12-
10-5-93 (1)

UCRL-ID-114972

SERS Internship Fall 1992 - Spring 1993
Abstract and Research Papers

Barry Goldman
Technical Coordinator

August 5, 1993

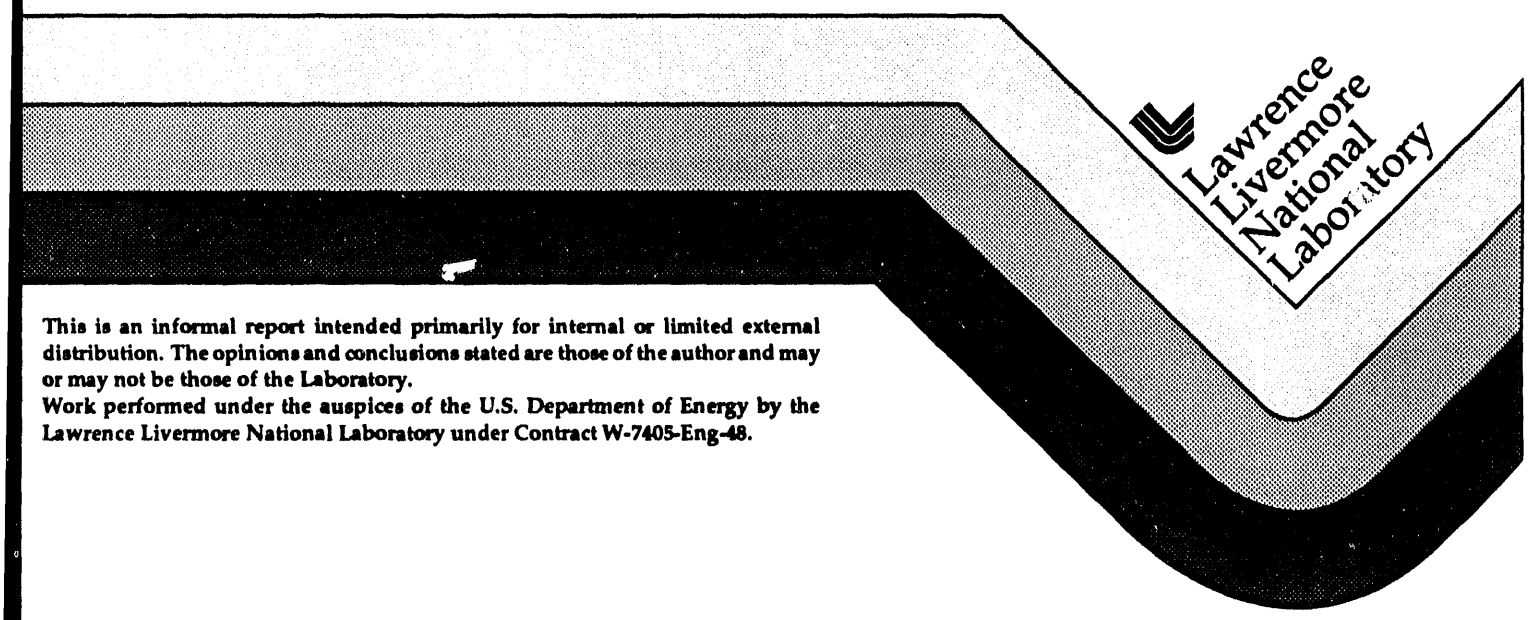

This is an informal report intended primarily for internal or limited external distribution. The opinions and conclusions stated are those of the author and may or may not be those of the Laboratory.
Work performed under the auspices of the U.S. Department of Energy by the Lawrence Livermore National Laboratory under Contract W-7405-Eng-48.

DISCLAIMER OF THIS DOCUMENT

DISCLAIMER

This document was prepared as an account of work sponsored by an agency of the United States Government. Neither the United States Government nor the University of California nor any of their employees, makes any warranty, express or implied, or assumes any legal liability or responsibility for the accuracy, completeness, or usefulness of any information, apparatus, product, or process disclosed, or represents that its use would not infringe privately owned rights. Reference herein to any specific commercial products, process, or service by trade name, trademark, manufacturer, or otherwise, does not necessarily constitute or imply its endorsement, recommendation, or favoring by the United States Government or the University of California. The views and opinions of authors expressed herein do not necessarily state or reflect those of the United States Government or the University of California, and shall not be used for advertising or product endorsement purposes.

This report has been reproduced
directly from the best available copy.

Available to DOE and DOE contractors from the
Office of Scientific and Technical Information
P.O. Box 62, Oak Ridge, TN 37831
Prices available from (615) 576-8401, FTS 626-8401

Available to the public from the
National Technical Information Service
U.S. Department of Commerce
5285 Port Royal Rd.,
Springfield, VA 22161

LLNL/SERS Fall'92 Students

Name	Program	Mentor	Phone
Benita Dair	Lasers	Jim De Yoreo	3-8945
Randall Hickman	NCD/NTS	Greg Nimz	3-2766
Dorrine McKinney	NTOD/NTS	Bob Knipes	702-295-6768 (NTS)
Rebecca Prince	BioMed	Rod Balhorn	3-4563
Mary Gable	BioMed	Harvey Mohrenweiser	3-1934
John Muller	Comp.	John Feo	3-0325
Vilmarie Lao	Comp.	John Feo	3-0325
Jeffrey Haslam	C&MS	B. Watkins	3-5543
Timothy Onasch	C&MS	Lucy Hair	2-8104
Justin Crockett	AIS	Tim Sharick	2-7983
Michael Stolze	Engr.	Steve Swierkowski	3-9374
Gerald Blycker	EPD	Michael Meltzer	3-5856

LLNL/SERS Spring'93 Students

Name	Program	Mentor	Phone
Bayliss, Jessica	Engr/EE	Shin-Yee Lu	2-6882,
Brown, Analisa	Bio-Med	Harvey Mohrenweiser	3-0534
Callaway, Duncan	Lasers	Ray Smith	2-7802
Friz, Alex	Physics	Jay Davis	3-1414
Krasovec, Mary	Physics-IGPP	Charles Alcock	3-0666
Lehr, Dana	Lasers	Dave Ress	3-8195
Mack, Larry	NCD	Bob Silva	3-1977
Montoya, Dustin	EPD	Michael Meltzer	4-6923
Palusinski, Iwona	Lasers	Scott Burkhart	3-2061
Persad, Ria	Env. Sci.	Ken Bogen	2-0902
Tang, Chris	Bio-Med	Andy Wyrobek	2-6296
Veir, Jennifer	Earth Sci	Robert Taylor	2-5652
West, Jonathan	Engr/ME	Dale Schauer	3-0303
Wildes, Gregg	C&MS	Lucy Hair	3-7823

MASTER

SCIENCE & ENGINEERING

SERS

RESEARCH SEMESTER

LAWRENCE LIVERMORE NATIONAL LABORATORY

FALL 1992

ABSTRACTS

FOR

STUDENT SYMPOSIUM

SPONSORED BY:

THE U.S. Department of Energy

Office of Energy Research

SERS FALL 1992 Symposium Abstract

Table of Contents

NAME	PAGE
Gerald M. Blycker	1
Justin M. Crockettt	1
Benita Dair	2
Mary Gable	3
Jeffery J. Haslam	4
Randy J. Hickman	4
Vilmarie Lao'	5
Dorrine McKinney	5
John S. Muller	6
Sean Mattingly	6
Tim Onasch	7
Rebecca M. Prince	8
Michael A. Stolze	8

Alternative Cleaners for Hazardous Solvents

Gerald M. Blycker
Dickinson College
Environmental Protection Department

ABSTRACT

We determined which alternative cleaners are suitable to replace hazardous solvents. The alternative cleaners consisted of citrus and pine based terpenes and aqueous detergents. These cleaners are safer on humans and the environment than traditional hazardous solvents such as alcohol's, CFCs and chlorinated solvents. The performance of the cleaners was evaluated by cleaning cutting oil from glass slides and aluminum and cleaning flux from printed circuit boards. We obtained quantitative measurements of cleaning by three methods. Particles on glass were counted with an image analyzer. An infra-red method was used to detect contamination on aluminum. Ionic contamination on the circuit boards was measured using an ionograph. We found several cleaners to clean as well as or better than traditional hazardous solvents.

Electronic Authentication Systems

Justin Crockett
Tennessee Technological University
Advanced Technology Center

ABSTRACT

The emerging information systems at Lawrence Livermore National Laboratory (LLNL) are network based, using client/server designs, and employing large numbers of clients and servers. New technologies such as electronic forms, are also available that enable end users to automate their business processes without the need for programming. Lack of two key elements are retarding progress: a secure authentication mechanism for initial identification of the user to the "network" of information services, and a digital signature capability which would enable transactions requiring authorization to be paperless. To address these two problems, electronic authentication and surrounding issues were explored, including encryption algorithms, digital signatures, privacy enhanced mail, and electronic forms. The Kerberos authentication system, the digital signature technology developed by RSA Data Security, Inc., as well as other technologies were evaluated for possible use at LLNL, Legal, societal, and security issues pertaining to LLNL were also taken into account. Finally, a set of recommendations was made.

KDP Growth Dynamics

Benita Dair
Cornell University
Lasers Division

ABSTRACT

Potassium dihydrogen phosphate (KH_2PO_4, or KDP) is a crystalline material used as a frequency converter in the Nova Laser, a high-power Nd:glass laser system employed in Inertial Confinement Fusion (ICF) research. KDP cyrstals convert the infrared laser beams into green and ultraviolet light, which are more effective in ICF and for physics applications. Presently, a crystal large enough for the Nova laser takes about 9 to 12 months to grow. Increasing the growth rate induces strain in the crystal, which degrades its optical quality. In order to grow a high quality crystal (with a strain density of $<10^{-5}$), we are observing the growth dynamics of KDP to learn how and why strain originates. In addition, the study of KDP growth dynamics will provide insight into how impurities are incorporated into the crystal structure, and more fundamentally, how impurities are incorporated into the crystal structure, and more fundamentally, how crystals using the atomic Force Microscope (AFM), a force-based microscope with a resolution of $<10^{-9}$m. We have found growth islands and hillocks on the surfaces, and further studies into their characteristics are being conducted.

Identification and Organization of Genes on Human Chromosome 19

Mary Gable
University of California, Davis
Biology and Biotechnology Research Program

ABSTRACT

A major goal of the Human Genome Project is to identify and determine the organization of the -100,000 genes distributed across the 24 human chromosomes. Cosmid contigs associated with -80% of chromosome 19 have been ordered, and -200 of the expected 2000 genes have been assigned. Chromosome 19 has a unusually large number of gene families, multiple copies of a gene that have apparently arisen as a series of tandem duplications. One family, the RFX genes regulate class II HLA expression; mutations at these loci cause combined immunodefieiency disease (SCID). RFX2 and RFX3 are linked on an -8kb contig located on p13.2 to p13.3, while RFX resides at p13.1 in an -56kb contig. In a parallel effort, an anonymous cDNA fragment (l.1kb) from fetal brain is being characterized. This gene is expressed as a 3-4kb mRNA found in high levels in the heart, brain, placenta, lung, liver, and skeletal muscle. Using the 1.2 kb to be scattered throughout an -175kb contig localized to 19p12. This organization suggests either a very large gene or a family of genes. Several of these cosmids contain zinc finger (regulatory) elements. Future efforts will focus on obtaining a full length cDNA and determining the function and organization of this gene.

Boron Carbide-Aluminum Cermet Processing

Jeffery J. Haslam
University of Kansas
Chemistry and Materials Science

ABSTRACT

Discussion of challenges encountered in the preparation of boron carbide powder and the slip casting procedures used to form boron carbide compacts. Data is given relating the volume percentage of boron carbide in the slip with the solids density in the boron carbide compacts formed from the slip casting process. A description is given of the aluminum infiltration process and some possible effects of various alloying constituents upon the infiltration. Discussion of challenges for large-scale production and potential solutions for producing boron carbide-aluminum cermet parts.

Chlorine-36 Distribution in the Unsaturated Zone

Randy Hickman
Virginia Tech
Nuclear Chemistry Division

ABSTRACT

Chlorine-36 has been used in many studies as a vadose zone ground water tracer. Nuclear weapons tests conducted from 1953 to 1962 in the Pacific Ocean produced a bomb pulse of ^{36}Cl which subsequently fell back to Earth and infiltrated the soil. The geological insignificance of 30 years since fallout led most hydrologists to believe that the bomb pulse should be concentrated at a single depth. This study instead demonstrates that multiple bomb pulses exist at various depths in a single soil column. Certain soil minerals have a great capacity to absorb free ions from the soil water. We are correlating bomb ^{36}Cl with mineralogy present at the depths of the pulses. Desert soil samples were taken from the Nevada Test Site. These are being analyzed for ^{36}Cl by Ion Chromatography (IC) and Accelerated Mass Spectrometry (AMS) and for soil mineralogy by X-ray diffraction (XRD).

Implementing Neural networks in a functional language

Vilmarie Lao
Metropolitan University, Puerto Rico
Computer and Mathematics Research Division

ABSTRACT

We developed a parallel code to execute a multilayer feed forward neural network in a functional language called Sisal. Functional languages support implicit parallelism and high performance. We studied the parallel properties of neural networks and their performance on different parallel machine architecture's. The network uses the back error propagation algorithm as a learning rule. Properties of the input and output were predefined based on the operations that we wanted the network to perform. Our code is short, easy to read, and portable. We present performance numbers for a scalar multiprocessor and a vector supercomputer.

SMES: Special Measurement and Emplacement System

Dorrine McKinney
Peru State College
NTOD Division

ABSTRACT

SMES is designed to lower cables safely into the ground during downhole operations. Presently, on and off switches manually lower cables and potenionmeters control the speed. SMES is being automated by interfacing a Robershaw controller to the existing SMES. The automated SMES will improve safety, fielding proficiency, and operational control.

Inertial Fusion Reactor Design Using the CTA Solving the Ejecta Problem

Sean Mattingly
Andrews University
Lasers Division

ABSTRACT

Concern has been expressed about the conceptual design of fusion reactors using a Compact Torus Accelerator (CTA). A CTA accelerates a plasma torus lineraly toward a fusion target. When the torus nears the target, it is compressed and focused down to a small volume, creating a very high energy density. The torus then impacts the target, initiating a fusion explosion. The focusing cone is destroyed with each shot due to the stress from the torus passing through it as well as from the force of the explosion.

The problem with this design is that when the focusing cone is shattered, the resulting small pieces (ejecta) are blown by the explosion and may enter the CTA itself causing damage and shortening the life of the CTA. The proposed solution for this possible problem is to bend the focusing cone so that the ejecta no longer have a clear path to the CTA. Calculations show that the plasma torus may be sent through a focusing cone bent with a radius of curvature on the order of a few meters without significantly disturbing the plasma.

Implementation of the Schwarz Alternating Method Using a Functional Language

John S. Muller
University at Stony Brook
State University of New York
Computing Research Group

ABSTRACT

Using SISAL, a portable functional language, we implemented Schwarz Alternating Method (SAM) on multi-processor architecture's. SAM is a numerical technique used for solving elliptic partial differential equations with boundary conditions, while SISAL is a portable functional language with syntax similar to other high level languages such as Pascal or Ada. In SISAL it is easy to parallelize algorithms for different multi-processor architecture's. As a result, it is the ideal language for those with little or no knowledge of parallel computing. We use SISAL to exploit SAM's natural parallelism, but also demonstrate how it takes advantage of parallelism no matter what architecture is used and can be employed with minimal effort by the programmer. We show performance results on a variety of architecture's.

Adsorption Characteristics of Nitric Oxide on Copper Catalysts

Tim Onasch
Carleton College
Physical Chemistry

ABSTRACT

Previous experiments have shown that copper reduces nitric oxide (NO) gas to N_2 and O_2, indicating the potential use of copper as a catalyst to control exhaust emissions from cars. We will be carrying out infrared studies of the vibrational frequencies of NO adsorbed onto copper ions matrixed in zeolite and aerogel supports. To augment these studies, we used the Columbus system of computer codes to investigate a simple NO-copper model in the restricted Hartree-Fock (H-F) approximation. This is a preliminary theoretical study of NO interacting with copper ion on a catalytic surface. We compared the total H-F energies of the model at the equilibrium bond distances in the

a) linear Cu^{+1}-N=O b) linear Cu^{+1}-O=N and c) bent Cu^{+1}-N(=O)

conformations, to determine the preferred geometry of adsorption. Preliminary results indicate that the linear Cu^{+1}-ON system is lowest in energy. We characterized the NO-copper interation by examining the electron densities, the total potential energy curves, and the vibrational frequencies of the free and adsorbed NO molecule. Similar studies have also been done on NO adsorbed onto copper oxide, an overall neutral system.

Sperm Cells as Vectors in the Production of Transgenic Animals

Rebecca M. Prince
California State University at Hayward
Biology and Biotechnology Research Program

ABSTRACT

Transgenic animals are used in industry and in biomedical research in order to provide *in vivo* experimental model systems. Sperm cells have been reported used as vectors in the production of transgenic animals before, however no approach has of yet proven to be successful. Fertilizing eggs with genetically modified sperm would be advantageous in that sperm are readily accessible and stable, and eggs can be fertilized by modified sperm cells *in vivo*. Recent elucidations regarding the unique manner of DNA packaging in sperm chromatin by protamines has provided us with the insight of developing a method of introducing foreign DNA into sperm which is likely to succeed where others have failed.

We have developed a method for mimicking the *in vivo* system of sperm chromatin toroid subunits *in vitro*, concentrating these toroids, and fluorescent visualization. Our present work concerns development of a method to successfully deliver DNA across the cell membranes and into the nucleus.

Fabrication of Silicon Membranes Using Electrochemical Etching

Michael A. Stolze
Washington University in St. Louis
Engineering Research and Development

ABSTRACT

An electrochemical etch-stop has been evaluated as a technique for producing silicon membranes. To begin the process, n-type layers were formed on the back of p-type silicon wafers. The wafers were then etched in hot potassium hydroxide under reverse-biased voltage. The etching continued only until the p-type material had been etched through. At that point, current flow through the n-type material caused an oxide layer to form. This layer stopped the etching process.

While this technique is not new, it is not widely used at Lawrence Livermore. These membranes are flexible and can be used in very small mechanical devices, such as pumps and valves. This thickness of these membranes can be selected by controlling the thickness of the n-type layer.

SCIENCE & ENGINEERING

SERS

RESEARCH SEMESTER

Lawrence Livermore National Laboratory

Spring 1993

ABSTRACTS FOR STUDENT SYMPOSIUM

May 17, 1993

Sonsored by:

The U.S. Department of Energy
Office of Energy Research

SCIENCE & ENGINEERING
SERS
RESEARCH SEMESTER

Spring 1993 Student Symposium Abstract

Table of Contents

NAME	PAGE
Jessica D. Bayliss	1
Analisa Brown	1
Duncan S. Callaway	2
Alexander M. Friz	2
Mary L. Krasovec	3
Dana E. Lehr	3
Larry H. Mack, Jr.	4
Dustin W. Montoya	4
Iwona A. Palusinski	5
Ria N. Persad	5
Chris W. Tang	6
Jennifer K. Veir	7
Jonathan D. West	8
Gregg S. Wildes	9

The Use of Computer Vision and Force Control for Tight Tolerance Assembly

Jessica D. Bayliss
California State University, Fresno
Intelligent Mechatronics Laboratory Engineering Directorate

ABSTRACT

Computer vision and force control provide feedback for robot manipulation during the assembly of objects. Both techniques have weaknesses, but their complementary strengths enable them to work well together, achieving assembly with tight tolerances. For instance, camera resolution limits the accuracy of computer vision, but it can locate approximately where the part should be placed and is an excellent choice for coarse placement of the part. Force control senses the force induced by object contact and if used extensively could damage a delicate part, but when used for fine placement of an object, it compensates for the error in coarse placement. It is our goal to utilize the best features of force sensing and computer vision to reduce the error in placement of an object.

The results of placing a peg in a 0.15mm tolerance hole with different camera resolutions will be presented. We have chosen to use computer vision to move the peg as close to its correct placement point as possible and force control to make minor adjustments, achieving the correct positioning of the peg.

Physical Mapping and Localization of Genes on Chromosome 19

Analisa Brown
University of Wyoming
Biology and Biotechnology Research Program

ABSTRACT

The Human Genome Project is an attempt to find the sources of nearly 4000 human disorders caused by single genes, to understand how genes interact with one another, and to physically map the entire human genome. The goal of my project is to complete a map of chromosome 19 around the area of two DNA repair genes, ERCC1 and ERCC2 and a muscle specific creatine kinase (CKM) gene. There is strong evidence suggesting that these genes are in close proximity to each other on chromosome 19. Secondly, I am trying to locate unknown genes on chromosome 19. My project will help further the physical mapping of the entire chromosome. Once physical maps are completed for every chromosome and the genetic causes of diseases are identified, suffering from genetic disease will be vastly reduced.

First Wall Problem

Duncan S. Callaway
University of Rochester
Laser Division, Inertial Confinement Fusion Program

ABSTRACT

Materials which could act as a "first wall" in the target chamber of the National Ignition Facility (NIF) have been studied. Fusion reactions within NIF will produce very high intensity, high energy X-rays. Potential first wall materials have been chosen because of their ability to withstand this X-ray exposure. Six low average atomic number materials have been determined to be good first wall candidates-- beryllium, beryllium oxide, boron, boron carbide, boron nitride, and lithium oxide. The materials are of low atomic number because of their correspondingly small photon interaction cross-sections. They were also chosen for their thermophysical properties-- high melting and vaporization points, high specific heats, and high heats of fusion and vaporization-- and for their relatively low cost. The list of materials will be narrowed down to one with further contact with vendors to understand the cost of producing and machining these materials, with computer modeling of the problem, and with tests on the current ICF facility, Nova.

PIXE: Surface Contamination on Al

Alexander M. Friz
Ohio State University
Center for Accelerator Mass Spectrometry (CAMS)

ABSTRACT

Our group primarily uses 3 to 5 MeV proton beams to perform Particle Induced X-ray Emission(PIXE) for elemental analysis. PIXE can yield element concentrations down to parts per million. I am presently investigating the application of PIXE to surface contamination of aluminum as opposed to conventional methods such as chromatography for LLNL's Environmental Protection Department.

Dust Accretion onto White Dwarf Stars

Mary L. Krasovec
University of Nebraska at Lincoln
Physics IGPP

ABSTRACT

In this paper I outline a method for examining the possibility of micron sized dust particles reaching the atmospheres of white dwarf stars. Using a stellar dust cloud model similar to that observed in the solar system, I apply equations governing the Poynting-Robertson drag and the effects of the dwarf's magnetic field to the calculation of the scale of such accretion. I have found that the Poynting-Robertson drag is an effective method of transfer for the particles, moving large quantities of dust into a magnetosphere around the dwarf where the dust particles evaporate and the resulting molecules ionize. Preliminary calculations show that the dwarf's magnetic field will not prevent the dust ions in the magnetosphere from reaching the atmosphere of the star.

Moiré Deflectometry For High-Density Plasma Characterization

Dana E. Lehr
Bucknell University
Y-Division

ABSTRACT

We report the development of a soft-x-ray Moiré deflectometer at the Nova laser facility. Moiré deflectometry is a scheme for plasma density diagnosis which provides line-integrated measurements of the electron density gradient along a single dimension. A 15.5-nm yttrium x-ray laser beam is collimated and sent through a plasma subject, where the initially parallel rays of incident light are refracted in relation to the electron density gradient. We measure these deflections as fringe shifts in a Moiré interference pattern produced by two angularly-offset Ronchi rulings. In our experiments we have produced a high-contrast Moiré deflectogram of a laser-irradiated CH plasma in which the electron density exceeded 4×10^{21} cm^{-3}. This is well above the limits of any previous methods of plasma density characterization.

Diffusion of Analyte Molecules into the Silicone Cladding of Fiber Optic Sensors

Larry H. Mack, Jr.
University of Houston
Nuclear Chemistry Division

ABSTRACT

A fiber optic evanescent field absorption sensor has been developed for the remote detection of volatile organic compounds in aqueous solutions. Diffusion mechanisms of specific analyte molecules into the polydimethylsiloxane (PDMS) cladding of optical fiber is being investigated. It is important to determine the diffusion rate of certain compounds into the fiber polymer for long term sensor applications and multiple component systems. Changing different parameters, such as, concentration of analyte, temperature of the solution, and the physical properties of the analyte, provides information in determining the theory behind the diffusion of siloxane polymers. We are using near infrared(NIR) spectroscopy to examine the analyte/polymer interaction. In particular we are looking at hydrogen bonding and the rates of diffusion. Trichloroethylene (TCE), dichloroethylene (DCE), water and various phosphates were used to help understand the chemistry behind the polymer/analyte interaction in the PDMS cladding of the optical fiber.

Replacing Hazardous Solvents with Alternative Cleaners

Dustin W. Montoya
Metropolitan State College of Denver
Environmental Protection Department

ABSTRACT

Because traditional hazardous solvents like Freon TE, 1,1,1 Trichloroethane, Isopropyl Alcohol, and Acetone are being "phased out" by environmental regulations, non-hazardous, environmentally benign alternatives must be developed, tested, and implemented. The goal of the Alternative Cleaning Testing Program is to identify non-hazardous, environmentally safe cleaning agents for use at the Laboratory in order to enhance worker safety, reduce solvent costs, and limit the Laboratory's contribution to stratospheric ozone depletion. Tests are currently being conducted using over forty different cleaning agents to clean three different materials: glass, aluminum, and printed board assemblies. Quantitative data is being collected using Optical Image Analysis, Fourier Transform Infrared Spectroscopy, or Ionography, depending on the material cleaned.

Beamlet Front-End Harmonic Conversion Experiment

Iwona A. Palusinski
University of Arizona
Laser Division

ABSTRACT

With the Beamlet Front-End down-collimated to produce 4GW/cm^2, this experiment will determine the reduction in harmonic generation as bandwidth increases on the fundamental beam to suppress transverse stimulated Brillouin scattering (SBS). We will show, that for applied bandwidths sufficient to suppress SBS in the Beamlet output optics, the conversion efficiency to the third harmonic will remain around 70% thus allowing the Beamlet milestone of 5kJ of energy in a 3ns pulse at 351nm to be attained.

Correlation of Mutagenic and Carcinogenic Chemical Potencies

Ria N. Persad
Princeton University
Environmental Sciences Division

ABSTRACT

Correlations between mutagenic and carcinogenic potency based on "in vitro" test results enable us to perform preliminary, upper-bound assessments of potential carcinogenic risk of complex mistures or unidentified compounds such as mixed-waste samples from hazardous waste sites. This project analyzes dose-response relationships of mutagenicity data for over 200 carcinogens using a polynomial regression-correlation model and calculates the Pearson correlation coefficient between carcinogenic and mutagenic potency for these compounds.

Hierarchical Chromosome Organization of Human Sperm Detected by Fluorescence In Situ Hybridization

Chris W. Tang*, Art Kobayash, and Andy Wyrobek
***University of California, Los Angeles**
Biodosimetry Group, Biology and Biotechnology Research Program

ABSTRACT

The organization and packaging of DNA into human sperm nuclei remains essentially unknown. Fluorescence in situ hybridization was used to visualize segments of 2 to 10 megabases of highly repetitive DNA in sperm. Two DNA probes were used for these experiments: pY3.4 which was specific for ~ 10 Mb of sequence on chromosome Y and CEP8 which was specific for ~ 2 Mb of repeat sequence on chromosome 8. Sperm nuclei were decondensed to provide various state of chromatin decondensation. The morphology and substructure of the fluorescent domains for these probes was visualize by fluorescence and confocal microscopies. We observed that the overall length of repetitive DNA segment and degree of chromatin decondensation determined the size and number of fluorescent domains. Four classes of fluorescence domains were noted, which were named A, B, C and D. A hierarchical model of chromatin organization is proposed in which chromatin domain A contains two B domains, domain B contains two C domains, and domain C contains two D domains. The preliminary estimate of the amount of DNA contained in each domain is 8. 4. 2. and 1 Mb respectively. [Work performed under the auspices of the U.S. DOE by the Lawrence Livermore National Laboratory under contract W-7405-ENG-48.]

Characterization of PHB Production in a TCE-Degrading Methanotroph

Jennifer K. Veir
Ohio University
Division of Earth Sciences

ABSTRACT

A quantitative gas chromatographic assay was developed for poly-ß-hydroxybutyrate (PHB), an energy storage polymer, and poly-ß-hydroxyvalerate (PHV) in microbial biomass. Samples were acetone dried and subjected to a hydrochloric acid propanolysis. Total elapsed time between sampling growing cultures and final PHB quantification was successfully reduced to 4 hours. As little as 0.005 mg PHB can be accurately detected by this methodology. Bioreactor grown *Methylosinus trichosporium* OB3b cells examined under nitrate growth conditions ranging from 18.4 mM down to 0.03 mM and optical densities (A_{660}) of 0.78 to 18.75 were found to produce a maximum of 4.2% (w/w) PHB under nitrate depletion and an A_{660} of 9.9. At an A_{660} of 0.188 and sufficient nitrate PHB was at 3.4%. Shake-flask cells at A_{660}s of less than 1.0 showed 1.1-2.1% PHB production at nitrate deficiency and 4.0% PHB with sufficient nitrate. Shake flask cells of higher optical densities are being examined currently. No PHV was detected in either culture. Significantly, the peak PHB level corresponds with the previously observed optimal whole-cell TCE-degrading longevity.

Site 300 Contained Firing Facilities

Jonathan D. West
Texas A&M University
Defense Technology Engineering Division

ABSTRACT

The Site 300 Contained Firing Facilities are being developed to minimize hazardous emissions to the environment and reduce quantities of hazardous waste while still allowing design engineers to conduct tests on the high explosives component of a nuclear weapon. Currently, the design of the firing chamber in these facilities is being reviewed and a quarter-scale model will be tested to examine the strength and durability of the chamber. My SERS project is to provide engineering analysis support for this quarter-scale testing. This will involve using the non-linear finite element code Nike3D to simulate the blast loading and model the resultant forces and strains created in the firing chamber. I used INGRID to develop the three dimensional grid of the firing chamber and create the input deck for Nike3d. The grid currently models the initial drawings for the quarter-scale model and may be modified to analyze possible design changes. I am approximating the pressure loading conditions using the peak pressure, pressure impulse, impulse duration and arrival times corresponding to the appropriate scaled distance (z-factor). In my closing weeks, I plan to finish defining various loading scenarios, refine the INGRID mesh and verify its accuracy, and examine possible improvements in the firing chamber design.

Aerogel Surface Modification and Alternative Processing Techniques

Gregg S. Wildes
University of Michigan
Chemical Sciences Division

ABSTRACT

We investigated non-supercritical processing methods as alternatives to current aerogel drying methods involving supercritical solvent extraction. The objectives of the experiments were to both reduce the large capillary stresses during aerogel drying and to increase the initial strength of the gel. By strengthening the initial material and reducing the stresses during processing, our goal is to avoid the expensive and time consuming use of supercritical drying in aerogel production. We chose eight solvent systems of varying surface tensions to examine their evaporative effects during drying under controlled conditions. Resorcinol formaldehyde gels were dried in a vapor environment, and then directly exposed to air. A direct correlation was established between the amount of induced gel shrinkage and the surface tension and boiling point of each solvent. We also examined the effects of five post-treatments chosen to induce additional, post-synthesis condensation reactions. We hypothesize that a higher concentration of active surface groups at the aerogel's neck regions causes localized, preferential syneresis that strengthens the material's string-of-pearls structure. Post-synthesis processes included the addition of excess monomer, heat and acid treatments.

Lawrence Livermore National Laboratory Science and Engineering Research Semester (SERS) students are participants in a national program sponsored by the Department of Energy/Office of Energy Research. The SERS program provides students the opportunity to participate in research at one of seven Department of Energy facilities during the academic year. Argonne National Laboratory in Illinois, Brookhaven National Laboratory in New York, Lawrence Berkeley National Laboratory in California, Lawrence Livermore National Laboratory in California, Los Alamos National Laboratory in New Mexico, and Pacific Northwest Laboratory in Washington place students in research appointments in this program. The Department of Energy initiated the SERS program to encourage undergraduates to pursue advanced degrees and careers in science or engineering.

The Use of Computer Vision and Force Sensing for Tight Tolerance Assembly

Jessica D. Bayliss

California State University, Fresno

Lawrence Livermore National Laboratory
Livermore, California 94550

May 19, 1993

Prepared in partial fulfillment of the requirements of the Science and Engineering Research Semester under the direction of Shin-yee Lu, Research Mentor, at the Lawrence Livermore National Laboratory.

* This research was supported in part by an appointment to the U.S. Department of Energy Science and Engineering Research Semester (hereinafter called SERS) program administered by LLNL under Contract W-7405-Eng-48 with Lawrence Livermore National Laboratory.

By acceptance of this article, the publisher or recipient acknowledges the U.S. Goverment's right to retain a non-exclusive, royalty-free license in and to any copyright covering this article.

ABSTRACT

Computer vision and force control provide feedback for robot manipulation during the assembly of objects. Both techniques have weaknesses, but their complementary strengths enable them to work well together, achieving assembly with tight tolerances. For instance, camera resolution limits the accuracy of computer vision, but it can locate approximately where the part should be placed and is an excellent choice for coarse placement of the part. Force control senses the force induced by object contact and if used extensively could damage a delicate part, but when used for fine placement of an object, it compensates for the error in coarse placement. It is our goal to utilize the best features of force sensing and computer vision to reduce the error in placement of an object.

The results of placing a peg in a 0.15mm tolerance hole with different camera resolutions will be presented. We have chosen to use computer vision to move the peg as close to its correct placement point as possible and force control to make minor adjustments, achieving the correct positioning of the peg.

Background

The peg-in-the-hole experiment demonstrates different methods for tight tolerance assembly. Each method solves a particular problem with tight tolerance assembly. For instance, Remote Center Compliance (RCC), or passive force sensing, uses a set of springs above a robot's gripper for tolerance to assembly error caused by slight angular or lateral misplacement of the peg as discussed in [8]. Active force sensing tries to solve the same problems while providing feedback information to perform more complex tasks in assembly as in [7]. In order to give active force sensing the same kind of error tolerance as RCC, a compliance/damping matrix has been proposed to provide the same kind of error tolerance in [6]. While these methods provide invaluable aid in inserting the peg once it is very close to the hole, they fail to offer any help in getting the peg close to the hole except to imply that a tight tolerance in robot performance and repeatability in placing the hole in the same location is necessary.

As an alternative to force sensing, computer vision could be used to place the peg in the hole. Here there are also problems, as computer vision is only as accurate as the image resolution being used. While a tight tolerance on robot accuracy can be exchanged for image accuracy in this case, the system will only work in a small amount of situations. For example, given the categories of possible errors that can be made in peg placement as shown in Figure 1, computer vision can only solve A, B, and C and then only if the angle of the peg can be determined correctly.

The main goal of this project is to develop a system for tight tolerance assembly that solves all the errors in Figure 1 without specifying ultra-tight tolerances on the equipment involved in placing and inserting the peg. The complementary use of force sensing and computer vision satisfy this goal. Computer vision can be used as the "eyes" of the robot for coarse placement of the peg and force control for fine placement and insertion of the peg. This way, the strengths of both methods can be used to provide a fault tolerant assembly system.

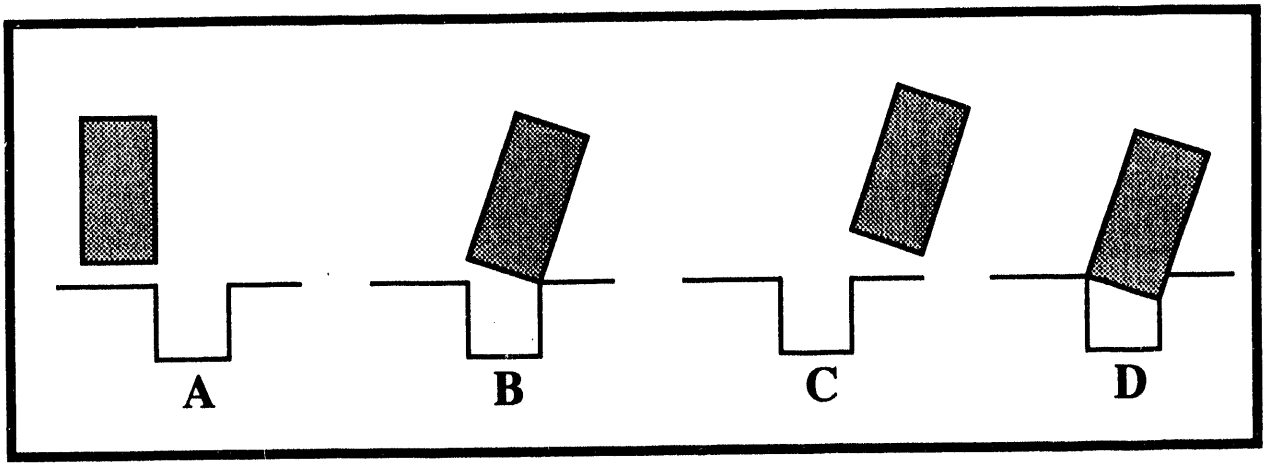

Figure 1 - A) The peg misaligned laterally with the hole, B) The peg angularly misaligned with the hole, C) The peg misaligned angularly and laterally with the hole, and D) The peg jammed in the hole because of angular misalignment.

General Approach

In our experiment, a Zebra Zeroforce robotic arm, shown in Figure 2, is utilized for placement and insertion of an aluminum peg into a 0.15mm tolerance hole in an aluminum box. Two cameras are set up to monitor the x and y directions of robot movement as shown in Figure 3. The z axis is assumed to be a constant for the sake of simplicity and the x and y cameras are calibrated individually to make sure the peg will be in the camera's field of view when the robot moves it from its resting position. Before the robot moves, an image is taken and the box hole located. The peg is then brought to where the robot thinks the hole should be. To compensate for gear slippage and robot inaccuracy, a vision feedback loop makes sure the centroid of the peg is within two pixels of the centroid of the hole. Once the peg is over the hole, force control (both active and compliant force sensing) is used to insert the peg. As an added benefit, if the robot somehow manages to miss the hole, the peg is brought back up and computer vision again attempts to correctly place the peg over the hole.

Computer Vision

The computer vision system consists of two Sony XC-999 cameras with 6mm lenses connected to Data Translation's DT2867 frame grabber board located in an expansion slot on a 486 pc. Image resolution is 640 X 480 pixels. The only component of the computer vision system that is not off-the-shelf is the vision processing software. The program used was an in-house program called Vision that is run in a Lisp environment from a Sparcstation-2 over a network. This was done for convenience as the necessary image processing techniques were already in existence in Vision.

Figure 2 - Zebra Zeroforce Robotic Arm Inserting the Peg in the box hole.

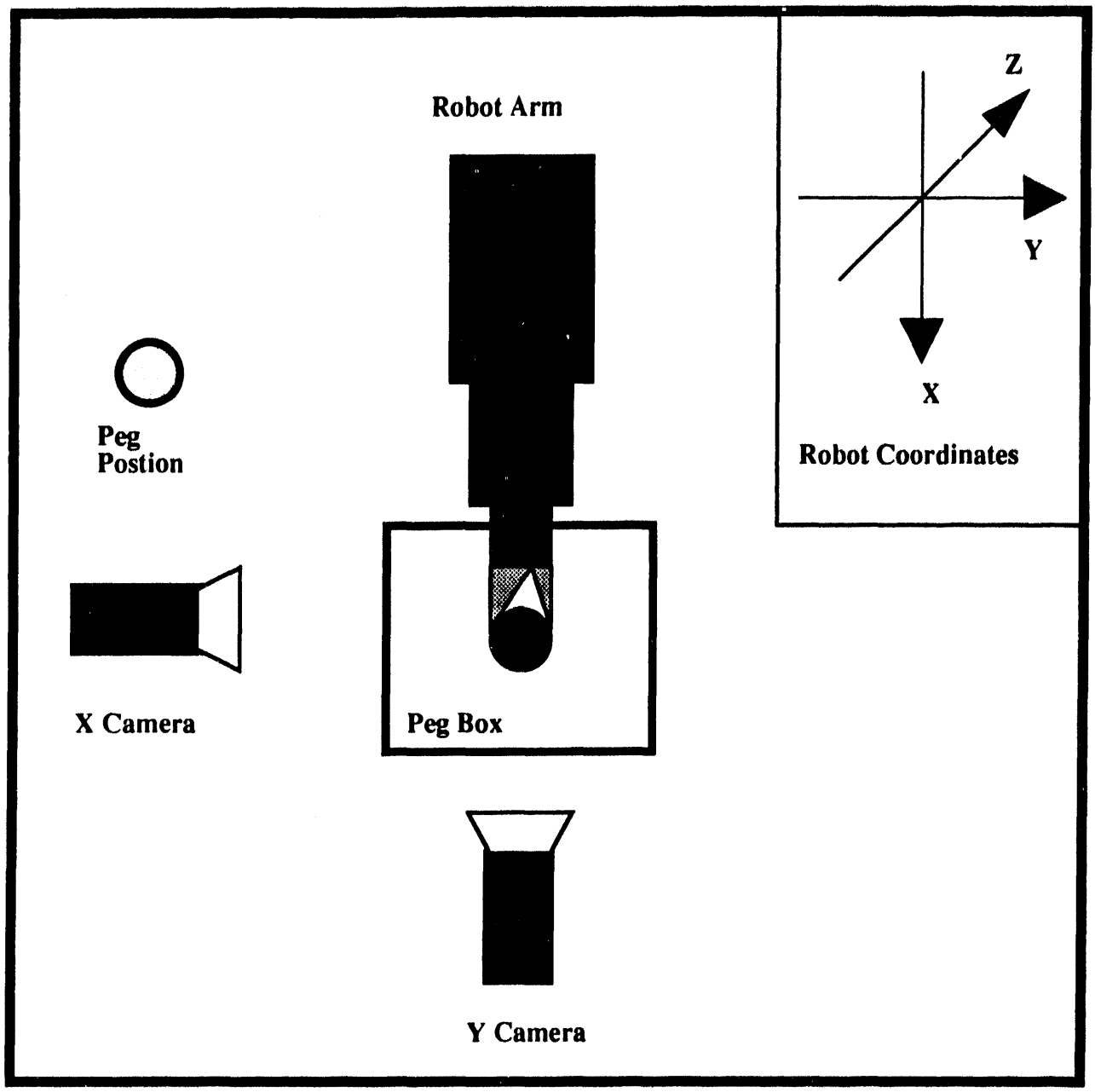

Figure 3 - Experimental Setup

Camera Calibration

The computer vision feedback loop makes camera calibration almost unnecessary. However, camera calibration was found to improve the first time performance of placing the peg. Thus, both the x and y camera were calibrated independently with three calibration points. The location of a light source held in the robot's gripper was found in camera coordinates as well as robot coordinates. As we were concerned with a relatively small work area (the area of the 19.5 mm hole), the transformation from camera to robot coordinates was assumed to be linear and follow the equation of a line ($y = mx + b$) where y was an x or y robot coordinate, m was the change in robot over the change in camera coordinates, x was the camera coordinate, and b was the constant offset gotten from looking at a particular point. Each camera was only responsible for one robot coordinate and the z axis was assumed to be constant. We realize that there are more complex calibration techniques and camera setups as described in [2] and [5], but they did not seem necessary and would have reduced the flexibility of the system.

Image Processing

A 640x480 pixel image is taken of the box with the hole before the robot moves. Region-based methods, where the image is thresheld at a set value and segmented with an 8 neighbor pixel growing algorithm are used to find the regions of interest in the image. The hole is then located by filtering out non-circular regions that are outside of a 10 to 250 pixel region size and the centroid of the hole region is found. For a more in-depth description of region-based algorithms see [2] and [3]. This process is repeated for both the x and y cameras. The robot was then given the calculated x and y coordinates from the x and y cameras (respectively) and told to move the peg to that location.

Experimental testing showed that the hole algorithm was sturdy and could be used in a room with florescent lights and open windows with the cameras being from 90-450mm (0.19mm/pixel

to 0.83mm/pixel) away from the hole. Changes in light are currently compensated for by changing the static threshold value of a camera, but in the future we hope to automate this process.

After locating the hole, the robot places the peg 1mm over where the computer vision system claims the hole is in the x and y directions. A peg-finding algorithm uses a similar region-based method to the hole-finding algorithm except in the peg algorithm the background noise is first screened out by subtracting the image of the hole from the image of the peg. The centroid of the peg is found and compared with the location of the centroid of the hole. The peg image and processing steps for the Y camera are shown in Figure 4. Region-based processing was used to locate the peg.

The peg algorithm is more sensitive to light than the hole algorithm and had a tendency to break down when the camera was greater than 450mm away from the hole due to the wider field of view of the cameras. Surprisingly enough, even when the whole peg was not located due to shadows and reflections off of its aluminum surface, the centroid of the peg corresponded fairly close to that of the true centroid of the peg.

Computer vision feedback is used in case the robot's gears slip and it places the peg erroneously and because of slight errors in the transformation of camera to robot coordinates. An attempt to insert the peg is made when the centroid of the peg and the centroid of the hole are aligned within two pixels of each other. Two pixels was chosen because the image pixels could be off one pixel in any direction when taking the same picture and because a one pixel tolerance substantially raised the time for placement of the peg without any noticeable improvements in performance. Even with the two pixel tolerance, it took an average of four times to place the peg correctly over the hole.

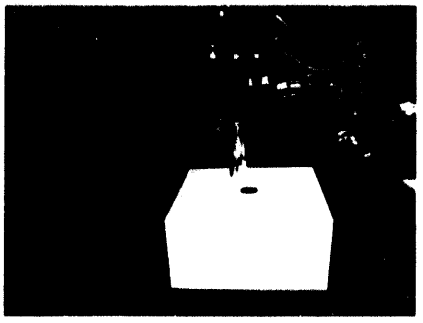

A

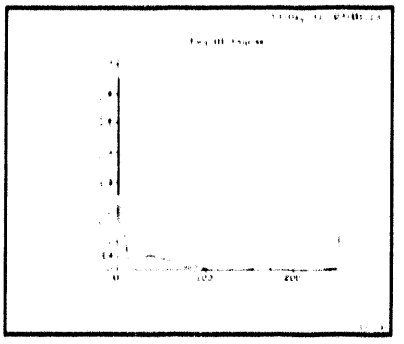

B

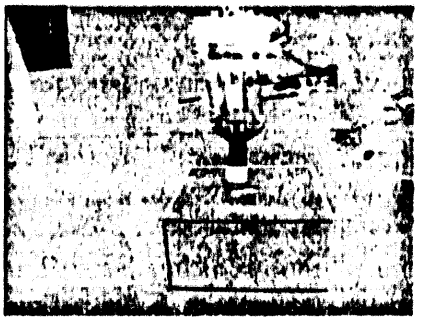

C

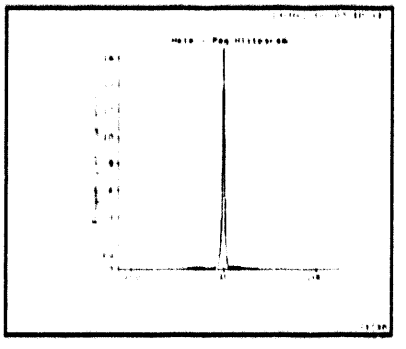

D

E

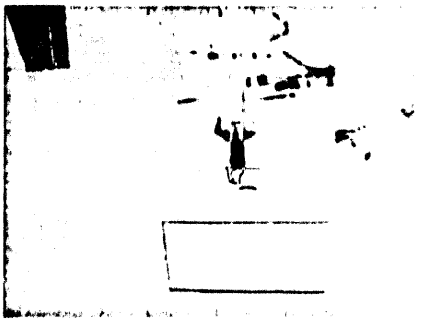

F

Figure 4 - A) The original peg image from the Y camera, B) The histogram of image intensities for A, C) The difference of the peg and box images, D) The histogram of image intensities for B, E) The segmented regions for C, and F) The peg has been found.

Force Control

The Zebra Zeroforce robot force sensor is mounted between the wrist and end-effector of the robotic arm and measures forces and moments in the x, y, and z directions. To add a measure of compliant force sensing to the robot in the x and y directions, a rubber band was foam-taped to the inner part of the robot's grippers. Thus, both active and passive (compliant) force sensing were used to insert the peg into the hole.

The active force sensing was programmed in software on the 486 pc to be compliant in the x and y positions while remaining stiff in the z direction. This method of active force sensing with the compliant force sensing gives the error tolerance of Remote Centre Compliance without losing the sensory feedback that enables the robot arm to perform more complicated tasks. As a last measure protection against the peg jamming into the hole, a one degree wobble was added near the beginning of the insertion. In this way the error of Figure 1d was solved. Experimentally, the peg was inserted into the hole thirty-eight times with the cameras from 90-450mm away and the peg never failed to enter the hole although it jammed at 450mm when the true centroid of the peg was incorrect.

Discussion

The complementary use of computer vision and force sensing not only worked well in placing a peg into a tight tolerance hole, but provided for a fault tolerant and easily adaptable system. Surprisingly, this complementary usage has not been tried by many and when it is, usually computer vision dominates the experiment [1, 4]. Although the peg-finding routine was somewhat sensitive to lighting conditions, it is possible to automate finding the peg threshold and make the algorithm applicable to a broader range of conditions.

Another area of concern is that of time. In this experiment it was near impossible to measure

the time of an operation as the robot and frame grabber were located in a pc and the computer vision software was located on a Sun Sparcstation-2. The two were constantly communicating over a network which made timing the system very difficult. In the future, all software and hardware will be located on the same computer to enable real time processing of information.

Acknowledgments

This work is performed under the auspices of the U.S. Department of Energy and Engineering Research Semester (SERS) program administered by the Lawrence Livermore National Laboratory under Contract W-7405-Eng-48. The author would like to thank Shin-yee Lu, Robert Johnson, Jose Hernandez, and Eric Breitfeller for technical explanations and support..

References

1. R. L. Anderson, "Dynamic Sensing in a Ping-Pong Playing Robot", *IEEE Transactions on Robotics and Automation*.Vol. 5, No. 6, pp. 728-739, Dec. 1989.

2. D. H. Ballard and C. M. Brown, *Computer Vision*. Prentice-Hall, 1982.

3. P. J. Besl and R. c. Jain. "Range Image Segmentation", *Machine Vision: Algorithms, Architectures, and Systems*. Academic Press, pp. 221-257, 1988.

4. G. C. Burdea and H. J. Wolfson, "Solving Jigsaw Puzzles by a Robot", *IEEE Transactions on Robotics and Automation*.Vol. 5, No. 6, pp. 752-761, Dec. 1989.

5. B. Jahne, *Digital Image Processing: Concepts, Algorithms, and Scientific Applications*. New York: Springer-Verlag, pp. 23-39, 1991.

6. M. A. Peshkin, "Programmed Compliance for Error Corrective Assembly", *IEEE Transactions on Robotics and Automation*.Vol. 6, No. 4, pp. 473-482, Aug. 1990.

7. H. Van Brussel and J. Simons, "Automatic Assembly by Active Force Feedback Accommodation", *Robot Sensors (International Trends in Manufacturing Technologies): Vol. 2 Tactile and Non-Vision*, UK: IFSPublications, pp. 53-66, 1986.

8. D. E. Whitney and J. L. Nevins, "What is Remote Centre Compliance (RCC) and what Can It Do?", *Robot Sensors (International Trends in Manufacturing Technologies): Vol. 2 Tactile and Non-Vision*, UK: IFSPublications, pp. 3-15, 1986.

Physical Mapping and Localization of Genes on Chromosome 19

Analisa Brown

University of Wyoming

Lawrence Livermore National Laboratory
Livermore, California 94550

May 26, 1993

Prepared in partial fulfillment of the requirements of the Science and Engineering Research Semester under the direction of Harvey Mohrenweiser and Susan Hoffman, Research Mentors, at the Lawrence Livermore National Laboratory.

* This research was supported in part by an appointment to the U.S. Department of Energy Science and Engineering Research Semester (hereinafter called SERS) program administered by LLNL under Contract W-7405-Eng-48 with Lawrence Livermore National Laboratory.

ABSTRACT

The Human Genome Project is an attempt to find the sources of nearly 4000 human disorders caused by single genes, to understand how genes interact with one another, and to physically map the entire human genome. The goal of my project is to complete a map of chromosome 19 around the area of two DNA repair genes, ERCC1 and ERCC2, and a muscle specific creatine kinase (CKM) gene. There is strong evidence suggesting that these genes are in close proximity to each other on chromosome 19. Secondly, I am trying to locate unknown genes on chromosome 19. My project will help further the physical mapping of the entire chromosome. Once physical maps are completed for every chromosome and the genetic causes of diseases are identified, suffering from genetic disease will be vastly reduced.

INTRODUCTION

The Human Genome Project is a large collaborative effort that was started in 1990 and is expected to last for 15 years. The main goal of the Human Genome Project is to complete a physical and genetic map for all the human chromosomes.[4] The Lawrence Livermore National Laboratory's (LLNL) main focus is on chromosome 19. The first part of my project consists of trying to develop a more detailed map around a certain area on the long arm of the chromosome. Secondly, I am trying to localize new genes on the chromosome.

Gaps in the physical map of the chromosome are currently posing the biggest obstacles in completing the reconstruction. I am trying to physically map a certain area on the q13.2 region of the chromosome and fill up one of the many gaps. Located in this area of the chromosome are three genes, ERCC1, ERCC2, and CKM. ERCC1 and ERCC2 are excision repair cross-complementary genes that are responsible for repairing DNA.[5] People with defects in one of these two genes become more susceptible to cancer. Xeroderma pigmentosum is a disease caused by a defect in the ERCC2 gene. Patients with this disease are prone to skin cancer because they lack the ability to repair their DNA after damage caused by the sun's UV rays.[2] CKM is a muscle-specific creatine kinase gene that produces ATP by catalyzing the reverse transfer of a phosphate from phosphocreatine to adenosine diphosphate. This gene is especially important in tissues such as the brain and muscle that need large amounts of energy.[3]

One of the reasons we want clonal continuity is that it allows us to search for and identify important stretches of DNA. There are many ways to find a gene, but an ordered clone library is very advantageous. Approximately 4000 genes have been identified out of approximately 100,000 genes.[4] This is where the second part of my project comes in. I am trying to localize unknown genes onto the chromosome by using expressed sequence tagged (EST) DNA generated from cDNA libraries.[1] The cDNA is a sequence of DNA that is complementary to a mRNA that is used to synthesize proteins. Once the gene is identified, it becomes necessary to understand the organization and structure of the gene and then to find its location on the chromosome.

The Human Genome Project is expected to revolutionize biology and the way medicine will be practiced in the next century. Once all the human chromosomes are physically mapped and the structural organization and function of all the genes are identified, we will have a foundation for reducing the suffering caused by genetic diseases. In the future are the possibilities of gene and drug therapy, and the ultimate goal of replacing a defective gene with a functional one.[4]

MATERIALS AND METHODS

Cosmid Library

Since LLNL's part of the project involves chromosome 19, it was necessary to purify only chromosome 19 from all the other human chromosomes. Human somatic cells were fused with hamster cells to obtain a hybrid cell line with only chromosome 19. High speed flow sorting was used to purify the human chromosome from the human-hamster cell line. The chromosomes were dyed and passed through laser beams in single droplets. After the fluorescence signal was analyzed for each droplet, droplets containing chromosome 19 were electrically charged and deflected into a collection tube. The uncharged particles containing hamster chromosomes were discarded.

The DNA was cut into relatively small overlapping fragments by using restriction enzymes that cleave DNA at a specific site by recognizing a certain sequence. The DNA fragments were inserted into a cosmid vector and grown in E. coli bacterial cells. The cosmid vector accepts DNA inserts ranging from 25kb to 40kb in size. The bacteria then replicated, making many clones of the DNA fragments. Because the clones contained in the bacterial cells represent overlapping segments of DNA from chromosome 19, it is a library of overlapping clones.[4]

Fingerprinting

The DNA fragments were digested with EcoRI and Bgl II to obtain smaller fragments. The DNA fragments were tagged with fluorescent dyes and separated by size using gel electrophoresis. Laser beams were used to record the fluorscence signal from each fragment. The signals were processed to generate fingerprint waveforms that are displ[illegible]d as

a series of peaks by the computer. If any two clones contain overlapping segments of DNA, then a portion of the waveform fingerprint for each will be identical. Groups of two or more cloned fragments that represent overlapping regions of the chromosome are known as contigs.[4]

Contig Browser

The fingerprints were put into a computer algorithm and compared to one another to form contigs. This algorithm uses pattern recognition to estimate the statistical chances that two clones are from an overlapping piece of DNA. The program displays the contigs graphically and then links them by a relational database to all other information about the clones.[4]

Restriction Digest and Southern Blot for q13.2 Region

The transfer of DNA to the filter, as single stranded molecules allows for the detection of a specific DNA sequence within a complex mixture of DNA. The clones from the ERCC1, ERCC2, and CKM genes were digested with Hind III and then run on an electrophoretic polyacrylamide gel. The DNA was transferred from the gel to a nitrocellulose filter paper by using the Southern blot technique. The filter was then hybridized with ERCC1, ERCC2, CKM (600 bp fragment), and CKM (500 bp fragment) to demonstrate if the respective DNA sequence of interest was present. Restriction mapping was done by comparing the fragments to one another to find the overlapping clones. The cosmids were then lined up in the order that they occur on the chromosome.

Chromosome Walking

The purpose behind chromosome walking is to extend contigs and eventually fill up the gaps in the chromosome map (Fig. 1). The clone at the very end of the contig is made into a probe and used to screen the cosmid library arrayed on high density filters (Fig. 2). This process can be repeated until all the cosmids are found that fill up the gap.[4]

Random Probes

D19S15 and D19S16 DNAs were used as probes to screen the chromosome 19 cosmid libraries. There was evidence suggesting that these probes were in the area that I was investigating. This is just another way to try to fill in gaps in the physical map. If probes that are known to map into the area of interest are used to screen the cosmid libraries, there is the possibility of finding additional cosmids from that area.

Restriction Digests for ESTs

The five ESTs, G19P1, HHCH60Z, ATP4A, EST00708, and EST00875, were digested with EcoRI and run on an electrophoretic agarose gel. The DNA was transferred to a nitrocellulose filter by using the Southern blot technique. The filters were probed with their respective cDNAs and the fragments were compared to one another to complete a restriction map.

Fluorescence In Situ Hybridization

Fluorescence *in situ* hybridization (FISH) is a technique that localizes clones onto specific regions of the chromosome. A human sperm nucleus is fixed on a microscope slide and chemically treated to break open the nucleus and release all the chromosomes. The DNA is denatured so that the two strands of DNA separate. DNA from one of the cosmids is fluorescently tagged and added to the slide to act as a probe. When the probe finds the complimentary base sequence, it hybridizes to it. The fluorescent dots seen through the light microscope represent the location of the probe on the chromosome.[4]

Northern

Northern filters are bought commercially and are used to determine what tissue the gene is most actively expressed in. The filter contains RNA from different tissues including the liver, brain, kidney, heart, and lung. EST00708 and EST00875 were individually tagged with a radioactive label and hybridized to the Northern blot. Wherever there is a mRNA complementary to the probe on the blot, hybridization will occur, resulting in a radioactive band that can be detected by

autoradiography. Analyzing how strong the band is on the autoradiograph allows us to determine how actively the gene is transcribed in each tissue.[6]

RESULTS

Data from the restriction digest and the ERCC1, ERCC2, CKM (500bp), and CKM (600bp) hybridizations on the Southern blot were analyzed and a restriction map was completed (Fig. 3). The restriction map provided me with the information I needed to find the end cosmid on the ERCC1 gene. Hybridizations to the cosmid library with the end probe derived from cosmid 8697 provided me with list of cosmids. Additional cosmids were also found from the D19S15 and D19S16 probes that were used to screen the cosmid library.

For the second part of my project, a restriction map was completed for HH60Z, G19P1, ATP4A, EST00708, and EST00875 from the data derived from the restriction digests and the various hybridizations with the respective probes. The location of the five ESTs on chromosome 19 was determined by using the FISH mapping procedure (Fig 4). The Northern blots performed on EST00708 and EST00875 showed no hybridization whatsoever.

DISCUSSION

I have not yet completed the physical mapping of the area on the q13.2 region but I have obtained some results that may be promising. The cosmids I found from the chromosome walk may map into the area. I found two cosmids in one contig that my end probe actually hit. These cosmids, along with the ERCC1 cosmids, were run on another gel and a Southern blot was performed. The Southern was then probed with the 8697 T7 end probe to make sure that it indeed has some degree of overlap with these cosmids. There was a lot of background on the filter so it will be probed again.

Additional cosmids were found from the D19S15 and D19S16 DNA that were used to probe the cosmid library. I concluded that the cosmids found from the D19S16 probe were not in the area that I am trying to map. The cosmids that were found were located in other areas of the chromosome. The D19S15 probe may still be helpful in trying to

close the gap because it hit five cosmids in one contig. The cosmids will be run on a gel to determine which cosmid to use for FISH mapping. I will then know if the contig is in the area that I am trying to map.

The Northern blots performed on EST00708 and EST00875 were both unsuccessful. I may try to use a new technique to make a stronger probe and attempt to perform Northerns once again.

Restriction maps have helped order the clones for each EST and FISH mapping has enabled us to know the location of each EST on the chromosome. I have also found where the genes are located within the contigs. I plan on screening the cosmid libraries to find more clones that will take me a step further in finding where the genes are located on the chromosome. Once the genes are located, it will then be useful to understand the structural organization and function of the genes.

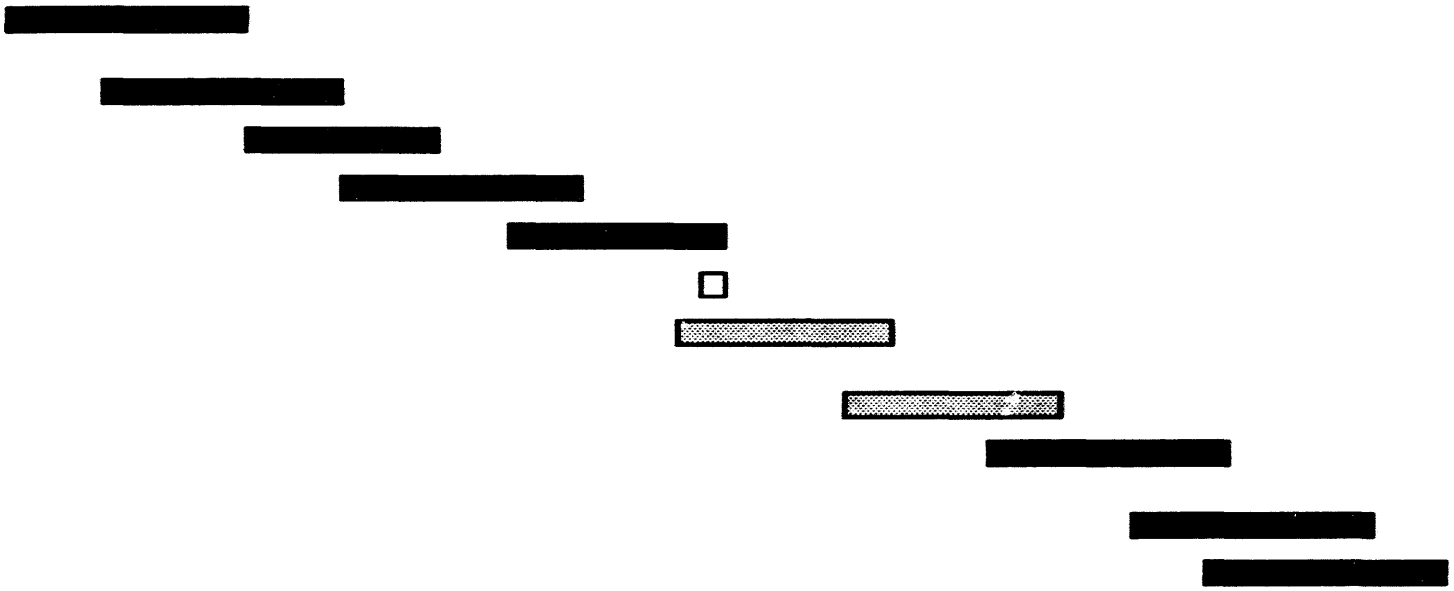

Fig. 1. This is an example of chromosome walking. The solid boxes represent clones in a contig. The dotted boxes represent the clones in the walk. The small non-shaded square represents the end probe used to find the new clones that fill the gap.

26230	22		
15123	22	5.6	
8697	22	5.6	6.5

Fig. 2. Restriction map of ERCC1 region showing fragment sizes in kb. The numbers on the left represent clones. The underlined numbers represent the location of the gene on the contig. Cosmid 8697 was the end cosmid used for the chromosome walk.

26293	19	12	2.2	7	3.8											
25251	18	11	2.2	7	3.8											
14455					3.8	19.5	12.5	5		6.9						
14581						19.5	12.5	5		6.9	10	9	2.7			
20341						19.5	12.3	5	2.8							
28304								5	2.8					17	20	5.5
14344								5			10	9	2.7		13	
27588									2.8					18	22	16
16570										6.9				16.8	20	

Fig. 3. Restriction map of ERCC2-CKM region on q13.2 area of chromosome 19. The underlined numbers represent the location of the ERCC1 gene on the contig. The numbers in bold represent the location of the CKM gene on the contig.

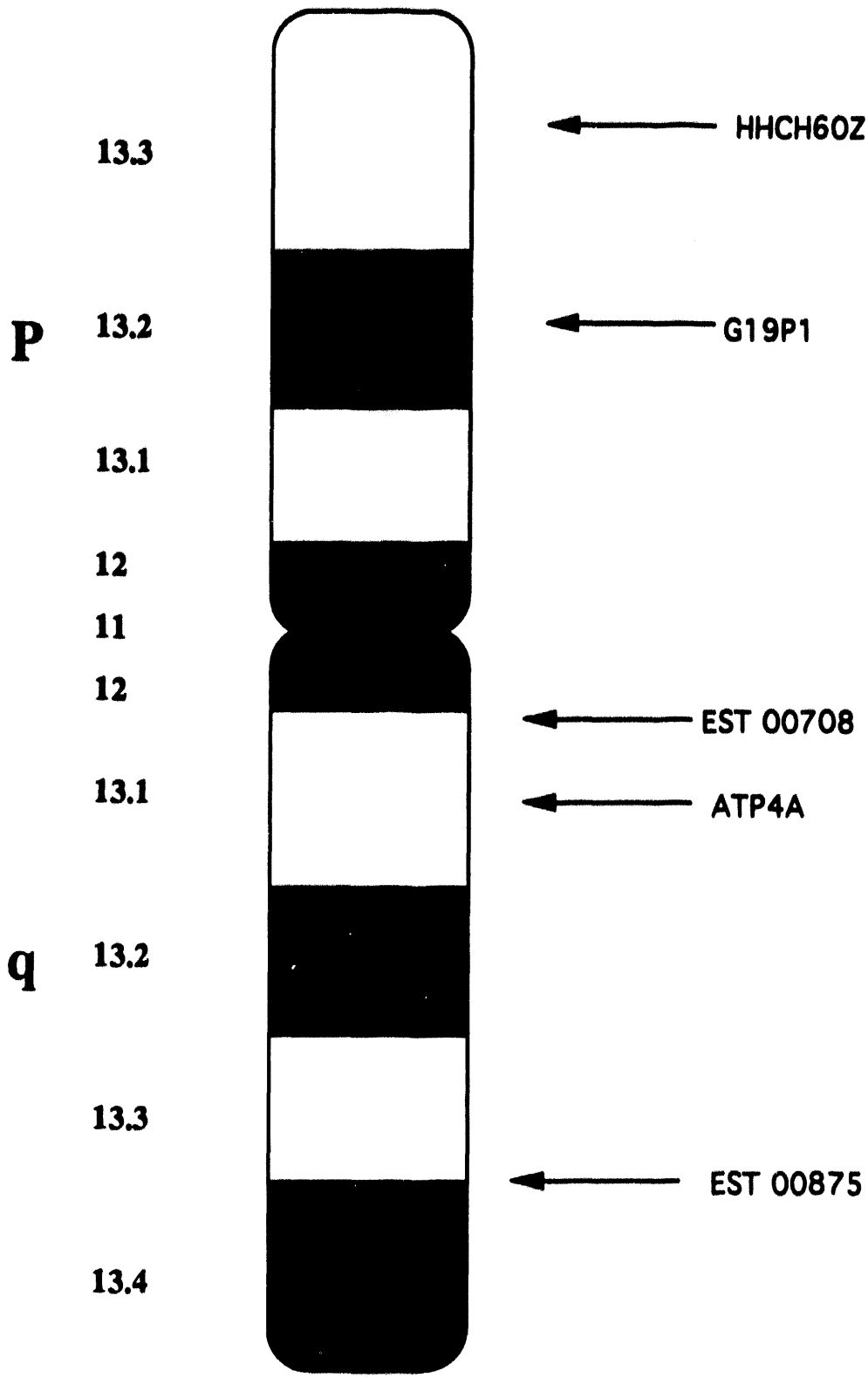

Fig. 4. Location of the five ESTs on chromosome 19.

REFERENCES

1. Adams, M. D., et al. (1992). Sequence identification of 2,375 human brain genes. *Nature* **355**:632-634

2. Mohrenweiser, H. W., et al. (1989). Refined mapping of the three DNA repair genes, ERCC1, ERCC2, and XRCC1, on human chromosome 19. *Cytogenet Cell Genet* **52**:11-14.

3. Nigro, J. M., et al. (1987). cDNA cloning and mapping of the human creatine kinase M gene to 19q13. *Am. J. Hum. Genet.* **40**:115-125.

4. Sefcik, J. A. (1992). The Human Genome Project. *Energy and Technology Review* **2**:29-56.

5. Smeets, H., et al. (1990). A long-range restriction map of the human chromosome 19q13 region: close physical linkage between CKMM and the ERCC1 and ERCC2 genes. *Am. J. Hum. Genet.* **46**:492-501.

6. Weaver, Robert F. and Philip W. Hedrick. 1989. *Genetics.* WM. C Brown Publishers, Dubuque, IA USA.

ACKNOWLEDGEMENTS

I would like to give a special thanks to the following people for all their help: Harvey Mohrenweiser, Susan Hoffman, Susan Tsujimoto, Chris Conner, Gisela Shonnard, and Barbara Zingg.

First Wall Studies for the Target Chamber of the National Ignition Facility

Duncan S. Callaway

University of Rochester

Lawrence Livermore National Laboratory
Livermore, California 94550

May 19, 1993

Prepared in partial fulfillment of the requirements of the Science and Engineering Research Semester, under the direction of Ray Smith, Research Mentor, at the Lawrence Livermore National Laboratory

* This research was supported in part by an appointment to the U.S. Department of Energy Science and Engineering Research Semester (hereinafter called SERS) program administered by LLNL under Contract W-7405-Eng-48 with Lawrence Livermore National Laboratory.

Abstract

Materials which could act as a "first wall" in the target chamber of the National Ignition Facility (NIF) have been studied. Fusion reactions within NIF will produce very high intensity X-rays. Potential first wall materials have been chosen for their ability to withstand this X-ray exposure without vaporizing and damaging the final optics of the laser. Seven low atomic number materials have been determined to be good first wall candidates– beryllium, beryllia, boron carbide, boron nitride, boron, lithium oxide, and graphite. Materials of low atomic number elements have correspondingly small photon interaction cross sections. They were also chosen for their thermophysical properties– high melting and vaporization points, large specific heats, and high heats of fusion and vaporization. They were also chosen for their relatively low cost. The list of materials will be narrowed down to one with further contact with vendors to understand the cost of producing and machining these materials, with computer modeling of the problem, and with tests on the current ICF facility, Nova.

SERS

LawrenceLivermore National Laboratory Science and Engineering Semester (SERS) students are participants in a national program sponsored by the Department of Energy/Office of Engineering Research. The SERS program provides students the opportunity to participate in research at one of seven Department of Energy facilities during the academic year. Argonne National Laboratory in Illinois, Brookhaven National Laboratory in New York, Lawrence Berkeley National Laboratory in California, Lawrence Livermore National Laboratory in California, Los Alamos National Laboratory in New Mexico, and Pacific Northwest Laboratory in Washington place students in research appointments in this program. The Department of Energy initiated the SERS program to encourage undergraduates to pursue advanced degrees and careers in science and engineering.

Introduction

Inertial confinement fusion (ICF) is being studied at Lawrence Livermore National Laboratory (LLNL) as a potential future energy source. Nova, LLNL's current facility for studying fusion, achieves fusion by heating and compressing a small pellet of deuterium-tritium mixture. Nova drives the fusion reaction with ten laser beams, amplified to a maximum total energy of 120kJ at 1.053 micron. The maximum fusion yield Nova has produced is 62J. The reaction takes place inside a 4.6 meter diameter aluminum target chamber.

It is the goal of the proposed National Ignition Facility (NIF) to take this process a step further and initiate ignition and gain, i.e., to create a reaction hot enough to drive itself (ignition) and produce energy gains of 2 to 10 times the input laser energy. This will require large amounts of input energy– NIF will use between 192 and 288 beams to achieve a total target laser energy of 1.8 MJ. Fusion yields of 20-30 MJ are anticipated. The reaction will take place in an aluminum chamber 10 meters in diameter.

For NIF, direct X-irradiation will pose a large problem at the inner or first wall of the target chamber. An estimated 15% of the total fusion yield plus 1MJ from the original laser energy will result in X-ray energy. The maximum resulting X-ray fluence would be about 3.2 J/cm^2 from a 30MJ yield; this peak accounts for the expected Lambertian distribution of X-rays. Absorption of X-ray fluence levels this high by aluminum will result in melting and vaporization.[1] The chamber operates at 10^{-6} torr, and the resulting mean free path of an atom is about 10 meters, or the diameter of the chamber. This enables a vaporized atom to travel the diameter of the chamber, depositing upon and damaging the final optics of the laser. In order to prevent this, another material can be plasma sprayed on or placed over the aluminum in sheets. This first wall material must

be able to withstand high X-ray fluences to minimize ablation to extend the life of the final optics. Figure 1 shows a preliminary drawing of what the chamber might look like if plates are used. There are 343 plates of 8 basic shapes.

Low energy X-rays (high energy photons) interact with the wall primarily via the photoelectric effect, whereby an atom absorbs a high energy photon. A portion of the photon's energy causes the atom to eject an electron from a bound state, the rest increases the atom's vibrational energy. The probability that a photon will interact with an atom is determined by the atom's photon interaction cross section. The absorption cross section of a material is the effective target area of an atom when subject to bombardment by, in this case, photons. Cross section depends directly on, and increases with, atomic number. Figure 2 illustrates this. The smaller this area, the lower the chance of a photon-atom interaction.[2] Also, smaller cross sections distribute energy through a greater depth of the material, and a lower energy deposition per unit mass results. As photons are absorbed, and energy per unit mass increases, the material can get hot enough to melt or vaporize. Shock waves may propagate through the material due to rapid thermal expansion of the heated material.

For the above reasons, a first wall which has a very low atomic number, or Z, is necessary. Furthermore, a material should possesses thermophysical properties that would enable it to absorb large amounts of energy before melting or vaporizing. Heat of fusion, heat of vaporization, specific heat, melting point and vaporization point are all properties which, if high in number, will help prevent a material from melting and vaporizing by increasing the total amount of input energy to reach those phase changes. A low linear coefficient of thermal expansion will reduce shock generation in the material, minimizing possible spalling of its back surface. This material must be of very high purity, for a small

amount of a high-Z material could increase the average cross section enough to be detrimental to the energy deposition per unit mass.

Goal

The goal of this four month study has been to select a small number of materials (half a dozen or less) whose characteristics prove attractive for use as a first wall. The attempt has been to identify materials which should be more thoroughly studied, specifically through advanced theoretical calculations and testing on Nova.

Procedure

First, materials were examined via library research. A book titled Thermophysical Properties of High Temperature Materials[3] was used to single out ceramics and metals which were low Z and possessed attractive thermophysical properties as discussed above. Cross sections were determined with the aid of photon absorption data tables.[4] Next, price and availability checks were made with vendors to determine which materials were inexpensive, which could be supplied in plates (preferably 1 meter square), which could be sprayed (at high densities), and which could be supplied in high purities. Vendor names were retrieved from the Thomas Register.[5] Lastly, a radiation hydrodynamics code called Hyades[6] was used to simulate high X-ray fluences incident upon various materials. Unfortunately there was insufficient time to develop an accurate problem to run with Hyades, and its results will not be included in this report. See Appendix A for a discussion of the problems identified in using Hyades.

Results

Nine materials were chosen solely on the basis of their atomic number and thermophysical properties. They are:

beryllium (Be)

beryllium carbide (Be_2C)

beryllium nitride (Be_3N_2)

beryllia (BeO)

boron (B)

boron carbide (B_4C)

boron nitride (BN)

graphite (C)

lithium oxide (Li_2O)

Their thermophysical properties are presented in table 1. For some materials, certain values were not published in the reference book used-- those columns were left blank. Most especially, vaporization point was unavailable for every material. Cross section, melting point, and heat of vaporization are values which could be calculated or were published for most of the materials; they are graphed in figures 3 through 5.

Searching for accurate prices and availability for these materials proved to difficult. Many of these materials are uncommon, and manufacturing techniques are expensive. Some materials have large price ranges from manufacturer to manufacturer-- I attribute this to limited knowledge of the materials and the processes involved in manufacturing large sized plates (most of the materials are rarely, or never have been, supplied in 1 meter-square plates). Price quotes for each material are listed below. Plates were quoted at 1 cm thicknesses, and at the highest available purities. Because the prices quoted are only preliminary, rough

estimates, the vendor's names have been replaced with letter codes in order to avoid any inference that LLNL has selected specific vendors. For LLNL employees, the vendor code and corresponding vendor names are available from Ray Smith or Mike Tobin.

Beryllium: This is the only material for which I was able to find vendors that supply 1 meter square plates. Vendor A quoted a price of $880/kg, which corresponds to $2.7 million for plating to cover the entire chamber (314 m^2).

Beryllium Carbide/Beryllium Nitride: Two vendors (B&C) agreed that these materials can cost up to 100 times the amount of beryllium– this cost appears prohibitive.

Beryllia: Vendor D is able to produce (hot press) .5m x .5m plates of beryllia at $4500 each. This corresponds to $5.7 million to cover the chamber. Vendor A, however, is unable to produce plates larger than 10 cm x 10 cm. Discussions with Vendor A are continuing, and they may be able to produce larger plates with more development.

Boron: Only one vendor (E) was able to quote a price for boron. The request was made for .5m x .5m plates, and Vendor E quoted a price of $29,340/plate– each plate in 12-14 sections, though. This would correspond to $37 million to cover the chamber.

Boron Carbide: Vendor D was able to quote a price of $1500/plate for .5m x .5m plates, or $1.9 million to cover the chamber. The process involved is hot pressing. Vendor E quoted 5 times as much, $7807, for the same size plate in 6 to 8 sections ($9.9 million/chamber).

Boron Nitride: The largest boron nitride plate size Vendor F can manufacture is .25m x .3m, at $915/plate ($3.8 million/chamber). Vendor E quoted a .5m x .5m plate in 6-8 sections at $9,616/plate ($12 million/chamber).

Graphite: Graphite was not considered until late in the study, because its vapor can be extremely detrimental to the final optics of the system. We were

made aware of a process by which carbon can be removed from the system– in essence, a low density oxygen plasma is used to getter carbon off the laser optics.[4] Vendor G can produce graphite plates 1 m x .3 m for about $550, which would correspond to $.58 million to cover the chamber.

Lithium Oxide: Based on my studies, this material is no longer regularly supplied. Vendor H has produced it in the past for use in batteries, but at low purities (96%). Such a large order, though, may be incentive for a supplier to develop a higher purity material in plate form. Li_2O was previously supplied by Vendor G for $275/kg ($1.6 million/chamber)

The options for plasma spraying were lightly searched. Discussions with people at Vendor I produced the following information: Beryllium compounds cannot be plasma spayed in an open environment, due to its toxicity. It may be difficult to find an enclosed chamber large enough contain the NIF chamber, or parts of it. The characteristics of boron carbide prohibit spraying at thicknesses greater than .5 mm– this thickness is too small to filter out the high intensity X-rays present under NIF conditions. The same is true for plasma sprayed graphite. Vendor H has not sprayed boron nitride, boron, and lithium fluoride, but believes it is possible. Costs would involve set up for the job, labor, and the price of the material in powder form. Representatives of Vendor H believe that the bulk of the cost will be for the material. Speaking with other vendors showed that costs for materials were significantly less in powder form (for plasma spraying) than plates.

Discussion

The toxicity of beryllium is a concern if the material vaporizes: it then may enter the bloodstream through the lungs. Therefore, if further studies can

show that either beryllium or beryllia does not vaporize when exposed to expected X-ray fluences, they will be viable candidates. Beryllium's strong points are relatively low cost, high heat of vaporization, and very low X-ray cross section. Beryllia's cross section is larger than any other material considered, but its high melting point may be able to compensate. The manufacture of large BeO plates may be difficult, though.

Due to their cost, beryllium carbide and beryllium nitride have been removed form the study. It is possible that all of the other materials may be brought to within the NIF budget-- some prices are currently too high, but they have not been thoroughly investigated.

Due to low purities and unavailability, lithium oxide has also been removed from the study.

A thickness of 1 cm was chosen for structural reasons-- it will be necessary for the material to be able to support 150 to 200 lbs/ft^2 (technician weight). Its possible that some materials might be used at lower thicknesses if their strengths indicate it; this would lessen their costs.

Figure 6 graphs a figure of merit for ranking the remaining six materials. The figure of merit is the ratio of energy to bring each material from room temperature to its melting point (using an average specific heat), to the material's cross section at 1 keV (peak intensity at 350 eV blackbody temperature).

Conclusions/Recommendations

Because of their cost, photon cross sections, thermophysical properties, and availability, studies of the following materials should continue:

- beryllium
- beryllia

- boron carbide
- boron nitride
- boron
- graphite

Further contacts should be made with vendors to establish firm prices of these materials. Computer simulation of the X-ray material interaction with Hyades should provide accurate calculations of energy deposition per unit mass, and allow determination of fluences at which these materials will vaporize.

Tests on Nova, at close range to the target, will subject materials to X-ray fluences comparable to those which NIF will produce, thus validating that a material will vaporize and spall as predicted by the Hyades code. I recommend that all the materials above are studied in this fashion.

Appendix A: Hyades

Hyades was designed as a radiation hydrodynamics code for high energy density plasma studies. I have used it to study lower temperature physics, in an effort to gather information on energy deposition and shock propagation in different materials for varied fluences and blackbody X-ray temperatures. The advantages Hyades offers are an accurate representation of blackbody curves, use of the Sesame equation of state tables, and relatively simple operation. It was designed to take very little training to learn how to use, and run on a P.C. Unfortunately, there are many pitfalls. The code has a number of "bugs" which have yet to be fixed, and crashes very easily, especially when working in relatively low temperatures. The input file might be changed to keep the program from crashing, but it is up to the user to determine what that change might be, and unfamiliarity with the code hinders this. These constraints prevented me from ever achieving any accurate results with the Hyades code.

I believe that Hyades can be used to benefit the first wall study, but the time and effort required to generate an accurate simulation may be too large to be cost effective. There will be new a version arriving soon which will perform more efficiently at low temperatures, and include the strength of materials in its calculations. This could yield interesting results, and I recommend that further use of Hyades on the first wall problem is stopped until this version arrives.

Table 1: Thermophysical Properties

Symbol	Material	Heat of Fusion (cal/g)	Heat of Vapor-ization (cal/g)	Melting Point (K)	Density (g/cm^3)	Specific Heat (cal/g·K)	Thermal Expansion (C^{-1})
Be	Beryllium	310.7	7816	1556	1.86	.5 - .85	41 e -5
Be_2C	Beryllium Carbide	559	6524	2373	1.9	>.5	9.7 e -6
Be_3N_2	Beryllium Nitride	561	5613	2473			
BeO	Beryllia	551	4013	2843	3.03	.4 - .525	6.8 e -6
B_4C	Boron Carbide			2723	2.5	.375 - .55	5.7 e -6
BN	Boron Nitride		2603	3273	2.25	.4 - .475	
LiF	Lithium Fluoride	250	1850	1133	2.64	.38**	
Li_2O	Lithium Oxide	468.5	4697	1973	2.013	.53 - .73	
B	Boron		11182	2310	2.5	.264**	
C	Graphite		5500	4500*	1.78	.17**	

*sublimation point

** at room temperature.

Figure 1: NIF Target Chamber

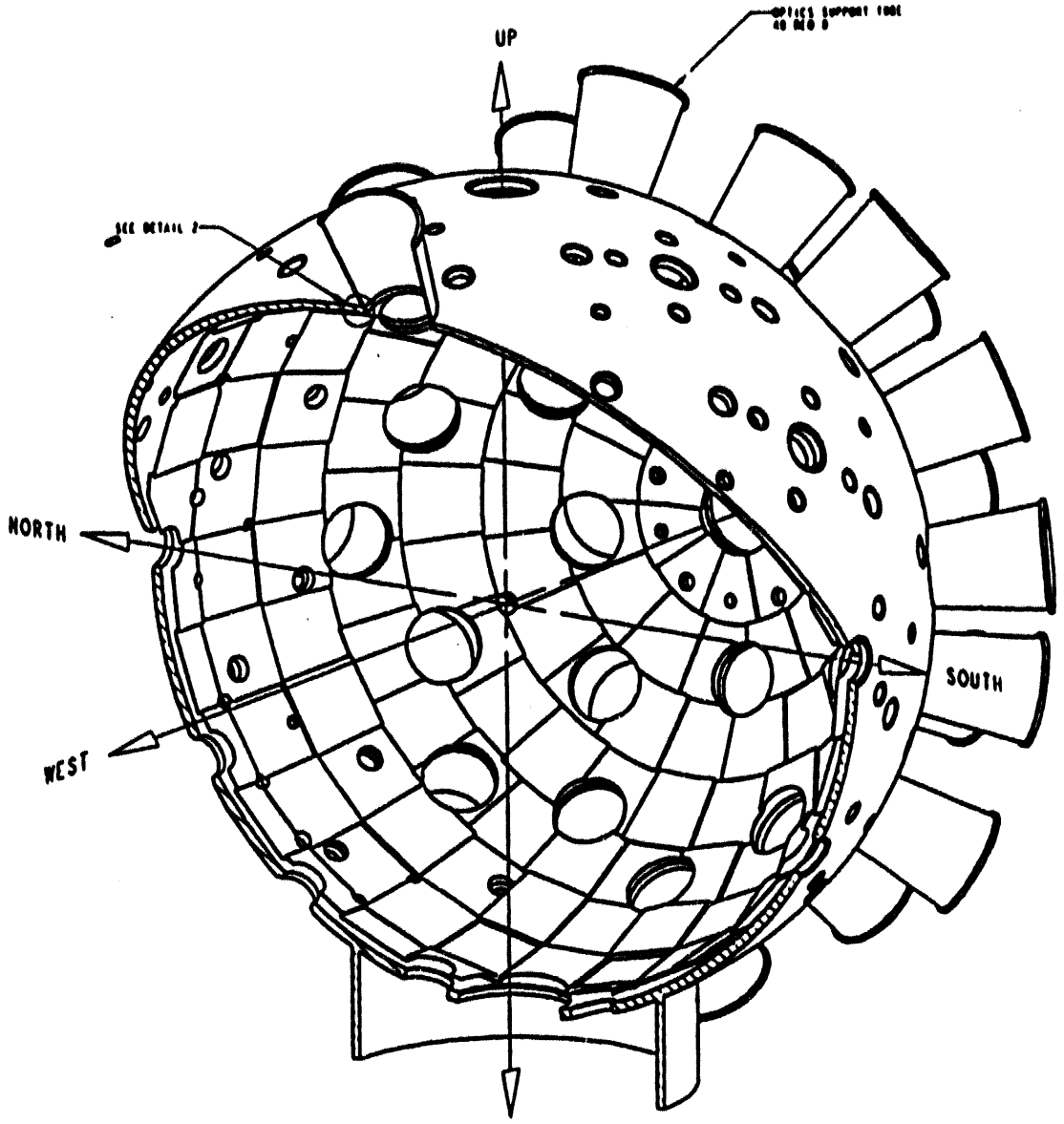

Figure 2: Cross section vs. Atomic number

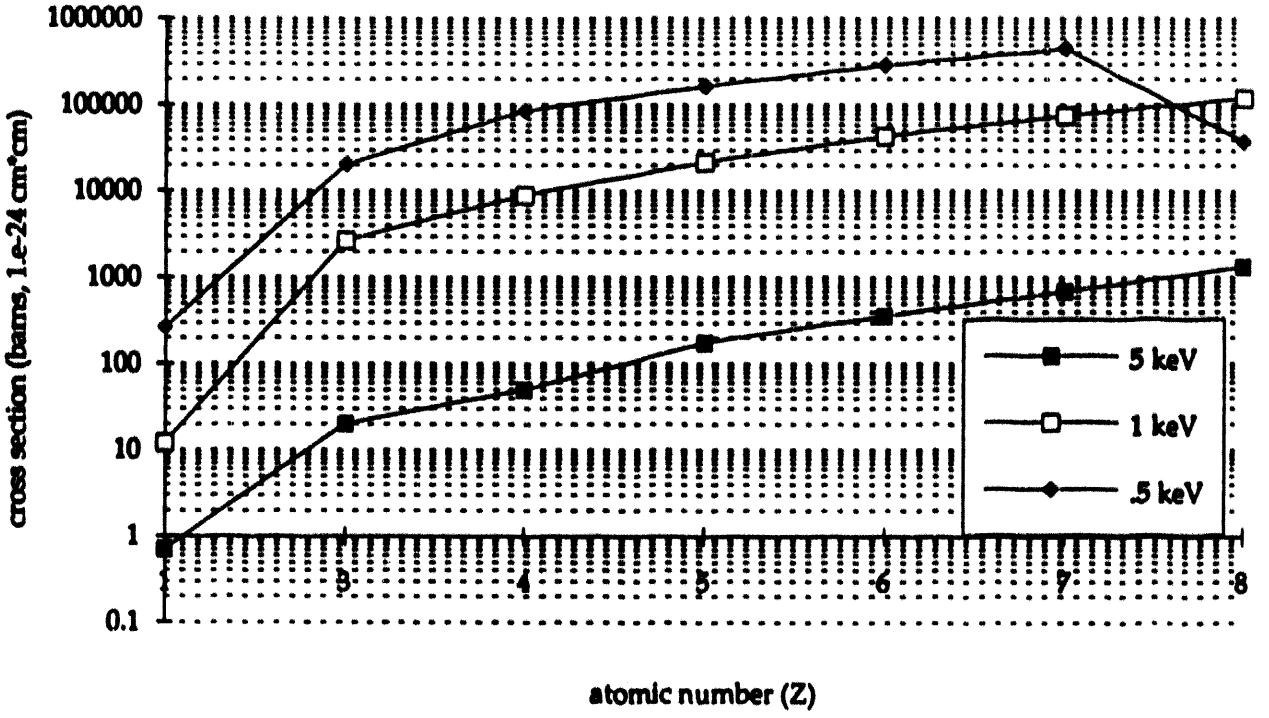

Figure 3: Cross section in barns, at 1 keV

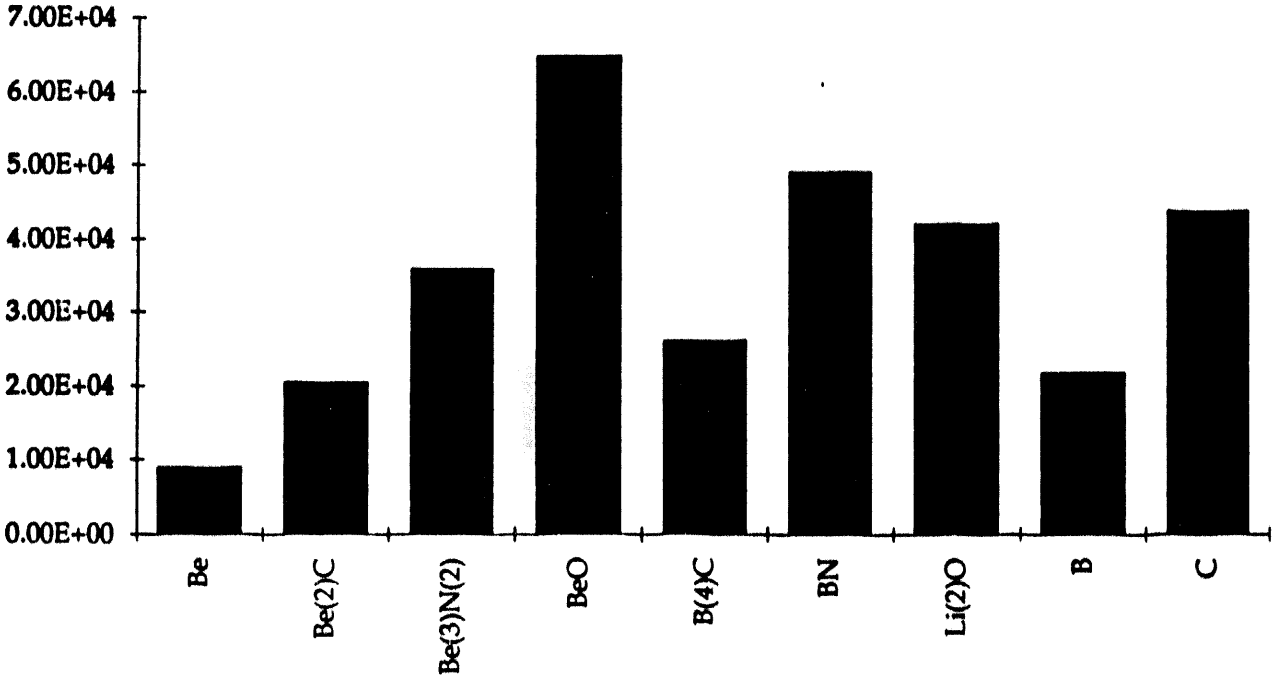

Figure 4: Melting point (K)

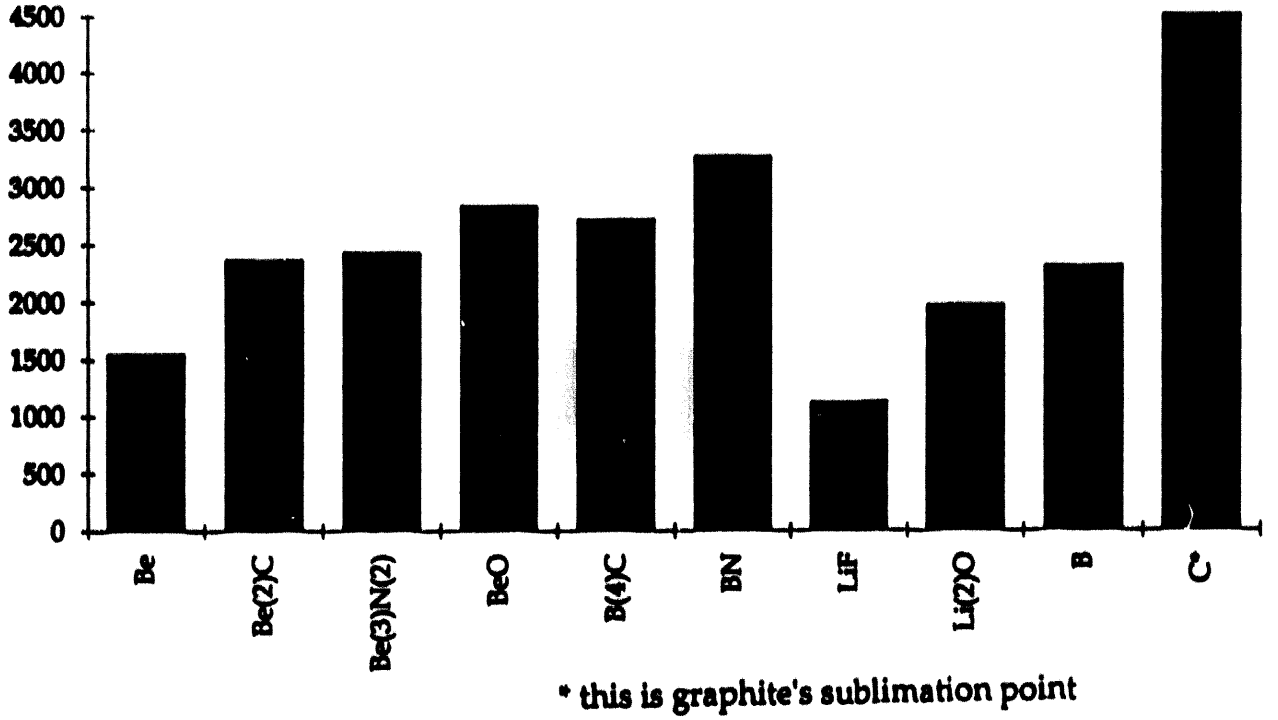

* this is graphite's sublimation point

Figure 5: Heat of vaporization (cal/g)

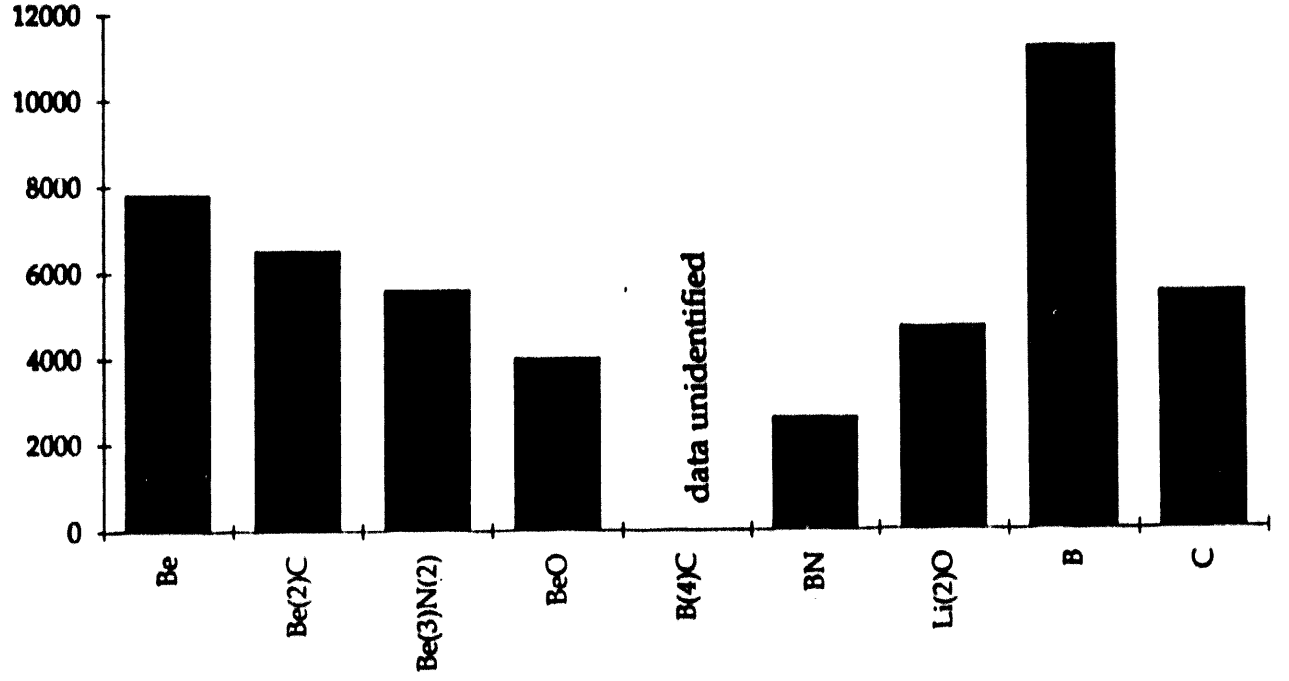

Figure 6: Figure of merit (energy required per gram to heat to melting point divided by photon cross section at 1 keV)

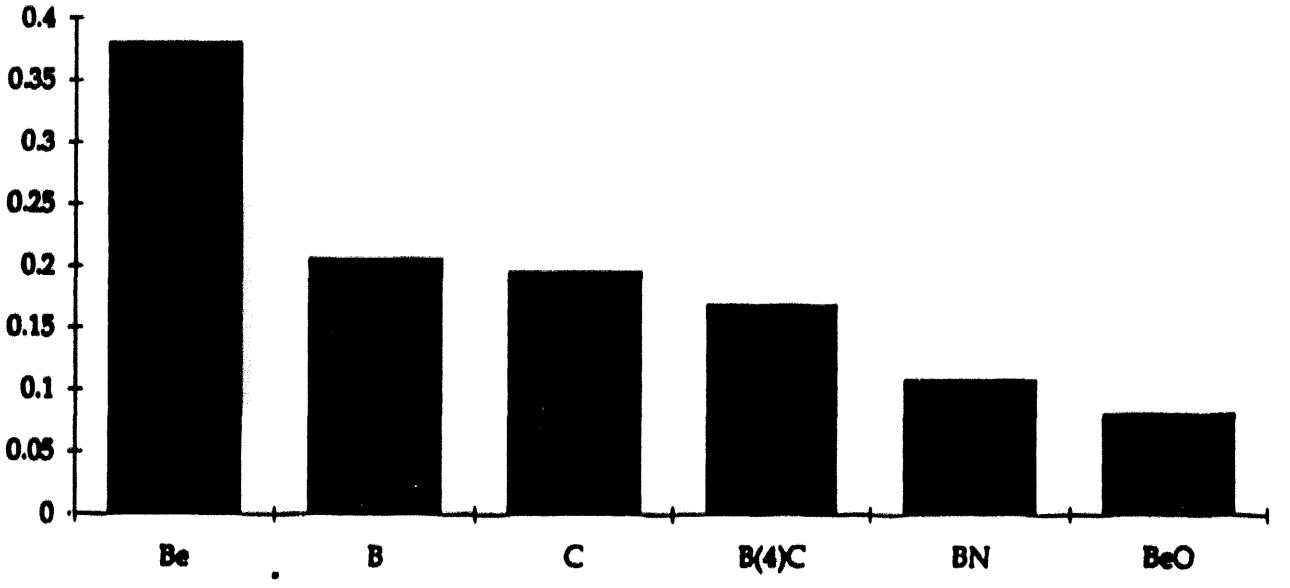

References

1.) Tokheim, R.E., et al, "Threats From Radiation Effects in the Proposed Nova Upgrade," SRI International, September 1992, Subcontract No. B160484, Sections 1,2.

2.) Glasstone, Samuel, *Nuclear Reactor Engineering*, D. Van Nostrand Company, Inc., Princeton, 1967.

3.) Touloukian, Y.S., ed., *Thermophysical Properties of High Temperature Solid Materials*, Macmillan Company, New York, 1967.

4.) Cullen, D.E., Chen, M.H., Hubbell, J.H., et al, "Tables and Graphs of Photon-Interaction Cross Sections From 10eV to 100GeV Derived From the LLNL Evaluated Photon Data Library. (EPDL)," *UCRL-50400*, Lawrence Livermore National Laboratory, Livermore, CA (Oct 1989).

5.) Duchaine, R.J., *Thomas Register of American Manufacturers*, Thomas Publishing Company, New York, 1993

6.) "Hyades," Version 01.05.06, 1993. Written by John Larson, Cascade Applied Sciences, P.O. Box 4477, Boulder, CO 80306.

Acknowledgments

I would like to thank Steve Lane for his gracious time and effort helping me to understand and work with Hyades. Most especially I'd like to thank my mentor, Ray Smith, for his patience, encouragement, and dedication to the leaning process.

P.I.X.E. as an elemental analysis tool*

Alexander M. Friz

The Ohio State University

Lawrence Livermore National Laboratory
Livermore, California 94550

May 20, 1993

Prepare in partial fulfillment of the requirements of the Science and Engineering Research Semester under the direction of Jay C. Davis and Charles Westbrook, Research Mentor, at the Lawrence Livermore National Laboratory.

* This research was supported in part by an appointment to the U.S. Department of Energy Science and Engineering Research Semester (hereinafter called SERS) program administered by LLNL under Contract W-7405-Eng-48 with Lawrence Livermore National Laboratory.

If this paper is to be published, a copyright diclaimer must also appear on the cover sheet as follows:

> By acceptance of this article, the publisher or recipient acknowledges the U.S. Govenment's right to retain a non-exclusive, royalty-free license in and toany copyright covering this article.

P.I.X.E. as an elemental analysis tool

Alexander Friz
The Ohio State University
Center for Accelerator Mass Spectrometry (CAMS)

Abstract

Our group primarily uses 3 to 5 MeV proton beams to perform Particle Induced X-ray Emission(PIXE) for elemental analysis. PIXE can yield element concentrations down to parts per million. I am presently investigating the application of PIXE to surface contamination of aluminum as opposed to conventional methods such as chromatography for LLNL's Environmental Protection Department (EPD). In addition to the EPD investigation, I am looking into elemental concentration measurements on Aluminum infiltrated Boron Carbide (B_4C) of various composition for LLNL's Chemistry and Material Science Division (C&MS).

Particle induced x-ray emission (P.I.X.E) is a technique based on x-ray spectrometry and can be used as an elemental analysis tool for elements heavier than sodium i.e. $Z \geq 11$. P.I.X.E. is a very sensitive and quantitative method and can yield concentrations down to parts per million such as in impurity concentration measurements. A variety of ions are available for use for P.I.X.E. at our facility but the most commonly used ones are hydrogen and oxygen. Our accelerator facility allows us great flexibility in the energy we choose for the ion beam. Typical values for protons and for oxygen are 3 MeV and 40 MeV, respectively. For the spectra I have collected and have presented in this paper, the ion beam I used was a 3 MeV proton beam. Minimum detection for the highest number of elements is the reason for this beam energy choice. Working at these energies and at reasonable current densities, P.I.X.E. is nondestructive to the sample material which is very favorable

in many cases.

Below is the tandem Van der Graaff lab which is run at LLNL (Fig. 1).

The Tandem Accelerator Lab.

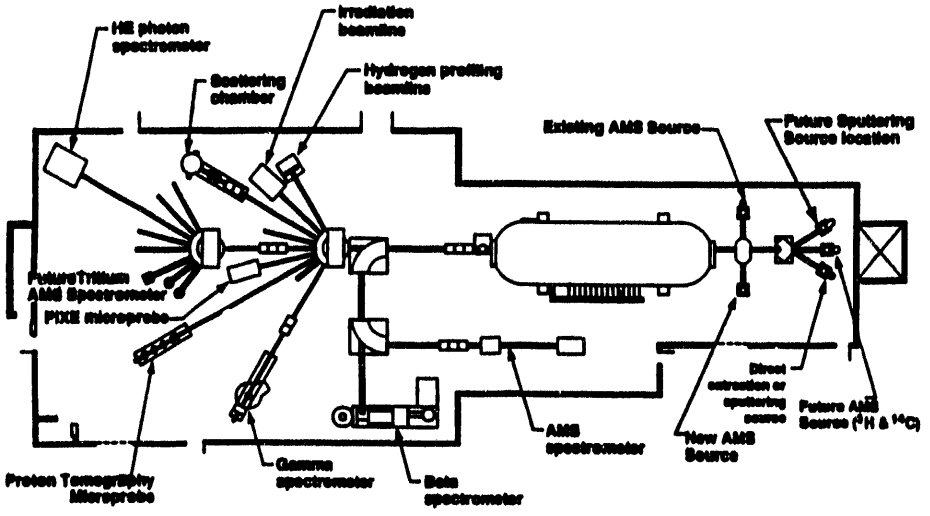

Figure 1

As can be seen, the lab is a multi-user lab with 9 separate beamlines. For P.I.X.E. the path of the ions starts in the direct extraction source. This is where negative ions are produced. The ions are then guided by magnets and beam steerers to the front end of the accelerator. The path until this point is called the low energy end of the accelerator. The ions are accelerated by a potential of approximately 3-4 MV and stripped by carbon foil to their final charge state and then accelerated again to their final energy before leaving the accelerator. Any point beyond the back end of the accelerator is called the high energy end. From here the beam is again guided by magnets and beam steerers down to our target chamber. Below is close-up of the beam focusing strategy (Fig. 2). It consists of two sets of slits, aperture slits and object slits. These two sets of slits roughly define the beam and the fine tuning of the beam is done by the quadrapole doublet magnet right before the target chamber. Typical

beam spot sizes are ~100μm but smaller sizes are frequently used.

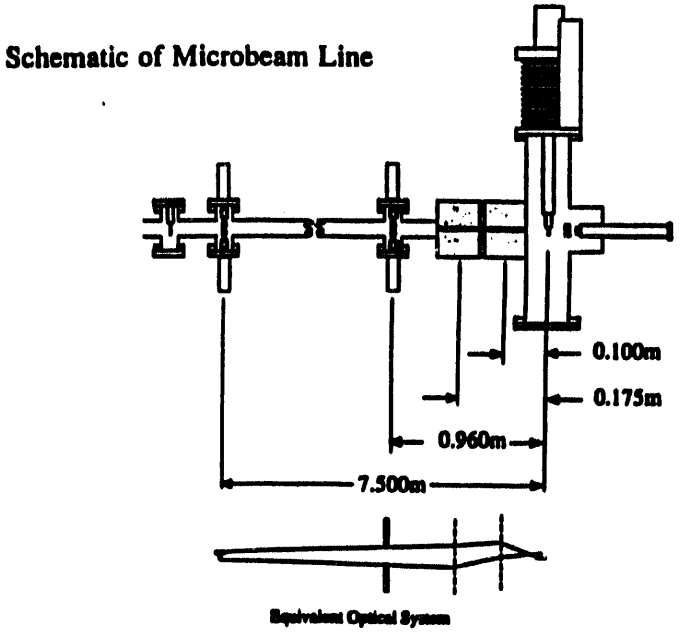

Figure 2

As the beam enters the chamber which is typically at 10^{-6} Torr it impinges on the target and introduces inner-shell vacancies in the atom. As outer-shell electrons fill these vacancies, the atom emits a spectrum of characteristic x-rays inherent to that element (Fig. 3).

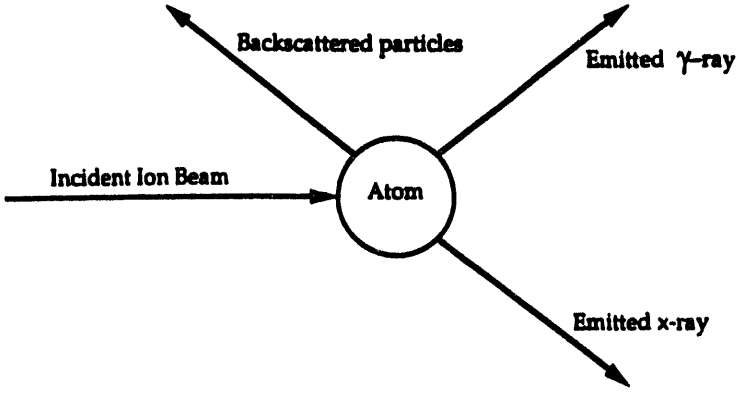

Figure 3

The energy range for proton-induced x-rays which we can resolve is 2-12 keV. Data acquisition is via a lithium-drifted silicon (SiLi) x-ray detector and charge collection from a Faraday cup or directly from the sample. This data is reduced by a computer code developed partially by two coworkers, G. Bench and A. Antolak. The

computer code contains a spectrum fitting part which subtracts background caused by electronics noise and unwanted signals from bremsstrahlung from the acquired spectrum.

As an initial project, I entered cross-sections for elements heavier than aluminum into this computer code. These cross-sections are used to correct for secondary fluorescence caused by excitation of the atom other than by direct excitation the beam. The data which have been entered are the K-shell and all L-shell cross-sections. Although we cannot see the difference in the background fit created by the code, secondary fluorescence corrections are reflected by a difference in peak area numbers.

LLNL's Environmental Protection Dept. (EPD) was interested in accurately measuring hydrocarbon surface contamination on aluminum to test alternative solvents. I considered this a good possibility since our limits of detection are on the order of their present method, Fourier transform infrared spectrometry (FT/IR). Normally P.I.X.E.'s detection limit for a thin sample is on the order of the picogram (10^{-12}g) level, but since the contaminated aluminum was fairly thick (3mm) this detection limit increased to approximately the nanogram (10^{-9}g) level. Apparently if we were to "look" for Cl content this would give a computational link to hydrocarbon contamination. Below is a fitted spectrum of a uncontaminated Al blank (Fig. 4). We need to test a blank, untreated sample before we test the treated samples to obtain a reference .

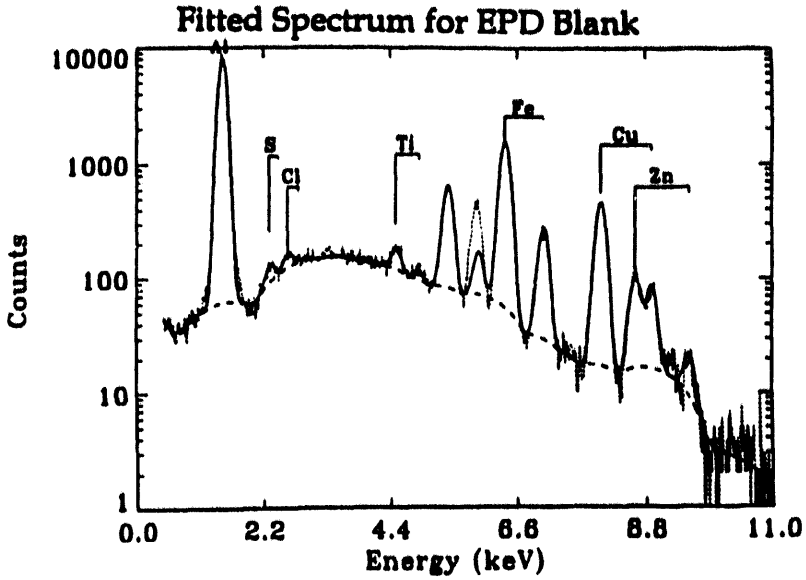

Figure 4

As we can see there is already some background Cl present. This may effect the results we are able to obtain. In general, this is a fairly "dirty" sample and we would prefer a cleaner one, but are limited by the aluminum composition. Figure 5 represents an Al sample which has been contaminated with dirty machine oil and then cleaned with Freon-FTE.

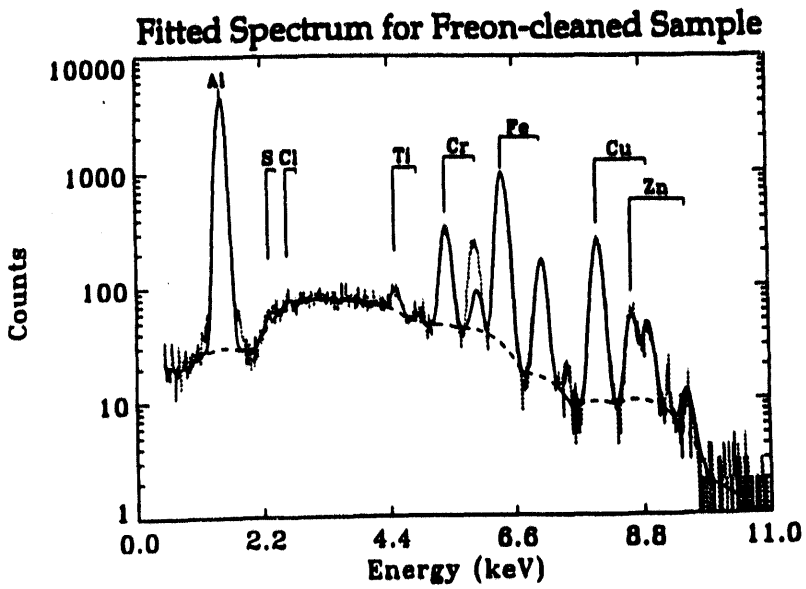

Figure 5

Here the Cl concentration (directly related to peak area) is lower than on the blank. The lower Cl level on the cleaned sample is obviously a good thing for EPD,

but bad thing for quantifying the amount of contamination due to the dirty machine oil. We were unable, for this reason, to calculate the amount of hydrocarbon remaining on the sample. The inherent high amount of background at the lower end of the spectrum also affected the sensitivity of the Cl measurement. Even though P.I.X.E.'s detection limit is competitive with that of FT/IR hydrocarbon contamination via Cl measurements does not look hopeful.

In addition to the EPD data we acquired a few spectra for LLNL's Chemistry & Materials Science Division (C&MS). The particular group we contacted was working on aluminum infiltrated boron carbide (B_4C), a ceramic. This group was interested in looking for compositional variations between samples with the same Al alloy and on samples with fractures i.e. differences in composition on and off the fracture. Figure 6 shows a fitted spectrum for B_4C infiltrated with a common Al alloy, namely Al-6061.

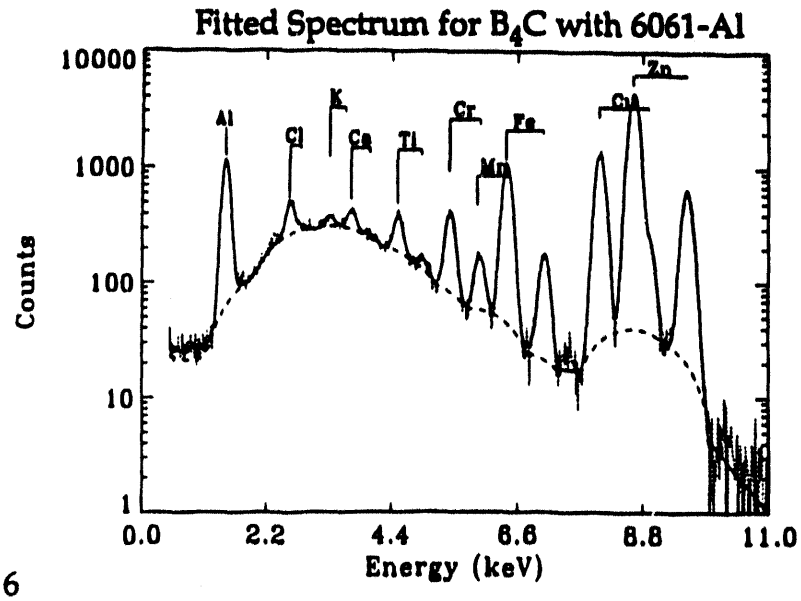

Figure 6

This spectrum shows us reasonable values for the elements present in the samples. Notice that samples are also "more dirty" than we would like. This is due,

as in the EPD samples, to the composition of the Al alloy. Although quantitative concentrations have not been calculated, qualitative ratios of the peak areas indicates promise.

Figures 7 and 8 show spectra of B_4C infiltrated with Al-1100.

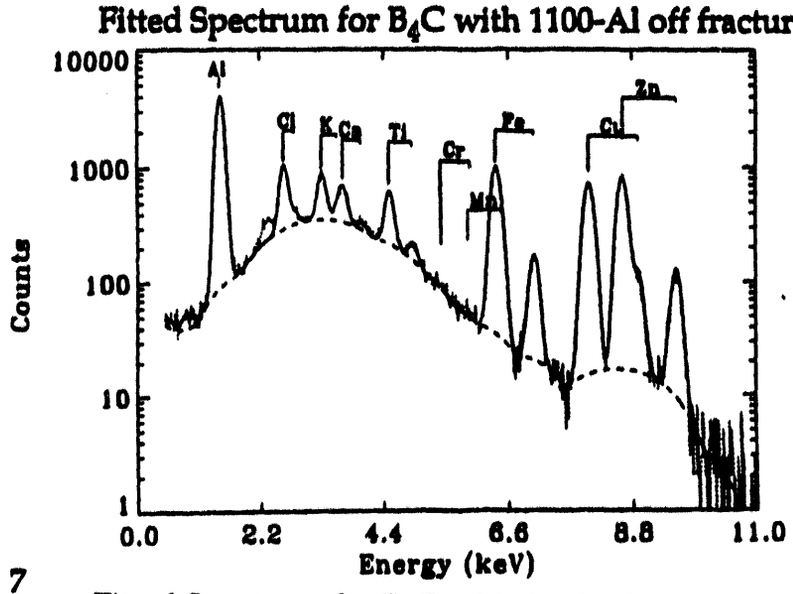

Figure 7

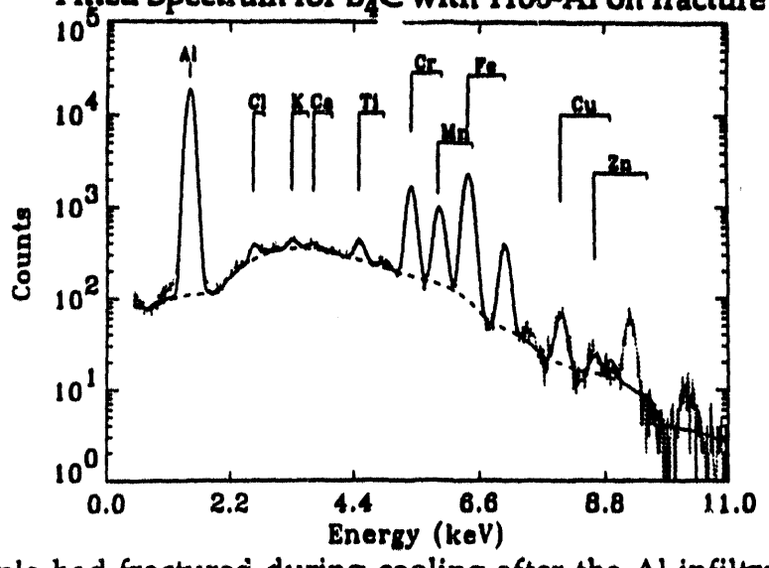

Figure 8

This sample had fractured during cooling after the Al infiltration. As indicated one spectrum was taken off the fractured area of the sample and the other was taken on the fractured surface. It is interesting to note the differences in elemental composition on and off the fracture. Of particular interest are the

differences in Cu/Zn as opposed to Cr/Mn levels off and on the fracture. Cu and Zn are higher off the fracture whereas Cr and Mn levels are lower. The opposite is true for the spectrum taken on the fracture in addition to some other elements having lower concentrations such as Cl, K Ca. This variation may be able to tell us something about the infiltration process and/or the cooling process. Initial, rough calculations indicate the accepted elemental concentrations for the Al alloy. This gives great promise for continuation of concentration measurements for C&MS.

Our group is also presently building a new beamline dedicated to Rutherford backscattering measurements and ion microtomography (IMT). IMT is a method in which 3-D density images are formed by proton energy loss measurements (PEL). An incident proton beam of known energy moves through the sample losing energy via electronic interactions. This energy is then measured by a detector at the back of the target chamber. After data reduction we can actually choose a slice anywhere through the sample and get a density image of that slice. I have been working with technicians through every stage of the beamline's construction. Our group hopes to have this beamline up and running by Aug. 1993.

In conclusion, P.I.X.E. is a very sensitive, nondestructive elemental analysis tool. Initial attempts for EPD contamination measurements did not show potential, but EPD has shown interest in taking measurements for contamination on printed circuit boards. These measurements may not present as great a problem because of the different substrate. Compositional analysis of B_4C is very promising. The data gathered from these measurements may change the way the ceramic is processed. When the IMT beamline is finished and running I hope to be able to do a

morphology study of aerogels. Aerogels are also made be a C&MS group which is interested in maximizing surface area for catalysis reasons.

References:

[1] S.A.E. Johansson and J.L. Campbell, P.I.X.E A Novel Technique for Elemental Analysis, John Wiley & Sons, 1988

Dust Accretion onto White Dwarf Stars*

Mary Krasovec

University of Nebraska at Lincoln

Lawrence Livermore National Laboratory
Livermore, California, 94550

May 7, 1993

Prepared in partial fulfillment of the requirements of the Science and Engineering Research Semester under the direction of Charles Alcock, Research Mentor, at the Lawrence Livermore National Laboratory.

*This research was supported in part by an appointment to the U.S. Department of Energy Science and Engineering Research Semester (hereinafter called SERS) Program administered by LLNL under Contract W-7405-Eng-48 with Lawrence Livermore National Laboratory.

By acceptance of this paper, the publisher or recipient acknowledges the U.S. Government's right to retain a non-exclusive, royalty-free license in and to any copyright covering this article.

Dust Accretion onto White Dwarf Stars

Mary Krasovec
University of Nebraska at Lincoln
Physics IGPP

ABSTRACT

In this paper I outline a method for examining the possibility of micron sized dust particles reaching the atmospheres of white dwarf stars with luminousities from .01 to .001 times solar luminousity. Using a stellar dust cloud model similar to that observed in the solar system, I apply the equations governing the Poynting-Robertson drag and the effects of the dwarf's magnetic field to the calculation of the scale of such accretion. I have found that the Poynting-Robertson drag is an effective method of transfer for iron, silicate, and graphite particles up to a distance of .5 to 4.5 solar radii from the dwarf where the dust particles evaporate and the resulting molecules ionize. Further calculations show that the dwarf's magnetic field causes a magnetosphere to form around the dwarf, but that enough particles can escape to the surface of the dwarf that large scale accretion is not prevented.

PART 1: INTRODUCTION

One of the major goals of astrophysicists is the development of models of the atmospheric conditions of various stars. White dwarfs, in particular, exhibit properties that are not yet understood. Small, hot, very dense stars in the last stage of their evolution, white dwarves have passed through the red giant phase of their evolution and burnt off most of their lighter elements. They lack the high mass needed for collapse into neutron stars or black holes, but end up in a stable state with cores made up of degenerate electron gas. In their remaining lifetime, white dwarves continuously radiate off their remaining energy as they slowly fade into black dwarves.

Studies of the spectral lines emitted by white dwarfs show that eighty percent, called DA dwarfs, have nearly pure hydrogen atmospheres (atmosphere being defined as the outer part of the star that can be seen, since it's difficult to find a definite surface on a ball of degenerate matter and hot plasma.) This has been explained as a result of the extremely high surface gravity of white dwarf stars that makes the heavier elements settle below the "see-able" depth. The presence of traces of heavier elements was explained as the result of comet accretion. (Alcock et. al., 1986) The event of a comet falling into a dwarf star causes enough of a disturbance to mix its elements with the star's pure hydrogen, causing a detectable level of heavier elements to be present in the star's atmosphere.

Most of the other twenty percent of known white dwarfs are DB dwarfs with nearly pure helium atmospheres. The absence of hydrogen in these dwarfs has not been yet been explained. Uncertainties about the details of stellar evolution probably hide the explanation for the surface chemistry of DB dwarfs, but it is very likely that accretion of dust particles from a stellar dust cloud could dramatically affect the contents of a dwarf's atmosphere.

PART II: THE SOLAR SYSTEM'S DUST CLOUD

The dust cloud in our own solar system is bound to be different from that surrounding a dwarf star, largely because of the solar wind. A stream of charged particles is constantly racing out of the sun, blown away by high coronal temperatures and activities like sunspots, flares, and prominences. This tends to push small dust particles out of the solar system. Because of their high surface gravity and lack of surface activity, it is doubtful that white dwarves have a stellar wind. Large differences in the magnitude and variance of the magnetic fields of the sun versus white dwarfs will also affect the properties of their dust clouds. But because most white dwarfs were probably stars much like the sun at one point in their evolution, it is helpful to study the observed solar dust cloud to get some idea of what the dust cloud of a white dwarf star might be like.

The solar system's dust cloud is made up of primarily two populations, as shown in Figure 1. Population I is flattened into the orbital plane and slow in radial density decrease, extending out through the entire solar system. The particles are easier to detect with infrared than with visible light and exhibit lower albedo and higher polarization then Population II dust. (Levasseur-Regourd, et. al., 1991) The temperature of the dust, which ranges from 100 to 500 degrees Kelvin as opposed to the Population II temperature range of 20 to 100 degrees Kelvin, (Greenberg, 1991) suggests that Population I dust is made up of silicates with few volatiles. Population II dust has an isotropic distribution that ends somewhere around the asteroid belt at 2.8 to 3.7 au from the sun (Hovenier and

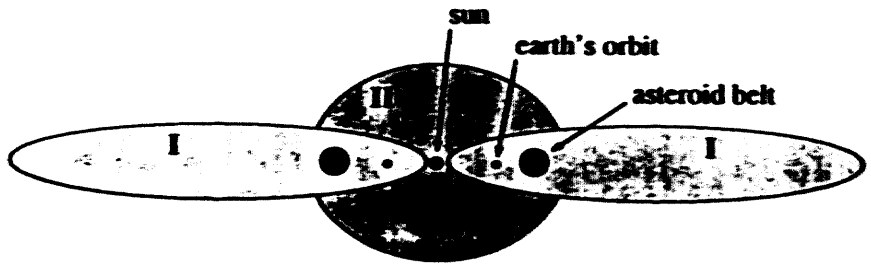

FIGURE 1: Model of the solar system's dust cloud.

Bosma, 1991). The high albedo and low polarization of the dust makes it best detected with visible light and accounts for the gegenschein, or zodiacal light, visible in earth's sky. The lower temperature range as well as the high albedo suggests that there are more ices and volatiles. The sources of Population I dust appear to be mostly asteroids and short period comets, whereas Population II dust probably comes from long period comets and asteroids with large inclinations that allow the dust to move above and below the orbital plane. (Kneissel and Mann, 1991),

The most useful information for my purposes is the source of the dust. Having a good idea of where the dust comes from allows a guess at the amount of dust produced per unit time. Kumar (1989) estimated this at 10^4 kg/s. In the solar system, a large portion of this dust is blown away from the sun by the solar wind and only a small amount reaches the sun's atmosphere. In a dwarf star, there is no wind to blow the dust away, so all or at least most of it could very likely reach the dwarf. In this paper I explore the contributions of the Poynting-Robertson effect and the dwarf's magnetic field to the path dust particles take in dwarf star accretion.

PART III: POYNTING-ROBERTSON DRAG

The Poynting-Robertson effect is based on the principle that light scattered off of a moving object will have it's wavelength Doppler-shifted, which, according to modern physics, implies a momentum change to the photon. Momentum is conserved by an equal but opposite change in the momentum of the object. In the case of a micron sized dust particle moving through a vacuum, this change will add up over time and significantly influence the particle's motion.

At this point it is significant to note that a photon reflected off the dust particle causes the same amount of momentum change as the same photon absorbed and re-emitted by the material in the dust particle. Therefore it is not necessary to take the albedo α, which gives the fraction of light absorbed by the dust material, into account for this part of the calculation.

Consider a particle orbiting a dwarf star with a velocity v that scatters a photon of frequency ν with scattering equally likely in any angle from the particle's frame of reference. If ϕ is the angle measured clockwise from the direction of forward velocity in the orbital plane and θ is the angle measured from the vertical axis, (see Figure 2), then the corresponding momentum change experienced by the dust particle is

$$\delta p = \frac{-h\nu}{c}\left(1 + \frac{v}{c}\cos\theta\right)\cos\theta$$

for momentum p, Planck's constant h, and the speed of light c. Summing up the momentum change over all θ and ϕ results in the average momentum change to the particle per photon:

$$\Delta p = 4\pi \int\int \delta p \sin\theta \, d\phi \, d\theta$$

$$= 4\pi \int_0^{\pi} \int_0^{2\pi} \frac{-h\nu}{c}\left(1 + \frac{v}{c}\cos\theta\right)\cos\theta \sin\theta \, d\phi \, d\theta$$

$$= \frac{-h\nu\nu}{3c^2}$$

The number of photons per second (n) hitting a particle of radius a at a distance r from a star of luminosity L_* (where ν is the average frequency of a photon from the sun) can be calculated:

n = # incident photons * area ptl ÷ surface area of sphere with radius r

$$= \frac{L_*}{\langle h\nu \rangle} \frac{\pi a^2}{4\pi r^2} = \frac{L_*}{4\langle h\nu \rangle} \frac{a^2}{r^2}$$

The momentum change of the particle can then be written:

$$\frac{dp}{dt} = n\,\Delta p = \frac{-L_* \nu a^2}{12 c^2 r^2} \qquad (1)$$

A particle of mass m with a Keplerian velocity v has angular momentum A defined by:

$$A = mrv \qquad (2)$$

and

$$\frac{dA}{dt} = r \frac{dp}{dt} \qquad (3)$$

Combining (1) and (3) yields

$$\frac{dA}{dt} = r \frac{-L_* \nu a^2}{12 c^2 r^2} = \frac{-L_* \nu a^2}{12 c^2 r} \qquad (4)$$

and with the orbital velocity $v = (G M_* / r)^{1/2}$ for the gravitational constant G and the mass of the white dwarf M_*, differentiate (2) to get:

$$\frac{dA}{dt} = \frac{d}{dt} m (G M_* r)^{1/2} = \frac{m}{2} (G M_* / r)^{1/2} \frac{dr}{dt}$$

$$= \frac{m v}{2} \frac{dr}{dt} \qquad (5)$$

Combining (4) and (5) and solving for dr/dt:

$$\frac{dr}{dt} = \frac{- L_* a^2}{6 m c^2 r}$$

but $m = (4/3) \pi a^3 \rho$, where ρ is the density of the dust grain, so that

$$\frac{dr}{dt} = \frac{- L_*}{8 \pi \rho c^2} \frac{1}{a r} \qquad (6)$$

Since the rate at which the particle moves into the star depends on its radius *a* and *a* will change as the particle approaches the star, it will be necessary to have an expression for *a* as a function of r. MacQueen (1968) provides an such an equation for sublimation rate of a spherical particle:

$$\frac{da}{dt} = \frac{-1}{\rho} \left(\frac{m_H \mu}{2 \pi k T} \right)^{1/2} P \qquad (7)$$

where m_H is the atomic weight of hydrogen, μ is the molecular weight of the substance in question, k is the Boltzmann constant, T is the temperature of the particle, and P is the vapor pressure, given by the Clausius-Clapeyon expression involving the material constants A and B:

$$\log_{10} P = \frac{- A}{T} + B \qquad (8)$$

The temperature of a particle with albedo α can be found as a function of r. A spherical particle absorbs the energy E_a from the star, which is the following fraction:

$$E_a = \frac{\pi a^2}{4 \pi r^2} L_* (1-\alpha)$$

The particle will emit, according to the blackbody flux law with the Stefan-Boltzmann constant σ,

$$E_e = \sigma T^4 \pi a^2$$

In a system in equilibrium $E_a = E_e$, so

$$T = \left(\frac{L_* (1-\alpha)}{4 \pi \sigma r^2}\right)^{1/4} = \frac{t_0}{r^{1/2}} \quad \text{for } t_0 = \left(\frac{L_* (1-\alpha)}{4 \pi \sigma}\right)^{1/4} \tag{9}$$

Combining (7), (8), and (9) yields:

$$\frac{da}{dt} = -c_0 \, r^{1/4} \, 10 \wedge (-c_1 \, r^{1/2}) \tag{10}$$

where $c_0 = \frac{10^B}{\rho} \frac{m_H \, \mu}{2 \pi k t_0}$ and $c_1 = \frac{A}{t_0}$

Equation (6) can be simplified by writing it as:

$$\frac{dr}{dt} = \frac{-c_2}{a \, r} \tag{11}$$

where $c_2 = \frac{L_*}{8 \pi \rho c^2}$

Equations (10) and (11) are interdependent and best solved numerically. Using a C code to apply the fourth order Runge-Kutta method to the differential equations, I found approximate values for the distance of sublimation from the center of the star for three different materials. The graphic result of a single run of the program is shown in Figure 3, and the numerical results for various values of a and L_* are shown in Figure 4.

Note: for all calculations in Figure 4 I started with a stepsize of one year, but for accuracy had functions built in to the code to lengthen or shorten the stepsize according to whether the radius of the particle was changing rapidly or not. This led to the strange oscillation of step size apparent at the top right hand portion of the graph, but produced more accurate results once the particle started to evaporate.

PART IV: THE EFFECTS OF THE DWARF'S MAGNETIC FIELD

The molecules from the dust particles are likely to be quickly ionized after sublimation. In the absence of a stellar magnetic field, the ions will continue to experience the Poynting-Robertson drag which, in addition to the growing gravitational field and the absence of a stellar wind (as is

Figure 3: Sublimation Distance

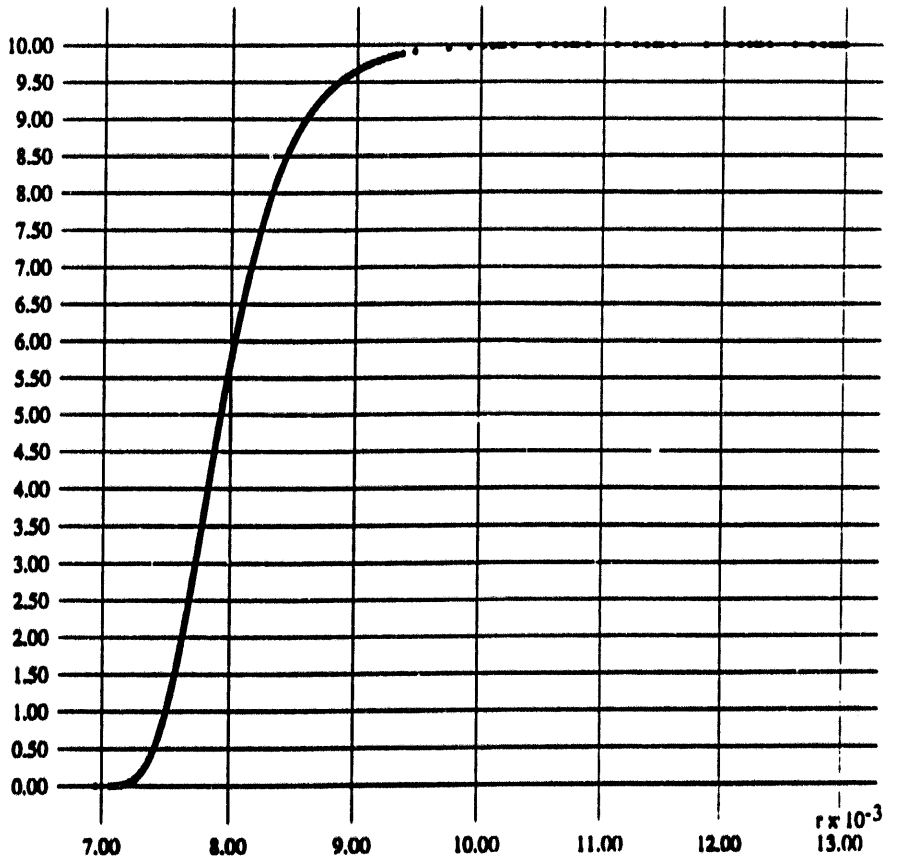

Figure 3: A graph of sun-particle distance (r in a.u.) versus particle radius (a in microns). A 10 micron graphite particle is used for this calculation and dwarf luminousity is .01 times solar luminousity.

dwarf lum.	grain radius in microns: 10 μ	1 μ	.1 μ	.01μ
	a: iron grains			
.001 Lo	1.33	1.34	1.37	1.40
.005 Lo	2.91	2.99	3.07	3.14
.01 Lo	4.14	4.15	4.18	4.44
	b: silicate grains			
.001 Lo	.837	.839	.846	.859
.005 Lo	1.87	1.88	1.90	1.92
.01 Lo	2.64	2.66	2.67	2.72
	c:graphite grains			
.001 Lo	.477	.478	.484	.493
.005 Lo	1.06	1.06	1.08	1.10
.01 Lo	1.51	1.52	1.53	1.56

Figure 4: Sublimation distance in solar radii for various types of grains as a function of initial grain radius and dwarf luminousity. (Lo is solar luminousity.)

assumed for the high surface gravity dwarf stars), will pull the ions into the dwarf's atmosphere. However, it seems very unlikely that a dwarf star will have no magnetic field. Because observed white dwarfs show no detectable magnetic field and it is suggested that a field greater than 10 kilogauss would be detectable (Schmidt et. al., 1992), I will use 10 kilogauss as the value of my model star's magnetic field. This insures that any calculation done involving the effects of the magnetic field are at a maximum, so I'm considering a worst case scenario.

Just to be safe, I did a quick calculation of the Lorentz force caused by the stellar magnetic field as compared to the pull of gravity on the pre-sublimized grains. (Figure 5) If the Lorentz force becomes larger than gravity, then the particle will not have the Keplerian velocity used in equations 2 through 10 and it's movements will be controlled be the magnetic field lines, not the Poynting-Robertson drag. However, Figure 5 shows that gravity is the dominate force on dust grains at the point of sublimation. The particles will therefore reach sublimation distance and evaporate before the magnetic force becomes strong enough to control their motions. After sublimation occurs, on the other hand, I find that the Lorentz force will strongly dominate the motions of ions (Figure 6) at sublimation distance. So my model dwarf will now have a magnetosphere made up of ions from interstellar dust particles. To find out how these ions can reach the atmosphere, it is necessary to explore how charged particles move in a dipole magnetic field.

Charged particles in the presence of a magnetic field follow the path shown in Figure 7. Point S is at the point of sublimation where the ions begin their movement under the influence of the magnetic field. As the particle moves along the field line towards the north or south pole of the star, the strengthening of the field forces all of the particle's kinetic energy into gyration, which is perpendicular to the magnetic field line. Energy must be conserved, so the ion's motion parallel to the field line (towards the surface of the star) decreases as the gyration increases and finally the inward motion stops at the mirror point M. The magnetic force then pushes the ion away, so that the ion follows the field line back around to the opposite pole, in effect oscillating between the north and south mirror points as it gyrates around the field lines and slowly drifts east or west according to its charge. The height of the mirror point M above the surface of the dwarf depends on the angle β that the initial velocity of the ion makes with the B field, so that there is a loss cone defined by β that allows a fraction of particles to mirror close enough to the white dwarf to be caught up in the atmosphere and escape the magnetosphere.

Parks (1991) contains a detailed analytical explanation of the probability that a particle will escape the magnetosphere. To calculate this probability, Parks defines a loss cone of certain values of the angle β (introduced above) that will allow particles to be lost. Using geometry known about plasmas in magnetic "bottles," he then shows that β can be written as a function of the relative strengths of the magnetic field encountered by the charged particle so that the probability of particle loss P is a function of these magnetic field strengths and the unknown angle β is out of the calculation. If B_m is the strength of the magnetic field at the mirror point and B_s is the strength of the field when the particle is at its furthest distance from the star, which in this case is the sublimation distance, then

$$P = 1 - \left(1 - \frac{1}{R}\right)^{1/2} \qquad (12)$$

where, for the sublimation distance r_s corresponding to B_s and the mirror distance r_m corresponding to B_m,

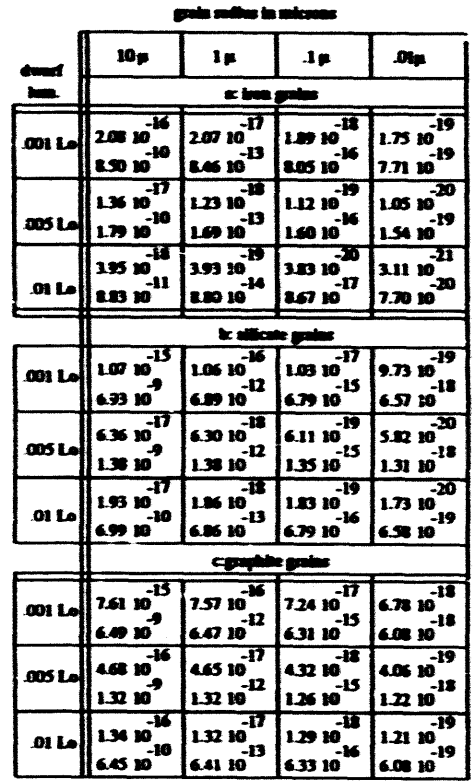

dwarf lum.	grain radius in microns: 10μ	1μ	.1μ	.01μ
	a: iron grains			
.001 Lo	$2.08\ 10^{-16}$ $8.50\ 10^{-10}$	$2.07\ 10^{-17}$ $8.46\ 10^{-13}$	$1.89\ 10^{-18}$ $8.05\ 10^{-16}$	$1.75\ 10^{-19}$ $7.71\ 10^{-19}$
.005 Lo	$1.36\ 10^{-17}$ $1.79\ 10^{-10}$	$1.23\ 10^{-18}$ $1.69\ 10^{-13}$	$1.12\ 10^{-19}$ $1.60\ 10^{-16}$	$1.05\ 10^{-20}$ $1.54\ 10^{-19}$
.01 Lo	$3.95\ 10^{-18}$ $8.83\ 10^{-11}$	$3.93\ 10^{-19}$ $8.80\ 10^{-14}$	$3.83\ 10^{-20}$ $8.67\ 10^{-17}$	$3.11\ 10^{-21}$ $7.70\ 10^{-20}$
	b: silicate grains			
.001 Lo	$1.07\ 10^{-15}$ $6.93\ 10^{-9}$	$1.06\ 10^{-16}$ $6.89\ 10^{-12}$	$1.03\ 10^{-17}$ $6.79\ 10^{-15}$	$9.73\ 10^{-19}$ $6.57\ 10^{-18}$
.005 Lo	$6.36\ 10^{-17}$ $1.38\ 10^{-9}$	$6.30\ 10^{-18}$ $1.38\ 10^{-12}$	$6.11\ 10^{-19}$ $1.35\ 10^{-15}$	$5.82\ 10^{-20}$ $1.31\ 10^{-18}$
.01 Lo	$1.93\ 10^{-17}$ $6.99\ 10^{-10}$	$1.86\ 10^{-18}$ $6.86\ 10^{-13}$	$1.83\ 10^{-19}$ $6.79\ 10^{-16}$	$1.73\ 10^{-20}$ $6.58\ 10^{-19}$
	c:graphite grains			
.001 Lo	$7.61\ 10^{-15}$ $6.49\ 10^{-9}$	$7.57\ 10^{-16}$ $6.47\ 10^{-12}$	$7.24\ 10^{-17}$ $6.31\ 10^{-15}$	$6.78\ 10^{-18}$ $6.08\ 10^{-18}$
.005 Lo	$4.68\ 10^{-16}$ $1.32\ 10^{-9}$	$4.65\ 10^{-17}$ $1.32\ 10^{-12}$	$4.32\ 10^{-18}$ $1.26\ 10^{-15}$	$4.06\ 10^{-19}$ $1.22\ 10^{-18}$
.01 Lo	$1.34\ 10^{-16}$ $6.45\ 10^{-10}$	$1.32\ 10^{-17}$ $6.41\ 10^{-13}$	$1.29\ 10^{-18}$ $6.33\ 10^{-16}$	$1.21\ 10^{-19}$ $6.08\ 10^{-19}$

FIGURE 5: A comparison of Lorentz force q(vxB) to gravitational force GmM/r on dust grains if they have a surface potential of about 1 volt. The top values are the Lorentz force, the bottom gravitational, both in Newtons. This shows that for grains larger than .01 micron, the dwarf's magnetic field doesn't control the grain's motion.

dwarf lum.	radius of source grain in microns: 10 μ	1 μ	.1 μ	.01μ
	a: iron ions			
.001 Lo	$3.00\ 10^{-20}$ $8.61\ 10^{-24}$	$2.97\ 10^{-21}$ $8.57\ 10^{-27}$	$2.72\ 10^{-22}$ $8.15\ 10^{-30}$	$2.52\ 10^{-23}$ $7.80\ 10^{-33}$
.005 Lo	$1.96\ 10^{-21}$ $1.81\ 10^{-24}$	$1.77\ 10^{-22}$ $1.71\ 10^{-27}$	$1.61\ 10^{-23}$ $1.62\ 10^{-30}$	$1.51\ 10^{-24}$ $1.56\ 10^{-33}$
.01 Lo	$5.69\ 10^{-22}$ $8.94\ 10^{-25}$	$5.65\ 10^{-23}$ $8.91\ 10^{-28}$	$5.50\ 10^{-24}$ $8.77\ 10^{-31}$	$4.48\ 10^{-25}$ $7.80\ 10^{-34}$
	b: silicon ions			
.001 Lo	$1.53\ 10^{-19}$ $1.10\ 10^{-23}$	$1.52\ 10^{-20}$ $1.09\ 10^{-26}$	$1.48\ 10^{-21}$ $1.08\ 10^{-29}$	$1.40\ 10^{-22}$ $1.04\ 10^{-32}$
.005 Lo	$9.14\ 10^{-21}$ $2.20\ 10^{-24}$	$9.06\ 10^{-22}$ $2.19\ 10^{-27}$	$8.78\ 10^{-23}$ $2.15\ 10^{-30}$	$8.36\ 10^{-24}$ $2.09\ 10^{-33}$
.01 Lo	$2.77\ 10^{-21}$ $1.11\ 10^{-24}$	$2.68\ 10^{-22}$ $1.09\ 10^{-27}$	$2.63\ 10^{-23}$ $1.08\ 10^{-30}$	$2.49\ 10^{-24}$ $1.04\ 10^{-33}$
	c:carbon ions			
.001 Lo	$1.09\ 10^{-18}$ $1.45\ 10^{-23}$	$1.09\ 10^{-19}$ $1.44\ 10^{-26}$	$1.04\ 10^{-20}$ $1.40\ 10^{-29}$	$9.75\ 10^{-21}$ $1.35\ 10^{-32}$
.005 Lo	$6.73\ 10^{-20}$ $2.94\ 10^{-24}$	$6.69\ 10^{-21}$ $2.93\ 10^{-27}$	$6.22\ 10^{-22}$ $2.81\ 10^{-30}$	$5.84\ 10^{-23}$ $2.71\ 10^{-33}$
.01 Lo	$1.92\ 10^{-20}$ $1.44\ 10^{-24}$	$1.90\ 10^{-21}$ $1.43\ 10^{-27}$	$1.86\ 10^{-22}$ $1.41\ 10^{-30}$	$1.73\ 10^{-23}$ $1.35\ 10^{-33}$

FIGURE 6: A comparison of Lorentz force q(vxB) to gravitational force GmM/r on ions at sublimation distance. The top values are Lorentz force, the bottom gravitational, both in Newtons. The Lorentz force was calculated for +1 ions, which give the lowest value possible, but it is still obvious that the magnetic field will dominate the particle's motion. Note: In part b silicon was used instead of oxygen since silicon ions are heavier and gravity will be greater on them.

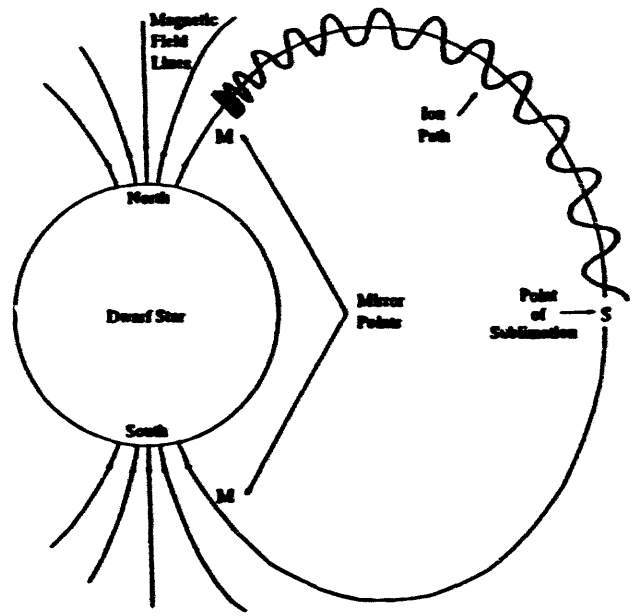

Figure 7: The trajectory of an ion in a dipole magnetic field. The ion will also drift east to west as it oscillates between the north and south mirror points.

$$R = \frac{B_m}{B_s} = \frac{r_s^3}{r_m^3} = \frac{r_s^3}{(R_* + h)^3} \qquad (12a)$$

Figure 8 shows calculated values of P for iron ions as a function of height h above the surface of the dwarf star with the dwarf's radius estimated at $R_* = .0115R_{sun}$, an average value of observed white dwarf radius. (Liebert, 1980) The probability of particle loss is small, in the range of 10^{-6} to 10^{-8}, but the fact that ions can escape the magnetosphere suggests that there exists a stable state where the same amount of material escapes the magnetosphere as enters through Poynting-Robertson drag.

But P represents the amount of loss when the particles pass the mirror point the first time only. The fraction lost after the ions travel to the opposite pole and mirror a second time depends on how many particles undergo Rutherford scattering and move into the loss cone defined by the angle β. To estimate the time needed to fill the loss cone, it is necessary to find the scattering cross section of the ions and calculate the time it takes for all of the ions to undergo at least one collision. After each particle has had a collision, the velocities of the ions in the plasma will be randomly scattered and the loss cone will be full. Therefore, if all ions undergo at least one collision in a relatively short amount of time, then a significant amount of particles will be able to escape at each mirror point and the eventual state of equilibrium descibed above can be reached.

I define a collision as the event that two ions come close enough to each other that their kinetic energy equals their electrostatic potential energy, or

$$\frac{1}{2} m v^2 = \frac{1}{4 \pi \varepsilon_o} \frac{q^2}{d}$$

for the charge on the ion q, the permittivity constant ε_o, the distance d, and each ion's mass and velocity m and v (assumed to be equal). Solving for d:

$$d = \frac{q^2}{2 \pi \varepsilon_o m v^2}$$

The collisional cross section σ_c is then defined as:

$$\sigma_c = \pi d^2 = \frac{q^4}{4 \pi \varepsilon_o^2 m^2 v^4} \qquad (13)$$

If the ion is moving at a velocity v for a time t, it sweeps out a volume $\sigma_c v t$

Next I make an approximation of the particle density η in the magnetosphere. To guess at the volume of the ion cloud, I model it as a cylinder from the surface of the dwarf to the sublimation point that extends from one stellar radii below the star to one stellar radii above it for a total height of 4 times the radius of the star (see Figure 9). This model of the shape of the magnetosphere gives an intentionally large volume so that the particles will be more spread out in my model than in a real

Figure 8: Probability of Ptl Mirroring at Height h

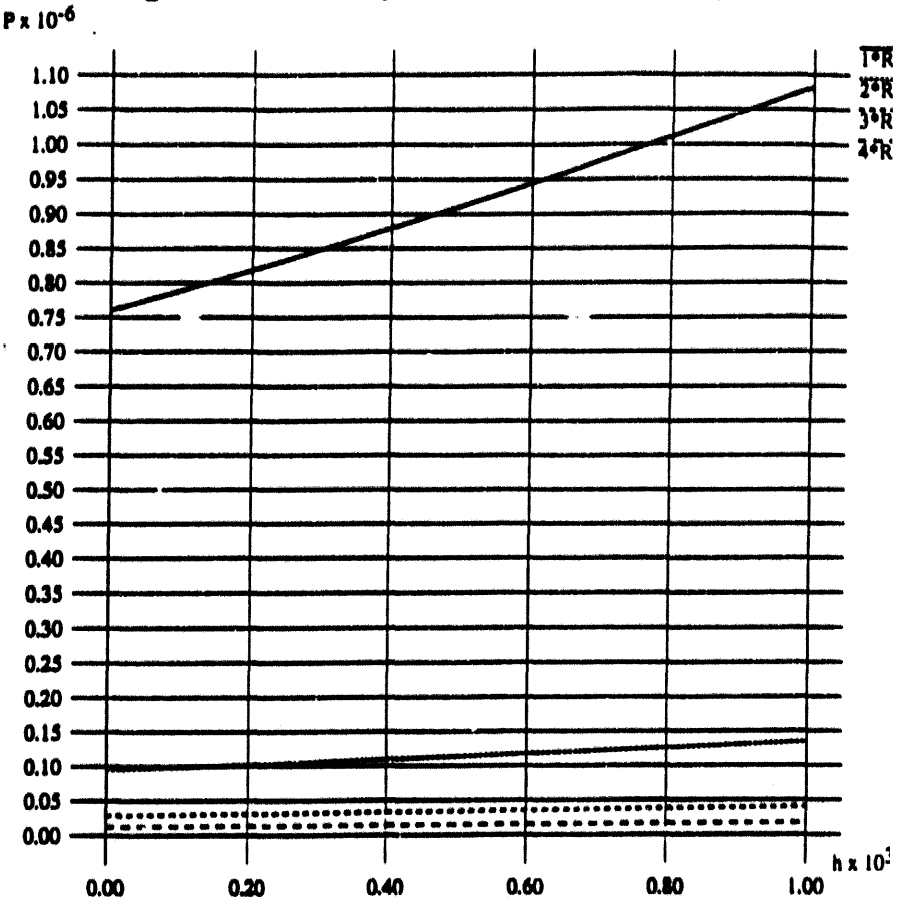

Figure 8: The probability of particle loss depends on the height at which it mirrors. There are four graphs shown, one for each of four different sublimation distances as labeled to the right of the graph. The vertical axis is the probability of the particle mirroring at height h above the dwarf's surface. (Rs is the solar radius.)

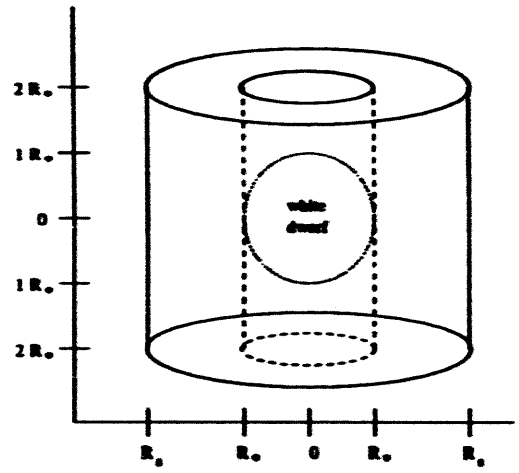

FIGURE 9: Model of the magnetosphere used to calculate ion density. The volume used in equation 14 is that of a cylinder with inner radius $R_\oplus$, outer radius Rs, and height 4 $R_\oplus$.

magnetosphere and the time calculated for all particles to collide and scatter will be an upper limit. The volume of the cylinder is $\pi (r_s^2 - R_*^2)\, 4 R_*$. If the total number of ions in this volume is N, the mass of a single ion is m, and the rate at which material enters the magnetosphere is δm, then the ion density is:

$$\eta = \frac{N}{V} = \frac{\delta m\, t}{m V} = \frac{\delta m\, t}{4 \pi m R_* (r_s^2 - R_*^2)} \qquad (14)$$

I assume all particles have collided when $\eta \sigma_c v t = 1$, so

$$\frac{\delta m\, t}{4 \pi m R_* (r_s^2 - R_*^2)} \; \frac{q^4\, t}{4 \pi \varepsilon_o^2 m^2 v^4} = 1$$

$$t = \frac{4 \pi \varepsilon_o}{q^2} (m v)^{3/2} \left(\frac{R_* (r_s^2 - R_*^2)}{\delta m} \right)^{1/2} \qquad (15)$$

The velocity of the ions is found as the Keplerian velocity $(G M_*/\langle r \rangle)^{1/2}$ (with $M_* = .6\, M_{sun}$ and $\langle r \rangle = .15\, R_{sun}$) minus the average velocity of stellar rotation, 8 km/s. (Liebert, 1980) Kumar et. al. (1989) estimate that the solar dust cloud needs 10^4 kg/s of dust to replentish that lost to Poynting-Robertson drag, so I use 10^4 kg/s as the value of δm for my model system's star. With the following values:

$q (Fe^{+2}) = 2 (1.6 \times 10^{-19}\, C) = 3.2 \times 10^{-19}\, C$
m (1 Fe ion) $= 9.33 \times 10^{-26}$ kg
$R_* = .0115\, R_{sun} = 8.0 \times 10^6$ m
$r_s = .291\, R_{sun} = 2.03 \times 10^8$ m

I find the scattering times shown in Figure 10 which range from 2 to 17 years, depending on the sublimation distances as found in Part II of this paper (Figure 4).

PART V: CONCLUSION

In this paper I have shown that it is possible to trace the motions of accreting dust particles mathematically and I have reached two main conclusions: 1) the Poynting-Robertson drag is an effective means of transport for micron sized dust particles, and 2) the presence of a small magnetic field around the dwarf will not hinder dust accretion.

The calculations done in this paper further show that the presence of a magnetosphere around a white dwarf may be important to the observed spectrum of the white dwarf. Because the probability of particle escape from the magnetosphere is constant but very small, there must be a

Figure 10: Scattering Time

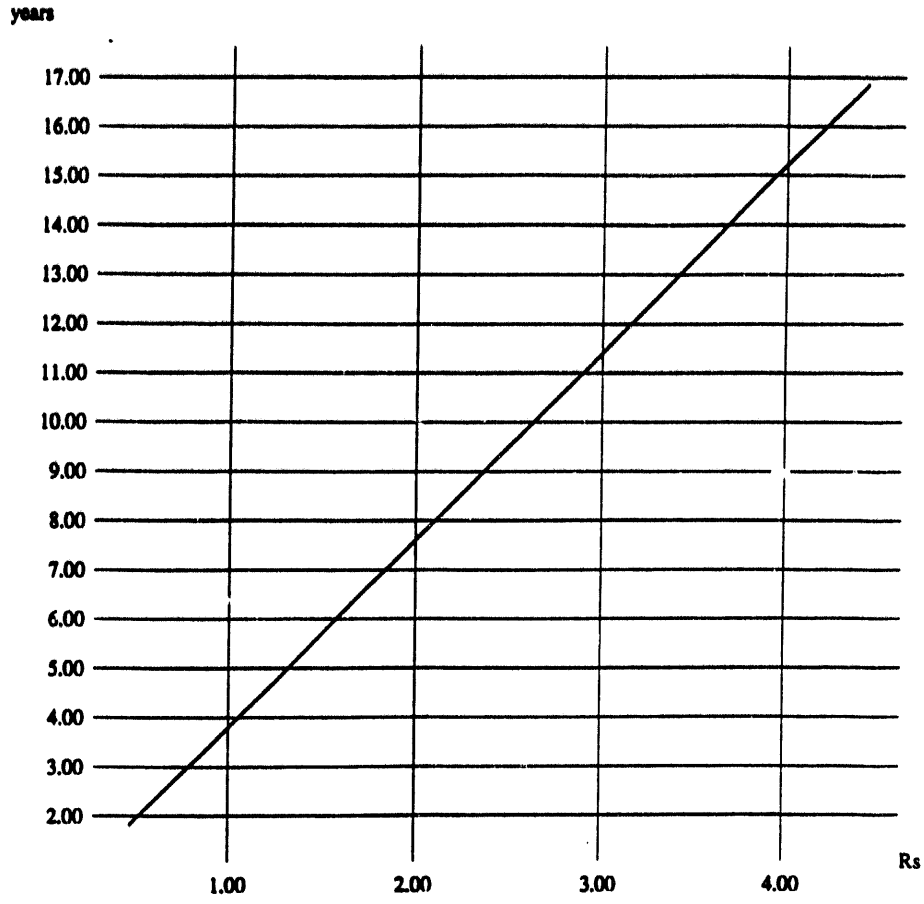

Figure10: A graph of equation 15 shows the time to fill the loss cone (in years) as a function of sublimation distance (in solar radii).

large build up of ions around the star before a state of equilibrium between the entering and escaping material is reached. The effects of a dense magnetosphere on the absorption lines of the light emitted by the star is a good topic for further research.

Also left for further study is the relative amounts of ions in the dwarf's magnetosphere, which may lead to a deeper understanding of why there is no hydrogen observed in DB dwarves. A more detailed model of the dust environment of a white dwarf's system, such as what could survive the red giant phase, would make to the calculations done in this paper more applicable to observed situations.

BIBLIOGRAPHY

Alcock, C. and Illarionov (1980) *Astrophys. J.* **235**, p. 534.

Bohm, K.H. (1971) in IAU Symp. 42, *White Dwarfs* ed. W.J. Luyten, (Dordrecht, Holland: D. Reidel Publishing Co.) p. 130.

Greenberg, J.M. (1991) in *Origin and Evolution of Interplanetary Dust* ed. A.C. Levasseur-Regourd and H. Hasegawa, (Dordrecht, Netherlands: Kluwer Academic Publishers Group) p. 155.

Hovenier, J.W., and Bosma, P.B. (1991) in *Origin and Evolution of Interplanetary Dust* ed. A.C. Levasseur-Regourd and H. Hasegawa, (Dordrecht, Netherlands: Kluwer Academic Publishers Group) p. 155.

Kneissel, B., and Mann, I. (1991) in *Origin and Evolution of Interplanetary Dust* ed. A.C. Levasseur-Regourd and H. Hasegawa, (Dordrecht, Netherlands: Kluwer Academic Publishers Group) p. 139.

Koester, D., and Finley, D. (1992) in Lecture Notes in Physics 401, *The Atmospheres of Early-Type Stars* ed. U. Heber and C.S. Jeffrey, (Berlin: Springer-Verlag) p. 314.

Kumar, C.K., Davila, J.M., and Rajan, R.S. (1989) *Astrophys. J.* **337**, p. 414.

Levasseur-Regourd, A.C., Renard, J.B., and Dumont, R. (1991) in *Origin and Evolution of Interplanetary Dust* ed. A.C. Levasseur-Regourd and H. Hasegawa, (Dordrecht, Netherlands: Kluwer Academic Publishers Group) p. 131.

Liebert, J. (1980) in *Ann. Rev. Astron. Astropys.* ed. B. Burbidge, D. Layzer, and J.G. Phillips, (Palo Alto, CA: Annual Reviews, Inc.) **18**, p. 363.

MacQueen, R.M. (1968) *Astrophys. J.* **154**, p. 1059.

Mihalas, D., and Binney, J. (1981) *Galactic Astronomy* (San Francisco: W.H. Freeman and Co.).

Oke, J.B. (1971) in IAU Symp. 42, *White Dwarfs* ed. W.J. Luyten, (Dordrecht, Holland: D. Reidel Publishing Co.) p. 67.

Parks, G.K. (1991) *Physics of Space Plasmas* (Redwood City, CA: Addison-Wesley Publishing Co.)

Schmidt, G.D., Stockman, H.S., and Smith, P.S. (1992) *Astrophys. J. Letters* **398**, p. L57.

van Horn, H.M. (1971) in IAU Symp. 42, *White Dwarfs* ed. W.J. Luyten, (Dordrecht, Holland: D. Reidel Publishing Co.) p. 97.

Wiedermann, V. (1971) in IAU Symp. 42, *White Dwarfs* ed. W.J. Luyten, (Dordrecht, Holland: D. Reidel Publishing Co.) p. 81.

Zielik, M., Gregory, S.A., and Smith, E.v.P. (1992) *Introductroy Astronomy and Astrophysics* (Orlando, FL: Saunders College Publishing).

MOIRÉ DEFLECTOMETRY FOR HIGH-DENSITY PLASMA CHARACTERIZATION*

Dana E. Lehr

Bucknell University

Lawrence Livermore National Laboratory
Livermore, California 94550

May 19, 1993

Prepared in partial fulfillment of the requirements of the Science and Engineering Research Semester under the direction of David Ress, Research Mentor, at the Lawrence Livermore National Laboratory.

*This research was supported in part by an appointment to the U.S. Department of Energy Science and Engineering Research Semester (hereinafter called SERS) program administered by LLNL under Contract W-7405-Eng-48 with Lawrence Livermore National Laboratory.

Abstract

We report the development of a soft-x-ray Moiré deflectometer at the Nova laser facility. Moiré deflectometry is a scheme for plasma density diagnosis which provides line-integrated measurements of the electron density gradient along a single dimension. A 15.5-nm yttrium x-ray laser beam is collimated and sent through a plasma subject, where the initially parallel rays of incident light are refracted in relation to the electron density gradient. We measure these deflections as fringe shifts in a Moiré interference pattern produced by two angularly-offset Ronchi rulings. In our experiments we have produced a high-contrast Moiré deflectogram of a laser-irradiated CH plasma in which the electron density reached 2 x 10^{21} cm^{-3}. This is well above the measured limits of any previous methods of plasma density characterization.

Introduction

In experimental plasma research it is often desirable to measure the spatial density distribution of a given plasma subject. Currently, the predominant method of density diagnosis makes use of interferometry, a scheme which is presently restricted to the use of ultraviolet light or lower-frequency radiation. These measurements are typically limited to line-integrated electron densities of less than 2×10^{19} cm^{-2}. So, given a typical scale-length of 1 mm for laser-produced plasmas, UV-interferometry is a useful diagnostic up to densities of only about 2×10^{20} cm^{-3}. Research efforts in high-density plasmas, such as inertial-confinement fusion (ICF), weapons physics, laser-material interactions and hydrodynamics, require a diagnostic which can measure electron densities which exceed present capabilities. Hence, it is desirable to develop a new method of density characterization which can utilize higher-energy radiation to probe particularly dense plasmas. Specifically, the use of soft x-rays instead of UV light would increase the measurable density range by at least two orders of magnitude.

Using the Nova laser research facilities at the Lawrence Livermore National Laboratory (LLNL) in Livermore, California, we are developing a new method of density characterization which utilizes an x-ray laser as a probe to measure plasma densities. Specifically, using a yttrium x-ray laser at 15.5 nm, we can expect to measure a line-integrated electron density of up to 5×10^{21} cm^{-2}. Again assuming a typical 1-mm-scale-length plasma, this corresponds to an electron density of up to 5×10^{22} cm^{-3}, many times the critical density of 0.35-μm radiation. The use of x-ray radiation thus allows us to probe the higher- density plasmas which are under current study in ICF as well as in other areas of plasma research.

Moiré deflectometry is a simple scheme which can easily utilize an x-ray source to characterize plasma densities. This technique provides line-integrated measurements

of the electron density gradient along a single dimension. Here we have succeeded in using a yttrium x-ray laser as the illumination source to produce a high-contrast Moiré deflectogram of a laser-produced CH plasma in which the electron density reached 2×10^{21} cm^{-3}. This is well above the measured limits of any previous methods of plasma density characterization.

Principle of Moiré Deflectometry

Moiré deflectometry is a general, nondestructive technique for testing the optical properties of a given object.[1] Used as a technique for plasma density diagnosis, Moiré deflectometry provides a map of ray deflections corresponding to electron density gradients within an inspected plasma.

To produce a Moiré deflectogram, a collimated light source is directed through the subject plasma. As the beam propagates through the plasma, the initially parallel rays of incident light are refracted in relation to the gradient of the index-of-refraction in the plasma, where the total deflection is proportional to the line-integrated gradient of the refractive index. The plasma index-of-refraction, N, is, in turn, related to the electron density, n_e, by

$$N = \sqrt{1 - \frac{n_e}{n_c}}, \tag{1}$$

where n_C is the critical density of the probe radiation. (For 15.5-nm radiation, $n_C = 4.8 \times 10^{24}$ cm^{-3}.) Hence, the angular deflections in the probe beam are related to the electron density gradient in the plasma by

$$\phi(x,y) = \int \frac{\partial N(x,y)}{\partial x} dz \cong -\frac{1}{2} \int \frac{\partial}{\partial x} \left(\frac{n_e(x,y)}{n_c} \right) dz, \tag{2}$$

where we have assumed $n_e << n_C$.

In order to measure the actual deflections in the source beam, we utilize a geometrical interference pattern known as the Moiré effect. A Moiré pattern is produced whenever two transmitting materials of a similar motif are overlapped and illuminated. In the measurement of plasma densities we use a pair of one-dimensional transmission gratings (Ronchi rulings) consisting of equally spaced bands of opaque and transmitting materials to produce a Moiré pattern similar to that shown in Figure 1. When two rulings of pitch p are overlapped at an angle θ, a Moiré fringe pattern is produced. The actual pattern consists of chains of alternating dark and bright rhombic-shaped regions. When averaged by the eye or a detection system, however, the pattern reduces to a periodic series of dark and bright straight fringes. The dark fringes occur at the intersections of the opaque regions of the Ronchi rulings with spacing $s = p/\theta$.

When the collimated light source is propagated through a subject plasma prior to incidence on the Ronchi rulings, the angular deflections in the initially parallel rays appear as fringe shifts in the Moiré pattern. Specifically, for an angular deflection of ϕ, the spatial shift of a fringe is given by

$$\Delta s = \phi \frac{d}{\theta}. \tag{3}$$

where d is the separation between the two Ronchi rulings. Hence, from Eq. (2) we see that the fringe shifts in the Moiré pattern are proportional to the line-integrated density gradients in the plasma. By measuring the relative spatial shifts in the Moiré fringe pattern, we can integrate to find a one-dimensional density profile.

The sensitivity of Moiré deflectometry is ideally determined by the minimum discernible fringe shift, which, in turn, depends upon the spacing of the Moiré fringes. Recalling that the fringe spacing s is given by the ratio p/θ, from Eq. (3) we find that the relative fringe shift due to an angular deflection of ϕ is given by

$$\frac{\Delta s}{s} = \phi \frac{d}{p}. \tag{4}$$

It follows that a relative shift of one fringe corresponds to a deflection angle p/d. Hence, the measurement sensitivity of Moiré deflectometry is easily improved by decreasing the

ratio of the pitch of the rulings to the distance of their separation. Ultimately, however, the sensitivity of the experiment is determined by the diffraction limit of the system.

To produce Moiré deflectograms with good fringe visibility, one must minimize the effects due to diffraction. The Talbot self-imaging distance (or Fourier image plane) of a transmission grating is given by

$$d_t = \frac{p^2}{\lambda}. \tag{5}$$

(For the 15.5-nm yttrium x-ray laser and Ronchi rulings of 10-μm pitch, d_t = 6.45 mm.) When a grating is illuminated by a collimated light source, exact replicas of the object grating are imaged at distances that are integer multiples of d_t. More specifically, at even multiples of d_t the image is equivalent to the object grating, while at odd multiples of d_t a negative image is produced. Thus, in our Moiré experiment the diffraction due to the Ronchi rulings is minimized and the Moiré fringe visibility reaches a maximum when the second Ronchi ruling is placed at one of the even-numbered Talbot planes of the first. Similarly, the fringe contrast is reversed when the two gratings are separated by an odd number of Talbot planes. As the second ruling moves off of a Talbot plane, the absolute fringe visibility decreases until, at a point midway between the Talbot planes, the contrast goes to zero (i.e., the Moiré pattern disappears completely).[2] Hence, to produce Moiré deflectograms with good fringe visibility the separation between the two Ronchi rulings, as well as the separation between the second ruling and the detector, must be close to an integer multiple of the Talbot self-imaging distance.

Experimental Apparatus

The experimental program to utilize Moiré deflectometry as a plasma density diagnostic is being conducted at the two-beam Nova laser facility at LLNL. Nova

consists of a 120-kJ (at 1.06 μm), ten-beam Nd:glass laser facility. One or two of these ten beams can be diverted into a two-beam target chamber and used to pump an x-ray laser. To produce an x-ray laser, the Nova beams are line-focused onto a metal thin-foil target placed at the center of the two-beam chamber, which is maintained at a high vacuum (10^{-6} torr). The beams deposit their energy into the foil target, converting it into a plasma with a short-lived population inversion between excited states. Unlike most lasers, there is no cavity to support oscillations for multiple-pass gain in the lasing region. Rather, the Nova-driven x-ray laser emits a short burst of amplified spontaneous emission with a single pass through the gain channel. With suitable geometry of the foil target, one can make a directional beam with substantial coherence.

An x-ray laser produced at the two-beam Nova facility is used as the probe beam for the development of Moiré deflectometry. Our experimental set-up utilizes a yttrium x-ray laser which operates at 15.5 nm to probe the subject plasma.

A schematic of the optical arrangement for Moiré deflectometry is shown in Figure 2. The plasma to be characterized is produced by illuminating a plastic or foil target with one of Nova's beams. The second of the two Nova beams is line-focused onto a thin-foil yttrium x-ray laser target to produce the x-ray laser probe beam. The x-ray beam strikes a collimating mirror before returning to pass through the laser-produced plasma. The mirrors used in this experiment are special multi-layer mirrors designed to give high reflectance over a bandpass which includes the 15.5-nm x-ray laser probe. As the probe beam propagates through the subject plasma, the initially parallel rays of the collimated x-ray laser beam are deflected by density gradients within the plasma. After exiting the plasma subject, the probe beam reflects off an imaging mirror and passes through the two angularly-offset Ronchi rulings and into an x-ray detector. In early experiments x-ray film was used to record the Moiré deflectogram; more recently we use a x-ray CCD camera to image the fringe pattern.

Unwanted radiative emissions from the subject plasma can reduce fringe visibility and increase the noise level at the detector. To reduce the amount of unwanted light which reaches the detector, filters are positioned in the course of the x-ray probe beam which attenuate undesirable radiation. Spatial filters are placed between the x-ray laser source and the collimating mirror and between this mirror and the plasma subject, and the apertures of the multi-layer mirrors serve to reduce the line-of-sight of the detector. Within the line-of-sight, hard x-rays are attenuated by x-ray filters positioned directly in front of the Ronchi rulings, and the multi-layer mirrors provide low reflectance outside a narrow bandpass centered on the 15.5-nm line of the x-ray laser.

The alignment of the Moiré deflectometry set-up is done prior to each experiment using a red diode laser placed at the center of the target chamber to mock the x-ray laser. The diode laser is focused to a known point which is aligned at chamber center. After the optics and detector have been aligned using this visible beam, the diode laser is replaced with the x-ray laser target such that the x-ray laser beam will follow the same course as the beam of the diode laser.

Results

The first demonstration of a simple Moiré fringe pattern was successful in an early experiment using a selenium x-ray laser and 40-μm rulings separated by 1.3 cm. The Moiré pattern showed excellent fringe contrast with a fringe separation of about 400 μm. The pattern was recorded with 1:1 imaging on x-ray film placed 4 mm behind the second ruling.

Using the same 40-μm rulings and a yttrium x-ray laser, a crude Moiré deflectogram of a CH laser-irradiated plasma was produced which showed slightly

shifted fringes in the region of the plasma. Again no imaging optics were used, and the deflectogram was recorded on x-ray film. The image shows a maximum relative fringe shift of about 0.6, which corresponds to a deflection of about 1 mrad within the plasma.

In our more recent experiments, we have improved the sensitivity of this density diagnostic by adding an imaging mirror to increase the magnification of the imaging system and by decreasing the ratio of the pitch of the Ronchi rulings to their relative separation. In addition, we now use an x-ray CCD camera rather than film to image the plasma.

In the first experiment using this high-resolution system, we attempted to image a plasma produced from a Mylar ($C_{10}H_8O_4$) target. A 600-ps, 2.5-kJ at 532 nm square pulse was line-focused onto a 3-cm yttrium x-ray laser target to produce the probe beam. After a 1.5-ns delay, a 2-ns, 0.6-kJ at 532 nm square pulse irradiated a 50-μm-thick Mylar target in a 3-mm spot focus to produce the subject plasma. A delay between the two Nova beams ensured that the x-ray laser probe would arrive at the subject plasma near the end of the 2-ns heating pulse. Filtering consisted of 1951 Å of Lexan and 825 Å of aluminum which was placed in front of the Ronchi rulings. The rulings consisted of 10-μm-pitch gold-on-silicon gratings which were separated by three Talbot planes (19.35 mm). A 23-μm-diameter-pixel x-ray CCD camera recorded a time-integrated image of approximately 10 s. The result of this first experiment was saturation of the CCD image.

In the second attempt to produce a high-resolution Moiré deflectogram, we increased the filtering by adding an additional 3000 Å of aluminum to the existing filters to reduce the amount of radiation that was entering the CCD detector. All other specifications remained the same as in the first experiment. Again, the result was saturation of the CCD image.

The attenuation profiles of the filtering systems for the first two experiments are shown in Figure 3. Plot (a) shows the system throughput versus wavelength for the filters and two multi-layer mirrors used in the first Nova shot; this is the attenuation as seen by

the x-ray laser. Plot (b) shows the system throughput as seen by the plasma subject; here the radiation must pass through the same filters and only one multi-layer mirror. From this plot we see that substantial hard x-ray and lower-frequency radiation was capable of entering the detector.

Plots (c) and (d) show the attenuation profiles of the filters and mirror(s) as seen by the x-ray laser and the subject plasma, respectively, for the second experiment. It is clear that this filtering is unsuitable for deflectometry since it is biased against the x-ray laser. (Lower-frequency radiation is more easily transmitted than the x-ray laser at 155 Å.) A better choice of filters would attenuate radiation outside a narrow bandpass centered on the x-ray laser line.

A more suitable selection of filters is shown in Figure 4. Here the system throughput versus wavelength is plotted for a filter combination of 1000 Å each of Lexan, aluminum, and titanium, plus four multi-layer mirrors. The additional two multi-layer mirrors are flat, 45° mirrors placed between the imaging mirror and the Ronchi rulings in order to improve the rejection outside a narrow bandpass (see Figure 2).

In order to determine the source of the excessive radiation experienced in the previous attempts at deflectometry, a third experiment tested the brightness of the x-ray laser without attempting to image a plasma. Here a Mylar target was placed in the course of the x-ray probe beam but was not irradiated to produce a subject plasma. The Nova pump beam for the x-ray laser was shot with the same specifications as before, and a Moiré fringe pattern was recorded with an x-ray CCD camera. Filtering for this experiment consisted of 2000 Å each of Lexan and Si_3N_4 and 1000 Å each of aluminum and titanium. (The additional two multi-layer mirrors were not yet in place for this experiment.)

The resulting Moiré pattern had a fringe spacing of 220 μm at the detector (magnification = 7.5), and the Mylar target was visible at the center of the image. The expected fringe visibility of the Moiré pattern was 25% for this experiment. (A different

CCD camera was used for this shot that did not allow the detector to be located exactly at a Talbot plane.) The measured fringe visibility, however, was only 10 to 15%. This suggests that a substantial soft x-ray background source was present within the line-of-sight of the detector.

It was hypothesized that a substantial amount of the Nova beam which pumped the x-ray laser burned through the x-ray target and irradiated the Mylar to produce unwanted x-ray emission. In addition, it was noted that lithium-like oxygen (OVI) exhibits a bound-bound emission line at 150.1 Å, a wavelength which is significantly transmitted through our system of mirrors and filters. To prevent the production of this undesirable background radiation in future experiments, pure CH targets are used to produce the subject plasma rather than oxygen-containing Mylar, and an aluminum shield is placed between the x-ray laser target and the plasma target in order to prevent burn-through radiation from heating the plasma target.

The most recent pair of experiments was successful in producing a high-contrast Moiré deflectogram of a dense plasma. In the first of these experiments, our objective was to produce a high-contrast Moiré fringe pattern without imaging a plasma. As before, a collimated x-ray laser beam was propagated through a pair of angularly-offset, 10-μm-pitch Ronchi rulings separated by three Talbot planes (19.35 mm). A pure CH target was placed in the course of the x-ray laser beam, but was not directly irradiated. Filtering consisted of 1000 Å each of Lexan, aluminum, and titanium, and the additional two multi-layer mirrors were placed in the course of the probe beam to produce a narrow bandpass of high transmission to the detector. A 27-μm-diameter-pixel x-ray CCD camera recorded a 20-s time-integrated image.

The resulting Moiré fringe pattern for this experiment is shown in Figure 5. The image shows 145-μm fringe spacing at the detector (magnification = 10) with an excellent contrast of about 50%.

The final experiment to date repeated the above shot while attempting to image a plasma. A 50-μm CH target was irradiated with a 0.5 mJ of 532-nm laser light for 1 ns to produce the subject plasma. The resulting high-contrast Moiré deflectogram is shown in Figure 6. Fringe shifts in the straight-line Moiré pattern are clearly evident near the irradiated face of the target, indicating density gradients within the CH plasma.

Analysis

Using the successful Moiré deflectogram, we calculated the electron density profile within the imaged plasma as a function of the distance from the face of the target. In this analysis, we assume a slab model of the plasma. In this model for laser-produced plasmas, the density of the plasma varies only as a function of distance from the target (i.e., in Eq. (2) the index of refraction and, equivalently, the electron density do not depend on z).

To calculate a density profile for the CH plasma shown in Figure 6, a typical fringe was traced from the CCD image, and spatial fringe shift versus distance from the target was measured from an undeflected baseline extrapolated from the plasma-free regions of the image. Recalling the approximately tenfold magnification of the imaging system and using Eq. (4), the recorded spatial fringe shifts were converted to angular deflections in the x-ray probe beam at the object plane. These angular deflections are plotted in Figure 7 as a function of the distance from the face of the target. We can then use Eq. (2) to find the density gradient versus distance from the target and integrate to get a density profile.

To calculate a more accurate density profile of the plasma, however, we must account for effects due to refraction in the plasma. Recall, as the parallel rays of the x-

ray laser beam propagate through the plasma, they are refracted in relation to the gradient of the index of refraction within the plasma such that the final deflection angle is proportional to the line-integrated gradient of the index of refraction. When we image the plasma, we measure final deflection angles in the x-ray probe beam as a function of position (i.e., distance from the target face) as measured in the object plane, rather than as a function of the positions of the x-rays upon incidence to the plasma (see Figure 8). Therefore, the density profile that is calculated from the measured angular deflections is not the same as that which produced those angular deflections.

In order to correct for this effect, a computer code was written which finds a profile for the index of refraction that produces angular deflections that are consistent with measurement. The procedure begins by using the measured angular deflections and Eq. (2) to calculate a first guess for the profile of the index of refraction in the plasma. A grid of light rays is propagated through the plasma using this index-of-refraction profile, and the total deflection and imaged position of each exiting ray is calculated to produce a simulated deflection profile. For each position at which a measured deflection is known, the measured deflection is compared to the predicted deflection as interpolated from the simulated deflection profile. The gradient of the index of refraction at this position is corrected to compensate for the error between the simulated and measured deflections, and the grid of light rays is again propagated through the plasma using the new profile for the index of refraction. This procedure is repeated until an index-of-refraction profile is found that produces angular deflections which are consistent with measurement. The electron density profile is then calculated using Eq. (1).

The refraction-corrected electron density profile corresponding to the angular deflections measured from the Moiré deflectogram of a CH plasma is shown in Figure 9. The electron density approaches 2×10^{21} cm^{-3} and decreases to zero within 110 μm from the target face. This rapid fall-off may be due to the limited resolution in measuring the fringe shifts from the CCD image. The angular deflection profile demonstrates a sudden

drop to zero at a distance of about 110 μm from the target where the fringe shifts become undetectable (see Figure 7). The computer code to correct for refraction effects iterates until a smooth density profile is found which produces no deflections in the probe beam at a distance further than 110 μm from the target face. Hence, the actual density profile may decrease less rapidly since a lower-density plasma may exist at larger distances that produces angular deflections below the resolution of our measurements.

Conclusions

We have successfully measured a one-dimensional density profile of a high-density, laser-induced CH plasma using Moiré deflectometry. This scheme utilizes an x-ray laser source to measure line-integrated electron density gradients along a single transverse dimension. In our most recent experiment, measured electron densities within the imaged plasma reached 2 x 10^{21} cm^{-3}, well above the limits of any previous methods of plasma density characterization.

As a plasma density diagnostic, Moiré deflectometry has limited capability. The main drawback of this method is its intrinsic limitation to one-dimensional density information. In order to increase its use to two-dimensional density profiles, we would need to produce simultaneous images along orthogonal directions. In addition, deflectometry measures density gradients; we must integrate to recover the desired density information.

In general, however, Moiré deflectometry is a simple method to characterize plasma densities. The scheme requires few components which are easily aligned. In addition, the x-ray laser illumination source has already been developed with the required beam coherence and brightness. Finally, we can easily control the sensitivity of this

diagnostic by varying the magnification of the imaging system as well as adjusting the pitch and relative separation of the Ronchi rulings.

Future extensions of Moiré deflectometry would include the development of a fully two-dimensional x-ray deflectometer, as well as attempts to produce one-dimensional deflectograms of exploding foils and higher-Z plasmas such as nickel and gold. This would fully demonstrate the usefulness of Moiré deflectometry as a general density diagnostic for numerous ongoing studies in plasma physics.

References

[1]O. Kafri and I. Glatt, *The Physics of Moiré Metrology* (Wiley, New York), 1990.

[2]E. Keren and O. Kafri, J. Opt. Soc. Am. A, **2**, 111 (1985).

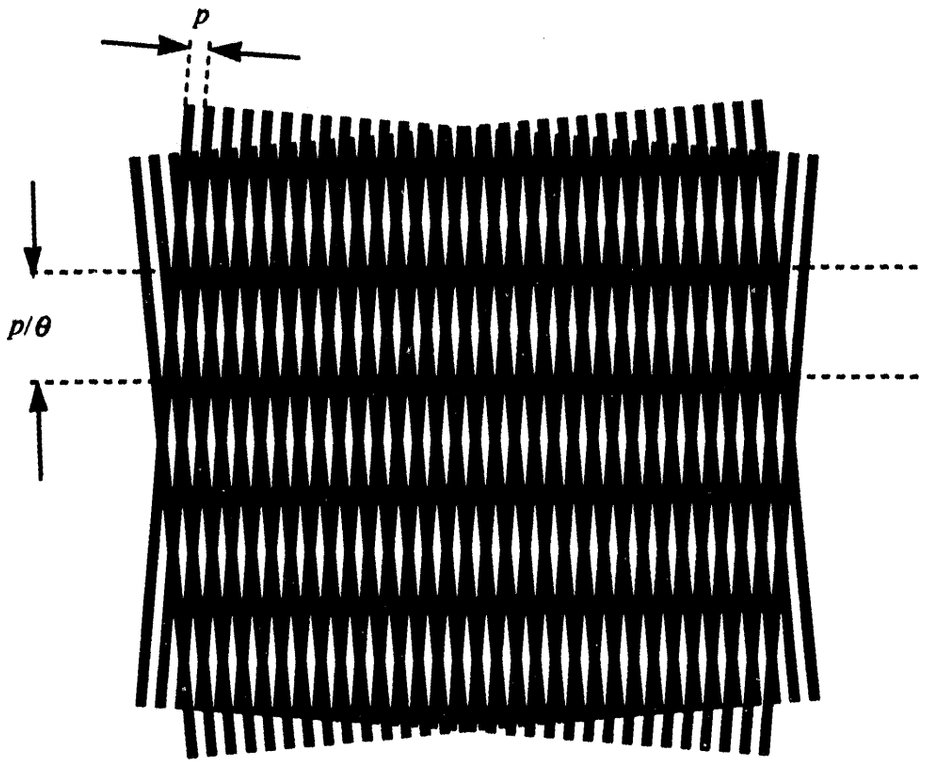

Figure 1

A one-dimensional Moiré fringe pattern is produced when two Ronchi rulings of pitch p are overlapped with a relative angle offset θ. Dark fringes occur at the intersections of the opaque regions of the Ronchi rulings with spacing p/θ.

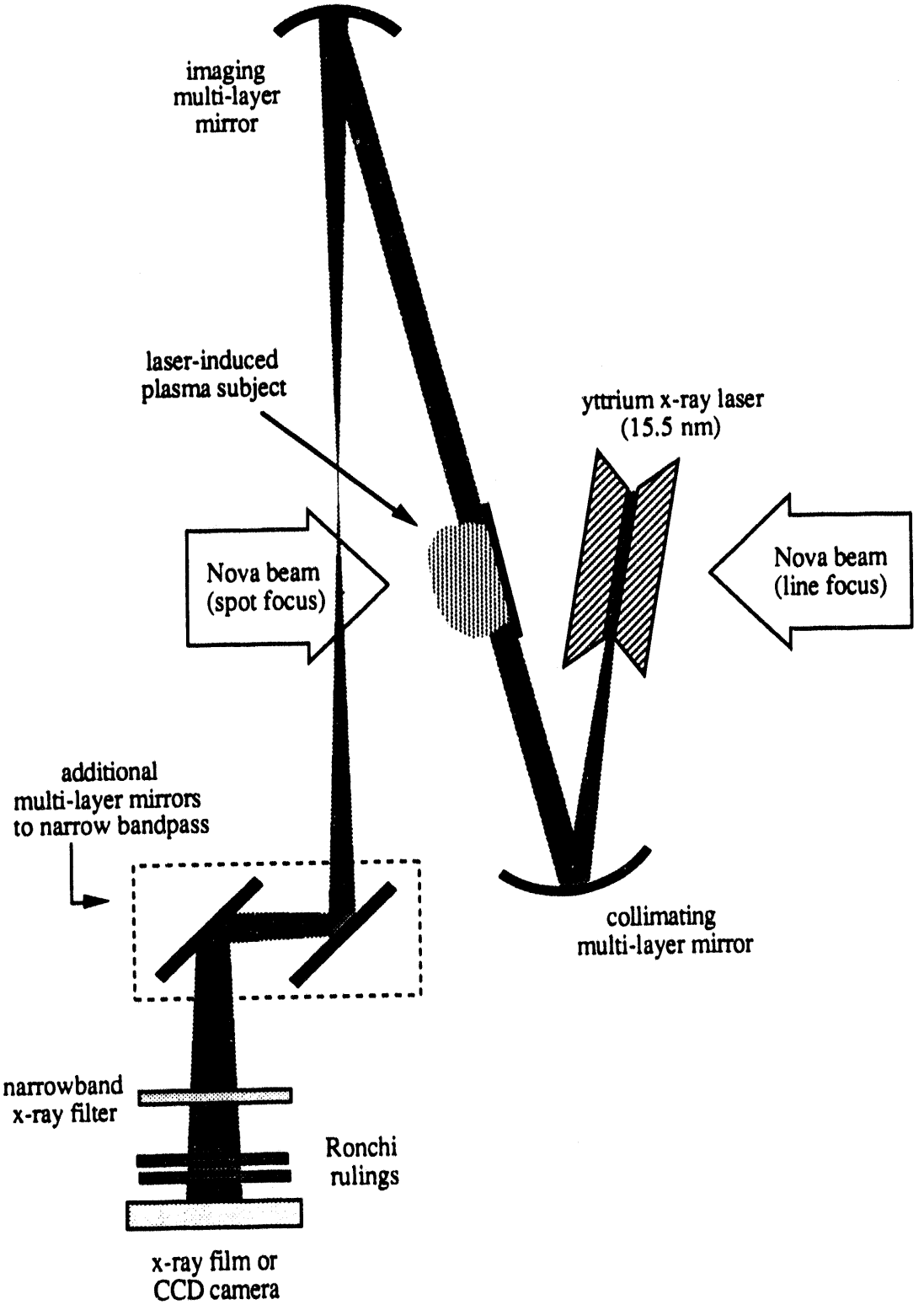

Figure 2

Schematic of optical arrangement for Moiré deflectometry.

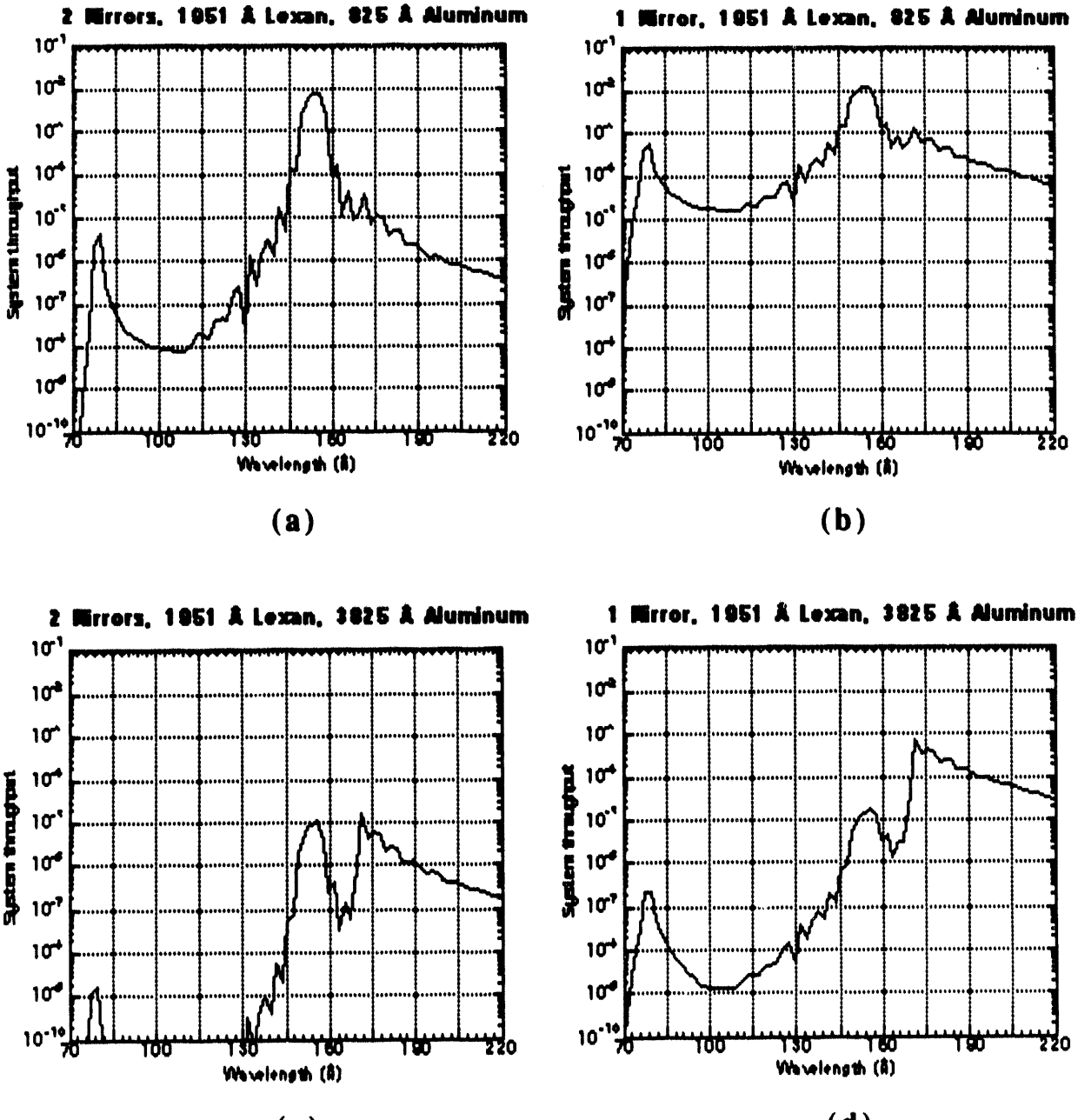

Figure 3

Attenuation profiles for filter and mirror systems in Moiré deflectometry experiments:
(a) System throughput for 1951-Å Lexan, 825-Å aluminum, and two multi-layer mirrors.
(b) System throughput for 1951-Å Lexan, 825-Å aluminum, and one multi-layer mirror.
(c) System throughput for 1951-Å Lexan, 3825-Å aluminum, and two multi-layer mirrors.
(d) System throughput for 1951-Å Lexan, 3825-Å aluminum, and one multi-layer mirror.

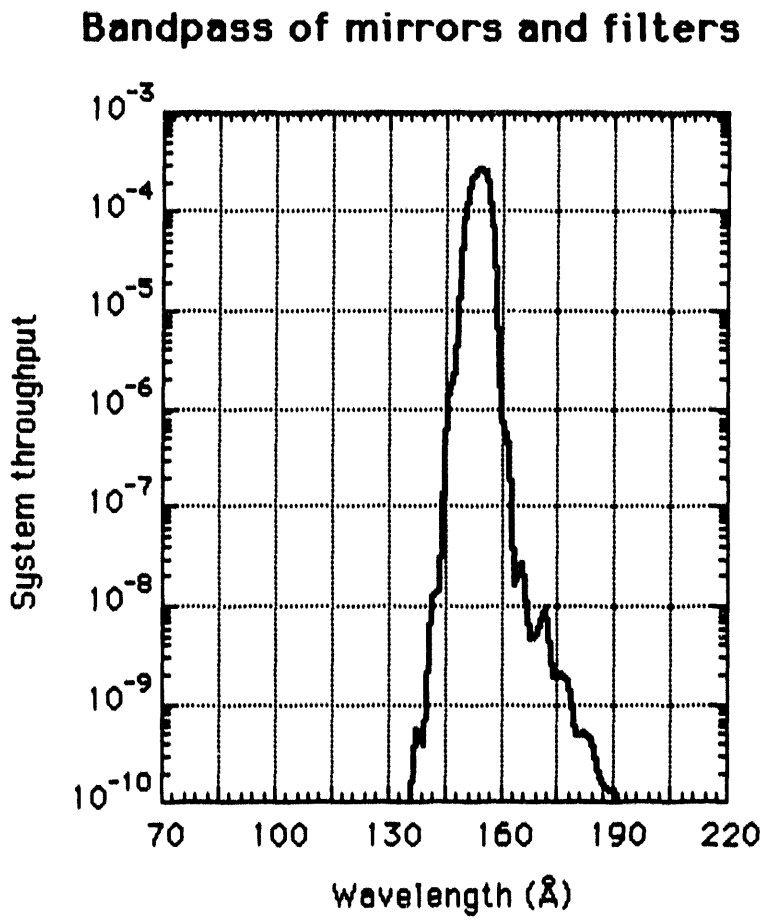

Figure 4

System throughput for multi-layer mirrors and filters for Moiré deflectometry. Plotted here is total attentuation for four multi-layer mirrors plus 0.1-μm Lexan, 0.1-μm aluminum, and 0.1-μm titanium. Narrow bandpass is centered around the yttrium x-ray laser at 155 Å.

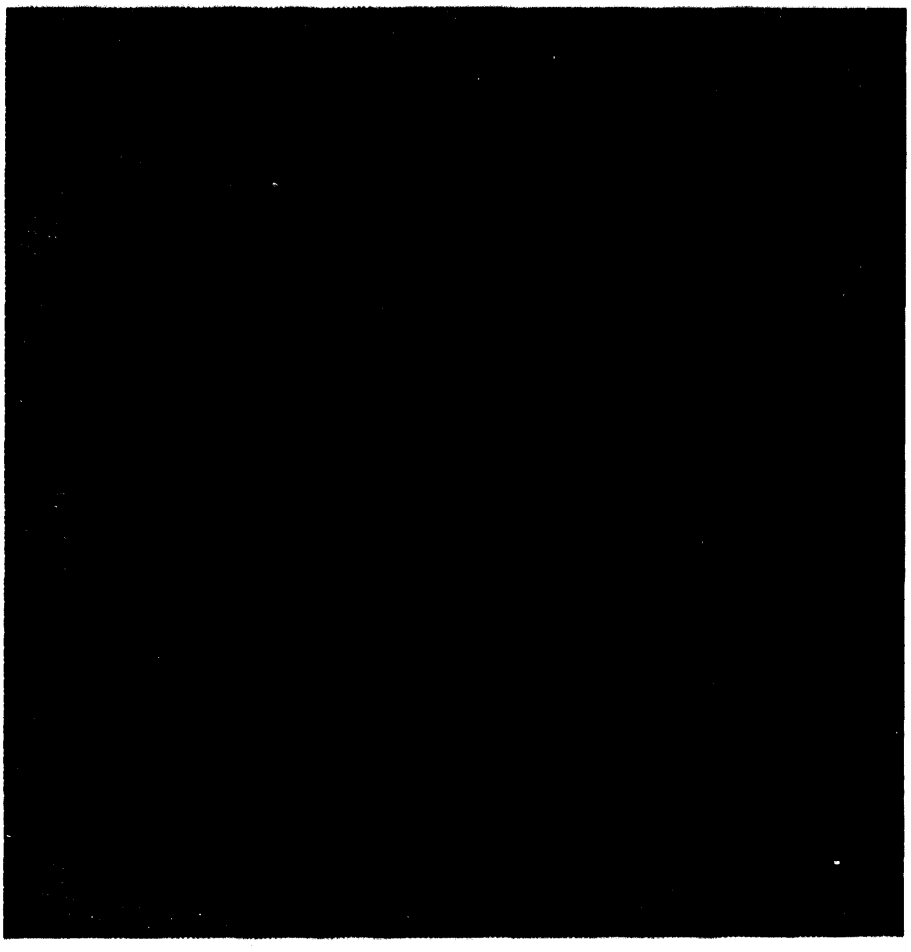

Figure 5

X-ray CCD image of a Moiré straight-line fringe pattern. A collimated x-ray laser beam was propagated through a pair of angularly-offset Ronchi rulings to produce the Moiré pattern. Dark image is the plastic target which will be irradiated to produce a subject plasma. The target was not directly irradiated in this shot.

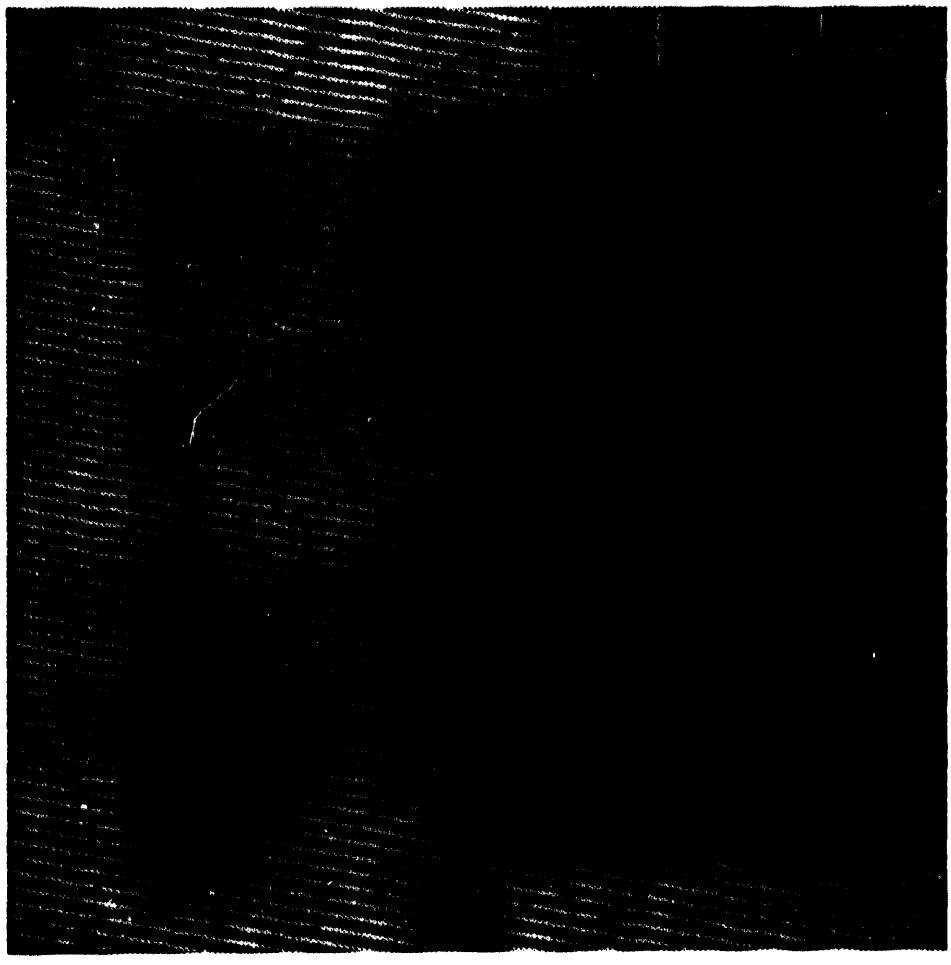

Figure 6

Moiré deflectogram of a CH plasma. The target was irradiated from the west side with 0.5 mJ of 532-nm laser light for 1 ns to produce the subject plasma. Fringe shifts in the straight-line Moiré pattern are evident near the west face of the target.

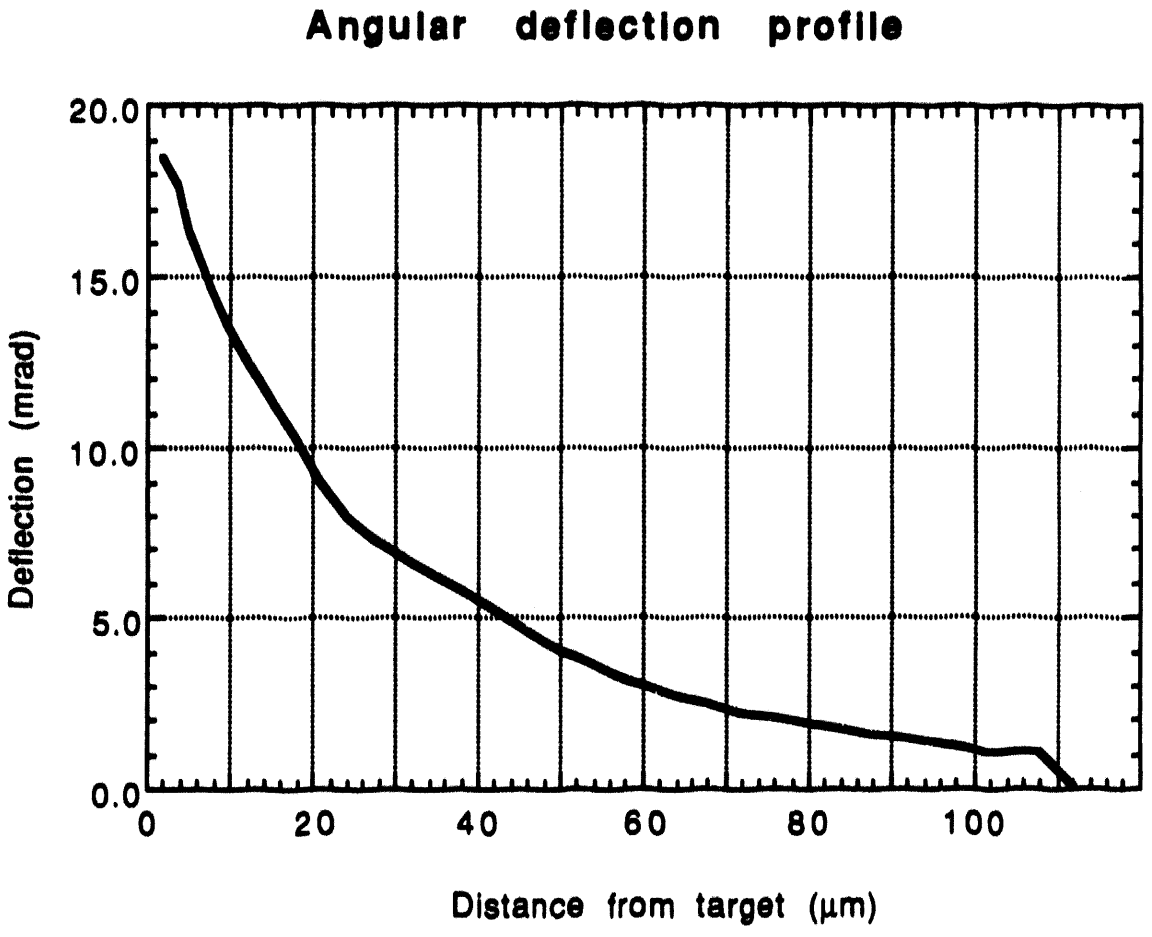

Figure 7

As collimated x-rays propagate through a plasma, they are refracted in relation to the electron density gradient in the plasma such that the total deflection is proportional to the line-integrated density gradient. Plotted here is total deflection (in mrad) as a function of distance from the face of the target (in μm).

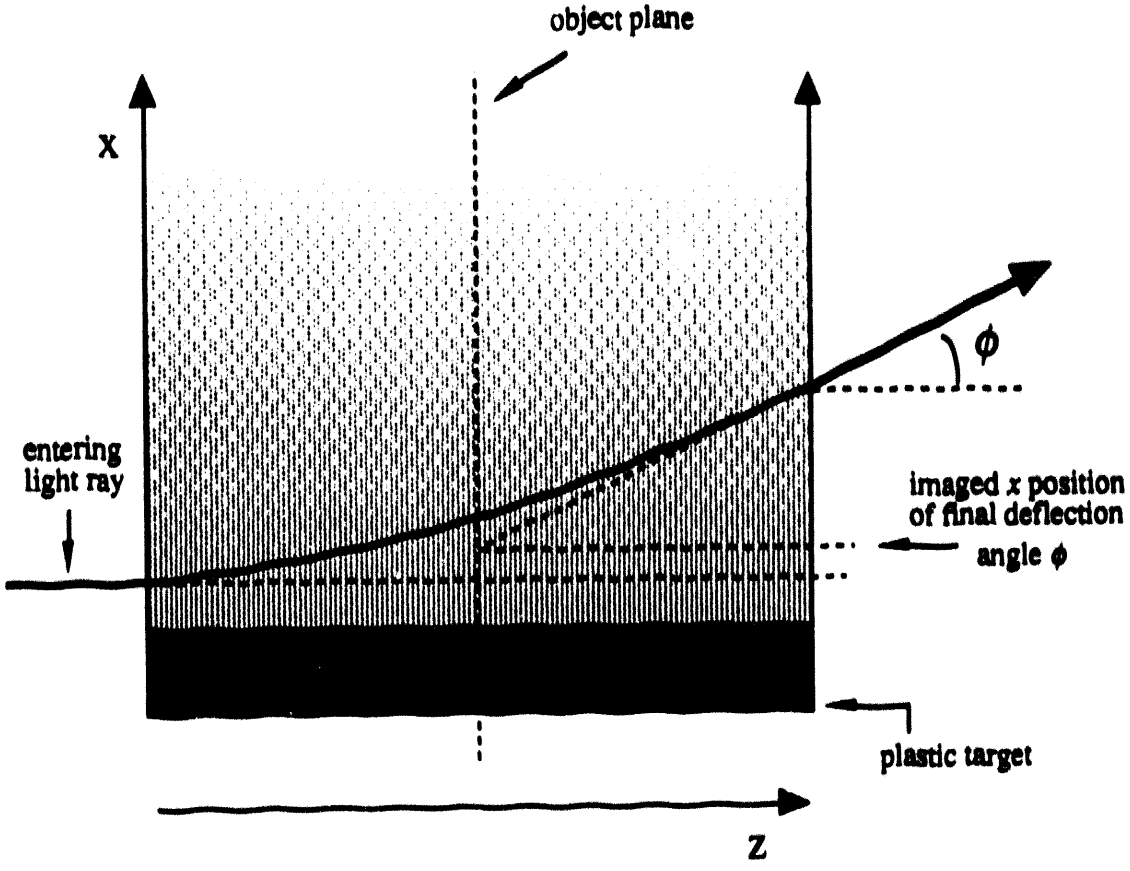

Figure 8

Refraction within a plasma. As light rays propagate through the plasma, they are refracted in relation to the gradient of the plasma index of refraction. When the plasma is imaged, the imaged position for a given final deflection angle differs from the incident position of the light ray.

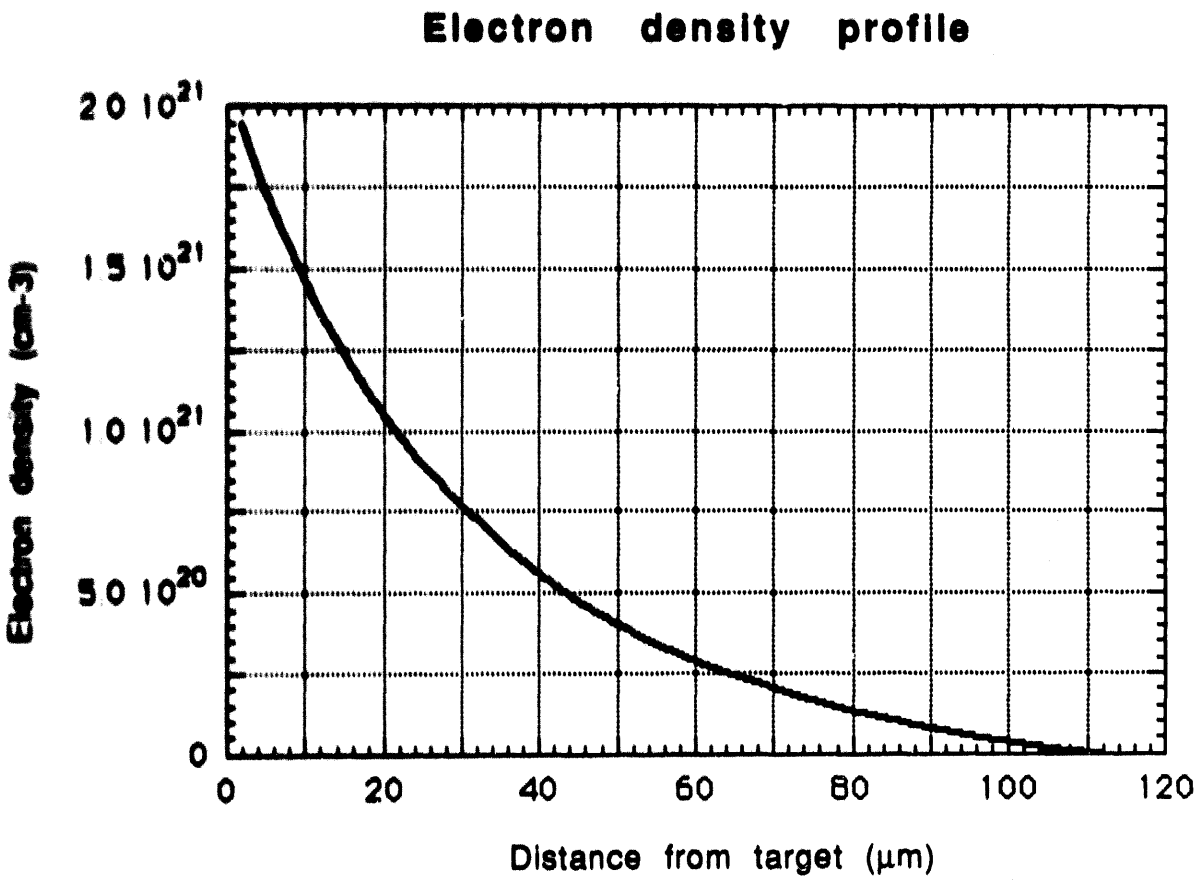

Figure 9

Electron density profile of a CH plasma after correcting for refraction. Plotted here is density (in cm-3) as a function of distance from the face of the target (in μm).

DIFFUSION OF ANALYTE MOLECULES INTO THE SILICONE POLYMER CLADDING OF A FIBER OPTIC SENSOR

Larry Mack *(Nuclear Chemistry Division - Lawrence Livermore National Laboratories)*

Abstract

A fiber optic evanescent field absorption sensor has been developed for the remote detection of volatile organic compounds in aqueous solutions. Diffusion mechanisms of specific analyte molecules into the polydimethylsiloxane (PDMS) cladding of optical fiber is being investigated. It is important to determine the diffusion rate of certain compounds into the fiber polymer for long term sensor applications and multiple component systems. Changing different parameters, such as, concentration of analyte, temperature of the solution, and the physical properties of the analyte, provides information in determining the theory behind the diffusion of siloxane polymers. We are using near infrared(NIR) spectroscopy to examine the analyte/polymer interaction. In particular we are looking at hydrogen bonding and the rates of diffusion. Trichloroethylene (TCE), dichloroethylene (DCE), water and various phosphates were used to help understand the chemistry behind the polymer/analyte interaction in the PDMS cladding of the optical fiber.

Introduction

Increasing potential hazards to the population due to groundwater pollution results in the design of remote sensors. Even though enviromental regulations are becoming stronger the contamination of our groundwater is still a valid concern. This is the reason for the developement of an inexpensive, in situ detection system. This system would take accurate analysis of contaminated groundwater and it would also take continuous data for long term contamination monitoring.[3]

Various fiber optic techniques have been introduced for the developement of sensor systems, such as, basic fiber optic probes that send light through a medium and collect spectroscopic information of the analyte to flourescent dyes that are specific to the analyte and placed on an optical probe. The former mentioned method has the problems of data collection and optical interference of the medium. The latter has the problems of being specific to the analyte where only one analyte at a time could be detected and bleaching of the dye .[3]

The evanescent field absorption sensor (EFAS) has the ability to be used in aqueous solutions with no electrical hazard. Only light carrying optical fiber is submersed into the groundwater system. The approach discussed here uses the optical fiber as a remote sensor that will absorb the analyte into its cladding material. As light passes through the fiber small amounts of light (called the evanescent wave) will penetrate into the cladding material. As the light passes through several meters of optical fiber, near infrared (NIR) spectroscopic absorption information about the analyte, that has diffused into the polymer cladding, will be detected.

Diffusion of analyte molecules into the polymer cladding is the focus of this research. In the past, diffusion of water into the cladding material has been overlooked because of its hydrophobic properties of the polymer cladding. The present research would tend to say that diffusion of water occurs although the equilibration time is on the order of days.

Diffusion of the organic molecules is on the order of minutes and therefore water absorption would not interfere in shortterm measurements. The diffusion mechanism of the polymer is important to predict what will take place with different compounds.

When describing the diffusion mechanisms in silicone rubber two possibilities need to be considered. First, the physical ability of the polymer to accomodate the compound and to offer continuous voids for the compound to flow through representing a free flowing model. Second the ability of the molecule to interact, temporarily, with the polymer thus slowing the diffusion rate. It is important to know the diffusion rate to determine how long the sensor must be exposed to a solution and obtain accurate equilibrium data. Also knowledge of diffusion rates would aide in the analysis of multicomponent systems, taking into consideration that different size and structure molecules will diffuse into the polymer at different rates. Understanding the diffusion mechanisms of the polymer could lead to better designs and materials used in the fiber optic system.

Theory

Sensor

Evanescent field spectroscopy (EFS) is a derivative of the attenuated total reflection (ATR) method.[2] The EFS uses optical fiber to transmit light from a source to a detector. Internal Reflection Theory states that as light passes through the core of the optical fiber it will reflect off the core/cladding interface when the cladding refractive index (RI) is lower than the core RI and when the incident angle of the incoming light is greater than the critical angle. Therefore, $n_1 > n_2$ where n_1 is the core RI and n_2 is the cladding RI and eq.1:

$$\sin\theta_c = \frac{n_2}{n_1} = n_{21} \qquad (1)$$

Where θ_c is the critical angle of the incoming light. Some light will penetrate into the cladding and this will be called the evanescent wave. The energy that is transmitted into the polymer cladding at each reflection is defined in eq.2. [2]

$$E = E_o e^{\frac{-z}{d_p}} \qquad (2)$$

where E_O is the wave amplitude at z=0 and z is the distance normal to the optical interface and d_p is the penetration depth of the light given by eq.3:

$$d_p = \lambda / \left[2\pi n_1 \left(\sin^2\theta - n^2_{21} \right)^{\frac{1}{2}} \right] \qquad (3)$$

λ is the wavelength of the light in the core medium. The penetration depth is normally on the order of a wavelength, yet, as the angle of incidence reaches the critical angle the d_p will go to infinity and light will not be totally internally reflected. Similarly as the wavelength increases or the core/cladding RI's approach unity the d_p will increase.

The evanescent light will have more opportunity for absorption as the penetration depth is increased in the EFS system. Therefore, more information

about the cladding and the molecules that have diffused into the cladding will be relayed to the photodiode detector.

The EFS system can provide simultaneous information about the medium surrounding the core of the optical fiber, such as, the RI and absorbance of the matrix (polymer and analyte in this case). If the RI of the polymer changes, the penetration depth of the light will also change as seen in eq.3. The intensity of the evanescent field is dependent on the RI matrix of the polymer/analyte combination (as seen in eq.4). The RI depends upon the analyte absorption coefficient, hence, the transmitted intensity of the field will depend upon this analyte absorption.[1]

$$I = I_o\left(NA^2 / NA_o^2\right) \qquad (4)$$

This equation represents the transmitted intensity at a nonabsorbing wavelength of the cladding or matrix combination where NA_o is the numerical aperture of the sensor in reference and NA is the numerical aperture in the analyte solution given by: [1]

$$NA_o = \left(n_{co}^2 - n_{cl}^2\right)^{1/2} \qquad (5)$$

$$NA = \left(n_{co}^2 - n_m^2\right)^{1/2} \qquad (6)$$

where n_{co} is the core RI (1.456), n_{cl} is the cladding RI (1.436), and n_m is the matrix RI given by the polymer/analyte solution. At an absorbing wavelength the intensity relationship includes the combination of Beer's Law and eq.4. From Beer's Law:

$$I' = I_o' 10^{-\alpha_e \ell c} \qquad (7)$$

where α_e is the effective absorptivity, ℓ is the effective optical path length, and c is the analyte concentration. Getting $I_o = I'$ and ratioing eqs.4 and 7 the intensity at an absorbing wavelength can be determined by: [1]

$$-\log(I / I') = \alpha_e \ell c + \log\left(NA_o^2 / NA^2\right) \qquad (8)$$

where $\alpha_e = \eta_p \alpha_c$ and η_p is the fraction of total light intensity in the evanescent field given by:

$$\eta_p = \kappa / V \qquad (9)$$

where V is the normalized frequency shown in eq.10 and κ is the proportionality constant.

$$V = (2\pi r / \lambda) \cdot \left(n_1^2 - n_2^2\right)^{1/2} \qquad (10)$$

The cladding matrix RI dependence can be seen in both the first and second term of eq.8. The first term accounts for the absorption in the cladding and the slope of the baseline. The second term results from refractive light losses which effect the numerical aperture of the sensor in the analyte solution.

Diffusion

Diffusion mechanisms of silicone rubber are still being examined to a large degree. Diffusion into the polydimethyl siloxane(PDMS) polymer is still not fully understood. Two independent theories exist that explain the process by which molecules permeate into the polymer. Free volume polymer model, in which the analyte is able to flow into and out of the

silicone polymer without interaction. And the bonding interaction in which the molecules temporarily and reversibly bond to the polymer. These are the two theories that will be considered in our study. The first model that will be discussed is the free volume model.

Diffusion of molecules largely depends on size, shape and the ability of the polymer to physically accept and continuously provide a channel for them to flow through. Recently, it has been examined that molecule/polymer interactions or, bonding, contribute more to the diffusion process[4]. Eqs.(11)-(14) will be helpful mathematical interpretations in order to understand the bonding interaction.[4]

$$\tau = \tau_o \exp(E / \kappa T) \tag{11}$$

where τ is the dwell time at each individual absorption site, and E is the energy representing the bond at each activation site, and τ_o is the vibrational frequency given by: [4]

$$\tau_o = h / \kappa T \tag{12}$$

The diffusion coefficient is then given by the expression: [4]

$$D = \lambda^2 / 6\tau \tag{13}$$

where λ represents the jump length from one interaction site to the next. After substituting eqs.(11) and (12) into eq(13) the diffusion coefficient is given by: [4]

$$D = \left(\lambda^2 \kappa T / 6h\right) \exp(-E / RT) \tag{14}$$

This equation is identical to the free-volume model equation except that here E is the physical/chemical nature of the molecule instead of the size and shape representation of the molecule.

For the case of a hydrocarbon molecule it will jump randomly through the polymer at a jump length of about $\lambda \cong .5nm$ and held at each bond site by Van der Waals forces for the approximate time length of 10^{-10} seconds if $E = 15kJ / mol$. These dispersive forces happen at all molecule/polymer interaction sites and without much change between them.

Non hydrocarbon molecules, containing O, N, S with free electron pairs will have the tendency to create hydrogen bonds between the molecule and the polymer. Different molecules could bond more strongly to the polymer than others. The stronger bonding molecules would increase the dwell time at each site which would decrease the diffusion rate. However, if the first molecules are delayed by strong hydrogen bonds the next "layer" of molecules would not neccesarily be held up by the bonding process and depending on size and shape could be allowed to pass through to the next layer of the polymer. From this process Watson (4) developes a concentration dependent diffusion coefficient. Taken from the fractional occupancy, ϕ of the available absorption site and given as:

$$\phi = f\tau_s / \left(f\tau_s + C_s\right) \tag{15}$$

where f is the number of times that the molecule will encounter strong absorption sites per unit volume of the polymer. The concentration dependent coefficient is then given as: [4]

$$D_c = \frac{\left(1+\frac{C_m\tau_s}{C_s\tau_t}\right)^2 D}{\left(1+\frac{C_m\tau_s}{C_s\tau_t}\right)^2 + \frac{\tau_s}{\tau_t}} \qquad (16)$$

where C_m / C_s is the ratio of the mobile permeant concentration to the absorption site concentration, τ_s / τ_t is the ratio of the dwell site time to the lag or delay time between sites. D is the diffusion coefficient in the absence of strong interaction sites.

From equation(16) determination of a structural unit concentration of 1.4×10^4 mol/m^3 for the polymer can be calculated.[4] This calculation will lead to a volume per unit of $1.2 \times 10^{-28} m^3$, and therefore, extracting a .49nm cube in which each unit will occupy. This corresponds well with the jump length of .5nm as calculated previously. This suggests that the molecules jump from one site to the next without skipping sites. This will continue until the layer is saturated. Then the following molecules could pass to the next layer of the polymer. This process could change as the diffusion rate of the different concentrations increases.

Therefore, small molecules should interact with the polymer as well as larger molecules, although, larger molecules will be diffusion limited by their size and shape. This suggests that there is a free volume within the polymer in which the molecules can move and are influenced by the Van der Waals forces at the interaction sites. Also taken from this theory is the fact that the stronger interacting molecules will have a decreasing interaction energy as their concentration increases.

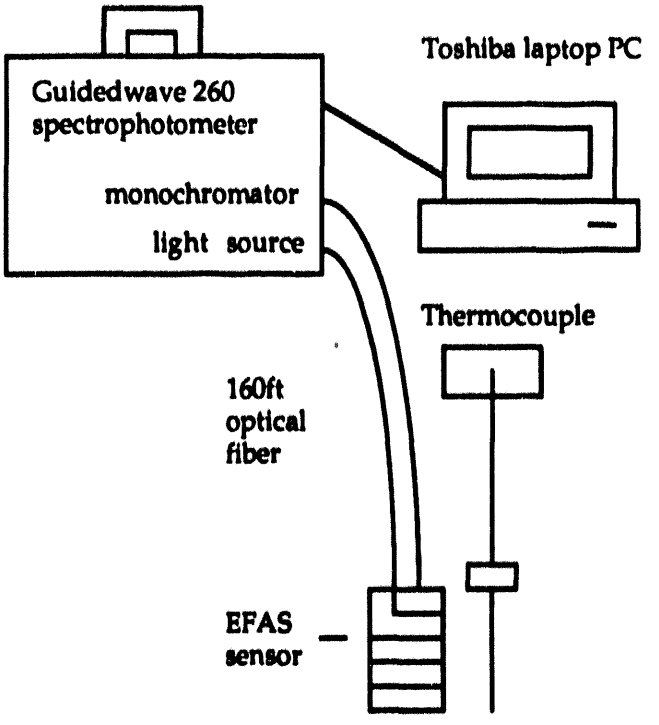

FIGURE 1: The portable, analyte compound detecting system. Including the spectrometer, computer, thermocouple, and EFAS sensor.

Experimental

Reagents

The analyte compounds were used in the experiments were trichloroethylene (TCE), dichloroethylene (DCE), tributyl phosphate (TBP), tripropyl phophate (TPP), trimethyl phosphate (TMP), tributylamine, and tripropylamine. All the above compounds were 99%+ in purity.

Each sample was weighed carefully for accurate amounts of concentration. Each was then dilluted in 2 liters of deionized water. The solutions were

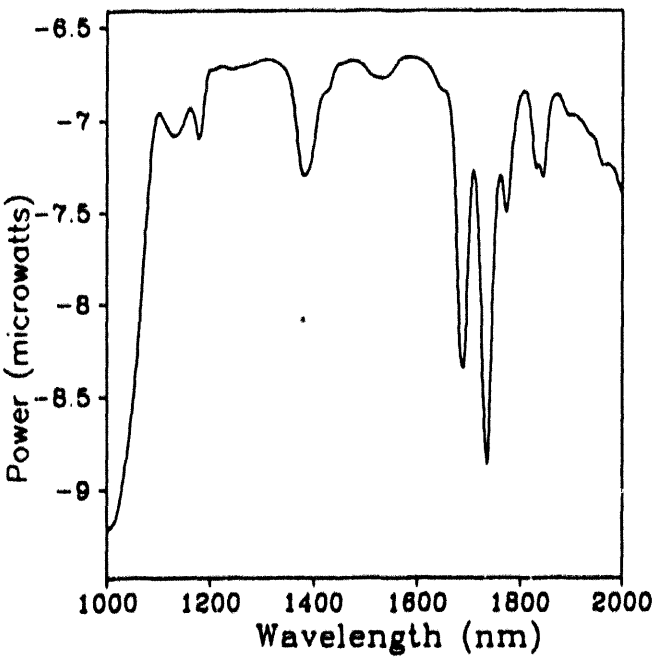

FIGURE 2: The reference power taken with the EFAS sensor. This transmitted power will the basis from which all of the spectra is taken.

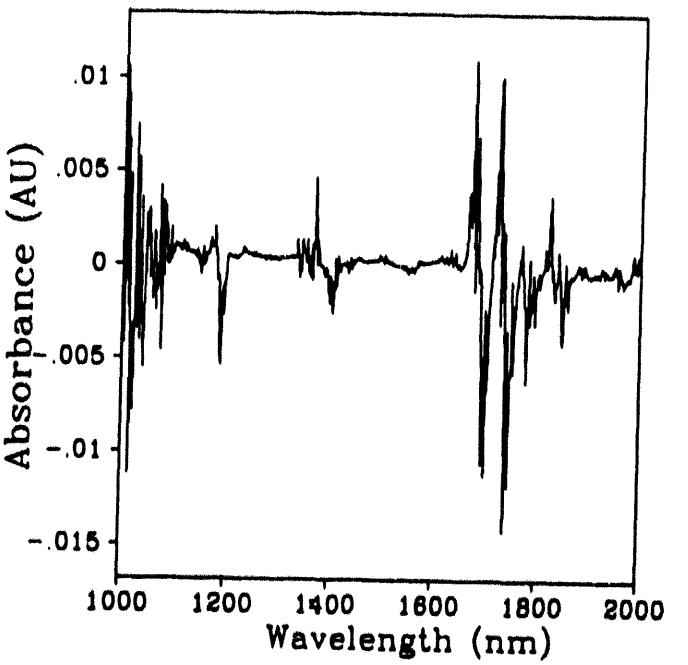

FIGURE 3: The background spectra taken in water at 18 degrees C. This is the effective signal in the sensor and must be taken into consideration when determining the spectra of the analytes.

contained in double walled cylindrical glass beakers that were kept at a constant 18°C. The solution was mixed homogenously by a magnetic stirrer set at a constant speed. Concentrations of 12-150 parts per million (ppm). Because of the volatility of the organic compounds, the glass container was sealed with an O-ring and glass lid. This lid has two seperate holes for the fiber optic inputs. The glass beakers were filled to capacity to insure that no containment bubbles of air were trapped at the top of the glass beaker.

Sensor

A polymer cladding/silica core optical fiber, from Fiberguide Industries, was used in the sensor. This fiber had a core refractive index (RI) of 1.456 and a cladding RI of 1.436 with a numerical aperture of .24. The core thickness is 400 microns, the cladding thickness is 500 microns and the fiber has a 700 micron nylon jacket. To remove the jacket, the fiber was placed in a propylene glycol solution for several hours as the temperature was raised slowly to 150°C. After a few a minutes the temperature was lowered back to room temperature and the exposed cladding surface was cleaned and dried.

Twelve meters of optical fiber were coiled on a 4cm diameter stainless steel brace. The brace was coiled with approximately 95 turns of optical fiber and the ends of the fiber were connected to the top portion of the brace with SMA connectors. The fiber optic leads from the

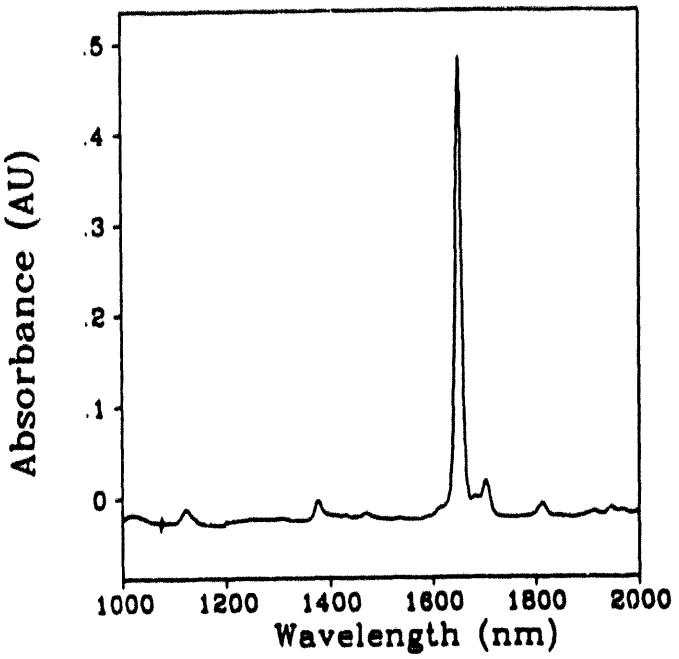

FIGURE 4: Pure TCE spectra taken from a 1mm cuvette. Notice the sharp peak at 1650nm.

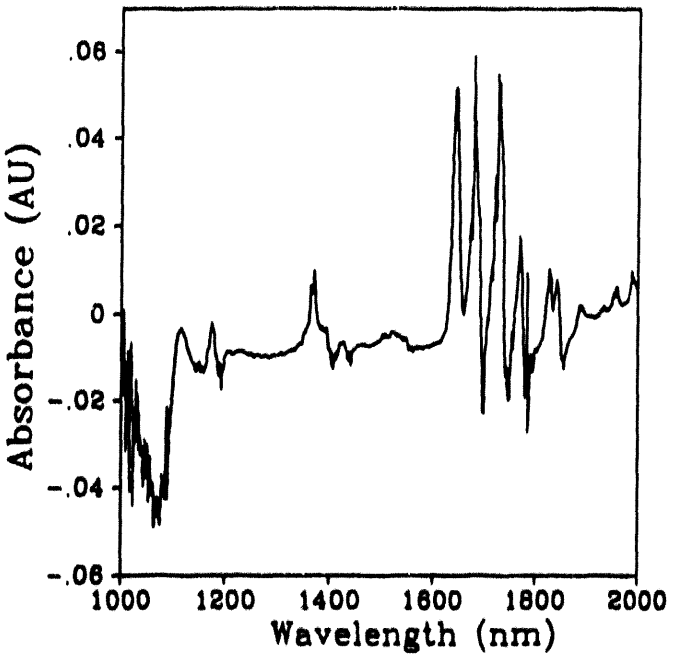

FIGURE 5: this spectra of TCE, about 40ppm, was taken from the EFAS sensor. Notice that the 1650nm peak is not overlapped by the background spectra.

spectrophotometer were connected to the SMA connectors which made a continuous optical path loop. The fiber coil and brace were then connected to a fitted, stainless steel cage to protect from physical damages. [see figure 1]

Instrument

The rest of the system consisted of a Guidedwave model 260 spectro-photometer, Toshiba laptop PC, and a thermocouple. The spectrometer has an incandescent tungsten light source with two focusing lenses, a 300 line/mm transmission grating, and two photodiode detectors. The first detector is lead sulphide with an 1100 EFLP filter for the NIR and a 1mm slit. The second detector is germanium with no filter and a .5mm slit.

Results and discussion

Sensor stability is crucial to obtain accurate data for any detection system. The EFAS has shown no fluctuation or drift in its background spectra to indicate any instability in the measurement of the analytes. Fig.2 shows the reference power of the sensor outside of any solution(in air). Fig.3 shows the background spectra of the sensor taken from reference. The background (noise) is relatively low and stable over the 1000-2000nm range with exception of 1650-1850nm range.

Each analyte has a different absorbance in the near infrared making it

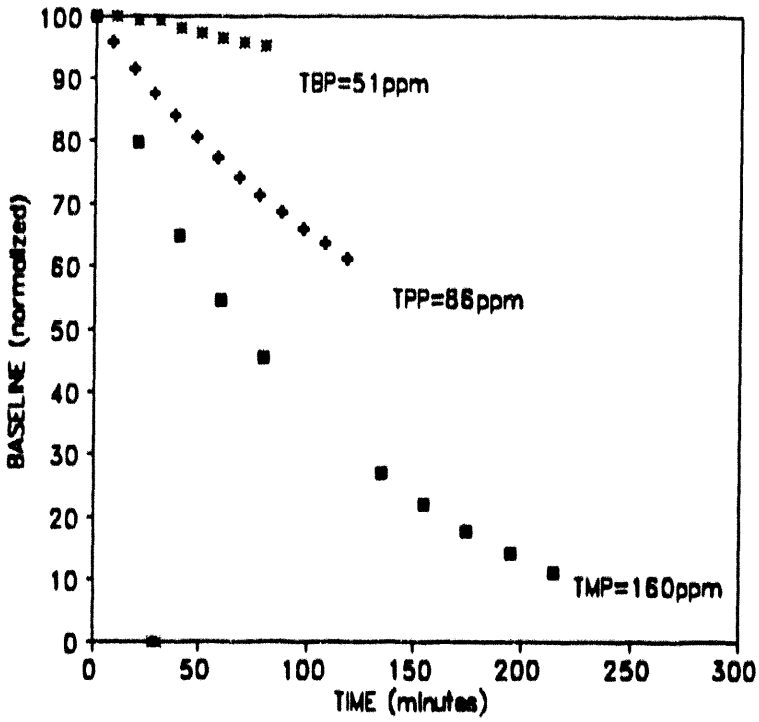

FIGURE 6: The diffusion rates of TBP, TPP, and TMP. The 1250nm wavelength is used to determine this rate in each case. The vertical axis is normalized to the first data point.

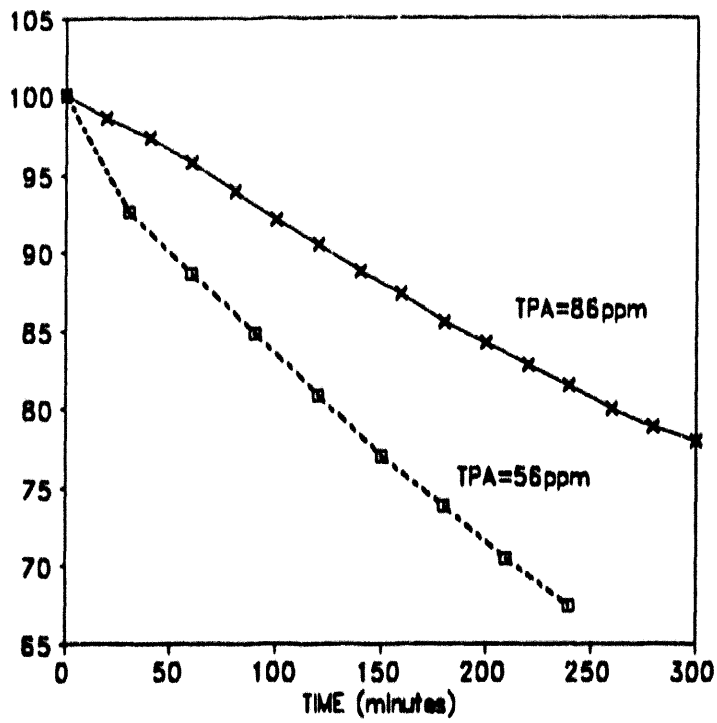

FIGURE 7: The diffusion rates of TPA at 56ppm and 86ppm. The 1250nm wavelength is used as the baseline and the vertical axis is normalized to the first data point.

possible for the EFAS to be partially selective in the detection process of these compounds. The detection of organic species in water presents the problem of strong OH overtones in many detection systems. Since the EFAS is strongly hydrophobic, although not completely, these large Oh bands are eliminated from the spectra and the organic compound spectra is predominant.

As seen in fig.4 pure trichloroethylene (TCE) will absorb strongly at 1625nm. This absorption peak is easily detected by the EFAS as well because it is out of the background noise range of the sensor. From the reverse kinetic experiment of TCE in the EFAS it was found that as concentrations of TCE in water were reduced from 125ppm to under 60ppm the equilibration time also reduced. This suggests that the diffusion of the analyte depends somewhat on the concentration of the analyte to the polymer.

An interesting experiment came about from the TCE diffusion measurements. It was discovered that an OH peak began to increase as the EFAS was left in solution for several days. This peak at 1888nm (as seen in fig.5) is believed to be due to water diffusing into the polymer.The peak increased steadily up until 120 hours and then it reached equilibrium at approximately 12 x 10^{-3} absorption units (AU). This data is important when considering the fact that the EFAS has the ability to be a long term

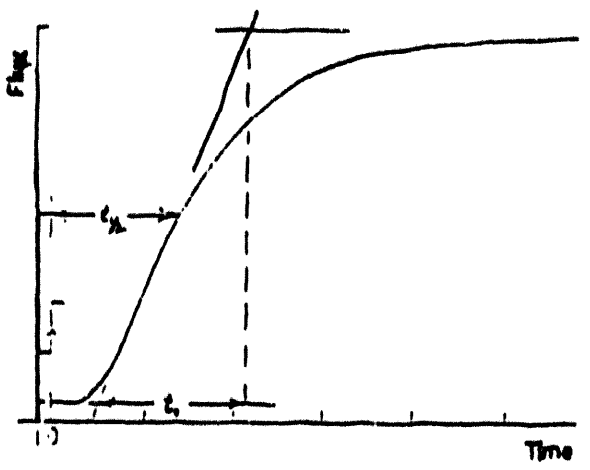

FIGURE 8:This is the graph for the ideal flux transient for a permeating molecule in the silicone polymer. This is the smooth curve for flux .v. time.

monitoring sensor. And whether or not OH bands will interfere with the detection limits is a fact worth considering. Although, the data here is inconclusive and further examination would be appropriate to form any conclusion about the water diffusing into the polymer overlong periods of time.

The peak at 1888nm also caused concern when looking at tributyl phosphate (TBP). It was discovered that the peak grew much more as the TBP diffused into the sensor. This leads us to believe that, because TBP has a free electron oxygen in its molecular makeup, there is some OH interaction between the analytes with free electrons and the polymer.

The diffusion process of the polymer cladding was the target of the phosphate and amine experiments. The idea was to understand the diffusion mechanisms of the polymer when it is exposed to similar analytes. Knowledge of polymer/analyte interaction can be obtained if similar hydrocarbons are analyzed. The phosphate set used was tributyl phosphate (TBP), $[CH_3(CH_2)_3O]P(O)$; trimethyl phosphate (TMP), $[CH_3O]P(O)$; and tripropyl phosphate (TPP), $[CH_3(CH_2)_2O]P(O)$. If diffusion rates and baseline shifts of the analyte spectra are considered based on the RI dependence, as shown in eq.8, then this interaction can begin to be understood to some extent. The results show that the diffusion process follows eq.8 and TBP diffused in slower than TPP which diffused in slower than TMP. This suggests that smaller molecules have less binding energy with the polymer than the larger molecules and therefore less interaction time between sites. On the other hand it could suggest that the smaller molecules move more freely through the polymer and interact at fewer sites than the larger molecules. This could help explain the different diffusion rates as seen in Fig.6.

Figure 6 shows the diffusion of TBP, TPP, and TMP into the silicon cladding. Note that the concentrations are different in each case, although, the difference in the diffusion rates is large enough to suggest that the larger molecule has a greater interaction energy and a greater interaction time between sites in the polymer.

Looking at Fig.7 we can assume that the concentration of the analyte in the sensor has less effect on the diffusion rate than is observed in Fig.6. Although, the fact that tripropylamine(TPA) diffuses in

slower than tripropyl phosphate(TPP) and TPP has an oxygen with free electrons where TPA does not, is still not completely understood.

The experimental data also suggests that the CH bands of the polymer (1183nm and 1381nm) decrease as the concentrations of the analyte in the polymer increase. And because TPP has a larger RI the bands decrease more than the TMP with a smaller RI. This relationship can again be attributed to eq.8.

Conclusion

From the results of the experiment using the EFAS sensor it can be determined that effective measurements of hydrocarbons down to the parts per million range can be made. Many different parameters, independently influence the transmitted intensity of the system, such as: refractive index, concentration, absorptivity and size of the analyte molecule; temperature of the solution; and refractive indexs of the core and cladding.

Although, each parameter is known to a high degree of accuracy, what is not known is the interaction process between the polymer cladding and the analyte molecule. The results from this experiment show, inconclusively, that there is some hydrogen bonding thta will effect the diffusion rate of the molecule into the cladding. The size of the molecule will also effect the diffusion rate and more study into this area should be considered before any conclusions can be drawn.

If these diffusion models can be fully developed, then an accurate assesment of the permeating molecules could be determined. When the diffusion rate is directly associated with different hydrocarbons or sets of hydrocarbons it could be possible to expand the limits of the EFAS sensor. To restate, if polymer/analyte interaction is known, then further designs on the sensor could be possible. This could increase the detection limits of the system or increase the number of detectable analyte compounds.

References

[1] Michael D. Degrandpre and Lloyd W. Burgess, *Applied Spectroscopy*. 44, 273-279 (1990).

[2] Michael D. Degrandpre and Lloyd W. Burgess, *Anal. Chem.* 60, 2582-2586, (1988).

[3] J. Burck, J.P. Conzen and H.J. Ache, *Anal. Chem.* 394-398, (1991).

[4] J.M. Watson, G.S. Zhang and P.A. Payne, J. Membrane Science 73, 55-71 (1992).

Replacing Hazardous Solvents with Alternative Cleaners

Dustin W. Montoya
Metropolitan State College of Denver
Environmental Protection Department
Lawrence Livermore National Laboratory

ABSTRACT

Because traditional hazardous solvents like Freon TE, 1,1,1 Trichloroethane, Isopropyl Alcohol, and Acetone are being "phased out" by environmental regulations, non-hazardous, environmentally benign alternatives must be developed, tested, and implemented. The goal of the Alternative Cleaning Testing Program is to identify non-hazardous, environmentally safe cleaning agents for use at the Laboratory in order to enhance worker safety, reduce solvent costs, and limit the Laboratory's contribution to stratospheric ozone depletion. Tests are currently being conducted using over forty different cleaning agents to clean three different materials: glass, aluminum, and printed board assemblies. Quantitative data is being collected using Optical Image Analysis, Fourier Transform Infrared Spectroscopy, or Ionography, depending on the material cleaned. Recent test results have identified nine alternative cleaning agents which can effectively replace traditional solvents in cleaning Trimsol from aluminum.

INTRODUCTION

Laboratory, military, and industry specifications require that certain materials be free of contamination during fabrication and/or use. Unfortunately, traditional cleaning methods are hazardous to the environment as well as workers. In fact, the Montreal Protocol, the Clean Air Act of 1990, a Presidential Mandate, and DOE directives have required the "phasing out" of Ozone Depleting Compounds (ODCs) like CFCs and 1,1,1 Trichloroethane. In addition,

permit requirements for the use of Volatile Organic Compounds (VOCs) limit the use of solvents like Acetone and Alcohol.

Because traditional solvents, like Freon-Te (CFC 113), 1,1,1 Trichloroethane (methyl chloroform), Acetone, and Isopropyl Alcohol, will soon be commercially unavailable or economically unfeasible, alternative cleaning agents must be identified, tested, and implemented as safe, cost effective substitutes for traditional solvents.

The growing demand for alternative cleaning processes has triggered the establishment of the Alternative Cleaning Testing Program at LLNL. The goal of this program is to identify environmentally benign cleaning processes for use at the Lab to minimize the problems associated with traditional cleaning methods. The scope of the program is to include testing of several substrate/contaminate combinations. Up to this point, the major substrate/contaminate combinations tested have been glass/oil, aluminum/Trimsol, and Printed Board Assembly/Flux. Of these primary combinations, my project has consisted of identifying alternative cleaners that perform as good as or better than a baseline of traditional cleaning methods. The following is an explanation of the methods used, presentation of the data, discussion and analysis of the results, and a brief summary.

EXPLANATION OF METHODS USED

Our testing process can be applied to any material and contaminate so that any application can be tested. My major contribution to the program has been testing the cleaning effectiveness of over 40 various cleaning agents and comparing their performance with an established baseline in an attempt to identify alternative cleaning processes for cleaning Trimsol off of Aluminum Parts.

MATERIAL

The material that we selected was 6061 Aluminum. This material was chosen on the basis that it accurately represents aluminum commonly worked with at LLNL machine shops as well as in industry. For example, 6061 aluminum is commonly used in the fabrication of electronic chassis' and system enclosures at LLNL. Aluminum in these applications must often be contaminant free before being coated with alodine (a coating which keeps aluminum from oxidizing while adding electrical conductivity to the chassis).

CONTAMINATE

The contaminate that we have chosen is Trimsol. Trimsol is a water miscible cutting and grinding fluid concentrate commonly used for applications with aluminum in machining shops at LLNL and in industry.

CLEANLINESS SPECIFICATIONS/REQUIREMENTS

Unfortunately, no standard cleanliness specifications/requirements exist for cleaning Trimsol from 6061 Aluminum. Consequently, we have established a baseline set of cleanliness specifications/requirements by: (1) identifying traditional cleaning processes actually used at LLNL shops and labs for the application being tested, (2) cleaning our test coupons (1/2x2 1/2 samples of 6061 Aluminum contaminated with Trimsol) using traditional cleaning processes, and (3) evaluating the cleanliness of these samples using Fourier Transform Infrared Spectroscopy (FTIR).

IDENTIFY TRADITIONAL CLEANING METHOD

Because no cleaning specifications/requirements had existed prior to our tests, our first step was to identify traditional cleaning methods and evaluate their cleaning performance. The cleaning methods that we have identified as representing those actually used for cleaning Trimsol from aluminum at LLNL and industry are as listed:

- Freon-TE Vapor Degreaser with on Freon-TE rinse
- Freon-TE Vapor Degreaser with two Freon-TE rinses
- 1,1,1 Trichloroethane Vapor Degreaser
- Freon-TE Ultrasonic Cleaner
- 1,1,1 Trichloroethane Ultrasonic Cleaner (Ambient)
- 1,1,1 Trichloroethane Ultrasonic Cleaner (raised temperature)
- Isopropyl Alcohol Ultrasonic Cleaner
- Acetone Ultrasonic Cleaner

IDENTIFY ALTERNATIVE CLEANING METHOD

Over thirty different alternative cleaning agents were chosen to be tested on the basis that they were marketed as being environmentally benign cleaning agents. The actual method of application chosen was ultrasonic cleaning. An ultrasonic cleaner was chosen because this process allows for constant time, temperature, and agitation. In addition, thus ultrasonic cleaning process helped create a testing atmosphere that was not operator sensitive while optimizing cleaning effectiveness. Each sample was cleaned in this unit at 50 kHz, 40 degrees Celsius, for 5 minutes. The samples were then rinsed in the ultrasonic cleaner with deionized water for 5 minutes under the same conditions. Following the rinse, the samples were allowed to air dry. The manufacturers recommended application was not followed for each cleaning agent. Instead, each cleaning agent was applied in the same fashion so as to keep the variables constant throughout testing. In addition, the temperature was set at 40 degrees Celsius to avoid meeting the flash points of some of the cleaners tested.

CLEANING PROCEDURE

As illustrated in figure 1, each test coupon was contaminated with Trimsol before being ultrasonically cleaned in a bath containing a chosen cleaning agent. Next, each sample was placed in a deionized water rinse under the same conditions. Finally, each sample was allowed to air dry. Once dried, the cleaned

Figure 1

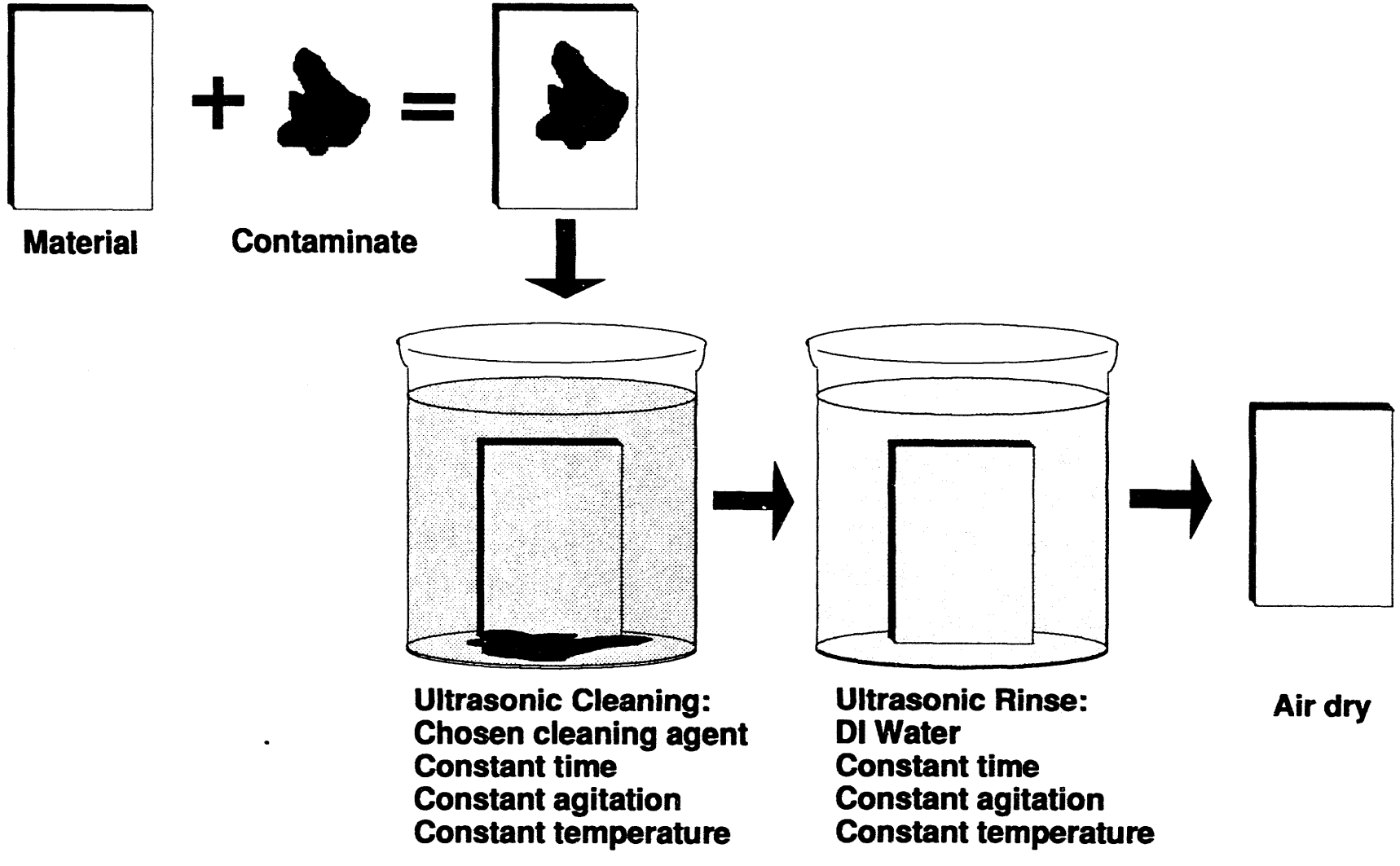
Material
Contaminate
Ultrasonic Cleaning:
Chosen cleaning agent
Constant time
Constant agitation
Constant temperature
Ultrasonic Rinse:
DI Water
Constant time
Constant agitation
Constant temperature
Air dry

test coupons were individually packaged in petri dishes in preparation for FTIR cleanliness evaluation testing.

EVALUATION OF CLEANLINESS

Fourier Transform Infrared (FTIR) Spectroscopy is the method which is used to measure the layer thickness of hydrocarbon contamination on the surface of aluminum. This method takes advantage of a molecule's characteristic of absorbing infrared frequencies of light that correspond to the molecules vibrational modes. The frequencies absorbed during the FTIR tests relate directly to the compounds remaining on the aluminum surface after being cleaned. We are interested in the frequency absorbed at 2900 wavenumbers because this wavelength corresponds to hydrocarbons. In turn, Hydrocarbons are a major constituent of Trimsol.

PRESENTATION OF DATA

The cleaning effectiveness of each cleaner was tested three times using the above cleaning procedure and FTIR technique. Figures 2 and 3 illustrate the average results of these three test runs.

As mentioned, a baseline specification of cleanliness had to be established for cleaning Trimsol off of aluminum before we could compare the cleaning effectiveness of traditional and alternative cleaning processes. Figure 2 illustrates hydrocarbon contamination in nanometers of thickness on those test coupons cleaned with traditional solvents and methods.

With an established baseline for cleaning performance with traditional solvents (Figure2), this baseline can now be compared to the performance of alternative cleaners (Figure 3). Of the alternatives tested, we are only concerned with those performing as good as or better than the baseline.

Figure 2

HYDROCARBON CONTAMINATION: BASELINE SOLVENTS

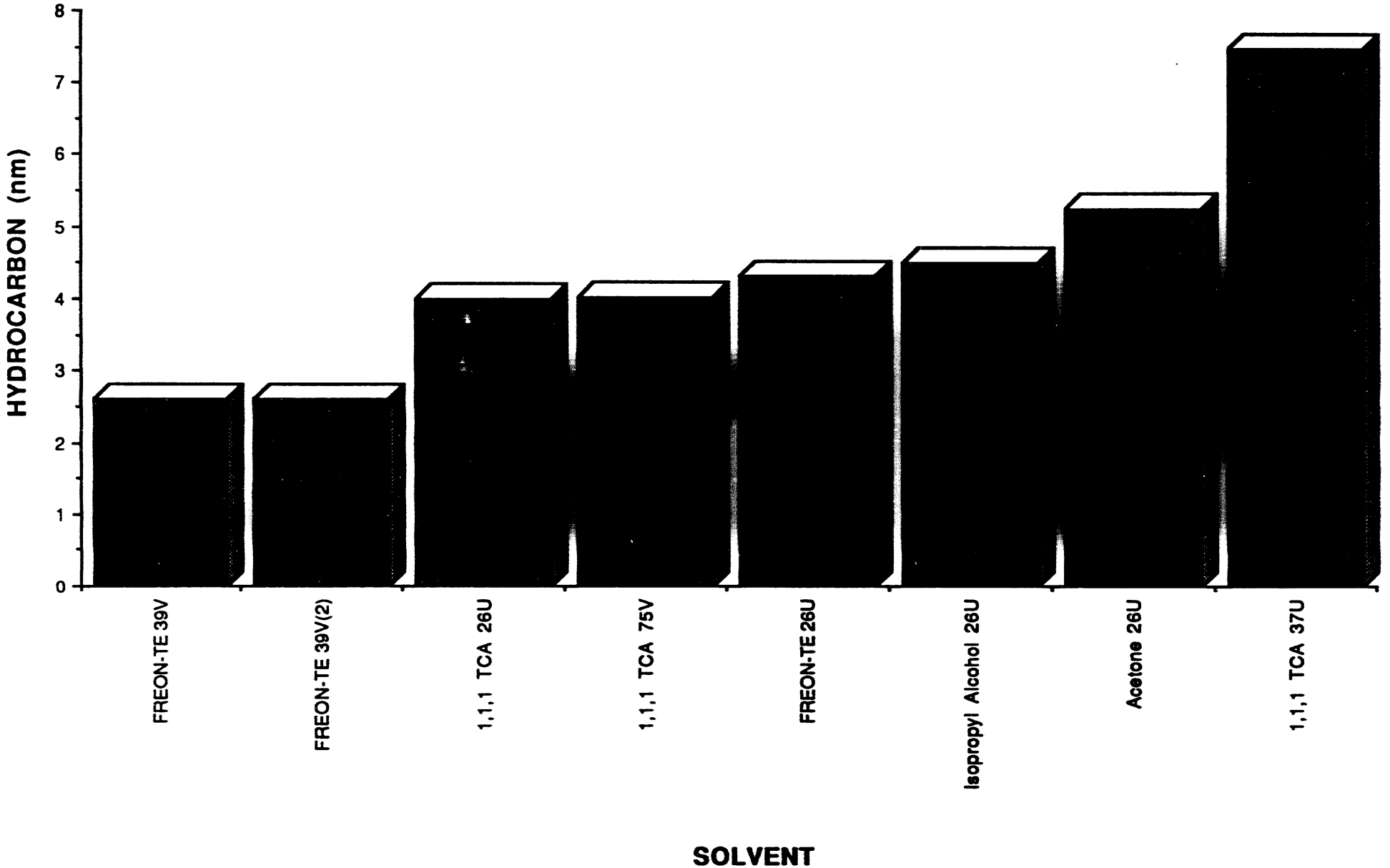

Figure 3

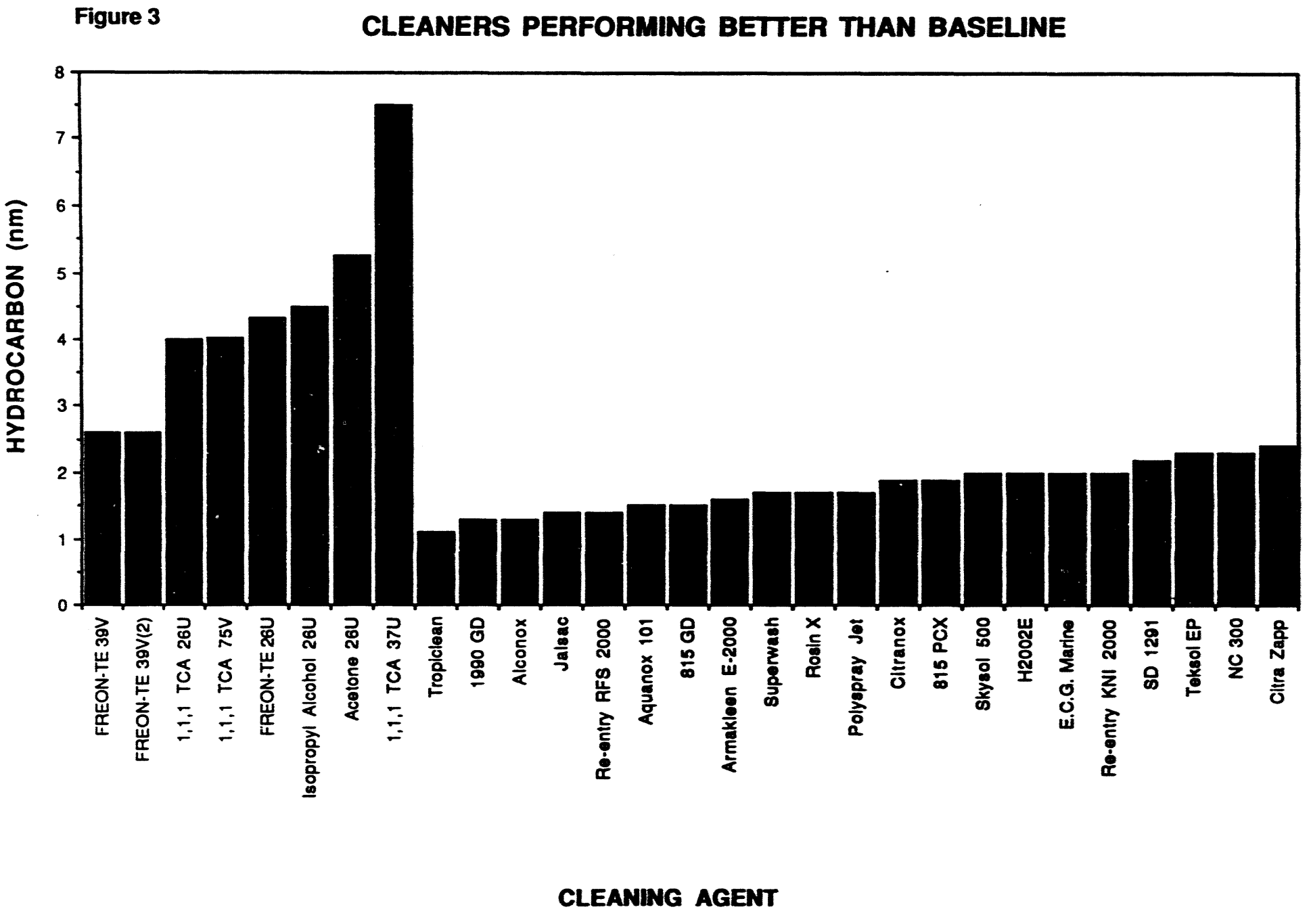
CLEANERS PERFORMING BETTER THAN BASELINE
HYDROCARBON (nm)
0
1
2
3
4
5
6
7
8
FREON-TE 39V
FREON-TE 39V(2)
1,1,1 TCA 26U
1,1,1 TCA 75V
FREON-TE 26U
Isopropyl Alcohol 26U
Acetone 26U
1,1,1 TCA 37U
Tropiclean
1990 GD
Alconox
Jalsac
Re-entry RFS 2000
Aquanox 101
815 GD
Armakleen E-2000
Superwash
Rosin X
Polyspray Jet
Citranox
815 PCX
Skysol 500
H2002E
E.C.G. Marine
Re-entry KNI 2000
SD 1291
Teksol EP
NC 300
Citra Zapp
CLEANING AGENT

DISCUSSION AND ANALYSIS OF DATA

The test coupons cleaned using Freon-TE in a vapor degreaser at 39 degrees Celsius and rinsed once in an ambient Freon-TE rinse tank performed the best leaving only 2.6 nm of hydrocarbon contamination on the surface. The test coupons cleaned using the same method with an additional Freon-TE rinse at ambient temperature performed equally as good. This would indicate that the contamination removal took place during the raised temperature wash and /or the ambient rinse. Moreover, this data may show that Freon-TE cannot remove the contamination beyond 2.6 nm.

1,1,1 Trichloroethane in an ultrasonic cleaner at ambient temperature (26 degrees Celsius) cleaned the test coupons to an average of 4.0 nm of hydrocarbon thickness. Test coupons cleaned in a 1,1,1 Trichloroethane vapor degreaser at 75 degrees Celsius also left a 4.0 nm hydrocarbon contamination.

Freon-TE in an ultrasonic cleaner at ambient temperature left a 4.3 nm thick hydrocarbon contamination. Isopropyl Alcohol in these same conditions left a 4.5 nm hydrocarbon contamination. Acetone was also tested in an ultrasonic cleaner at ambient temperature and left a 5.3 nm hydrocarbon contamination.

The highest level of contamination remaining on those coupons cleaned with baseline cleaning processes was 7.5 nm and occurred on those samples cleaned ultrasonically with 1,1,1 Trichloroethane at 37 degrees Celsius. This figure is suprising because the samples cleaned under the same conditions, but at 26 degrees Celsius, only left 4.0 nm of hydrocarbon contamination. Normally, chemical reactions are accelerated and cleaning effectiveness would increase as a function of temperature. However, in this case, the samples cleaned at 26 degrees Celsius cleaned nearly twice as good as those cleaned at 37 degrees Celsius. (explanation?)

NOTE: These baseline cleaning processes were carried out under the same conditions as would normally be done with aluminum parts contaminated with Trimsol with traditional solvents.

Of the twenty-one cleaning agents that performed as good as or better than the baseline, nine have been identified as being acceptable substitutes based on quantitative and qualitative data. Although the samples that were eliminated cleaned the Trimsol off effectively, they also reacted or left a residue with the aluminum. Listed below are the nine alternative cleaning agents which performed the best against the baseline.

- 1990 GD 1.3nm
- Alconox 1.3nm
- Jalsac 1.4nm
- 815 GD 1.5nm
- Citranox 1.9nm
- E.C.G. Marine 2.0nm
- SD 1291 2.2nm
- Teksol EP 2.3nm
- Citra Zapp 2.4nm

SUMMARY

Our goal is to identify high performance, environmentally benign cleaning processes for use at the lab to minimize the problems associated with traditional solvents. One step we have taken in meeting that goal is in identifying alternative processes for cleaning a common type of aluminum contaminated with a common cutting oil. Less formal tests than these have already contributed to minimizing the use of Freon-TE, 1,1,1 Trichloroethane, Acetone, and Isopropyl Alcohol at LLNL. Future tests are scheduled to include removing vacuum grease from glass and stainless steel. In addition, tests will also be custom designed to meet the requirements of any application as demand for alternative cleaning processes grow.

Beamlet Front End Harmonic Generation Experiments*

Iwona A. Palusinski
University of Arizona
Laser Division

University of California
Lawrence Livermore National Laboratory
Livermore, CA 94550

ABSTRACT

With the Beamlet Front End down-collimated to produce up to 4 GW/cm^2, this experiment will determine the reduction in harmonic generation efficiency as bandwidth increases on the fundamental beam to suppress transverse stimulated Brillouin scattering (SBS). We will show that for applied bandwidths sufficient to suppress SBS in the Beamlet output optics, the harmonic generation efficiency to the third harmonic will remain around 70%, thus allowing the Beamlet milestone of 5 kJ of energy in a 3 ns pulse at 351 nm to be attained.

2. INTRODUCTION

The Beamlet laser is a 1.053 μm Nd:glass laser within the Inertial Confinement Fusion (ICF) Division at the Lawrence Livermore National Laboratory. The project's overall goal is to achieve 5 kJ of energy at 351nm in a 3 ns pulse.

The 351nm wavelength is of great importance to the ICF program because plasma targets absorb energy from shorter wavelengths of light more readily than longer wavelengths of light. Plasmas absorb 93% of the energy from 351 nm light while only

*This work was supported in part by an appointment to the U.S. Department of Energy Science and Engineering Research Semester (hereinafter called SERS) program administered by LLNL under Contract no. W-7405-ENG-48 with Lawrence Livermore National Laboratory.

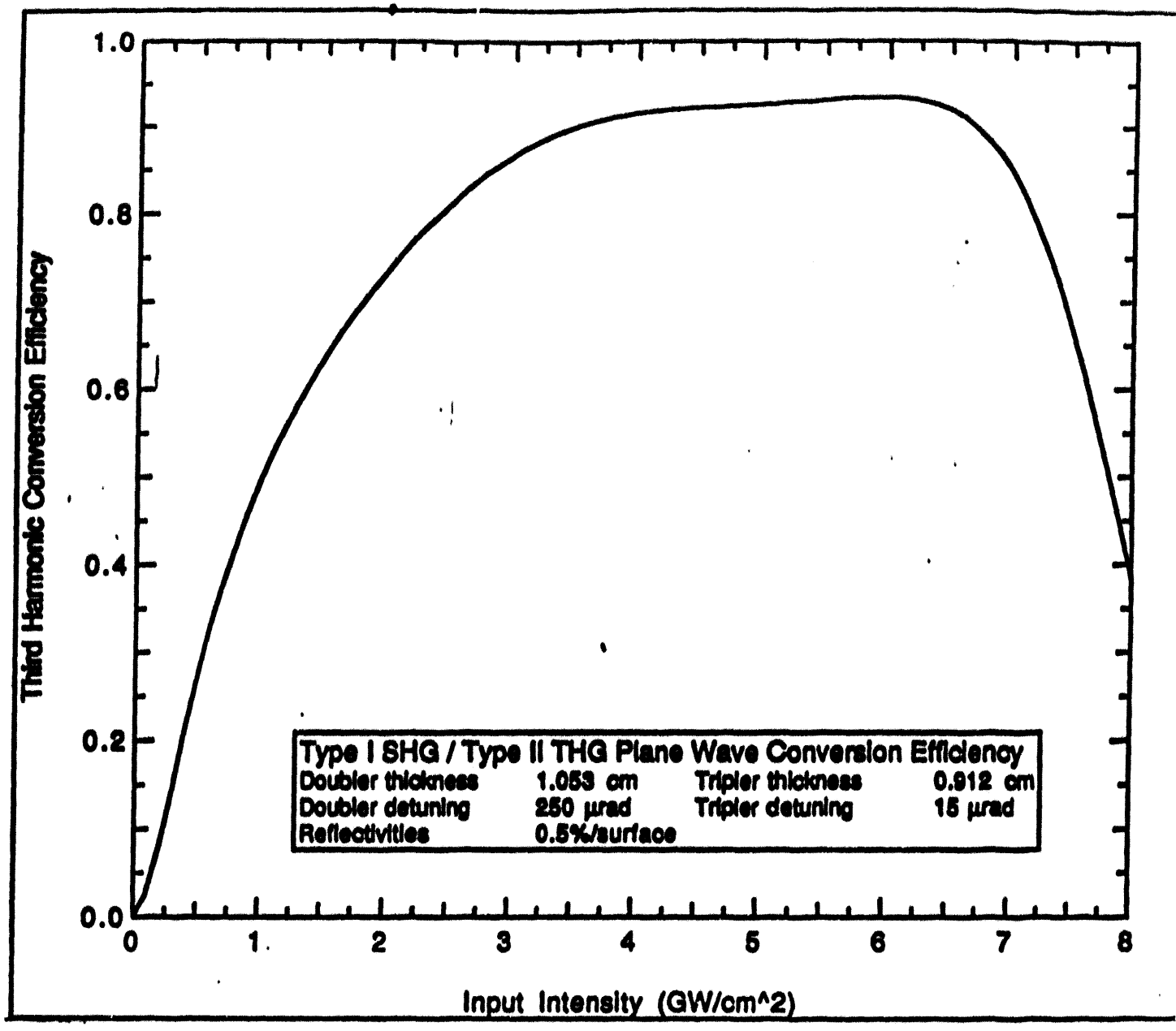

Figure 1. Efficiency of Type I Second harmonic conversion/ Type II Third harmonic conversion is plotted against intensity. It is demonstrated that efficiency of third harmonic generation on Beamlet will be severely limited when intensities go beyond 6.75 GW/cm^2.

49% of the energy from 1.053 μm[1]. The ICF program uses glass lasers that operate at 1.053 μm because they are the shortest wavelength lasers in existence that are capable of delivering high energy to targets[2]. The energy produced by a 1.053 μm laser is easily converted to the more useful 351 nm wavelength by harmonic generation.

Due to high fluences on the Beamlet laser, a large bandwidth is required to overcome the risk of stimulated Brillouin scattering (SBS) at the output. As high intensity light passes through large aperture optics, some of the energy is side–scattered and hits o–rings and other supports. The o–rings and supports absorb this energy and send out an acoustic wave focused on the center of the optic. This wave can be strong enough to shatter the optic[3]. Murray et. al., have demonstrated that for fused-silica lenses, which are used on the Beamlet laser, a bandwidth of 8 GHz reduces SBS to an insignificant level. Large bandwidths however, reduce the efficiency of harmonic generation.

We performed a series of experiments to asses quantitatively the influence of bandwidth on harmonic generation efficiency. We wanted to determine whether at high intensities (greater than 2 GW/cm^2), bandwidth for sufficient suppression of SBS on Beamlet would reduce harmonic generation efficiency below 70%. This was of concern because as Figure 1 shows, bandwidth reduces harmonic generation efficiency more severely as intensity increases[4].

We used the Front End of the Beamlet laser for these experiments because of its capabilities to generate bandwidth of up to 90 GHz by phase modulation in an

integrated waveguide modulator. Bandwidth is produced in two ways. The phase modulators are driven by single rf frequency and by a sum of two rf frequencies.

The Front End is also capable of generating over 10 J of energy with an adjustable pulse shape. The pulses can vary in length (200 ps to 3 ns) and have a bandwidth of up to 90 GHz[5].

3. EXPERIMENTAL SETUP

The Beamlet Front End was modified to produce up to 4 GW/cm^2 by use of a 5X reducing telescope. The telescope was used so that fluences that will be present on the Beamlet laser could be simulated. The beam was diverted from the output beamline to the telescope by a turning mirror placed at the end of spatial filter 4 (Figure 2). The beam was then directed to the doubling and tripling crystals on the harmonic generation table (Figure 3). Beamlet Front End harmonic generation of 351 nm (3ω) from 1.053 μm light (1ω) took place using a Type I/Type II orientation of the KDP doubler and tripler crystals respectively. The crystals are 5x5 cm square with a 10 mm thickness. The various wavelengths produced were then sent to an array of energy and pulse shape diagnostics.

Before the harmonic generating crystals were put in place, we characterized the diagnostics on the harmonic generating table. The beam paths of the 1ω, 2ω, and 3ω were mapped out and directed into appropriate calorimeters. These calorimeters measured the energy of the 1ω input and output beams as well as the 2ω and 3ω output beams. The calorimeters were calibrated by resistive calibration heaters and a program

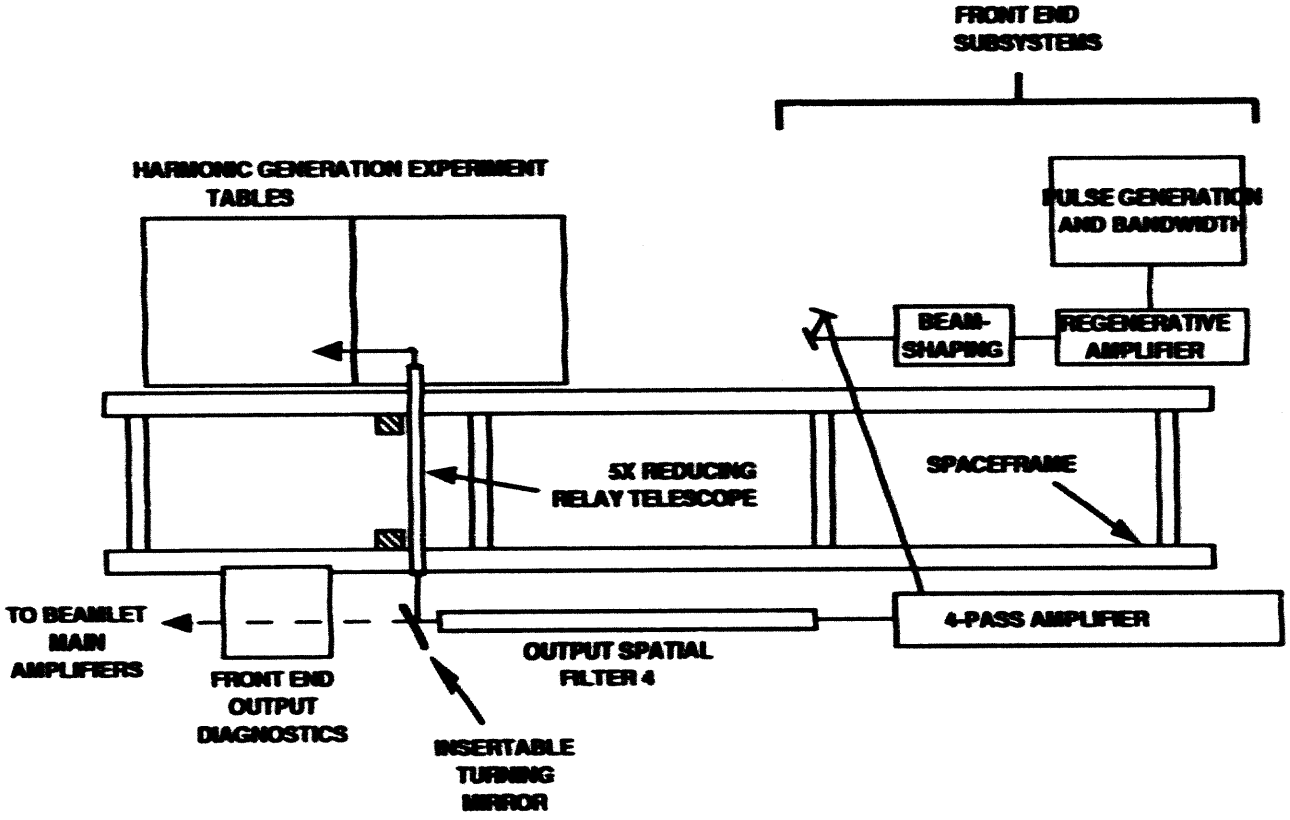

Figure 2. The Front End of the Beamlet laser was modified to produce up to 4GW/cm^2. A turning mirror was inserted at the end of spatial filter four to direct the 1w beam onto the harmonic generation table.

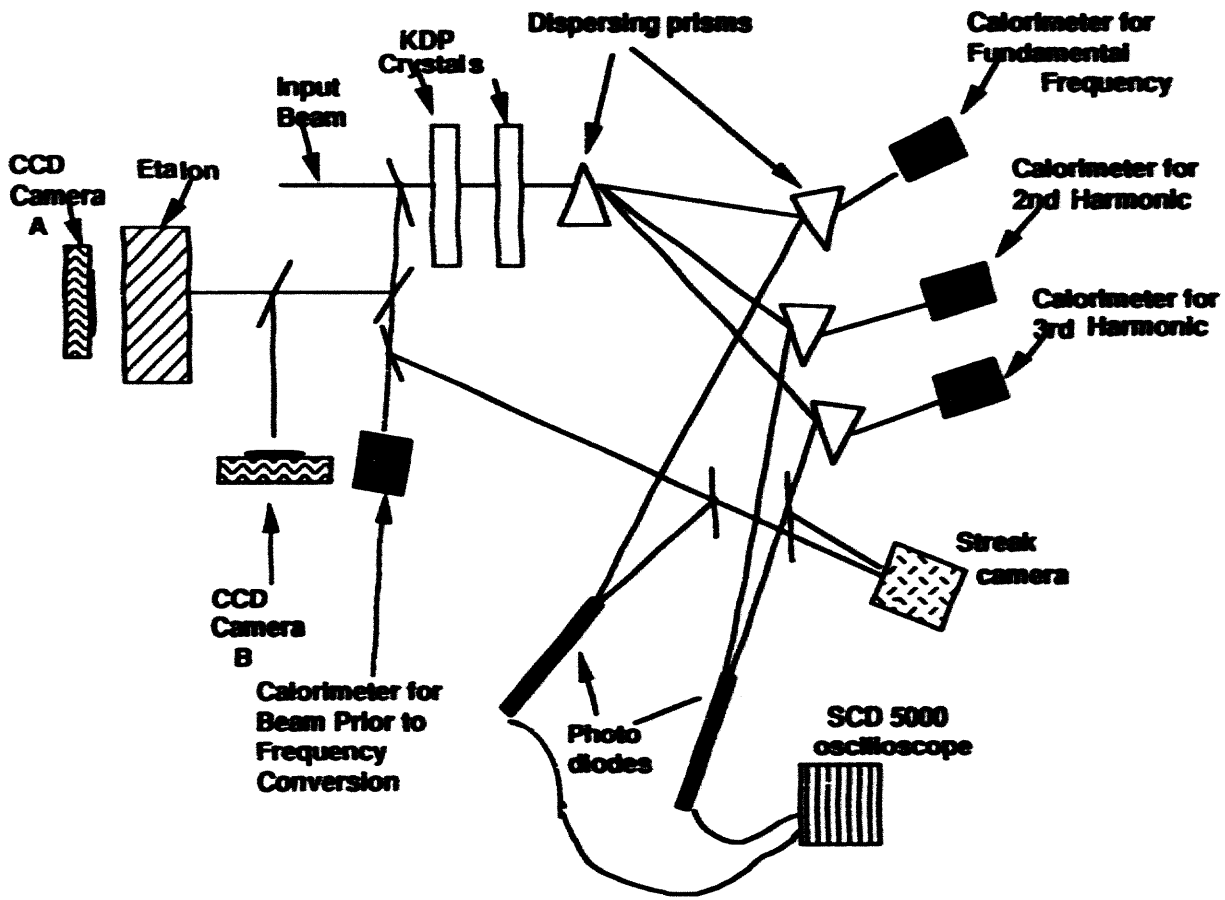

Figure 3. Harmonic Generation Table (schematic).
The input beam comes from the 5X reducing telescope onto the table and is diverted into the Fizeau etalon for bandwidth monitoring. CCD camera B looks at the near field of the beam profile and verifies beam centering on the crystals. The input beam is also diverted to a calorimeter to record energy levels prior to harmonic conversion. The other part of the input beam goes through the KDP crystals and is harmonically converted. The 1w, 2w, and 3w output beams are then dispersed by a prism to calorimeters for energy readout. The prisms directly in front of the calorimeters are used to counteract beam distortion caused by the first prism. The photodiodes and streak camera register beam pulse shapes.

developed by using *LabView* software. The program was designed to record the energy readings of each of the calorimeters with an accuracy of +– 2%. The program accounted for reflections and transmissions at optical surfaces so that a total energy balance for each of the harmonics could be calculated.

Two CCD cameras were tested and characterized by dark current measurements and variance vs. signal graphs. The cameras were connected to monitors and cooled to –50 C. Camera A was used to record bandwidth spectra using a Fizeau etalon. Camera B was used to record near field beam profile and verify beam centering on the crystals.

A third non–cooled CCD camera was used to verify beam pointing and crystal alignment using surface reflections form each of the crystals.

The Fizeau etalon was tested and produced a finesse of 89.1 and set to a free spectral range of 100 GHz. This etalon was aligned with camera A such that bandwidth spectra could be imaged.

Temporal pulse shape analysis was done by fast photodiodes and a streak camera. Photodiodes recorded the pulse shapes on an oscilloscope (SCD 5000). One photodiode traced the 1ω input and 1ω output harmonics and the other photodiode traced the 2ω and 3ω output harmonics. A more detailed analysis of the pulse shape was done with the 1ω input and 3ω output harmonics directed into a streak camera.

Once the diagnostics were aligned and calibrated, the KDP crystals were put in place. The crystals were placed in mounts with calibrated angular adjustments, and the

resolution was approximately 8 μrad. However, the actual alignment resolution was limited by the beam pointing stability of the laser and thus was approximately 20 μrad. Low energy regen amplifier pulses were used for rocking curves because of their high repetition rate of 5 seconds. If the laser were to be used, data points could only be gathered every 20 minutes.

The doubler was mounted first and a rocking curve was generated to find the best orientation for optimum 2nd harmonic generation (Figure 4). An energy meter was placed behind the crystal to measure the energy of the converted green light and the red light that was not converted. It was of interest to use relative measurements from the energy meter to locate the angular position for maximum 2nd harmonic generation.

When the tripling crystal was in its mount, a rocking curve was also generated to find the position for maximum 3rd harmonic generation. This test was done using the *LabView* calorimeter program instead of using the energy meter because the meter could not detect energy from the 3ω beam. Attaining maximum 3ω generation was difficult because the doubler had to be detuned and matched with the tripler to create the red to green intensity ratio of 1:2 to enter the tripler. The task of detuning the doubler was very crucial because it was a Type I instead of a Type II doubler. Type I doublers are very sensitive to angular tuning especially when incident intensities exceeded 2.5 GW/cm^2. The Type I doubler was chosen for Beamlet because of its degree of insensitivity to beam depolarization. Beam depolarization is considered a high possibility on Beamlet.

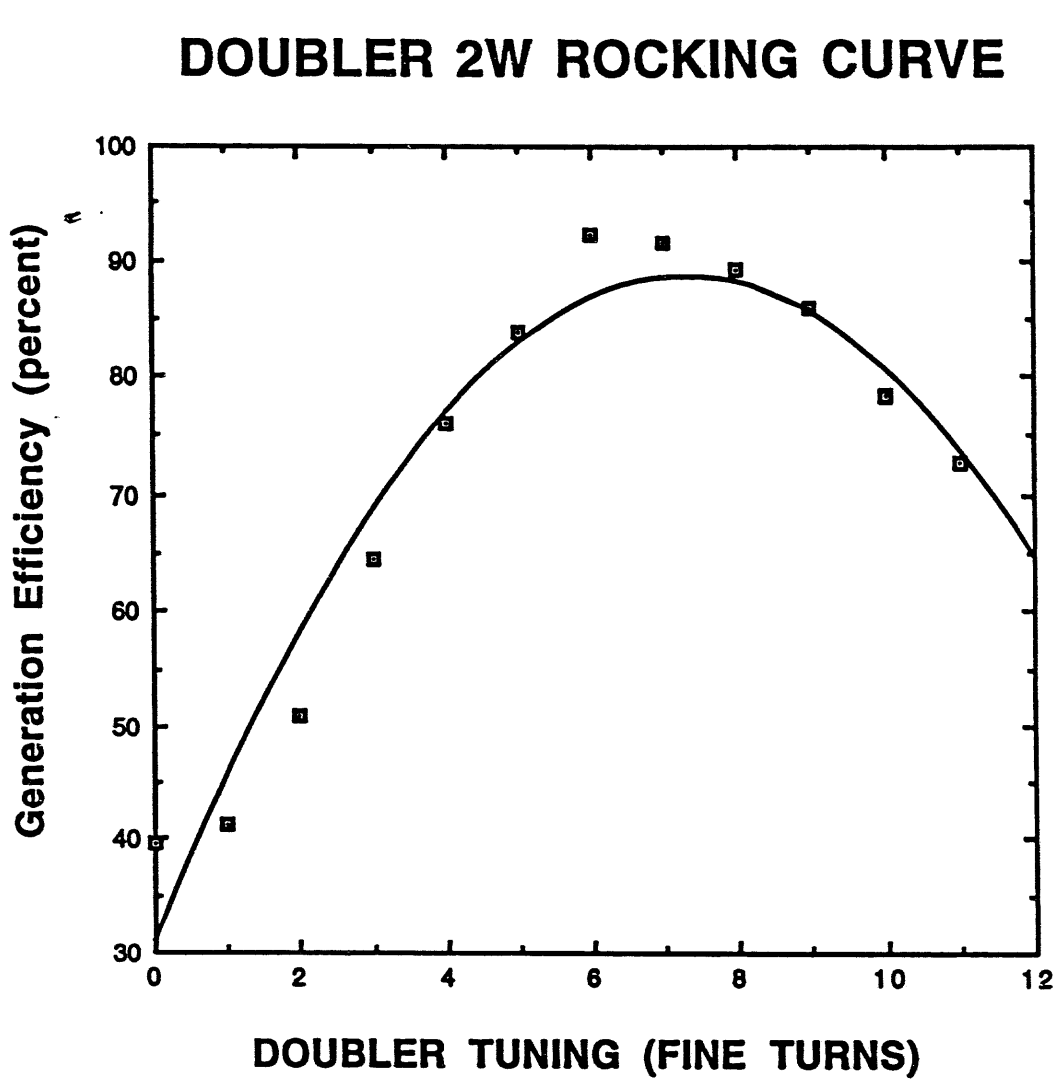

Figure 4. The doubler rocking curve was used to align the doubling crystal. It was only of interest to find the tuning position where the generation efficiency was a maximum. The optimum generation efficiency was achieved on the seventh fine turn.

Rocking curves were measured at lower intensities where back conversion was not present. Once optimum crystal alignment was established, incident 1ω intensity was increased to 3.5 GW/cm^2. It was of interest to achieve 70% conversion from 1ω to 3ω energy at high intensities.

4. BANDWIDTH EXPERIMENTS

Prior to conducting harmonic generation experiments with bandwidth, we studied the effects of bandwidth and pulse length on spectral stability. Regen pulses with bandwidth from the master oscillator were imaged onto camera A through the Fizeau etalon. The master oscillator pulse was varied by changing the bandwidth and the pulse length. Tests were done with the following configurations: 4 GHz 2W rf power from 0.5 ns to 3 ns; 8 GHz 2.1W rf power 0.5 ns to 3 ns; 4 GHz(1W rf power)/5 GHz(0.6W rf power) 1 ns to 3 ns; and 5.3 GHz(1W rf power)/8 GHz(0.6W rf power) at 3 ns. Three spectra were recorded at each pulse length. As the pulse length was shortened in 0.5 ns increments, the amplitudes of the spectral peaks decreased because of the reduced exposure time to regen output intensity. Shortened pulse lengths also diminished the resolution of the Fizeau etalon.

The spectral lineouts were recorded, corrected for background, and normalized. The graphs were analyzed shot-to-shot during the same pulse length, same frequency at all pulse lengths, and then a comparison was made between mixed modulation frequency and single modulation frequency.

From the bandwidth data, it was possible to draw a general conclusion on single and mixed modulation frequencies. Single modulation frequencies were found to be more stable shot-to-shot and varied less with pulse length modulation than mixed modulation frequencies.

The comparison of shot–to–shot stability between single and mixed frequencies was demonstrated by the 4 GHz and 4 GHz/5.3 GHz data. Figure 5 shows the stability of the 4 GHz bandwidth at 0.5 ns and 3 ns. The stability is characterized by keeping the same general shape and number of the peaks, but some amplitude variation of individual peaks is allowed due to variation in the output of the regen. It was sufficient to show stability of the spectra at the two extremes of 0.5 ns and 3 ns because the spectral stability increases as the pulse length increases.

The 4 GHz/5.3 GHz data in Figure 6 shows the instability of mixed frequencies when the inverse of the pulse length is very close to the frequency separation of the two modulating frequencies. We can see in Figure 6 that the basic spectral shape varies quite considerably between shots. This instability can occur because a complete cycle of the difference frequency takes about 0.769 ns while the full pulse length is only 1ns. The short pulse length prevents many cycles from appearing thus allowing variations in oscillation of the frequency to become more apparent.

Figure 7 shows the stability of single modulation frequencies when pulse length is varied. Each of the peaks of the 8 GHz spectra falls on top of the previous peaks. This did not occur at mixed modulation frequencies because of the instability in spectral patterns at short pulse lengths.

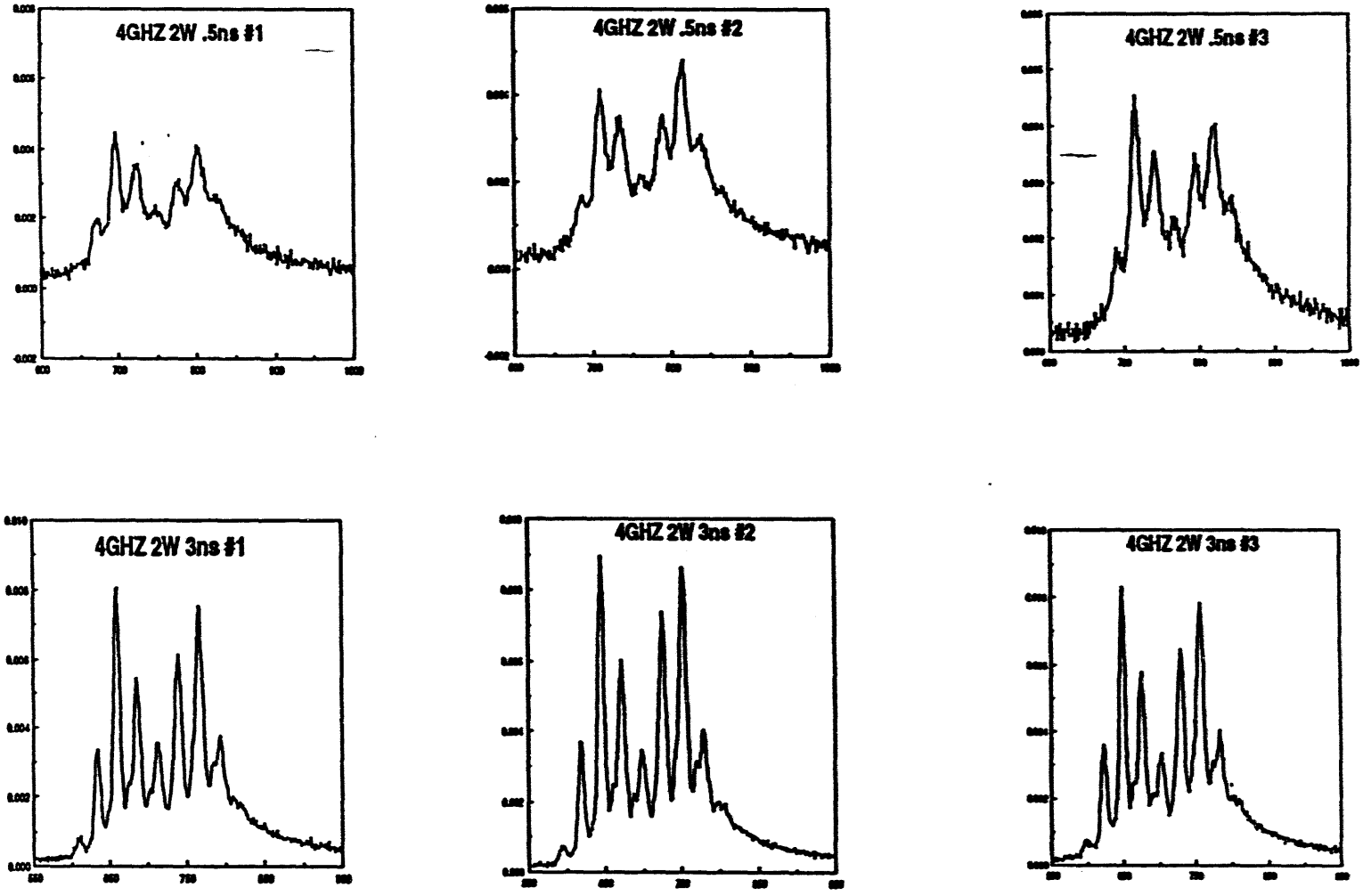

Figure 5. These spectra at 4 GHz demonstrate the shot-to-shot stability of single modulation frequency. There are 7 peaks in each spectra at the 0.5 ns and 3 ns pulses. The stability of spectra is evaluated by the number of peaks and not the relative amplitudes of the peaks. The amplitudes may vary slightly due to the variation in regen output.

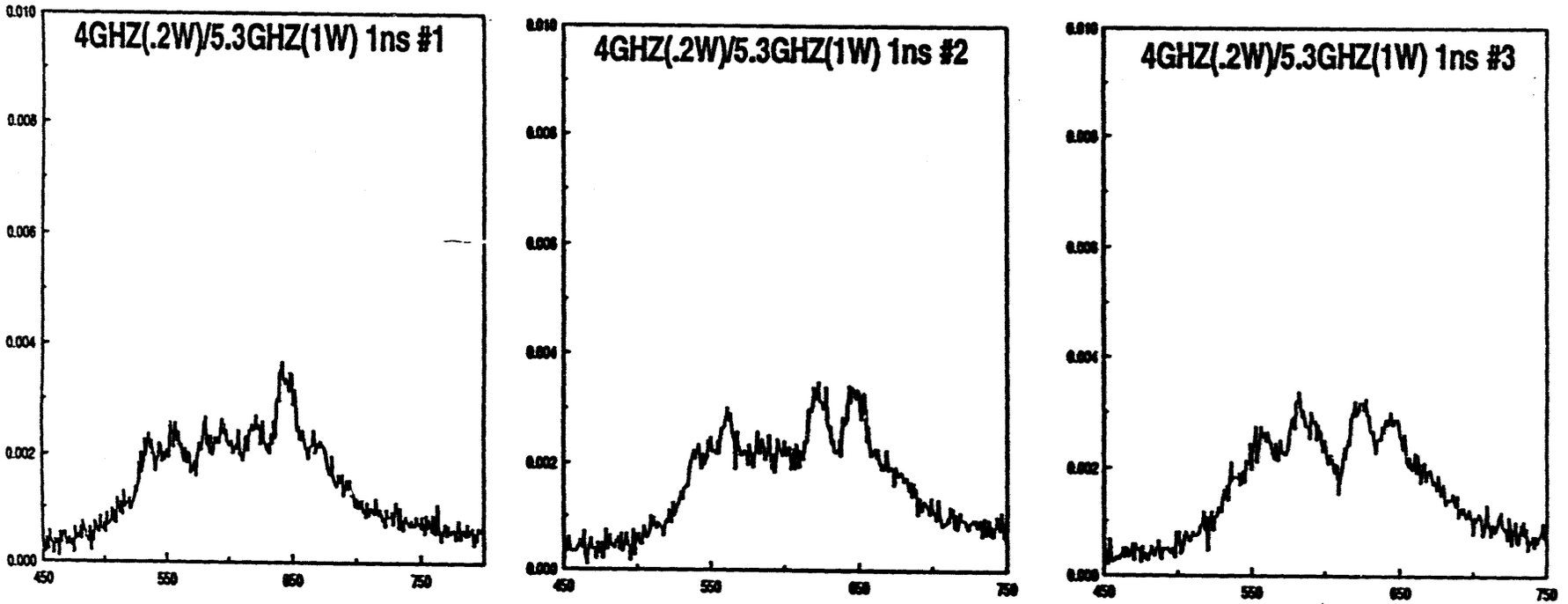

Figure 6. These spectra for the 4 GHz/5.3 GHz data vary greatly at a 1 ns pulse length. The shape is not constant and neither is the number of peaks. This did not occur for pulse lengths greater than 1 ns. If the pulse length is longer than the inverse of the beat frequency, the spectral pattern is stable.

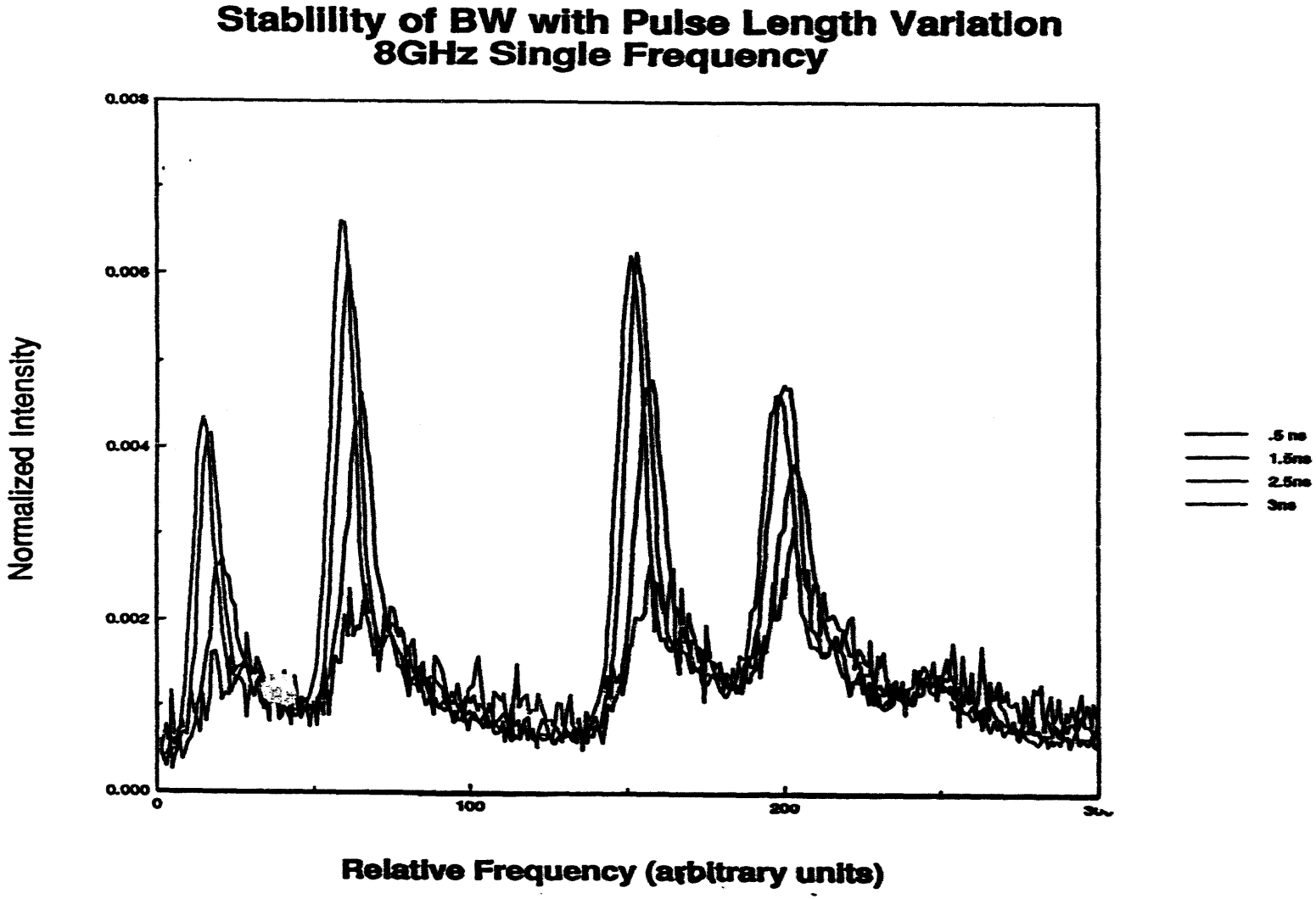

Figure 7. This plot of the 8 GHz data shows the stability of single modulation frequency spectral patterns when pulse length is varied. The number of peaks is constant and so is their spacing. The amplitude of the peaks is higher as the pulse length increases due to longer exposure to intensities on the regen.

Amplitude modulation on the pulse shape occurred at 5.3 GHz/8 GHz mixed modulation frequency. While observing the spectral patterns on the computer from CCD camera A at the 3 ns pulse length, we noticed the pattern changed distinctively between shots (Figure 8). Spectral side bands appeared and disappeared in a cyclical manner. The spectral pattern changes correlated to low and high amplitude modulation on the pulse shape at the output of the regen. Figure 9 shows the modulating pulse shapes. The reason for this modulation and its effects are not yet known. However, there are some possible explanations: the presence of intermodulation products in the rf amplifier used to drive the phase modulator, the nonlinear effects and dispersion in the long transport optical fiber between the master oscillator and the preamplifier, and the presence of etalon effects in the regenerative amplifier.

5. HARMONIC GENERATION EXPERIMENTS

Once analysis of spectral lines was completed, we began our experiments to quantify the effects of bandwidth on harmonic generation efficiency. Bandwidth generated by phase modulation of a single frequency beam can have two effects on harmonic generation. Phase modulation is a periodic frequency modulation which modulates generation efficiency and causes intensity modulation to occur. These effects are accompanied by an overall reduction in harmonic generation efficiency.

However, experiments using 32 GHz bandwidth (8 sidebands separated by 4 GHz) showed no significant effect of bandwidth on harmonic generation efficiency at intensities of up to 3.5 GW/cm^2 (Figure 10). Tests with and without bandwidth attained harmonic generation levels of 68%. Amplitude modulation did occur as theory

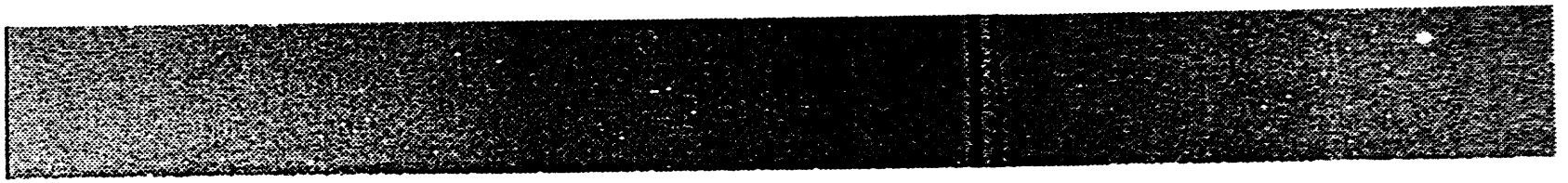

High modulation

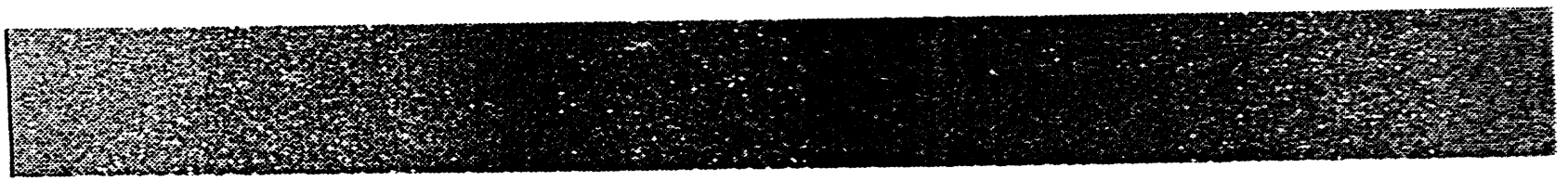

Medium modulation

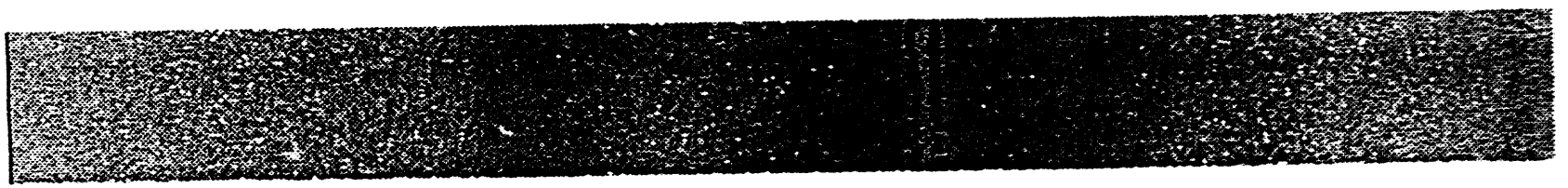

Low modulation

Figure 8. Pictures directly from the CCD camera and Fizeau elaton show the variation in fringes as pulse shape amplitude modulation occurs on the regen at 5.3 GHz/8 GHz mixed modulation frequency. The medium amplitude modulation spectra is present during the transition from high to low amplitude modulation on the pulse.

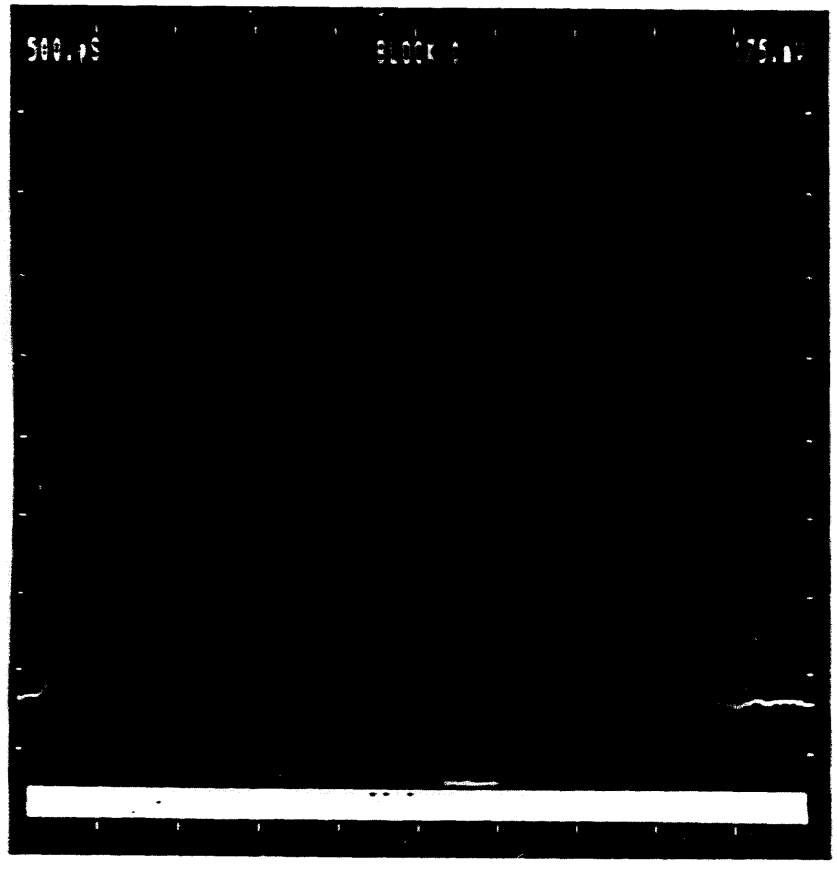

5.3 GHz (1ω)/8 GHz (0.6ω)
3 ns pulse
Regen output, low modulation

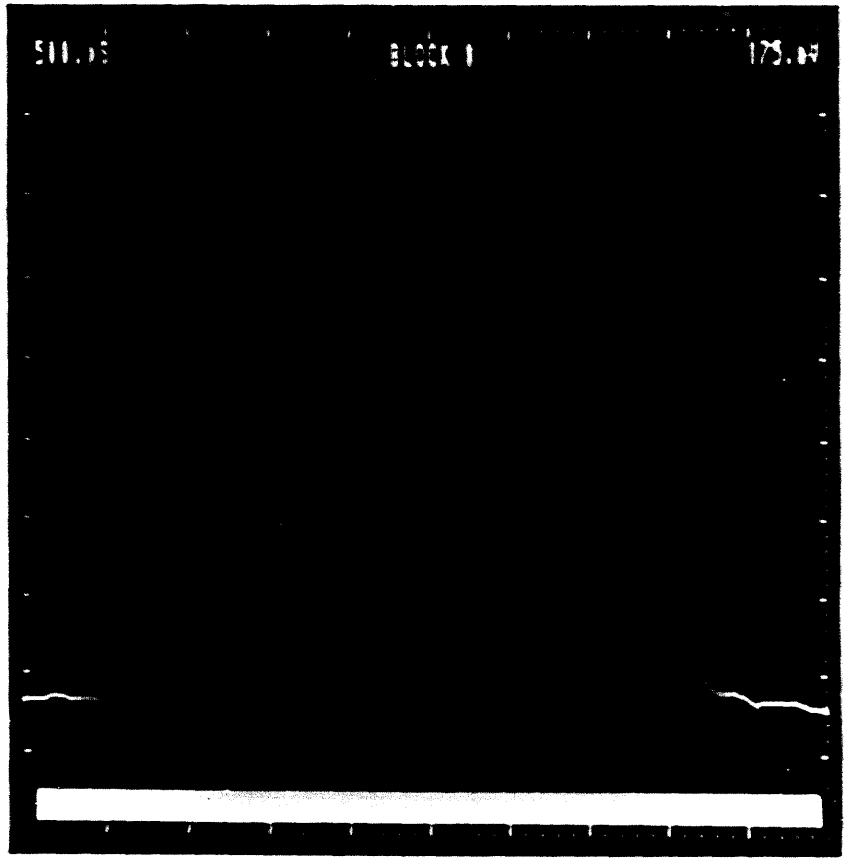

5.3 GHz (1ω)/8 GHz (0.6ω)
3 ns pulse
Regen output, high modulation

Figure 9. These oscilloscope pictures show low and high amplitude modulation on the pulse shape at the output of the regen at the mixed modulation frequency of 5.3 GHz/8 GHz. The 8 peaks on the high amplitude modulation pulse correspond to the number of cycles of the 2.7 GHz beat frequency present in a 3 ns pulse length. The low amplitude modulation pulse shows approximately twice the number of peaks in the pulse shape possibly from a doubling of frequency when low amplitude modulation is present.

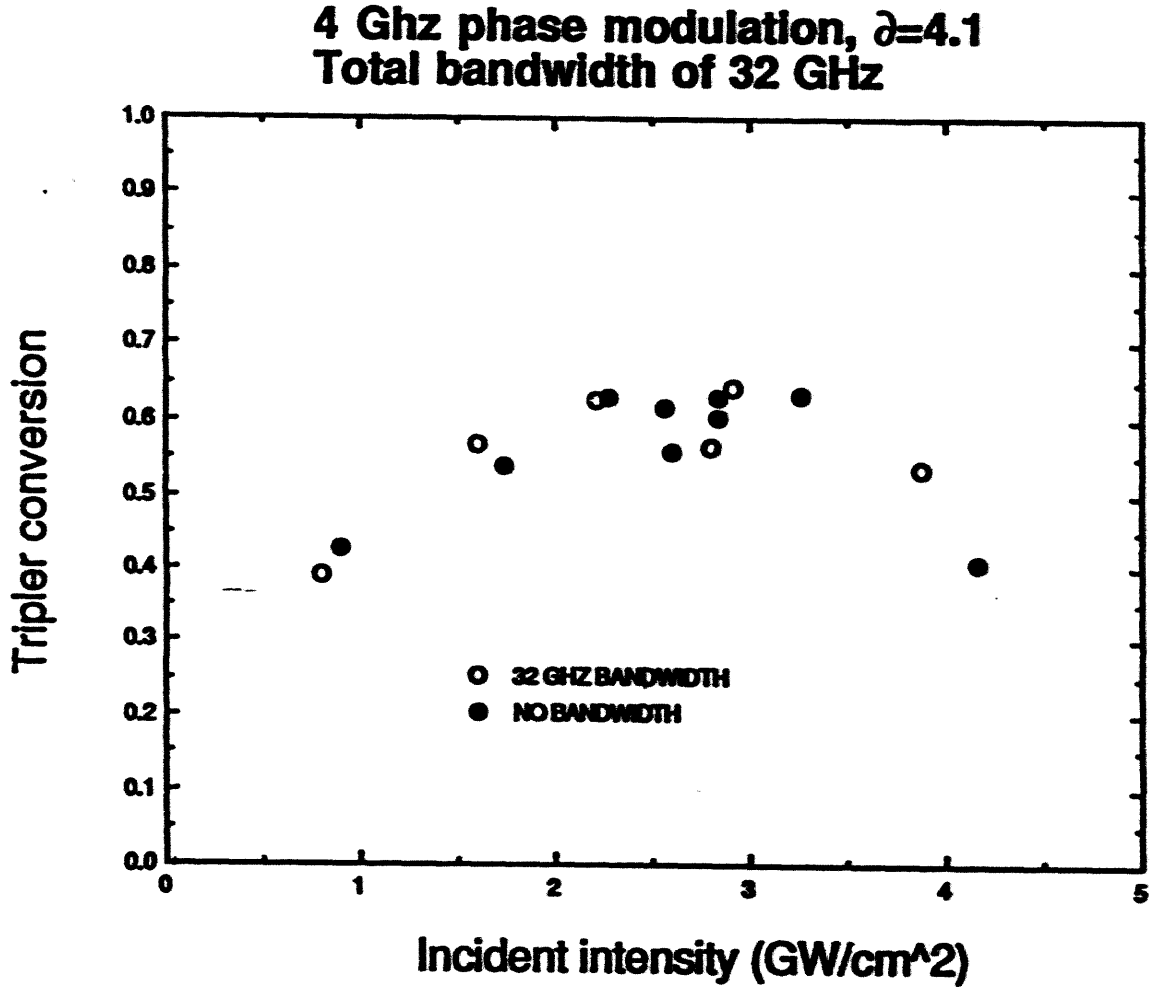

Figure 10. The graph shows that for a 4 GHz phase modulation and a 32 GHz bandwidth, there is no significant effect of bandwidth on harmonic generation efficiency. Tests with and without bandwidth resulted in approximately 65% harmonic generation efficiency.

predicted. Streak camera output results showed an intensity modulation up to 15% peak to peak in the 3ω output pulse.

6. CONCLUSION

To completely characterize the effects of bandwidth on harmonic generation efficiency, it will be necessary to use mixed modulation frequency sidebands where known instabilities of spectra and pulse shape exist. Analysis of these types of sidebands will be crucial as mixed modulation frequency sidebands are ones that will reduce the risk of SBS most significantly on Beamlet. Future experiments will involve mixed modulation frequency sidebands. We hope that the results from our experiments will lead to a better understanding of the bandwidth requirements necessary to significantly limit SBS with mixed modulation frequencies without severely decreasing the efficiency of harmonic generation efficiency.

7. ACKNOWLEDGMENTS

Charles Barker, Don Browning, Scott Burkhart my mentor, Mike Norman, and Bruno Van Wonterghem for their support and help throughout the semester in the Laboratory. Jack Campbell for his hospitality.

8. REFERENCES

1. W Kruer, *Physics Laser Plasma Interaction* (Addison Wesley, New York, 1988).
2. Energy and Technology Review, February 1985, Lawrence Livermore National Laboratory, Livermore, CA. UCRL-52000-85-2 pp. 2.
3. Murray et at., J. of the Opt. Soc. of Am. B, 8, 2410 (1989).
4. Charles Barker et al., Memo April 29, 1993, Lawrence Livermore National Laboratory, Livermore, CA. BLT-FC-93-01 Figure 2.
5. Van Wonterghem et al., Preprint, Lawrence Livermore National Laboratory, Livermore, CA. UCRL-JC-111452 pp. 1.

A STATISTICAL ANALYSIS OF MUTAGENIC AND CARCINOGENIC CHEMICAL POTENCIES

Ria Persad, SERS Participant
Princeton University
Environmental Sciences
Mentor: Dr. Kenneth Bogen

STATISTICAL ANALYSIS OF MUTAGENIC AND CARCINOGENIC CHEMICAL POTENCIES

Ria Persad
Princeton University
Lawrence Livermore National Laboratory
Livermore, CA 94550

May 21, 1993

Prepared in partial fulfillment of the requirements of the Science and Engineering Research Semester under the direction of Dr. Kenneth T. Bogen, Research Mentor, at the Lawrence Livermore National Laboratory.

*This research was supported in part by an appointment to the U.S. Department of Energy Science and Engineering Research Semeseter (hereinafter called SERS) program administered by LLNL under Contract W-7405-Eng-48 with Lawrence Livermore National Laboratory.

By acceptance of this article, the publisher or recipient acknowledges the U.S. Government's right to retain a non-exclusive, royalty-free license in and to any copyright covering this article.

PROJECT

I am involved in a statistical analysis and expansion of a database which consists of mutation and cancer-causing potency information for environmental chemicals found to cause cancer and damage DNA.

Correlations between mutagenic and carcinogenic potency based on "in vitro" test results enable us to perform preliminary, upper-bound assessments of potential carcinogenic risk of complex mixtures or unidentified compounds such as mixed-waste samples from hazardous waste sites.

Salmonella Mutagenicity Test Results: Preincubation Methodology

All chemicals were tested using the preincubation procedure of the Salmonella assay [Ames, et al, 1975]. Briefly, 0.5 ml of S-9 mix was dispensed into 13 X 100 mm culture tubes maintained at 37C, and then 0.05 ml of cells and 0.05 ml of solvent was added to each tube. There was a preincubation period for 20 minutes at 37C in open laboratory followed by 2.5 ml (EGG) or 2.0 ml (CWR, SRI) of molten top agar at 45C supplemented with 0.5 mM L-histidine and 0.5 mM D-biotin. The contents were poured onto 25 ml of minimal glucose bottom agar. After the overlay solidified, plates were inverted and incubated at 37C for 48 hours. Three plates were used, and highest dose tested was 10 mg/plate.

THE DATABASE

The database consists of selectively extracted information from

(1) seven published volumes of Ames-test data from *Environmental Mutagenesis*, Supplements 1, 2, 5, 7, 9, 12, and 21, relating to bacterial mutagenicity with and without liver-enzyme activation,

(2) four published volumes of rodent bioassay cancer potency data.

Associated with each chemical is the following data:

(1) Cancer potency reported in TD50's by species (rat, mouse, hamster)

(2) Bacterial test strain used and indication for whether data is for rat liver induced or non-induced test

(3) Mutagenicity Dose , Response, and Standard Error data sets for each tester strain with or without metabolic activation.

Sample data set for mutagen/carcinogen beta-Propiolactone:

```
{Compound identification}
Propiolactone,beta- 57-57-8  s1-207    72.07
{Cancer Potency Data}
Mouse 1.47 1.43 Rat 1.34 1.61
{Mutagenic Potency Data}
{Strain:}       TA100  N
{Doses:}        0    .33    1   3.3   10   33
{Responses:}    115  118  137   153  230  448
{Errors: }      8.4  7.3  6.4   2.8  6.7
{Strain:}       TA100  I
{Doses: }       0    .33    1   3.3   10   33
{Responses: }   167  200  201   300  492  977
{Errors:  }     3.5  2.3  14.8  4.9  20   54.6
```

This format is continued throughout the database for over 1,000 compounds. The database is then used as input in the *Mathematica* program **DataVariance**, a package written by Ken Bogen and co-written by Ria Persad to perform the Statistical Analysis of the Database.

The following is the documented *Mathematica* program **DataVariance**.

■ Test

■ MakeData

```
Off[General::spell]; Off[General::spell1];
Prn[x_]:=Print[HoldForm[x],"= ",x];
Attributes[Prn]={HoldAll};

MakeData[filename_, start_:Automatic]:=
Module[{s1,s2,s3,m1,marker=1,numspecies,numstrains,numdoses,
     cancerpotlist,mutpotlist,datalist,compoundlist,
     specieslist,all={},range,test=True,n,auto=True,a,b,
     types,i},

(* MakeData converts a string of carcinogenic-mutagenic
     data to a list of the following form:
     {Chemical info, {Carcinogenic Potency info by species},
     {Mutagenic Strains and Dose-Response-Error sets}}
*)

Open[filename];
m1 = ReadList[filename,Word];
n = Length[m1];
If[IntegerQ[start] && start>0, auto=False; marker=start];
While[test,
     If[Not[IntegerQ[ToExpression[m1[[marker+1]]]]]===True,
          m1[[marker+1]] =
               StringJoin[ m1[[marker]], " ", m1[[marker+1]] ];
          marker++
     ];

     compoundlist = Join[ m1[[{marker,marker+1,marker+2}]],
          ToExpression[ m1[[{marker+3,marker+4}]] ] ];
     marker = marker + 5;
     numspecies = ToExpression[m1[[marker]]];
     cancerpotlist={};
     For[eachspecies = 1, eachspecies<=numspecies,eachspecies++,
          numTD50 = ToExpression[m1[[marker+2]]];
          specieslist = {m1[[marker+1]],
               m1[[Range[marker+3, marker+2+numTD50]]]};
          AppendTo[cancerpotlist, ToExpression[specieslist]];
          marker = marker + 2 + numTD50
     ];
     numstrains = ToExpression[m1[[marker+1]]];
     mutpotlist = {};
     marker = marker+2;
     For[eachstrain = 1, eachstrain<=numstrains, eachstrain++,
          datalist = {};
          numdoses = ToExpression[m1[[marker+2]]];
```

```
            If[numdoses != 0,
                range = Range[marker+3, marker+2+(3*numdoses)];
                datalist = Partition[m1[[range]],numdoses];
            ];
            datalist=ToExpression[{{m1[[marker  ]],
                                    m1[[marker+1]]},datalist}];
            AppendTo[mutpotlist, datalist];
            marker = (marker+3)+(3*numdoses)
        ];
        types = Union[First/@mutpotlist];
        datalist = Table[
            Select[mutpotlist,#[[1]]==types[[i]]&],
            {i,Length[types]}      ];
        mutpotlist = Transpose[{types, (Last/@#)&/@datalist}];
        AppendTo[all, {Sequence@@compoundlist,
            cancerpotlist, mutpotlist} ];
        test=(marker<=n);
        If[Not[auto], test=False; all={all[[1]], marker}]
    ];
    all
    ]
```

■ FIT (Regression for General Linear Models) (from *RiskQ*)

```
Needs["Statistics`NormalDistribution`"];
Needs["Statistics`InverseStatisticalFunctions`"];

Off[General::spell ];
Off[General::spell1];
Prn[x_]:=Print[HoldForm[x],"= ",x];
Attributes[Prn]={HoldAll};
$DefaultFont={"Helvetica",10};
```

```
FIT::usage = "FIT[xy, fxn_List, x_Symbol, options]
fits the General Linear Model (GLM), y(x) = Sum[qi Fi(x)] for
i=1...np, to xj-yj data (for j=1...n) given in xy (an n-by-2
matrix) by direct or generalized least-squares regression,
assuming yj are all normally distributed as N(0,1/wj) with
wj=1 by default. Use NYatX->nyj, with integer nyj>0 (ny=1 by
default) or nyj an n-lengthed such list, to treat yj as
means, in which case corresponding sample stand. devs. sj of
nyj y-values must be specified using Errors->sj. Use
Weights->wj to similarly specify KNOWN weights wj; or use
Weights->{Wyhat, yhat, df} to specify that wj=(Wyhat/.
yhat->y(xj)) for a Wyhat expression involving the symbol
yhat, in which case the fit is obtained by iterative
reweighting assuming df (=0 if not specified) degrees of
freedom are lost in estimating Wyhat from the data (& use
MaxIterations ->maxit and/or Tolerance->tol to override
defaults). If Report->True, SDs and 100p% conf. limits on ai,
R^2, a chi-square test-of-fit, ANOVA table, F-tests of
GLM-fit and nonzero qi for i>0, and a plot are all printed
(use Report->NoPlot to suppress plot). The qi estimates are
output (along with: covariance matrix, the list
{xval,yhat,yLCL, yUCL}, a sum-of-squares & assoc. degr.-
of-freedom matrix, the F-test p-values, the chi-square
p-value, and/or a plot using Outputs->{CV, xval, SumSquares,
PvalF, PvalX2, [and/or] Plot}, where xval may be a list. Use
Confidence->p to change p from 0.95, and use Xmin->xlo,
etc.(see PlotData Options) to change plot defaults.";

CV::usage = "CV: See FIT, Plot.";
Confidence::usage = "Confidence is an option of FIT,
 UncertaintyAnalysis.";
Errors::usage = "Errors is an option of FIT.";
Outputs::usage = "Outputs is an option of FIT.";
PvalF::usage = "PvalF: See FIT.";
PvalX2::usage = "PvalX2: See FIT.";
SumSquares::usage = "SumSquares: See FIT.";

Options[FIT]={Report->False,Confidence->.95,
 Outputs->Automatic,Weights->Automatic,
   Errors->Automatic,NYatX->1,Tolerance->10.^-4,
   MaxIterations->50};

FIT[xy_List, Fxns_List, x_Symbol, options___Rule]:=
Module[{n=Length[xy],nn,np=Length[Fxns],ny,fxns,
   i,X,Xbar,SSX,Y,Ybar,Yhat, Wyhat,yhat,dfW=0,
   W,SW,w,s,s2,errors=True,P,verbose,noweights,
   xval,dy,ylim,ylims,Ylim,draw,cv,Fxiscon,
   b,a,sa,da,number, aold,tol,its=0,nits,iterate,
   report,conf,conf2,cs,csu="%UCL",csl="%LCL",out,o,
```

```
    Fx,A,tA,V,x2,plot,fit,data,
    xmin,xmax,ymin,ymax,labels,dotsize,
    qs,tval,sumsq,SSvals, msr,msa,msw,mss,
    SSreg,SSa,SSw,SSres,SS,dfreg,dfa,dfw,dfres,df,
    pvalF,pmod,fmod,pqi,fqi,pvalX2,px2},
pvalX2=pvalF=number=draw=cv=sumsq=iterate=ylims=
     verbose=noweights=Fxiscon=False;
fxns=Sort[Fxns];
If[D[Plus@@fxns,x]==0,  Fxiscon=True];
P:=Print[" "];

xmin=         Xmin  /. {options} /. Options[PlotData];
ymin=         Ymin  /. {options} /. Options[PlotData];
xmax=         Xmax  /. {options} /. Options[PlotData];
ymax=         Ymax  /. {options} /. Options[PlotData];
labels=     Labels  /. {options} /. Options[PlotData];
dotsize=  DotSize  /. {options} /. Options[PlotData];
outs =     Outputs  /. {options} /. Options[FIT];
report=     Report  /. {options} /. Options[FIT];
If[report, draw=True];
conf=  Confidence  /. {options} /. Options[FIT];
tol=      Tolerance  /. {options} /. Options[FIT];
nits=  MaxIterations  /. {options} /. Options[FIT];
W=         Weights  /. {options} /. Options[FIT];
s=          Errors  /. {options} /. Options[FIT];
ny=          NYatX  /. {options} /. Options[FIT];

(*** TEST INPUTS AND SETUP ********************************)
(***********************************************************)
If[Not[(IntegerQ[ny] && ny>0)===True ||
          ( Length[ny]==n && (And@@((IntegerQ[#] && #>0
               )&/@ny)) )===True],
     Return["FIT: Bad NYatX value(s)"],
     If[NumberQ[ny], ny=Table[ny,{n}]];
          sqrtny=N[Sqrt[ny]];
          nn=Plus@@ny;
          dfres= nn - np - dfW
];
If[dfres<1, Return["FIT: Too few degrees of freedom"]];
Which[
     report===NoPlot,        report=True;                  draw=False,
     report===Verbose,       verbose=report=True;          draw=False
];
conf2=1. - (1.-conf)/2.;
If[Not[(0<conf<1)===True],
   Return["FIT: Bad Confidence option"]
];
Which[
     s===Automatic,                s=Table[0,{n}]; errors=False,
```

```
      NumberQ[s] && s>0,              s=Table[N[s],{n}],
      (VectorQ[s] && Length[s]==n && (And@@(#>0&/@s)))===True,
                                      s=N[s],
      True,                           Return["FIT: Bad Errors"]
];
s2=s^2;
Which[
      W===Automatic,      W=1&/@s; noweights=True,
      NumberQ[W],         W=N[W]&/@s,
      (VectorQ[W] && Length[W]==n && (And@@(#>=0&/@W)))===True,
                          W=N[W],
      (VectorQ[W] && Length[W]>1 && Head[W[[2]]]===Symbol &&
      NumberQ[ N[ W[[1]]/.W[[2]]->1 ] ]),
                          {fWyhat,yhat}={W[[1]],W[[2]]};
                               iterate=True;
                               If[Length[W]>2, qs=W[[3]];
                                    If[IntegerQ[qs] && qs>0,dfW=qs]
                               ];
                               W=1&/@s,
      True,               Return["FIT: Bad Weights"]
];
w=N[Sqrt[W]];
If[NumberQ[outs], number=True];
If[Not[Head[outs]===List],  outs={outs}];
If[outs=!={Automatic},
      If[MemberQ[outs,SumSquares],          sumsq=True];
      If[MemberQ[outs,PvalF],               pvalF =True];
      If[MemberQ[outs,PvalX2],              pvalX2=True];
      If[MemberQ[outs,Plot],                draw=True];
      If[MemberQ[outs,CV],                  cv=True];
      xval=Select[outs,VectorQ[#] || NumberQ[#]&];
      If[xval!={},
            If[xval==outs && VectorQ[outs],
                ylims=True;
                     outs={YLim},
                xval=xval[[1]];
                    ylims=True;
                    outs=If[VectorQ[#] || NumberQ[#],YLim,#]&/@outs
            ];
            If[ number, xval=xval[[1]] ]
      ];
      If[ Union[{draw,pvalF,pvalX2,cv,ylims}]===False,
           Return["FIT: Bad Outputs option"]
      ]
];
If[(Length[Union[xy]]-np) < 0, Return[
      "FIT: Too few unique yj to fit model parameters"]
];
```

```
(*** FIT ***************************************************)
(************************************************************)
{X,Y}=Transpose[xy];
Fx=N[(fxns /. x->#)&/@X];
aold=Table[Infinity,{np}];
While[its<=nits, its++;
If[Fxiscon,
     V={{1}};
          a={(Plus@@( ny W Y))/Plus@@( ny W)},
     A=sqrtny w Fx;          (*** A = the "design matrix"  ***)
     tA=Transpose[A];
     b=sqrtny w Y;
     V=tA.A;
     a=N[LinearSolve[V, tA.b]];
     V=N[Chop[Inverse[V]]];
];
     Yhat=a.#&/@Fx;
     SSw=Plus@@(W(ny-1)s2);
     x2=N[ (Plus@@( ny W(Y - Yhat)^2 )) + SSw ];
     V= N[V x2/Max[1,dfres]];
     If[Fxiscon, V=N[V/nn]];
     sa=N[Sqrt[ Table[V[[i,i]],{i,np}] ]];
     If[iterate,
          b=Plus@@(Abs[a-aold]/sa);
          If[verbose, Print[its,": qi=",a," RelErr=",b] ];
          If[ b<tol, Break[] ];
               aold=a;
               W=N[Wyhat/.yhat->Yhat];
               w=Sqrt[W],
          Break[]
     ]
];

(*** SUM OF SQUARES & OTHER STATS ***************************)
(************************************************************)
tval=N[ Quantile[StudentTDistribution[dfres],conf2] ];
If[report || pvalX2,
     px2=N[1-CDF[ChiSquareDistribution[dfres],x2]]
];
W=ny W;
SW=Plus@@W;
If[report || pvalF || sumsq,
     Ybar=(Plus@@(W Y))/SW;                    dfw=   nn-n;
     SSreg=N[Plus@@( W(Yhat - Ybar)^2)];       dfreg= np+dfW-1;
     SSa=  N[Plus@@( W(Y    - Yhat)^2)];       dfa=   dfres-dfw;
     SSres=SSa   + SSw;
     SS=    SSreg + SSres;                     df=    nn-1;
];
If[report || pvalF,
```

```
        If[Chop[SSw]==0 || dfw==0,
            fmod=0; pmod="1 (Assumed)",
            fmod=N[(SSa/dfa)/(SSw/dfw)];
                pmod=N[ 1 - CDF[FRatioDistribution[
                                    dfa,dfw],fmod] ]
        ];
        If[Chop[SSres]==0,
            fqi=Infinity; pqi=0,
            If[np==1,
                fqi=N[(a[[1]]^2)/V[[1,1]]],
                fqi=N[(SSreg/dfreg)/(SSres/dfres)]
            ];
            pqi=N[ 1 - CDF[FRatioDistribution[
                                    Max[1,dfreg],dfres],fqi] ]
        ]
    ];
    If[report || sumsq,
        {msr,msa,msw,mss}=Which[
                    #[[2]]==0 && Chop[#[[1]]]==0,        Undefined,
                    #[[2]]==0,                           Infinity,
                    True,                          N[#[[1]]/#[[2]]]
                    ]&/@{{SSreg,dfreg},{SSa,dfa},
                        {SSw,dfw},{SSres,dfres}};
        out={{"SOURCE","SumSqrs","DegFr","MeanSq"},
            {"Regression", SSreg,       dfreg,    msr},
            {" AboutRegr", SSa,         dfa,      msa},
            {" WithinY|x", SSw,         dfw,      msw},
            {"Residual",   SSres,       dfres,    mss},
            {"Total (Y)",  SS,          df,       N[SS/df]}};
        If[sumsq, SSvals={#[[2]],#[[3]]}&/@Rest[out] ]
    ];
    If[report,
        cs=100 conf;
        If[(cs-Floor[cs])==0, cs=Floor[cs]];
        cs=ToString[cs];
        csu=StringJoin[cs,csu];
        csl=StringJoin[cs,csl];
        da=sa tval;
        qs=Array["q",np,0];
        Print["General Linear Model (GLM):"];
        Print["E[Y|",x,"] = ", qs.fxns]; P;
        Print[ TableForm[Transpose[{Join[{"Coef"},qs],
            Join[{"LS Est."}, a],       Join[{"SD"},  sa],
            Join[{csl}, a-da],          Join[{csu}, a+da]
            }],TableSpacing->{0,3}]          ];
        Print["R",Superscript[2],"= ",N[SSreg/SS]];
        Print["Chi-Square Goodness-of-Fit Test",
            " (Null hypoth: Fit OK):"];
        If[noweights,
```

```
            Print[" WARNING: Var[Y|x]=1 assumed for all x"]
        ];
        Print["Chi-Square(",Max[dfres,1],")= ",x2,
             "   1-tail p= ",px2];                                    P;
        Print["Analysis of Variance for GLM Regression:"];  P;
        Print[TableForm[out, TableSpacing->{0,5}]];
        If[SSw==0,
             P; Print["GLM is assumed here to be true"],
             P; Print["F-Test for GLM (Null hypothesis: ",
                      "GLM is true):"];
                Print["F(",dfa,",",dfw,")= ",
                     fmod,"   p= ",pmod]
        ]; P;
        Print["F-Test for Regression, Conditional on GLM:"];
     If[np==1,
        Print["(Null hypothesis: q[0]=0)"],
        Print["(Null hypothesis: q[i]=0 for i=1,...,",np-1,")"]
     ];
       Print["F(",Max[1,dfreg],",",dfres,")= ",fqi,"   p= ",pqi]
];

(*** PLOT & OUTPUT ***************************************)
(**********************************************************)
If[draw,
       fit=a.fxns;
       If[weights,
             data={xy,Transpose[{X,Y-s}],Transpose[{X,Y+s}]};
             plot=PlotData[data, Style->{O,M,J,M},
                  JoinPoints->False, FitTo->{fit,x},
                  Xmin->xmin, Ymin->ymin, Xmax->xmax,
                  Ymax->ymax, Labels->labels, DotSize->dotsize],
             plot=PlotData[xy,
                    JoinPoints->False, FitTo->{fit,x},
                  Xmin->xmin, Ymin->ymin, Xmax->xmax,
                  Ymax->ymax, Labels->labels, DotSize->dotsize]
       ]
];
If[outs===Automatic, Return[a]];
If[ylims,
     Xbar=(Plus@@(W X))/SW;
     SSX=  Plus@@(W(X-Xbar)^2);
     dy=tval Sqrt[(x2/dfres)(SW^-1 +((xval-Xbar)^2)/SSX ) ];
     If[NumberQ[dy],
          Fx=fxns /. x->xval;
               Yhat=a.Fx;
               ylim={xval, Yhat, Yhat-dy, Yhat+dy},
          Fx=(fxns /. x->#)&/@xval;
               Yhat=a.#&/@Fx;
               ylim=Transpose[Join[{xval},
```

```
                                                    Yhat+#&/@{0,-dy,dy}]]
      ]
];
a=(a);
Do[
     Switch[outs[[i]],
               CV,     a=Append[a,V],
            PvalF,     a=Append[a,{pmod,pqi}],
           PvalX2,     a=Append[a,px2],
       SumSquares,     a=Append[a,SSvals],
             Plot,     a=Append[a,plot],
             YLim,     a=Append[a,ylim]
     ],{i,Length[outs]}
]; a
] /; (MatrixQ[xy] && 2<=Dimensions[xy][[2]]<=3 &&
      Length[xy]>1)
```

■ DataVariance

```
Remove[DataVariance];

DataVariance::usage = "DataVariance[data, ny:] finds most
significant positive linear fit of the dataset data=(x,y,sy),
where x (= values of the independent variate), y
(corresponding mean values of the dependent variate) and sy
(= corresponding standard deviations) are all n-lengthed
lists with n>2. Values of y and sy are all presumed to be
based on ny (>2) observations.";

DataVar::usage = "DataVar is a function called by
DataVariance.";

FixY::usage = "FixY is a function called by DataVariance.";

VarianceScale::usage = "VarianceScale is an option of
DataVariance.";

Options[DataVariance]={Confidence->0.95, VarianceScale->1};
```

```
DataVariance[data_List, options___Rule]:=
Module[{i,out,o,Z,fit, x,y,v,xy,p,pin,
     n,yspan,c,clo,r2,vscale},
pin =      Confidence /. {options} /. Options[DataVariance];
vscale=VarianceScale /. {options} /. Options[DataVariance];
pin=1.- pin;
{x,y,v}=N[data];
n=Length[x];
v=Last/@FixY[Transpose[{y, vscale v^2}]];
out=DataVar[x,y,v];
xyv=Transpose[{x,y,v}];
If[n>3,
     o=Table[
          xy=Transpose[Take[#,i]&/@{x,y}];
          Append[FIT[xy,{1,Z},Z,Outputs->{PvalF}], i]
          , {i,n,3,-1}
     ];
     o=Transpose[o];
     o[[2]]=Last/@Hommel[Last/@o[[2]]];
     o=Last/@Sort[ {#[[2]],#}&/@Transpose[o] ];
     o=Select[o, (#[[1,2]]>0 && #[[2]]<= pin)& ];
     If[Length[o]>0,
          {i,p}={o[[1,3]],o[[1,2]]};
          {x,y,v}=Take[#, i]&/@{x,y,v};
          o=DataVar[x,y,v];
          o[[2]]=p;
          AppendTo[out, o]
     ];
];
out
]
```

```
DataVar[X_List, y_List, v_List]:=
Module[{x,z,fit,OK,p,n,c,pc0,vbar,SSv,R2,o},
OK[xx_]:=Which[
     NumberQ[xx],          True,
     Length[xx]===0,       False,
     (And@@(NumberQ[N[#]]&/@Flatten[xx]))===True, True,
     True,                 False
];

n=Length[X];
fit=FIT[Transpose[{X,y}],{1,x},x,Outputs->{PvalF}];
Which[
     Length[fit]==0,
          Return["DataVar: FIT failed"],
     Not[OK[fit[[1]]]===True],
          Return["DataVar: FIT failed"],
     True,     p=fit[[2,2]]
];
z=(v/y)-1;
fit=FIT[Transpose[{y,z}],{1},x,Outputs->{PvalF}];
Which[
     Length[fit]==0,
          Return["DataVar: FIT failed"],
     Not[OK[fit[[1]]]===True],
          Return["DataVar: FIT failed"],
     True,     {c,pc0}={fit[[1,1]]+1,fit[[2,2]]/2}
];
vbar=(Plus@@v)/n;
SSv=Plus@@( (v - vbar)^2 );
R2=Max[0, 1 - N[( Plus@@( (v - c y)^2 ) )/SSv] ];
o={n,p,N[Max[y]/y[[1]]],{c,pc0,R2}};
fit=FIT[Transpose[{y,z}],{x},x,Outputs->{PvalF}];
Which[
     Length[fit]==0,
          Return["DataVar: FIT failed"],
     Not[OK[fit[[1]]]===True],
          Return["DataVar: FIT failed"],
     True,     {c,pc0}={fit[[1,1]],fit[[2,2]]/2}
];
R2=Max[0, 1 - N[( Plus@@( ( y(1 + c y) - vbar)^2 ) )/SSv]];
Append[o,{c,pc0,R2}]
] /; Length[X]==Length[y]==Length[v]  && Length[v]>2
```

```
FixY[XY_List, interpolate_:0, order_:1]:=
Module[{xy=XY,n=Length[XY],z=interpolate,yhat},
xy=Select[XY, #[[2]]=!=z&];
If[Length[xy]==n, Return[XY]];
If[Not[OrderedQ[Transpose[XY][[1]]]],
    Return["FixXY: Bad input"]
];
If[Length[xy]<2, Return["FixXY: Cannot interpolate"]];
If[XY[[1,2]]==z,    xy=Prepend[xy,{XY[[1,1]],xy[[1,2]]}]];
If[Last[XY][[2]]==z,xy=Append[xy,{Last[XY][[1]],Last[xy][[2]]}]];
yhat=Interpolation[xy,InterpolationOrder->order];
If[#[[2]]==z, {#[[1]], yhat[#[[1]]]}, #]&/@XY
] /; (MatrixQ[XY] && Length[XY]>2 &&
    Dimensions[XY][[2]]==2)
```

■ PlotData (from *RiskQ*)

□ Shapes for Plotting 2-D Data

□ PlotData Function

■ Hommel (from *RiskS*)

```
Hommel::usage = "Hommel[p_List] performs Hommel's modified
Bonferroni procedure on an input list of p-values, and
returns the list {{p1,a1},{p2,a2},...}, where p={p1,p2,...}
and {a1,a2,...} are the corresponding adjusted p-values.
(See Wright, S.P. 1992. Biometrics 48, 1005-1013.)";
```

```
Hommel[x_List]:=
Module[{a,p=x,n=Length[x],r,m,i,c,cmin},
r=Range[n];
r=Last/@Sort[
     Transpose[
          Append[Transpose[Reverse/@Sort[Transpose[{x,r}]]],r]
     ]];
(*Print["r= ",r];*)
c=a=p=Sort[x];
Do[
     i=Range[n, n-m+1,-1];
     If[Not[i=={}],
          ( c[[#]]=m p[[#]]/(m+#-n) )&/@i;
          cmin=Min[ c[[i]] ];
          If[a[[#]]<cmin, a[[#]]=cmin]&/@i;
          (*Print["m=",m];
          Print["i=",i];
          Print["cmin=",cmin];
          Print["c=",c];
          Print["a=",a];*)
     ];
     i=Range[n-m];
     If[Not[i=={}],
          (c[[#]]= Min[cmin, m p[[#]]])&/@i;
          If[a[[#]]<c[[#]], a[[#]]=c[[#]]]&/@i;
          (*Print["i=",i];
          Print["c=",c];
          Print["a=",a];*)
     ],{m,n,2,-1}
];
Transpose[{x,a[[r]]}]
] /; (And@@((0<=#<=1)&/@x))===True
```

■ [Blank Space]

SUMMARY

We have seen how to apply an analysis of variance and linear regression to model the behavior of mutagenic dose-response curves. Through the application of this program, we are now able to analyze dose-response patterns and structural relationships of standand errors for over 1,000 compounds, an approach never taken before on such a large amount of data.

REFERENCES

Agnese, G., D. Risso, and S. De Flora (1984) Statistical Evaluation of inter-and intra-laboratory variations of the Ames test, as related to the genetic stability of Salmonella tester strains, Mut. Res., 130: 27-44.

Couch, D. B., and A. W. Hsie (1978) Mutagenicity and Cytotoxicity of Congeners of Two Classes of Nitroso Compounds in Chinese Hamster Ovary Cells, Mut. Res., 57: 209-216.

Haynes, R. H., and F. Eckardt (1979) Analysis of Dose-Response Patterns in Mutation Research, Can. J. Genet. Cytol., 21:277-302.

Horn, L., J. Kaldor, and J. McCann (1983) A comparison of alternative measures of mutagenic potency in the Salmonella (Ames) test, Mut. Res.

Leo, A., A. Panthananickal, C. Hansch, J. Theiss, M. Shimkin, and A. W. Andrews (1981) A Comparison of Mutagenic and Carcinogenic Activities of Aniline Mustards, J. Med. Chem., 24, 859-864.

McCann, J., L Swirsky Gold, L. Horn, R. McGill, T.E. Graedel and J. Kaldor (1987) Statistical Analysis of Salmonella test data and comparison to results of animal cancer tests, Mutation Res., 205, 183-195.

Piegorsch, W. and D.B. Hoel (1988) Exploring relationships between mutagenic and carcinogenic potencies, Mutation Res., 196, 161-175.

Zeiger, E., B. Anderson, S. Haworth, T. Lawlor, and K Mortelmans (1992) Salmonella Mutagenicity Tests: Results from the Testing of 311 Chemicals, Env. and Mol. Mutagenesis, 19, 21:2-141.

Hierarchical Chromosome Organization of Human Sperm Detected by Fluorescence in Situ Hybridization

Chris Tang*, Art Kobayashi, and Andy Wyrobek

*University of California, Los Angeles

Biodosimetry Group, Biology and Biotechnology Research Program,

LLNL.

Abstract:

The organization and packaging of DNA into human sperm nuclei remains essentially unknown. Fluorescence in situ hybridization was used to visualize segments of 2 to 8 megabases of highly repetitive DNA in sperm. Two DNA probes were used for these experiments: pY3.4 which was specific for ~ 8 Mb of sequence on chromosome Y and CEP8 which was specific for ~ 2 Mb of repeat sequence on chromosome 8. Sperm nuclei were decondensed to provide various state of chromatin decondensation. The morphology and substructure of the fluorescent domains for these probes was visualize by fluorescence and confocal microscopies. We observed that the overall length of repetitive DNA segment and degree of chromatin decondensation determined the size and number of fluorescent domains. Four classes of fluorescence domains were noted, which were named A, B, C and D. A hierarchical model of chromatin organization is proposed in which chromatin domain A contains two B domains, domain B contains two C domains, and domain C contains two D domains. The preliminary estimate of the amount of DNA contained in each domain is 8. 4. 2. and 1 Mb respectively. [Work performed under the auspices of the U.S. DOE by the Lawrence Livermore National Laboratory under contract W-7405-ENG-48.]

Introduction:

Much of the organization and higher order structure of mammalian sperm DNA remains unknown despite recent research efforts. The study presents a unique obstacle because mammalian sperm DNA is tightly packaged. Sperm cells contain half as much DNA as somatic cells, yet its nucleus volume is fortyfold less (Wyrobek et al 1976). This translates to a sixfold increase in condensation for sperm DNA (Pienta and Coffey 1984; Balhorn 1982), making it the most compacted eukaryatic DNA. Studies on chromatin condensation during spermatogenesis and decondensation during sperm nuclear swelling showed that sperm DNA, although compact, is highly organized (Zirkin et al 1982; Risley et al 1986).

Unlike somatic cell DNA, sperm DNA is packaged in linear array rather than the nucleosome structures (Balhorn 1982). This is made possible by the presence of the highly basic protamines, the DNA binding proteins of sperm nuclei. Protamines bind to DNA by lying lengthwise inside the minor groove, neutralizing the phosphate groups on DNA. This protamine-DNA complex does not induce any coiling, and would fit into the major groove of another protamine-DNA complex, thus allowing the strands to be pack side by side linearly (Balhorn 1982). This allowed DNA to be tightly package into very small volume. Investigations have further elucidate that sperm DNA is organize via loop domains attaching to nuclear matrix (Ward and Coffey 1991), similar to their somatic counterparts. However, little more is know about the higher order of organization.

Fluorescence in situ hybridization with probes specific for certain chromosomes had been successfully used for detecting chromosomes in

sperm (Robbins et al. 1993). However, one recurring problem for FISH is that sperm cells hybridized with probes specific for a contiguous DNA sequence consistently display multiple fluorescent domains. While it is unlikely that each of the fluorescent spots represent an individual chromosome, they could represent substructures of chromatin and possibly lead to uncovering of higher orders of sperm DNA organization. In the current study, fluorescence in situ hybridization was used to visualize segments of 2 to 10 megabases of highly repetitive DNA in sperm. Two DNA probes were used for these experiments: pY3.4 which was specific for ~ 10 Mb of sequence on chromosome Y and CEP8 which was specific for ~ 2 Mb of repeat sequence on chromosome 8. Fluorescence and confocal microscopy were used to visualize segments of contiguous sperm DNA at various stages of decondensation to determine a hierarchical model of chromatin organization.

Materials and Method:

Semen Samples: All samples were obtained from healthy volunteers enrolled in an ongoing semen donor program at Lawrence Livermore National Laboratory. For this study, all samples were taken from the same donor.

Probe Preparation: Two probes were used: probe pY3.4 was derived from a 3.4kb fragment of a highly repeated sequence on the distal arm of Yq (Cooke and McKay 1978; Smith et al. 1987). It is specific for about 8 Mb of sequence on chromosome Y. Probe CEP8 is a centromeric probe specific for approximately 2 Mb of repeated sequence on chromosome 8 (Ge et al 1992). pY3.4 is labeled with rhodamine and CEP8 is labeled with biotin using nick translation.

Sperm Preparation and Fluorescence In Situ Hybridization: 7 μ l of semen samples were spread into thin smears on clean microscope slides and allowed to air-dry. Smears were stored at room temperature for at least 24 hours prior to sperm decondensation. Decondensation and hybridization were performed as described by Wyrobek et al (1990).

Scopes and Image Collecting: A Zeiss Axioplan microscope with camera and a Nikon confocal microscope were used to obtain all images. Sperms were observed at 2000X and 1200X, respectively. The images collected by the confocal scope (Nikon) is then processed by Art Kobayashi using Interactive Data Language (IDL) from Research Systems Inc.. Diameter measurements were done via the COMOS software on the confocal microscope. Volume calculations were done by Art Kobayashi using IDL software.

Results:

Sperms were hybridized with probe p3.4 to mark a continuous piece of DNA about 8 megabases along the Y chromosome. The pattern of the fluorescence within the sperm nuclei differed among sperm. Some contained a single large fluorescence domain while other sperm had various numbers of domains of various sizes. The domains were classified into four groups.

*A: largest, domain observed, usually no more than one per sperm (figure 1a).

*B: Second largest domain observed, usually in cluster of 2 to 3 per sperm (figure 1b).

* C: Third largest domain observed, usually in cluster of 4 to 6 per sperm (figure 1c).
* D: smallest domain observed, usually in cluster of 6 to 8 per sperm (figure 1d).

The number of domains increase as their sizes decrease. As shown in table 1 approximately 70% of the hybridized cells showed domains that can be class into one of the four sizes. Of those, 33% of the cell showed only A domain, 36% of the cells showed at least one B domain (19% showed only B domains), 42% of the cells have at least one C domain and 22% of the cells have at least one D domain. Majority of the sperms display combinations of different size domains.

CEP8 hybridizes a contiguous strand of DNA about 2 Mb. Sperms hybridized with probe CEP8 showed smaller, single C domain most of the time. Occasionally, two D domains can be seen. Over 87% of the cells showed only one C domains, and 13% of the cells showed D domains. (Table 1).

By using the software (COMOS) equipped on the confocal microscope, the diameters of domains can be measured at a specific plane. Measurements were done on the section showing the best resolution of domain sizes. For Y chromosome, the diameter ratio of A domain to C domain is about 2.2. The diameter ratio of C domains in chromosome Y to the C domains in chromosome 8 is determined to be 0.94 (Table 2). Volume of chromosome Y and 8 were calculated via computer imaging software (IDL). The preliminary average volume ratio of repeat sequence on chromosome Y to repeat sequence on chromosome 8 is determined to be 3.8 (Table 3).

Discussion:

A gradual increase in the number of domains for Y chromosome was observed (figure 2). The progression starts from a single, compact, very large size domain (designate as A) to two large size domains (designate as B). B domains subsequently give rise to two C domains each. Subsequent decondensation results in C domains progressing to two D domains.

As mentioned in result section, chromosome 8 consistently gives signals with one or two domains, and the domain sizes are very small compared with those for chromosome Y. They are about the same size as domains C for Y chromosome. This can be explain by the fact that the CEP8 has a much smaller target site compared with the one for Y chromosome. As a result, CEP8 is only able to attach to a small region of chromosome 8. Thus, regardless of how condense or decondense chromosome one is, the site that probe X is accessible to only spans one small domain (maximum of two if that region of DNA is packaged between domains).

On the other hand, there are many more repeated sequences for pY3.4 to bind to compared to CEP8. Consequently, the DNA strand that pY3.4 hybridize to is larger, and will give us more information on the organization of the chromosome over a larger distance. As a result, when the chromosomes are in a condensed state, the signals we observed is very compact and the domains are large and few in number. As the chromosome decondenses, the signal breaks into smaller, multiple domains. The number of domains subsequently increase and with it, decrease in the size of the domains.

Based on the preliminary data gathered, we proposed a hierarchical model of chromatin organization in sperm, where domain A consists of two B domains, domain B consists of two C domains, and domain C consists of two D domains (figure 3).

The images taken by the confocal microscope showed that domains usually are contained within 3 μm. The Y and 8 chromosome always fade in and out of focus at about the same planes (within 0.4μm) This suggests that the domains have about the same thickness. The 0.94 diameter ratio between the C domains of chromosome Y to chromosome 8 indicated that they are approximately the same in cross section area, and thus the volume. The 2.07 diameter ratio for chromosome Y's A domain to chromosome Y's C domain suggest that A domain is about four times the size of C domain. This is further supported by the 3.8 volume ratio obtained by the IDL software. Furthermore, when only C domains were observed in chromosome Y, the number of domains is always four (data not shown). These led us to conclude that domain A contains four times the DNA as domain C. Since the repeat sequence in chromosome 8 is about 2 Mb (Ge et al 1992), we can conclude that the pY3.4 is hybridizing to about 8 Mb of DNA (fourfold). This is within the range of 6 to 10 Mb that previous studies have determined (Bauman et al 1989; Cooke and McKay 1978). Following the proposed model, this leads to the conclusion that domain A contains about 8 Mb, domain B contains approximately 4 Mb, domain C contains 2 Mb, and domain D contains about 1Mb of DNA (figure 3).

We have been able to observed up to 16 domains under the Axioplan microscope. This indicates that there is another order of organization (hereon called E domain) beyond the D domain. The size of

the E domain is smaller, and a maximum of 16 E domains can be seen at a particular cell. Cells showing intermediate stages between 8 D domains and the 16 E domains led us to believe that each D domain consists of two E domains, which would be about 0.5 Mb (data not shown).

Our current study is limited by the resolution of the Axioplan cameras, as well as the laser of confocal scope. Our immediate goal now is to determine how the domains are linked together. This can be achieve using 3 dimensional reconstruction of the images obtained by the confocal microscope. This would give us a better understanding on how the domains are arranged in relation to each other, and subsequently more understanding on how chromosome is packaged in sperm. Future studies should concentrate on getting images of E domains, and determine their spatial relations.

Reference:

Balhorn R (1982). A model of for the structure of chromatin in mammalian sperm. J Cell Biol 93:298-305.

Bauman JG, Pinkel D, Trask BJ, and Van Der Ploeg M (1989). Flow cytometric measurements of specific DNA and RNA sequences. Flo Cytogenetics. pp265-301

Cooke HJ and McKay RD (1978). Evolution of a human Y chromosome-specific repeated sequence. Cell 13:453-460.

Ge Y, Wagner MJ, Siciliano M, and Wells DE (1992). Sequence, higher order repeat structure, and long-range organization of alpha satellite DNA specific to human chromosome 8. Genomics 13:585-593.

Pienta KJ and Coffey DS (1984). A structural analysis of the role of the nuclear matrix and DNA loops in the organization of the nucleus and chromosome. J Cell Sci Suppl 1:123-135.

Risley MS, Einheber S, and Bumcrot DA (1986). Changes in DNA topology during spermatogenesis. Chromosoma 94:217-227.

Robbins WA, Segraves R, Pinkel D, and Wyrobek AJ (1993). Variation among donors in frequencies of sperm disomic for chromosomes 1 and Y detected by fluorescence in situ hybridization. Amer J Hum Gen 52(4): 799-807.

Smith KD, Young KE, Talbot CC Jr, Schmeckpeper BJ (1987): Repeated DNA of the human Y chromosome. Development (Suppl101):77-92.

Ward WS, Coffey DS (1991). DNA packaging and organization in mammalian spermatozoa: Comparison with somatic cells. Biology of Reproduction 44:569-574.

Wyrobek AJ, Meistrich ML, Furrer R, Bruce WR (1976). Physical characteristics of mouse sperm nuclei. Biophys J 16:811-825.

Wyrobek AJ, Alhborn T, Balhorn R, Stanker L, Pinkel D (1990): Fluorescence In Situ Hybridization to Y chromosomes in decondensed human sperm nuclei. Mol Reprod Dev 27:200-208.

Zirkin BR, Soucek DA, Chang TSK (1982). Sperm nuclear packing and regulation during spermatogenesis and fertilization. Johns Hopkins Med J 151:101-112.

Figure 1: Images of domains from the Y and 8 chromosome. The Y chromosome is the larger of the two in all panels. Panel A showed a singular donut shape A domain. Panel B showed two pair shape B domains. Panel C showed four ball shape C domains. Panel D showed eight individual D domains.

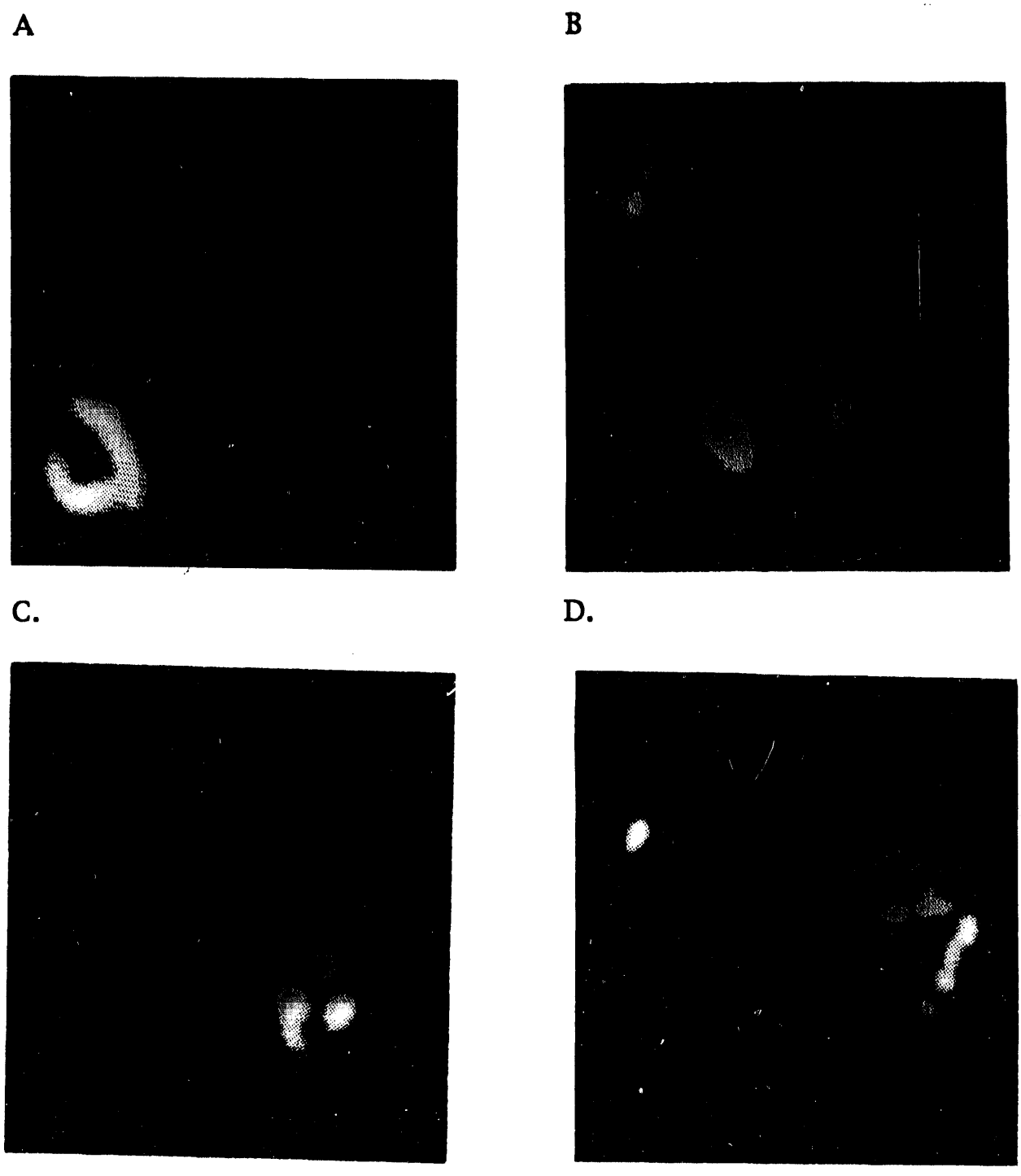

Figure 2. Sketches of the organization of fluorescent domains in human sperm after hybridization to a 8 megabase long repetitive sequence on the Y chromosome. The patterns of fluorescence were organized by increasing number of fluorescent domains per sperm nucleus. Four different sizes of fluorescent domains were observed: A, B, C and D. A progression from the compact, donut shaped A domain to eight ball shaped D domains are shown.

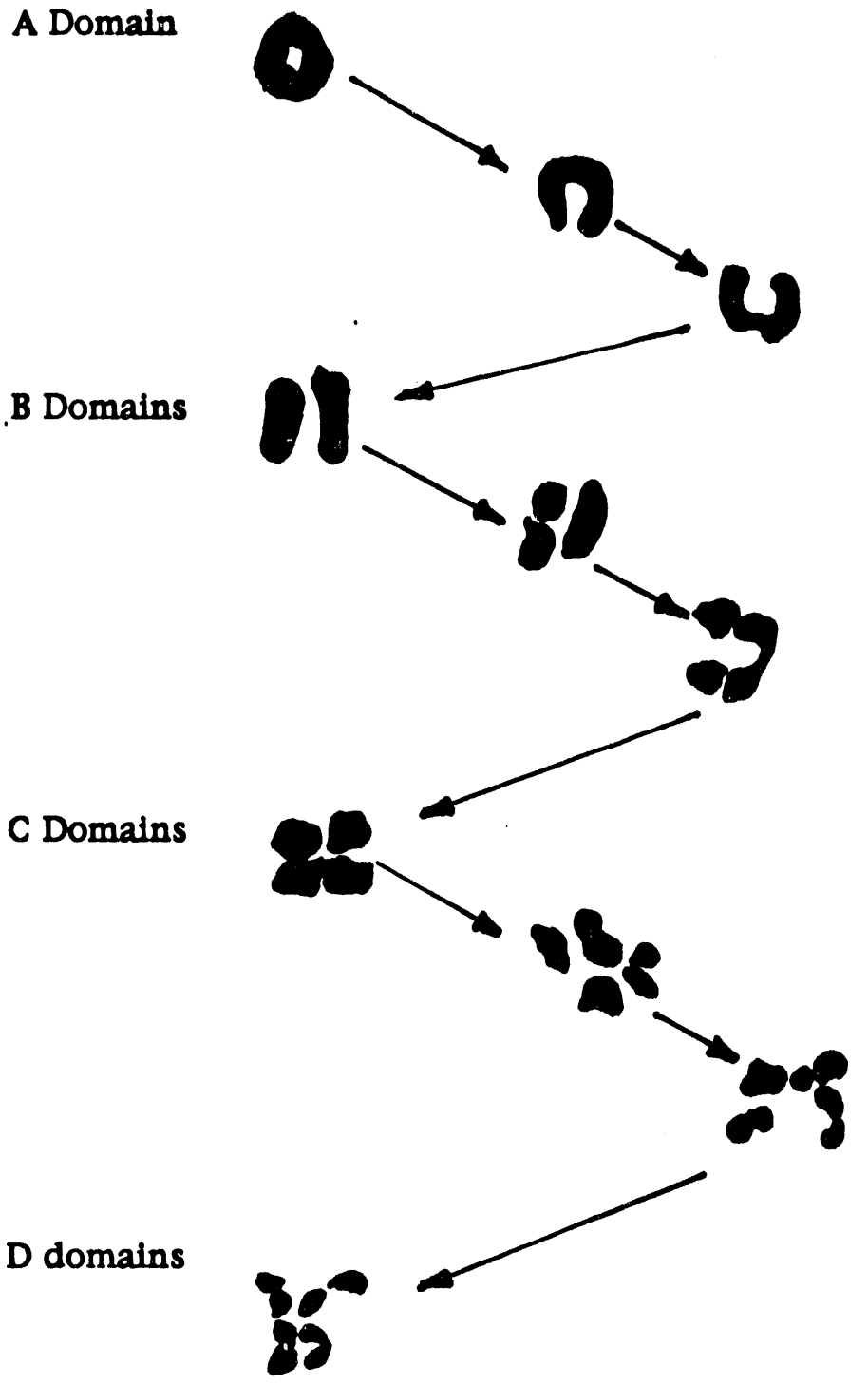

Figure 3: PROPOSED MODEL OF CHROMATIN ORGANIZATION: Based on the size, location, and number of domains observed, we propose the following model for the organization of chromatin in human sperm nuclei. According to the model, the "A" domain consists of an aggregation of two "B" domains. Each "B" domain consists of two "C" domains. Each "C" domains consists of two "D" domains, and each "D" domain consists of two "E" domains.

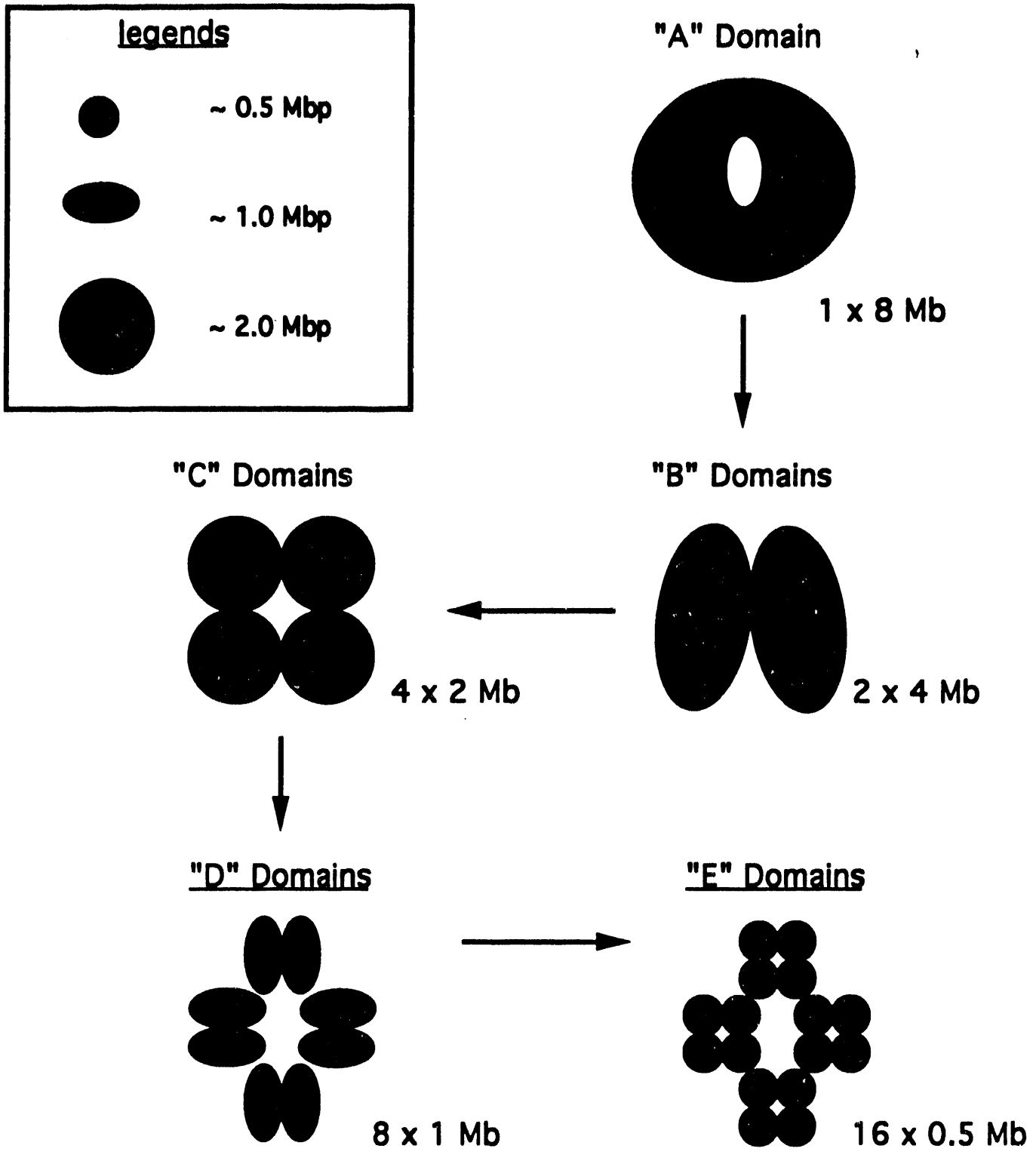

Table 1: Percentage of cells that showed A, B, C, or D domains in chromosome Y and 8. For chromosome Y, cells showing domain A does not contain any other domain sizes. Cells, showing B, C, or D domains often has combinations of other domain sizes. For chromosome 8, cells showing either C or D domains do not display combination of different domain sizes.

	Domain Sizes				No of cells scored
	A	B	C	D	
Chromosome Y:					
Percentage of cells: with at least one of the domains:	33%	37%	42%	22%	200
Percentage of cells showing only one type of domain:	33%	26%	8%	3%	200
Chromosome 8:					
Percentage of cells with at least one of the domains	0%	0%	87%	13%	200
Percentage of cells showing only one of the domains.	0%	0%	87%	13%	200

Table 2: A. The average diameters (mm) of domains in chromosome Y and chromosome 8. B. The diameter ratios of chromosome Y domains to chromosome 8's D domain.

A.

	Chromosome Y		Chromosome 8
Domain Size	A	C	C
Average Diameter: (μm, n=10)	1.76	0.80	0.85

B. **Diameter ratios**

$$\frac{\text{Chromosome Y, domain C}}{\text{Chromosome 8, domain C}} = 0.94$$

$$\frac{\text{Chromosome Y, domain A}}{\text{Chromosome Y, domain C}} = 2.07$$

Table 3. The volume ratio of chromosome Y to chromosome 8.

Volume ratio (Y : 8)				
Cell 1	Cell 2	Cell 3	Cell 4	Average
3.6	4.0	3.8	3.7	3.8

CHARACTERIZATION OF POLY-ß-HYYDROXYBUTYRATE PRODUCTION IN A TRICHLOROETHYLENE-DEGRADING METHANOTROPH*

Jennifer K. Veir

Ohio University

Lawrence Livermore National Laboratory
Livermore, California 94550

May 28, 1993

Prepared in partial fulfillment of the requirements of the Science and Engineering Research Semester under the direction of Dr. Robert T. Taylor, Research Mentor, at the Lawrence Livermore National Laboratory.

* This research was supported in part by an appointment to the U.S. Department of Energy Science and Engineering Research Semester (hereinafter called SERS) program administered by LLNL under Contract W-7405-Eng-48 with the Lawrence Livermore National Laboratory.

By acceptance of this article, the publisher or recipient acknowledges the U.S. Government's right to retain a non-exclusive, royalty-free license in and to any copyright covering this article.

ABSTRACT

A quantitative gas chromatographic (GC) assay was developed for poly-ß-hydroxybutyrate (PHB), an energy storage polymer, and poly-ß-hydroxyvalerate (PHV) in microbial biomass. Washed, centrifuged cell pellet samples were either lyophilized or acetone dried. They were then subjected to a hydrochloric acid hydrolysis and propanol esterification of the released hydroxy acids (monomers) for GC analysis. Total elapsed time between sampling the growing cultures and the final PHB quantification was successfully reduced to 4 hours, when the cells were acetone-dried. As little as 0.005 mg of PHB can be accurately measured by this methodology. Batch bioreactor grown *Methylosinus trichosporium* OB3b bacteria, when examined under nitrate growth conditions ranging from 18.4 mM down to 0.03 mM and cell densities (measured by the A_{660}) of 0.78 to 18.75 were found to produce a maximum of 5.8% (w/w) PHB under nitrate depletion conditions and an A_{660} of 9.9. Early log phase bioreactor cells at an A_{660} of 0.188 and sufficient nitrate contained 5.0% PHB. It was most likely derived from the shake-flask inocula. Gaseous-substrate-limited shake-flask cells at A_{660}s of less than 1.0 contained only 1.1-2.1% PHB when they were nitrate deficient, but they displayed a 4.0% PHB content in the presence of excess nitrate. No PHV was detected in either bioreactor or shake-flask cultured cells. Significantly, the peak PHB level in bioreactor grown *M. trichosporium* OB3b corresponds with the previously observed optimal whole-cell TCE-degrading longevity.

INTRODUCTION

Due to its former common use as an industrial solvent, trichloroethylene (TCE), a carcinogen, is frequently found to contaminate groundwater aquifers. Currently, the standard method of remediation is via a pump-and-treat process. Contaminated groundwater is brought to the surface by many wells and cleansed above ground (15). Not only is this an expensive process, but the resulting degree of decontamination is also quite uncertain due to preferential flow of extracted fluids caused by heterogenicity of subsurface material (3,16). In situ microbial filtration may lessen the problems of current technology. It has been demonstrated that TCE can be degraded by a variety of bacteria, one class of which includes methanotrophs. *Methylosinus trichosporium* OB3b produces an enzyme, methane mono-oxygenase (MMO), which oxidizes both TCE and methane, a source of cellular carbon and energy. Hence methane is a competitive inhibitor (4,9). To eliminate this competition methane may be removed and TCE can be digested by resting cells ().

Recent experimentation has proven the feasibility of an in situ microbial filter composed of resting *M. trichosporium* OB3b cells to degrade TCE. TCE was completely eliminated as it passed through an area of the sand bed in which a zone of attached bacteria had been created by a prior injection (15). Although this technology successfully degraded two successive pulse of TCE over one week, the bioactive zone of enhanced degradative activity must remain active for a period of ~30 days or more to be more economically advantageous than traditional pump-and-treat operations. The

limiting factor of the bacterial capacity to oxidize TCE is either the availability of electrons from an intracellulr biological source such as NADH or the creation of a toxic environment by TCE degradation reaction intermediates (2,7,9). Studies of suspension stored resting cells had established that bioreactor cells grown for ~90-100 hours retained 100% of their ability to degrade TCE for up to ~30 days, followed by a sharp decline in activity (15). This pattern indicates the depletion of an internal electron or energy source at the onset of the decreased whole-cell biocatalytic activity.

Further evidence of the necessity of an additional energy source for extended TCE degradation is given by the findings of Henry an Grbic-Galic that non-growing methanotrophs which possessed storage granules exhibited longer TCE degradation activity than those that did not (7). Kallio and Harrington had previously demonstrated that these granules actually contained the energy storage lipid PHB (8). This polymer is an excellent source of the electron donor NADH as three molecules of NADH are produced for every unit of PHB that is catabolized (1).

PHB storage levels are highest under conditions of stress, especially when a carbon source is present, but nutrients such as nitrogen are deficient (6). PHB production is also of interest because it is used as a polymer in the manufacture of biodegradable plastics. Findlay and White claim that PHB is actually a mixed polymer of short chain ß-hydroxy fatty acids, of which PHB is most prevalent, followed by poly-ß-hydroxyvalerate (PHV) (6). The PH(B-coV) copolymer of PHB and PHV is especially interesting to the plastics industry due to its similar characteristics to polypropylene

and its ability to be completely digested by bacteria into water and carbon dioxide (11).

The purpose of my project was to develop a time-efficient assay for PHB and copolymer PHV in order to facilitate a characterization of the intracellular appearance of these compounds and to permit an adjustment of culture conditions, if needed, for optimizing accumulation. The precise relationship between PHB accumulation by *M. trichosporium* OB3b and the cells' extended ability to degrade TCE will be examined in detail in the near future.

MATERIALS AND METHODS

Materials Poly-ß-hydroxybutyrate and poly(3-hydroxybutyric acid)/poly(3-hydroxyvaleric acid) copolymer used for standardization was purchased from the Sigma Chemical Company (St. Louis, MO) and Aldrich (Milwakee, WI), respectively. Concentrated HCl and propanol were obtained from J.T. Baker (Philipsburg, NJ) and were reagent grade. TCE was purchased from Aldrich (Milwaukee, WI) and was 99+% pure.

Culture conditions *M. trichosporium* OB3b was obtained from Professor R.S. Hanson (Gray Freshwater Biological Institute, University of Minnesota). The basal formulation employed for maintenenance of the strain was Higgin's nitrate minimal salts medium lacking copper (10). All incubation temperatures were 30.0°C. Fermentor-scale experiments were performed in a 5-L bioreactor (Bioflo II, New Brunswick, NJ) at pH 6.8-7.2. Gaseous substrates, 1:3 (v/v) methane and 10% CO_2-containing air, were

sparged continuosly at flow rates of 200-300mL/min for methane ant 600-900 mL/min for CO_2-containing air. The level of dissolved oxygen (DO) was maintained above 5% in most cases by controlling the agitation speed (300-500 rpm) and the gas flow rates. The media used was modified Higgin's media lacking copper (20 mM NO_3, 16μM Mo, 7.5 μM Ni, 80 μM Fe) (13,14). The bioreactor inocula were cultivated in 1-L shake-flasks with 100 mL of Higgin's media lacking copper under a 1:1 (vol/vol) air/methane gas mixture at 300 rpm (10).

Hydroxyalkanoate Analysis From the bioreactor, a 10 to 40 mL sample of cells was harvested by centrifugation at 4400g for 3 min, then washed with 10 mL of H_2O and recentrifuged. The pellet was then frozen and lyophilized. Ten mg of each dried cell pellet were weighed into a 5 mL screw-capped vial with a Teflon-lined seal and 2 mL of a 5:4:1 mixturev of TCE:dry propanol:concentrated HCl with 1mg/mL benzoic acid internal standard were added. The screw-capped cell mixture was incubated at 100°C for 0.5 h and 80°C for 2 h with occasional shaking. Samples were then cooled to room temperature, 2 mL of H_2O were added and the mixture was vortexed and centrifuged (3 min. at 4400g). The organic layer was then transfered to a separate clean vial with a septum in the cap. An equivalent volume of H_2O was added and the mixture was again vortexed and centrifuged. One μL injections were then made from the organic layer onto a 170°C Carbowax Chromosorb W-AW column (Alltech, Deerfield, IL), which was mounted in a HACH Carle Series 100 AGC gas chromatograph. The injection port temperature was 250°C and a flame ionization detector was used. PHB peak areas

(retention time = 2.5 min.) and PHV areas (retention time = 3.24) were then compared to a standard curve (Figure 1) to calculate actual PHB and PHV content. Values were also normalized to the corresponding internak benzoic acid peak areas.

Two steps in this procedure adapted from that described by Riis (12) were subsequently shortened, the cell pellet drying time and the HCl hydrolysis-propanol esterification time. The drying time was shortened from an overnight (~20 hour) vacuum lyophilization to a one hour combined acetone wash plus 60°C oven incubation. Identical samples prepared by these two methods give peak areas within 1.7% agreement. The hydrolysis-esterification reaction time was also was shortened from the 5 hours used by Riis (12) to 2 hours. Figure 2 shows that after 2 hours at 80°C the peak areasgiven by both PHB and benzoic acid have leveled within the assay range of error. These two modifications together allow the amount of PHB to be ascertained as soon as 4 hours after the cell sampling.

Biocatalysis Assays Whole-cell nitrogenase and TCE-degradation rate assays were performed as described by Shah (13,14).

RESULTS

PHB and PHV Accumulation as a function of nitrate concentration No PHV was detected in any of the samples examined. Figures 3-5 illustrate the results of three separate batch bioreactor cultivations in which *M. trichosporium* OB3b was grown on modified Higgins media. Figure 3A shows that PHB accumulation

is an inverse function of nitrate concentration. As soon as the medium nitrate is depleted, levels of stored PHB increase. If a pulse of nitrate equivalent to the amount in the original medium is given, PHB storage decreases, then rises again as nitrate is again depleted. Figures 3A, 4A, and 5A also show that the appearance of whole-cell nitrogenase activity corresponds with the amount of PHB stored. The presence of nitrogenase activity reflects the change in nitrogen source from the nitrate in the medium to the nitrogen gas in the air which *M. trichosporium* OB3b must fix (i.e., metabolically convert to ammonia). Figures 4A and 5A clearly reinforce that maximum PHB accumulation occurs during the early stages of the stationary growth phase, shortly following nitrate depletion . Although the disappearance rate assay for determining whole-cellTCE-degrading activity has a high degree of variability, Figures 3A, 4A, and 5A display the presence of a significant level of TCE-degrading activity throughout cell growth. nce these catalytic assays were performed less than one hour after the cells were harvested, they are not a measure of the cells' longevity, but it does show a significant amount of initial activity.

Figure 5A shows a`5.0% intracellular PHB level during the very early stage (~12 hours) of bioreactor growth when the nitrate concentration is still high. This is due to high PHB content of the shake-flask-grown inocula cells. Their rather high PHB content is believed to be caused by the depletion of a gaseous nutrient such as oxygen during their gas-phase-limited growth and stress in shake-flasks.

DISCUSSION

Significantly, peak PHB accumulation seems to coincide with previously observed enhanced whole-cell stability of TCE-degrading activity (15). Future experiments will elucidate more detailed time correlations between stored PHB levels and stored suspension whole-cell TCE-degrading activity, as well as the relationship between loss of TCE-degrading activity and loss of intracellular PHB in washed and stored resting cell preparations. Also, we plan to investigate the basis of high PHB content in the presence of ample nitrate by implementing alternative nutrient depletion stress conditions such as oxygen depletion. Lastly, the effects of the absence of nitrogen from the system will be examined by shifting the composition of feed gases from air and methane to argon-oxygen and methane in the bioreactor.

ACKNOWLEDGEMENTS

This research was supported in part by an appointment to the U.S. Department of Energy Science and Engineering Research Semester (hereinafter called SERS) program administered by LLNL under Contract W-7405-Eng-48 with Lawrence Livermore National Laboratory.

REFERENCES

1. Alvarez-Cohen, L., McCarty. 1991. Effects of toxicity, aeration and reductant supply on trichloroethylene transformation by a mixed methanotrophic culture. Appl. Environ. Microbiol. **57**: 228-235.

2. Anderson, A.J., Dawes, E.A. 1990. Occurrence, metabolism, metabolic role, and industrial uses of bacterial hydroxyalkanoates. Microbiological Reviews. **54**: 450-472.

3. Baker, K.H., Hersonn, D.S. 1991. In situ bioremediation of contaminated aquifers and subsurface soils. Geomicrobiology. **8**: 133-146.

4. Broholm, K., Christensen, T.H., Jensen, B.J. 1992. Modeling TCE degradation by a mixed culture of methane-oxidizing bacteria. Water Res. **26**: 1177-1185.

5. Cornish, A., Nicholls, K.M., Scott, D., Hunter, B.K., Aston, W.J., Higgins, I.J., Sanders, J.K.M. 1984. *In vivo* ^{13}C-NMR investigations of methanol oxidation by the obligate methanotroph, *Methylosinus trichosporium* OB3b. J. Gen. Microbiol. **130**: 2565-2575.

6. Findlay, R.H., White, D.C. 1983. Polymeric beta-hydroxyalkanoates form environmental samples and *Bacillus megaterium*. Appl. Environ. Microbiol. **45**: 71-78.

7. Henry, S.M., Grbic-Galic, D. 1991. Influence of endogeneous and exogeneous electron donors and trichloroethylene oxidation by methanotrophic cultres from a groundwater aquifer. Appl. Environ. Microbiol. **57**: 236-244.

8. Kallio, R.E., Harrington, A.A. 1960. Sudanophilic granules and lipid of *Pseudomonas methanica*. J. Bacteriol. **80**: 321-324.

9. Oldenhuis, R., Oedzes, J.Y., vander Waarde, J.J., Janssen, D.B. 1991. Kinetics of chlorinated hydrocarbon degradation by *Methylosinus trichosporium* OB3b and toxicity of trichloroethylene. Appl. Environ. Microbiol. **57**: 7-14.

10. Park, S., Hanna, M.L., Taylor, R.T., Droege, M.W. 1991. Batch cultivation of *Methylosinus trichosporium* OB3b. I: Production of soluble methane monooxygenase. Biotechnol. Bioeng. **38**: 423-433.

11. Pool, Robert. 1989. In Search of the Plastic Potato. Science 245:1187-1190.

12. Riis, V., Mai, W. 1988. Gas chromatographic determination of poly-ß-hydroxybutyric acid in microbioal biomass after hydrochloric acid propanolysis. J. Chromatography. **445**: 285-289.

13. Shah, N.N., Hanna, M.L., Jackson, K.J., Taylor, R.T. 1993. Batch Cultivation of *Methylosinus trichosporium* OB3b: IV. Production of hydrogen-driven soluble or particulate methane monooxygenase activity. Biotechnol. Bioeng., submitted.

14. Shah, N.N., Park, S., Taylor, R.T., Droege, M.W. 1992. Cultivation of *Methylosinus trichosporium* OB3b: III. Production of particulate methane monooxygenase in continuous culture. Biotechnol. Bioeng. **40**: 705-712.

15. Taylor, R.T., A.G. Duba, W.B. Durham, M.L. Hanna, K.J. Jackson, M.C. Jovanovich, R.B., Knapp, R. B. Knezovich, J.P. , Shah, N.N., Shonnard, D.R., Wijesinghe, A.M. 1992. *In Situ* bioremediation of trichloroethylene-contaminated water by a resting-cell methanotrophic microbial filter, in *Proceedings of the Symposium In Situ Bioremediation '92* , Niagara-On-The-Lake, Ontario, Canada,

September 20-24, 1992, Hydrological Sciences Journal (in press) 1993.

16. Travis, C.C., Doty, C.B. 1990. Can contaminated aquifers at superfund sites be remediated? Environmental Science and Technology. **55:** 3155-3161.

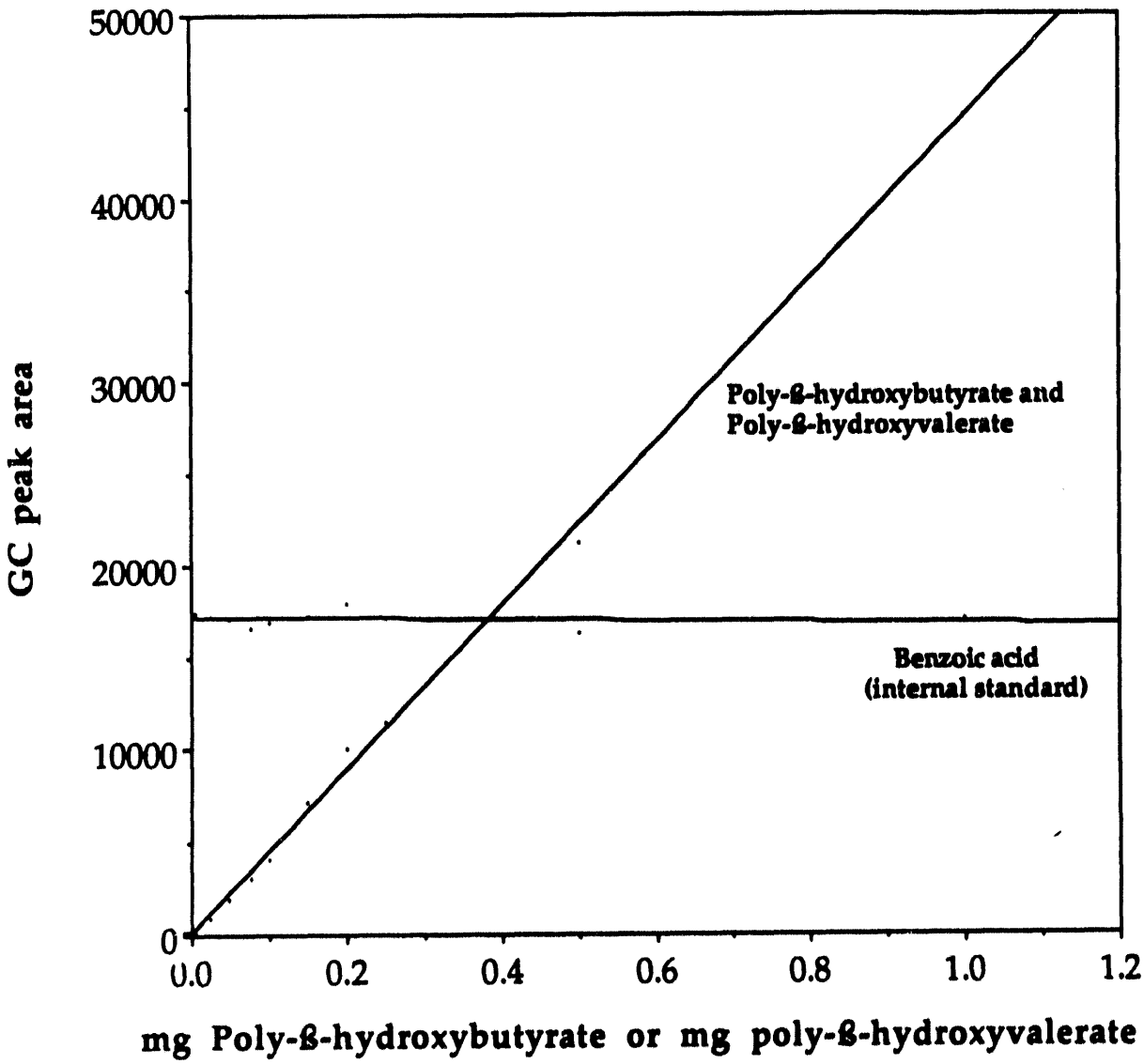

Figure 1. Standard Curve

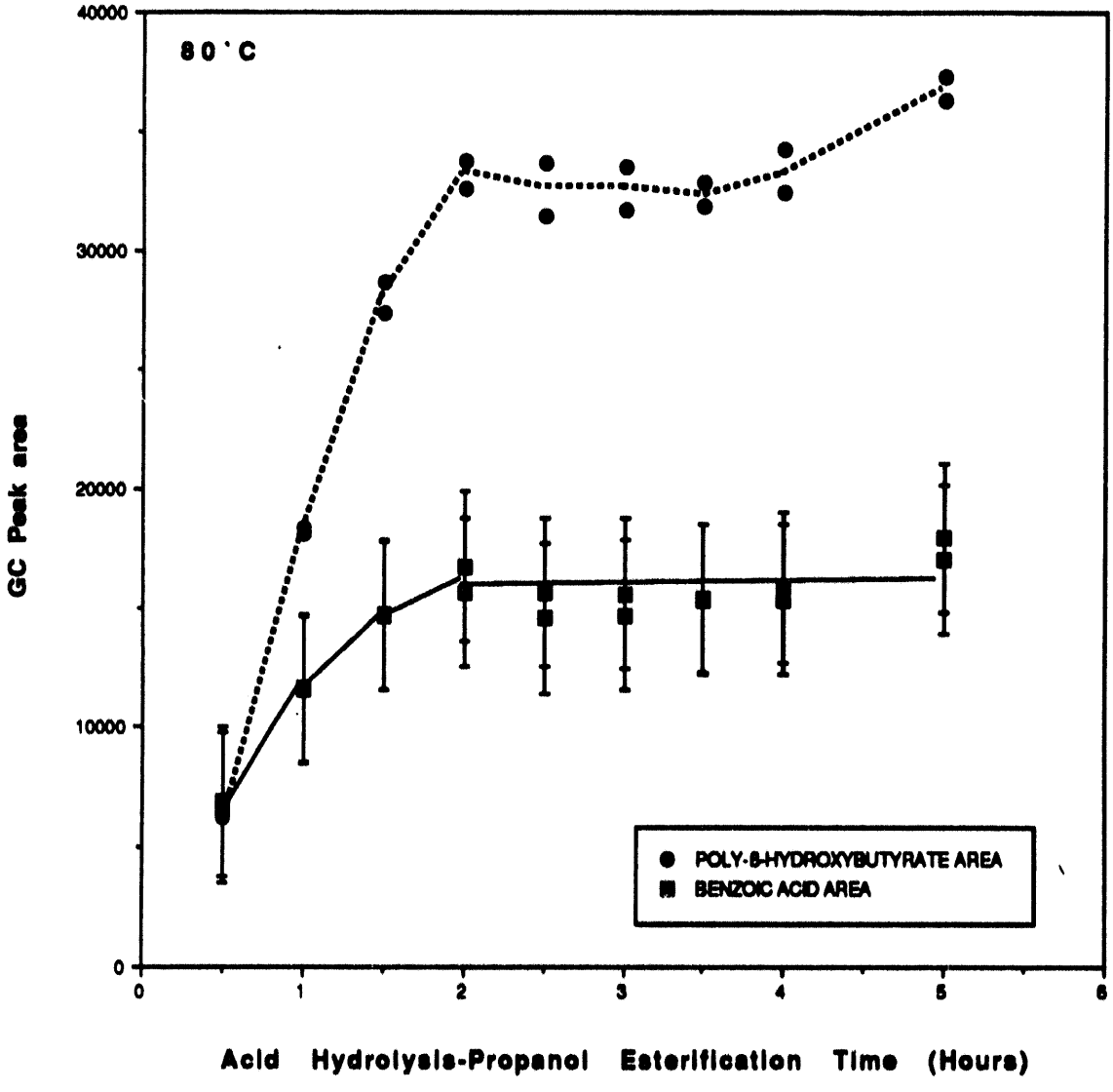

Figure 2. Incubation Time

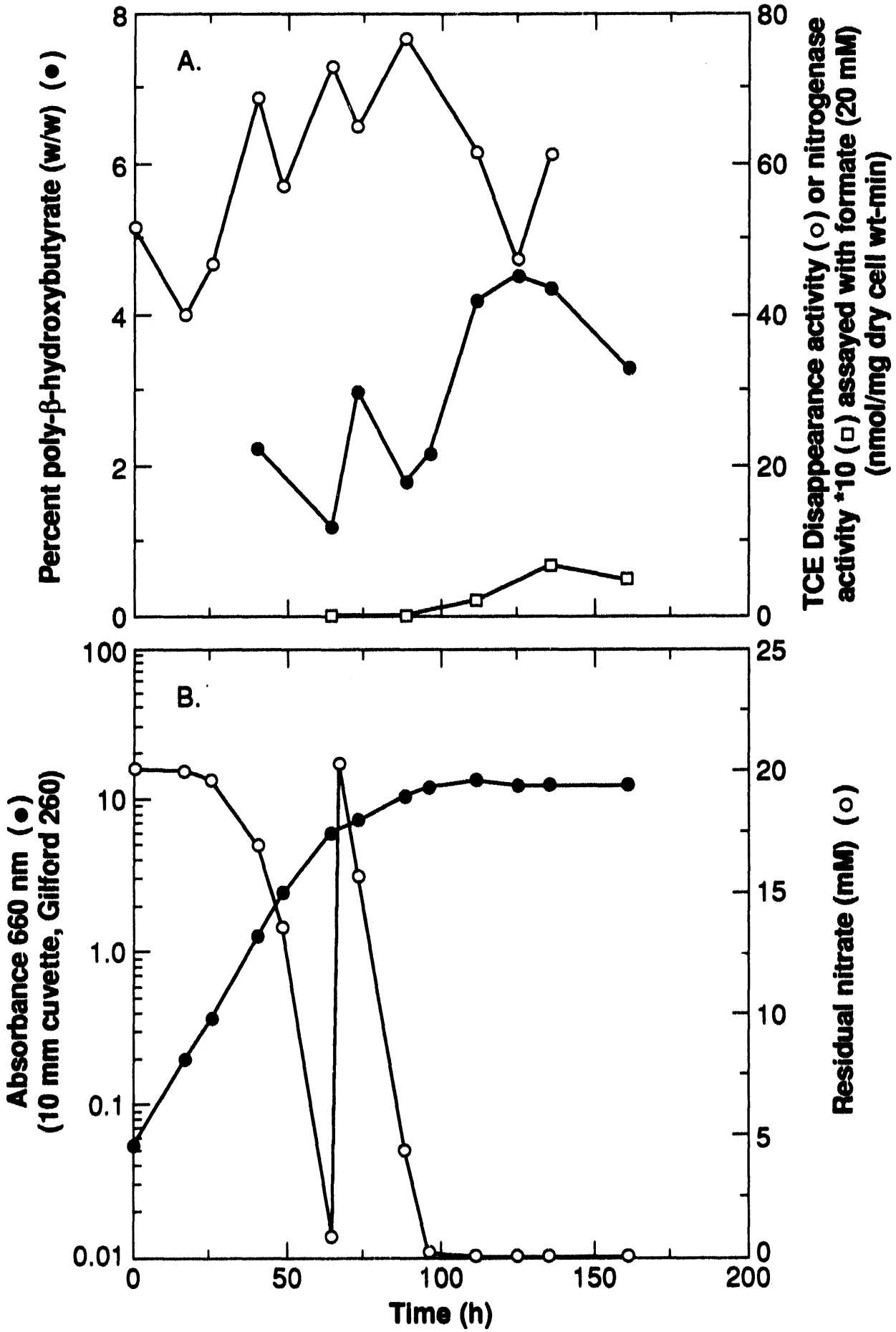

B-JV-3 (6-14-93) IL

Figure 1

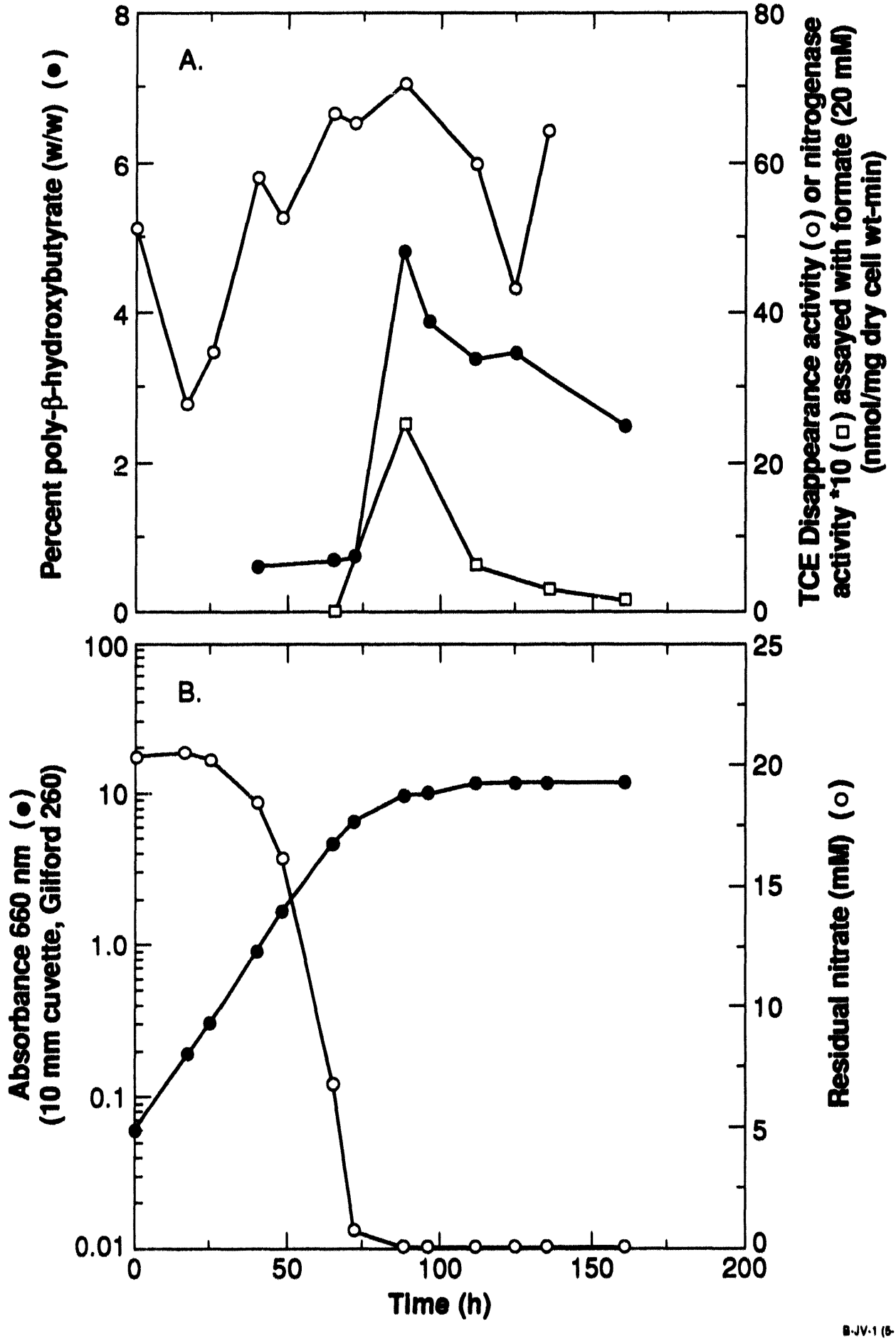

B-JV-1 (6-14-93) IL

Figure 2

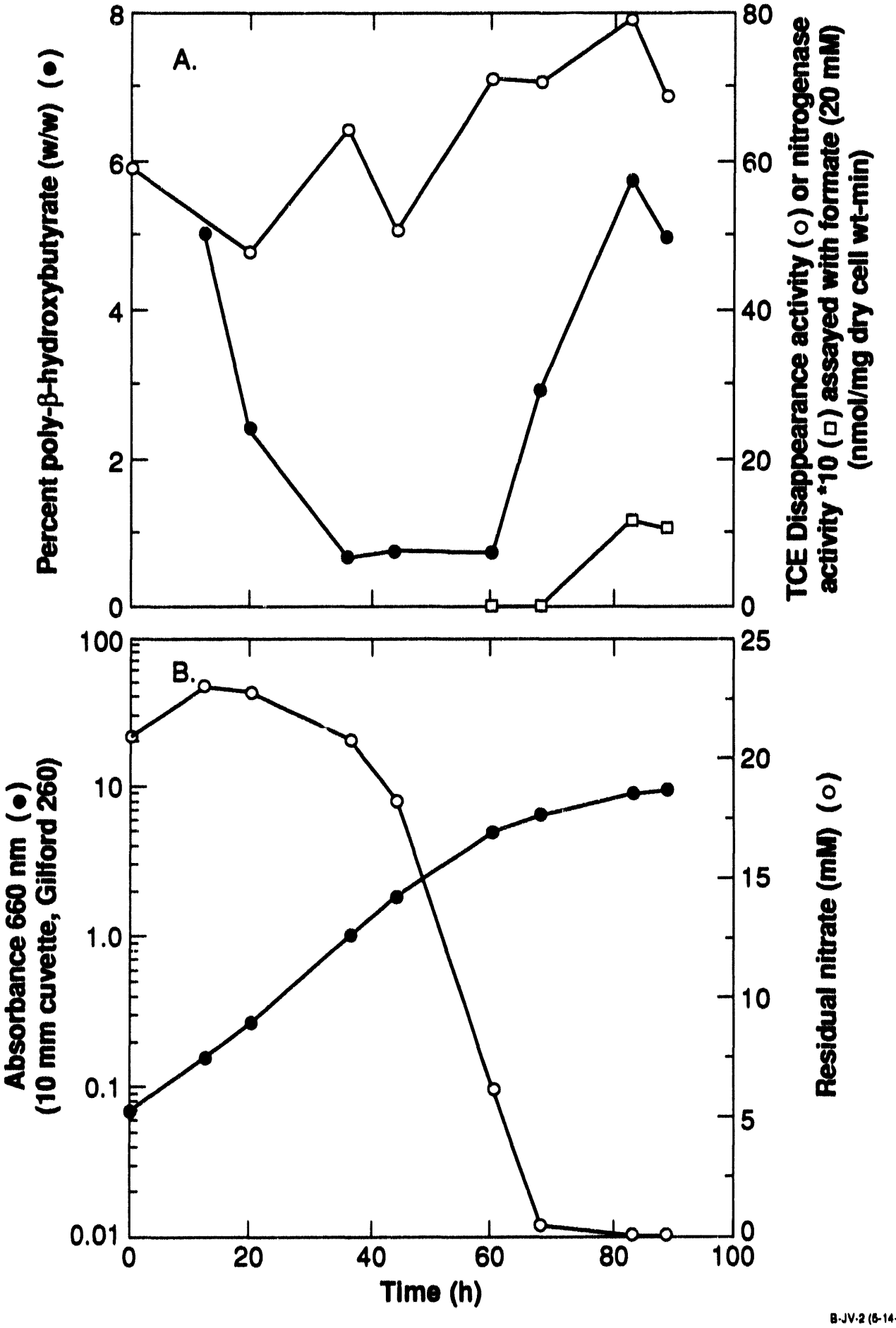

B-JV-2 (5-14-93) IL

Site 300 Contained Firing Facilities*

Jonathan West
Texas A&M University

Defense Technologies Engineering Division
Lawrence Livermore National Laboratory
Livermore, California 94550

May 19, 1993

Prepared in partial fulfillment of the requirements of the Science and Engineering Research Semester under the direction of Greg Kay, Sanjay Govindjee, and Dale Schauer, Research mentors, at the Lawrence Livermore National Laboratory.

*This research was supported in part by an appointment to the U.S. Department of Energy Science and Engineering Research Semester (hereinafter called SERS) program administered by LLNL under *Contract W-7405-Eng-48 with Lawrence Livermore National Laboratory.*

Site 300 Contained Firing Facilities

Jonathan West
Texas A&M University

Defense Technologies Engineering Division
Lawrence Livermore National Laboratory

ABSTRACT

The Site 300 Contained Firing Facilities are being developed at LLNL to minimize hazardous emissions to the environment and reduce quantities of hazardous waste while still allowing design engineers to conduct tests on the high explosives component of a nuclear weapon. To this point, the designers have conducted a series of tests on an open-air quarter scale section of the chamber floor. I analyzed the strain data to find evidence of non-linear effects. Currently, the design of the firing chamber in these facilities is being reviewed and a quarter-scale model will be tested to examine the strength and durability of the chamber. My SERS project is to develop a finite element model of the firing chamber. I have used INGRID to create the three-dimensional representation of the firing chamber, including the material specifications of the walls, anvil, doors, and soil. I used NIKE3D, a nonlinear, implicit, 3D finite element code to find the primary eigenvalues of the chamber. For the actual analysis, however, I used DYNA3D, a nonlinear, explicit, 3D finite element code to run two shot scenarios. Little quantitative data is available from the analysis at this time, but the results so far appear favorable and with further refinement, the model should be able to provide insight into the response of the firing chamber to the required blast loadings.

TABLE OF CONTENTS

Introduction 1

Quarter Scale Floor Tests 2

Figure 1: Full Scale Contained Firing Chamber 3

QSFT Data Analysis 4

Figure 2: QSFT Anvil/Floor Section 5

Figure 3: QSFT Strain Gage Data 6

Figure 4: QSFT Concrete Strain 7

Figure 5: QSFT Z-Axis Strain. 8

Quarter Scale Firing Chamber Analysis 9

Modelling Assumptions 9

Figure 6: Quarter Scale Firing Chamber INGRID Mesh 10

Pressure Loading Assumptions 11

Eigenvalue Analysis 11

Figure 7: Scaled Distance "Z" Relations 12

Figure 8: Eigenvalue #1 — 0.80 milliseconds/cycle 13

Figure 9: Eigenvalue #2 — 0.90 milliseconds/cycle 14

Figure 10: Eigenvalue #3 — 1.47 milliseconds/cycle 15

Figure 11: Eigenvalue #4 — 2.29 milliseconds/cycle 16

Transient Analysis 17

Conclusion 17

References 18

Appendix

Appendix A: Quarter Scale Firing Chamber INGRID Code A-1

Appendix B: Load Curve Generator FORTRAN Code B-1

Appendix C: QSFC Maximum Overall Loading. C-1

Appendix D: QSFC Maximum West Wall Loading D-1

INTRODUCTION

The Nuclear Weapon Design Program at Lawrence Livermore National Laboratory currently uses Site 300 to perform open-air high explosives testing. Although many of the devices involved in these tests contain toxic and/or low level radioactive materials (depleted uranium), the tests do comply with all applicable environmental standards. More constrictive regulations, however, may severely limit open-air testing in the future. Having the ability to execute tests close to the lab is crucial to the design process, so the Laboratory is currently working to design a fully enclosed test chamber. The Site 300 Contained Firing Facilities will minimize hazardous emissions to the environment and reduce quantities of hazardous waste while still allowing design engineers to conduct tests on the high explosives component of a nuclear weapon.[1]

In April, 1990, Holmes & Narver, an engineering architecture firm, prepared the conceptual design report for the Site 300 Firing Facilities. They estimated a total project cost of $46.2 million for the Firing Chamber, Support Facility, and Diagnostic Facility.[2] Before building such a costly structure, however, the project directors proposed a series of ¼ scale model tests to establish the final design criteria, to determine advantageous strain gage placement, and to verity that the firing chamber will reliably and safely contain the shock and debris from numerous high explosive blasts.[3] The approved testing plans called for prototype testing of a ¼ scale floor section and further testing of a complete ¼ scale firing chamber.[4]

QUARTER SCALE FLOOR TESTS

The initial design of the firing chamber[5] allows for six different firing zones on the floor as seen in Figure 1. Because the shots occur only three to four feet above the floor, the primary design concern was the ability of the floor to withstand the explosive blasts over a long lifetime (≈40 years) without cracking. The first series of tests proposed, therefore, focussed on the floor and consisted of steel-reinforced concrete block with a steel anvil on top, representative of an open-air ¼ scale section of the floor directly beneath firing zone one. The projected schedule of the Quarter Scale Floor Tests (QSFT) called for a total of sixteen shots with four each at explosive weights 50%, 125%, 200%, and 400% of the design yield.[6]

The weight of high explosive needed to simulate the full scale effects of the ¼ scale model is calculated using the scaled distance[7] Z. The scaled distance Z represents the relative severity of an explosive blast so for any given test, the Z-factor for each ¼ scale surface is equal to that of the full scale chamber. The scaled distance Z is calculated according to the following equation:

$$Z = \frac{R}{W^{1/3}}$$

R is the distance between the HE charge and the reference surface and W is the weigh of HE in equivalent pounds of TNT. The equivalent TNT weight of HE is based on the ratio of the effective explosive energy of HE versus TNT. The conservative upper bound applicable to the high explosives in use at Site 300 is that one pound HE is equivalent to 1.3 pounds of TNT.[8] Once the Z-factor has been calculated for the full scale chamber and explosive weights, the HE weight needed for the ¼ scale can be calculated by solving for the weight in terms of the Z-factor (same as full scale) and the known distance from the charge to the surface.

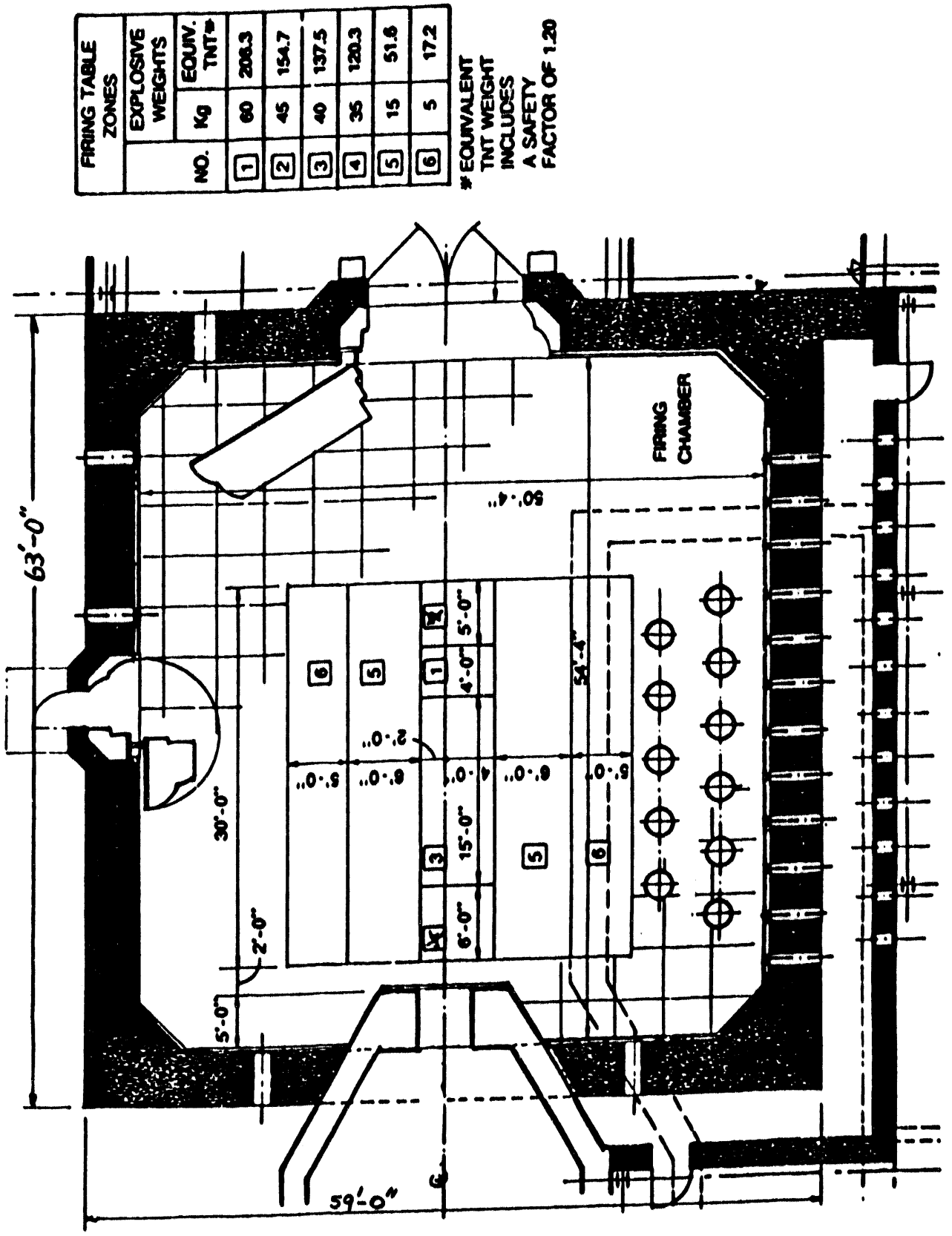

Figure 1: Full Scale Firing Chamber

QSFT DATA ANALYSIS

The actual test schedule for the ¼ scale floor section,[9] seen in Figure 2, consisted of eleven tests, ending in early 1993. The tests included two shots each at 25%, 50%, and 100% of the designed maximum explosive weight and five shots at 125%. During the testing, the strain gages hinted that the block was being strained non-linearly. As a result, testing was stopped and I was asked to consolidate and analyze the strain gage data to determine what could be learned from the tests.

The original data recorded by the strain gages was graphical in form, showing the plots of stress versus elapsed time for the fourteen strain gages. For each gage, I recorded the maximum positive and negative stress levels for each test and then found the average values for each test range (i.e. 25%, 50%, 100%, and 125%). Finally, I divided each stress value by its respective modulus to convert the data into readings of microstrain (10^{-6} in/in). The average strains for the various gages can be seen in Figure 3. To better see the trends occurring as the testing progressed, I also graphed the strains versus the weight of HE. The graph if Figure 4 shows the average positive peak of the strain gages inside the concrete block. The horizontal dotted line is the theoretical fracture limit[10] of 160 μin/in developed by Hatano in 1960 for dynamic uniaxial tensile strain in concrete. Based on this criteria, the lower section of the concrete started to fail during the 50% tests and the middle and upper sections failed at 100% and 125% respectively. Figure 5 compare the strain of the concrete and the enclosed rebar for the z-axis (vertical). Notices specifically that as the strain reaches a level higher than the fracture limit of the concrete, the two curves begin to separate. This implies that the concrete and rebar have debonded and the rebar becomes somewhat loose within the cracked concrete. As this occurs, the rebar is unable to transfer tne same proportion of the applied load as previously possible, causing the concrete to absorb the greater strain.

Instrumentation

Instrumentation will consist of a number of strain gages embedded in the concrete, on the reinforcing bars, and on the back side of the anvil. If possible we would like to measure the contact pressure between the steel anvil and the concrete below it.

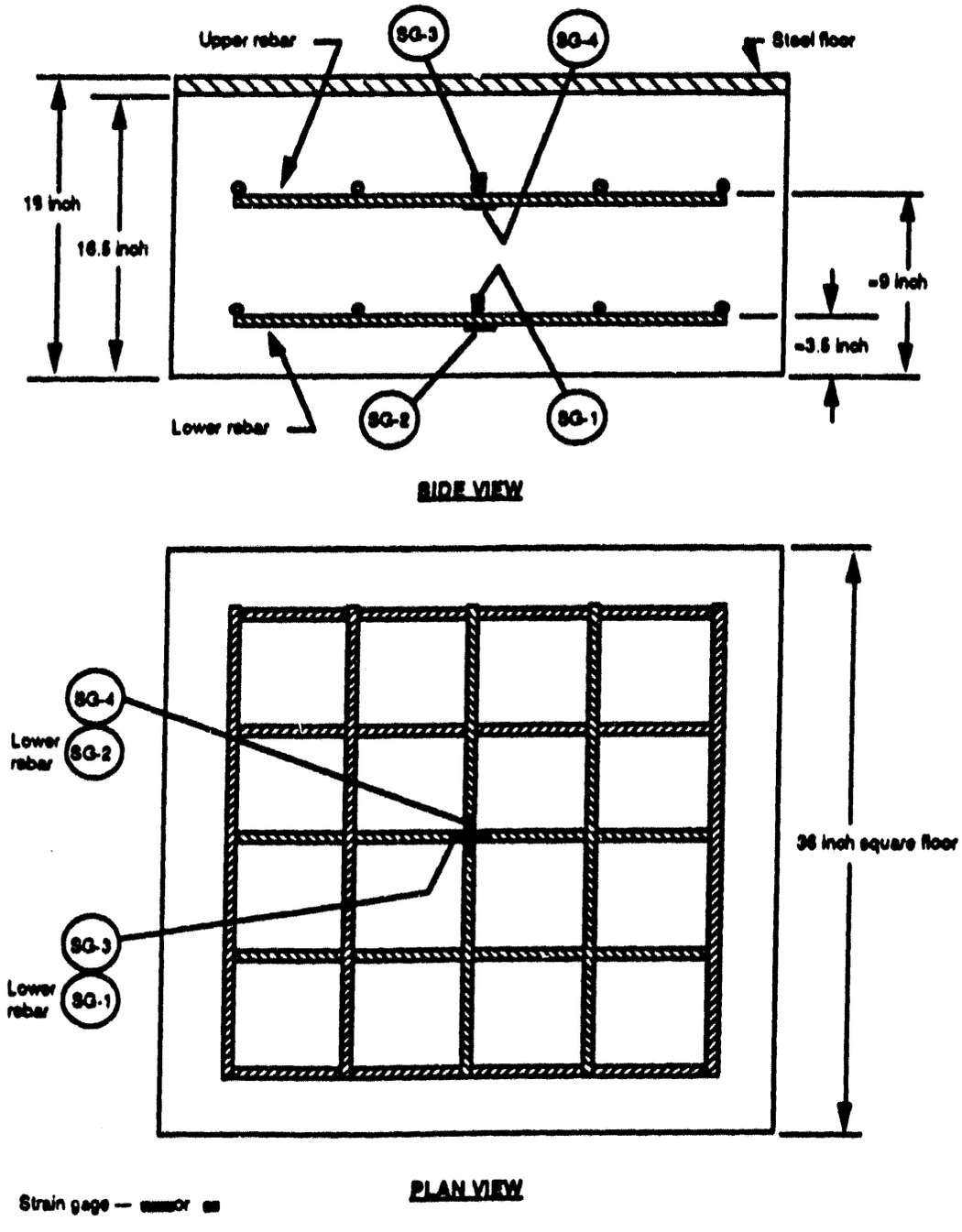

Figure 2: QSFT Anvil/Floor Section

Figure 3: QSFT Strain Guage Data

Maximum Positive Stress (Micro-in/in)

Test Level	25%	50%	100%	125%
Weight of HE [lb]	0.6	1.24	2.48	3.1
z-factor [1/(lb^1/3)]	1.09	0.85	0.68	0.63
Bolt 1 - Center Bolt	415	743.33	1066.67	1316.67
Bolt 2 - Side Bolt	303.33	500	641.67	783.33
Bolt 3 - Corner Bolt	139.17	150	205	421.67
SG 4 - Center Concrete Z	40	128	260	450
SG 5 - Top Rebar X	44.83	77.59	135.34	232.76
SG 6 - Top Rebar Y	0	0	0	0
SG 7 - Lower Rebar Y	65.52	189.66	525.86	663.79
SG 8 - Lower Rebar X	75	262.07	668.97	827.59
SG 9 - Upper Concrete X	45	84	108	196
SG 10 - Lower Concrete Y	84	435	1170	1410
SG 11 - Anvil X	115	115	425	226.67
SG 12 - Anvil Y	115	74.17	278.33	141.67
SG 13 - Lower Concrete X	35	64	42.6	40
SG 14 - Center Stirrup Z	51.72	118.1	208.62	322.41

Maximum Negative Stress (Micro-in/in)

25%	50%	100%	125%
0.6	1.24	2.48	3.1
1.09	0.85	0.68	0.63
90	150	266.67	200
191.67	125	166.67	153.33
75	63.33	66.67	76.67
88	189	335	412
39.66	25.86	29.31	89.66
0	0	0	0
43.79	65.52	50	70.69
39.31	65.52	160.34	163.79
34	25.6	66	92
49	108	40	100
100	117.5	200	85
90	130	196.67	143.33
30	56	67	80
100.86	203.45	332.76	362.07

Figure 4: QSFT Concrete Strain

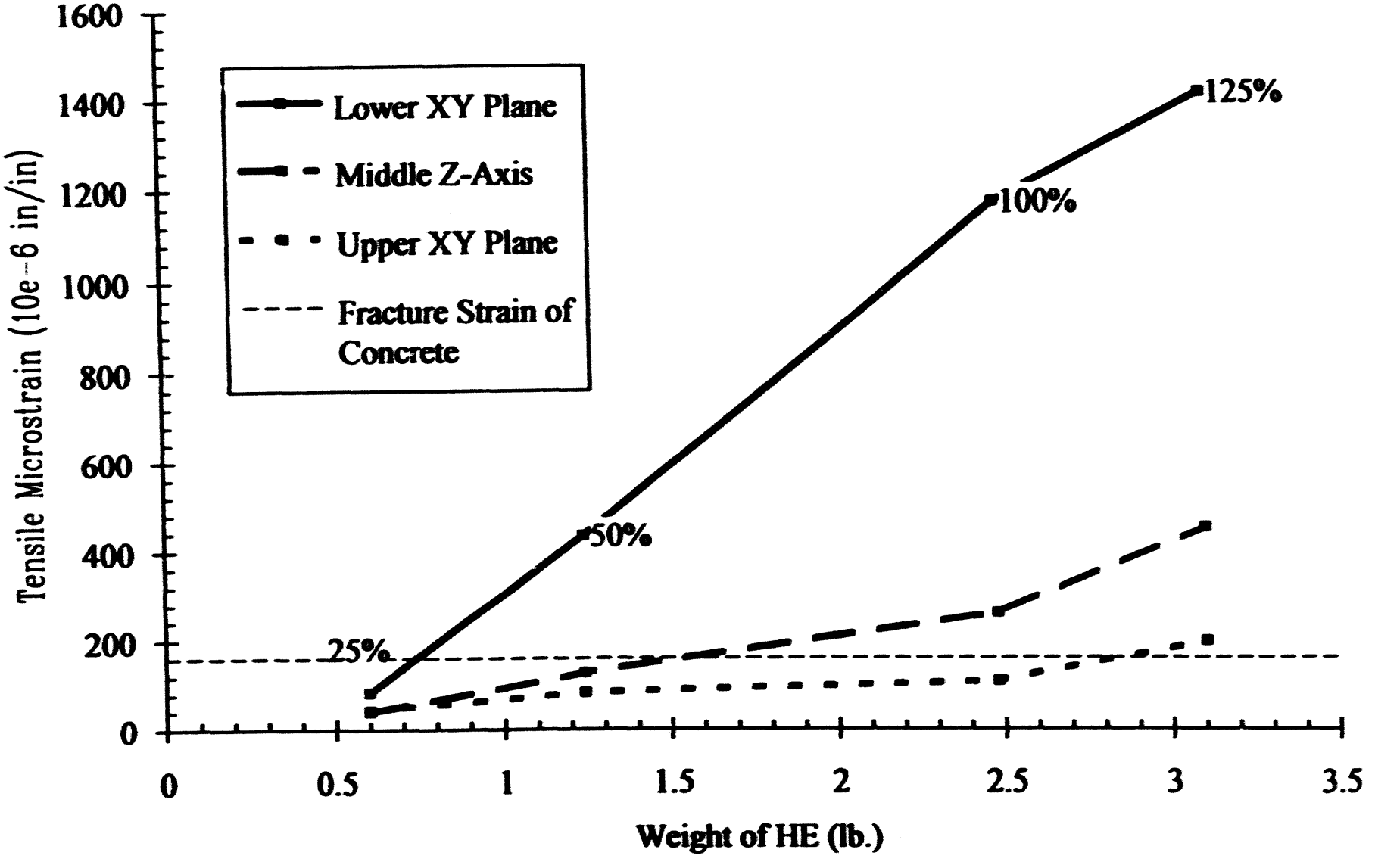

Figure 5: QSFT Z-Axis Strain

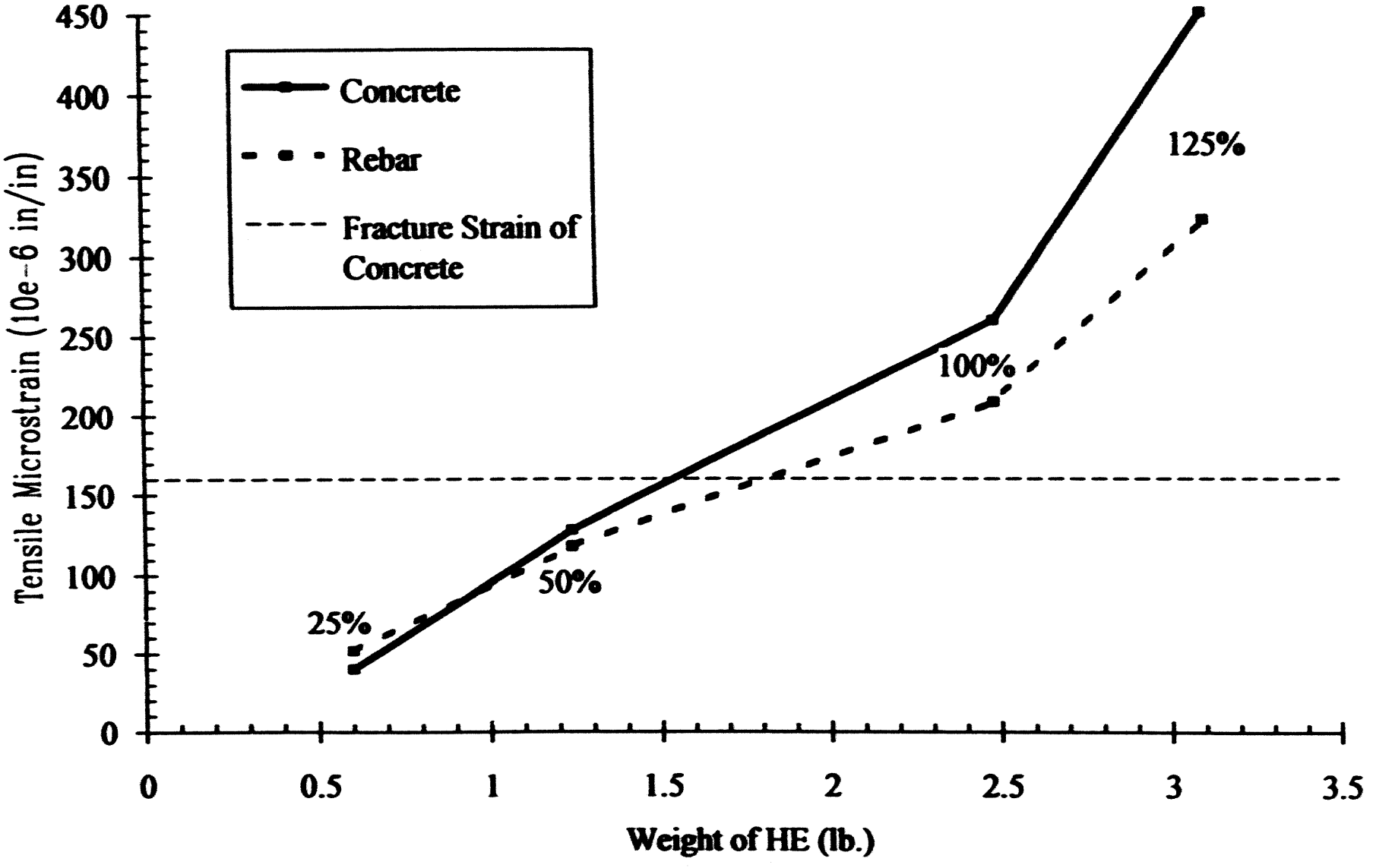

QUARTER SCALE FIRING CHAMBER ANALYSIS

From the performance of the floor in the open-air ¼ scale floor section tests, enough was learned to continue planning for the ¼ scale firing chamber tests. I have spent the majority of my SERS program term working on the finite element model of the ¼ scale model. To generate the model I have used INGRID to create the three-dimensional representation of the firing chamber, including the material specifications of the walls, anvil, doors, and soil. I used NIKE3D, a nonlinear, implicit, 3D finite element code to find the primary eigenvalues of the chamber. For the dynamic analysis, however, I used DYNA3D, a nonlinear, explicit, 3D finite element code to run testing scenarios for firing zones one and four. For post-processing the DYNA data, I used TAURUS to generate the displacement plots.

Modelling Assumptions

I spent the majority of my time simply learning INGRID to the extent necessary to develop a model of this magnitude (see Appendix A for the INGRID code). Do to the extreme complexity of the firing chamber, I made a number of simplifying assumptions to make the model's computational requirements reasonable. First, because the chamber is expected to remain elastic throughout its life cycle, I assumed that the walls were simply solid, elastic concrete rather than steel-reinforced brittle concrete. Second, I made the chamber symmetric about the path of the X-ray beam. The disparity between the two halves is only three inches (1.7%) and removing it allows me to cut the model size in half. Finally, the steel plate elements were modelled as two-dimensional thick shells to keep the mesh size from being too small. The 3D mesh created by the INGID code before blasting can be seen in Figure 6.

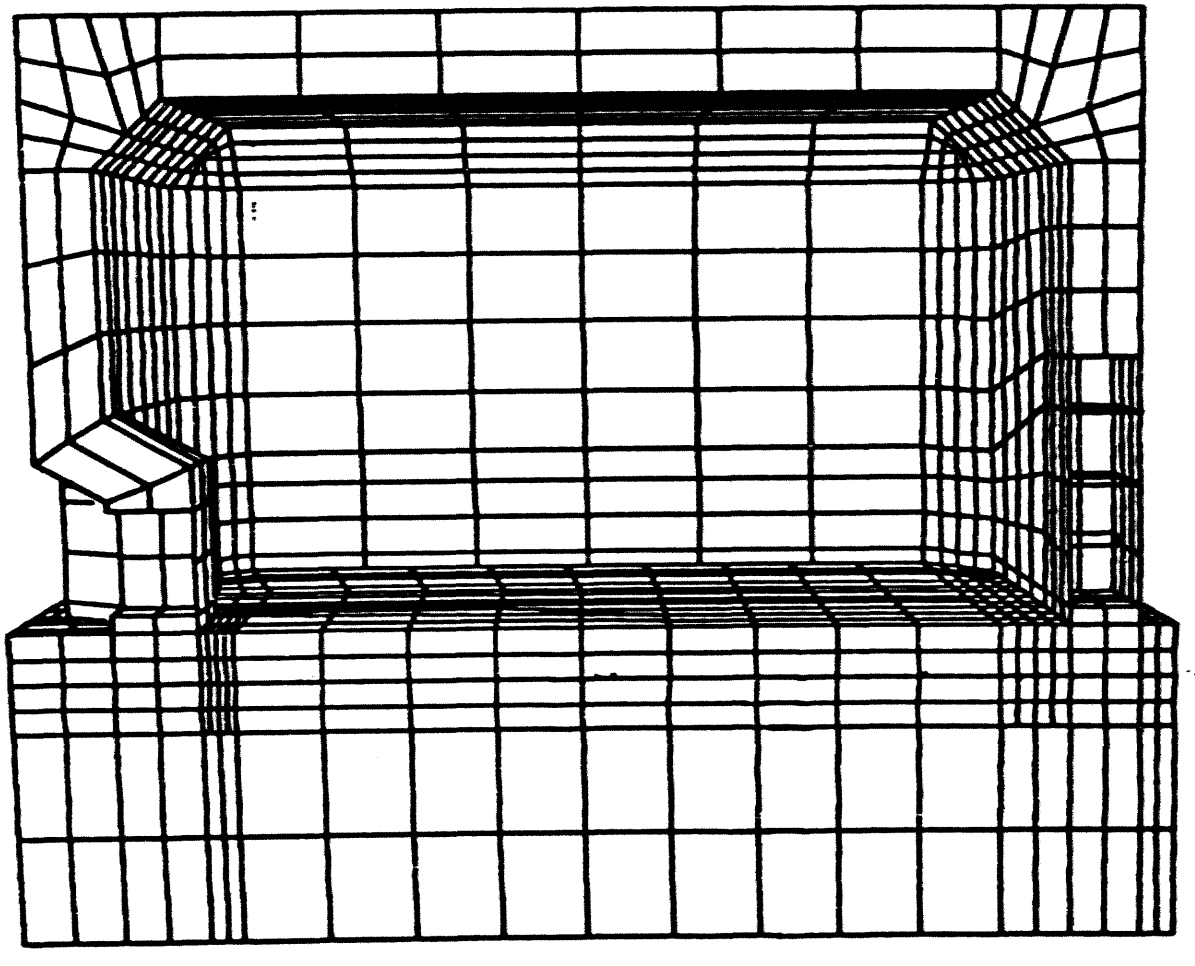

Figure 6: Quarter Scale Firing Chamber INGRID Mesh

Pressure Loading Assumptions

I made a number of assumptions about the pressure load curves which simulate the shock waves created by the high explosives blast. Holmes & Narver, in their original design, input average shock pressures and impulses (area under a 'Pressure vs. Time' graph) into the analysis program SHOCK to calculate the wall thicknesses and strengths needed. Although this is a reasonable method, I chose to make use of a different approximation. Using the maximum TNT weight limits for firing zones one and four, I calculated the Z-factor for the floor, ceiling, and three walls (East, West, & North). Then for each Z-factor I read the shock pressure (P_r) and calculated the arrival time (t_a), shock impulse (i_r), and the impulse duration (t_o) from the graph[11] in Figure 7. I wrote a FORTRAN program (see Appendix B) to generate an approximation of the pressure wave produced by the blast. The load curve created by the program has the same peak pressure as the real shock and assumes an exponential decay coefficient which creates an accurate shock impulse. INGRID only allows for constant wave velocity, so I assigned each load curve a velocity which is approximately the distance to from the charge to the surface in question divided by the arrival time from Figure 7. The shock wave also decays with the cube of the distance so although the initial peak is as high as 22,000 psi for the floor, the shock pressure drops quickly as it travels. After the shock wave passes, however, the building does not release the gases created, so a residual gas pressure is left. So for when the decaying shock pressure falls below the final gas pressure predicted by Holmes & Narver, I set up a separate set of load curves which eventually exert an equal pressure on all the walls.

Eigenvalue Analysis

The first four eigenvalues predicted by NIKE can be seen in Figures 8 through 11. These eigenvalues correspond to the natural vibrational frequencies of the chamber. Basically, if the loading conditions create excitation waves with similar periods, the chamber can be expected to resonate with motions similar to those shown.

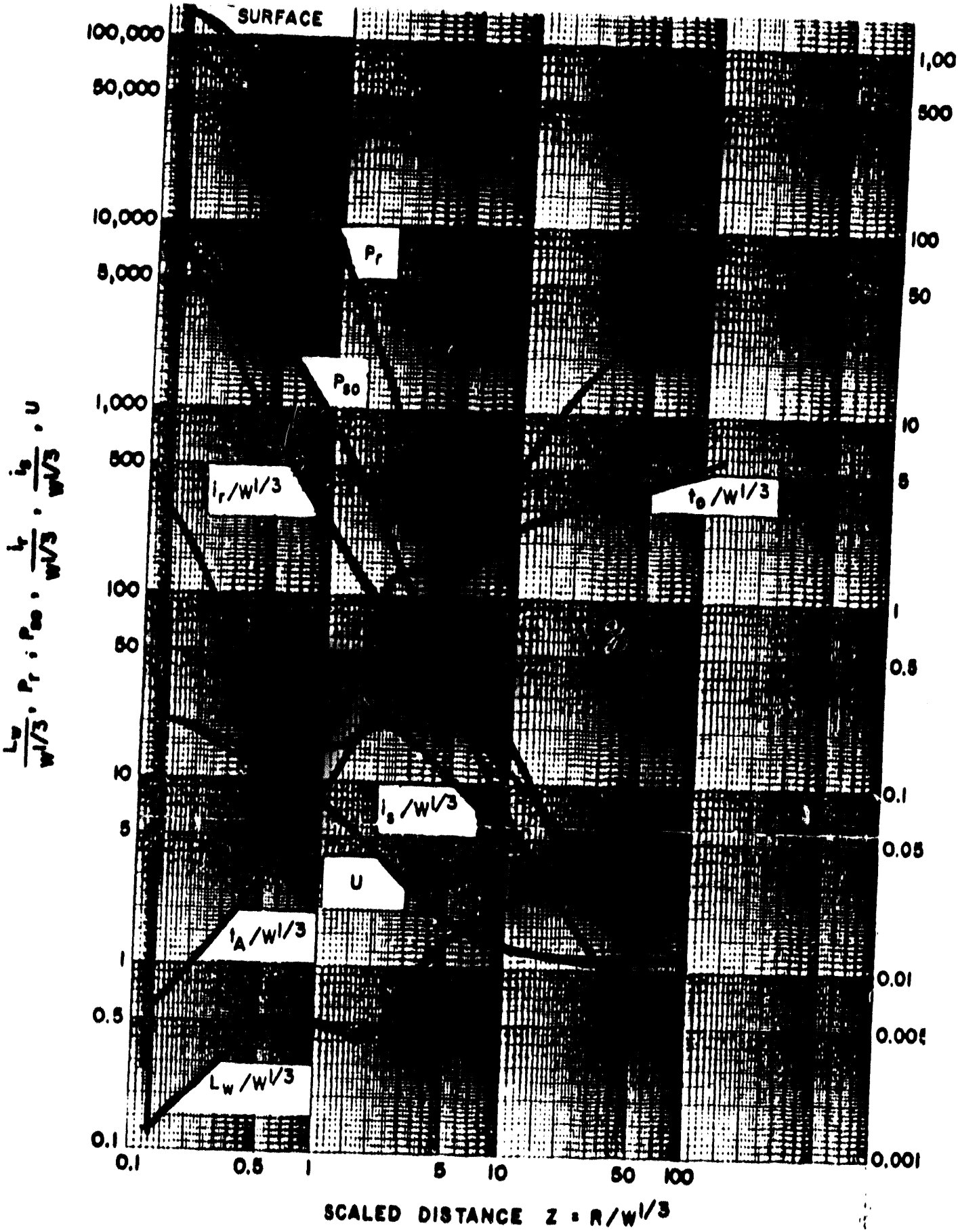

Figure 7: Scale Distance "Z" Relations

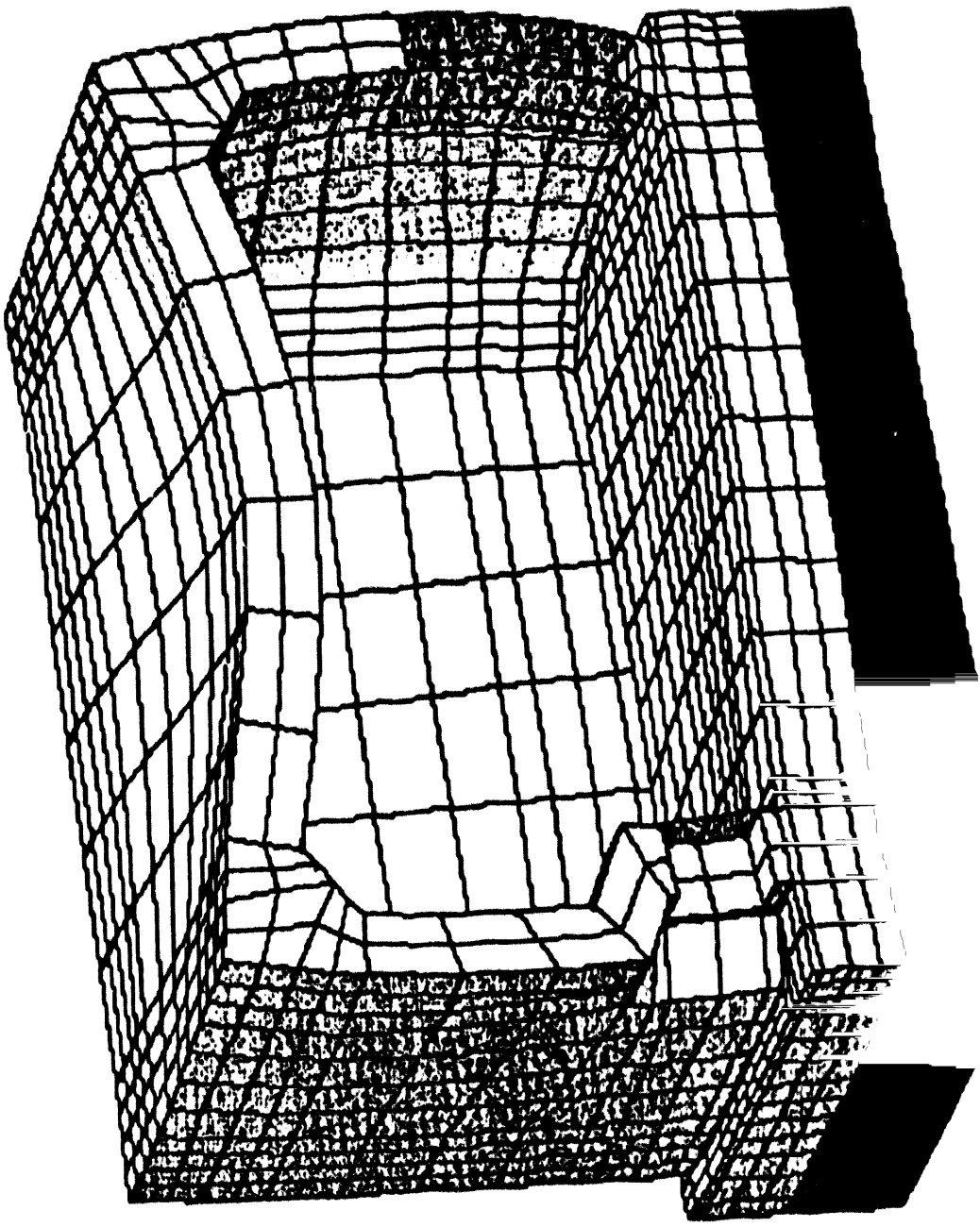

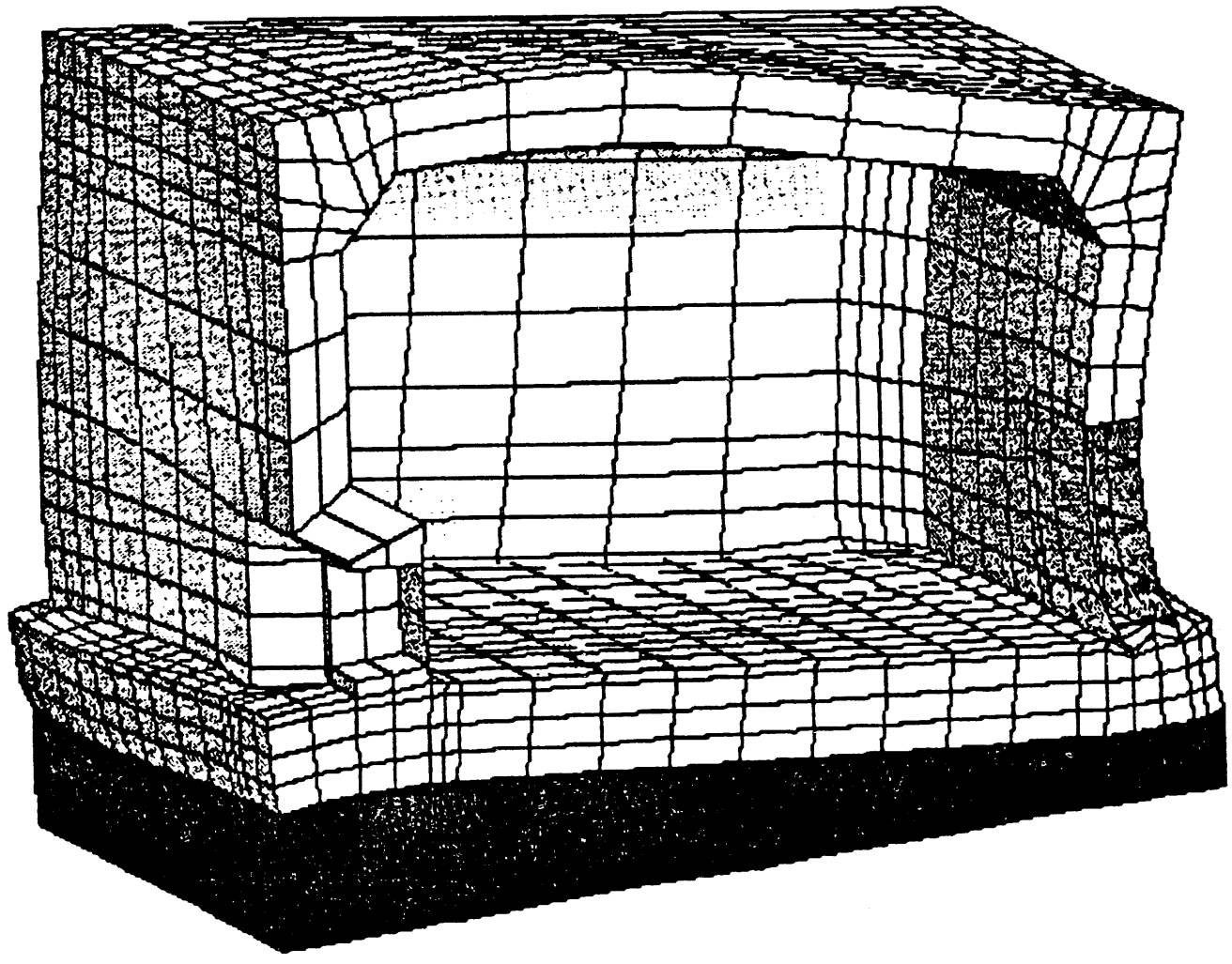

Figure 9: Eigenvalue #2 – 0.90 milliseconds/cycle

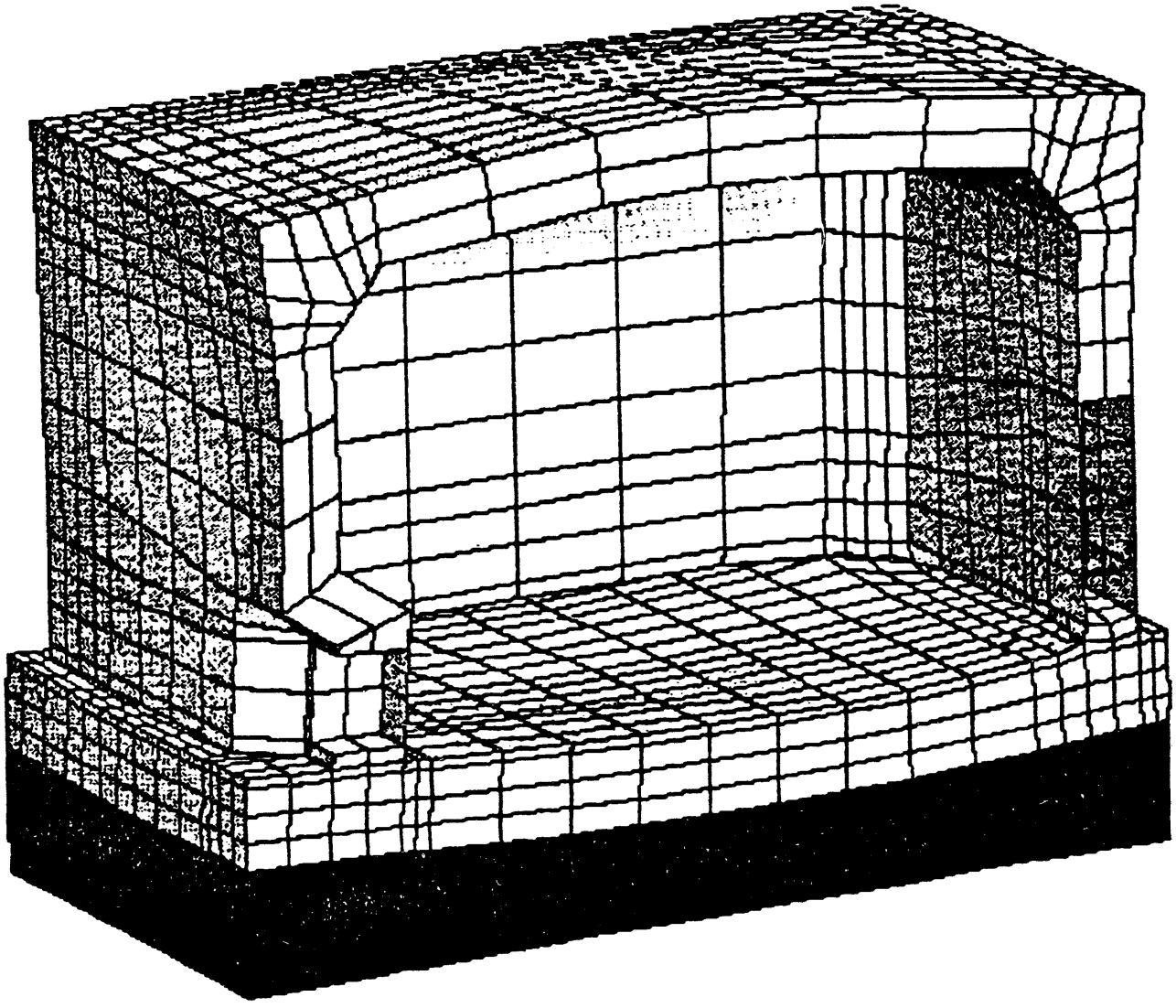

Figure 10: Eigenvalue #3 – 1.47 milliseconds/cycle

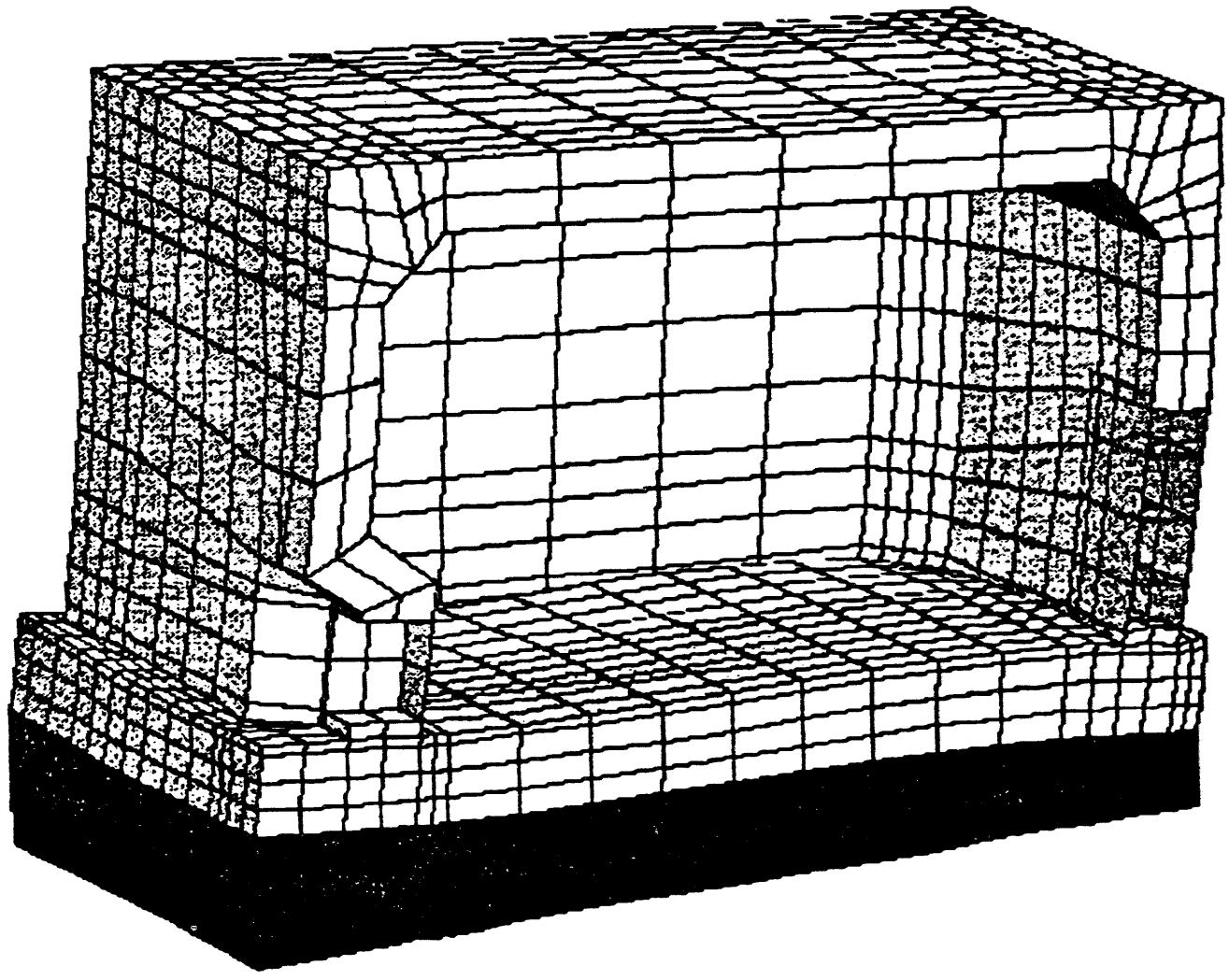

Figure 11: Eigenvalue #4 – 2.29 milliseconds/cycle

Transient Analysis

The first of the firing scenarios I ran with DYNA3D is the maximum overall loading of the firing chamber. When the ¼ scale model is finished, this test will consist of a 2.686 lb. HE charge (3.223 lb. TNT equivalent) detonated nine inches above firing zone one. The plots in Appendix C show the strain created in the firing chamber during the first ten milliseconds after the blast. After two milliseconds (C-7), the entire floor is arched due to the blast and the shock wave is just reaching the walls. The oscillation of the chamber is as it reaches its peak at four milliseconds (C-11) and flattens out at six milliseconds (C-14). The second scenario is the maximum west wall loading and in the ¼ scale model will involve a 1.566 pound HE charge (1.880 lb.) fired nine inches above firing zone four and only fifteen inches from the end of the X-ray inlet. The plots in Appendix D show the strain created in the firing chamber by the second firing scenario. The shock wave hits off the west wall very hard, deforming the X-ray inlet after only 0.6 milliseconds (D-3). Although the other walls of the firing chamber receives less punishment in this test scenario than in the first, notice how the propagation of the shock wave from west side of the chamber to the east causes the ceiling to oscillate both vertically but also side to side. Also notice how the building tends to shift on its foundation due to the uneven loading (D-12 to D-16). It should be noted that due to the lack of rebar in the model, these results over emphasize the response of the building to the blast loading.

CONCLUSION

The Site 300 Contained Firing Facilities are being developed to minimize hazardous emissions to the environment and reduce quantities of hazardous waste while still allowing design engineers to conduct test on the high explosive component of a nuclear weapon. Currently, the design of the firing chamber in these facilities is being review and a ¼ scale model will be tested to examine the strength and durability of the chamber. As a preface to these tests, I have developed

a finite element model of the ¼ scale firing chamber using INGRID to create the nodal input for NIKE3D and DYNA3d to analyze. The ability to capture the dynamic response of the chamber has been demonstrated. With further refinement to the model, e.g. rebar modelling and material failure models, higher confidence results will be available which should be able to provide insight into the response of both the ¼ scale and full-sized firing chambers when subjected to explosive blast loadings.

REFERENCES

[1]*Conceptual Design Report* "Site 300 Contained Firing Facilities" by Holmes & Narver, April 1990, Sect. I, Page B-1.

[2]Holmes & Narver, Section II, page B-1.

[3]"Proposal for a Research Project to Prove the Concept of Site 300 Contained Firing Facilities" by J. Pastrnak, C. Baker, & L. Simmons, Sept. 13, 1990, p. 6.

[4]"Floor Section Testing Plan in support of the proposed Contained Firing Facilities" by J. Pastrnak, C. Baker, L. Simmons, J. Rubke, B. Shay, Nov. 23, 1991, p. 7.

[5]Holmes & Narver, Section IV, page F-1.

[6]Pastrnak, *et al.*, Nov. 23, 1991, p. 12.

[7]*Structure to Resist the Effects of Accidental Explosions*, ARMY TM5-1300, NAVY NAVFAC P-397, AIR FORCE AFM 88-2, Department of the Army, Navy, and the Air Force. June 1969.

[8]"LLNL Explosion Handbook" by B.M. Dobraty, UCRL - 52997, March 16, 1981, pp. 8-19.

[9]Pastrnak, *et al.*, Nov. 23, 1991, p. 13.

[10]"Concrete Behavior Under Dynamic Tensile–Compressive Loads" by P.F. Mlakar, K.P. Vitaya-Udom, and R.A. Cole, U.S. Army Engineering Waterways Experiment Station, Tech Report SL-84-1, 1984.

[11]*Structure to Resist the Effects of Accidental Explosions*, ARMY TM5-1300, NAVY NAVFAC P-397, AIR FORCE AFM 88-2, Department of the Army, Navy, and the Air Force. June 1969.

APPENDIX A

Quarter Scale Firing Chamber INGRID Code

```
QSFC - Maximum Overall Loading

c NOTE:  This is NOT working code.  All of the load curves except for
c        Load Curves 1 & 10 have been deleted to save space.  Load curve 1
c        is representative of the impulse pressure waves and Load curve 10
c        is representative of the residual pressure which is 32 psi for test
c        one and 22 psi for test 2.

dn3d88s

term .05
plti 5.0e-4
prti 5.0e-4
c
c DEFINE SYMMETRY PLANE
plane 1
94.5 0 0  1 0 0 .001 symm

c DEFINE CONTACT SURFACES
si 1 tied ;

c DEFINE BEAM ELEMENTS
bsd 1 sthi 1.25 tthi 1.25;
bsd 2 sthi 1.25 tthi .625;

c DEFINE PRESSURE ARRIVALS
arri 1                    c Floor
velo 2.0e5
point 94.5 108.0 30.0
decay 9. r3 ;

arri 2                    c Ceiling
velo 4.3450e4
point 94.5 108.0 30.0
decay 81. r3 ;

arri 3                    c East Wall & X-Ray Nose (West Wall)
velo 4.3450e4
point 94.5 108.0 30.0
decay 75. r3 ;

arri 4                    c North Wall
velo 4.3450e4
point 94.5 108.0 30.0
decay 78. r3 ;

arri 5                    c Floor - Test 2
velo 1.9e5
point 94.5 48.0 30.0
decay 9. r3 ;

arri 6                    c Ceiling - Test 2
velo 3.776e4
point 94.5 48.0 30.0
decay 81. r3 ;

arri 7                    c East Wall - Test 2
velo 2.5423e4
point 94.5 48.0 30.0
decay 135. r3 ;

arri 8                    c North Wall - Test 2
velo 3.776e4
point 94.5 48.0 30.0
decay 78. r3 ;
```

```
arri 9                    c X-Ray Nose (WEST WALL) - Test 2
velo 1.350e5
point 94.5 48.0 30.0
decay 15. r3 ;

arri 10                   c GAS OVERPRESSURE - Floor
velo 2.0e5
point 94.5 108.0 30.0
decay 9. constant ;

arri 11                   c GAS OVERPRESSURE - Ceiling
velo 4.3450e4
point 94.5 108.0 30.0
decay 81. constant ;

arri 12                   c GAS OVERPRESSURE - East Wall & X-Ray Nose
velo 4.3450e4
point 94.5 108.0 30.0
decay 75. constant ;

arri 13                   c GAS OVERPRESSURE - North Wall
velo 4.3450e4
point 94.5 108.0 30.0
decay 78. constant ;

arri 14                   c GAS OVERPRESSURE - Floor - Test 2
velo 1.9e5
point 94.5 48.0 30.0
decay 9. constant ;

arri 15                   c GAS OVERPRESSURE - Ceiling - Test 2
velo 3.776e4
point 94.5 48.0 30.0
decay 81. constant ;

arri 16                   c GAS OVERPRESSURE - East Wall - Test 2
velo 2.5423e4
point 94.5 48.0 30.0
decay 135. constant ;

arri 17                   c GAS OVERPRESSURE - North Wall - Test 2
velo 3.776e4
point 94.5 48.0 30.0
decay 78. constant ;

arri 18                   c GAS OVERPRESSURE - x-Ray Nose (WEST WALL) - Test 2
velo 1.350e5
point 94.5 48.0 30.0
decay 15. constant ;


c                    ##################################
c                    ####     DEFINE PARTS     ####
c                    ##################################


c ***************************
c Part #1: Concrete Floor *
c ***************************
start
1 2 4 8 11 13 15;
1 3 5 9 15 18 22 24 26;
1 4 7;
0. 6. 24. 51. 69.64 82.07 94.5
0. 6. 18. 30. 129. 171. 183. 195. 201.
0. 9. 18.
```

```
mate 1

c Pressure Application

c       Test #1 (Site #1)
pri 3 4; 3 7; 3; 1 1.0 47. 94. -1000.
pri 4 7; 3 4 0 5 7; 3; 1 1.0 47. 94. -1000.
pri 3 4; 3 7; 3; 10 1.0 47. 94. -1000.
pri 4 7; 3 4 0 5 7; 3; 10 1.0 47. 94. -1000.
(
c       Test #2 (Site #4)
pri 3 4; 3 7 ; 3; 5 1.0 47. 94. -1000.
pri 4 7; 3 4 0 5 7 ; 3; 5 1.0 47. 94. -1000.
pri 3 4; 3 7 ; 12; 5 1.0 47. 94. -1000.
pri 4 7; 3 4 0 5 7 ; 12; 5 1.0 47. 94. -1000.
)

c Shape angled corners
pb 3 2 1 3 2 3 x 26.
pb 3 3 1 3 3 3 x 30.
pb 3 4 1 3 6 3 x 18.
pb 3 7 1 3 7 3 x 30.
pb 3 8 1 3 8 3 x 26.

c Shape cutout for x-ray inlet

pb 5 1 1 5 2 3 x 77.5
pb 6 1 1 6 2 3 x 84.
pb 6 2 1 7 2 3 y 18.
pb 5 3 1 5 3 3 x 69.75
pb 6 3 1 6 4 3 x 78.
pb 6 3 1 7 3 3 y 33.
pb 4 4 1 7 4 3 y 39.

c Adjust floor to mesh w/ rear door
pb 6 7 2 6 9 3 x 82.5
pb 5 7 2 5 9 3 x 70.5

c Contact with Concrete Walls
sii+ 2 3; 2 8; 3 3; 1 s 47 94 1000
sii+ 3 7; 2 3 0 7 8; 3 3; 1 s 47 94 1000

end

c *************************
c Part #2: Concrete Walls *
c *************************
start
1 3 5 9 10 11 12;
1 3 5 11 13 15;
1 2 4 5 6 9 11 13;
6. 18. 30. 72. 81. 85.5 94.5
6. 18. 30. 171. 183. 195.
18. 21. 36. 42. 54. 96. 108. 121.5

mate 1

c Pressure Application

c       Test #1
pri 2 7; 2 5; 7; 2 1.0 47. 94. 1000.    c CEILING
pri 2 7; 2; 1 7; 3 1.0 47. -1000. 60.   c WEST WALL
pri 2 7; 5; 1 7; 3 1.0 47. 1000. 60.    c EAST WALL
pri 2; 2 5; 1 7; 4 1.0 -1000. 94. 60.   c NORTH WALL
pri 2 7; 2 5; 7; 11 1.0 47. 94. 1000.   c Overpressure CEILING
```

```
pri 2 7; 2; 1 7; 12 1.0 47. -1000. 60.   c op WEST WALL
pri 2 7; 5; 1 7; 12 1.0 47. 1000. 60.    c op EAST WALL
pri 2; 2 5; 1 7; 13 1.0 -1000. 94. 60.   c op NORTH WALL
(
c       Test #2
pri 2 7; 2 5; 7; 6 1.0 47. 94. 1000.     c CEILING
pri 2 7; 2; 1 7; 9 1.0 47. -1000. 60.    c WEST WALL
pri 2 7; 5; 1 7; 7 1.0 47. 1000. 60.     c EAST WALL
pri 2; 2 5; 1 7; 8 1.0 -1000. 94. 60.    c NORTH WALL
pri 2 7; 2 5; 7; 15 1.0 47. 94. 1000.    c op CEILING
pri 2 7; 2; 1 7; 18 1.0 47. -1000. 60.   c op WEST WALL
pri 2 7; 5; 1 7; 16 1.0 47. 1000. 60.    c op EAST WALL
pri 2; 2 5; 1 7; 17 1.0 -1000. 94. 60.   c op NORTH WALL
)

c Cut out interior of building
di 2 7 ; 2 5 ; 1 7 ;

c Cut out holes for doors
di 6 7 ; 1 2 ; 2 3 ;
di 4 7 ; 5 6 ; 2 5 ;

c Angle wall edges
pb 2 2 1 2 2 7 xy 24. 24.
pb 2 2 7 7 2 7 yz 24. 102.
pb 2 2 7 2 5 7 xz 24. 102.
pb 2 5 1 2 5 7 xy 24. 177.
pb 2 5 7 7 5 7 yz 177. 102.

c  Angle wall for x-ray inlet
pb 4 1 3 7 2 3 z 39.
pb 4 1 1 4 1 5 x 77.5
pb 5 1 1 5 1 5 x 84.
pb 5 1 1 7 1 4 y 18.
pb 5 1 4 7 1 4 z 40.5
pb 4 1 5 7 1 5 z 47.
pb 4 2 1 4 2 4 x 69.75
pb 5 2 1 5 2 4 x 78.
pb 5 2 1 7 2 4 y 33.
pb 5 2 4 7 2 4 z 46.25
pb 4 2 5 7 2 5 z 54.5

c Shape hole for back door
pb 4 5 1 4 6 5 x 76.5
pb 4 5 5 7 6 5 z 63.
pb 4 5 3 7 6 3 z 42.
pb 4 5 4 7 6 4 z 54.
cpl 4 5 1 7 6 5 i
cpl 4 1 6 7 6 8 i

c Contact with concrete floor
sii+ 1 7; 1 2 0 5 6; 1; 1 m 47 94 -1000
sii+ 1 2; 2 5; 1; 1 m 47 94 -1000

end

c ************************
c Part #3:  Steel Anvil *
c ************************
start
1 4 6 8; 1 7; -1;
51. 69.64 82.07 94.5
39. 129.
18.

mate 2
```

```
c Pressure Application

c       Test #1
pri ; ; ; 1 1.0 47. 94. -1000.
pri ; ; ; 10 1.0 47. 94. -1000.
(
c       Test #2
pri ; ; ; 5 1.0 47. 94. -1000.
pri ; ; ; 14 1.0 47. 94. -1000.
)

pa 3 1 1 x 78.
thic [1.5]

end

c ************************
c Part #4:  Front Door *
c ************************
start
1 2 3; -1;1 2 4 5;
78. 85.5 94.5
33.
18. 21. 39. 46.25

mate 2
thic [1.5]

c Pressure Application

c       Test #1
pri ; ; ; 3 1.0 47. -1000. 60.
pri ; ; ; 12 1.0 47. -1000. 60.
(
c       Test #2
pri ; ; ; 9 1.0 47. -1000. 60.
pri ; ; ; 18 1.0 47. -1000. 60.
)
end

c ***********************
c Part #5:  Back Door *
c ***********************
start
1 2 4; -1 -2; 1 2 3 4 5;
76.5 82.5 94.5
183. 195.
21. 31.5 42. 54. 63.

mate 2
thic [2.0]


c Pressure Application
c       Test #1
pri ; 1; ; 3 1.0 47. 1000. 60.
pri ; 1; ; 12 1.0 47. 1000. 60.
(
c       Test #2
pri ; 1; ; 7 1.0 47. 1000. 60.
pri ; 1; ; 16 1.0 47. 1000. 60.
)

end
```

```
c ************************************
c Part #6:  Beams inside Back Door *
c ************************************
beam
rt 000000 82.5 183. 31.5
rt 000000 82.5 195. 31.5
rt 000000 82.5 183. 42.
rt 000000 82.5 195. 42.
rt 000000 82.5 183. 54.
rt 000000 82.5 195. 54.
rt 000000 82.5 189. 84.
0
1 2 1 3 3 7
3 4 1 3 3 7
5 6 1 3 3 7
0
bad 1
end

c ************************************
c Part #7:  Beams inside Back Door *
c ************************************
beam
rt 000000 94.5 183. 31.5
rt 000000 94.5 195. 31.5
rt 000000 94.5 183. 42.
rt 000000 94.5 195. 42.
rt 000000 94.5 183. 54.
rt 000000 94.5 195. 54.
rt 000000 94.5 189. 84.
0
1 2 1 3 3 7
3 4 1 3 3 7
5 6 1 3 3 7
0
bad 2
end

c **********************
c Part #8:  Soil Base *
c **********************

start
1 2 4 8 11 13 15;
1 3 5 7 13 16 18 20 22;
1 3 5;
0. 6. 24. 51. 69.64 82.07 94.5
0. 6. 18. 30. 129. 171. 183. 195. 201.
-36. -18. 0.


c Shape angled corners
pb 3 2 1 3 2 3 x 26.
pb 3 3 1 3 3 3 x 30.
pb 3 4 1 3 6 3 x 18.
pb 3 7 1 3 7 3 x 30.
pb 3 8 1 3 8 3 x 26.

c Shape cutout for x-ray inlet

pb 5 1 1 5 2 3 x 77.5
pb 6 1 1 6 2 3 x 84.
pb 6 2 1 7 2 3 y 18.
pb 5 3 1 5 3 3 x 69.75
pb 6 3 1 6 4 3 x 78.
pb 6 3 1 7 3 3 y 33.
```

```
pb 4 4 1 7 4 3 y 39.

mate 3

end


c DEFINE TOLERANCES
tp .01

c                       ################################
c                       ####   DEFINE MATERIALS   ####
c                       ################################

mat 1 1
head
Elastic Concrete
ro 2.2465e-07 e 5000. pr .20
endmat

mat 2 3 shell
head
ASTM-A36 steel plate
ro 7.7708448e-07 e 30.e3 pr .29
sigy 3.6e1 etan 67.e1 beta 1.
endmat

mat 3 3 beam
head
ASTM-A307 Back Door Bracing
ro 7.7708448e-07 e 30.e3 pr .29
sigy 3.6e1 etan 67.e1 beta 1.
endmat

mat 4 1
head
Elastic Soil
ro 1.4977e-07 e 20. pr .20
endmat

c                       ################################
c                       ####  DEFINE LOAD CURVES  ####
c                       ################################

c Define Load Curve for FLOOR - test 1
lcd 1 123
     0.0000000000000000E+00       0.0000000000000000
     0.4432000000000000E-05   22000.0000000000000000
     0.8864000000000000E-05   19875.7654302366822776
     0.1329600000000000E-04   17956.6387017177989947
     0.1772800000000000E-04   16222.8153977660331293
     0.2216000000000000E-04   14656.4033392740670934
     0.2659200000000000E-04   13241.2379464704081329
     0.3102400000000000E-04   11962.7154286361223967
     0.3545600000000000E-04   10807.6420803747657828
     0.3988800000000000E-04    9764.0981292492738248
     0.4432000000000000E-04    8821.3147297623354461
     0.4875200000000000E-04    7969.5628343203578652
     0.5318400000000000E-04    7200.0527943856197908
     0.5761600000000000E-04    6504.8436557513058460
     0.6204800000000000E-04    5876.7612119125549270
     0.6648000000000000E-04    5309.3239698857906887
     0.7091200000000000E-04    4796.6762644810446545
     0.7534400000000000E-04    4333.5278308004171777
     0.7977600000000000E-04    3915.0992113814313029
     0.8420800000000000E-04    3537.0724346146342327
```

0.8863999999999999E-04	3195.5464554616657438
0.9307199999999999E-04	2886.9968986445610426
0.9750399999999999E-04	2608.2396888763672678
0.1019360000000000E-03	2356.3981928154629486
0.1063680000000000E-03	2128.8735336651714647
0.1108000000000000E-03	1923.3177720803646196
0.1152320000000000E-03	1737.6096766215794105
0.1196640000000000E-03	1569.8328337199967280
0.1240960000000000E-03	1418.2558712592001484
0.1285280000000000E-03	1281.3145916910826543
0.1329600000000000E-03	1157.5958303087022614
0.1373920000000000E-03	1045.8228721016286897
0.1418240000000000E-03	944.8422767031086380
0.1462560000000000E-03	853.6119754691713837
0.1506880000000000E-03	771.1905178575544966
0.1551200000000000E-03	696.7273561345229638
0.1595520000000000E-03	629.4540681526706152
0.1639840000000000E-03	568.6764276232133994
0.1684160000000000E-03	513.7672400519980442
0.1728480000000000E-03	464.1598704097097254
0.1772800000000000E-03	419.3423957451112400
0.1817120000000000E-03	378.8523223992414515
0.1861440000000000E-03	342.2718133048966038
0.1905760000000000E-03	309.2233761195403403
0.1950080000000000E-03	279.3659676953561402
0.1994400000000000E-03	252.3914746865444130
0.2038720000000000E-03	228.0215339755125221
0.2083040000000000E-03	206.0046601063650868
0.2127360000000000E-03	186.1136500822613087
0.2171680000000000E-03	168.1432387454625150
0.2216000000000000E-03	151.9079805447771498
0.2260320000000000E-03	137.2403358313158215
0.2304640000000000E-03	123.9889419340972410
0.2348960000000000E-03	112.0170511738796915
0.2393280000000000E-03	101.2011196963114337
0.2437600000000000E-03	91.4295325618723354
0.2481920000000000E-03	82.6014519361800534
0.2526240000000000E-03	74.6257764945674715
0.2570560000000000E-03	67.4202013025133393
0.2614880000000000E-03	60.9103684703678514
0.2659200000000000E-03	55.0290998175598114
0.2703520000000000E-03	49.7157036277681303
0.2747840000000000E-03	44.9153483411221002
0.2792160000000000E-03	40.5784967202506008
0.2836480000000000E-03	36.6603946510604262
0.2880800000000000E-03	33.1206093029263906
0.2925120000000000E-03	29.9226118823399876
0.2969440000000000E-03	27.0334006742455704
0.3013760000000000E-03	24.4231604810412328
0.3058080000000000E-03	22.0649549448273623
0.3102400000000000E-03	19.9344485778240781
0.3146720000000000E-03	18.0096556324521182
0.3191040000000000E-03	16.2707132195435964
0.3235360000000000E-03	14.6996763333772558
0.3279680000000000E-03	13.2803326683003620
0.3324000000000000E-03	11.9980353159385094
0.3368320000000000E-03	10.8395516165131576
0.3412640000000000E-03	9.7929266044890175
0.3456960000000000E-03	8.8473596393794491
0.3501280000000000E-03	7.9930929486022424
0.3545600000000000E-03	7.2213109322044108
0.3589920000000000E-03	6.5240491903317571
0.3634240000000000E-03	5.8941123346527069
0.3678560000000000E-03	5.3249997355919042
0.3722880000000000E-03	4.8108384391225928
0.3767200000000000E-03	4.3463225606530285

```
    0.3811520000000000E-03        3.9266585319845641
    0.3855840000000000E-03        3.5475156321073954
    0.3900160000000000E-03        3.2049812983574735
    0.3944480000000000E-03        2.8955207497476606
    0.3988800000000000E-03        2.6159405100167075
    0.4033120000000000E-03        2.3633554525702631
    0.4077440000000000E-03        2.1351590274344274
    0.4121760000000000E-03        1.9289963629790436
    0.4166080000000000E-03        1.7427399648341442
    0.4210400000000000E-03        1.5744677612246530
    0.4254720000000000E-03        1.4224432681623231
    0.4299040000000000E-03        1.2850976698097082
    0.4343360000000001E-03        1.1610136290946145
    0.4387680000000001E-03        1.0489106615087444
    0.4432000000000001E-03        0.9476319211555540
    0.4476320000000001E-03        0.8561322626860151
    0.4520640000000001E-03        0.7734674559275004
    0.4564960000000001E-03        0.6987844419062239
    0.4609280000000001E-03        0.6313125297103163
    0.4653600000000001E-03        0.5703554433496170
    0.4697920000000001E-03        0.5152841365398015
    0.4742240000000001E-03        0.4655303012630520
    0.4786560000000001E-03        0.4205805031169016
    0.4830880000000001E-03        0.3799708829310212
    0.4875200000000001E-03        0.3432823699753137
    0.4919520000000001E-03        0.3101363573620481
    0.4963840000000001E-03        0.2801907950143694
    0.5008160000000001E-03        0.2531366598825970
    0.5052480000000001E-03        0.2286947669827320
    0.5096800000000001E-03        0.2066128883487007
    0.5141120000000001E-03        0.1866631501673845
    0.5185440000000001E-03        0.1686396812361808
    0.5229760000000001E-03        0.1523564884763735
    0.5274080000000001E-03        0.1376455375786799
    0.5318400000000001E-03        0.1243550189742123
    0.5362720000000001E-03        0.1123477812365489
    0.5407040000000001E-03        0.1014999157484178

c Define Load Curve for CEILING - test 1
lcd 2 75

c Define Load Curve for EAST WALL & X-Ray Nose (West Wall) - test 1
lcd 3 65

c Define Load Curve for NORTH WALL - test 1
lcd 4 67

c Define Load Curve for FLOOR - test 2
lcd 5 123

c Define Load Curve for CEILING - test 2
lcd 6 77

c Define Load Curve for EAST WALL - test 2
lcd 7 83

c Define Load Curve for NORTH WALL - test 2
lcd 8 81

c Define Load Curve for X-Ray NOSE (West Wall) - test 2
lcd 9 99

c Define Load Curve for GAS OVERPRESSURE - FLOOR - test 1
lcd 10 136
    0.0000000000000000E+00        0.0000000000000000
    0.4432000000000000E-05        0.0000000000000000
```

0.8864000000000000E-05	0.0000000000000000
0.1329600000000000E-04	0.0000000000000000
0.1772800000000000E-04	0.0000000000000000
0.2216000000000000E-04	0.0000000000000000
0.2659200000000000E-04	0.0000000000000000
0.3102400000000000E-04	0.0000000000000000
0.3545600000000000E-04	0.0000000000000000
0.3988800000000000E-04	0.0000000000000000
0.4432000000000000E-04	0.0000000000000000
0.4875200000000000E-04	0.0000000000000000
0.5318400000000000E-04	0.0000000000000000
0.5761600000000000E-04	0.0000000000000000
0.6204800000000000E-04	0.0000000000000000
0.6648000000000000E-04	0.0000000000000000
0.7091200000000000E-04	0.0000000000000000
0.7534400000000000E-04	0.0000000000000000
0.7977600000000000E-04	0.0000000000000000
0.8420800000000000E-04	0.0000000000000000
0.8863999999999999E-04	0.0000000000000000
0.9307199999999999E-04	0.0000000000000000
0.9750399999999999E-04	0.0000000000000000
0.1019360000000000E-03	0.0000000000000000
0.1063680000000000E-03	0.0000000000000000
0.1108000000000000E-03	0.0000000000000000
0.1152320000000000E-03	0.0000000000000000
0.1196640000000000E-03	0.0000000000000000
0.1240960000000000E-03	0.0000000000000000
0.1285280000000000E-03	0.0000000000000000
0.1329600000000000E-03	0.0000000000000000
0.1373920000000000E-03	0.0000000000000000
0.1418240000000000E-03	0.0000000000000000
0.1462560000000000E-03	0.0000000000000000
0.1506880000000000E-03	0.0000000000000000
0.1551200000000000E-03	0.0000000000000000
0.1595520000000000E-03	0.0000000000000000
0.1639840000000000E-03	0.0000000000000000
0.1684160000000000E-03	0.0000000000000000
0.1728480000000000E-03	0.0000000000000000
0.1772800000000000E-03	0.0000000000000000
0.1817120000000000E-03	0.0000000000000000
0.1861440000000000E-03	0.0000000000000000
0.1905760000000000E-03	0.0000000000000000
0.1950080000000000E-03	0.0000000000000000
0.1994400000000000E-03	0.0000000000000000
0.2038720000000000E-03	0.0000000000000000
0.2083040000000000E-03	0.0000000000000000
0.2127360000000000E-03	0.0000000000000000
0.2171680000000000E-03	0.0000000000000000
0.2216000000000000E-03	0.0000000000000000
0.2260320000000000E-03	0.0000000000000000
0.2304640000000000E-03	0.0000000000000000
0.2348960000000000E-03	0.0000000000000000
0.2393280000000000E-03	0.0000000000000000
0.2437600000000000E-03	0.0000000000000000
0.2481920000000000E-03	0.0000000000000000
0.2526240000000000E-03	0.0000000000000000
0.2570560000000000E-03	0.0000000000000000
0.2614880000000000E-03	0.0000000000000000
0.2659200000000000E-03	0.0000000000000000
0.2703520000000000E-03	0.0000000000000000
0.2747840000000000E-03	0.0000000000000000
0.2792160000000000E-03	0.0000000000000000
0.2836480000000000E-03	0.0000000000000000
0.2880800000000000E-03	0.0000000000000000
0.2925120000000000E-03	2.0773881176600124
0.2969440000000000E-03	4.9665893257544296

0.3013760000000000E-03	7.5768395189587672
0.3058080000000000E-03	9.9350450551726377
0.3102400000000000E-03	12.0655514221759219
0.3146720000000000E-03	13.9903443675478818
0.3191040000000000E-03	15.7292867804564036
0.3235360000000000E-03	17.3003236666227442
0.3279680000000000E-03	18.7196673316996383
0.3324000000000000E-03	20.0019646840614906
0.3368320000000000E-03	21.1604483834868424
0.3412640000000000E-03	22.2070733955109825
0.3456960000000000E-03	23.1526403606205511
0.3501280000000000E-03	24.0069070513977576
0.3545600000000000E-03	24.7786890677955891
0.3589920000000000E-03	25.4759508096682428
0.3634240000000000E-03	26.1058876653472933
0.3678560000000000E-03	26.6750002644080957
0.3722880000000000E-03	27.1891615608774071
0.3767200000000000E-03	27.6536774391469717
0.3811520000000000E-03	28.0733414680154358
0.3855840000000000E-03	28.4524843678926045
0.3900160000000000E-03	28.7950187016425265
0.3944480000000000E-03	29.1044792502523393
0.3988800000000000E-03	29.3840594899832928
0.4033120000000000E-03	29.6366445474297371
0.4077440000000000E-03	29.8648409725655726
0.4121760000000000E-03	30.0710036370209566
0.4166080000000000E-03	30.2572600351658556
0.4210400000000000E-03	30.4255322387753471
0.4254720000000000E-03	30.5775567318376771
0.4299040000000000E-03	30.7149023301902919
0.4343360000000001E-03	30.8389863709053853
0.4387680000000001E-03	30.9510893384912555
0.4432000000000001E-03	31.0523680788444461
0.4476320000000001E-03	31.1438677373139847
0.4520640000000001E-03	31.2265325440724997
0.4564960000000001E-03	31.3012155580937761
0.4609280000000001E-03	31.3686874702896836
0.4653600000000001E-03	31.4296445566503833
0.4697920000000001E-03	31.4847158634601985
0.4742240000000001E-03	31.5344696987369479
0.4786560000000001E-03	31.5794194968830984
0.4830880000000001E-03	31.6200291170689787
0.4875200000000001E-03	31.6567176300246862
0.4919520000000001E-03	31.6898636426379521
0.4963840000000001E-03	31.7198092049856308
0.5008160000000001E-03	31.7468633401174030
0.5052480000000001E-03	31.7713052330172681
0.5096800000000001E-03	31.7933871116512994
0.5141120000000001E-03	31.8133368498326154
0.5185440000000001E-03	31.8313603187638190
0.5229760000000001E-03	31.8476435115236267
0.5274080000000001E-03	31.8623544624213202
0.5318400000000001E-03	31.8756449810257876
0.5362720000000001E-03	31.8876522187634510
0.5407040000000001E-03	31.8985000842515820
0.2436108800000000E-02	32.0000000000000000
0.4327081600000000E-02	32.0000000000000000
0.6218054400000000E-02	32.0000000000000000
0.8109027200000000E-02	32.0000000000000000
0.1000000000000000E-01	32.0000000000000000
0.1500000000000000E-01	32.0000000000000000
0.2000000000000000E-01	32.0000000000000000
0.2500000000000000E-01	32.0000000000000000
0.3000000000000000E-01	32.0000000000000000
0.3500000000000000E-01	32.0000000000000000
0.4000000000000000E-01	32.0000000000000000

```
    0.4500000000000000E-01       32.0000000000000000
    0.5000000000000000E-01       32.0000000000000000

c Define Load Curve for GAS OVERPRESSURE - CEILING - test 1
lcd 11 88

c Define Load Curve for GAS OVERPRESSURE - EAST WALL & X-Ray Nose Test 1
lcd 12 78

c Define Load Curve for GAS OVERPRESSURE - NORTH WALL - test 1
lcd 13 80

c Define Load Curve for GAS OVERPRESSURE - FLOOR - test 2
lcd 14 136

c Define Load Curve for GAS OVERPRESSURE - CEILING - test 2
lcd 15 90

c Define Load Curve for GAS OVERPRESSURE - EAST WALL - test 2
lcd 16 96

c Define Load Curve for GAS OVERPRESSURE - NORTH WALL - test 2
lcd 17 94

c Define Load Curve for GAS OVERPRESSURE - X-Ray NOSE (West Wall) - test 2
lcd 18 112

end
```

APPENDIX B

Load Curve Generator
FORTRAN Code

```
      Program Load Curve Generator
*
*     Jonathan West
*     Lawrence Livermore National Laboratory
*     Applied Mechanics Group
*
*     NON CLASSIFIED MATERIAL
*
      Double Precision  t,to,ta,dt,P,Ps,Pr,Pa,Ir,Ix
*             t - (real) time after explosion
*             to - impulse duration (input from file)
*             ta - arrival time (iff)
*             dt - time step between calculations
*             P - Dynamic Pressure at time (t)
*             Ps - Static Pressure at time (t)
*             Pr - Peak pressure (iff)
*             Pa - Residual (average) pressure (iff)
*             Ir - Shock Impulse (iff)
*             Ix - Shock Impulse (calculated)
      Integer x,y
      Character*3 DynamicOutput, StaticOutput
      Character*9 InputName
*
      Open (unit=7,File='lcv.list',status='Old')

    Do 50, y=1,9
      Read (7,*) InputName
      Open (unit=8,File=InputName,status='Old')
      Read (8,*) DynamicOutput,StaticOutput
      Open (unit=9,File=DynamicOutput,Status='New')
      Open (unit=10,File=StaticOutput,Status='New')
      Read (8,*) Pr,Pa,to,ta,Ir

      t = 0.000000000000000
      P = 0.000000000000000
      Ps = 0.000000000000000
      Ix = 0.000000000000000
      dt = to / 50
 5    Format (e26.16,f25.16)

20    write (9,5) t,P
        write (10,5) t,Ps
        t=t+dt
        P=Pr*exp(-1000.0000*(t-dt)*Pr/Ir)
        if (P.lt.Pa) Ps = Pa - P
        if (t.le.to) Ix = Ix + dt * P * 1000.000000000
      if (P.gt.0.1) goto 20

      Ps = Pa
      dt = (1.000000e-2 - t)/5
        Do 30, x=1,5
          t=t+dt
          write (10,5) t,Ps
30      Continue
*     Print *,Outputname,Ix
      Close (8)
      Close (9)
      Close (10)
50  continue

      Close (7)

      End
```

APPENDIX C

Quarter Scale Firing Chamber
Maximum Overall Loading

QSFC Maximum Overall Loading
Displacement Fringes

Time = 0.2 milliseconds

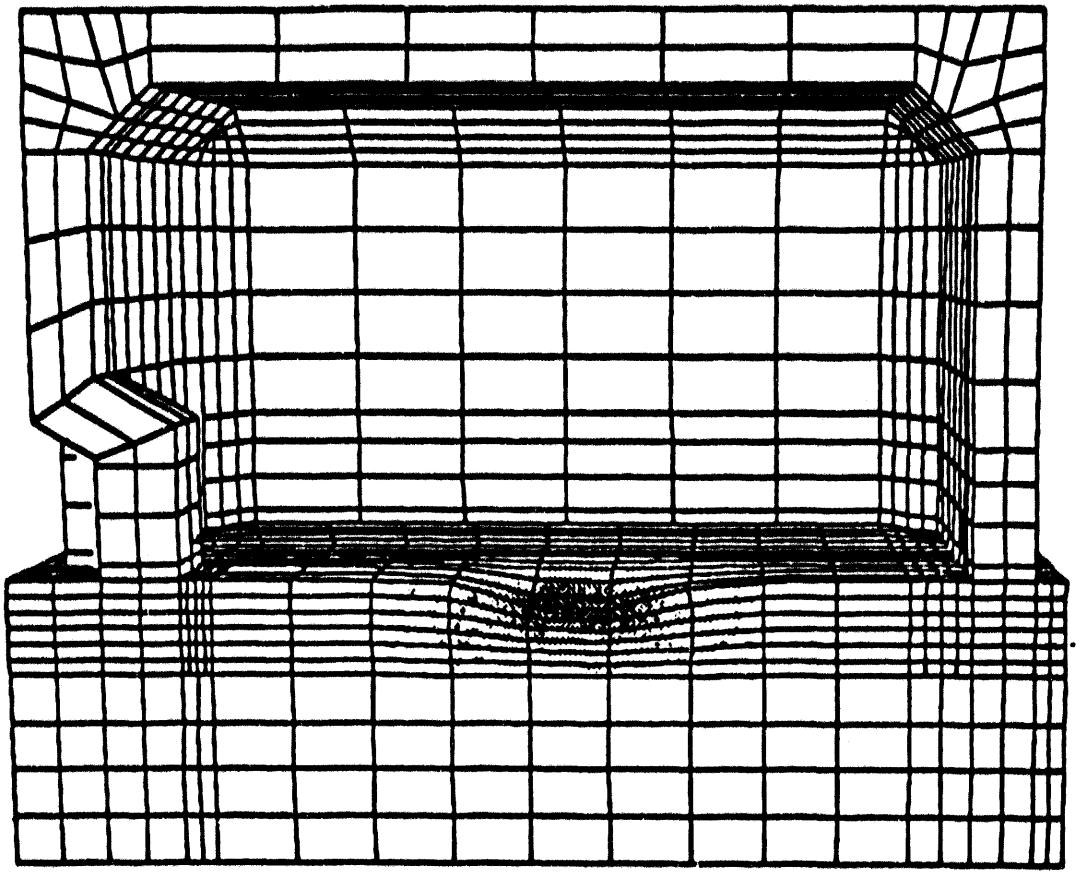

QSFC Maximum Overall Loading Displacement Fringes

Time = 0.4 milliseconds

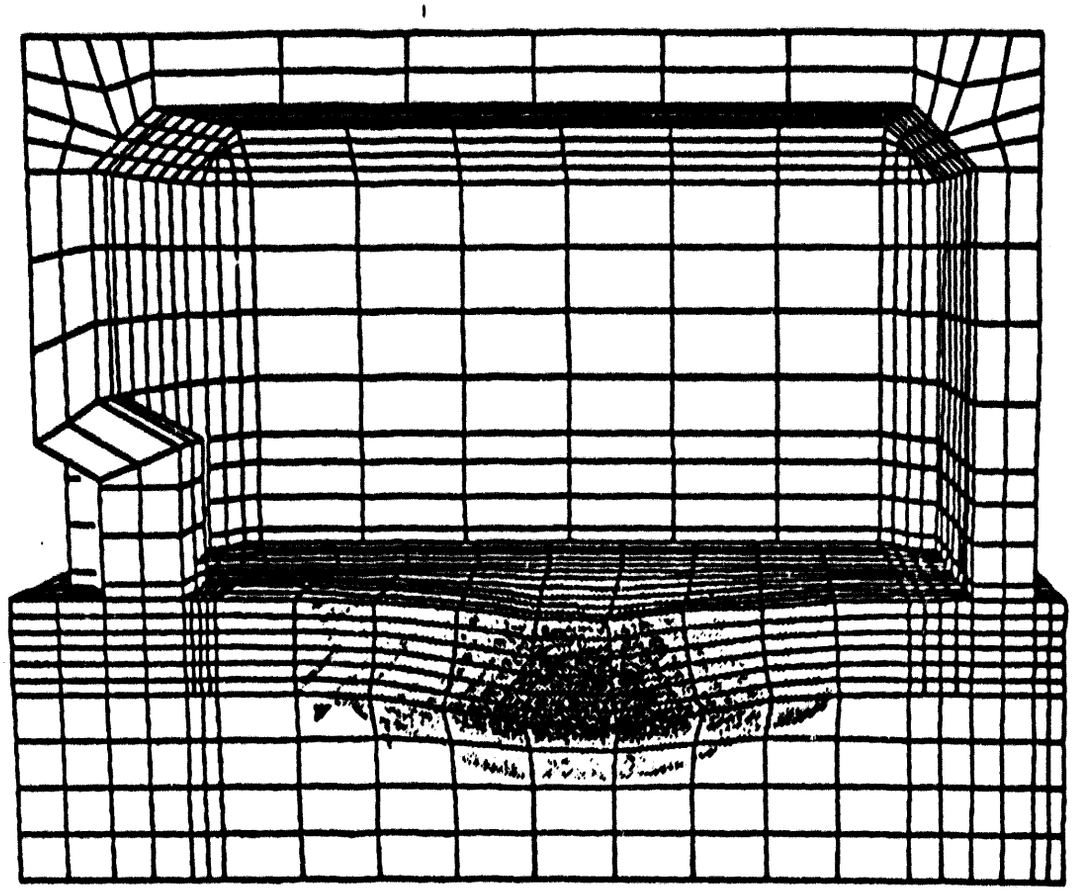

QSFC Maximum Overall Loading Displacement Fringes

Time = 0.6 milliseconds

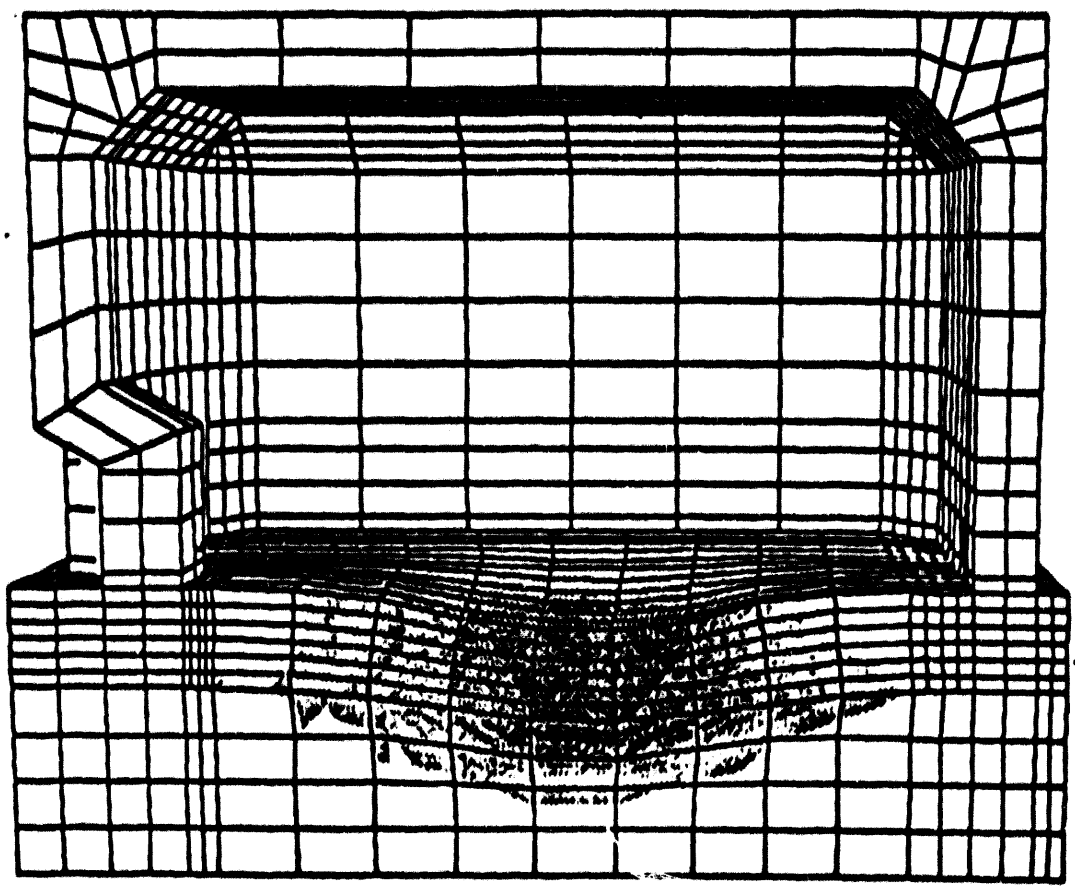

QSFC Maximum Overall Loading Displacement Fringes

Time = 0.8 milliseconds

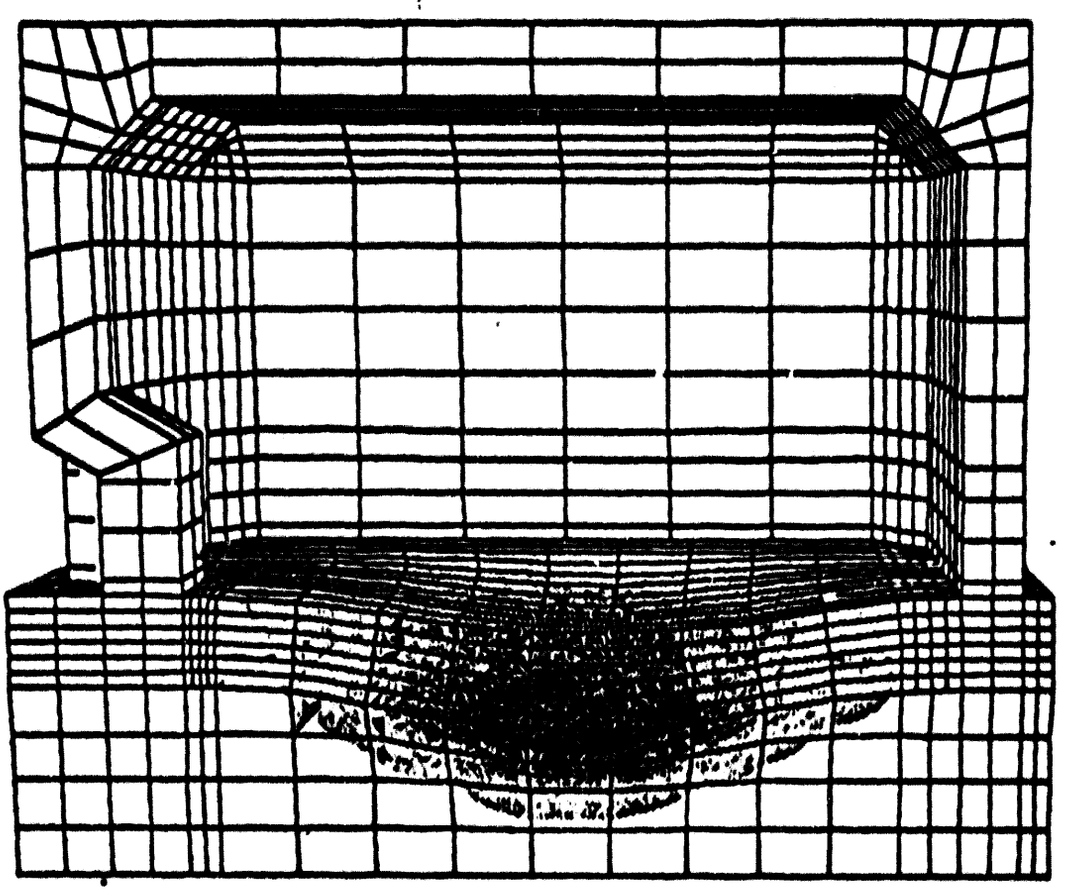

QSFC Maximum Overall Loading Displacement Fringes

Time = 1.0 milliseconds

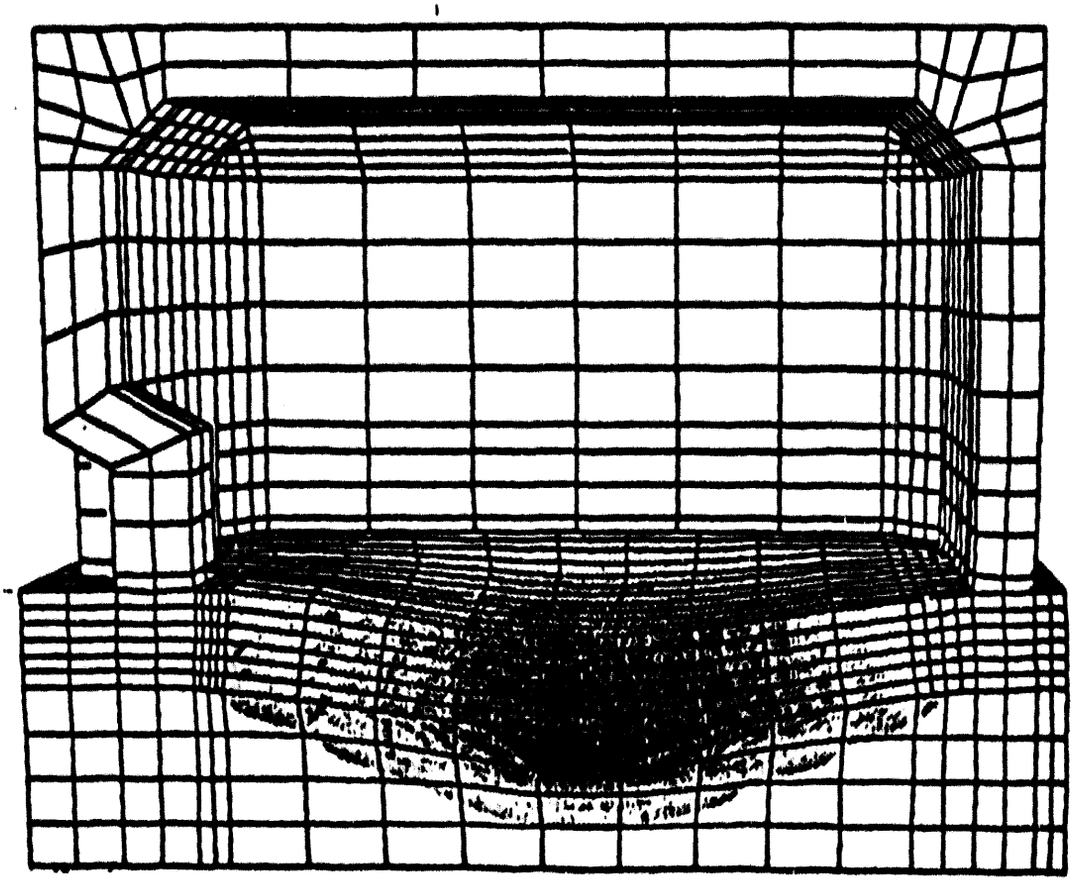

QSFC Maximum Overall Loading Displacement Fringes

Time = 1.5 milliseconds

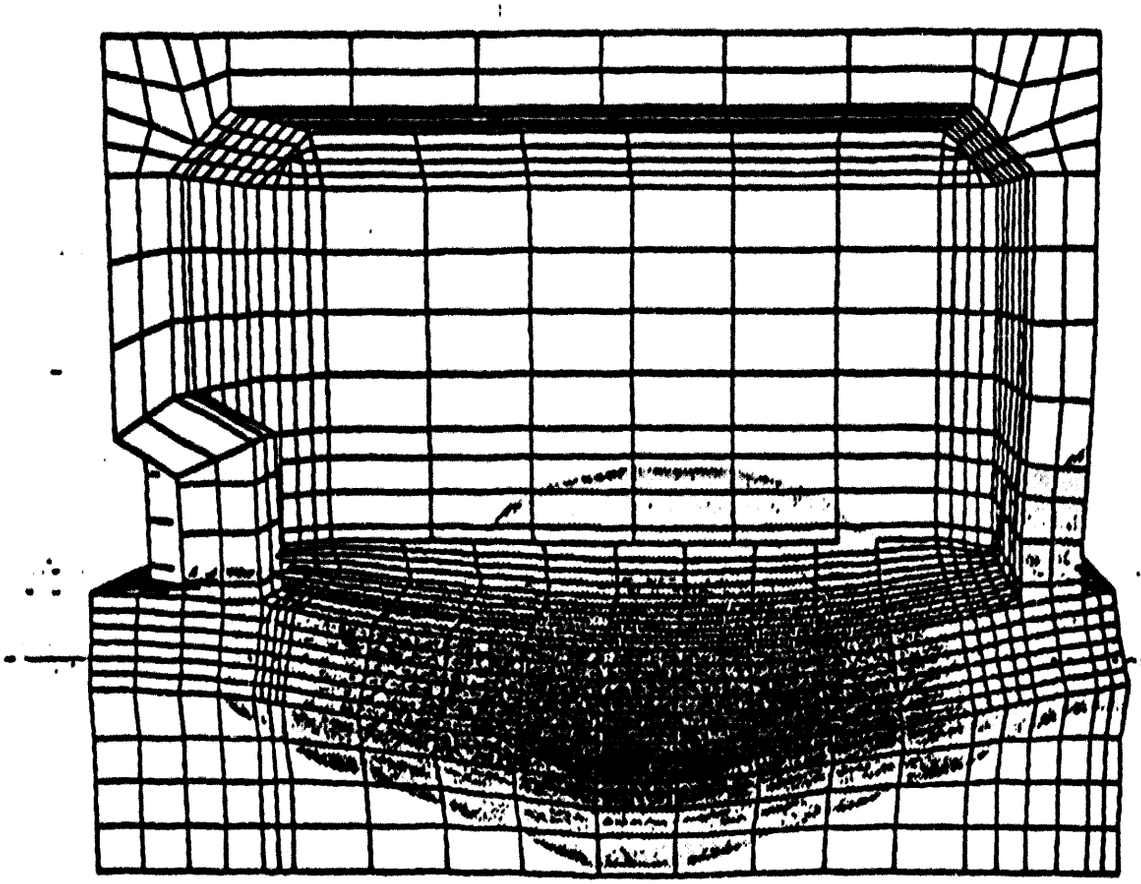

QSFC Maximum Overall Loading Displacement Fringes

Time = 2.0 milliseconds

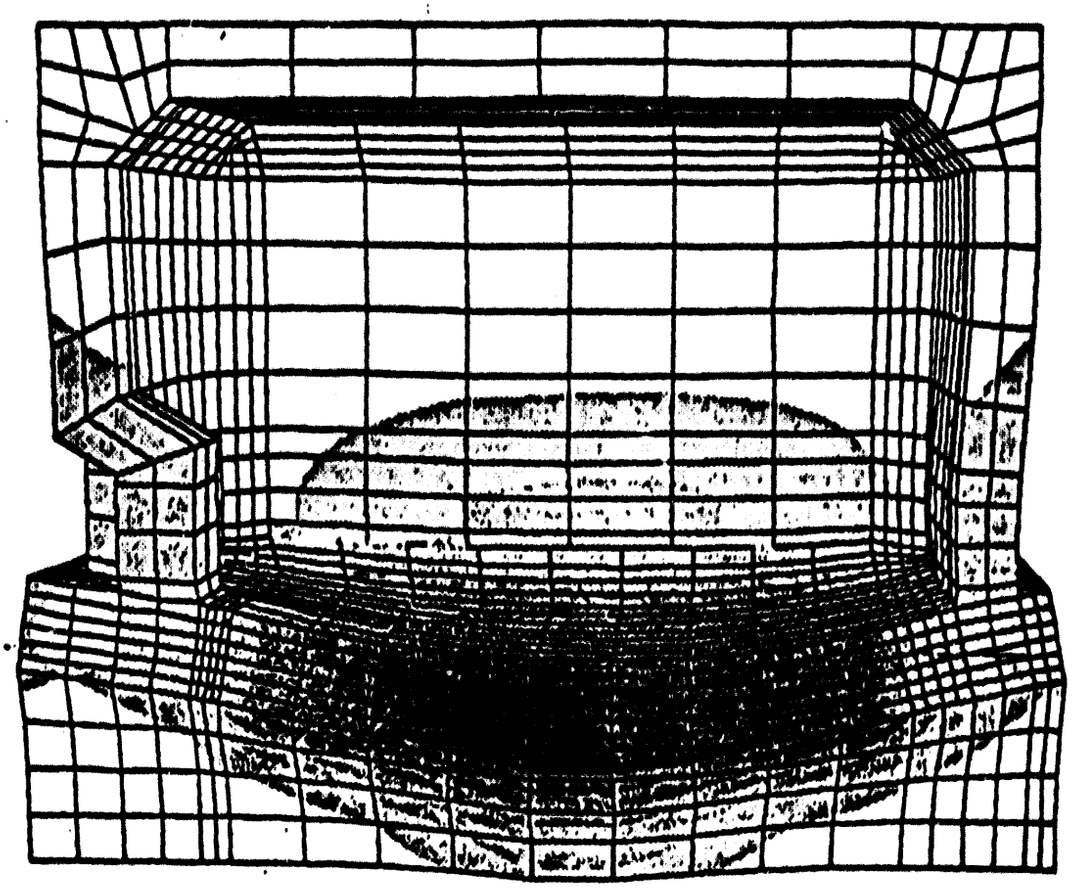

QSFC Maximum Overall Loading Displacement Fringes

Time = 2.5 milliseconds

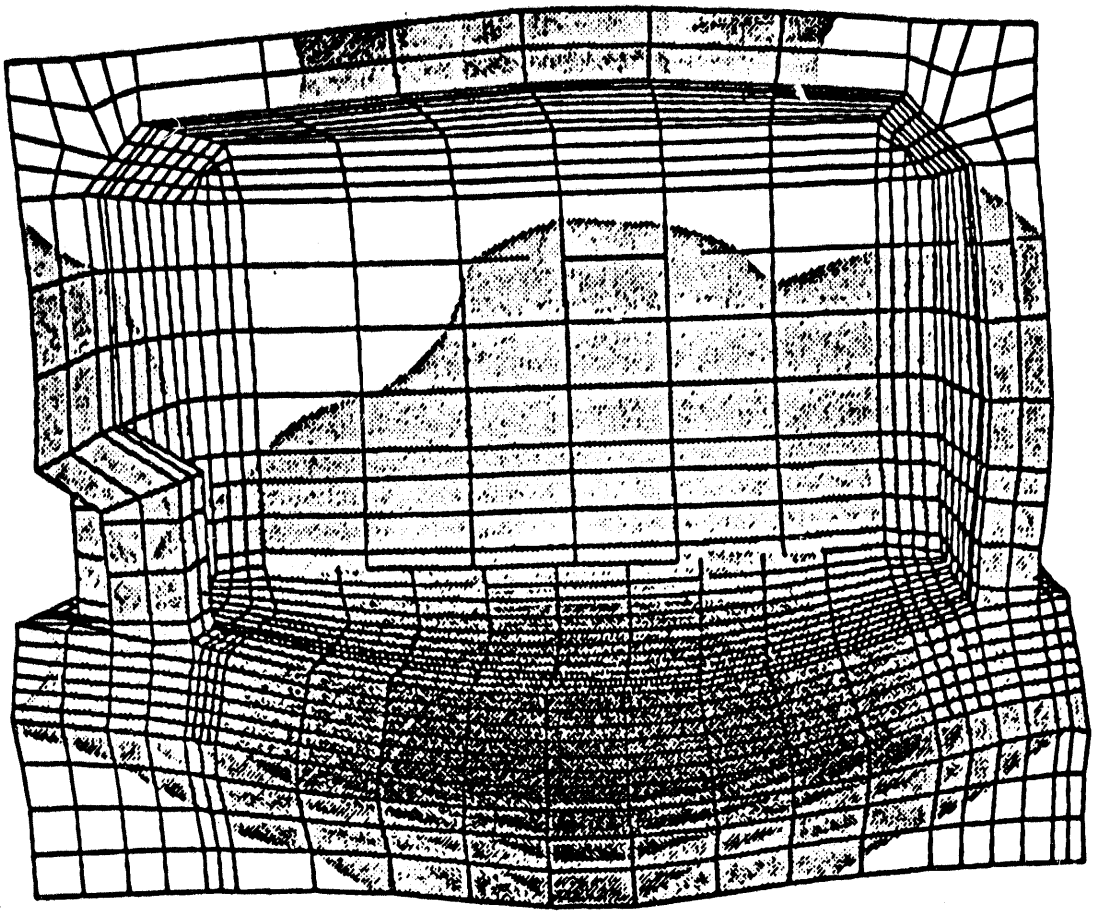

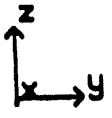

.0025

QSFC Maximum Overall Loading Displacement Fringes

Time = 3.0 milliseconds

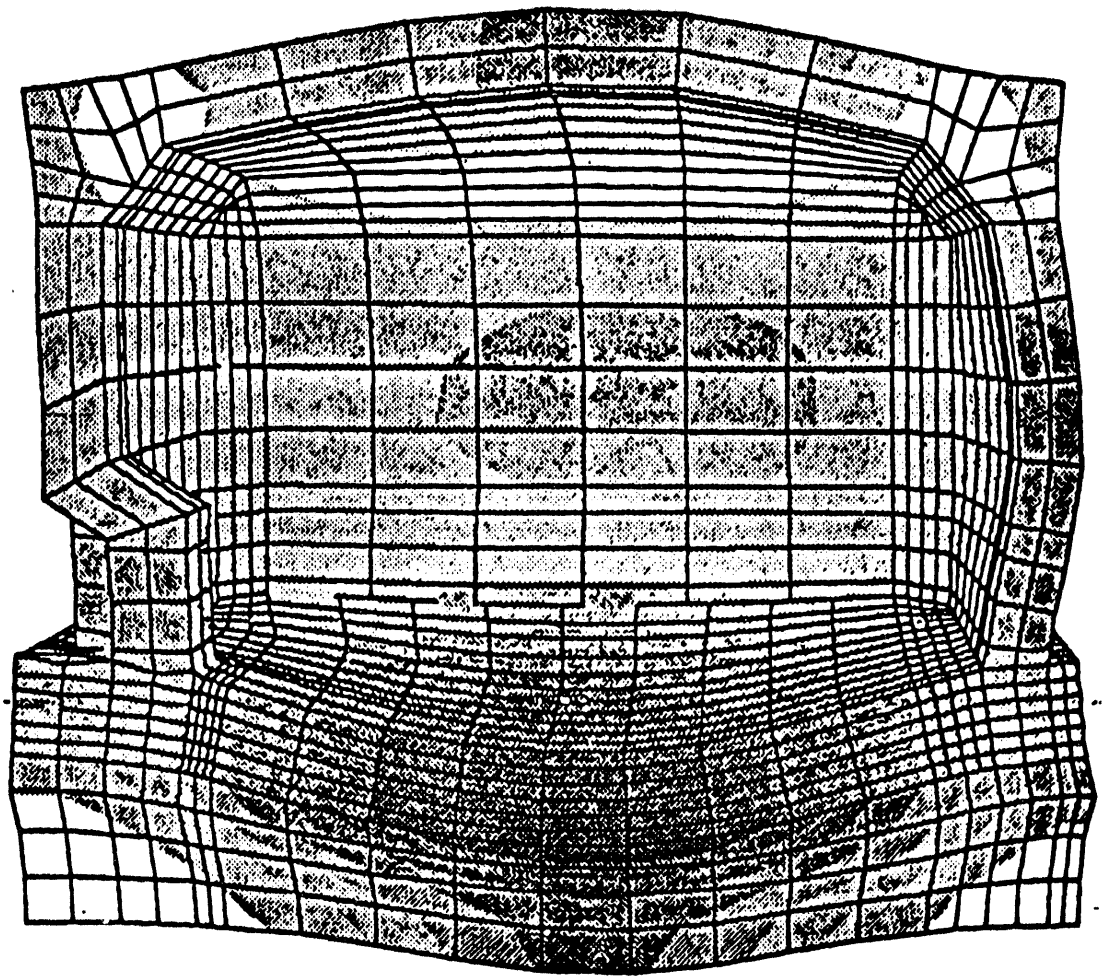

003

QSFC Maximum Overall Loading Displacement Fringes

Time = 3.5 milliseconds

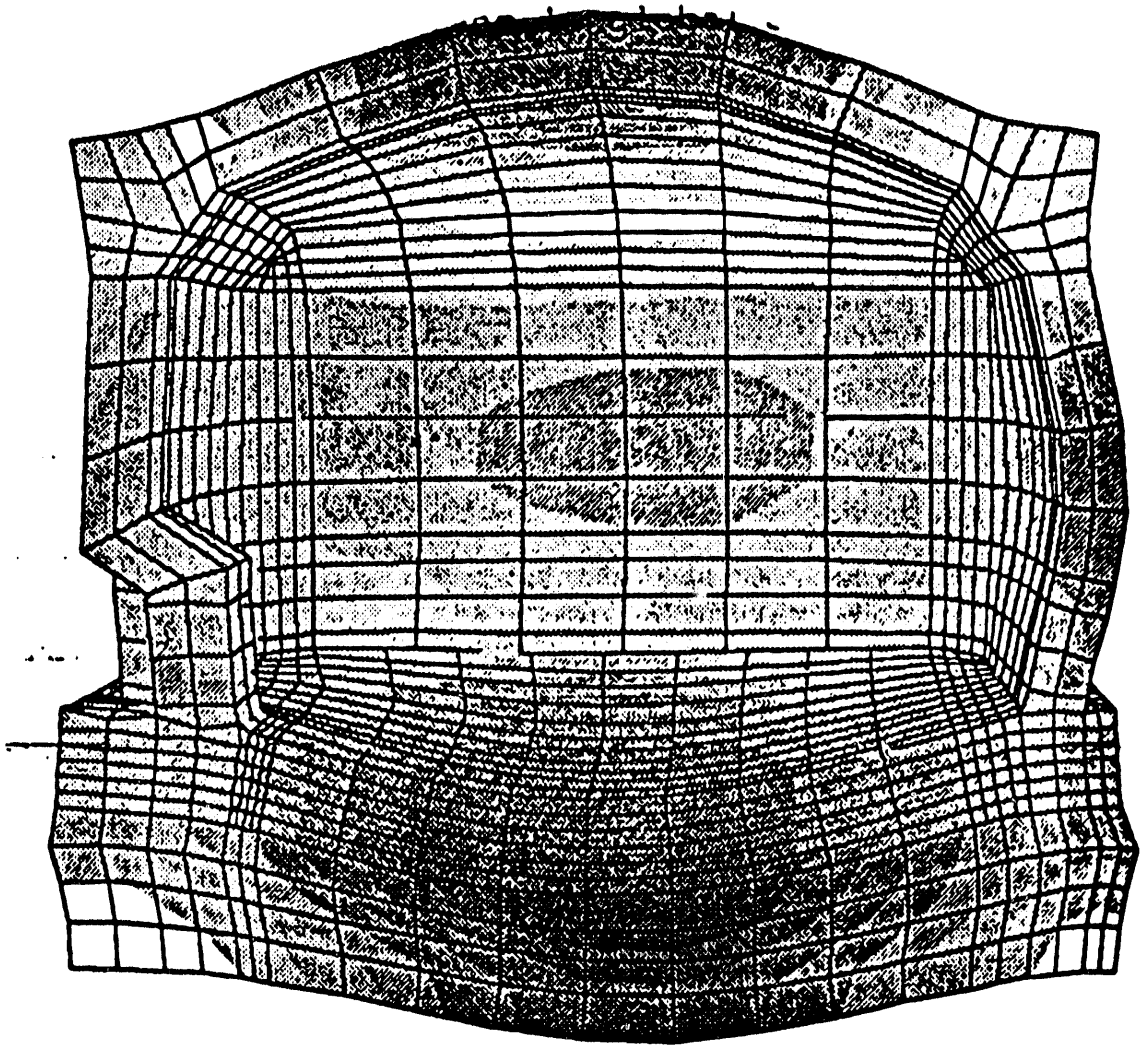

QSFC Maximum Overall Loading Displacement Fringes

Time = 4.0 milliseconds

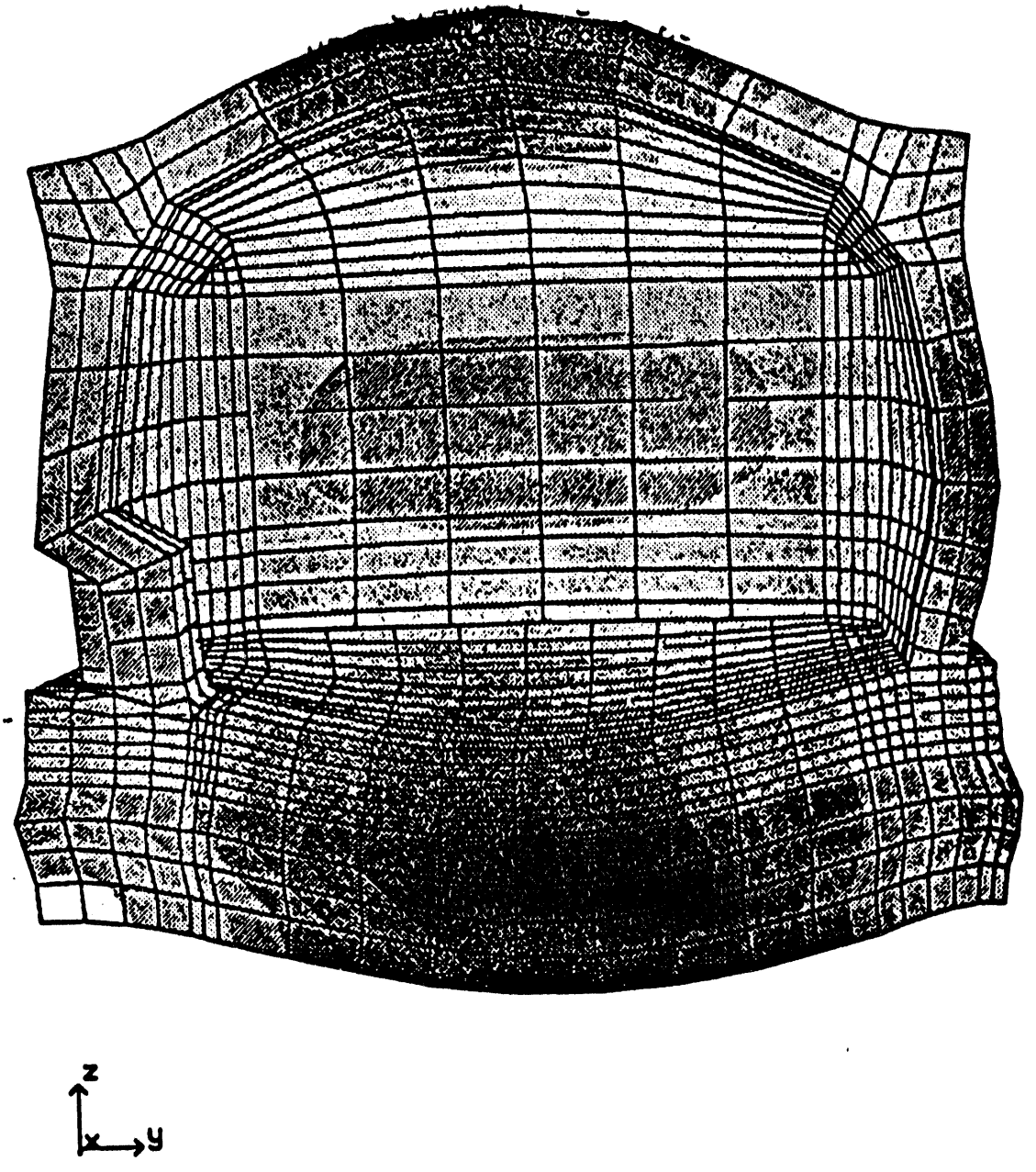

QSFC Maximum Overall Loading Displacement Fringes

Time = 4.5 milliseconds

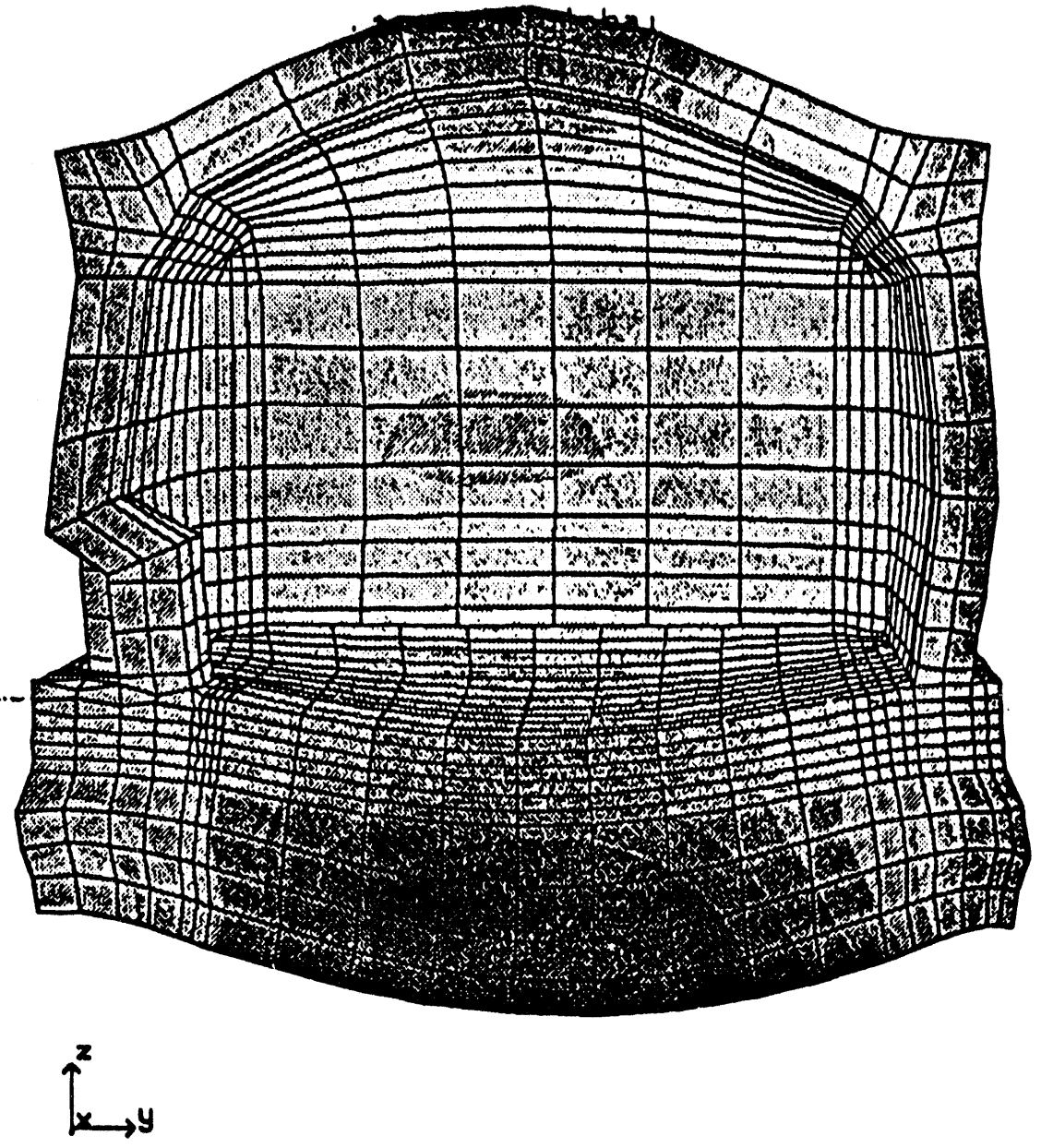

QSFC Maximum Overall Loading Displacement Fringes

Time = 5.0 milliseconds

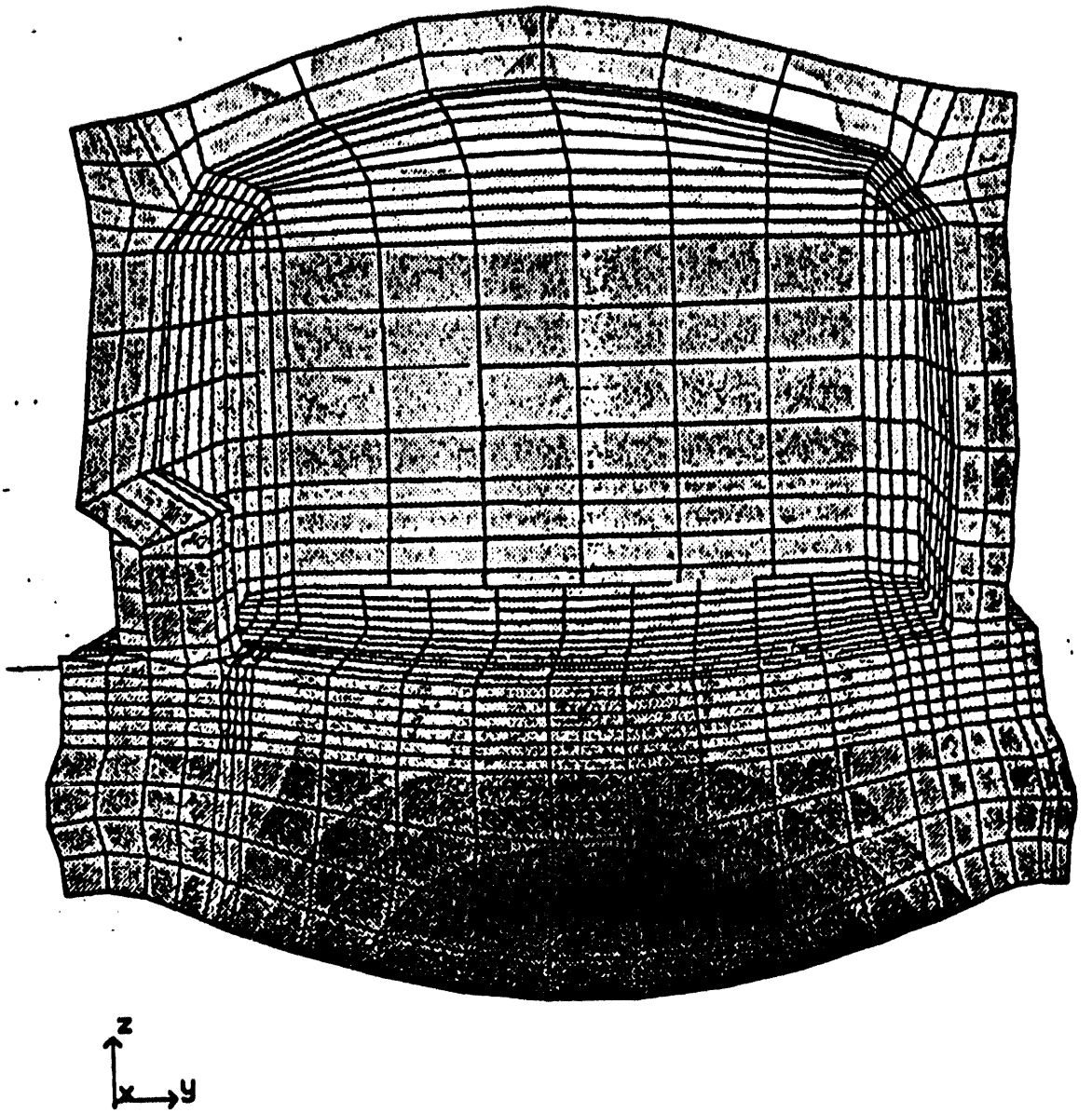

QSFC Maximum Overall Loading Displacement Fringes

Time = 6.0 milliseconds

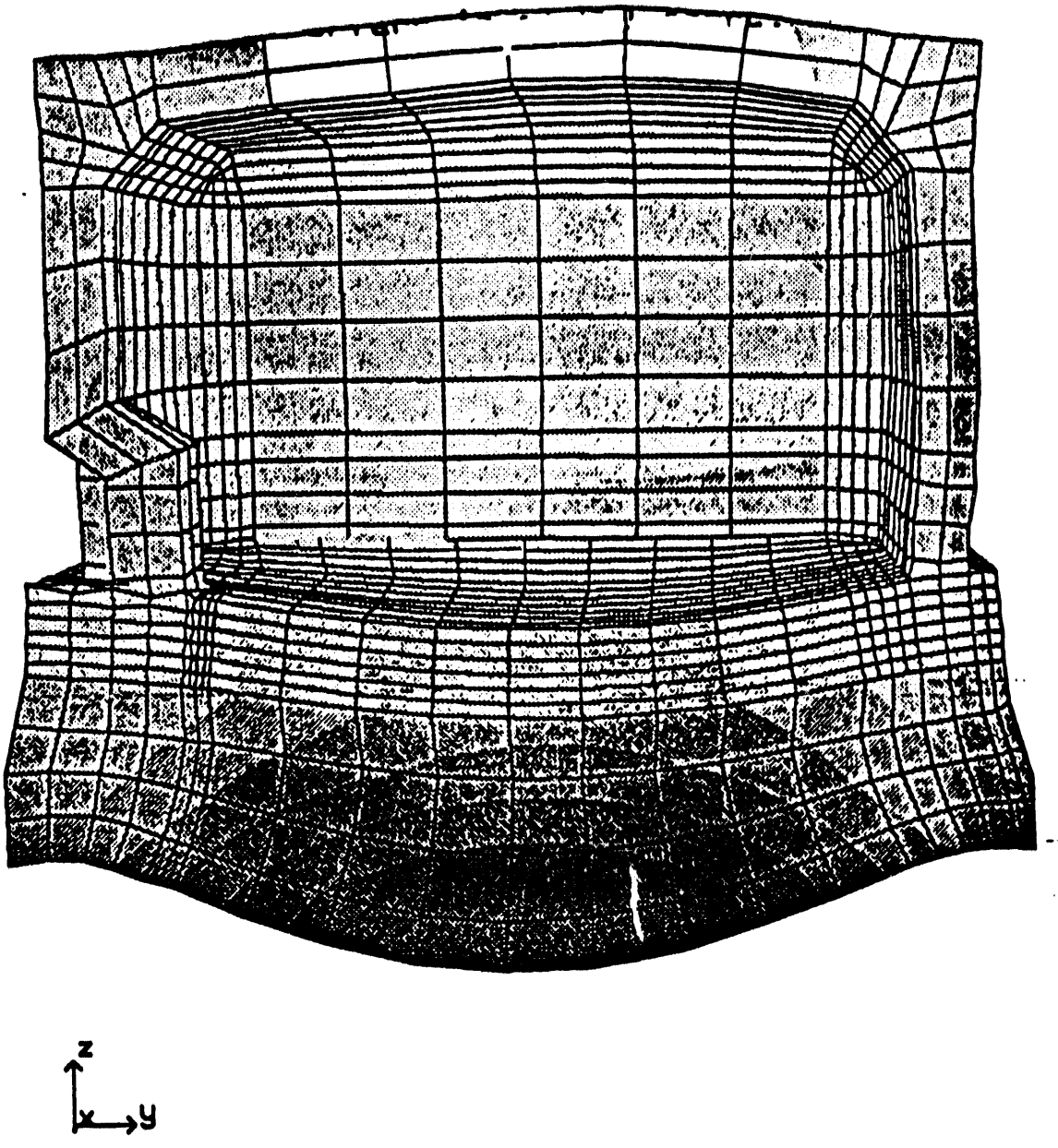

QSFC Maximum Overall Loading Displacement Fringes

Time = 7.0 milliseconds

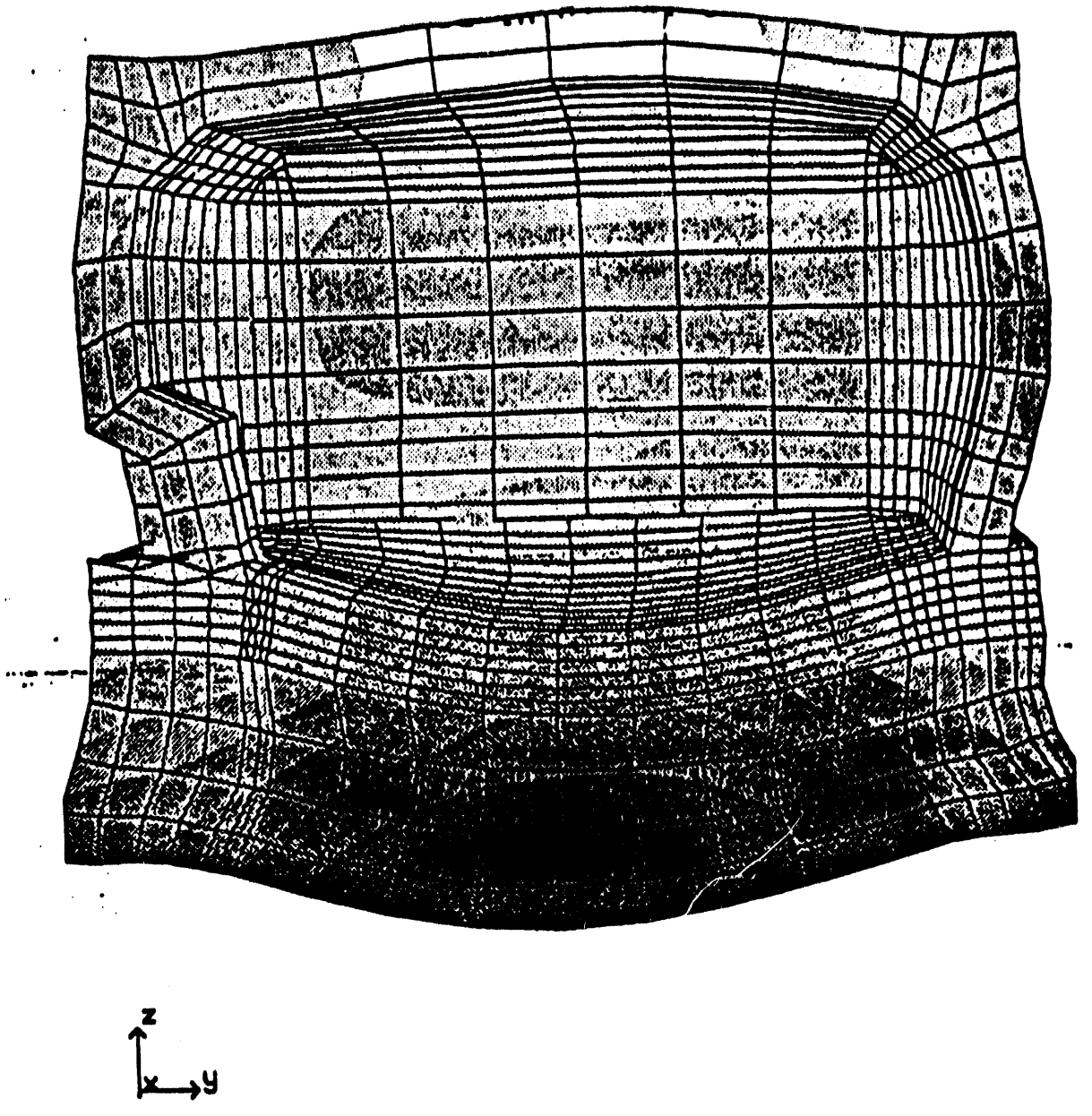

QSFC Maximum Overall Loading Displacement Fringes

Time = 8.0 milliseconds

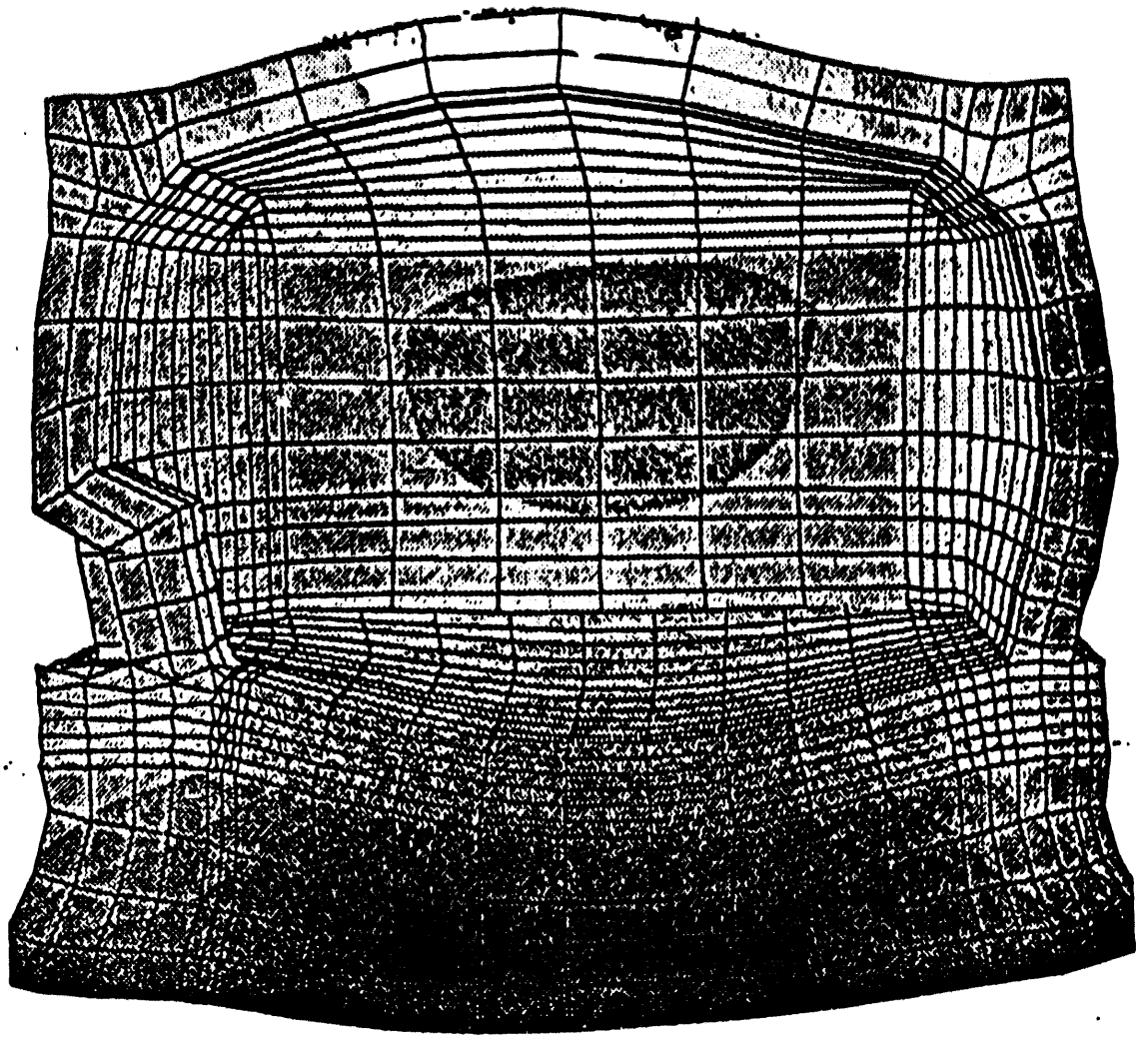

QSFC Maximum Overall Loading Displacement Fringes

Time = 9.0 milliseconds

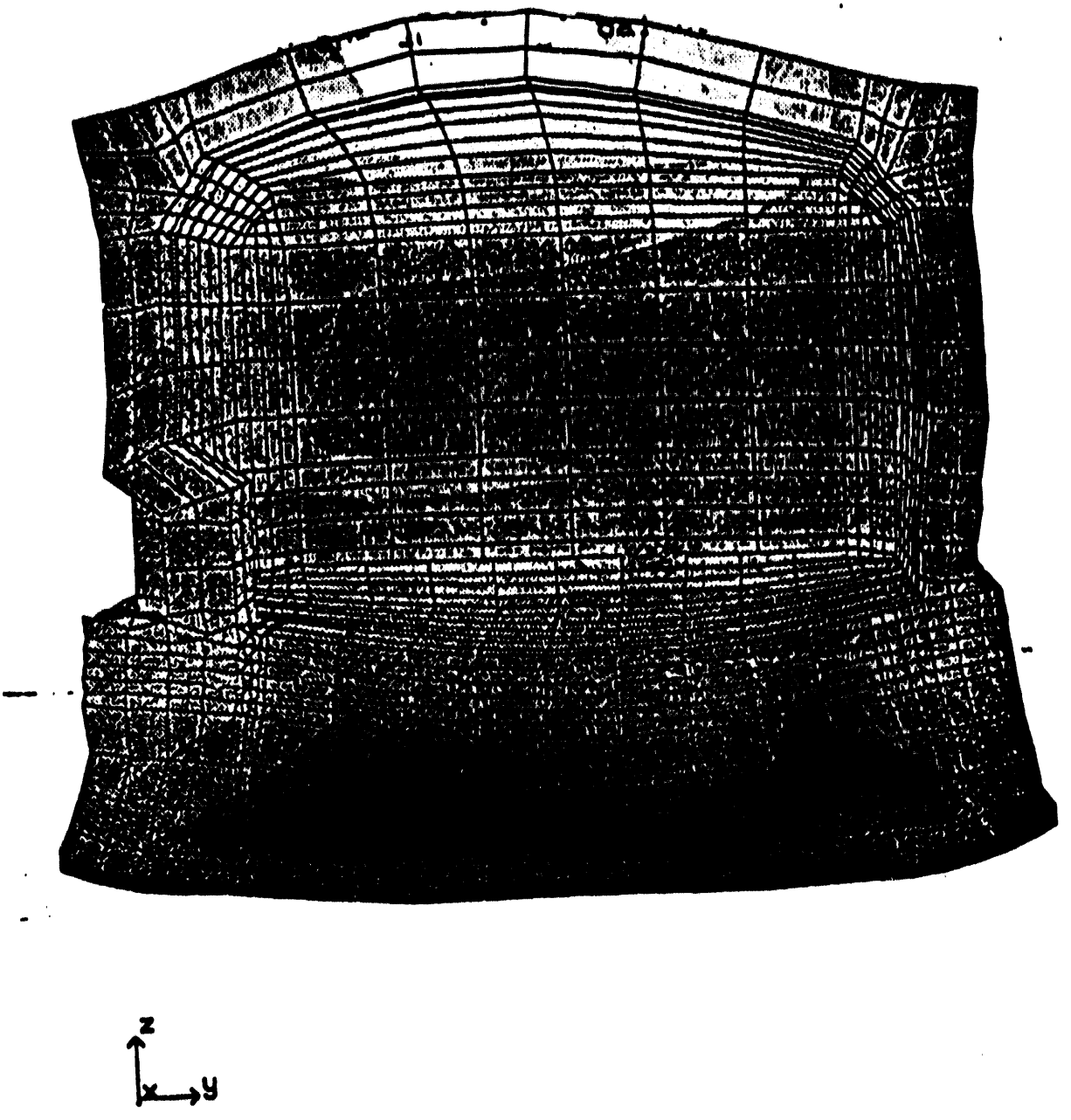

QSFC Maximum Overall Loading Displacement Fringes

Time = 10.0 milliseconds

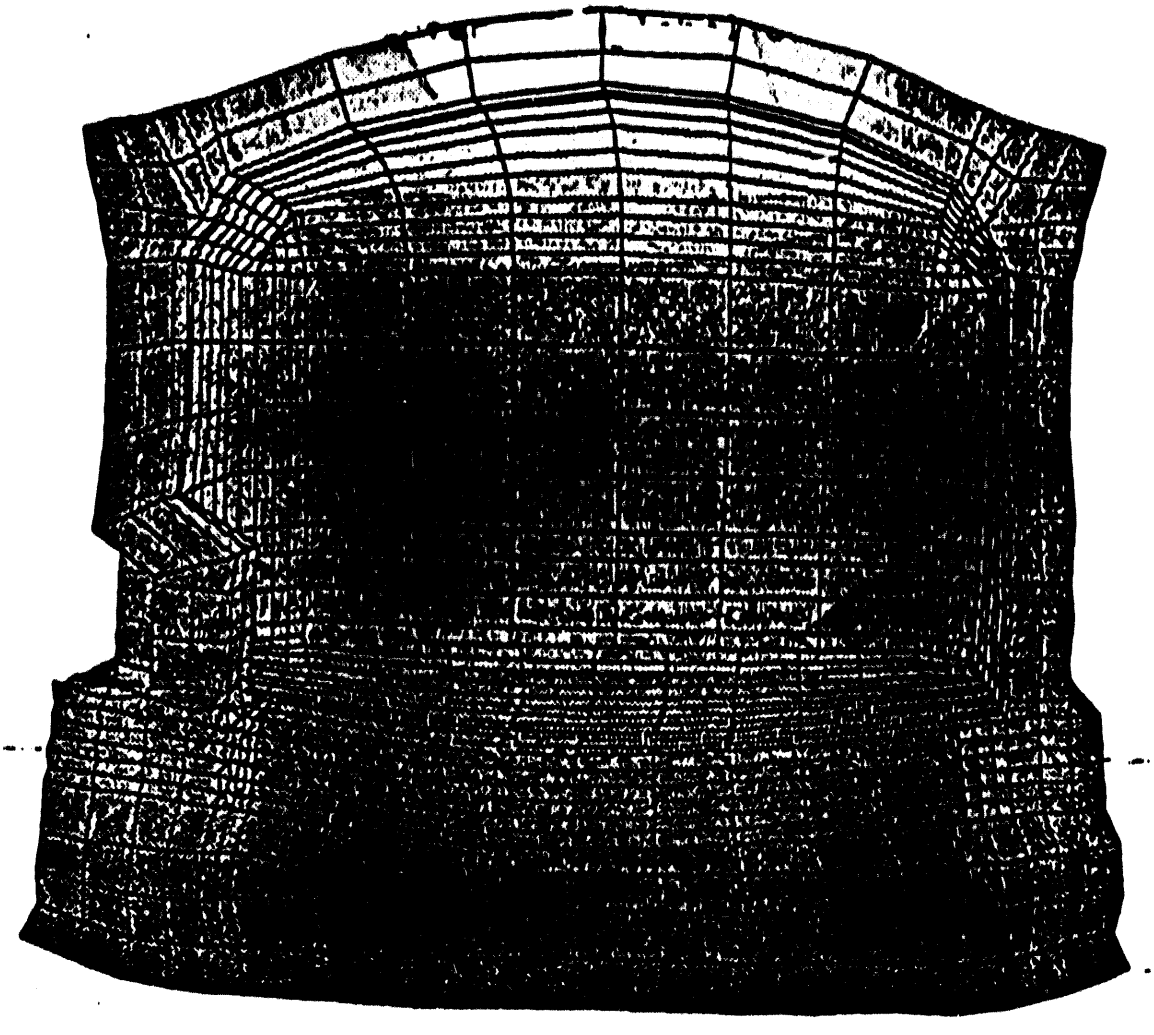

APPENDIX D

Quarter Scale Firing Chamber
Maximum West Wall Loading

QSFC Maximum West Wall Loading
Displacement Fringes

Time = 0.2 milliseconds

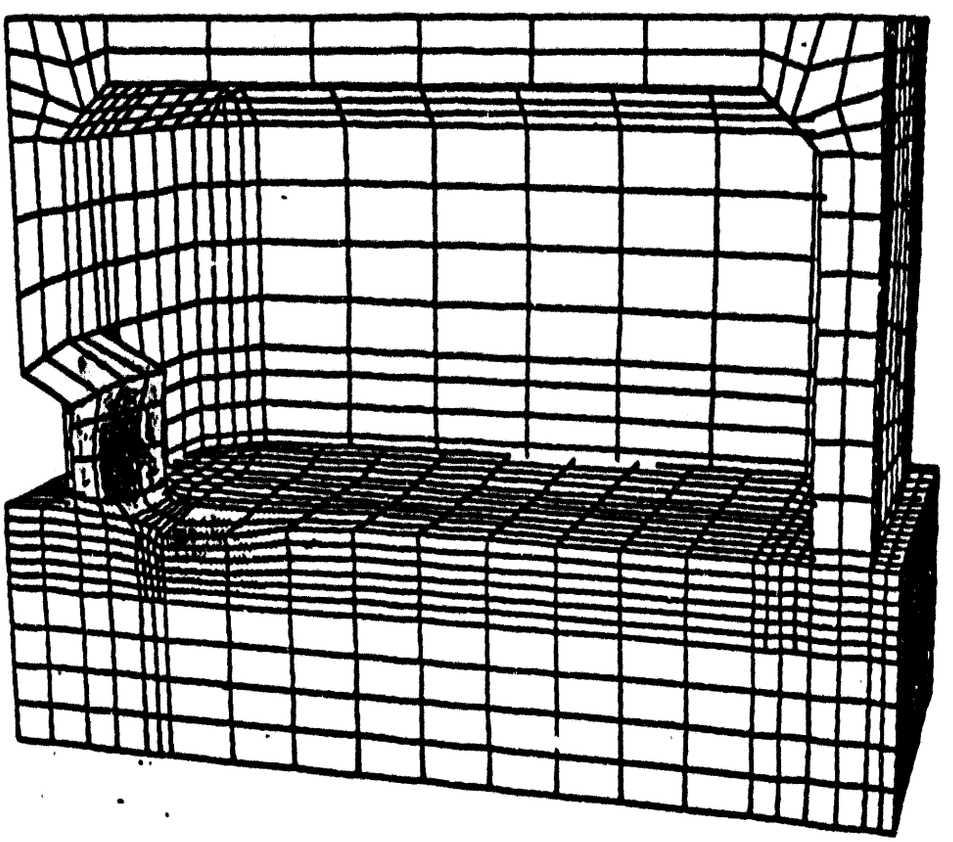

QSFC Maximum West Wall Loading
Displacement Fringes

Time = 0.4 milliseconds

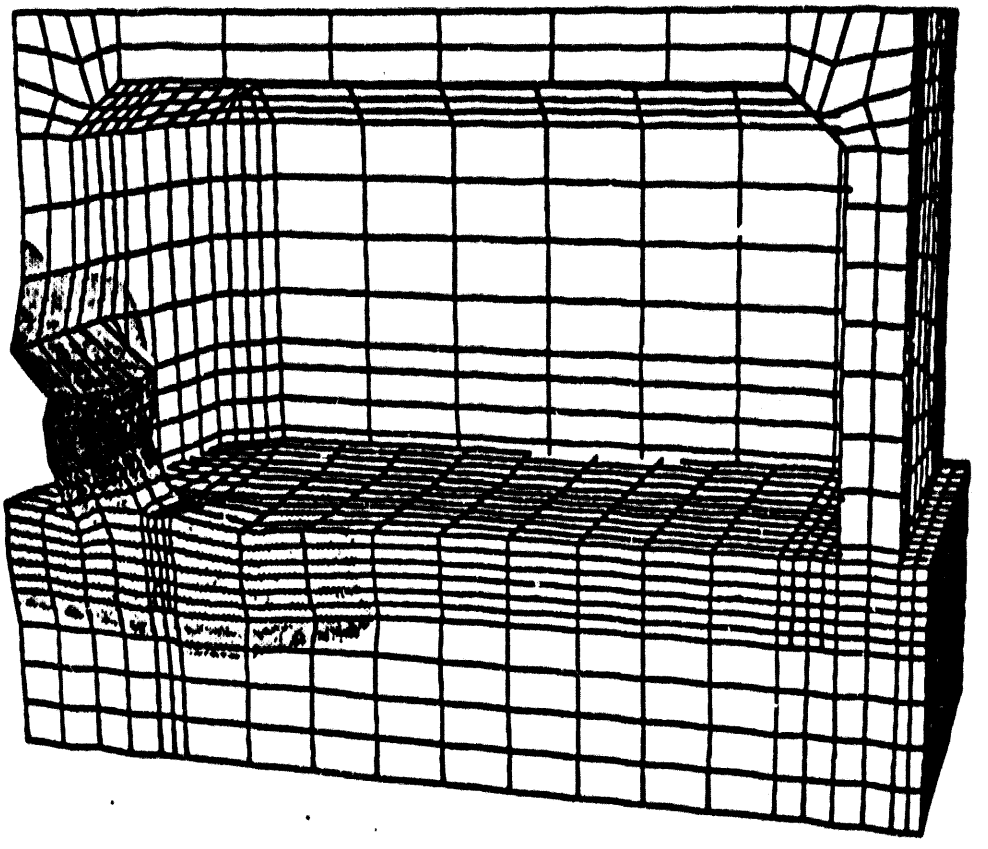

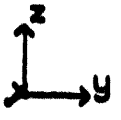

QSFC Maximum West Wall Loading
Displacement Fringes

Time = 0.6 milliseconds

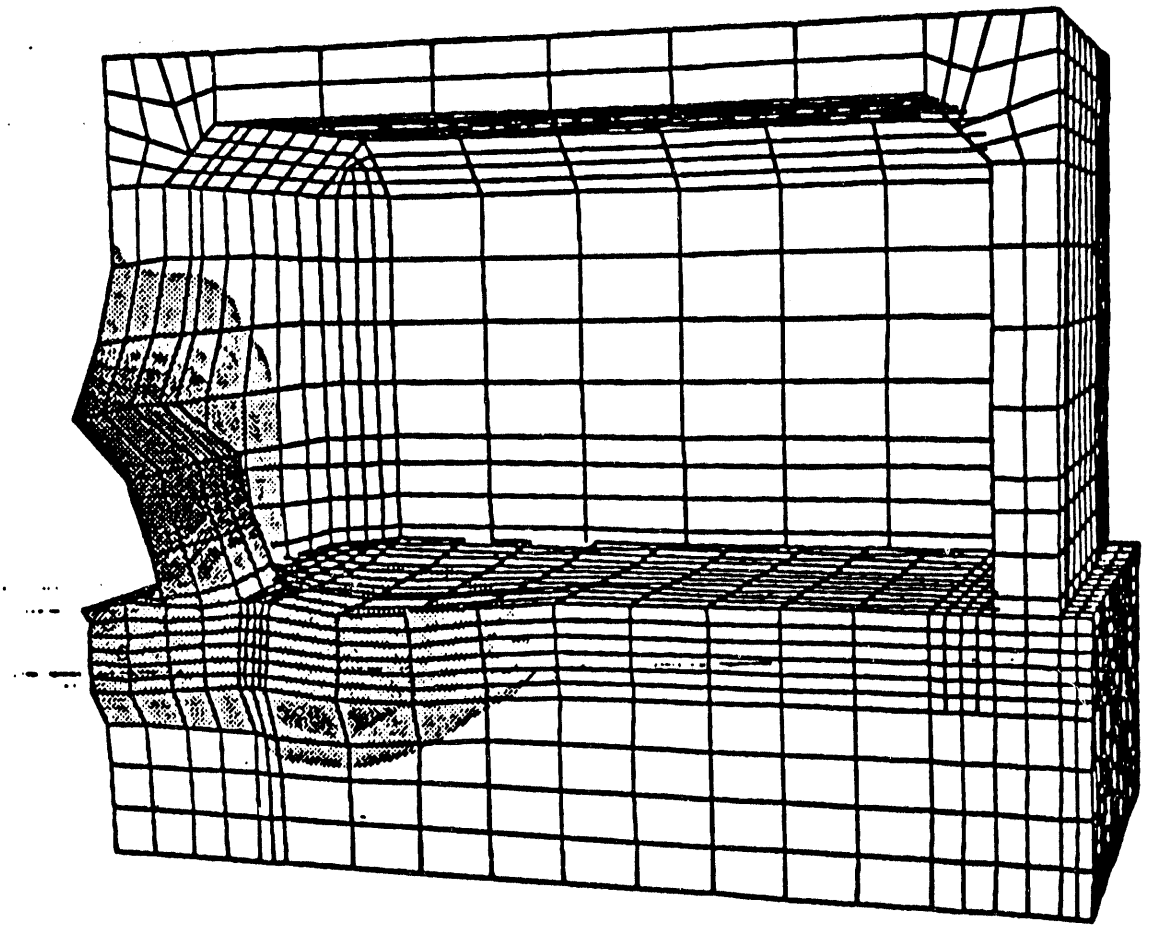

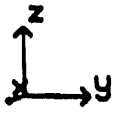

QSFC Maximum West Wall Loading
Displacement Fringes

Time = 0.8 milliseconds

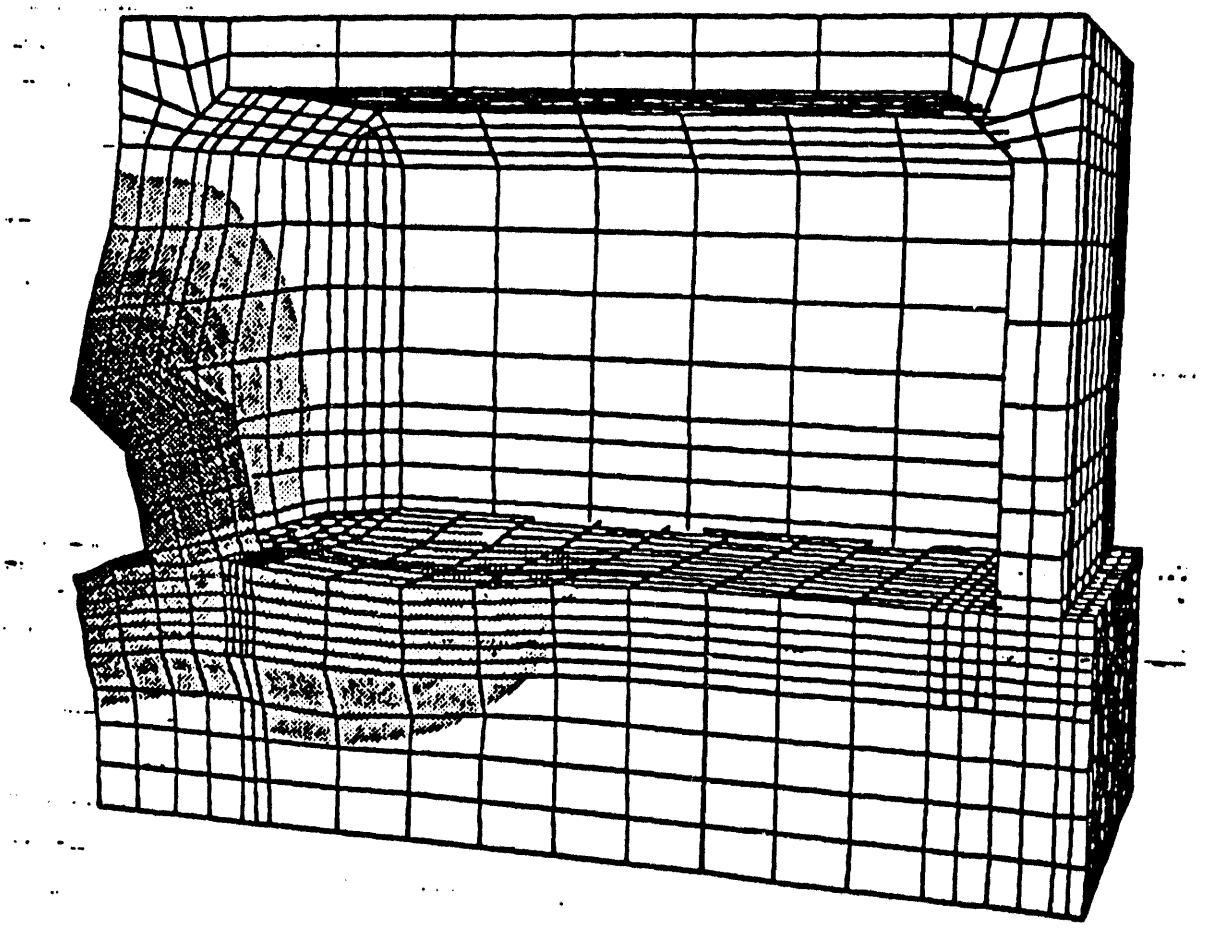

QSFC Maximum West Wall Loading
Displacement Fringes

Time = 1.0 milliseconds

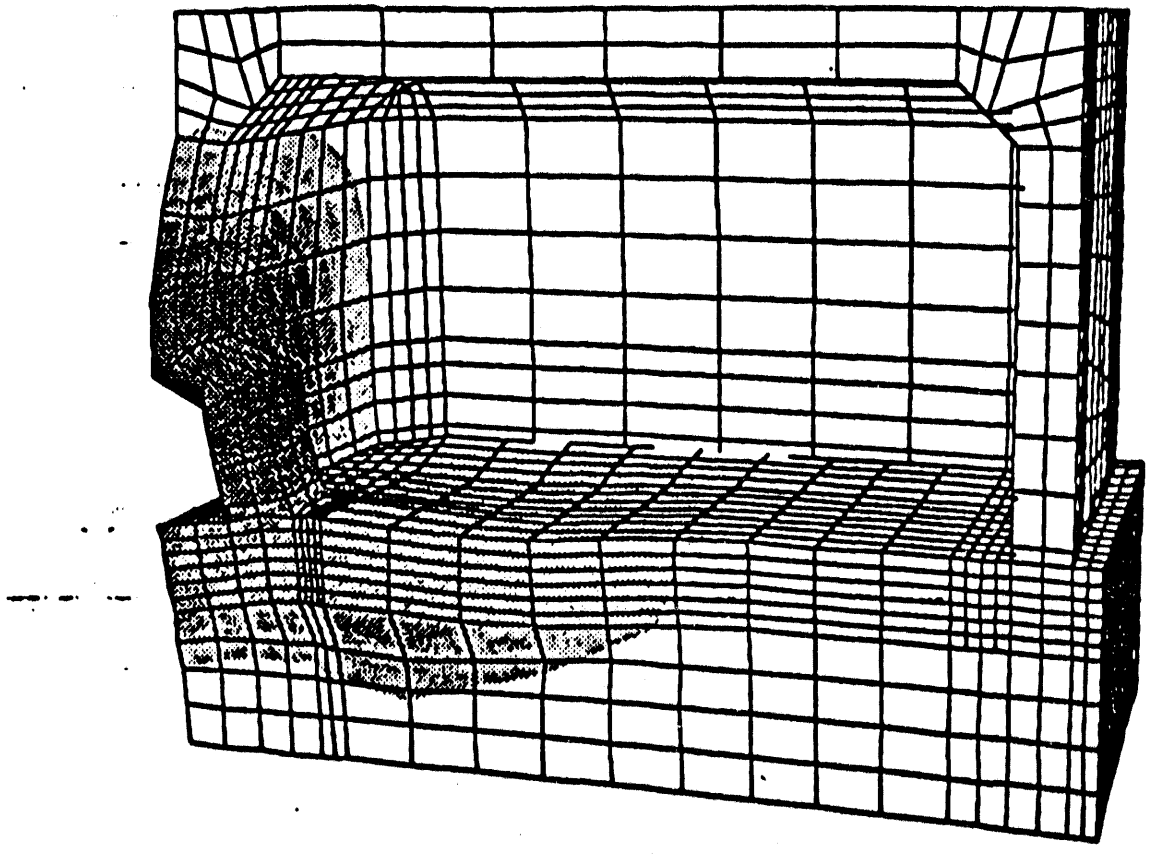

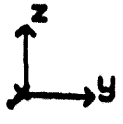

QSFC Maximum West Wall Loading
Displacement Fringes

Time = 1.5 milliseconds

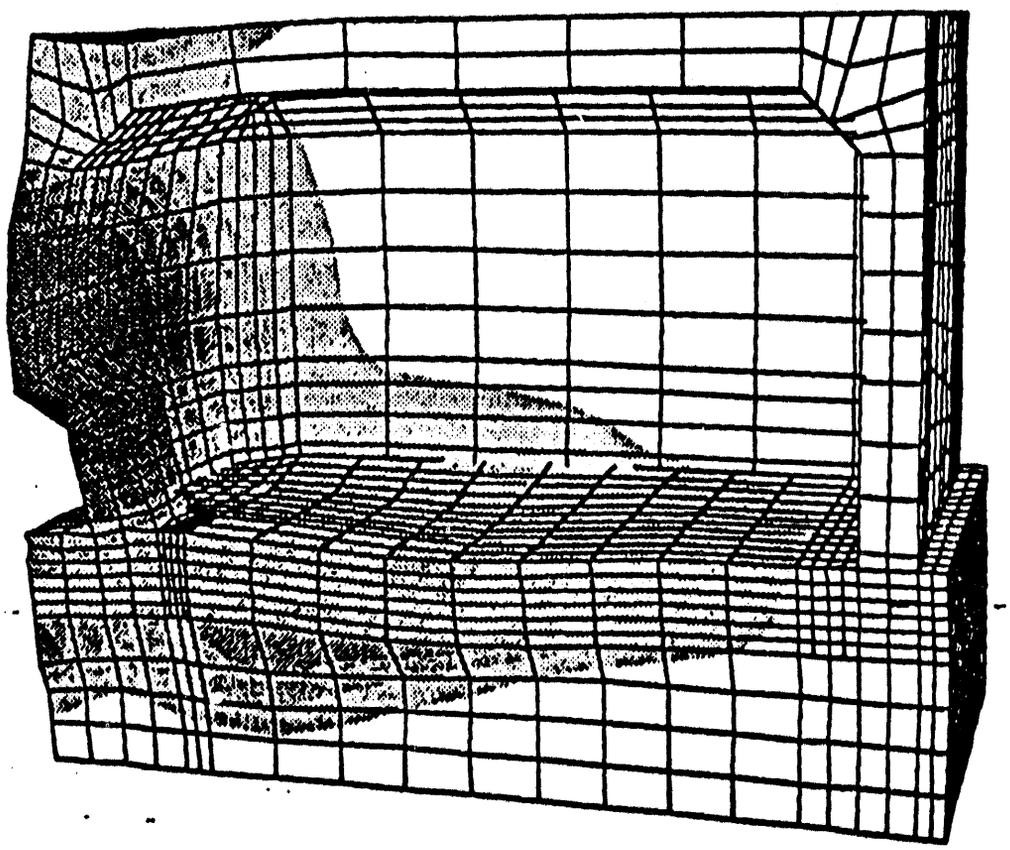

QSFC Maximum West Wall Loading
Displacement Fringes

Time = 2.0 milliseconds

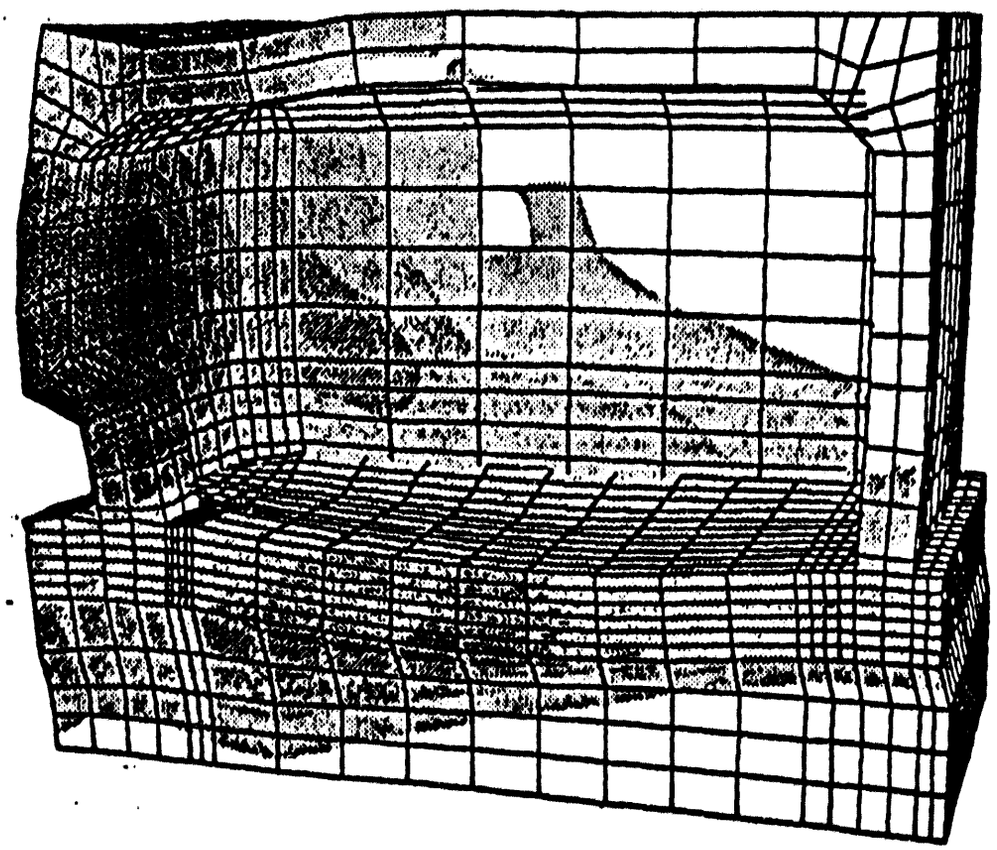

QSFC Maximum West Wall Loading
Displacement Fringes

Time = 2.5 milliseconds

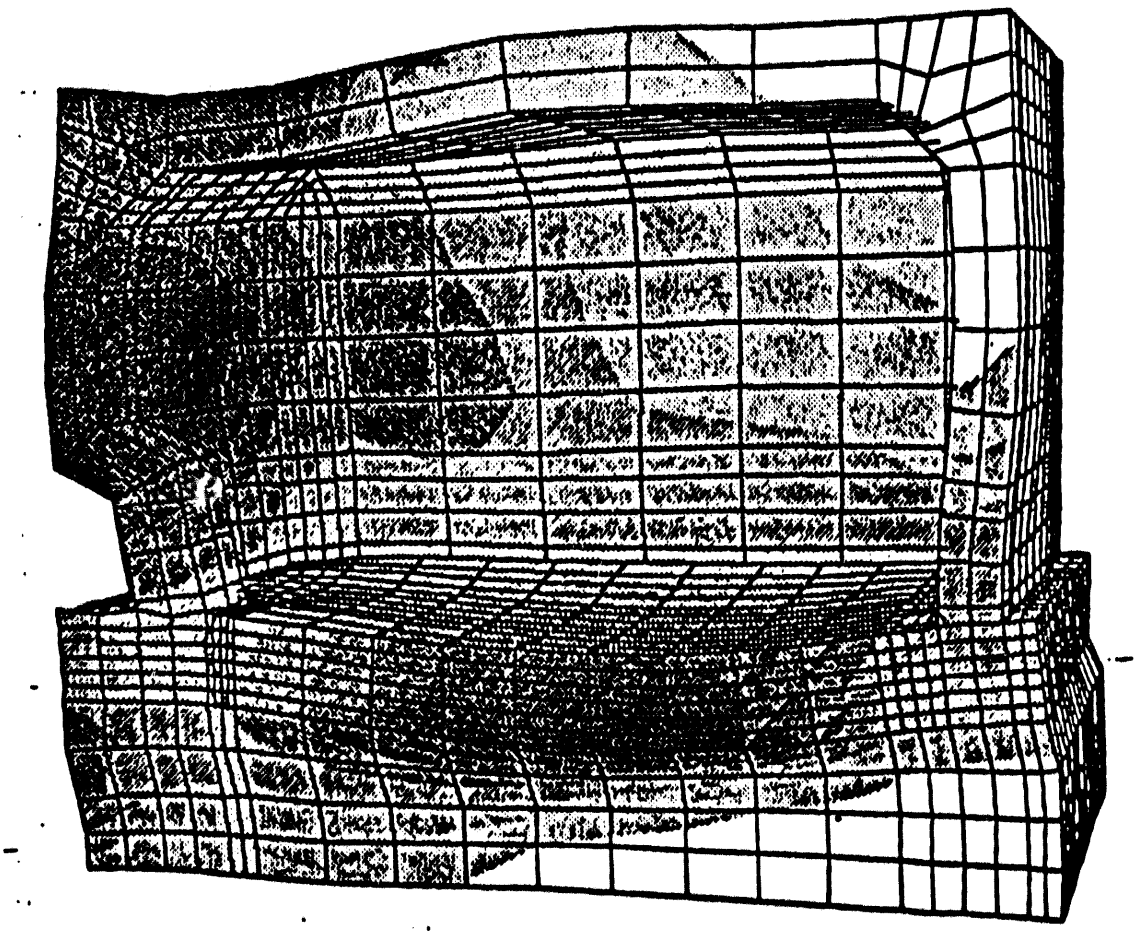

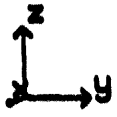

5.2

QSFC Maximum West Wall Loading
Displacement Fringes

Time = 3.0 milliseconds

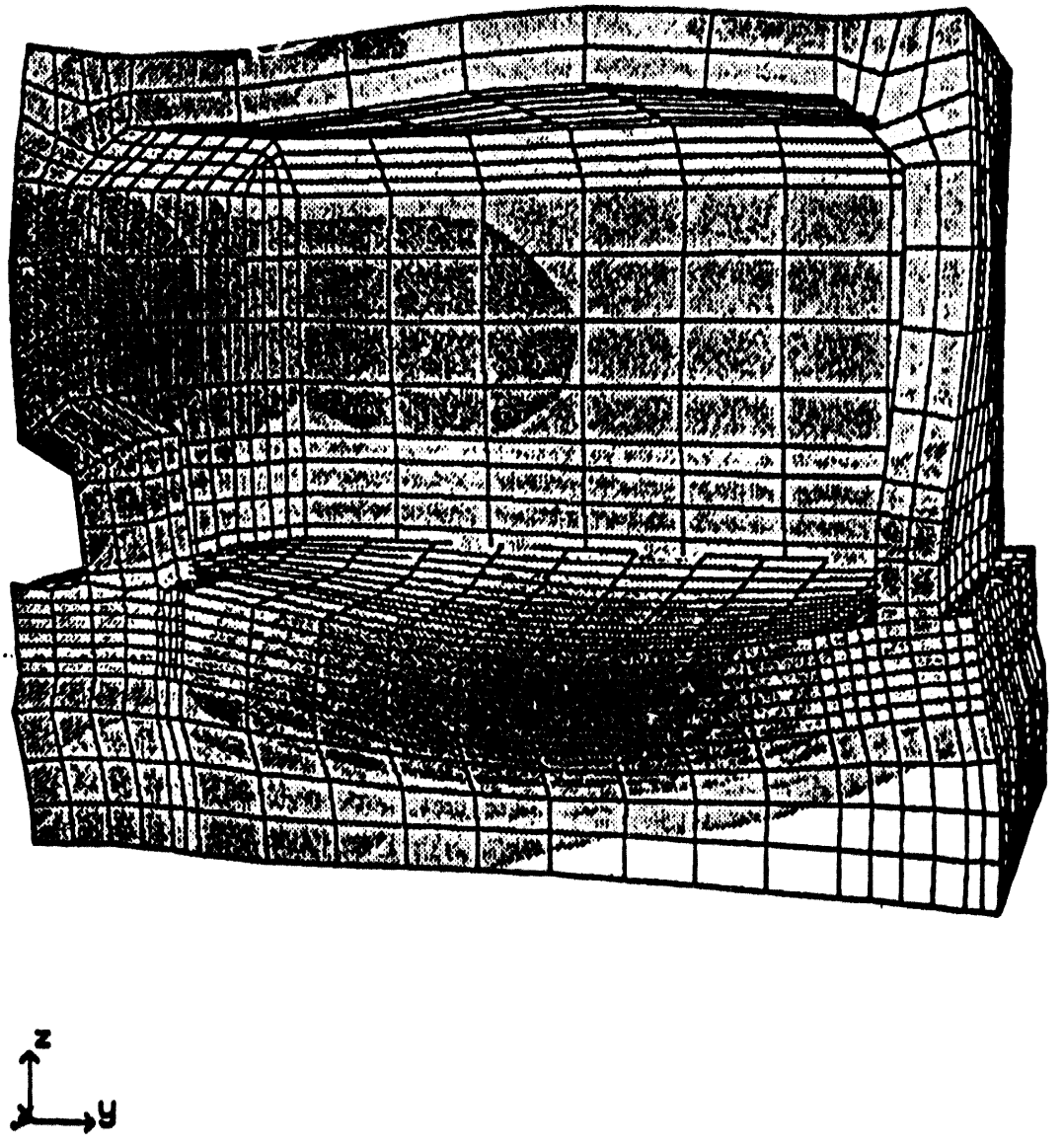

QSFC Maximum West Wall Loading
Displacement Fringes

Time = 3.5 milliseconds

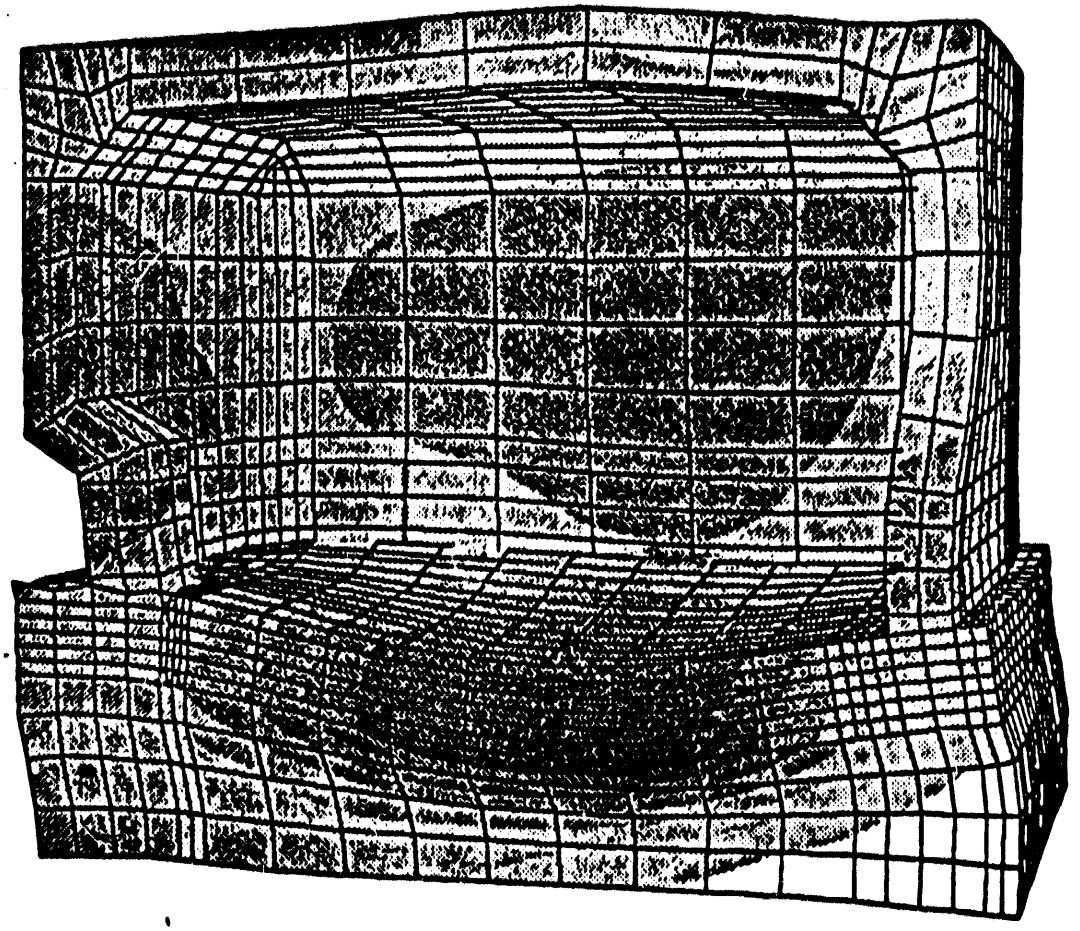

QSFC Maximum West Wall Loading
Displacement Fringes

Time = 4.0 milliseconds

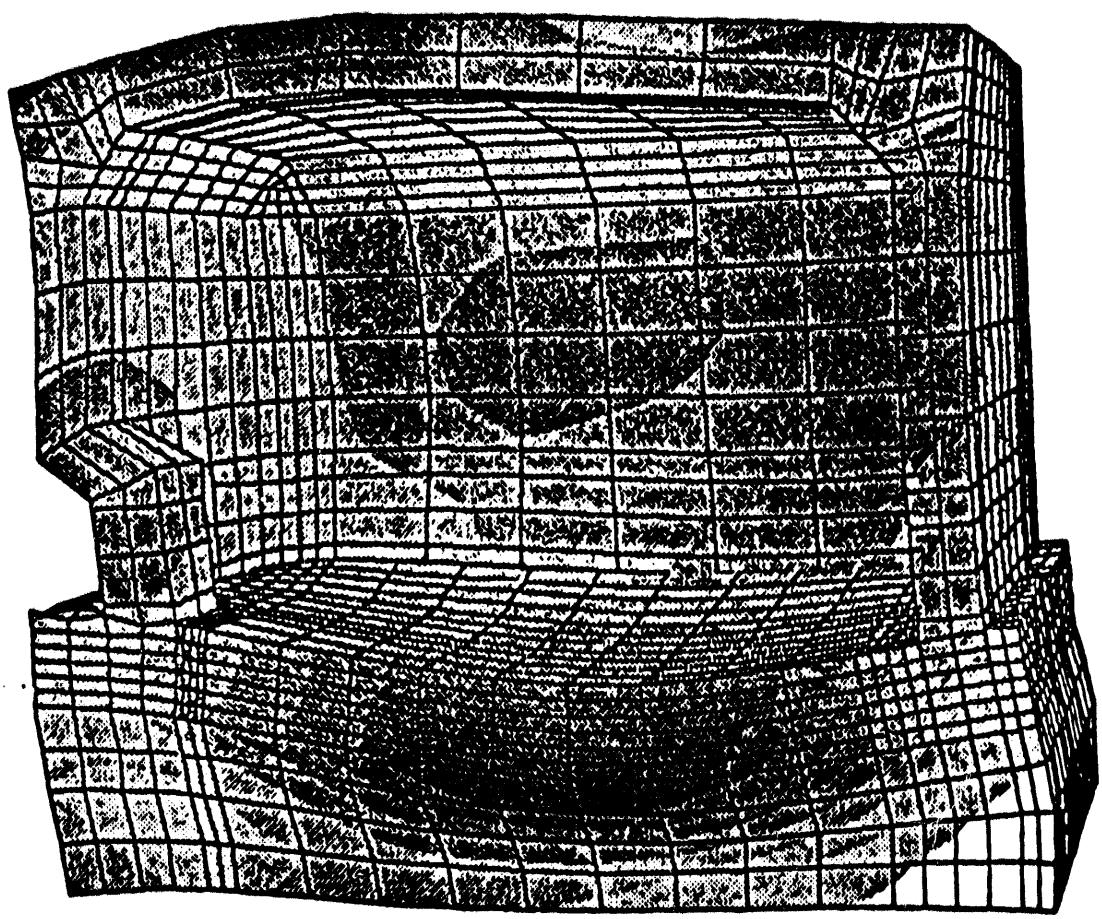

QSFC Maximum West Wall Loading
Displacement Fringes

Time = 4.5 milliseconds

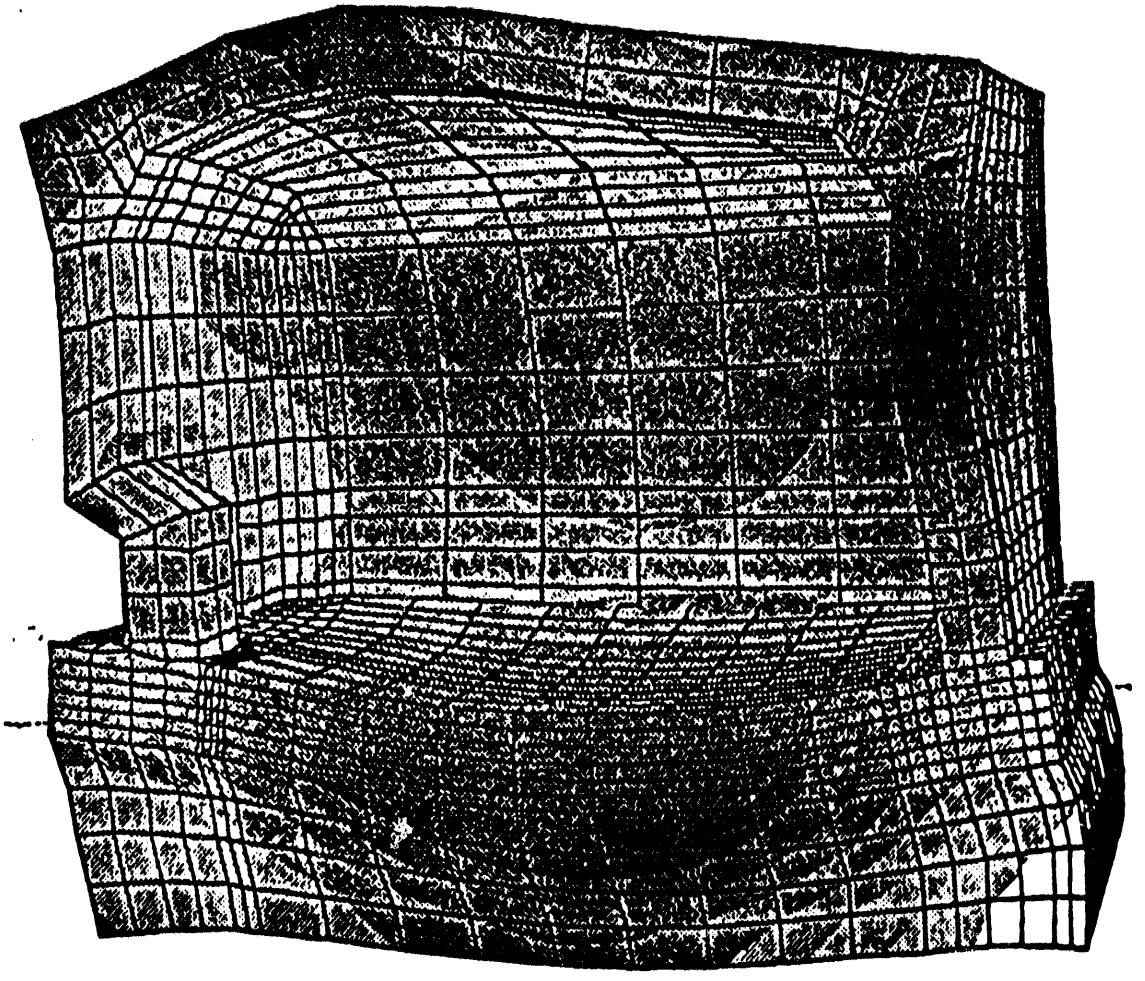

QSFC Maximum West Wall Loading
Displacement Fringes

Time = 5.0 milliseconds

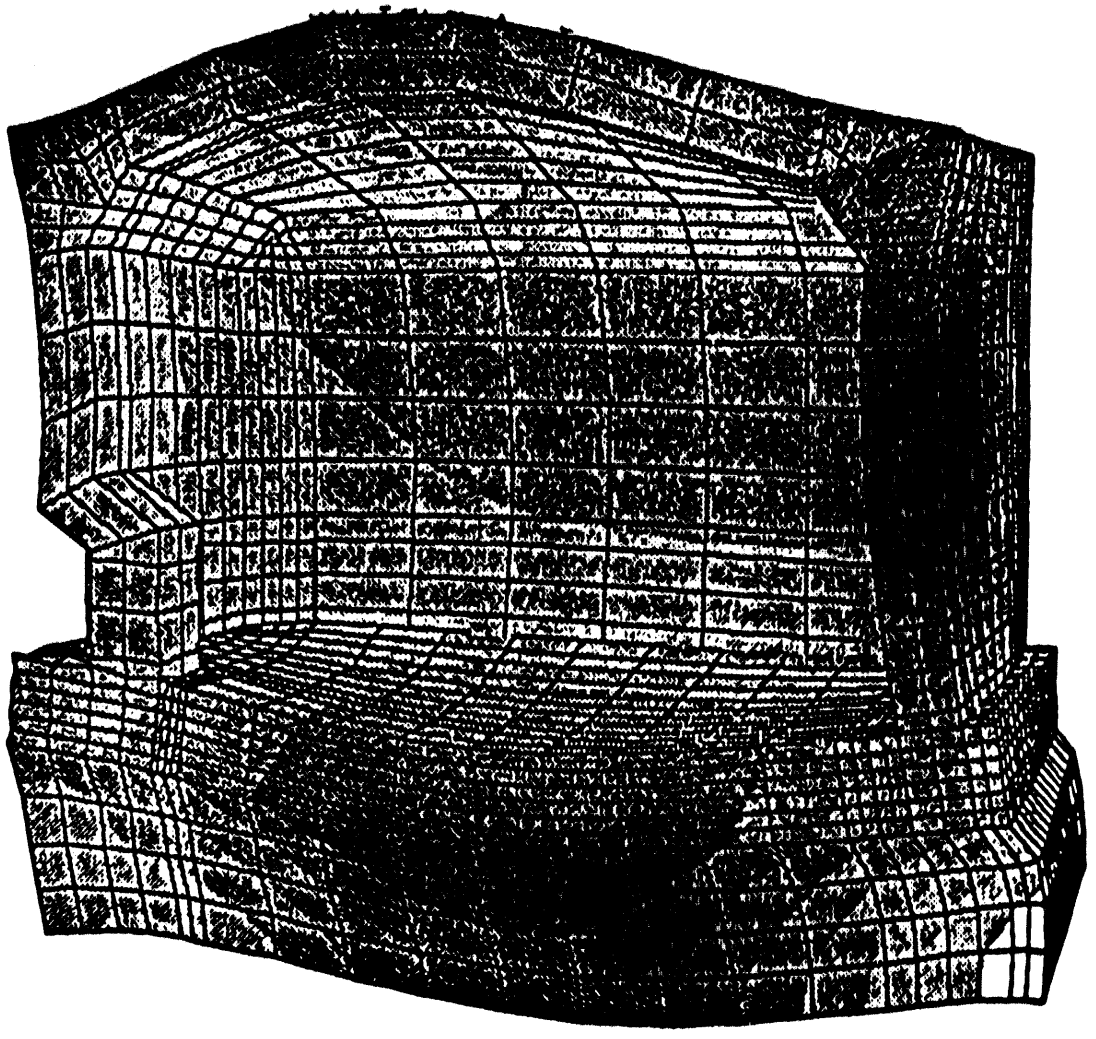

QSFC Maximum West Wall Loading
Displacement Fringes

Time = 6.0 milliseconds

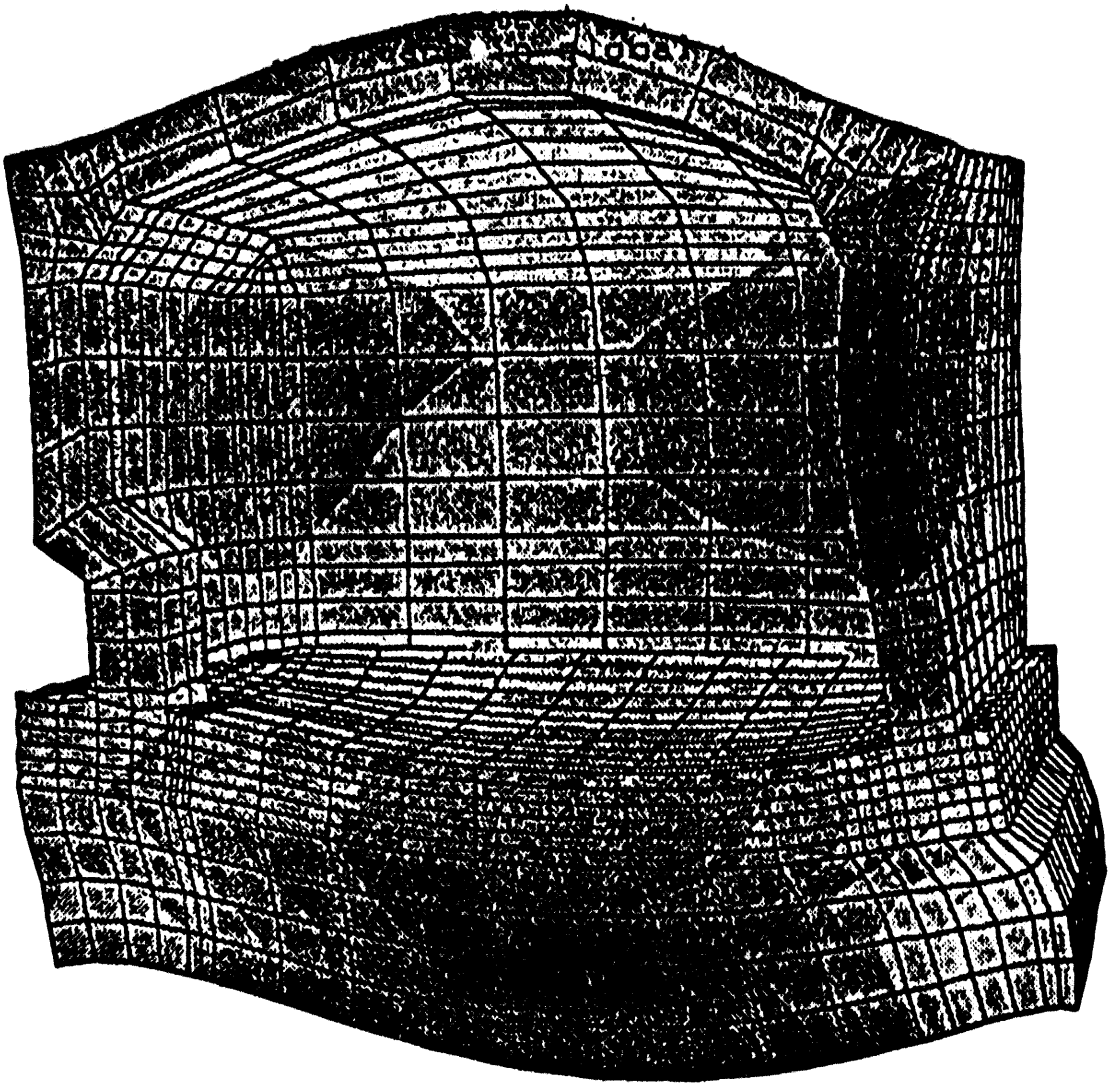

QSFC Maximum West Wall Loading
Displacement Fringes

Time = 7.0 milliseconds

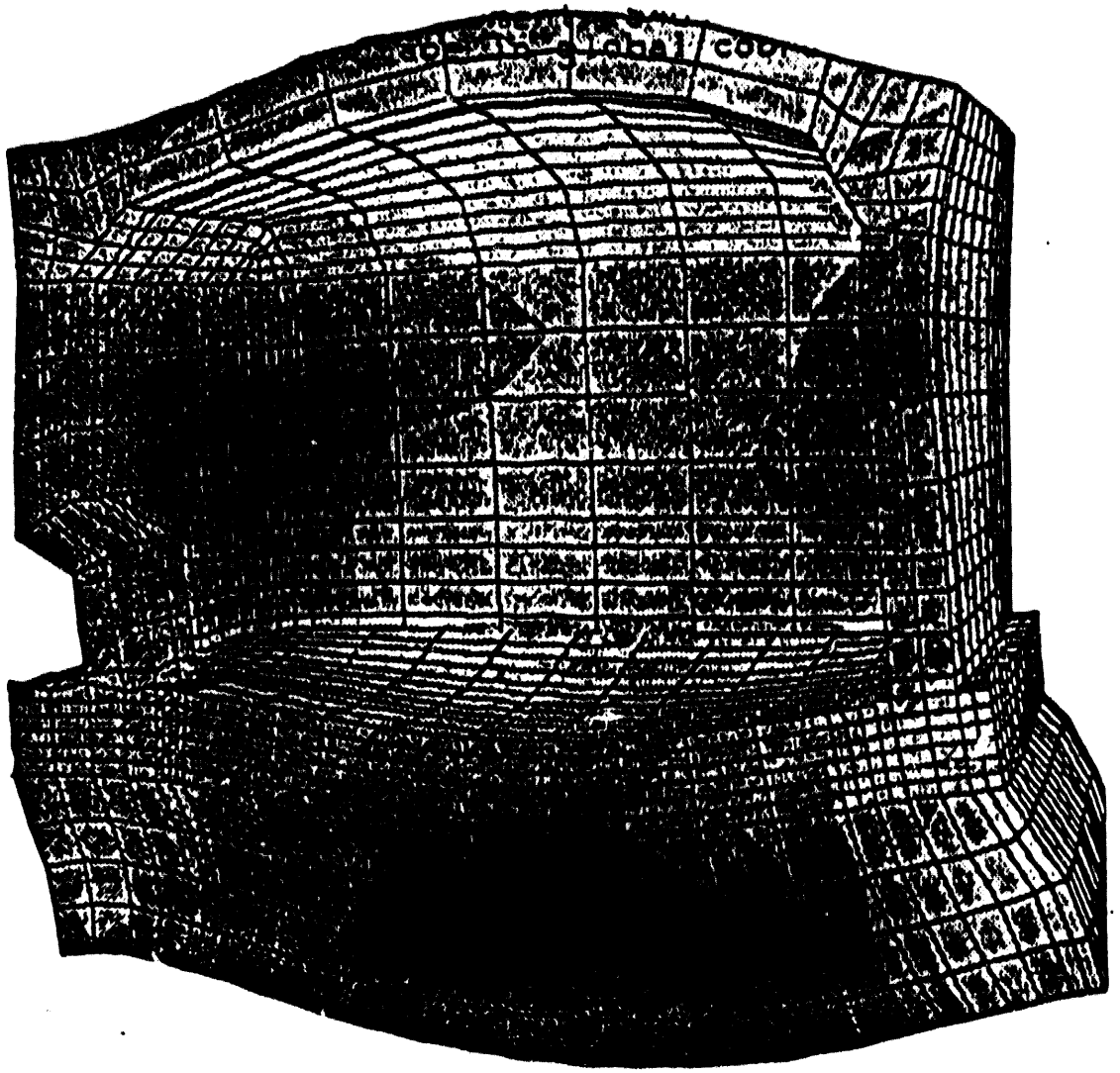

QSFC Maximum West Wall Loading
Displacement Fringes

Time = 8.0 milliseconds

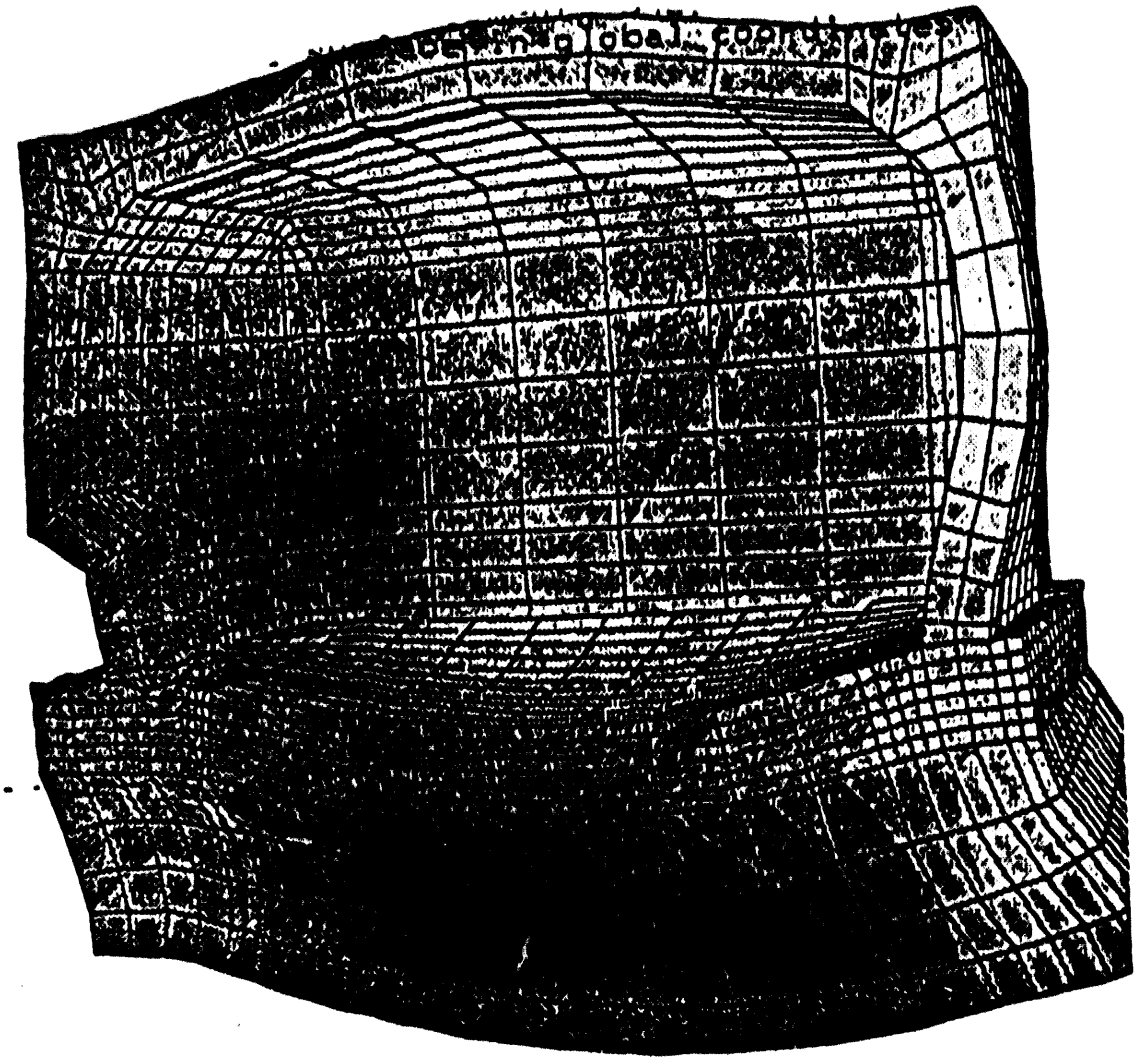

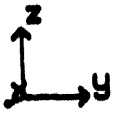

QSFC Maximum West Wall Loading
Displacement Fringes

Time = 9.0 milliseconds

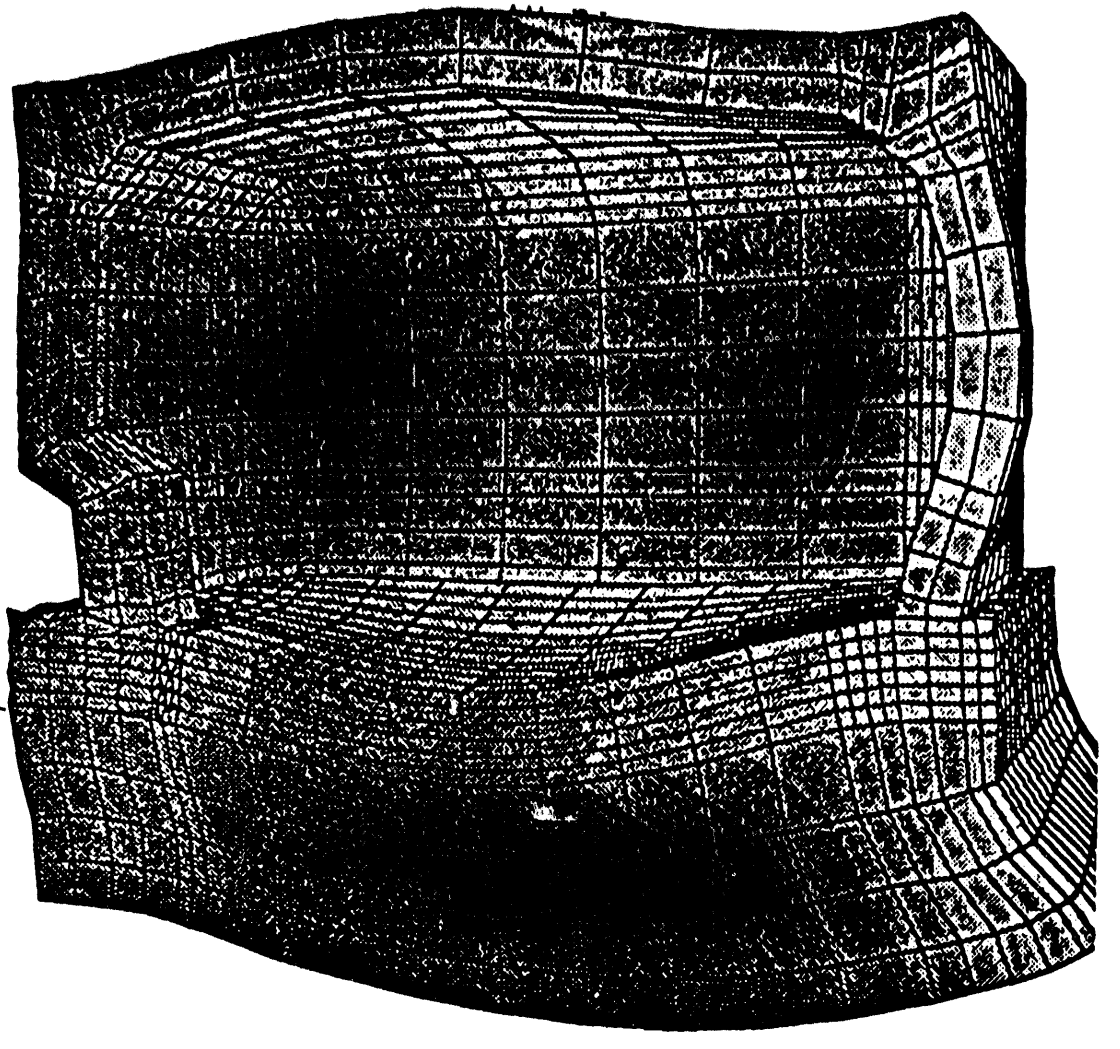

QSFC Maximum West Wall Loading
Displacement Fringes

Time = 10.0 milliseconds

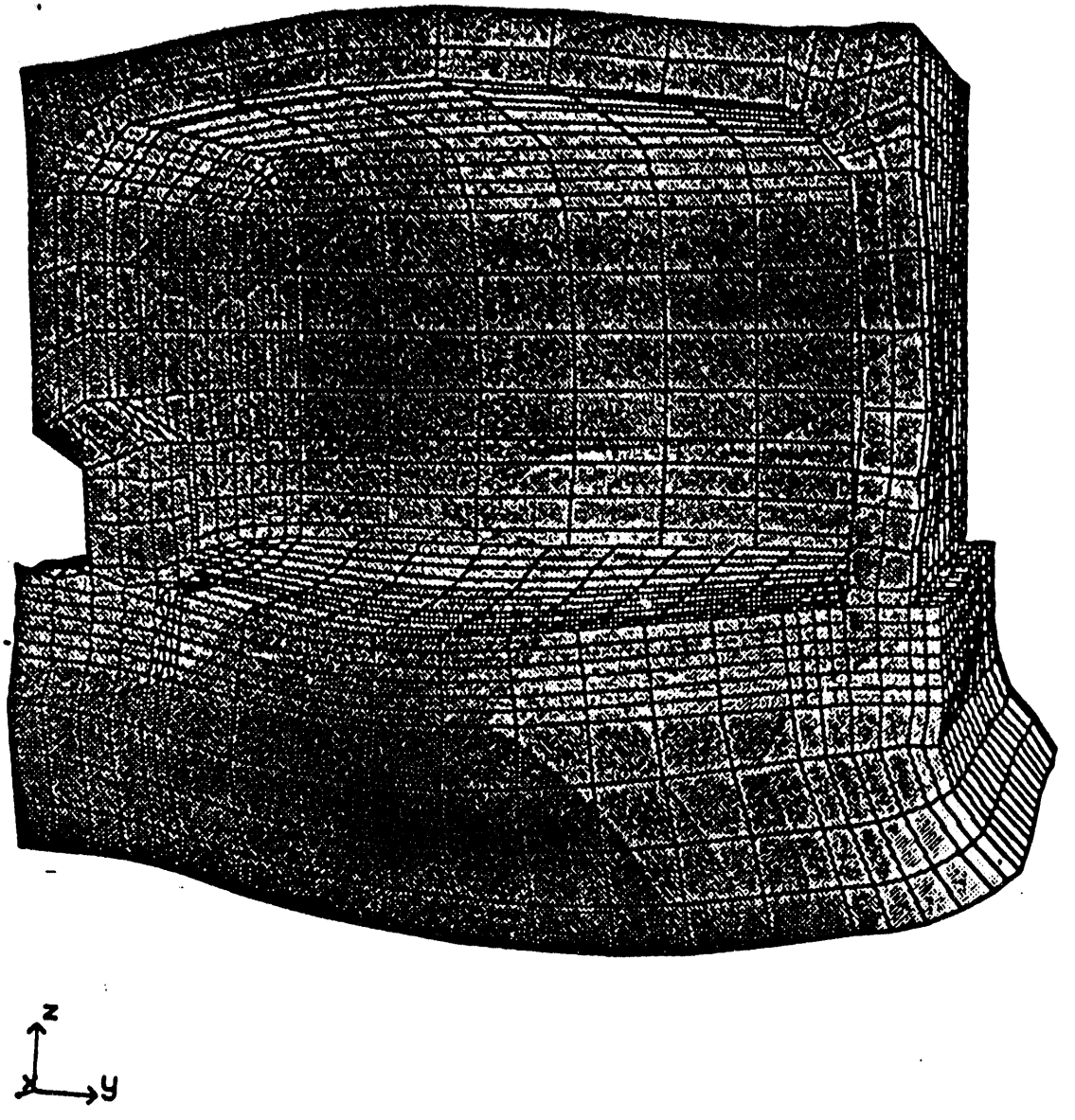

Organic Aerogel Surface Modification and Alternative Processing Techniques*

Gregg S. Wildes

University of Michigan

Lawrence Livermore National Laboratory
Livermore, CA 94550

May 20, 1993

Prepared in partial fulfillment of the requirements of the Science and Engineering Research Semester under the direction of Lucy Hair and Rick Pekala, Research Mentors, at the Lawrence Livermore National Laboratory.

* This research was supported in part by and appointment to the U.S. Department of Energy Science and Engineering Research Semester (hereinafter called SERS) program administered by LLNL under Contract W-7405-Eng-48 with Lawrence Livermore National Laboratory.

If this paper is to be published, a copyright disclaimer must also appear on the cover sheet as follows:

> By acceptance of this article, the publisher or recipient acknowledges the U.S. Government's right to retain a non-exclusive, royalty-free license in and to any copyright covering this article.

Organic Aerogel Surface Modification and Alternative Processing Techniques

Gregg S. Wildes [a] and Rick Pekala [a,b]

[a] Chemical Sciences Division, Lawrence Livermore National Laboratory, Livermore, CA 94550, USA

[b] Author to whom comments should be addressed.

Non-supercritical processing methods were investigated as alternatives to current aerogel drying methods involving supercritical solvent extraction. The objectives of the experiments were to both reduce the large capillary stresses during aerogel drying and to increase the initial strength of the gel. By strengthening the initial material and reducing the stresses during processing, our goal was to avoid the expensive and time consuming use of supercritical drying in aerogel production . We chose seven solvent systems of varying surface tensions to examine their evaporative effects during drying under controlled conditions. Resorcinol formaldehyde gels were dried in a vapor environment, and then directly exposed to air. A direct correlation was established between the amount of induced gel shrinkage and the surface tension and boiling point of each solvent. We also examined the effects of four post-treatments chosen to induce additional, post-gelation condensation reactions [Higher concentrations of active surface groups at the aerogel's neck regions cause localized, preferential syneresis that strengthens the material's string-of-pearls structure]. Post-synthesis processes included the addition of excess monomer, heat and acid treatments.

1. Introduction

Aerogels are highly porous materials that consist of a solid matrix composed of colloidal-like particles or polymeric chains. The material is a class of open-cell foam characterized by its ultrafine cell and pore structure (<1000 Å). This fine nanostucture is responsible for aerogel's optical transparency [1], low longitudinal sound velocities (20 - 200 m/s), very low densities (.003 g/cm^3 has been achieved) [2] and low thermal conductivity [3]. Although most aerogel literature and current research involves inorganic, silica gels, there is an increasing interest in organic aerogels. Organic aerogels have shown great promise in many applications, especially as insulation or capacitor electrodes. The record for the lowest solid thermal conductivity for any

material is $\lambda = 0.012$ W/m•K [4], set by organic aerogel. Resorcinol-formaldehyde aerogels can also be pyrolyzed to produce a carbon aerogel which can be used as high surface area electrodes for double layer capacitors [5].

The synthesis of resorcinol formaldehyde gels begins with the addition and polycondensation reactions and results in an aquagel. The monomers react and form 3 - 20 nm clusters. These clusters then link together and form a continuous, three-dimensional network [6].

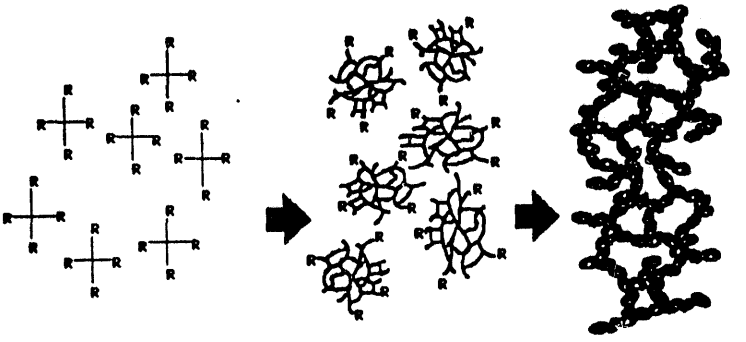

monomer 3 - 20 nm clusters 3-D gel network

Fig. 1. Sol-gel polymerization of resorcinol and formaldehyde ("R" is a reactive site).

The water-filled gel is then exchanged with acetone to displace water from the pores of the gel. This gel is placed in a pressure vessel that is subsequently filled with liquid CO_2. The acetone is flushed from the gel and the temperature and pressure of the vessel are brought to exceed the critical point of CO_2 ($T_C = 31°C$, $P_C = 7.4$ MPa). Under these operating conditions, there are no capillary stresses within the gel matrix during subsequent venting of the gas. The venting allows air to replace the CO_2 and effectively dries the gel. Unfortunately, due to the expensive and time consuming use of

supercritical drying, not enough aerogel can be produced to cost effectively supply interested businesses..

As described above, aerogels are made in a sol-gel process followed by supercritical extraction of the gel's solvent [7]. The supercritical extraction is done in autoclaves which are very limited in size. Currently the largest producer of monolithic aerogel tiles makes samples up to 40 x 40 x 2 cm^3 [8] in size and these are produced in small quantities. There are two key aspects of aerogel production that make large scale processing unlikely in the near future. Both limitations result from the batch nature of supercritical extraction. First, the extraction takes approximately 6-10 hours at best [9], making rapid production times impossible. Second, for large scale production, the capital requirements are massive. The autoclave, used for the supercritical extraction, is limited in size and produces relatively little product for its large volume. Because of the long cycle times for supercritical extraction, many autoclaves must be used to produce large scale quantities of aerogels. These pressure vessels are very expensive, especially for very large, custom made autoclaves. The mass production of aerogels is theoretically possible, yet, supercritical drying is a major limitation.

The main production processing objective would be to avoid the expensive and time consuming use of supercritical dying. To make this possible, post-gelation processing must either strengthen the initial gel, decrease the large capillary stresses present during drying, or do both without sacrificing the structure dependent properties of the material.

2. Experimental procedure

Resorcinol-formaldehyde gels were prepared by the base catalyzed, aqueous polycondensation of resorcinol (1,3 dihydroxybenzene) with formaldehyde [6]. A solids loading of 10 volume % (R = 100) was used, corresponding to a target density of 0.1 g/cm^3. The mole ration of [Resorcinol]:[Formaldehyde]:[$NaCO_3$] was 1:2:0.005. The solution was mixed and poured into 10 ml vials. These were then held at 333 K for 3 days and 363 K for one day to avoid bubble formation during gelation. The crosslinked gels were then broken out of the vials (batches of 15) and placed in a dessicator with 1.5 Liters of acetone for solvent exchange. The solvent was agitated and replaced three times over the next 36 hours. The acetone-filled gels were then exchanged into other solvents with a range of surface tensions. These solvent exchanges were performed in 400 ml beakers with agitation. A minimum of three samples were exchanged into each of the solvents of interest (see Table 1)

Table 1. Surface tension, Boiling points and relative temperatures of pore fluids employed (Water + surfactant is a 1% solution of Aerosol® OT, a 10% solution of Sodium Dioctyl Sulfosuccinate made by American Cyanamid Co.) [10 -13]

Final pore fluid (@298 K)	Surface Tension (dyne/cm)	Boiling Point (°K)	Relative Temp. (T/Bp)
Freon 22	9.5	232	1.28
Diethyl ether	16.5	307.6	0.97
Isopropanol	21.1	355	0.84
Ethanol	22.3	351.4	0.85
Acetone	23.0	329.5	0.90
Water + surfactant	26.0	373	0.80
Octanol	27.0	469	0.64

Some samples were subjected to chemical post-treatments. These treatments were also done three samples at a time in 400 ml beakers and stirred for 24 hours. The post-gelation treatments consisted of a solvent exchange into acetone, acetone with 0.1% trifluoroacetic acid (TFAA), acetone with 1% trifluoroacetic anhydride, acetone with 0.1% TFAA and 1% resorcinol monomer, and acetone with 0.1% TFAA and 1% resorcinol monomer at 333 K. All post-treated samples were then fully exchanged back into acetone before drying.

Drying of the gels was done in petri dishes with a Saran® cover. The Saran® had three small pin holes in it for vapor diffusion. Preliminary experiments examined the effect of vapor vs. direct air drying on the shrinkage of the samples. The solvent exchanged gel specimens were dried in a vapor environment, and then directly exposed to air after a specified interval of time. The results can be seen in figures 2 and 3.

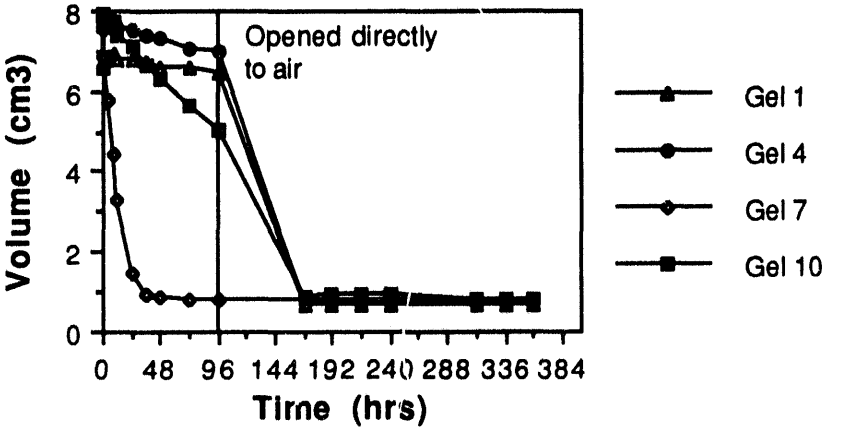

Fig. 2. Gel volume as a function of drying time for water (1), water + surfactant (4), acetone (7) and ethanol (10). Samples were directly exposed to air at 96 hrs.

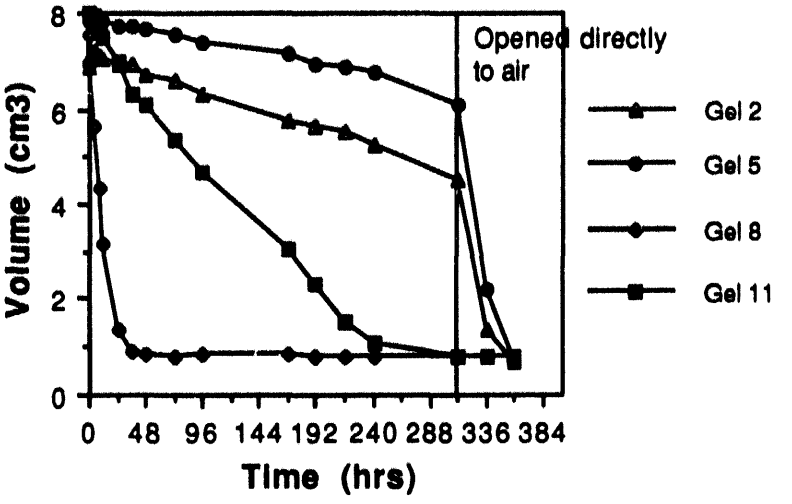

Fig. 3. Gel volume as a function of drying time for water (2), water + surfactant (5), acetone (8) and ethanol (11). Samples were directly exposed to air at 312 hrs.

Although the actual drying rates of the different gels varied (see Figs. 2, 3), due to the differences in relative temperature (see Table 1), the final densities were not significantly different for covered times over 96 hours. Therefore, the shortest time with minimal cracking was chosen as 96 hours under Saran® with three small pin holes. This time was used as our standard for all drying experiments.

3. Results and Discussion

Five post-gelation chemical treatments were employed with the objective of strengthening the neck region of the aerogel structure. The treatments were chosen to induce additional, post-gelation condensation reactions. Higher concentrations of

active surface groups at the aerogel's neck regions (see Figure 4) favor localized, preferential syneresis that strengthens the material's string-of-pearls structure.

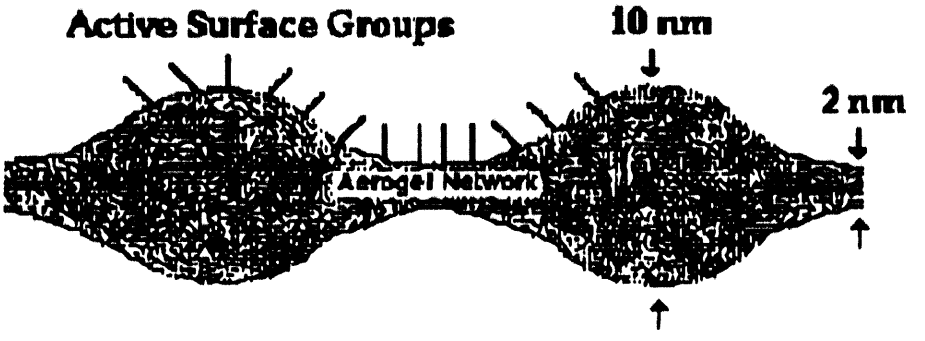

Fig. 4. Surface chemistry of an resorcinol formaldehyde gel.

However, all treatments actually induced additional gel shrinkage as seen below in figure 5.

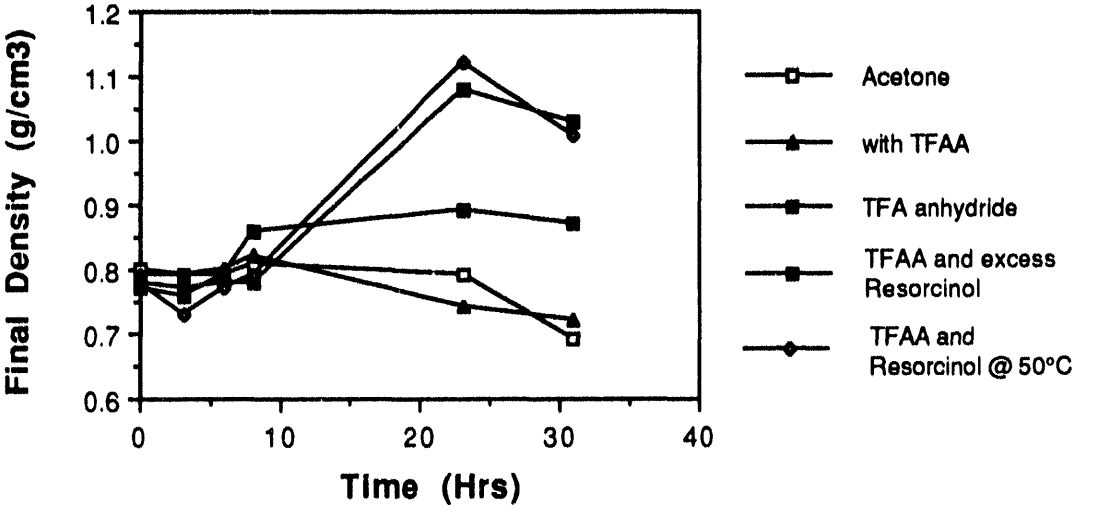

Fig. 5. Densification effects of post-gelation treatments

All samples were first exchanged into acetone to isolate any effects of the solvent. The post-treatments had varying effects on the volume, mass and density changes of the dried xerogel. However, the final volume and mass of the treated samples were all smaller than the samples exchanged only into acetone. Therefore, the treatments actually had a negative effect on the gels' ability to resist shrinkage and densification.

Two possible reasons for the increased shrinkage could be acid induced depolymerization of gel crosslinks or nonselective monomer condensation. In the presence of residual water, the acid could protenate and hydrolyze crosslink bonds. This could lead to widespread depolymerization and greatly weaken the gel, leading to increased gel shrinkage. Nonselective monomer condensation would decrease the average pore size (see Figure 6).

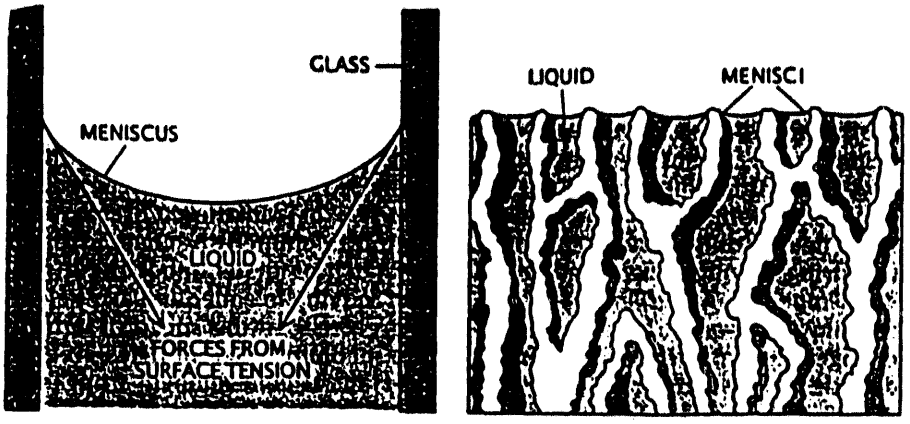

Fig. 6. Gel pore structure (right) and a model cylindrical capillary (left) [15].

This decrease in average pore size would cause increased capillary stresses during drying and increase gel collapse due to the equation:

$$P_r = \gamma \cos\theta / r$$

where P_r is the capillary stress, γ is the surface tension of the pore fluid, θ is the contact angle between the fluid and the solid, and r is the pore radius. The pore size at the meniscus (refer to Figure 6) is indirectly proportional to the capillary stress. Because areogels commonly have average pore sizes of 10 - 20 nm, stresses are very high. For ethanol (θ = 0 on glass, γ = 22.75 dyne/cm), the resulting stress is approximately 22.5 atm [15].

The phenomenology of gel drying was examined by looking at the weight and volume fraction lost as a function of time. This was investigated by drying three sets of samples in different solvents and comparing each relation between weight and volume loss. The experiment was modeled after a study by Kawaguchi *et al.* [14]. Similarities can be seen between figure 7 and the corresponding plot of silica gel drying data by Kawaguchi *et al.*, figure 8.

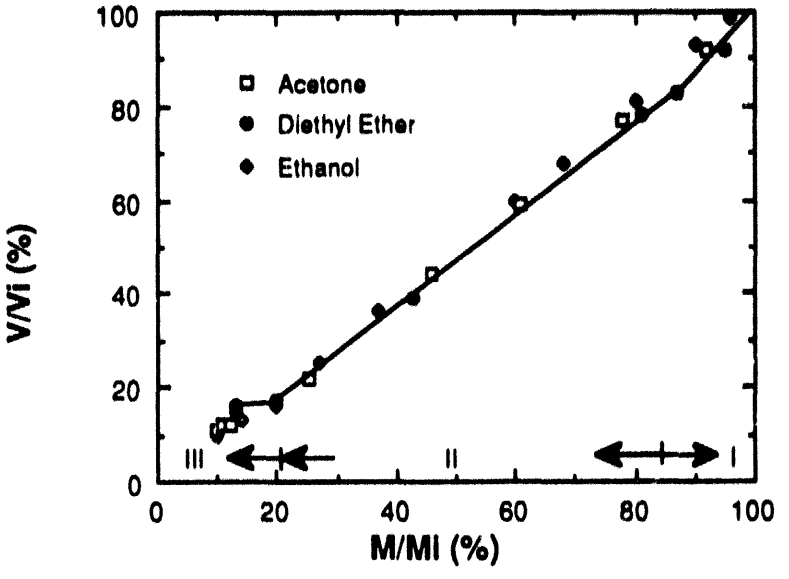

Fig. 7. The three stages of gel drying related by mass and volume loss, RF gel.

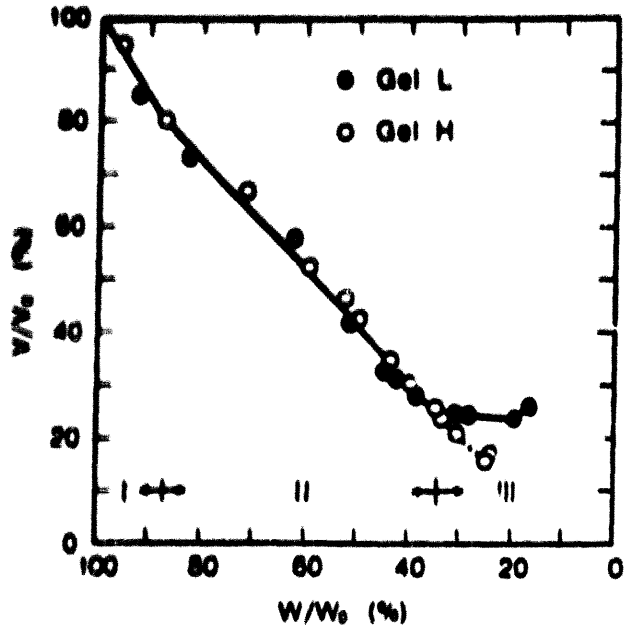

Fig 8 The three stages of gel drying related by mass and volume loss, silica gel (Gel L is acid catalyzed and Gel H is base catalyzed) [14].

Three regions of Figures 7 and 8 can be identified with three stages of gel drying. These are explained by Brinker and Sherer in their book, *Sol-Gel Science* [11]. In region I, recorded weight loss is less than the actual amount of escaping liquid because free liquid is collecting on the container bottom. In region II, the change in volume is proportional to the weight loss. During this time, the rate of evaporative loss is greater than the rate of liquid expulsion in I. After the transition to region III, the gel stops shrinking and only loses additional solvent weight[11].

This phenomenon can also be seen in the kinetics of gel densification. Each solvent system evaporated at a different rate (see Figure 9), due to relative temperature (see Table 1) and volatility. However, corresponding trends can be seen in the dynamics of the densification. The gels gradually dry and densify and eventually reach a maximum

density, corresponding to the end of region II. The gel then, only loses mass and its density falls until drying of the pore fluid is complete.

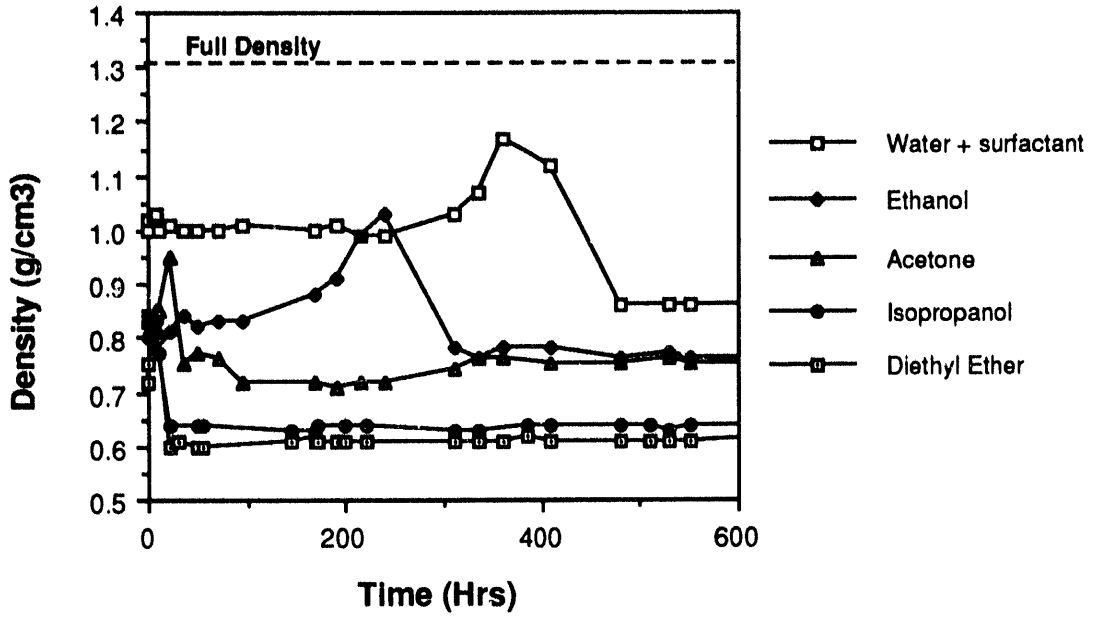

Fig. 9. Densification kinetics and phenomenology of RF gels

This densification relating to solvent loss can also be examined by plotting weight fraction vs. density. Again, the increase to a maximum density, region II transition to III, with a following sharp decrease is seen (figure 10).

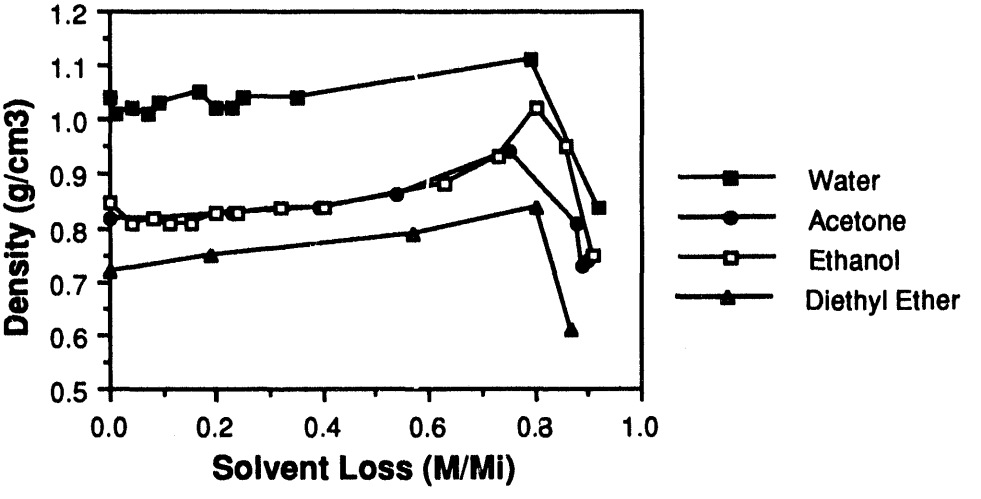

Fig. 10. Solvent loss induced densification for four RF gel solvents.

Each set of gel samples exhibited the same drying and densification phenomena; however, the final xerogel densities varied greatly as seen in Table 2.

Table 2. Final xerogel density related to pore fluid surface tension (subcritical exchange and drying of Freon was done in a Polaron®).

Final pore fluid (@298 K)	Final Density (g/cm3)	Surface Tension (dyne/cm)
Freon 22	0.49	9.5
Diethyl ether	0.61	16.5
Isopropanol	0.64	21.1
Ethanol	0.75	22.3
Acetone	0.75	23.0
Water + surfactant	0.84	26.0
Octanol	1.01	27.0

A direct correlation can be seen from the data which produces a linear plot (Figure 11).

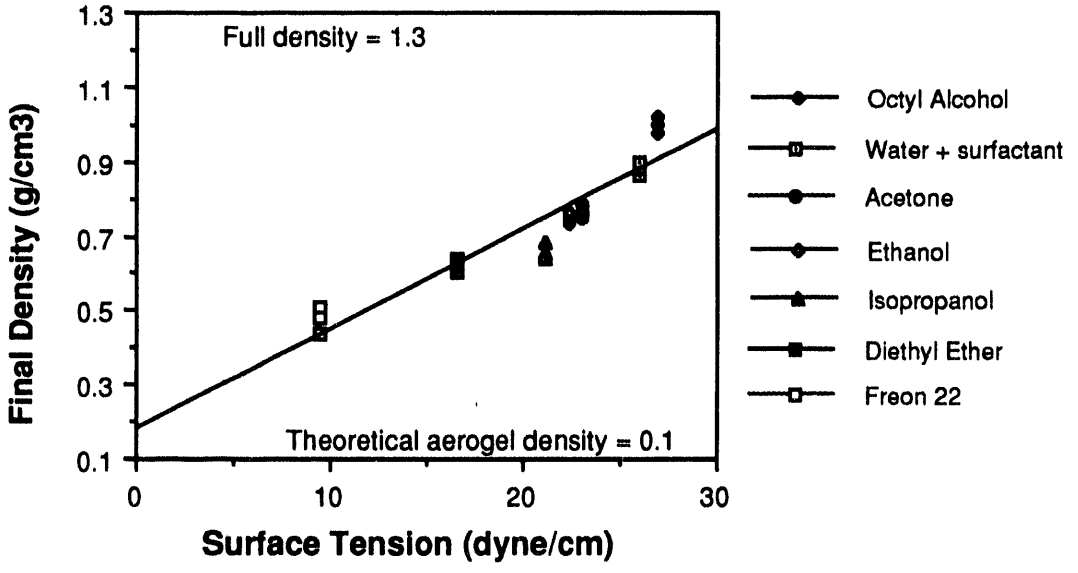

Fig. 11. Direct relation of gel pore fluid surface tension and final xerogel density (note full RF density and theoretical aerogel density based on solution solids loading during synthesis).

Three of the sets of gel samples reached more than 50% porosity (<0.7 g/cm^3), Freon 22, diethyl ether and isopropanol. Subcritical drying of gels with Freon 22 is easier than the supercritical process; however, it must still take place in a pressure vessel. Therefore, for minimum xerogel density, isopropanol and ether are the best choices of the solvents investigated. Current experiments are investigating other chemical, post-gelation treatments for network strengthening in combination with alternative, low surface tension solvents.

6. Summary

A direct correlation was established between pore fluid surface tension and the amount of induced gel shrinkage. Pore fluid surface tension and the amount of induced gel shrinkage gave a linear relation as predicted by theory [15]. Aerogel densification kinetics and phenomena were investigated and discussed. Solvent surface tensions and boiling points were plotted vs. final xerogel density and preferable solvent systems were identified. Five post-gelation chemical treatments were also employed with the objective of strengthening the neck region of the aerogel structure. However, all treatments actually induced additional gel shrinkage. This can be attributed to either non-selective condensation reactions which effectively decreased the average pore size, or acid present with any residual water hydrolyzed the crosslinks, thereby partially depolymerizing the gel network. Both of these effects would cause the observed increase in shrinkage, by increasing capillary stresses during drying or by weakening the resorcinol formaldehyde matrix, respectively. Future experiments will examine other chemical, post-gelation treatments for network strengthening in combination with alternative, low surface tension solvents.

References

1. T. Woignier, J. Phalippou, "Glasses from Aerogels, Part 2", Journal of Materials Science, 25, 1990.

2. L.W. Hrubesh, T.M. Tillotson, and J.F. Poco, "A Sol-Gel Route to Very High Porosity Silica Aerogels," in *Chemical Processing of Advanced Materials*, L.L. Hench and J.K. West, eds., (New York: John Wiley & Sons, Inc., 1992), pp. 19-27.

3. R. Siegel and J. R. Howell, *Thermal Radiation and Heat Transfer*, McGraw-Hill, Tokyo, 1972.

4. X. Lu, M.C Arduini-Schuster, J. Kuhn, O. Nilsson, J. Fricke, and R.W. Pekala, "Thermal Conductivity of Monolithic Organic Aerogels", Science, Feb. 21, 1992.

5. S.T. Mayer, R.W. Pekala, and J.L. Kaschmitter, "The Aerocapacitor: An Electrochemical Double Layer Energy Storage Device," J. Electrochem. Soc., in press.

6. J.D. LeMay, R.W. Hopper, L.W. Hrubesh, and R.W. Pekala, "Low Density Microcellular Materials," MRS Bulletin, 15(12), 19 (1990).

7. J. Fricke, Ed., *Aerogels* , Springer Proceedings in Physics, Vol. 6., Heidelberg, 1986.

8. J. Fricke, "Optimization of Monolithic Silica Aerogel Insulants", Int. J. Heat Mass Trans., 35(9), 1992.

9. A.J. Hunt and P.H. Tewari, "Process for Forming Transparent Aerogel Insulating Arrays; Hydrolysis and Condensation of Alkoxides to for Alcogels; Window, Appliance Insulation", Pat. No. US 4610863, Sept. 9, 1986.

10. R.C. Reid and T.K. Sherwood, *The Properties of Gases and Liquids* , (McGraw-Hill, Inc., USA, 1966).

11. C.J. Brinker and G.W. Sherer, *Sol-Gel Science: The Physics and Chemistry of Sol-Gel Processing* , (Academic Press, San Diego, CA, 1990).

12. Conversation with Brian McSwiggen, Technical Sales Associate, American Cyanamid Co., May 1993.

13. R.C. Weast, ed., *Handbook of Chemistry and Physics*, 56th Ed. (CRC, Cleveland, OH, 1975).

14. T. Kawaguchi, J. Iura, N. Taneda, H. Hishikura, and Y. Kokubu, J. Non-Cryst. Solids, 82,(1986) 50-56.

15. J. Fricke, "Aerogels," Sci. Am., 258(5), May 1988.

REPLACING HAZARDOUS SOLVENTS WITH ALTERNATIVE CLEANERS

Gerald M. Blycker
Dickinson College
Environmental Protection Department
Lawrence Livermore National Laboratory

ABSTRACT

The project identified alternative cleaners that are suitable to replace traditional hazardous solvents such as alcohols, CFCs and chlorinated solvents. The alternative cleaners consisted of citrus and pine based terpenes, aqueous detergents, hydrocarbons, and others. These cleaners present less risk to humans and the environment than traditional hazardous solvents. The performance of the cleaners was evaluated by removing dried flux from printed circuit boards, cleaning cutting oil from glass slides and cleaning cutting oil from aluminum. We obtained quantitative measurements of cleaning performance by three methods. Ionic contamination on the circuit boards was measured using an ionograph, which determined surface conductance. Particulate and oily contamination on glass was measured with an image analyzer to determine the percent contamination on the surface. Reflectance infra-red spectroscopy was used to detect contamination on aluminum. We found several cleaners that performed as well as or better than traditional hazardous solvents.

As a result of the regulatory climate, costly fines and disposal fees, environmental and human health concerns, legislation such as the Clean Air Act and international agreements such as the Montreal Protocol, hazardous solvents are on the way out and alternative cleaners are on the way in to replace them. Hazardous solvents such as Freon TE, 1,1,1 Trichloroethane, Trichloroethylene, Methyl Ethyl Ketone, Methylene Chloride, and Isopropyl Alcohol are used in a wide variety of applications at the Lawrence Livermore National Laboratory (LLNL) and throughout industry. Our goal was to determine which alternative cleaners are suitable replacements for these and other hazardous solvents.

In order to be a suitable replacement, these alternative cleaners must be non-hazardous with respect to their corrosiveness, flammability, toxicity and reactivity. They should also have little or no air emission issues associated with them. They cannot be stratospheric ozone depleting compounds (ODCs), and should not be precursors to smog formation. Vendor's information and Material Safety and Data Sheets (MSDS's) have been reviewed to confirm that they meet these requirements. Aquatic toxicity tests have also been performed on these cleaners at concentrated and working strengths.

Some working components of these alternative cleaners are natural terpenes (citrus and pine based), amines, detergents, alcohols, hydrocarbons, and glycol ethers. See Table 1 in the Appendix for a complete list of the alternative cleaners tested, their manufacturers, active components, uses and suggested cleaning methods.

We chose three common cleaning applications for our study: removing flux from soldered printed circuit boards, removing oil from glass and removing oil from aluminum. Evaluating cleaning performance can prove to be a difficult task. Our goal was to move beyond qualitative analysis such as visual inspection, white glove, and water break tests to a more quantitative analysis.

The method of testing PC board cleanliness was as follows. Five IC chips were hand soldered onto a PC board measuring roughly 7.5 cm X 13 cm. Twenty milliliters of cleaner was heated to the manufacturer's recommended temperature. This temperature varied, depending on the cleaner, from 23°C to 73°C. The front and back sides of the boards were brushed with a standard acid brush and a stiffer, short bristled acid brush from top to bottom for a total of 7 minutes. The PC boards were then placed in a beaker of heated deionized water and thoroughly rinsed. After being left to air dry, the PC board's cleanliness was analyzed by an Alpha Metals Ionograph Model 500. The Ionograph measures surface conductivity in µg NaCl/sq. in. equivalents.

This quantitative measurement is both useful and convenient in determining cleaning performance. We can compare the cleaning ability of the cleaners to Freon TE in a vapor degreaser, which is the traditional method at LLNL (and in many industrial shops) of cleaning PC boards. We can also compare the performance to the military specification, which states that all PC boards must be below 20 µg NaCl/sq. in.

The results from the four test runs can be seen below in Figure 1. Note that several alternative cleaners cleaned better than both Freon TE and Flux-off, which is a hazardous bench-top cleaner. Also note that all cleaners performed better than the military specification. This means that 815 PCX, Rosin-X, Citra Safe, Teksol EP, H2002E, and Armakleen are all acceptable alternative cleaners to replace Freon TE and Flux-off.

To test the general cleaning ability of the cleaners, as well as their ability to clean laser lenses and glass, we performed another set of tests. Glass slides measuring 3.7 cm X 2.5 cm X 0.1 cm were coated on both sides with Trimsol cutting oil. We then placed the slides in 20 ml cleaner and suspend the beaker in an ultrasonic bath for 5 minutes at 40°C. The slides were cleaned with acid brushes for the last 2 minutes and then placed in beakers of deionized water for 2 minutes of ultrasonic action at 40°C,

where they are again brushed. Upon removal from the rinse water, the slides are left to air dry.

Figure 1

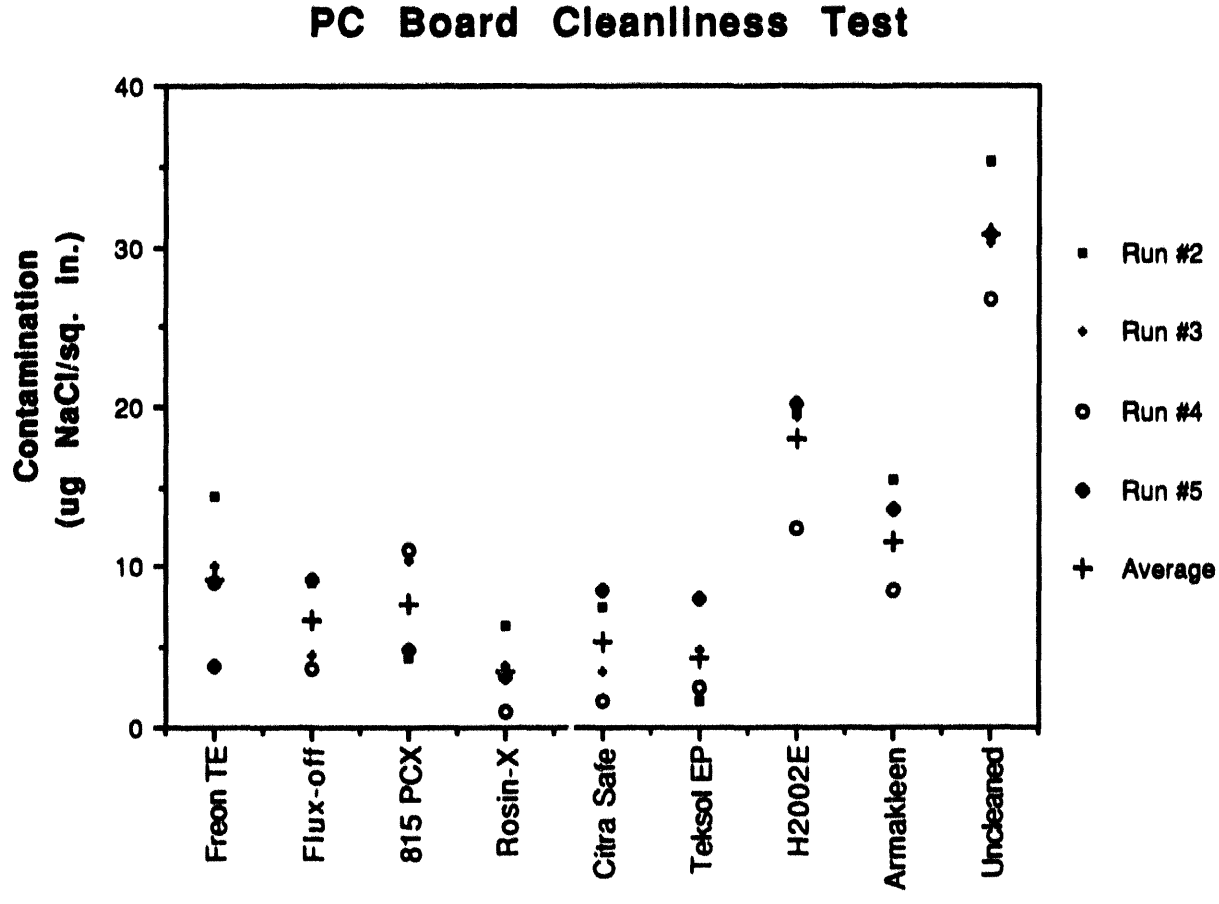

To quantitatively analyze the glass slide's cleanliness, we used an optical image analyzer, which calculated a percentage of the contaminated area on the slide. The image analyzer picked up both oily and particulate contamination. We captured and analyzed 16 images at unbiased locations on each slide. With the microscope at 50x magnification, the computer could detect particles as small as 8 microns in diameter. In total, 9% of each slide's surface area was analyzed to determine cleanliness.

Unfortunately, there is no military specification for glass surface cleanliness. LLNL users of hazardous solvents in these applications do not have a quantitative specification for how clean their parts and surfaces need to be. Therefore, our only option was to compare the alternative cleaners' performances with those of the traditional solvents presently being used. As depicted in Figure 2, almost all alternative

cleaners outperformed Trichlorotrifluoroethane, Methyl Ethyl Ketone, and Methylene Chloride. Re-Entry KNI 2000 and Perfect Way 147 cleaned as well as Freon TE. Tetrahydrofurfuryl Alcohol, EP 921, X-Caliber, UniClean VII, SD 1291, H2002E, NC-300, JALSAC, and PF-5060 all performed better than Freon TE.

Figure 2

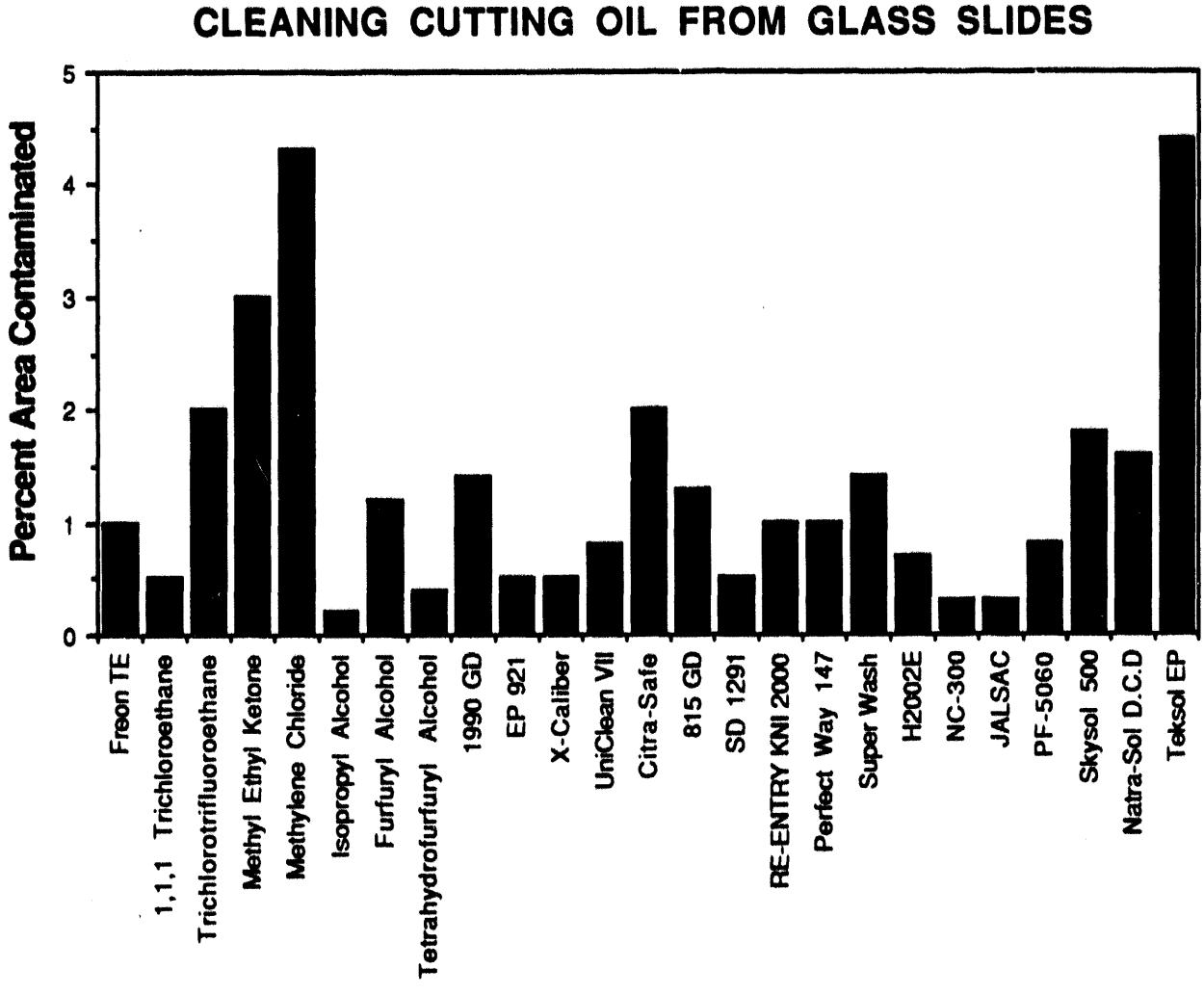

Removing Trimsol cutting oil from aluminum was chosen as another common cleaning application. We followed the same procedure as the glass slides for cleaning and rinsing the samples. Aluminum poses a difficult challenge for removing contamination because of it's rough, uneven surface. Many scratches and gouges remain after machining and cutting where the particles can remain trapped.

Several methods of analysis were performed on the cleaned aluminum samples, including: optical analysis of particles, x-ray fluorescence, gas chromatography/ mass spectrometry (GCMS), and reflectance IR spectroscopy. All but reflectance IR spectroscopy have proven to have limited success for various reasons. The optical analysis could not detect the particles in the scratches nor distinguish some particles from the background of aluminum. X-ray fluorescence was not sensitive enough to determine the performance of the better cleaners. Sulfur and chlorine were used as tracers in the cutting oil, but no counts of these were detected on the cleanest aluminum samples, so the best cleaners' performances could not be compared with each other. GCMS depends upon methylene chloride to remove all the contaminants on the cleaned sample. Therefore, it doesn't analyze how much contaminant remains on the sample after cleaning, but only how much of the contaminant the methylene chloride was able to remove. And as we discovered with the glass slide tests, methylene chloride does not remove cutting oil very well, even from a surface as smooth as glass.

Reflectance IR spectroscopy can identify and quantify hydrocarbon contamination remaining on the aluminum sample. It does not involve any wet chemistry, which can be unreliable, time-consuming and expensive. It has a sensitive detection limit and with a new detector should yield an order of magnitude increase in detection sensitivity. This method is currently being developed and samples are being analyzed. No quantitative data is available at this time.

We are currently in the middle of this project, with much more work lying ahead of us. New cleaners are developed continuously and must be tested as they come onto the market. More tests must be run to ensure that our methods are sound and our data are reproducible. Cleaners should be tested at different temperatures and concentrations to find their optimum cleaning parameters.

However, we have already observed that several cleaners exist which clean better than the traditional hazardous solvents for a variety of applications. No time should be wasted in replacing these hazardous solvents with the appropriate alternative cleaner.

APPENDIX

Table 1

Alternative Cleaners Being Tested

No.	Product Name	Manufacturer	Active Component
1	Rosin-X	Brulin	Blend of detergents, amines & solubilizers
2	Safety Strip HT	Brulin	Diethylene glycol n-butyl ether
3	SD 1291	Brulin	Non-petroleum solvent
4	1990 GD	Brulin	Detergents, phosphates, silicates & inhibitor
5	815 GD	Brulin	Blend of detergents, alkaline builders & inhibitors
6	815 PCX	Brulin	Blend of detergents & amines
7	Armakleen E-2000	Church & Dwight	Full aqueous cleaner
8	Axarel 32	DuPont	Hydrocarbon cleaning agent
9	RE-ENTRY KNI 2000	Envirosolv Inc.	Terpene mixture
10	Citra Safe	Inland Tech.	d-Limonene
11	EP 921	Inland Tech.	d-Limonene
12	SKYSOL 500	Inland Tech.	d-Limonene & C12-C13 Hydrocarbons
13	TEKSOL EP	Inland Tech.	d-Limonene & C10-C11 Hydrocarbons
14	X-Caliber	Inland Tech.	d-Limonene & Methylpyrrolidone
15	H2002E	O.C.S. Manufac.	x-butoxyethanol
16	Perfect Way 147	US Polychem	Blend of detergents, orange oil & mild alkali
17	JALSAC	US Polychem	Aqueous cleaner, sodium metasilicate
18	Polyspray -Jet 790	US Polychem	High alkaline cleaner
19	Tropiclean 281	US Polychem	d-Limonene,alkanol polyethoxylate, isopropanol
20	Alternative 2000	US Polychem	Terpene hydrocarbon, Glycol Monoethyl Ether
21	Natra-Sol D.C.D.	Sunshine Chem.	Citrus solvent
22	Super Wash	S.W.I. International	Alkaline cleaner
23	UniClean VII	Uniclean Products	Glycolethers
24	All Safe	Spartan Chem	Emulsifiers, surfactants, wetting agents
25	E.C.G Marine	Goode Chem	Surfactants, chelators, saponificate, n-butanol
26	NC-300	Ramco	Alkaline liquid, metasilicate, nonionic surfactants
27	Furfuryl Alcohol	QO Chemicals	Furfuryl alcohol
28	Tetrahydrofurfuryl Alcohol	QO Chemicals	Tetrahydrofurfuryl alcohol
29	Surfanol TG	Air Products	Surfactant
30	Surfanol 61	Air Products	Surfactant
31	Purasolv ELS	Purac Inc	Ethylester of natural lactic acid (Ethyllactate)

Table 1 (cont.)

No.	Uses	Cleaning Method
1	romove rosin & water soluble fluxes from PC boards	spray, wash, brush, ultrasonic
2	paint stripper	immersion, followed by water rinse
3	grease, caulk, ink, adhesives	wipe on/ wipe off
4	remove typical production soils & residues short term corrosion inhibitor	single or multi-stage spray wash
5	general degreaser short term ferrous metal flash rust inhibitor	hot tank, steam cleaning, ultrasonic, pressure washing
6	remove rosin & organic flux from PC boards	brushing, spray, ultrasonic
7	remove flux from PC boards	aqueous
8	electronics cleaner	semi-aqueous
9	degreaser	immersion, wipe on/ wipe off
10	remove grease, oil, tar, some resins cleans electrical parts	wipe, brush, spray, immersion
11	paint thinner/cleaner	wash
12	skydrol remover & general solvent cleaner	wash
13	cleans PC boards & other electrical components	wash
14	clean & remove unsaturated polyester resins, gel coat lines, paints, inks	wash, wipe
15	electronics cleaner	ultrasonic, pressure washer, vapor degreaser
16	remove tridolys, oil, buffing compounds & shop soils	ultrasonic, dip/soak tanks
17	general degreaser, cleaner	immersion, rinse
18	Remove oils, grease, dirt, buffing compounds	spray, pressure washer, immersion
19	general degreaser	dip, steam
20	semi-aqueous oul displacement	ultrasonic
21	degreaser, cleaner, deodorizer	immersion, spray
22	degreaser, cleaner	spray, immersion, rinse off
23	all purpose degreasing	wash, immersion
24	general degreaser, cleaner	ultrasonic, spray, dip
25	general degreaser, household cleaner	immersion, spray
26	general cleaner	spray, wipe, immersion
27	solvent	wipe, immersion
28	solvent	wipe, immersion
29	low-foaming, nonionic wetting agent	immersion
30	alcohol replacement	immersion, wipe
31	cleaning, coating, inks	immersion, wipe

ACKNOWLEDGEMENTS

This waste minimization project has been made possible through the collaboration of several individuals. I would like to sincerely thank the following people for their contribution to the study: Dave Shoemaker, Dave Miscovich, Russell Sanborn, Patricia Perry, Wigbert Siekhaus and G. Louis Powell. I would also like to thank Michael Metzer, who has been my personal mentor throughout this research project. Finally, I would like to thank the Department of Energy and the Science and Engineering Research Semester (SERS) program for giving me the opportunity to do this research.

Electronic Authentication Systems

Justin Crockett
Tennessee Technological University
Advanced Technology Center

ABSTRACT

The emerging information systems at Lawrence Livermore National Laboratory (LLNL) are network based, using client/server designs, and employing large numbers of clients and servers. New technologies, such as electronic forms, are also available that enable end users to automate their business processes without the need for programming. Lack of two key elements are retarding progress: a secure authentication mechanism for initial identification of the user to the "network" of information services, and a digital signature capability which would enable transactions requiring authorization to be paperless. To address these two problems, electronic authentication and surrounding issues were explored, including encryption algorithms, digital signatures, privacy enhanced mail, and electronic forms. The Kerberos authentication system, the digital signature technology developed by RSA Data Security, Inc., as well as other technologies were evaluated for possible use at LLNL. Legal, societal, and security issues pertaining to LLNL were also taken into account. Finally, a set of recommendations was made.

Electronic Authentication

Justin Crockett
Tennessee Technological University
SERS Program
Lawrence Livermore National Laboratory
ATC Tim Sharick
December 18, 1992

Computers have rapidly taken over many aspects of our business and personal life. In the workplace they have radically changed the way work is done. However, several problems have arisen that have prevented computers from truly revolutionizing the way we do business. These problems are authentication --how to verify the identity of a user over a computer network-- and digital signatures -- an electronic authenticator that could replace physical signatures and allow paperless transactions.

My goal on this research project was to investigate technology solutions to these two problems These problems are not only specific for AIS, but also apply to the Lab as a whole and any business or institution with large computer systems.

The first problem is primarily one of security. In AIS, users go across the network to work on various applications and must authenticate themselves to each application with an id and password. This is not only inconvenient but insecure. AIS is not the only department that will have this problem. All computing environments, as they become more distributed will have to face this issue of authentication.

The second problem involves overcoming a barrier that holds back computers from being vastly more useful than they currently are. Computers are extremely effective in managing and storing information. However, they are very poor at authenticating information. Most

systems have no way of telling where data came from, who authored it, and whether it has been tampered with. This makes the use of electronic transaction for business and official purposes highly insecure and untrustworthy.

One application hindered by this barrier of authentication is electronic forms. The Lab uses so many forms that the ability to store, fill out, and send forms through the computer is advantageous. The thrust for electronic forms has begun at the lab, but the lack of a signature alternative will hinder full implementation and usefulness.

There are a variety of solutions being developed for the authentication problem. Some of these solutions, like smart cards and biometric devices, are hardware based. Smart cards provide an extra level of security to the standard ID and password system. Biometric devices are hardware devices that detect some inherent quality about a person (such as retinal scans and voice prints). Unfortunately at this time, these devices are too unreliable and expensive for widespread use at the lab. The best solutions are software based because they are cheaper and easier to implement.

Kerberos is an authentication system that uses cryptography to solve the authentication problem in a distributed environment. Kerberos was developed at MIT for their Project Athena environment, a highly distributed environment with insecure, public workstations. Kerberos

uses the government DES (data encryption standard) for user and authentication and message security. It works as follows The user first authenticates himself to the Kerberos server using the password only he knows. Then the user can send requests to use other network services, like printing or mail. The Kerberos authentication server will issue tickets to be presented to the requested service.

Figure 1 shows the basic transaction that occurs for authentication. The client sends a request to the Kerberos Server, also know as the Key Distribution Center, or KDC. The c is the client's name, and the s the name of the server the client wishes to be authenticated to. The KDC then sends the client a ticket, to be presented to the server, and a session key, which can be used for secure communications. Both are encrypted in the client's secret key. To use these, the client must decrypt them using the proper key (this is the user's password for the initial transaction). It is important to note that instead of sending the password over the network in the clear, where it would be vulnerable to eavesdroppers, it is used locally to decrypt the Kerberos ticket. Once the ticket is decoded, it can be sent, along with an authenticator, to the server. The authenticator is generated by the client using the session key, and is used to prevent replay attacks by hackers. The server then checks the ticket and authenticator, and if everything is in order the server can be assured of the client's identity.

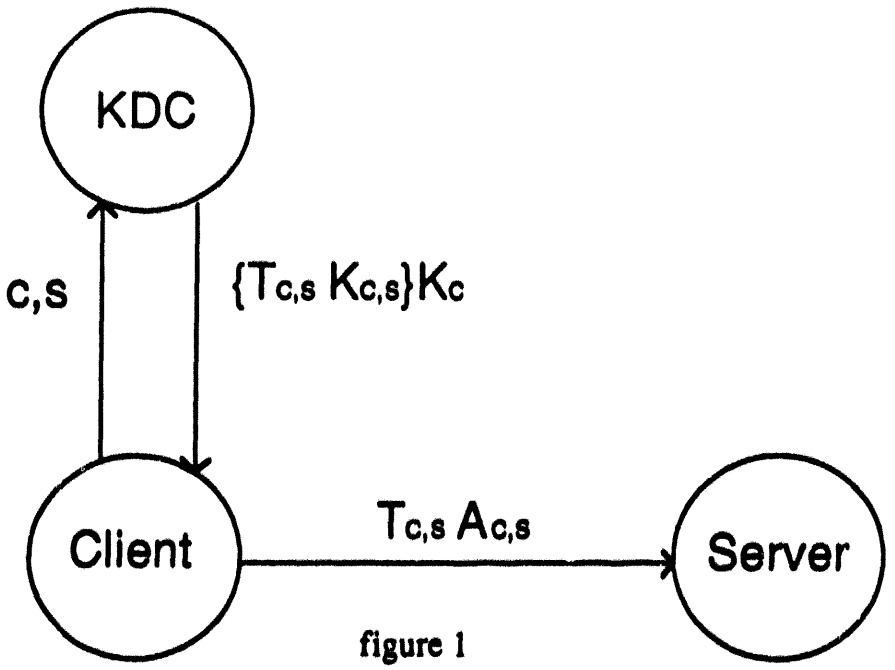

figure 1

The Kerberos system does not provide authorization. It's up to the service, once it knows whom it is dealing with, to decide what access, if any, the user is allowed. The main purpose of Kerberos is to enable trusted transactions on essentially untrustworthy, public workstation. It foils many of the common attack hackers use to gain unauthorized access to system resources.

Kerberos is seeing widespread acceptance as a useful network security product. Many major companies, like Digital Equipment Corp., are marketing their own versions of Kerberos or incorporating it into existing products. Because the code is distributed by MIT for free through anonymous FTP, there has been a large amount of testing and comment from the computing community. It has been in production use for five years at MIT.

Joe Ramus, who works at the Supercomputer Center, is looking at Kerberos for his users. The Livermore Computer Center, the Lab's classified computer center is also looking at Kerberos as a security solution. While Kerberos is a highly effective and useful system, it is not perfect. Properly implemented, Kerberos can solve the authentication problems presented in a highly distributed environment. However, the current version does not provide any capability for digital signatures. I had to look elsewhere for a technology that provided digital signature capability.

Public Key cryptography is a cryptographic innovation that allows principles to have trusted communications without the exchange of a secret. Instead of using a single key for both encryption and decryption, two keys are used. One, the private key, is kept secret by the user;the other, the public key, is known by all. Anything encrypted in the public key can only be decrypted by the private key. This means that if you send a message encrypted in a person's public key, only he can read it since only he has the private key necessary for decryption. Conversely, anything encrypted with private key can only be decrypted with the corresponding public key. This means if a person's public key is able to decode a message, that person must have originated it, since only he has that private key. This concept of non refutability of origin allows for digital signatures.

The RSA public key algorithm is rapidly becoming standard in commercial development of digital signature techniques.

Digital signatures provide a mechanism to allow a recipient to know that a message came from the specified sender. The RSA implementation works like as follows: The sender (A) of the message first computes a one-way hash function (also message digest function(MD)) of the message to generate a "hash code." A then encrypts this hash code with his private key. The result is appended to the message. (This is the "signature"). When the receiver(B) receives the message it computes the same one-way hash function of the message. B also decrypts the hash code appended to the message using the A's public key. If the results of the decryption match the one-way hash, the message was in fact sent by A and B knows that it was not altered in transmission. Figure 2 shows this process.

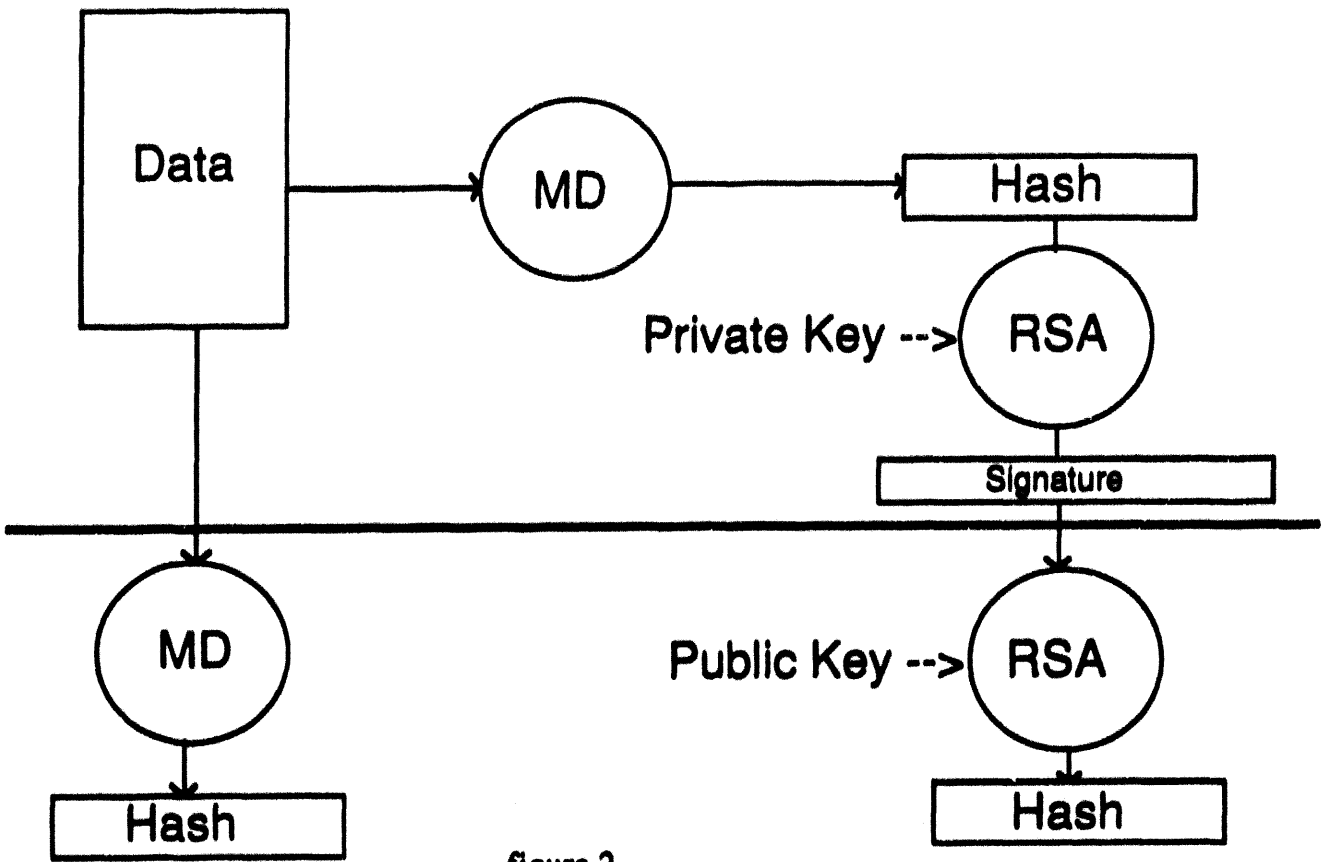

figure 2

Many major commercial software vendors have signed licensing agreements with RSA Data Security Inc. to utilize the digital signature capability in their own products. Apple Computer Inc. is one of these. Apple's OCE (Open Collaboration Environment), an extension to the System 7 operating system will include, among other things, digital signature support.

Electronic forms could make life easier at the lab. Currently authorization for forms is a long and arduous process. Some forms must be signed by more than one person before being approved. If forms could be sent using electronic mail, signed on a computer, and automatically

routed to the proper recipient, the process could be greatly accelerated. Electronic forms also make data storage and retrieval much easier. And of course they reduce paper consumption greatly.

Privacy enhanced mail is another use for digital signatures. Many people use the internet to correspond with colleagues and business partners using electronic mail. However, such mail is completely insecure. Most other electronic mail systems suffer from the same problem. There is no way to know if the message you have received has been changed in transmission or even if it was send by who it says it was. A digital signature capability could provide a greater level of security.

Even with the development of a technology solution, there are a variety of issues involved in implementing them.

A major concern with digital signatures is their regulatory and legal acceptance. Daniel Drake, a research fellow at Logistics Management Institute, has done research on the legal issues surrounding electronic signatures. He said that the US General Accounting Office and other high up agencies have accepted the idea of electronic and other high up government agencies have accepted the idea of electronic security alternatives as long as there are proper security measures. Drake says it is more a matter of educating the mid level officials about the technology and getting them to accept it. It requires a shift in thinking

about forms, information, computers and signatures. It would require a different way of doing business.

The FDA has realized the potential of alternatives to physical signatures, and is investigating possible regulatory changes to provide for these alternatives. In the July 21, 1992, issue of the Federal Register, the Food and Drug Administration put out a request for comments on electronic identification/signatures and electronic records. The FDA is considering whether to propose regulations that would allow an electronic substitute for the handwritten signatures called for in Title 21 of the Code of Federal Regulations. They are looking at many at many issues including regulatory acceptance, security, enforcement, and standards. They are accepting comments until December 18 of 1992, at which time they will come to some decision and put out another announcement in the federal register. Paul Motise, chairman of the working group on Electronic Identification and signatures, said the legal acceptance of electronic signature alternatives hinges upon system control. If the court can be shown the signature alternative is at least as secure as a physical signature they will accept it. In my opinion, due to the complexity of the RSA cryptosystem, the public key implementation of a digital signature is actually more secure than a physical signature.

The Electronic Identification/Signature Working Group put out a document detailing the major issues and areas of

concern. It also includes examination of the regulations and laws dealing with electronic signatures, and comments from various agencies within the FDA and what their specific concerns are.

From the research I've done, I believe that Kerberos or a Kerberos-like technology is a necessity for the future. It would be advantageous for AIS to prototype a Kerberos system, if not to eventually implement, than at least to be familiar with the issues involved with authentication and network security.

While ideally the best form of identification is something inherent to the individual, something that cannot be changed or forged, such technology does not yet exist. The digital signature technology based on public key encryption is cheap and relatively secure. It is achieving wide commercial support and it is possible to implement soon. The technology for digital signatures is rapidly becoming available. For AIS to use this technology they should stay current with the product offerings of the licensee's of the RSA technology. Products such as Apple's OCE have real potential for solving the digital signature problem. We should be on the look out for other mail, electronic forms, and other types of business packages. The conference RSA security is holding in January should be helpful in seeing what products are being offered currently and in the future.

Bibliography

Kerberos

Kerberos : An Authentication Service for Open Network Systems, Steiner,Neuman, and Schiller, presented at Winter USENIX, 1988, Dallas, TX

The Evolution of the Kerberos Authentication Service Kohl, Neuman, Ts'o,Presented Spring 1991 EurOpen Conference, Tromso, Norway

The Kerberos Network Authentication Service (INTERNET DRAFT V4.1), John Kohl and Clifford Neuman, MIT project Athena, June 30 1991

Limitations of the Kerberos Protocol, S.M. Bellovin and M. Merritt, AT&T Bell Laboratories, Murray Hill, New Jersey

Network Security via Private-Key Certificates, Don Davis and Palph Swick, MIT Project Athena Opening the gates on Kerberos: while Kerberos has earned its reputation as an excellent security system, public-key encryption is begin championed as an alternative. Bradford T. Harrison, DEC Professional v11,n6,p46(6) June, 1992

Public Key and PEM

Message Authentication Mechanisms, P. Halliden, 1988 European Seminar on Security in Communications Networks p.8, IBC Tech. Services, London

Privacy enhanced electronic mail, T.j. Casey, Fourth Aerospace Computer Security Applications p. 16-21, IEEE Comput. Soc. Press, Washington ,DC Call # TL3025 A1 1988

SuperForms: a security-enhanced smart electronic from management system, Dayao et al, GLOBECOM '90, p. 1079-83 vol. 2 , IEEE, New York, NY, Call # tk5101 g3,1990

Applying public key distribution to local area networks, B.P. Schanning, Computers & Security , vol.1 no.3 p.268-74, Nov. 1982, Netherlands

Electronic document authentication, Jueneman, R.R., IEEE Network, vol. 1 no.2 p17-23, April 1987

The design and implementation of an authentication system for the wide area distributed environment, Yamaguchi, Okayaman, Miyahara, IEICE Transactions, vol. 74 E, Iss. 11, Pages 3902-3909, Novemeber 1991

MEMO : Privacy and authentication for the automated office, Schanning, Powers, Kowalchuk, Conf Local Computer Networks 5th, Minn. MN, Oct 1980, IEEE p 21-30 Call # QA 76.5 C58 1980

Security IN Office Automation and Electronic Document Distribution, W. H. Murray, Proceedings - IEEE First International Conference on Office Automation, Pub by IEEE 1984 p117-124, Call # HF5547.5 I1 1984

Digital signatures: a tutorial survey, S.G. Akl, Computer, vol 16 no 2 p. 15-24 ,feb 1983

NIST Stumbles on Proposal for Public-Key Encryption, Ellen Messmer,NetworkWorld, v9n30 PP1, 42-43,52, jul 27, 1992

RSA Data Security to provide encryption software to entire US government.,Computergram INternational Issue n1383, March 13, 1990

Privacy Enhanced Electronic Mail, M. Bishop, DIALOG NTIS File 6, jun 90, 39p

Privacy Enhanced Mail : A user`s Perspective, Unisys Defense systems, DIALOG NTIS file 6, aug 91 19p

What's Happening In the privacy and securtiy of electronic mail data channels, Novemeber 09,1990, v 17, no. 22, Phillips Publishing, Inc

EDI held up by lack of public key standard, Newsbytes News Network, Dec 24, 1990

Microsoft acquires tools for software security, Newsbytes News network, June 4, 1991

The E-mail privacy dilemma and some solutions, Network computing February, 92, p.10

Public Keys for public Networks, CommunicationsWeek, November 18, 1991 p.15

Authentication of the Origin and Content of Paperless Transaction and Questions of Liability in Continental Law:Part 2, Amory and Thunis, International Computer law Adivser, vol3, no 3 p. 24-35, Dec. 1988

Authenticating Electronic Contracts: The location of a trusted record -keeper,
Benjamin Wright,Inform v4n8 pp.11-13 sep 1990

An authentication mechanism for USENET, M. Bishop, Proceedings of the Winter1991 USENIX conference p.281-7, jan 91, Berkeley , CA

Use of privacy-enhanced mail for software distribution,W.C. Barker,Fifth Annual Computer Security Applications Conference, Pub. IEEE Computer Soc. Press, 1990

Digital Signature Schemes, Tehcnical Report 81-120, Henk Meijer and Selim Akl,Queen's University,Kingston,Ont,April 1981

*******OCE*******

E-mail authentication coming to Mac; OCE will provide digital signatures.

(System 7 to include document authentication of electronic messages

through the Open Collaboration Environment), Mitch Ratcliffe, MacWEEK vol 5, n37 p4,Oct 29,1991

Apple, Mac developers come together over OCE. (Open collaboration Environment) Mitch Ratcliffe, MacWEEK v6,n3, p1(2), jan 20,1992.

Apple and RSA disclose technology agreement for integrating digital signature technology into O.C.E., March 3, 1992, PRNewswire

Apple announces directions for collaborative computing, October 15, 1991, PRNewswire

OCE opens new worlds: messaging interface :wrap, drag, drop.(Apple's upcoming Open Collaboration Environment), Mitch Ratcliffe, MacWeek v6,n6, p1(2), feb 10,1992

Apple, RSA show security blanket : digital signatures and data encryption in OCE., Brown and Ratcliffe, MacWEEk v6,n10, p14, March 9, 1992

Apple and RSA discolde technology agreement for integrating digital signature technology into OCE, March 3, 1992, PRNewswire.

Apple previews its open collaborative environment for Mac, Computergram International, March 9, 1992.

Apple Reveals Security Pact with RSA, CommunicationsWeeks, March 9, 1992, p.49

Open Systems Advisor: Open Apple,Nina Lytton, Open Systems Today, March 16,1992, p.10

Developers rally behind OCE; collaborative apps set for sneak peeks, Mitch Ratcliffe, D. Brown,MacWeek, v5 n42 p1(2),Dec 10, 1991

Memo: SPA is collaborating with NSA on encryption issues.,Mitch Ratcliffe,MacWeek v6 n13 p3(1),March 30, 1992

FDA Initiative

Feds to Erase Paper Signature Rules , Benjamin Wright, Corporate computing, p40,

Feds seek EDI contracting solution, Mitch Betts, ComputerWorld, September 14,1992, p109

Electronic Identification/Signatures;Electronic Records;Request For Information and Comments, Federal Register,Vol. 57, No. 140, Tuesday, July 21, 1992, p.32185

Electronic Identification/Signature Working Group, Progress Report Feburary 24, 1992

KDP Growth Dynamics

Benita Dair

Cornell University

Lawrence Livermore National Laboratory
Livermore, California 94550

December 18, 1992

Prepared in partial fulfillment of the requirements of the Science and Engineering Research Semester under the direction of Jim De Yoreo, Research Mentor, at the Lawrence Livermore National Laboratory.

* This research was supported in part by an appointment to the U.S. Department of Energy Science and Engineering Research Semester (hereinafter called SERS) program administered by LLNL under Contract W-7405-Eng-48 with Lawrence Livermore National Laboratory.

Abstract

Potassium dihydrogen phosphate (KDP) is a crystalline material noted for its nonlinear optical properties as a frequency converter for high power laser systems used in fusion research. We are observing the growth dynamics of KDP to learn how and why strain originates. The study of KDP growth dynamics has provided insight into the fundamental question of how crystals grow. Using Atomic Force Microscopy, we have successfully imaged growth and dissolution features on both the 100 and 101 faces.

We have observed pointed elongated growth hillocks on our 100 KDP faces. This indicates that the advancement of steps on the 100 faces was governed by kink integration, and not by impurities [9].

We have found that dissolution pits on the 101 face form by the spiraling down of screw dislocations. In addition, the fact that the tip of the 101 hillock is composed of layers, and not by spirals signifies that growth occurred by two-dimensional nucleation rather than by dislocation activity. Thus, we know that volume diffusion plays a very important role in KDP crystal growth, whereas surface diffusion, although present, does not play an important role.

Introduction

KDP and Crystal Growth

Potassium dihydrogen phosphate (KDP) is a crystalline material noted for its nonlinear optical properties as a frequency converter for high power laser systems used in fusion research. KDP crystals convert infrared laser beams into green and ultraviolet light, which are more effective in fusion research and in other physics applications. Presently, a crystal large enough for such applications takes about 9 to 12 months to grow and is therefore very expensive. Growing KDP crystals any faster would induce strain into the crystals, which would degrade optical quality. In order to grow high quality crystals (with a strain density of $<10^{-5}$), we need to learn how and why strain originates. Because dislocations and impurities are major sources of crystal strain, growing high quality crystals translates to preventing the incorporation of impurities and dislocations into the crystal structure. Therefore, we are observing the growth dynamics of KDP, which will provide insight into the mechanisms of how impurities are incorporated into the crystal, and more fundamentally, of how crystals grow. There are two competing mechanisms, or processes for crystal growth, that we are considering. The first is by the activity of screw dislocations, or by the rotation of the spirals. The second mechanism for crystal growth is by two-dimensional nucleation, or through the formation and growth of islands.

KDP grows in both the 100 (prismatic) and 101 (pyramidal) directions (figure 1). However, because KDP grows predominantly in the 101 direction, the net growth is in the 001 (z) direction.

We currently are examining the (100) and (101) faces of fresh KDP crystals using the Atomic Force Microscope (AFM), a scanned-probe microscope that uses force, rather than light or electrons, to image a sample surface. Because the AFM has atomic resolution, we should be able to image microscopic growth features to gain more insight into the mechanisms for hillock formation and growth.

Atomic Force Microscopy

The AFM is a scanned-probe microscope which scans a sample in a raster manner with an atom-sharp tip of diamond mounted on a gold-coated silicon cantilever. The electron cloud of the single-atom tip presses against the electron cloud of each atom in the sample (fig. 4). This produces a repulsive force, which deflects the tip. The movement of the tip is monitored by a laser reflected off the cantilever arm to a photodiode sensor. A feedback system responds to the laser movements by activating a piezoelectric control, which controls the z height of the sample (fig. 5). This enables the deflections, and thus the contact force, to keep constant. The tip movements are then transformed into a surface image. [3,4]

A fluid cell allows one to operate the AFM with the sample, tip, and cantilever immersed in a liquid. This would provide utility in allowing us to watch KDP grow from solution.

Experimental

We investigated the growth dynamics of small KDP crystals (<10x10x10 mm^3) grown from aqueous solution in conditions of natural convection. A solution of KDP with saturation temperature 53°C was prepared from deionized water and salt of 99% purity. The solution was heated to 73°C and was set aside for 24-30 hours to cool gradually to room temperature and to allow for small crystals to form. Crystals were plucked from solution using nylon tweezers and rinsed with hexane to stop any growth or dissolution from occurring [8]. They were patted dry and stored in lintless towelettes. Crystal surfaces were inspected for prospective AFM samples using optical microscopy. Pyramidal and prismatic faces were selected for abundance of growth hillocks and for smoothness.

The Nanoscope III AFM was used to image chosen crystal surfaces. AFM samples were prepared by cleaving and sanding the bulk crystal and mounting the resulting faces onto clay and/or tape.

Experimentally, we have found that dissolution pits are more abundant than growth hillocks on our crystals. We have realized four main procedural reasons for this occurrence:

--> Beforehand, we were reusing hexane so as not to generate a large volume of hazardous waste. Hexane is not miscible in, and is less dense than water; therefore, hexane floats on top of water. Because the squirt bottles draw liquid from the bottom of the container, we were rinsing the crystal surfaces with KDP solution

rather than with hexane. This allowed a less supersaturated solution to come in contact with the surface, and dissolution may have occurred before the crystal was patted dry from solution. Presently, only fresh hexane is used.

--> When one looks at a growing surface in solution, one may notice convection lines rising from the crystal. When these convection lines disappear, one knows that the equilibrium concentration of KDP in solution has been attained for that particular solution temperature. Because the temperature of the environment directly affects the solution temperature, any small fluctuation in room temperature will cause a fluctuation in solution temperature. If the solution should warm up, the equilibrium concentration of KDP in solution would increase, resulting in dissolution of the solid crystals. Therefore, we now are plucking crystals before convection lines disappear to ensure that only growth is occurring.

--> At times we have resorted to clay as a mounting material for KDP samples. Because clay is moist, some of the water molecules may have diffused to the surface of the crystals to cause slight dissolution.

--> When we leave samples exposed to air or mounted in the AFM for an extended period of time, the water vapor present in the environment may cause dissolution. Indeed, by using the optical set-up, we can notice water droplets collecting on the samples after the crystals have been exposed for only two days.

Results

Using Atomic Force Microscopy, we have successfully imaged growth and dissolution features on the 100 and 101 faces. As expected, triangular growth hillocks and dissolution pits were found on the 101 surface (see figures 6-8). Oblong growth features and dissolution features were found on the 100 faces (see figures 9-10).

We have also imaged larger growth islands on the 101 face (see figure 11) and steps and growth islands on the 101 growth hillocks (see figures 14-15).

Discussion

Previous work [9] has shown that the growth hillocks on the 100 face are in the shapes of either pointed ellipsoids or circular ellipsoids elongated along the 010 direction (figure 17). Indeed, we have noted optically that the growth hillocks found on the 100 surfaces of our crystals are pointed ellipsoids elongated in the 010 direction. Figures 9-10 show growth hillocks and dissolution pits on the order of 4μm long. Previous work [9] has also shown that step advancement in circular growth is governed by the density of adsorbed impurities, whereas pointed spiral growth is governed by kink integration. The pointed elongated shapes of our 100 growth hillocks indicate that the advancement of steps on the 100 faces was governed by kink integration, and not by impurities.

The optical image of the dissolving 101 face growth hillock (figure 7) shows that the dissolution of a 101 growth hillock occurs first at the center tip and down the edges of the hillock. This is a strong indication that dissolution pits form by the spiraling down of screw dislocations [7,8]. Because dislocations induce strain into a crystal, the material around a screw dislocation is strained in relation to the rest of the crystal. The free energy of the strained area is higher than the bulk crystal. This makes the area around the dislocation less stable. In addition, strain increases the saturation point of the surrounding area. Therefore, the material around the screw dislocation leaves before the bulk material.

There are two competing mechanisms, or processes for crystal growth. The first is by the activity of screw dislocations, or by the rotation of the spirals. This upwards rotation of the spiral generates a step for each revolution it undergoes. Atoms impinging on the crystal surface would diffuse around the area and eventually stick to the steps, propagating the crystal outwards [2,13].

Past work using Michelson interferometry [15] has confirmed the presence of screw dislocations, indicating that this mechanism of crystal growth does take place.

The second mechanism for crystal growth is by two-dimensional nucleation, or through the formation and growth of islands. In this process, atoms impinge onto the crystal surface, enter the adsorbed state, and diffuse around with no driving force. In an ideal model, the surface is a uniform distribution of equally

likely sites for adsorption. The adatoms may re-enter into solution or diffuse around the surface. Clusters are formed when diffusing atoms collide with one another. Clusters which are larger than the critical size are permanent and continue to grow by capturing more atoms. Forces are favorable for a diffusing atom to stick to an edge. In essence, then, a diffusing atom has three choices: it may re-enter into solution, form a new cluster, or stick to growing cluster or island. In this mechanism of crystal growth, surface diffusion is not very important; volume diffusion is the dominating factor [12].

There are two types of island growth: one is flat, quite similar to a sheet, and the other builds on top of the other layers. Figure 18 shows the flat island growth, while figures 13-16 show the layers that build on top of one another.

By looking at the images of the growth hillock (figure 13), we see that the tip of the hillock is composed of layers, and not by spirals. This indicates that growth occurred by two-dimensional nucleation rather than by dislocation activity. Close-ups of the steps (figures 14-15) show that islands are forming on top of the steps. If growth had been by dislocation activity, atoms would have been adsorbed at the step edges rather than on top of the steps. Figure 16 shows yet another close-up of the top of a hillock. The very island-like structures confirm that the mechanism of growth was by two-dimensional nucleation. The fact that we see island growth indicates that volume diffusion plays a very important role in crystal growth, whereas surface diffusion, although present, does not play an important role.

Future goals for this project include using a fluid cell to image KDP while it is in the process of growing to learn more about the mechanisms for atom incorporation and crystal growth.

Summary

Using Atomic Force Microscopy, we have successfully imaged growth and dissolution features on the 100 and 101 faces. As expected, triangular growth hillocks and dissolution pits were found on the 101 surface while oblong growth features and dissolution features were found on the 100 faces.

Dissolution of a 101 growth hillock occurs first at the center tip and down the edges of the hillock. This is a strong indication that dissolution pits form by the spiraling down of screw dislocations.

The pointed elongated shapes of our 100 growth hillocks indicate that the advancement of steps on the 100 faces was governed by kink integration, and not by impurities.

There are two competing mechanisms, or processes for crystal growth. The first is by the activity of screw dislocations, or by the rotation of the spirals. The second mechanism for crystal growth is by two-dimensional nucleation, or through the formation and growth of islands. The fact that the tip of the 101 hillock is composed of layers, and not by spirals indicates that growth occurred by two-dimensional nucleation rather than by dislocation activity. Thus, we know that volume diffusion plays a very important role in crystal growth, whereas surface diffusion, although present, does not play an important role.

References

1) W. K. Burton, N. Cabrera, F. C. Frank, "The Growth of Crystals and the Equilibrium Structure of Their Surfaces", Phil. Trans. Royal Society of London, Vol. 243 A.866, 40 (1951).

2) N. Cabrera, D. A. Vermilyea, "The Growth of Crystals from Solution", in: Growth and Perfection of Crystals, Eds. R. H. Doremus, B. W. Roberts and D. Turnbull (Chapman and Hall, London, 1958).

3) D. Rugar, P. Hansma "Atomic Force Microscopy" Physics Today, Vol. 261, 98 (October 1990).

4) H. K. Wickramasinghe "Scanned-Probe Microscopes" Scientific American, Vol. 43, 23 (October 1989).

5) V. V. Azarov, L. V. Atroshchenko, V. G. Vasil'chuk, M. I. Kolybaeva, and V. I. Salo, "Influence of the Imperfection of the Seed Crystal on the Structural Perfection of Potassium Dihydrophosphate Single Crystals" translated from Izvestiya Akademii Nauk SSSR, Neorganicheskie Materialy, Vol. 21, No. 2, pp. 335-337, February, 1985.

6) N. P. Zaitseva, I. L. Smol'skii, L. N. Rashkovich, "Study of Rapid Growth of KDP Crystals by Temperature Lowering", Soviet Physics Crystallography 36, 113 (1991).

7) P. G. Vekilov, Yu. G. Kuznetzov, A. A. Chernov, "Dissolution Morphology and Kinetics of (101) ADP Face; Mild Etching of Possible Surface Defects", Journal of Crystal Growth 102, 706-716 (1990).

8) W. J. P. Van Enckevort, R. Janssen-Van Rosmalen, W. H. Van Der Linden, "Evidene for Spiral Growth on the the Pyramidal Faces of KDP and ADP Single Crystals, Journal of Crystal Growth 49, 502-514 (1980).

9) J. W. Noor, B. Dam, "The Growth Spiral Morphology on {100} KDP Related to Impurity Effects and Step Kinetics", Journal of Crystal Growth 76, 243-250 (1986).

10) V. I. Bredikhin, V. P. Ershov, V. V. Korolikhin, and V. N. Lizyakina, "Influence of Impurities on the Growth Kinetics of a KDP Crystal",

Kristallografiya 32, 214 (1987) [Soviet Physics Crystallography 32, 122 (1987)].

11) A. A. Chernov, A. I. Malking, and I. L. Smol'skii, "Solution and Growth Kinetics of Dipyramid Face of ADP", Kristallografiya 32, 1508 (1987) [Soviet Physics Crystallography 32, 886 (1987)].

12) J. L. Robins, "Thin Film Nucleation and Growth Kinetics", Applied Surface Science 33/34, 379 (1988).

13) Y. Zundelevich, R. Glaser, "Activity of Growth Centers During Spiral Growth of KDP in Aqueous Solution: A Statistical Approach", Journal of Crystal Growth 102, 69 (1990).

14) A. A. Chernov, L. N. Rashkovich, A. A. Mkrtchan, "Solution Growth Kinetics and Mechanism: Prismatic Face of ADP", Journal of Crystal Growth 74, 101 (1986).

15) P. G. Vekilov, Yu. G. Kuznetsov, "Growth Kinetics Irregularities Due to Changed Dislocation Source Activity; (101) ADP Face", Journal of Crystal Growth 119, 248 (1992).

Captions for figures

Fig. 1: KDP grows in both the 100 and 101 directions.

Fig. 2: Screw dislocations are the components responsible for growth.

Fig. 3: Dislocations generated at the seed and cap extend in the 101 directions. (figure provided by J. De Yoreo)

Fig. 4: Atomic Force Microscopy is force based; the electron cloud of the tip presses on the electron clouds of the atoms in the surface. (figure taken from reference 3)

Fig. 5: AFM setup. Movements of the tip are monitored by a laser-to-photodiode set-up. The piezo controls the up-down movements of the sample to keep a constant contact force. (figure taken from reference 4)

Fig. 6: Growth hillock on the 101 surface.

Fig. 7: Dissolving growth hillock on the 101 surface.

Fig. 8: Dissolution pit on the 101 surface.

Fig. 9: Growth feature on the 100 surface.

Fig. 10: Dissolution feature on the 100 surface.

Fig. 11: Triangular growth island found on the 101 face.

Fig. 12: Dissolution of a hillock into a pit.

Fig. 13: Close up of the tip of a growth hillock.

Fig. 14: Close-up of steps - note the islands which have formed on top of the steps.

Fig. 15: Close-up of steps - note the islands which have formed on top of the steps.

Fig. 16: Close-up of another hillock - note island growth.

Fig. 17: Drawing of a 100 growth hillock (figure taken from reference 9)

Figures

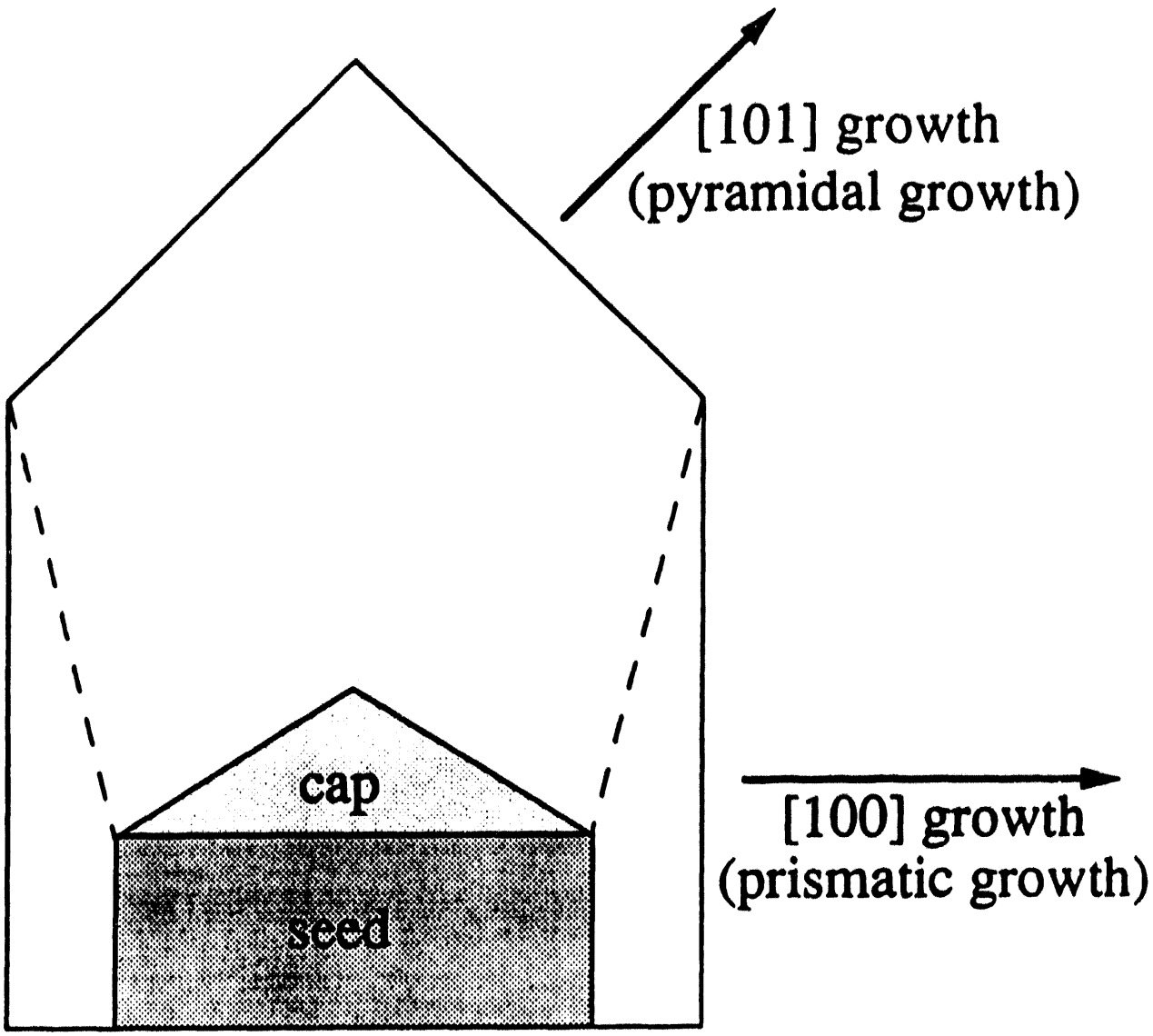
[101] growth
(pyramidal growth)
cap
seed
[100] growth
(prismatic growth)

Fig. 1

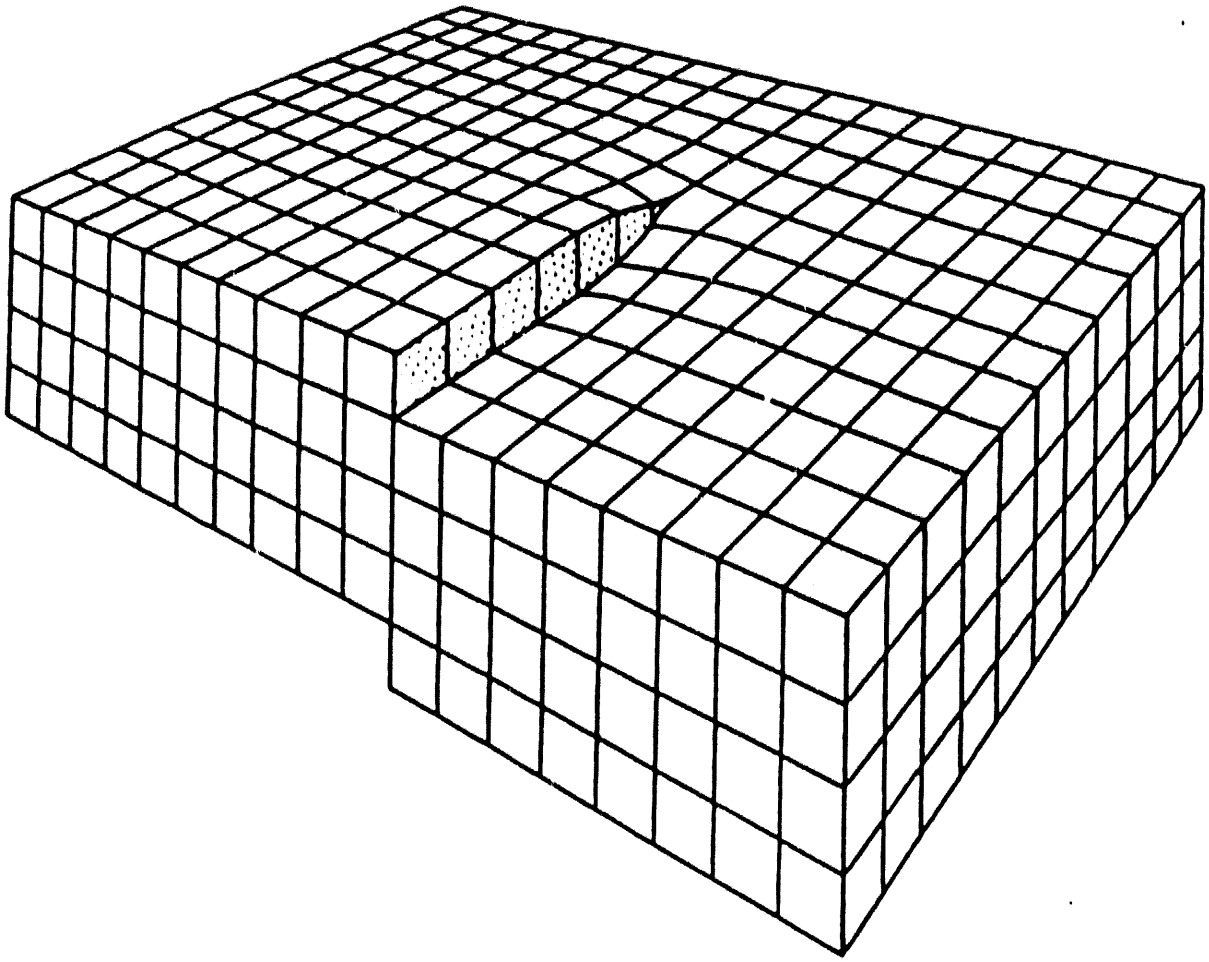

Fig. 2

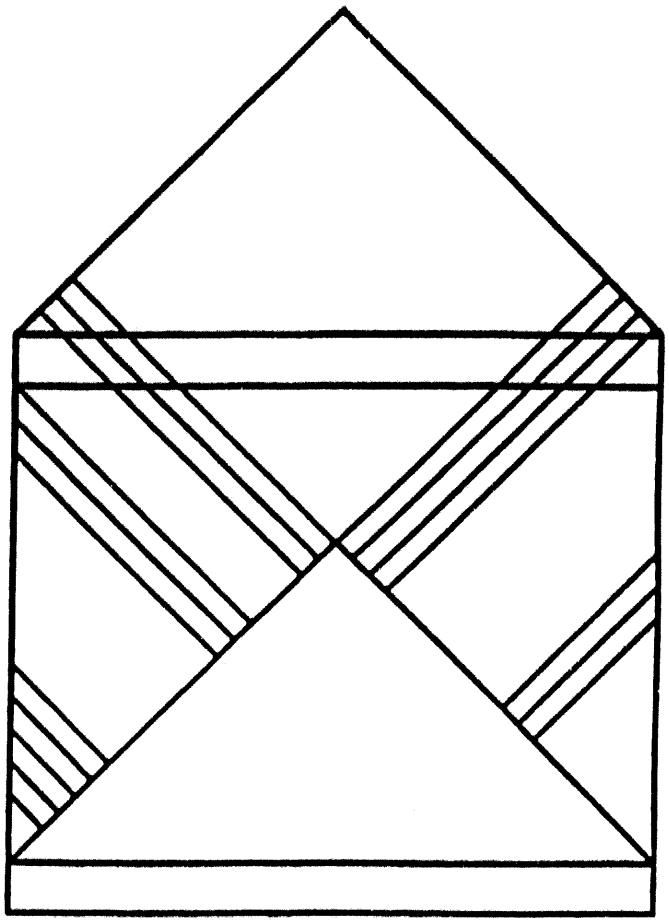

fig. 3

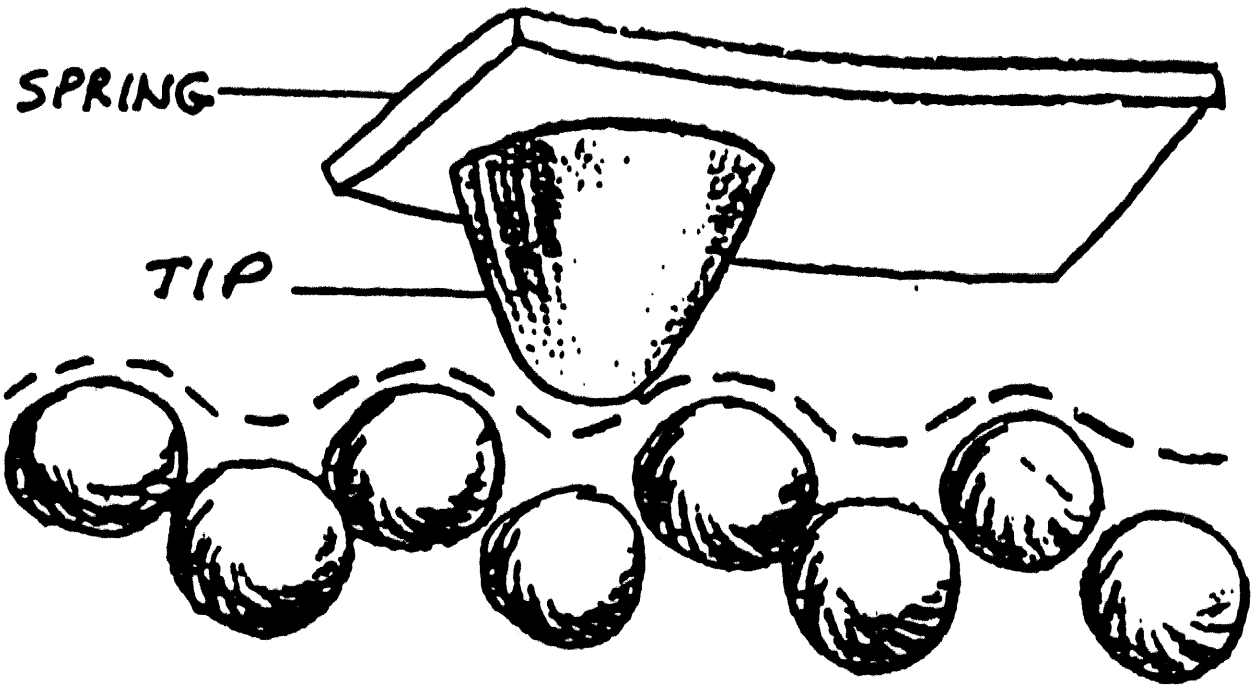

Fig 4

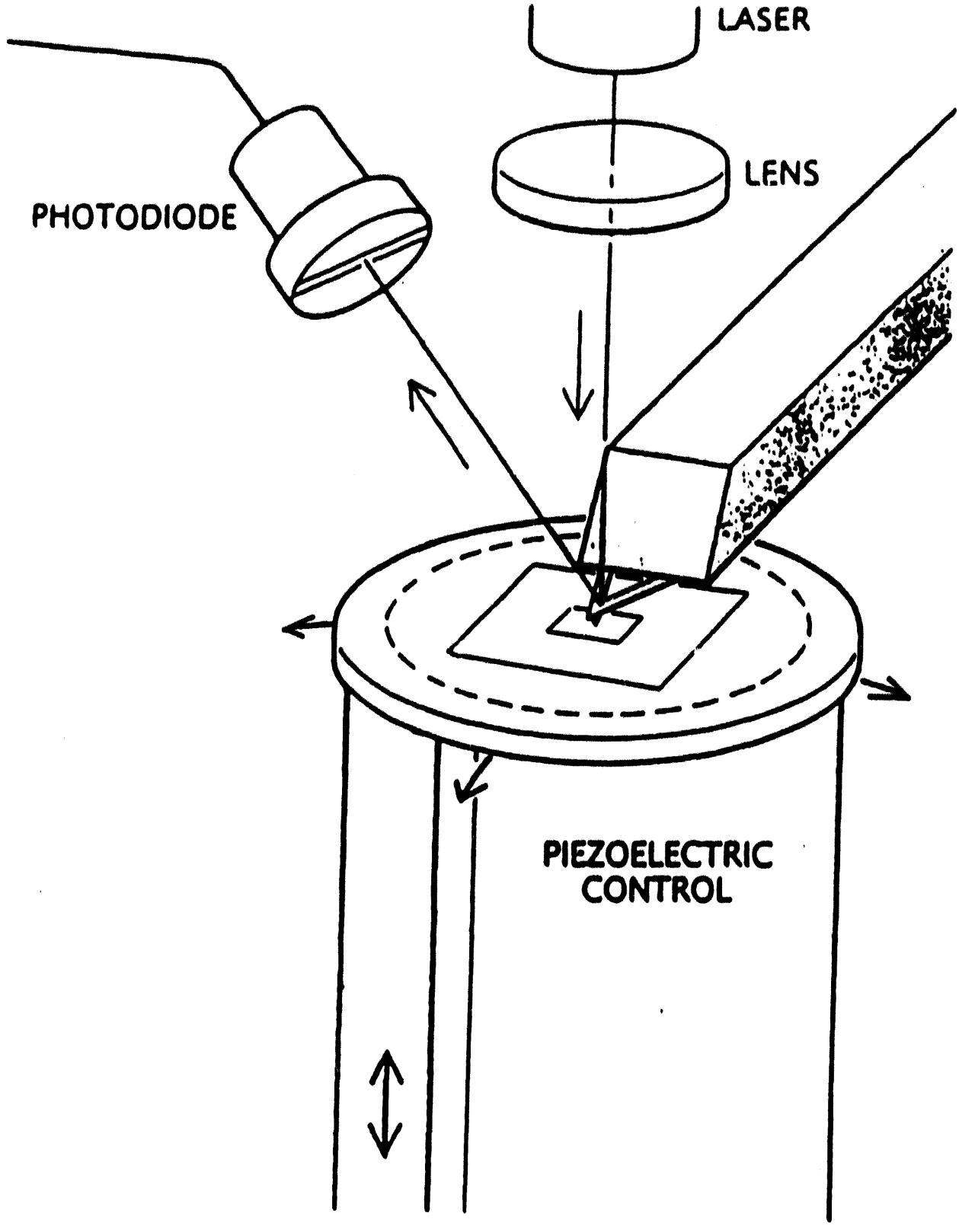

Fig. 5

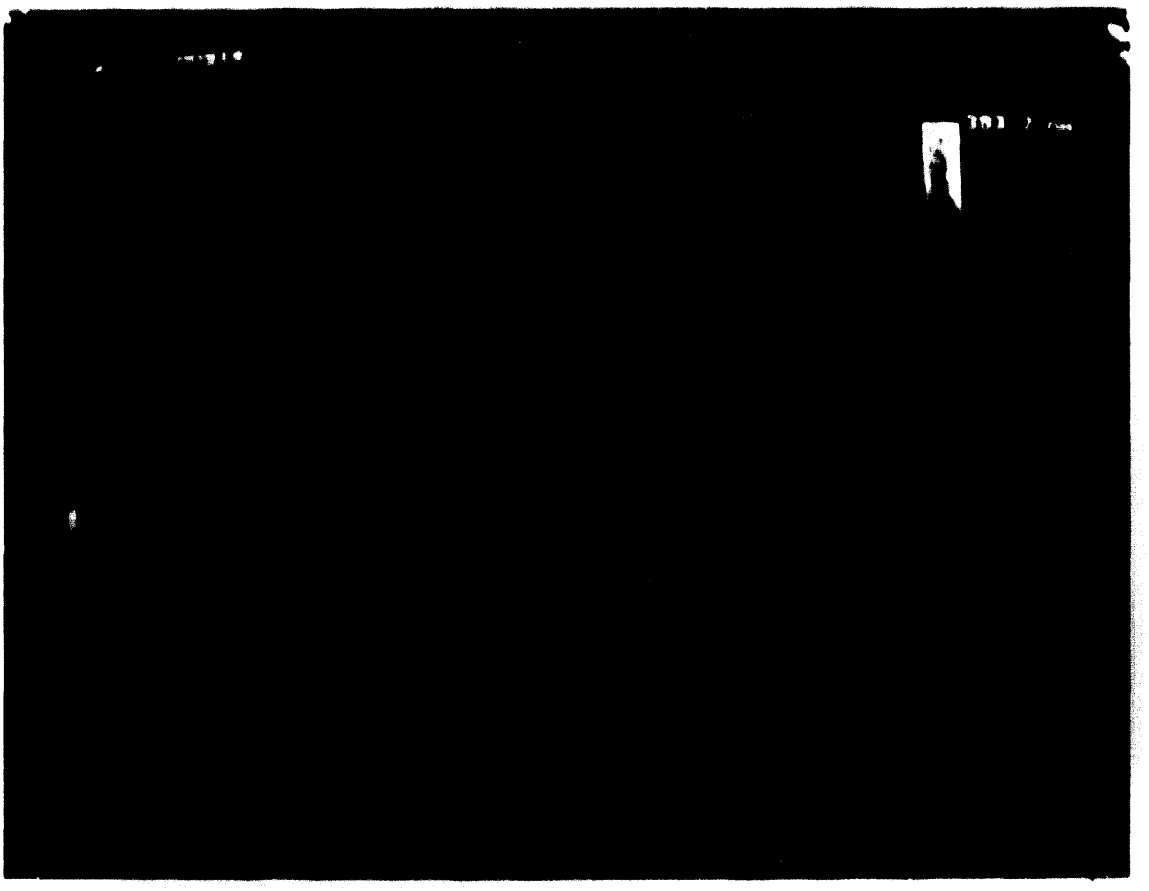

Fig. 6

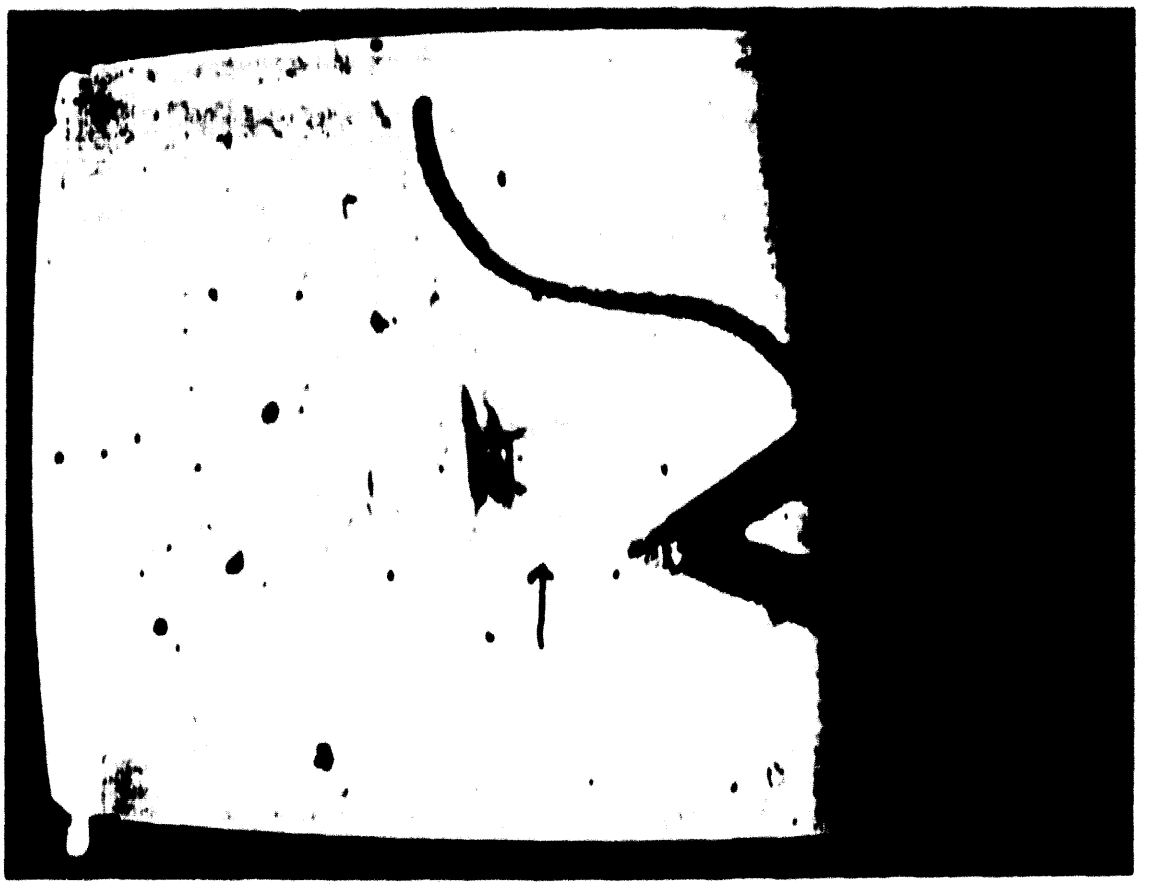

Fig. 7

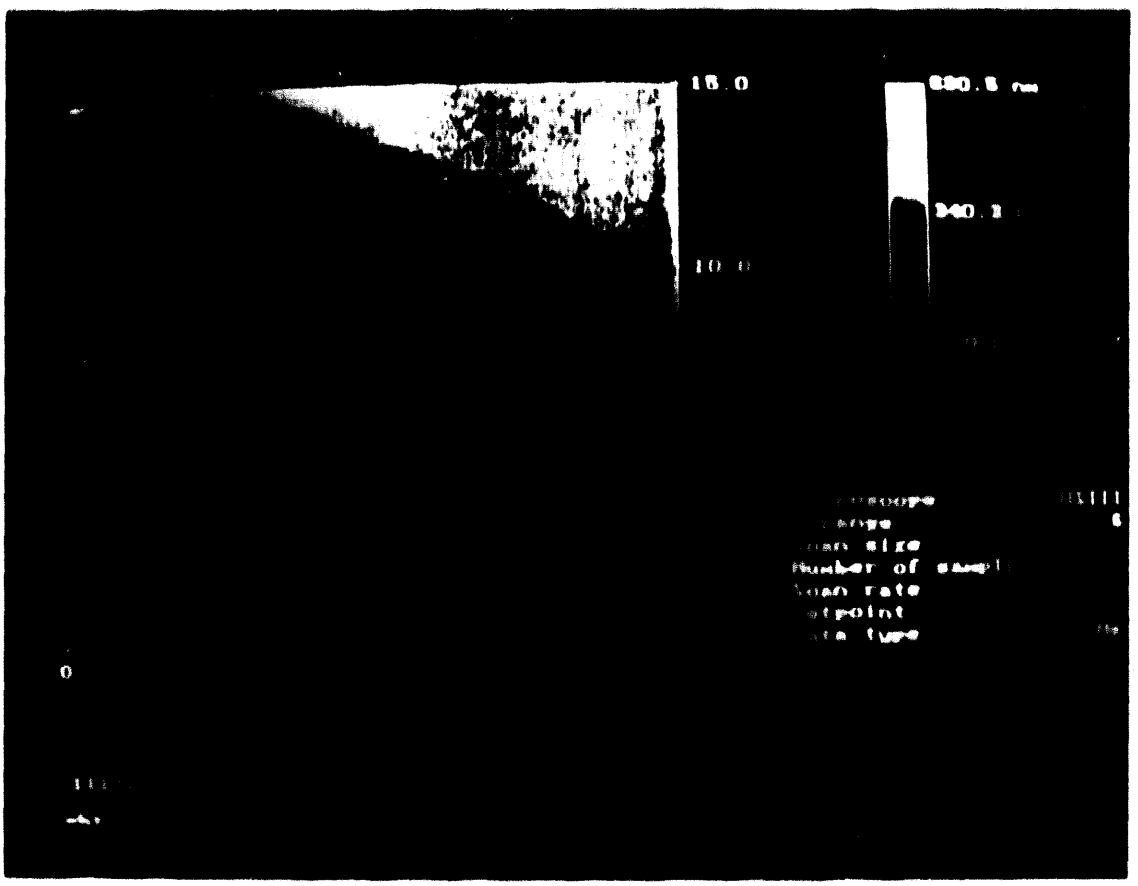

Fig. 8

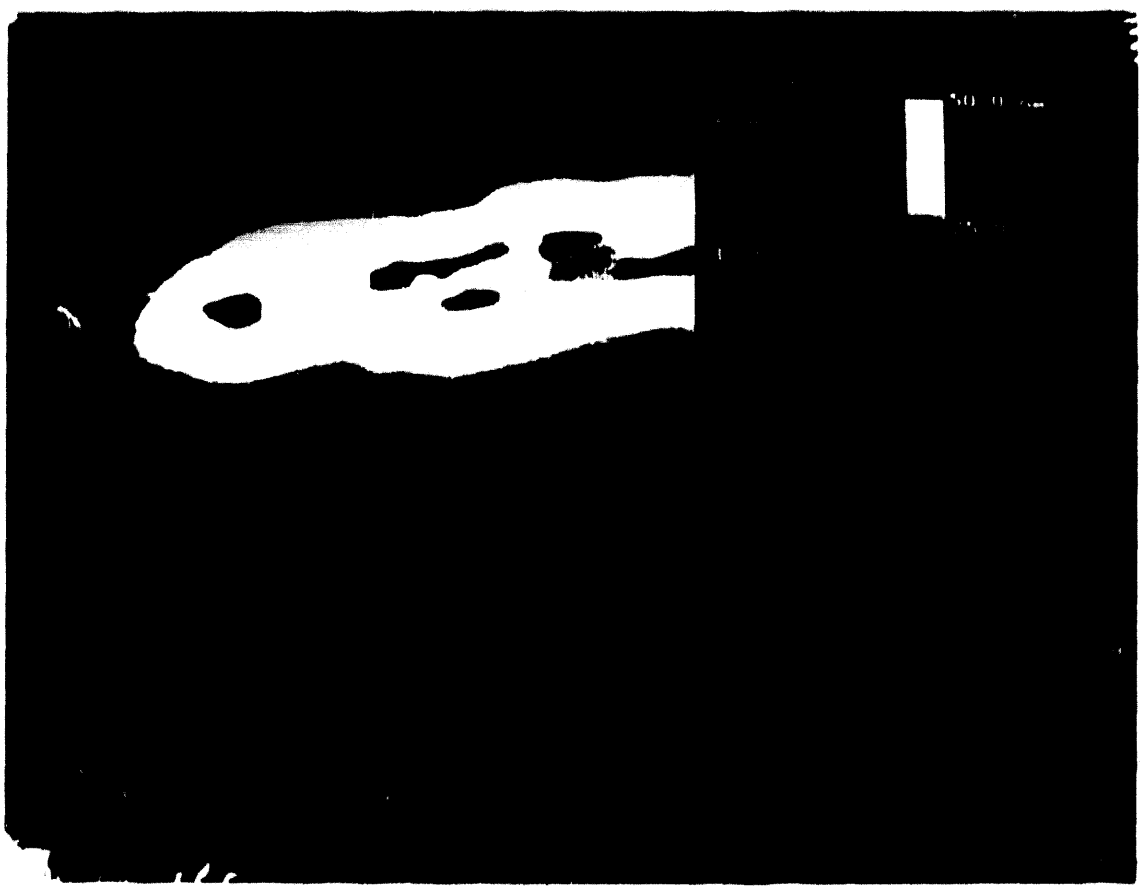

Fig. 9

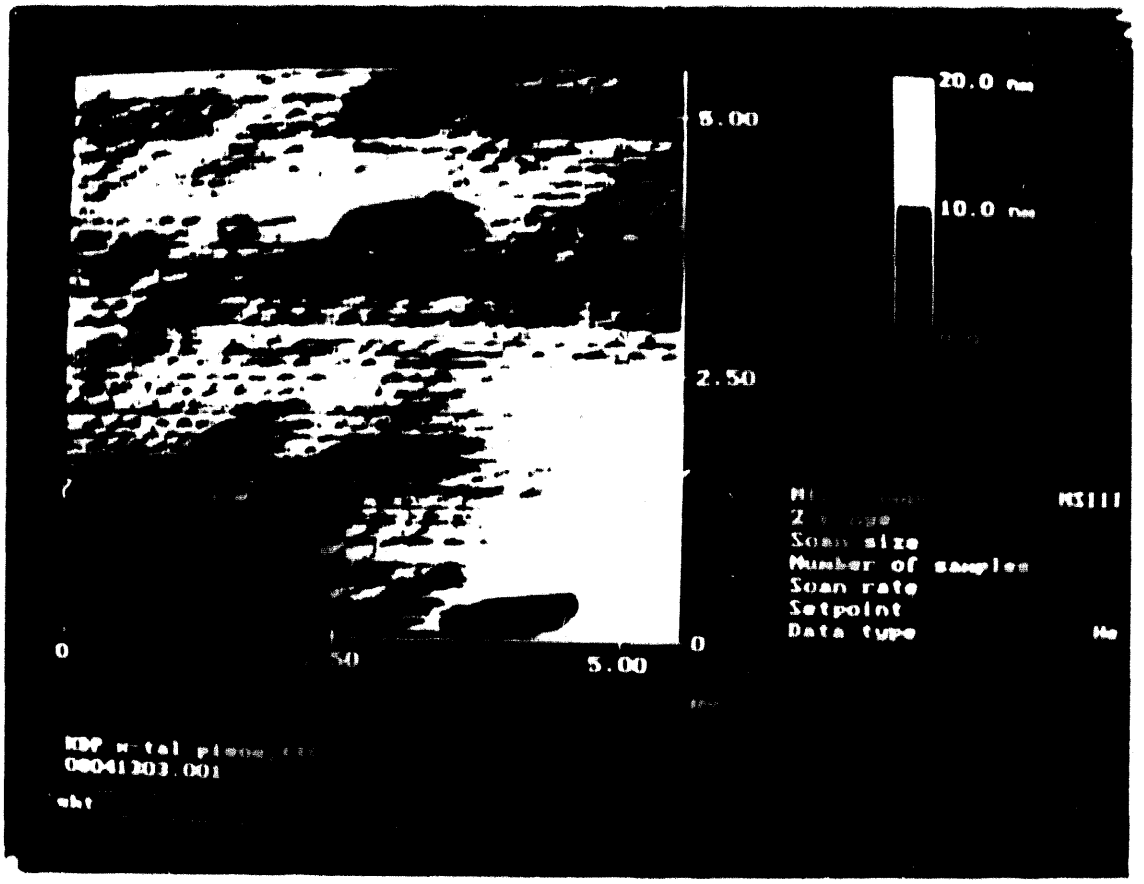
5.00
2.50
0
0
5.00
20.0
10.0
Scan size
Number of samples
Scan rate
Setpoint
Data type
08041303.001

Fig. 10

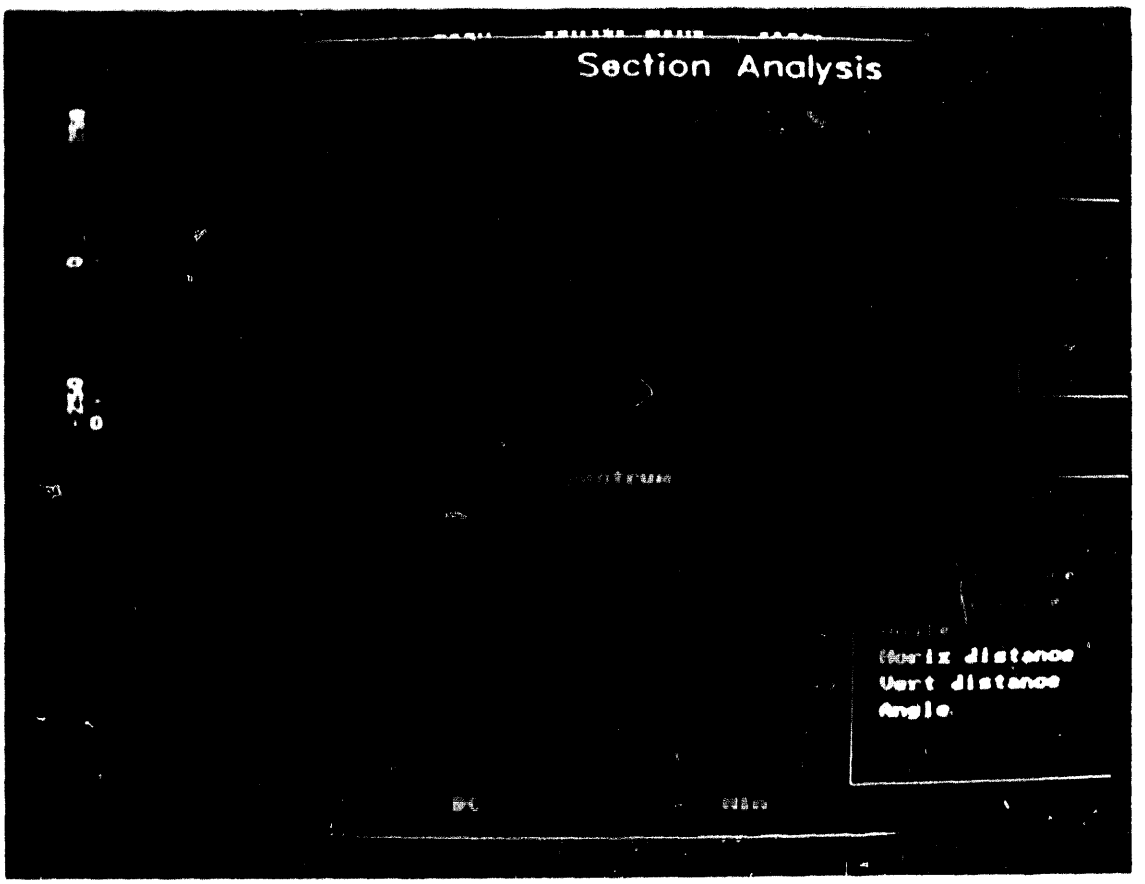

Fig. 11

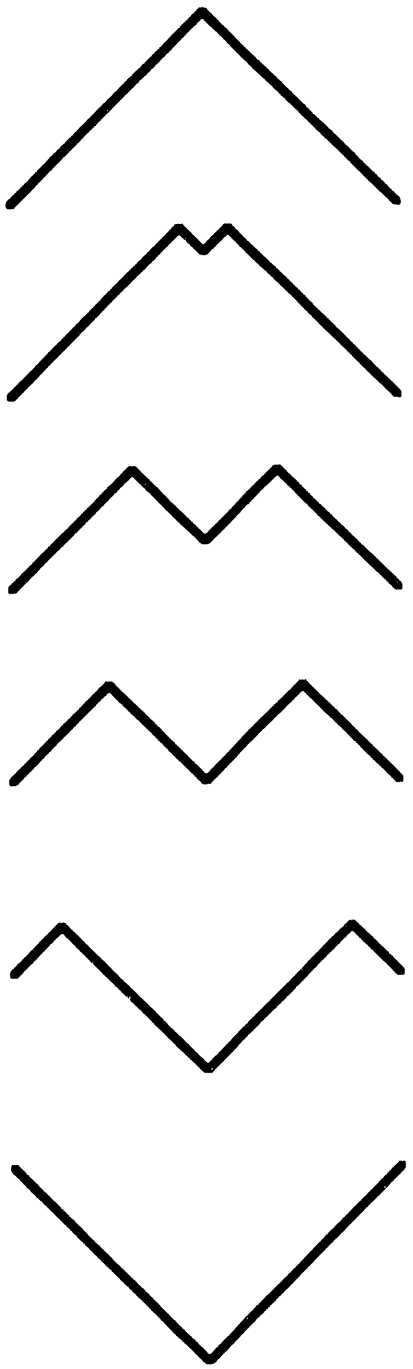

Fig. 12

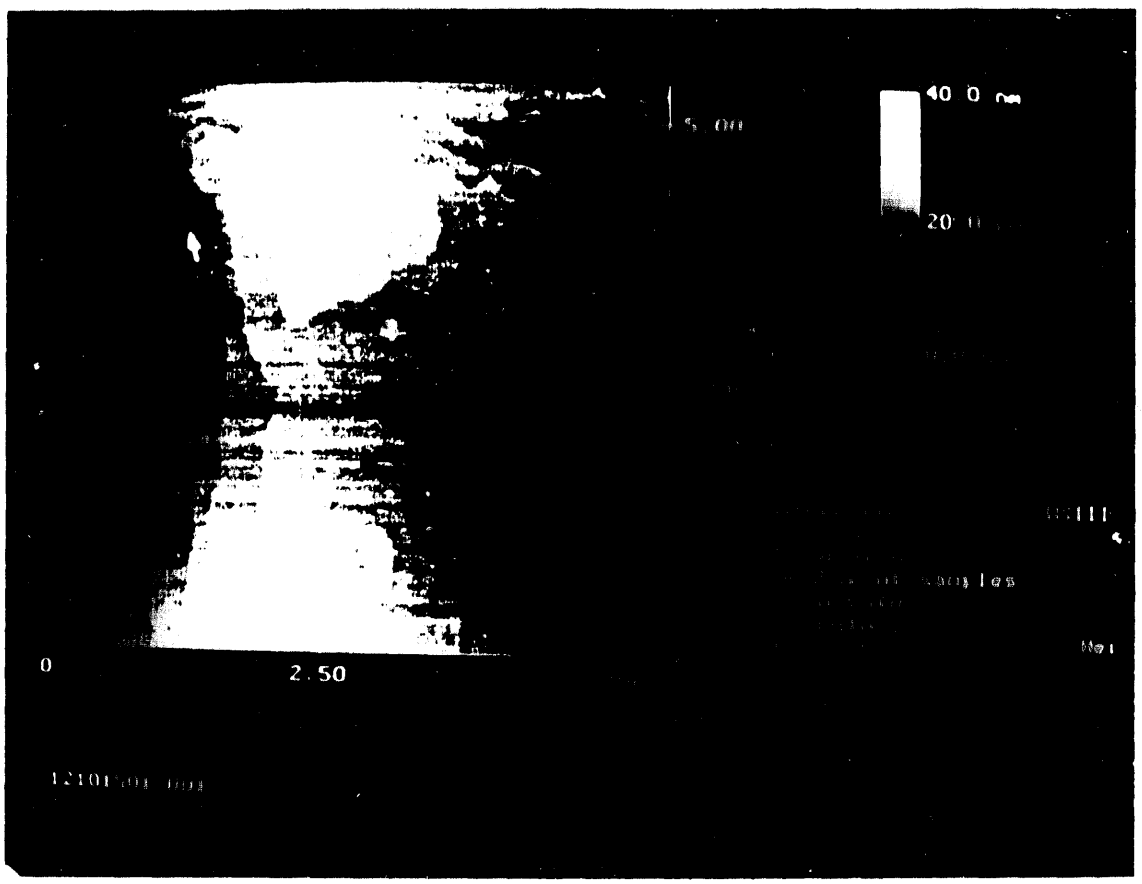

Fig. 13

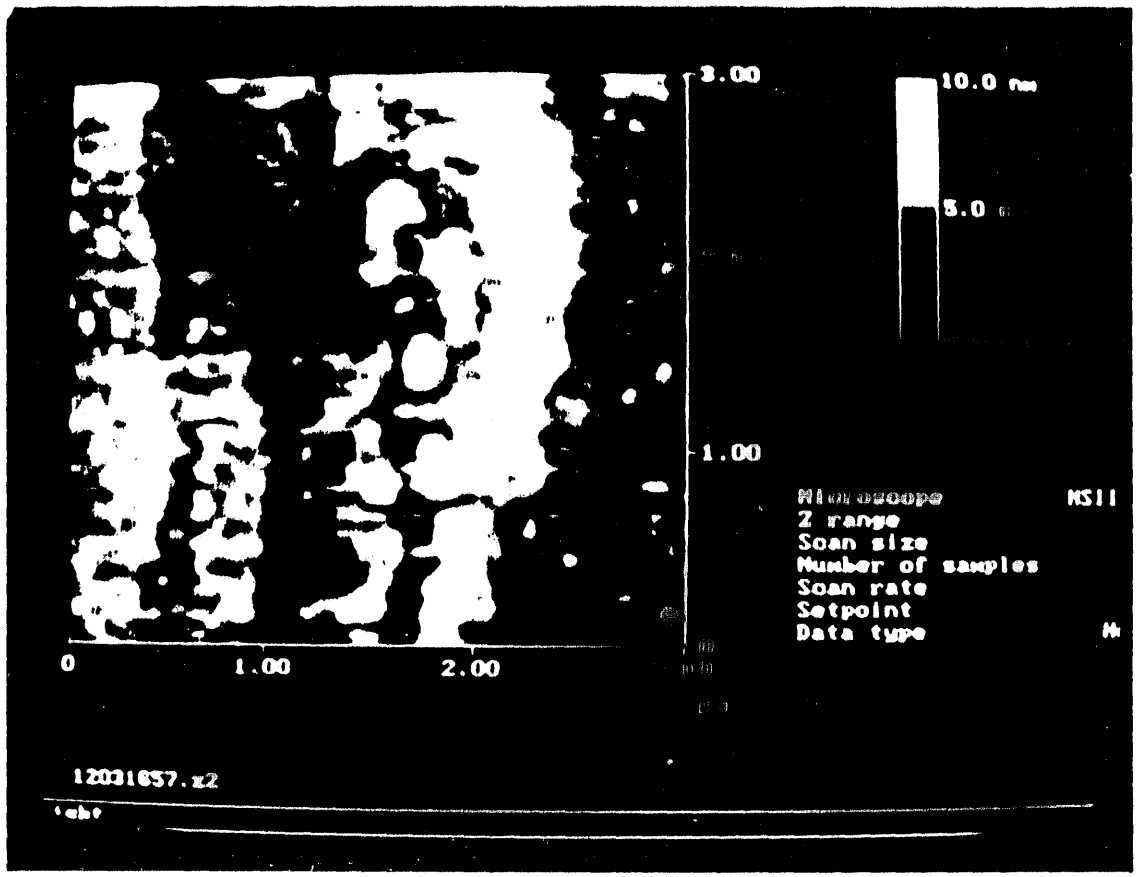
3.00
10.0
5.0
1.00
Z range
Soan size
Number of samples
Soan rate
Setpoint
Data type
0
1.00
2.00
12031657.x2

Fig. 14

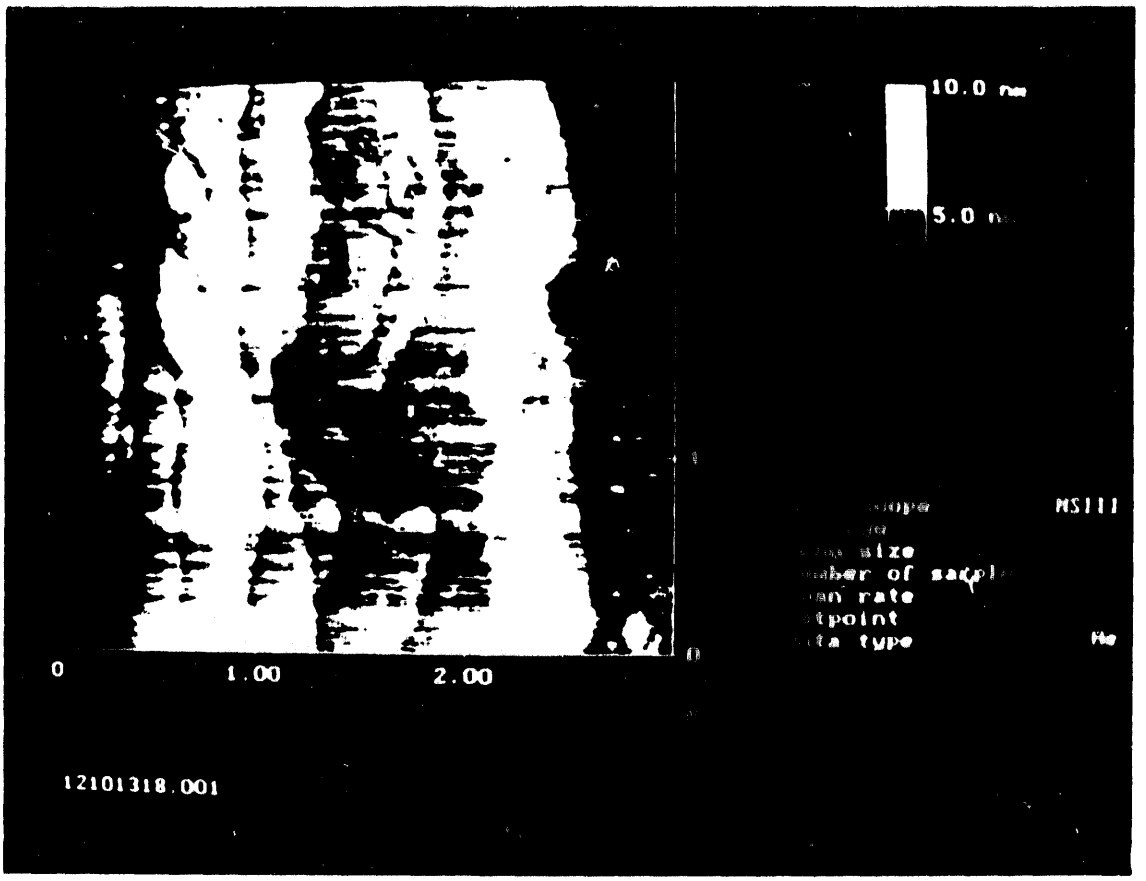

Fig 15

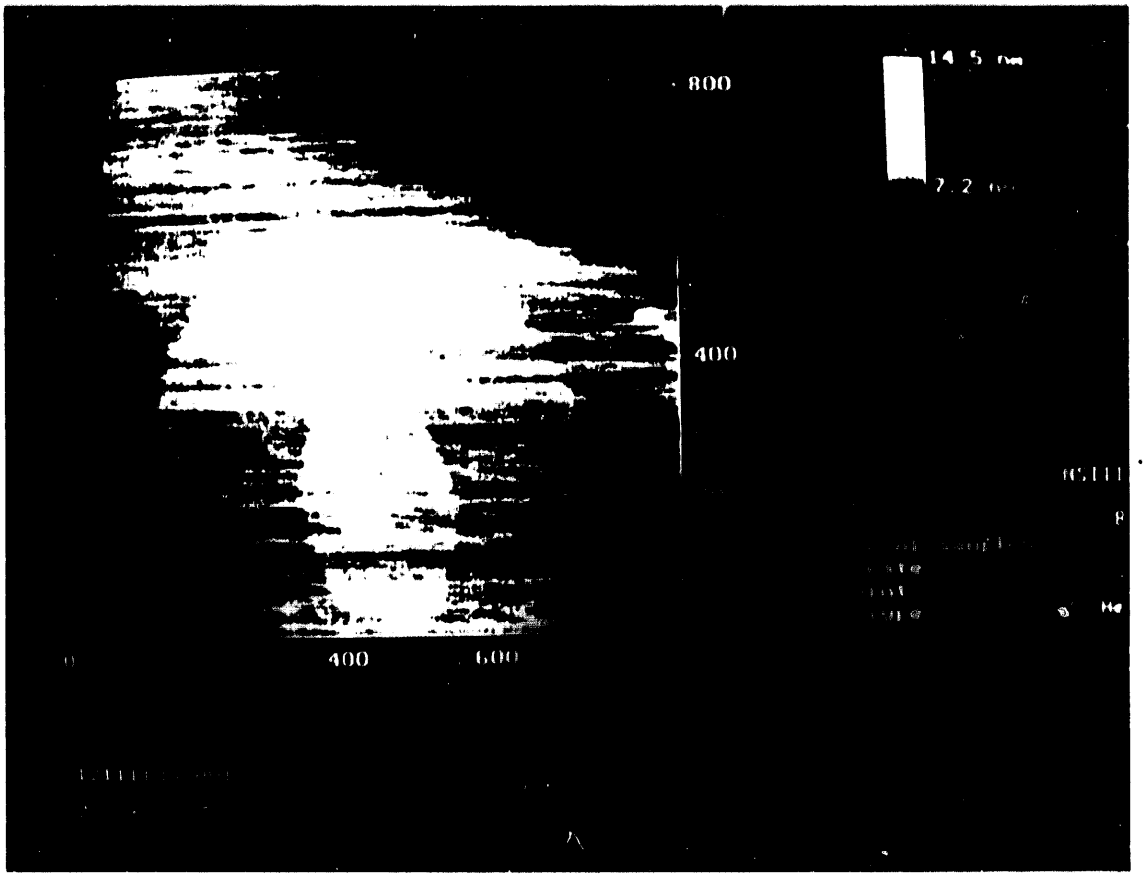

Fig. 16

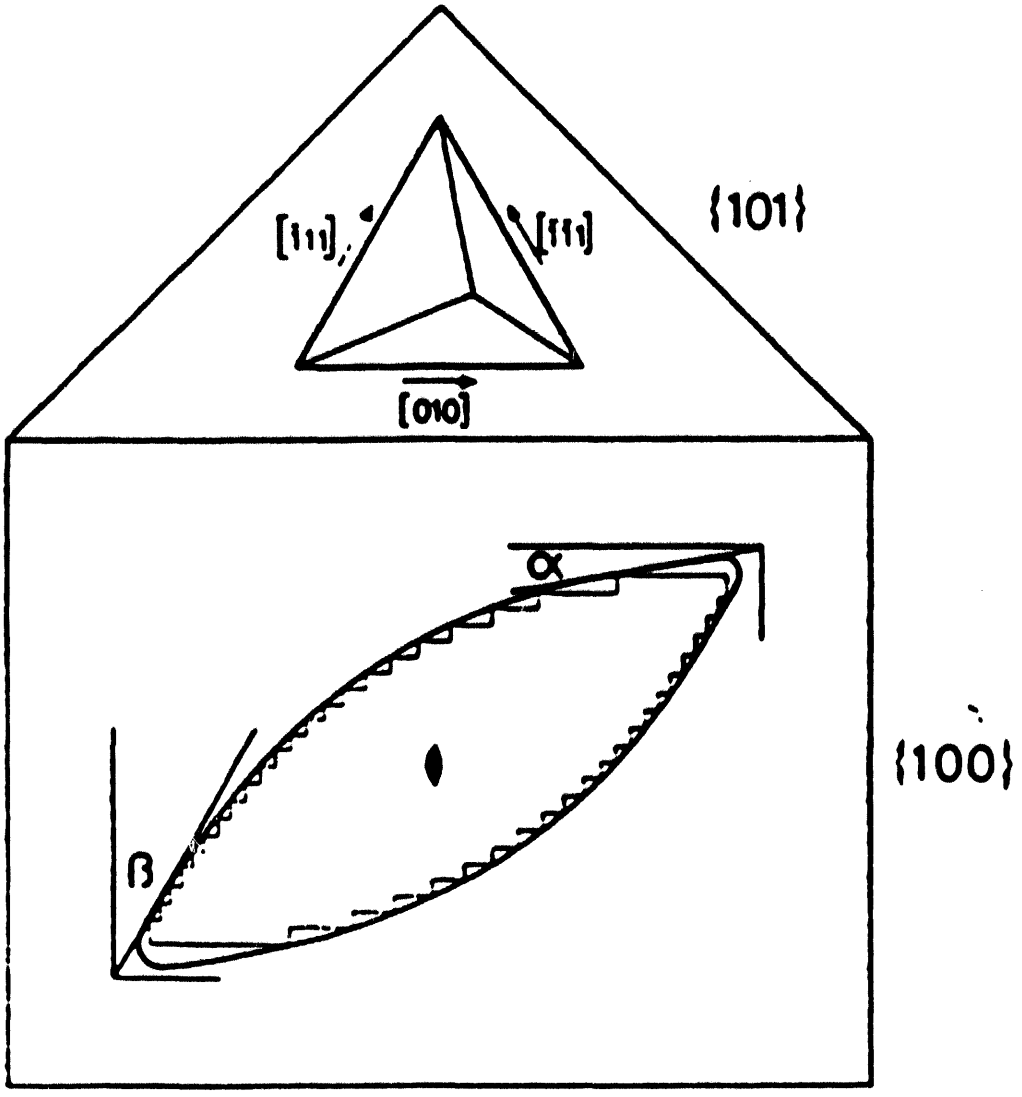

Fig. 17

Acknowlegements

I would like to thank these people for their incredible patience, support, and willingness to share knowledge, and whose help has made this semester very educational:

* Jim De Yoreo * (mentor)

Chris Ebbers

Terry Land

Phil Ambalal

Russ Vital

Kenneth Montgomery

Joe Lee

Identification and Organization of Genes on Chromosome 19

Mary Gable

University of California, Davis

Lawrence Livermore National Laboratory
Livermore, California 94550

December 18,1992

Prepared in partial fulfillment of the requirements of the Science and Engineering Research Semester under the direction of Harvey Mohrenweiser and Susan Hoffman, Research Mentors, at the Lawrence Livermore National Laboratory.

* This research was supported in part by an appointment to the U.S. Department of Energy Science and Engineering Research Semester (hereinafter called SERS) program administered by LLNL under Contract W-7405-Eng-48 with the Lawrence Livermore National Laboratory.

Abstract

One major goal of the Human Genome Project is to identify and determine the organization of the ~100,000 genes distributed across the 24 human chromosomes. Cosmid contigs associated with ~80% of chromosome 19 have been ordered and ~200 of the expected 2000 genes have been assigned. Chromosome 19 has an unusually large number of gene families, multiple, similar copies of a gene that have apparently arisen as a series of tandem duplications. One family, the RFX genes regulate class II HLA expression, and a mutation at the locus of RFX1 causes severe combined immunodeficiency disease (SCID). RFX2 and RFX3 are linked on an ~81kb contig, located on p13.2 to p13.3 while RFX resides at p 13.1 in an ~56kb contig. In a parallel effort, an anonymous cDNA fragment (1.2kb) from fetal brain is being characterized. This gene is expressed as a 3-4kb mRNA found in high levels in the heart, brian, placenta, lung, liver, and skeletal muscle. Using the 1.2kb fragment from the 3' end of the cDNA as probe, 9 probe-positive fragments were detected in an ~140kb contig while an additional 6 probe-positive fragments were detected in an ~40kb contig. Both were localized to 19p12. This organization suggests either a very large gene or a family of genes. Several of these cosmids contain zinc finger (regulatory) elements. Future efforts will focus on obtaining a full length cDNA and determining the function and organization of the gene.

Introduction:

The Human Genome Project is a collaborative effort which ultimately seeks to sequence each of the 24 human chromosomes. One of its major intermediate goals is to identify and determine the structure and organization of the ~100,000 genes distributed across the chromosomes. Once this map has been made, it should be possible to understand the origins of many genetic diseases. Individuals will likely always carry genetic defects, but as a result of these studies, newer, more advanced gene and drug therapies will be available to reduce suffering from genetic disorders. Also on the horizon are new molecules, proteins and natural pharmaceuticals, that may block disease-causing processes without altering the defective gene (3). But the ultimate therapy would be to substitute a normal gene for a defective one.

The Lawrence Livermore National Laboratory is participating heavily in this project by physically mapping chromosome 19. Chromosome 19 contains only about 2% of the total DNA in the human genome, but it is expected to contain approximately 2000 genes. Thus far, cosmid contigs associated with about 80% of this 60 megabase

chromosome have been ordered, and approximately 200 of the expected 2000 genes have been identified.

Chromosome 19 contains an unusually large number of gene families which are simply two or more structurally and functionally similar gene sequences. These multiple, similar copies apparently arise as a series of tandem duplications. It is often interesting to examine the evolutionary origins of these families. This can often provide insight in to the function of the various members of the family. This project concentrated on the RFX gene family and on an anonymous cDNA fragment which, from preliminary data, was originally thought to represent a gene family.

The RFX gene family has three known members, RFX1, RFX2, and RFX3, all of which are located on chromosome 19. RFX1 is a transacting DNA-binding regulatory factor which plays a role in the expression of the major histo-compatibility complex class II genes (2).

Three forms of major histocompatibility complex molecules called HLA-DR, HLA-DQ, and HLA-DP, have been identified. They are coded for by the α and β chain genes. These homologous and closely linked genes are found in the centromeric portion of the major histocompatibility complex, which is found on the short arm of chromosome 6 (6p). These class II molecules are involved in the presentation of antigens to T lymphocytes and are found as

receptors on the surface of many T cells. When the T cells are activated via these receptors by anything that is foreign to the body, they multiply to form a population of identical progeny which serve to activate the final steps in the immune response (2).

The expression of the HLA class II genes is controlled by two *cis* -acting DNA motifs, X and Y, which are located within the 150 base pairs upstream of the genes. Several protein factors, including the RFX's, have been found to bind to these sequences, and these factors show very specific contact points on the DNA (Figure 1). A form of hereditary immunodeficiency called HLA class II deficient severe combined immunodeficiency (SCID) is characterized by lack of expression of the HLA class II genes resulting from a defect in RFX1 (2).

Additional evidence for the role of RFX1 was obtained when it was shown that overexpression of RFX in transfected cells causes transactivation of the HLA class II promoter. It was also found that antisense RNA to the RFX gene expressed in transfected cells results in reduced expression of HLA-DR genes in these cells. Clearly, RFX is an important regulator of HLA class II gene expression. Another RFX gene, RFX2, has been found to show identical DNA binding characteristics, but definitive experiments

similar to those performed with RFX1 have not yet been conducted.

HHCC76 is a 1.2kb fragment of cDNA fragment which was isolated from a fetal brain tissue library and localized to chromosome 19 using PCR mapping. The small fragment sequenced thus far has no homology with any sequence currently in the GenBank and Pir data bases. Potential functions for this gene are unknown (1).

Purpose:

There were two major goals for this project: (1) to identify the structure and organization of the RFX gene family on chromosome 19 and (2) to characterize HHCC76 meaning that it was necessary to determine as much about the gene(s) as was possible. This entailed determining the gene or gene family's organization on the chromosome and characterizing the gene(s) in sufficient detail to suggest a function.

Methods and Materials:

Before a DNA library for chromosome 19 could be obtained, numerous copies of the chromosome were cut with a frequent-cutting restriction enzyme. By controlling

the experimental conditions so that the DNA was not cut at all possible sites, a population of overlapping fragments averaging 35 to 45kb in size was obtained. Then, COS genes were inserted into plasmids resulting in vector molecules (in this case, the Lawrist cosmid vector) that could have inserts of up to 45kb. These vector molecules were used to transport the individual fragments into *E.coli* , which were permitted to form bacterial colonies. The entire collection of bacterial colonies became the DNA library. Recombinant molecules were collected from the colonies, and the DNA was isolated from thousands of these clones. These clones or cosmids were arrayed in a high density fashion on filters which were probed with the relevant cDNA fragments in order to determine which cosmids contained the sequence of the gene in part or in whole (3).

Approximately 12,000 of these DNA clones have been "fingerprinted." This was done by cutting each clone into pieces which were tagged with a fluorescent dye. Next, the pieces were placed in a polyacrilimide gel and separated by electrophoresis. The pattern of DNA fragments down each lane of gel was visualized by exciting the fluorescent dye on each of them with a laser beam as they passed through a fixed window. The unique pattern of bands (number and size) for each clone was its fingerprint. A computer program used algorithms and the cosmids' fingerprint data

to compare the clones in a pair-wise fashion. Cosmids that shared a significant number of fragments were assumed to overlap and thus formed a contig . The contigs were graphically displayed and linked via a relational database to all other biological and notebook information using a display called Browser. In addition to assembling cosmids into contigs, the information from Browser was used to suggest additional experimental strategies (3).

Once contigs for HHCC76 and the RFX family had been ordered, the locations of these contigs were determined using fluorescence *in situ* hybridization (FISH). A representative clone was selected from each contig, fluorescently tagged, and hybridized to a metaphase spread of human chromosomes. Fluorescent dots appeared at specific sites on chromosome 19.

RFX Gene Family

A pool of probes consisting of the partial cDNAs, obtained from collaborators, for RFX1, RFX2, and RFX3 were hybridized to the library filters. Probes were made by radioactively tagging randomly located cytosine bases on the single strands of DNA. (Refer to the Figure 2 for information on the insert sizes and their restriction enzymes.) The three probes were combined and hybridized

to the library filters overnight. Altogether thirty-one probe-positive cosmids were isolated from the library; they were then examined by digesting them with EcoR1 and separating the restriction fragments by electrophoresis on a 1% agarose gel. The DNA fragments were then transferred to nitrocellulose membrane filters (Southern blotting). The blots were probed with RFX1, RFX2, and RFX3 separately.

HHCC76

HHCC76 was an anonymous cDNA fragment. The insert was 1.2kb in length, and when it was cut out of the vector by EcoR1, it was cut into two fragments (one of 0.4kb and one of 0.8kb). The cosmid library filters were probed with the 0.8kb fragment and the 0.4kb fragment on different occasions. The probe-positive cosmids were digested with EcoR1 and the fragments separated on a 1% agarose gel. The Southerns were made via neutral transfer. They were probed with the total 1.2kb insert, the 0.4kb fragment, and the 0.8kb fragment at different times.

Finally, a commercially-made northern blot of mRNA from various human tissues was probed with the 0.4kb and the 0.8kb fragments separately in order to define a pattern of gene expression.

Results:

Twenty-four cosmids were found to be probe-positive for RFX1 while 7 were positive for RFX2. RFX3 did not reveal any probe-positive cosmids when the unique 316bp fragment was used, so the entire 2kb insert was used to probe the Southerns a second time. The results of the second probing indicated that the same 24 cosmids that were positive for RFX1 were also positive for RFX3. It was discovered that RFX3 not only probed positive for the same band as RFX1 did, but that it probed positive for an additional smaller band. At present, there is no indication as to why the small fragment of RFX3 failed to probe positive for any of the cosmids, and further experimentation will be necessary in order to determine which cosmids are representatives of RFX1 versus RFX3.

Previous data placed RFX1 on 19p13.1 while RFX2 was found on 19p13.2-19p13.3 by *in situ* hybridizing on chromosome spreads obtained from phytohemagglutinin-stimulated peripheral blood lymphocyte cultures from three normal male donors (2). (A verification of these results using FISH data is forthcoming.) Therefore, RFX2 and RFX3 were placed on one contig while RFX1 was placed on its own contig. The results of these probings permitted the formation of two contigs using basic restriction mapping techniques. The restriction map for

the RFX1 positive cosmids contig was ~51kb in length and contained 10 cosmids, 5 of which were probe- positive. RFX1 was located on an 11.5kb EcoR1 fragment. RFX2 and RFX3 positive cosmids were found in the same contig of ~82kb in length containing 6 probe-positive cosmids for RFX2 and 9 probe-positive cosmids for RFX3. RFX2 was found on a 9kb EcoR1 fragment while RFX3 resided on a 4kb EcoR1 fragment (Figure 3). In addition to these two contigs, a third contig was assembled which contained the other 8 probe-positive cosmids for RFX1 and RFX3 (Figure 4).

HHCC76

Thirty library cosmids were found to be probe-positive for HHCC76. Most of these cosmids along with >12,000 others were displayed on Browser as being part of >1000 contigs. With the aid of Browser, subsequent EcoR1 restriction enzyme digest mapping resulted in the formation of an ~140kb contig containing 9 probe-positive fragments and an additional ~40kb contig containing 6 probe-positive fragments (Figure 5). No obvious functional motifs with the exception of zinc fingers (finger-shaped protein structures found in DNA binding proteins which help them to bind by inserting into the wide groove of the DNA) have been identified within these contigs. Analysis of the restriction

digest maps identified two cosmids which could be used for fluorescence *in situ* hybridization. Representative probe-positive cosmids for each contig mapped to 19p12 on metaphase spreads of chromosomes.

The northern blot probed with the 0.8 DNA fragment indicated that HHCC76 is expressed in high concentrations in the brain, lung, heart, and placenta, with minimal expression in the liver and skeletal muscle. Transcripts of different sizes are observed in different tissues. An ~3-4kb fragment is observed in the brain, lung, liver, and placenta while a slightly larger, ~4.5kb fragment is observed in the muscle tissue. Finally, an additional ~6kb fragment is observed in the lung.

When the 0.4kb fragment was hybridized to the northern, it was found to be expressed as an ~3-4kb fragment in the brain and lung tissues.

Discussion:

RFX Family

Details of the structure and organization of the RFX family will be useful for continuing studies of the functions and regulation of expression of the RFX family members. The location of the genes on the chromosome has now been

identified, and RFX1 in comparison to RFX2 and RFX3 has been found in a different location on the chromosome. Also, the fact that there is a third contig may point to the existence of a fourth RFX gene. This information will be essential as more is learned about the binding characteristics of the RFX members. For example, we may be able to heighten the immune response not only in those afflicted with SCID but in the average person, thereby decreasing a person's chance of contracting a disease or, at the very least, shortening the course of the infection. This could be done by regulating the expression of the class II immunoglobulins using the RFX proteins. But in order to successfully manipulate the proteins, the RFX genes' location and function must first be clearly understood.

HHCC76

HHCC76 is found on two contigs of ~140 and ~40kb in length which contain several zinc finger regulatory elements. The two contigs representing the structure of HHCC76 both contain probe-positive fragments at their tail ends which would indicate that there may be additional probe-positive regions on the chromosome which have not yet been identified. The *in situ* data places the contigs on 19p12 and indicates that they are ~4nm apart. Since they

digest maps identified two cosmids which could be used for fluorescence *in situ* hybridization. Representative probe-positive cosmids for each contig mapped to 19p12 on metaphase spreads of chromosomes.

The northern blot probed with the 0.8 DNA fragment indicated that HHCC76 is expressed in high concentrations in the brain, lung, heart, and placenta, with minimal expression in the liver and skeletal muscle. Transcripts of different sizes are observed in different tissues. An ~3-4kb fragment is observed in the brain, lung, liver, and placenta while a slightly larger, ~4.5kb fragment is observed in the muscle tissue. Finally, an additional ~6kb fragment is observed in the lung.

When the 0.4kb fragment was hybridized to the northern, it was found to be expressed as an ~3-4kb fragment in the brain and lung tissues.

Discussion:

RFX Family

Details of the structure and organization of the RFX family will be useful for continuing studies of the functions and regulation of expression of the RFX family members. The location of the genes on the chromosome has now been

identified, and RFX1 in comparison to RFX2 and RFX3 has been found in a different location on the chromosome. Also, the fact that there is a third contig may point to the existence of a fourth RFX gene. This information will be essential as more is learned about the binding characteristics of the RFX members. For example, we may be able to heighten the immune response not only in those afflicted with SCID but in the average person, thereby decreasing a person's chance of contracting a disease or, at the very least, shortening the course of the infection. This could be done by regulating the expression of the class II immunoglobulins using the RFX proteins. But in order to successfully manipulate the proteins, the RFX genes' location and function must first be clearly understood.

HHCC76

HHCC76 is found on two contigs of ~140 and ~40kb in length which contain several zinc finger regulatory elements. The two contigs representing the structure of HHCC76 both contain probe-positive fragments at their tail ends which would indicate that there may be additional probe-positive regions on the chromosome which have not yet been identified. The *in situ* data places the contigs on 19p12 and indicates that they are ~4nm apart. Since they

are not a large distance from one other, one immediate goal will be to try to link the two contigs together.

The organization of the HHCC76 "gene" indicates that there are several clusters of probe-positive fragments separated by probe-negative regions. This clustering could be indicate that there are a number of pseudogenes on the chromosome. That is, a portion of the sequence of the whole gene may be tandemly repeated along this region of the chromosome. A more straightforward conclusion could be that HHCC76 is a gene family containing 4 or possibly 5 members.

Once the final structure of the gene(s) has been determined, the next step will be to define the function of the gene. The results of the northern blots indicate three things. First they point out that HHCC76 is indeed an expressed gene because it binds to the mRNA in several tissues. Second, it indicates in which tissues the gene is expressed and by looking at how strong the probe-positive band on the filter is, an estimation of how strongly it is expressed in certain tissues can be made. If this is indeed a gene family, the various members may be causing different sized transcripts to be synthesized in the assorted tissues. Third, there is a different banding pattern for the 0.4kb fragment in comparison to the 0.8kb fragment, therefore the expression of the two is different. This information will

provide important clues in determining the ultimate function of the gene. As of yet, it is difficult to guess at a function for the gene, but once a full-length cDNA is identified, sequenced, and characterized, the exciting aspects of the problem, namely understanding the metabolic/physiological role of this gene(s), will be initiated.

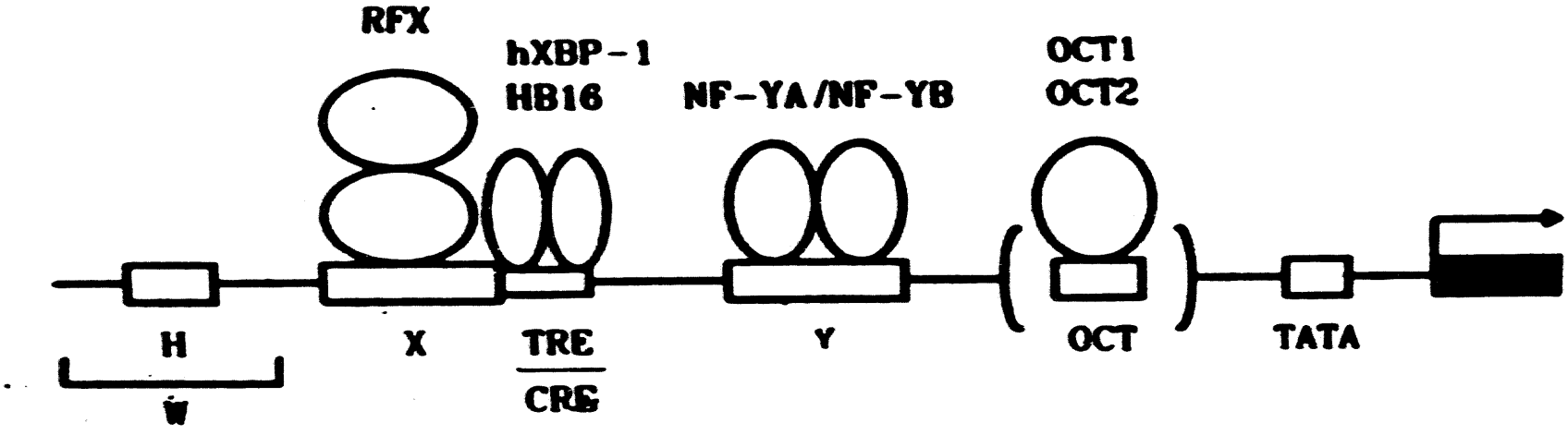

Figure 1. Schematic representation of the factors known to bind to the HLA DRA promoter.

Gene Family Member	Fragment Length	Restrict. Enzymes
RFX1	150bp	EcoR1
RFX2	300bp	BamHI + SalI
RFX3	316bp	XhoI + NcoI

Figure 2. Table indicating the sizes of the RFX fragments and their individual restriction enzymes.

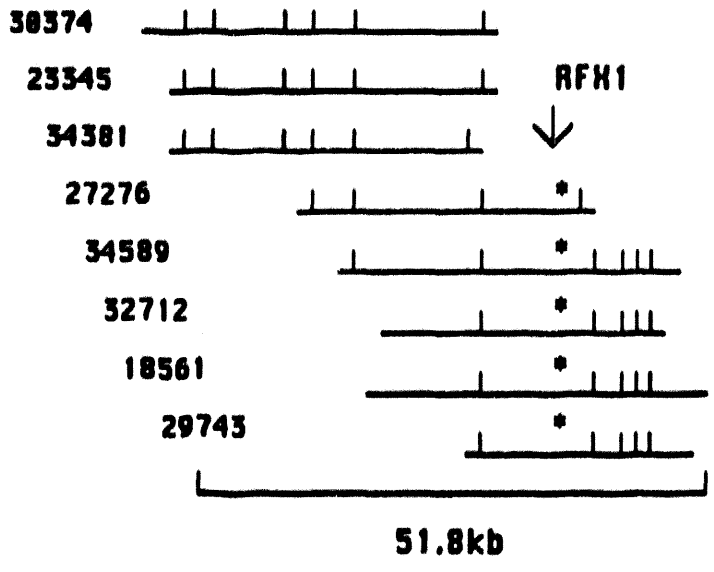

RFH1 is located on its own 51kb contig.

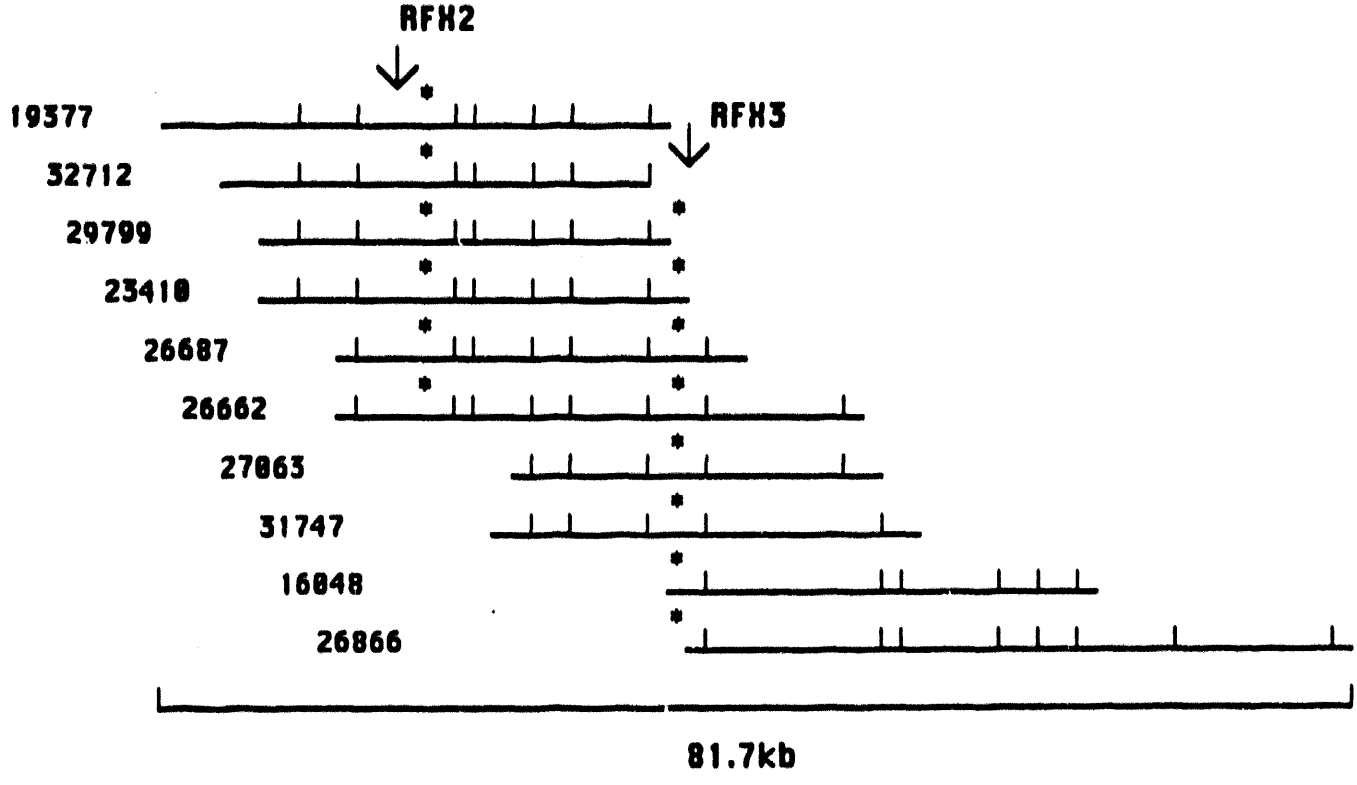

RFH2 and RFH3 are located on a separate 81kb contig.

Figure 3. Restriction maps of RFH1, RFH2 and RFH3.

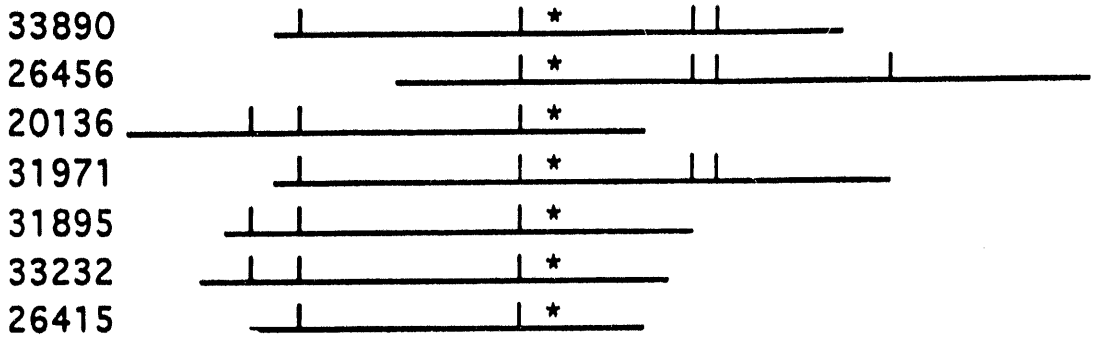

Figure 4. The third probe-positive contig for RFX family.

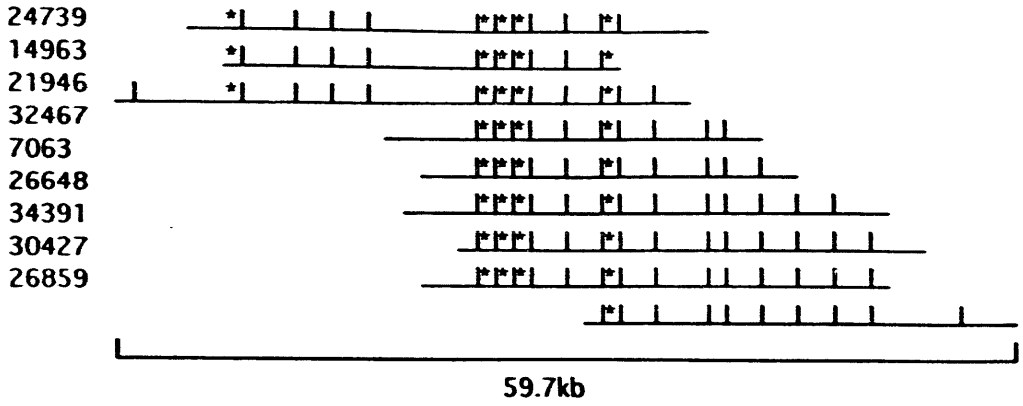

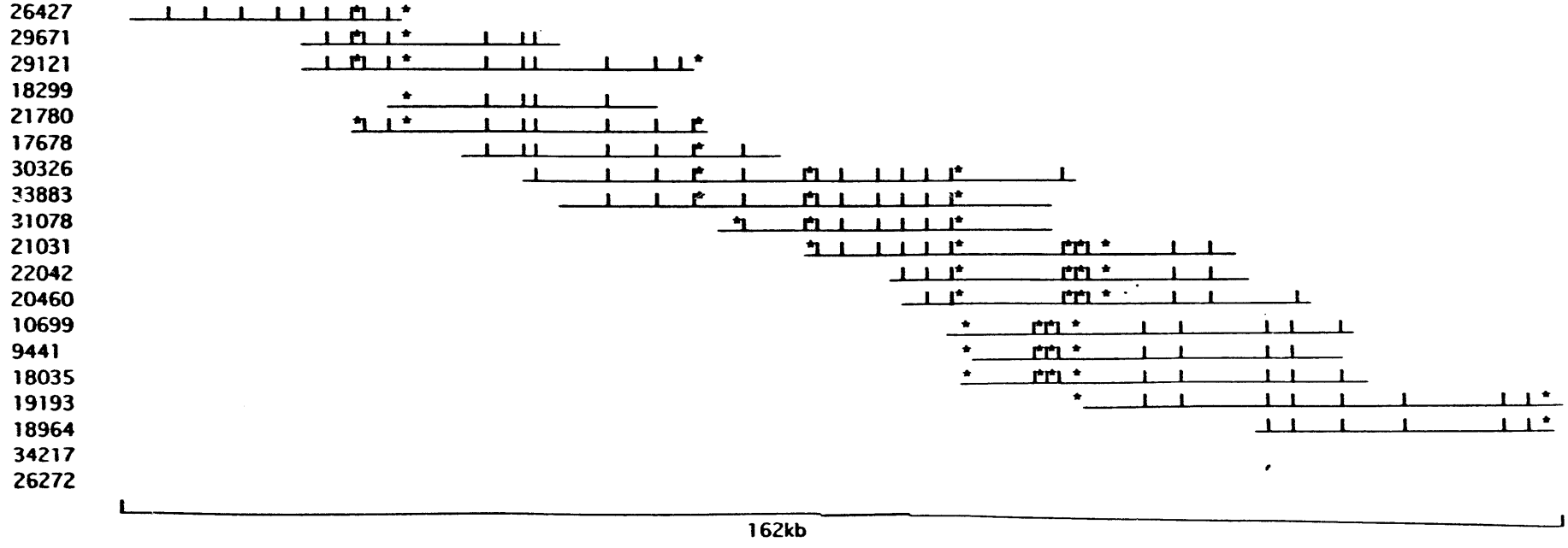

Figure 5. Restriction map of HHCC76.

References

1) Adams, M. D., Kelley, J. M., Gocayne, J. D., *et al.* (1984). Complemetary DNA sequencing: expressed sequence tags and the human genome project. Science. 252:1651-1656.

2) Pugliatti, L., Derre, J., Berger, R., Ucla, C., Reith, W., and Mach, B. (1992). Genes for MHC class II regulatory factors RFX1 and RFX2 are located on the short arm of chromosome 19. *Genomics.* 13:1307-1310.

3) Sefcik, J. A. (1992). The human genome project. *Energy and Technology Review.* 2:29-56.

Acknowledgements

I would like to thank the following people for their patience and understanding and most of all for sharing their vast knowledge with me:

Harvey Mohrenweiser
Susan Hoffman
Susan Tsujimoto
Gisela Shonnard
and
Chris Conner

Boron Carbide-Aluminum Cermet Processing

Jeffery J. Hasiam
University of Kansas
Chemistry and Materials Science

ABSTRACT

Discussion of challenges encountered in the preparation of boron carbide powder and the slip casting procedures used to form boron carbide compacts. Data is given relating the volume percentage of boron carbide in the slip with the solids density in the boron carbide compacts formed from the slip casting process. A description is given of the aluminum infiltration process and some possible effects of various alloying constituents upon the infiltration. Discussion of challenges for large-scale production and potential solutions for producing boron carbide-aluminum cermet parts.

Introduction

The Boron Carbide-Aluminum Cermet project has evolved considerably since the first attempts to produce this material. There are many methods for producing the cermet including: cold pressing and infiltrating, Hot Isostatic Pressing of B_4C and aluminum powders, slip casting and infiltration, and hot pressing and infiltrating. Each approach has its unique advantages and trade-offs and produces a similar chemistry but different microstructure and properties. For our purpose, slip casting was used to obtain B_4C compacts which were then infiltrated with molten aluminum. The slip casting process develops a reasonably dense, coherent compact. During infiltration and subsequent heat treatment, the aluminum reacts with the B_4C and forms binary and ternary phases of boron, carbon, and aluminum. The densities of the phases formed are comparable to the densities of boron carbide and aluminum. This prevents the formation of voids and reduces the risk of cracking and failure of the parts due to internal stresses created by volume changes of phases formed during the infiltration.

The formation of a good slip for slip casting is dependent on the ionic properties of the particles being suspended and the ionic behavior of the solvating solution. It is desired to disperse the particles in the slip so that the particles do not come near each other or have the opportunity to clump together. Clumping increases the viscosity of the slip, makes the casting difficult, and thus results in a compact of low density.

The goal of the project is to measure the physical properties of the cermet and to analyze the microstructure of the samples produced. The physical property measurements will be useful in demonstrating that the material is suitable for specific engineering applications. It is also likely to lead to further development and improvement of the material and new uses. Several issues currently under study are the effects of heat treatment, modifying the cermet by infiltrating with aluminum containing alloying elements, and the effects of the ratio of aluminum to boron carbide. Analysis of the microstructure by electron microprobe is expected to yield information about the location of constituent elements and the phases formed in the cermet. It will be useful to know whether specific alloying elements end up on grain boundaries and whether this correlates with changes in any of the physical properties. X-ray diffraction analysis will be used to identify the phases present in the samples and determine their proportions.

Procedure

Acid washing of the boron carbide powder followed by rinsing with water is effective in preparing the powder for slip casting. Hydrochloric acid dissolves calcium ions in aqueous solutions. The calcium ions are detrimental to the quality of the slip used in the slip casting. Boron carbide powder with a nominal 1500 grit size is used for the slip casting. The powder is weighed into 250 ml High Density Polyethylene (HDPE) bottles in 100 gram quantities. 150 ml of 1.5 Molar hydrochloric acid is added to each bottle. The bottles are agitated by hand several times over an 18 to 24 hr period to wet the powder with the acid. Sonicating with an ultrasonic probe is used to break up large particles that do not go into a suspension easily. It is believed, based on previous work, that calcium ions interfere with the dispersing agent used to form the slip. This is reasonable because the calcium ion is divalent and can readily displace ions from the surface of the boron carbide particles. The calcium ions do not cause sufficient repulsion between particles to form stable slips. Emission Spectroscopy analysis performed previously confirmed that acid washing followed by rinsing with water reduced calcium in the powder by a factor of 10 or more (Stuart L. Weinland, unpublished notes) Presently, two acid washing steps are used followed by two rinse steps to clean the powder sufficiently to cast tiles with 60% boron carbide by volume.

The wash and rinse steps are performed in the same way with the exception of the use of water or acid. After the bottles have been agitated and allowed to sit for 18-24 hours, the bottles are balanced to within 0.1 g with De ionized water and then centrifuged at approximately 10,000 RPM for one hour. After decanting the supernatant, the bottles are placed in an air circulated drying oven at approximately 80 degrees Centigrade for 24 hours or until measurements of the mass of the bottles do not differ by more than 0.1 g over a 2 hour period. Usually this requires 36 hours for the acid washing steps and 24 hours for the water rinse steps due to differences in packing in the two media.

After the powder was washed and rinsed, the dried material was broken up by squeezing the bottles and dumping the powder into a series of screens containing a #9 and #24 Tyler screens. The powder was then weighed and oven dried for 1 to 2 hours at 80 degrees Centigrade. Weight losses generally ranged from 0.5 to 0.8 grams for a 600 g batch of washed powder. This was accepted as sufficiently dry. It is important that the boron carbide is dried sufficiently because drying forms a pore structure between the particles. The pores absorb water when the powder is saturated in the next step of the process. When the water enter the pores

of the dry boron carbide, it breaks the particles apart so that they will be suspended in the liquid. The fine particle size (around one micron or less) facilitates the suspension of small particles because the gravitational effects on small particles are not large compared to the kinetic action from Brownian motion.

The slip is formed with a 0.0074 Molar solution of ammonium hydroxide. This solution gives a pH between 10.4 - 10.6 that has been found to be the best for forming slips of boron carbide based on past experience. The pH of the solution is measured when a volume of the base is measured into a graduated cylinder and after the solution has been transferred to the Stainless Steel beaker for mixing the slip. The pH generally does not change more than 0.1 pH unit. The pH meter used has an accuracy of approximately 0.2 pH units. The volume of ammonium hydroxide used is determined by estimating the volume required for a 50 volume percent (v%) mixture for the amount of washed boron carbide available. Boron carbide has a density of 2.52 g/cc. Whenever possible, the containers containing solutions of the ammonium hydroxide were covered to prevent excessive volatilization of ammonia from the solution. (It should be kept in mind that the ammonium hydroxide solutions are labeled by the weight percentage of ammonia and not ammonium hydroxide which usually makes up the balance of the solution.) The mixer is run at 500 RPM with a high shear blade. The boron carbide powder is added progressively to the ammonium hydroxide solution. The amount of boron carbide added is monitored and as the slip approaches 40 v% B_4C, the rate of powder addition is reduced and halted at about 45 v% B_4C. Properly prepared powder will achieve 48 v% B_4C in the slip, but the powder additions are stopped at 45 v% to allow sufficient mixing before reaching 48 v% B_4C. The slip is then mixed thoroughly for at least 5 minutes. When using powder washed as described above, the slip changes from a very watery character to a creamy and more viscous character at around 40 to 45 v% B_4C. If the powder is not cleaned sufficiently, the slip will not achieve 40 v% B4C before thickening extensively.

The slip begins to wrap around the spindle and forms a curved smooth surface above the blade as the maximum for the amount of boron carbide in the slip is reached. Powder is slowly added again and the consistency is observed by periodically dipping a mixing stick into the slip and pulling it directly up to observe the slip as it runs off the stick. When the slip forms drops shortly after leaving the stick it has not yet reached the maximum B_4C density. When the slip begins to pour off the stick in a thin continuous stream without breaking up into drops, the maximum B_4C density has probably been achieved. The amount of powder

used is recorded and a calculation of slip density using the amount of ammonium hydroxide solution can be made. The slip should be mixed for a few minutes, but excessive heating (due to Joule heating) of the slip should be avoided. After mixing is complete, the container with the slip is covered to prevent the formation of a skin layer on the surface due to the evaporation of ammonia.

The slip is poured through a screen before casting to catch large particles or "skin" layers that may remain. Samples of slip are transferred into graduated cylinders for density measurements.

Before pouring the slip into the molds, the interior of the mold is wetted a small amount of De ionized water unless the mold is still moist from a previous casting. The slip is then poured into the mold in a continuous stream. The molds are tapped to dislodge air bubble and tilted as they are tapped to bring air bubbles to the sprue. Tiles are allowed to cast until the sprue becomes solid. The lid of the mold is removed with the tile attached, the tile is cut from the sprue, and the sprue side of the tile trimmed flat. The tiles are allowed to dry in the open air. The mass of the tiles is measured on a regular basis (usually each day) to determine when the tile stops losing water. The tiles are then further dried in an oven by raising the temperature to 90 degrees Centigrade and then slowly ramping up through 110 degrees Centigrade.

The sprue face of the tile, (the top face), is sanded flat with sanding paper and the dimensions of the tile used to calculate a density of B_4C for the tile. Measurements of the tile dimensions are made. An average of several measurements of each dimension is used to determine the volume of the tile. The void space in the tile is calculated. An amount of aluminum equivalent to the void volume plus about 10 percent is used to infiltrate the tile. The excess aluminum is needed to account for losses due to volatization and oxidation. For alloys a correction is made for the amount of alloying.

The infiltration takes place in a flowing argon atmosphere in an inconel muffle. The tiles are placed in graphoil boats with the aluminum beneath the tile. The aluminum is bead blasted prior to the infiltration to remove any surface contamination on the aluminum. The graphoil boats are placed inside graphite boxes for support. Boron nitride is applied to the graphite boxes for added protection. This is done to gather any free oxygen inside the muffle. The graphite boats containing the tiles and aluminum are placed in the muffle and the muffle is evacuated to about 20 inches of mercury and held for 3 minutes or more. The muffle is then

filled with argon. This cycle is repeated three times to dilute or remove any oxygen present. Argon gas at 0.5 SCFH is allowed to flow through the furnace for 12 hours prior to infiltration to dilute and remove any oxygen which may still be present. Currently, the furnace is run on the following cycle during the infiltration:

Ramp from ambient temperature through 105 C. over 12 hours
Ramp to 1150 C. at 4 C./min. and hold at 1150 C. for 20 minutes
Ramp to 800 C. at 4 C./min.
Ramp from 800 C. to 15 C. at 1 C./min. and end program

The muffle temperature is approximately 50 C. below the furnace temperature when the furnace is at 1150 C. The ramping through 105 C. is used to remove any moisture that may still be present in the B_4C compact.

When the furnace has cooled to below 100 C., the tiles are removed and inspected for cracks. Excess aluminum must be cut from the tiles. The cermet may be cut by Electrical Discharge Machining (EDM). Heat treatments are performed at 800 C.

Results

Figure 1. is a graph of slip density and tile density in terms of the volume percentage of boron carbide in each. The plotted line is a linear curve fit to the data. There is a saturation level that limits the number of particles that can be suspended in the slip or packed together by slip casting. This limit is probably slightly above 60 volume percent boron carbide in the tile. Some deviation in the data on the graph may have resulted from slips that were pushed beyond the optimum viscosity and hence had a high slip density but did not cast to as high density because of the viscosity of the slip.

Hardness measurements are compared with the weight percentage of boron carbide in the tiles in figure 2. The circles represent the hardness of the top face. It is also the face that the aluminum is placed on for the infiltration. The squares represent the bottom face. The difference in hardness between faces may indicate the effects of longer reaction times upon the phases formed since the face into which the aluminum infiltrated would have a slightly longer time to react with the aluminum than the opposite face. The variation in hardness with the change in boron carbide content of the tiles does not seem to be statistically significant given the amount of scatter in the data. Figure 3. shows a comparison of the hardness obtained from various aluminum alloys used. The results are not conclusive. It will be useful to compare how the hardness values change for different heat treatments for these alloys.

Discussion

One of the first challenges that was encountered with this process was poor slip quality obtained when 0.25 Molar HCl was used to clean the B_4C powder. It was determined that this was not sufficient to remove enough of the calcium present. It was concluded later that new HDPE bottles may leach some calcium when acid is put in them for the first time. The bottles may also absorb acid when they are new. The concentration of acid was increased to 1.5 Molar to overcome this.

When excessive mixing times are used, the slip warms up due to Joule heating caused by friction between the mixer and suspended powder. This leads to the formation of a skin layer which if poured into the mold affects the quality of the tile. Cooling the slip during the mixing process was not an effective solution and it was difficult to control the slip.

One problem that has not been completely resolved is the cause of cracking that has occurred in many of the tiles processed by this procedure. The cracks that have formed have not been filled with aluminum. The conclusion is that these cracks formed during cooling because they would otherwise fill with aluminum during the infiltration. The cooling ramp rates were modified to attempt to correct this problem. A cooling rate of 4 degree Centigrade / min. was used, but cracks were still observed. A cooling rate of 4 degree Centigrade / minute to 800 Centigrade followed by a 1 degree Centigrade / minute cooling was also used. Cracking still occurred in these experiments. It may be that excess residual aluminum sets up stresses due to thermal expansion differences. Some tiles have come out with very little, if any, aluminum remaining and have still cracked in places. A related idea is that the fractures are in directions perpendicular to a bending moment stress caused by aluminum on the opposite side of the tile; although,this does not adequately explain the cracking when no aluminum is left on the tile. Another possibility, that is difficult to prove, is that stresses are developed as the aluminum infiltrates into the boron carbide. The infiltration always begins from one side or face, but never from all sides at once. One reason for avoiding this is to prevent gases from being trapped inside the tile as it infiltrates. The infiltration may cause cooling or heating of the infiltration side due to the heat of the reaction developed in forming the phases of the cermet. Some portion of the infiltration process may favor formation of some of the higher density phases including aluminum carbide.

The experimental design for research ongoing in this area is shown in Figure 4. Three parameters are being varied in the experiments: the

B_4C volume density in the tiles, the aluminum alloy, and the heat treatment conditions. The results of the physical property measurement for the three parameters varied in the samples should give insight to the trends in the physical properties for the material. The alloys were chosen for specific reasons. The 1100 Al alloy was chosen because it is essentially pure and therefore could serve as a baseline for comparison with other alloys. The 7075 alloy was selected because it has been used extensively in the past and many successful infiltrations have been accomplished using it. It contains a substantial amount of zinc and magnesium that become volatile and oxidize readily at temperatures below the infiltration temperature of 1100 Centigrade. This is helpful because these elements may act as a flux for the infiltration by preventing aluminum oxide from forming. The 6061 Al alloy was selected because it contains silicon which could form silicon carbide in the composite. Cermets using this alloy might be heat treated to a state of higher toughness while maintaining a comparable hardness compared to the other alloys.

Large scale production using this material will require substantial improvements in the process. Machining and removal of excess aluminum will need to be kept to a minimum to save cost. Net shape production will be helpful in keeping cost down due to the extreme expense and difficulty in machining the material. Excess aluminum is a nuisance and can cause surface defects when it is removed. Determining the exact amount of the aluminum needed for the infiltration or removal of the aluminum by some means after infiltration would improve the process. The 6061 Al alloy infiltration resulted in very little excess aluminum on one tile and no excess aluminum on the other tile. The tiles and the graphoil appeared to be crystallized on the surface after the infiltration was complete. The graphoil had become hard and brittle and came free from one tile with almost no effort and left the tile clean of aluminum. If this is reproducible and not detrimental to the material, it could be very useful for a production environment.

Conclusion

The work on this project thus far has yielded useful knowledge about the processing of this material and has suggested other issues that could be investigated to determine the mechanisms of the cracking problems and to solve processing problems. The initial results of hardness measurements indicate that the samples produced thus far are fairly good. Examinations of other physical properties such as flexure strength and fracture toughness and the microstructure analysis should provide useful comparisons and insight into the microstructure composition and material behavior of this material.

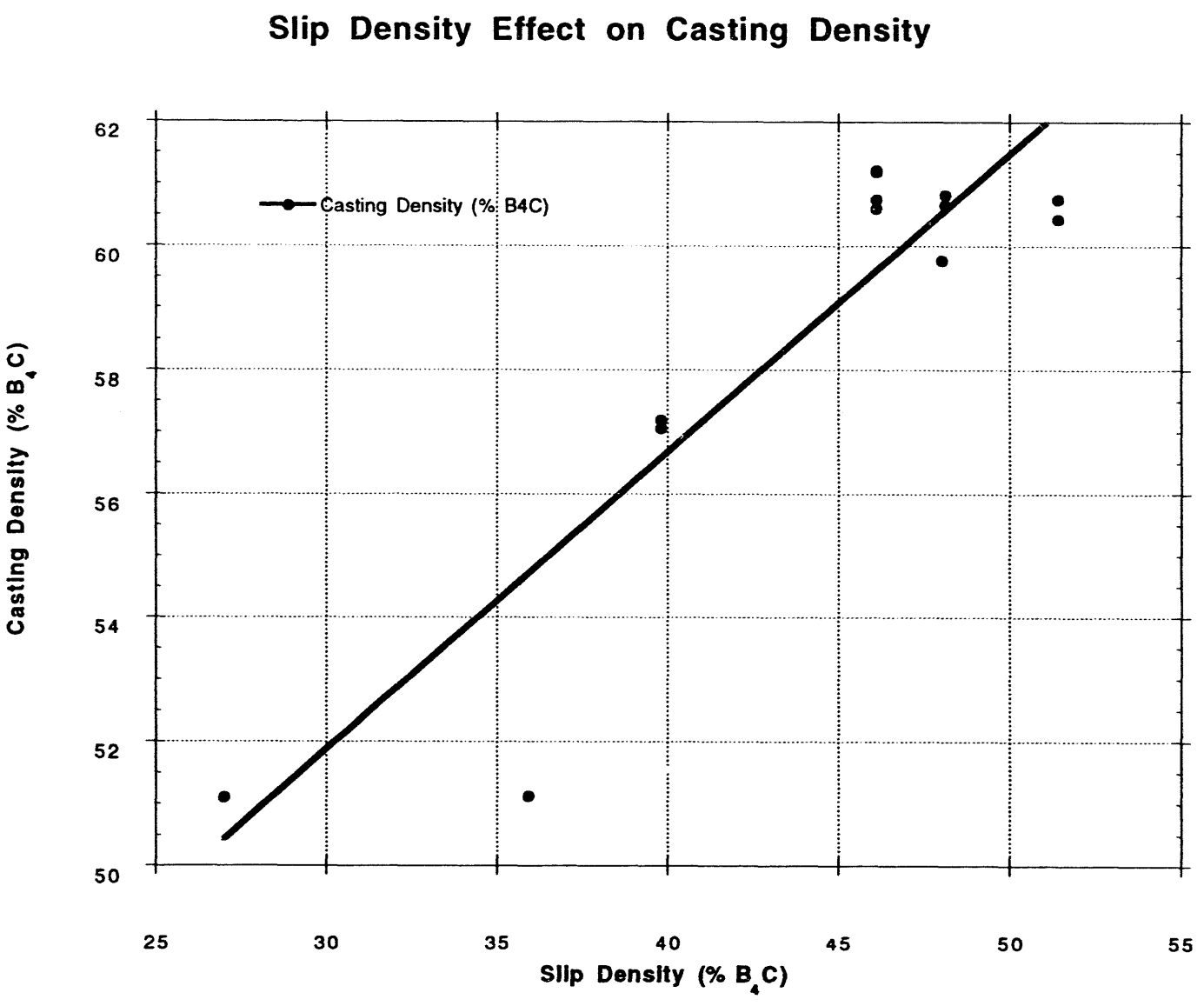
Slip Density Effect on Casting Density
Casting Density (% B4C)
62
60
58
56
54
52
50
Casting Density (% B4C)
25
30
35
40
45
50
55
Slip Density (% B4C)

Figure 1.

Boron Carbide-Aluminum Cermet, Rockwell Hardness, "A" Scale

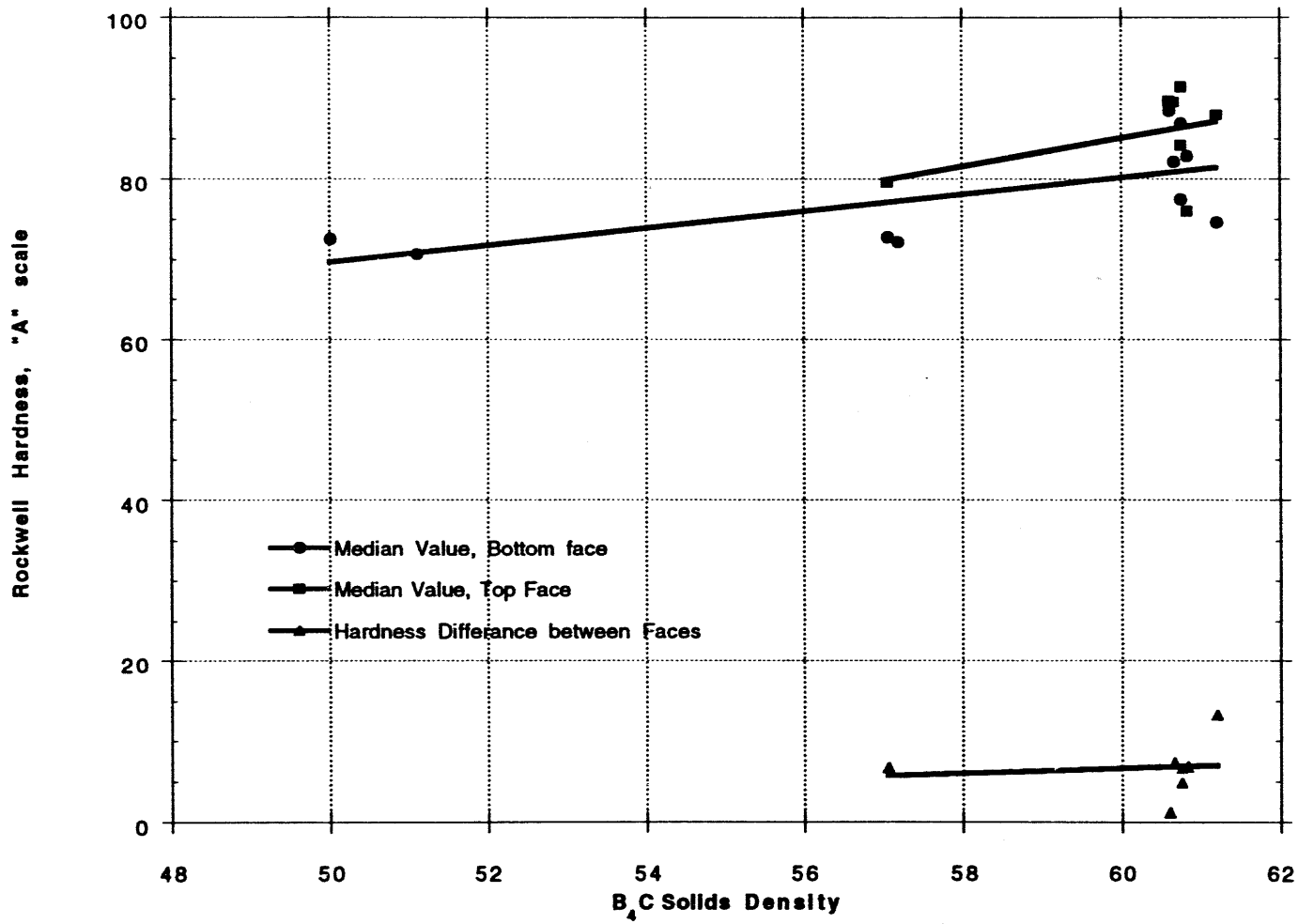

Figure 2.

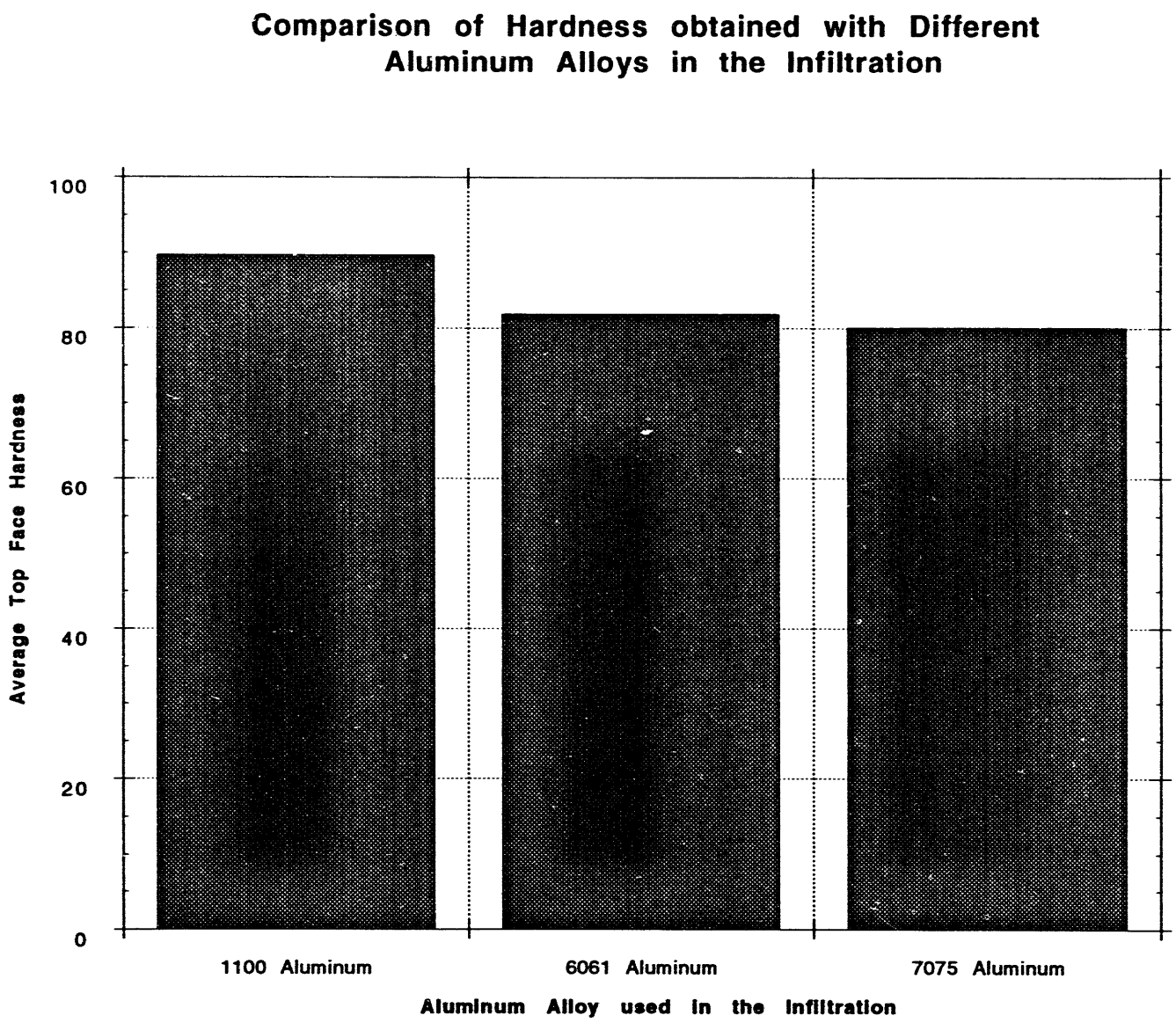
Comparison of Hardness obtained with Different Aluminum Alloys in the Infiltration
Average Top Face Hardness
100
80
60
40
20
0
1100 Aluminum
6061 Aluminum
7075 Aluminum
Aluminum Alloy used in the Infiltration

Figure 3.

Experimental Design

	B_4C Tile Density			Alloying
	50%	57%	61%	Elements
Alloys:				
1100 Al	X	X	X	none
6061 Al			X	Mg, Cr, Si
7075 Al			X	Zn, Mg, Cu

Additionally, three Heat Treatments for each cermet.

Figure 4.

Chlorine-36 Distribution in the Unsaturated Zone

Randy Hickman
Virginia Tech, Blacksburg, VA

Work performed under the auspices of the USDOE by
Lawrence Livermore National Laboratory under Contract W-7405-Eng-48.

ABSTRACT

A large influx of chlorine-36 was produced by nuclear weapons tests conducted from 1953 to 1963 over the Pacific Ocean. Fallout of 36Cl was concentrated in a short time span, leading hydrologists to believe that bomb ^{36}Cl would be similarly concentrated at a single depth in the soil column. However, recent studies indicate that ^{36}Cl becomes concentrated at many different depths within a soil column. This study attempted to correlate soil mineralogy with bomb pulses and thus explain the depth variations. Our ^{36}Cl analysis revealed a soil column with several bomb pulses; however, the mineral analysis showed that no anomalous minerals were present at the depths of the pulses. Mineralogy throughout the column consisted of smectite, illite, kaolinite, clinoptilolite (a zeolite), quartz, feldspars and calcite. This research concludes that no obvious correlation exists between bomb pulses and soil mineralogy.

INTRODUCTION/BACKGROUND

Chlorine-36 has been used in past research as a hydrologic tracer. It would seem to be an ideal groundwater tracer due to several of its properties: it had a large influx into the atmosphere/hydrosphere during nuclear weapons tests conducted over the Pacific Ocean from 1953-1963; it is a nearly conservative tracer (half-life = 3.01E+5 years), especially considering only 30 years have passed since the end of atmospheric tests. The influx is known as "bomb pulse," and increased ^{36}Cl concentrations globally.

Chlorine-36 is produced naturally both in the atmosphere and within the earth. Atmospheric ^{36}Cl is produced by spallation of argon, due to cosmic-ray fluxes. In situ ^{36}Cl is produced by neutron activation of ^{35}Cl; the neutrons are released during decay of natural uranium. However, these production methods of ^{36}Cl only account for a ^{36}Cl/total Cl background ratio of approximately 700E-15. Anthropogenic production gave a much greater ^{36}Cl/total Cl ratio. This enables the bomb pulse ^{36}Cl to be differentiated from natural ^{36}Cl.

The expected signature of the bomb pulse in the soil column is a peak in ^{36}Cl above background, concentrated at a single depth. The single spike would have given new hydrologic information, such as average infiltration rates, fallout variation with latitude and rainfall, and evaporation rates. The bomb ^{36}Cl has instead been seen at several depths in the same soil column; these depths vary from site to site. The only constant in bomb pulse research is the lack of a single bomb spike.

What, then, controls the distribution of chlorine in soil and rock? Infiltration in the vadose zone is expected to proceed nearly vertically downward. This leads to several theories to explain the existence of multiple bomb pulse peaks. One such theory is that chlorine is carried in solution by wetting fronts and deposited when the fronts dry.

Another theory, tested here, is that the soil contains "preferred sites" for chlorine deposition. Different soil minerals possess different ion exchange rates. The theory being tested is that anomalous minerals, especially clay minerals, control distribution of chlorine.

Understanding the processes that control ^{36}Cl distribution can help elucidate several geochemical phenomena: preferential minerals for adsorption, behavior of anionic solutes in the geosphere, and formation of ore bodies.

To minimize the difference between this and previous research, a similar (desert) environment was chosen as the field area. Desert soils contain few organics and field sites can be chosen that are relatively homogeneous. The sites chosen for this study were at the Nevada Test Site, located in southern Nevada. It is the most arid region of the most arid state in the U. S.

FIELD AND ANALYTICAL METHODS

Sampling was done at two trenches at NTS. Trench 5a in Midway Valley was sampled every 0.5 feet to a depth of 9.5 feet. Pit 6 in the Area 5, Radioactive Waste Management Site was sampled in two places: the east wall was sampled every 0.5 feet to 8.0 feet depth, and the west wall was sampled every 0.5 feet to 6.0 feet depth. All were taken using a channel sampling method, whereby each sample location is cleaned to obtain a fresh surface before the sample is taken. This provides a representative sample.

Lab analysis of the samples was twofold. One objective was to obtain chloride concentrations and ^{36}Cl/total Cl ratio; the second obective was to make a mineralogical analysis of the soil samples.

The chloride analysis proceeded as follows. Each sample was dry sieved into several size fractions, and a bulk sample was retained. Each sample was leached with water to remove chloride from the soil surfaces. The resulting soil-water mixture was filtered, centrifuged, and again filtered to remove all but colloidal (<.45 μm) particles from the water sample. Total chloride concentration of a water sample aliquot was obtained using a high-pressure liquid chromatograph (HPLC). Silver nitrate and nitric acid were added to the water sample to precipitate silver chloride. The precipitate was washed, dissolved with ammonium hydroxide, filtered to <.45 μm, re-precipitated, washed and oven dried. The clean precipitate was analyzed for ^{36}Cl/total Cl ratio using the LLNL Accelerated Mass Spectrometer. Only Pit 6 samples have been analyzed; Trench 5a samples are currently being analyzed.

The mineral analyses were performed on aliquots taken from the same depths as chloride analysis. The smallest size fraction (<37 μ m or <63 μm) of each sample was placed in a sample well to be analyzed for mineralogy by X-ray diffraction. The bulk sample was used to obtain a sample of only clay-size

particles (<2 μm). Soil sample and water were centrifuged to precipitate all particles >2 μm. The fraction <2 μm was reacted with magnesium chloride to flocculate magnesium salts, then centrifuged to precipitate all clay-sized particles. The precipitate was mixed with water, and the resulting slurry was dried on a slide to be analyzed for clay mineralogy by XRD (the clay slides were analyzed both before and after being dessicated with ethylene glycol, which resolves chlorides and smectites).

RESULTS

The chloride analysis of Pit 6 reveals what has become the common profile. Bomb pulses are present at 1 foot and 5 foot depths. These are mostly functions of the total chloride concentrations - the ^{36}Cl/total Cl ratio shows a single, well-defined peak at 3 feet depth. The total ^{36}Cl values are simply the products of the chloride concentrations and ^{36}Cl/total Cl ratios. Bomb pulse values are the products of chloride concentrations and above background ratios (the background was chosen as 700E-15 ^{36}Cl/total Cl). The bomb pulse value given - 3.43E+11 atoms ^{36}Cl/m2 - is obtained by integrating the values from the graph over the depth of sampling.

However, a mineralogical explanation for the presence of the bomb spikes is not apparent. The prelimenary mineral analysis shows that the same minerals, with few exceptions, are found throughout the soil column; the presence or absence of less common minerals does not coincide with presence or absence of bomb ^{36}Cl (a mineral's presence is all that can be determined from this analysis - quantitative abundances were not determined).

CONCLUSION

The mineralogy results of the X-ray diffraction testing are qualitative only. When the minerals are ranked by their peak intensities, no trends indicate that mineralogy correlates with bomb pulse spikes. No minerals are present

only at the bomb pulse depths, nor are there minerals present at all depths except those where bomb pulse exists. All clay minerals exist throughout the entire soil column. The few minerals that are less common among the others - dolomite and cristobalite - are scattered randomly. These observations indicate that unusual mineralogy does not control distribution of chlorine.

FUTURE DIRECTIONS

Many variables exist which control the flow of soil water and deposition of solutes. The most direct control is permeability, which is difficult to measure in a field setting. Other factors may control the distribution of chlorine. Clay content may control distribution locations, due to the anion exclusion effect - negatively charged ions are repulsed by the negatively charged clay surfaces. Evaporation and transpiration studies may locate the infiltration drying fronts. Another possible project is the determination of anion exchange rates in the field.

Many thanks to the following people for their help in completing the project:
JoAnn Rego, LLNL
Greg Nimz, LLNL
Brian Viani, LLNL
Marc Caffee, LLNL
Bob Finkel, LLNL
Jackie Kenneally, LLNL
Lee Davisson, LLNL
Dave Smith, LLNL
Jan Brown, LLNL
Layton O'Neill, NVO
Bruce Schneider, SAIC
Doc McNeely, SAIC

Chloride concentrations in Area 5, RWMS Pit 6

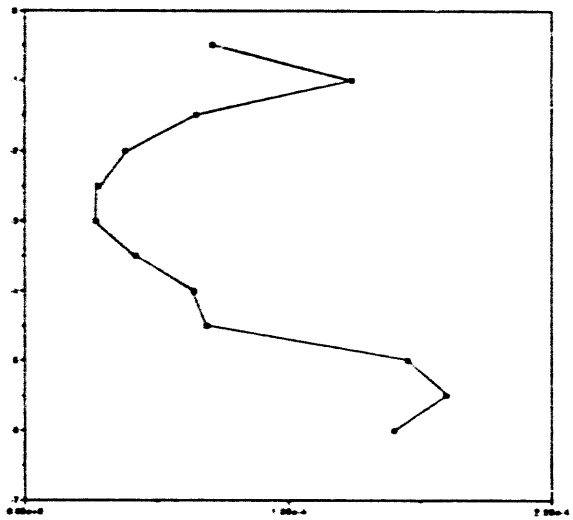

36Cl/Cl ratio in Area 5, RWMS Pit 6

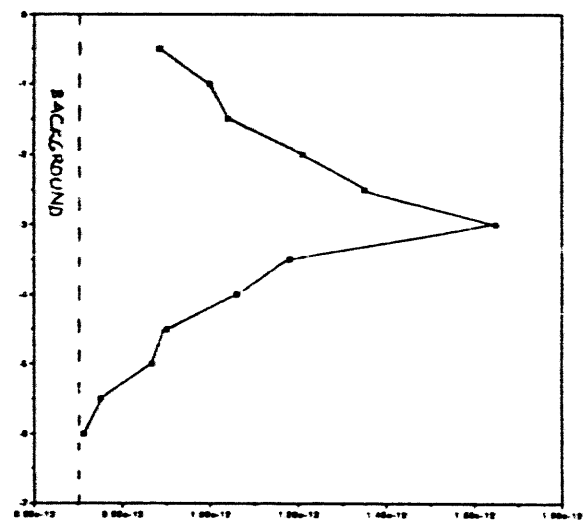

Total 36Cl in Area 5, RWMS Pit 6

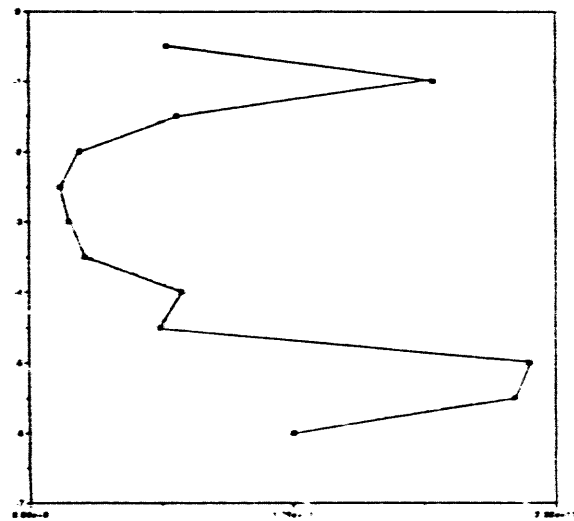

Bomb pulse at Area 5, RWMS Pit 6
3.43e+11 atoms 36Cl/m2

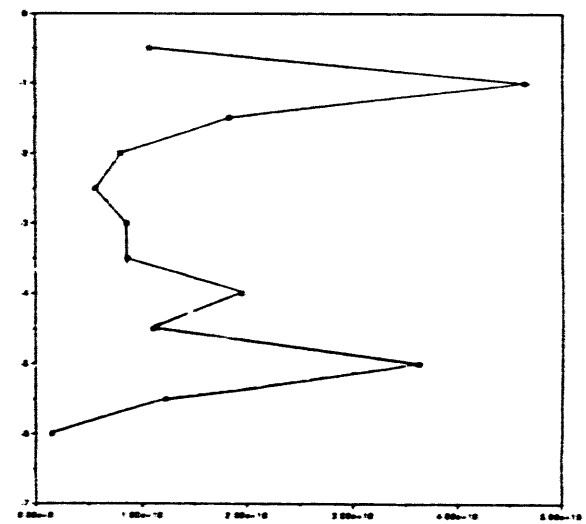

Pit 6 Prelimenary Mineralogy

Depth	Clay Minerals Present	Other Minerals Present
0.5 ft	Smectite, Illite, Zeolite, Kaolinite	Quartz, Calcite, Feldspar, Cristabolite
1.0	Smectite, Illite, Kaolinite, Zeolite	Quartz, Calcite, Feldspar, Dolomite
1.5	Illite, Smectite, Zeolite, Kaolinite	not tested
2.0	Illite, Zeolite, Smectite, Kaolinite	not tested
2.5	Illite, Zeolite, Smectite, Kaolinite	not tested
3.0	Illite, Zeolite, Smectite, Kaolinite	Calcite, Quartz, Cristobalite, Feldspar
3.5	Smectite, Illite, Zeolite, Kaolinite	not tested
4.0	Illite, Zeolite, Kaolinite	not tested
4.5	Illite, Zeolite, Smectite, Kaolinite	not tested
5.0	Illite, Smectite, Zeolite, Kaolinite	Quartz, Calcite, Feldspar, Dolomite
5.5	Smectite, Illite, Zeolite, Kaolinite	Quartz, Calcite, Feldspar
6.0	Illite, Zeolite, Smectite, Kaolinite	Quartz, Calcite, Feldspar, Dolomite

Minerals are listed in decreasing order of X-ray diffraction peak intensities.
The zeolite present is clinoptilolite.
Comparison of cation exchange capacities (CEC):
zeolite > smectite > illite > kaolinite

Implementing Neural Networks in a Functional Language •

Vilmarie Lao

Metropolitan University, Puerto Rico

Lawrence Livermore National Laboratory
Livermore, California 94550

Prepare in partial fullfilment of the requirements of the Science and Engineering Research Semester under the direction of John T. Feo Research Mentor, at the Lawrence Livermore National Laboratory.

Implementing Neural Networks in a Functional Language *

Vilmarie Lao, John T. Feo

Lawrence Livermore National Laboratory.
Livermore, CA 94550

December 18, 1992

Abstract: *We developed a parallel code to execute a multilayer feedforward neural network in a functional language called Sisal. Functional languages support implicit parallelism and high-performance. The network uses the backpropagation algorithm as a learning rule. Properties of the input and output were predefined based on the operations that we wanted the network to perform. Our code is short, easy to read, and portable. In this paper we discuss the parallel properties observed during the development of our code.*

1.0 Introduction

Artificial neural networks have been studied through the years in the hope of achieving human-like performance in cognitive tasks such as learning, recognition and optimization. They are based in our present understanding of the human brain. Instead of performing a program of instructions sequentially as in the von Neuman computer, neural net models explore many competing hypotheses simultaneously using massively parallel nets composed of many computational elements connected by links with variable weights[Lippmann87].

The nature of the operations performed in a neural network is highly parallel that eases the exploration of the properties of parallelism. Functional languages provide an easy-to-use environment ideal for the study of such properties. Sisal, as a functional language, provides the necessary constructions that ease the development and understanding of parallel applications.

* This research was supported in part by an appointment to the U.S. Department of Energy Science and Engineering Research Semester program administered by LLNL under Contract W-7405-Eng-48 with Lawrence Livermore National Laboratory

In this paper we discuss our study of the parallelism that we found during the implementation of a multilayer feedforward neural network in Sisal. In section 2.0 we provide a brief introduction to neural networks. In section 3.0 we discuss Sisal characteristics and features, and in section 4.0 we describe the implementation of the network to solve a pattern association problem and the parallelism observed.

2.0 Neural Networks : A definition

A neural network is a directed graph of interconnected computational units called neurons operating in parallel to carry out information processing by means of its state response to initial or continuous input. Each node in the network receives a fixed number of arguments supplied by the external environment or by other neurons and compute a single output.

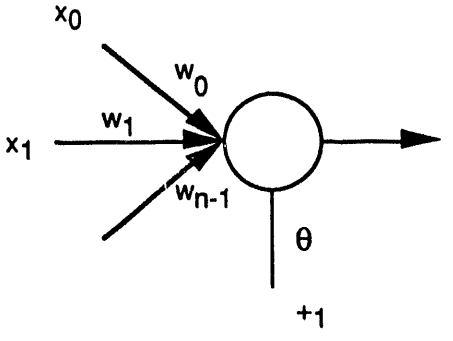

Figure - 1 A neuron

Feedforward neural networks are models in which the neurons are arranged in successive layers and each neuron is connected to a given neuron in the previous layer. Figure 2 illustrates a typical multilayer feedforward network architecture.

Input

First hidden layer

Second Hidden layer

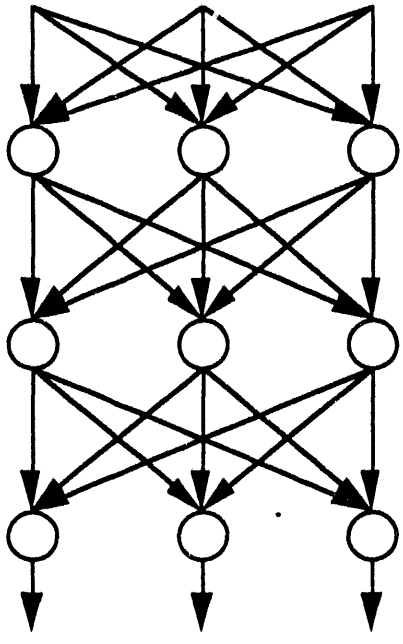

Output

Figure - 2 Multilayer feedforward network

The inputs to the network are shared by the neurons in the first layer while the neurons in each successive layer take inputs from the neurons in the preceding layer. The output of a given node is define by the function:

$$X_k = f(\sum_{i=1}^{I} W_{ik}X_k - \theta_k)$$

equation 1

where w_{ik} is the synaptic weight between the ith and kth node, X_i is the state of the node(-1 or 1) and θ_k is the internal threshold value for the jth node.

The result value of the function f determines if neuron "fires" and sends a signal to the next level. If the value of the sum of the inputs to the neuron exceeds the internal threshold, then the

neuron "fires" producing a single output. This is the key to the ability of the network to exhibits learning and memory.

The process of learning involves two steps: the forward step and the backward step. In the forward step an input pattern $X_n = [X_{0p}, X_{1p}, ... X_{(n-1)}]$ is propagated by computing the sum of the incoming arguments according to equation 1, and the maps of the input and output pattern in the form of $Y_n = [Y_{0n}, Y_1, ..., Y_{(n-1)}]$.

In the backward step the network uses the backpropagation algorithm to complete the process of learning. The output values Y which corresponds to the input pattern Xp are compared to a desired target pattern $D_n = [d_{0p}, d_{1p}, ..., d_{(n-1)}]$. The difference defines an error value given by :

$$E_p = \sum_{n=0}^{N-1} (d_{np} - Y_{np})^2$$

equation 2

Using a recursive algorithm the weights and the threshold for each neuron N in each layer l are updated. This process is repeated until the network learns; i.e. ., outputs the correct target signal for each given input.

3.0 Sisal

Sisal(Streams and Iterations in a Single Assignment Language) is a general purpose functional language developed as a collaborative effort between Lawrence Livermore National Laboratory and Colorado State University for the performance of highly parallel scientific applications. It bases its semantics in mathematically sound, side effect free functions.

As a functional language, Sisal gives the programmer the freedom to concentrate on the development of the algorithm without having to worry about the scheduling and synchronization of operations ,communication of data values, or the management of memory.

Sisal supports the execution of sequential and parallel operations. The parallel and sequential for loops constructions makes this possible. The `for initial` loop illustrated below resembles the sequential iteration in conventional languages[Feo90].

```
for initial
 i := 1;
 x := Y[1]
while i < n repeat
 i := old i +1;
 x := x + Y[i]
returns array of x
end for
```

It consists of four segments: initialization, loop body, termination test, and a result clause. The initialization segment defines the loop constants and assigns initial values to the loop-carried names. It is the first iteration of the loop. In the loop body new values for the loop-carried names are computed. Loop values modified by the old prefix refer to values obtained in previous iterations of the loop. The termination test can appear before or after the loop and can be executed using a while or until construction. The result clause defines the arity and the type of the results.

The construction that observes parallelism in Sisal is the `for` loop. It consist of three parts : a range generator, a loop body and a returns clause.

```
for i in 1, N
 x := A[i] * B[i]
returns value of sum x
end for
```

The range generator is a dot or cross product of a set of sequences or scatters. As in the for initial loop the loop body new loop-carried values are computed. The returns clause performs in the same manner as the return clause in a for initial construction. Due to its mathematical nature Sisal program are easy to read and understand. They can be ported

from an uniprocessor architecture to multiprocessor architecture without any difficulties that deals in reducing the program development cost by 80% to 90%.

4.0 Simulation Results

We conducted simulations to study the properties of parallelism in a totally connected multilayer neural network based on the backpropagation algorithm. The study was conducted in order to observe the properties of portability, performance and the simplicity of the code written in Sisal. In the following section we discuss the results obtained after solving a pattern association problem.

4.1 Pattern association problem

We used a totally connected multilayer network as the one in figure 3 to perform the task of pattern association. Our network consists of 4 layers: an input layer, 2 hidden layers and an output layer consisting of 3 neurons.

The initial weights where chosen at random in the range, 0.2 - 0.5 and we set the learning rate (η) be 0.7.

We trained our network to recognize the patterns given in Table1.

Input	Output
000	000
001	001
010	010
100	100
101	101
110	110
111	111

Table 1

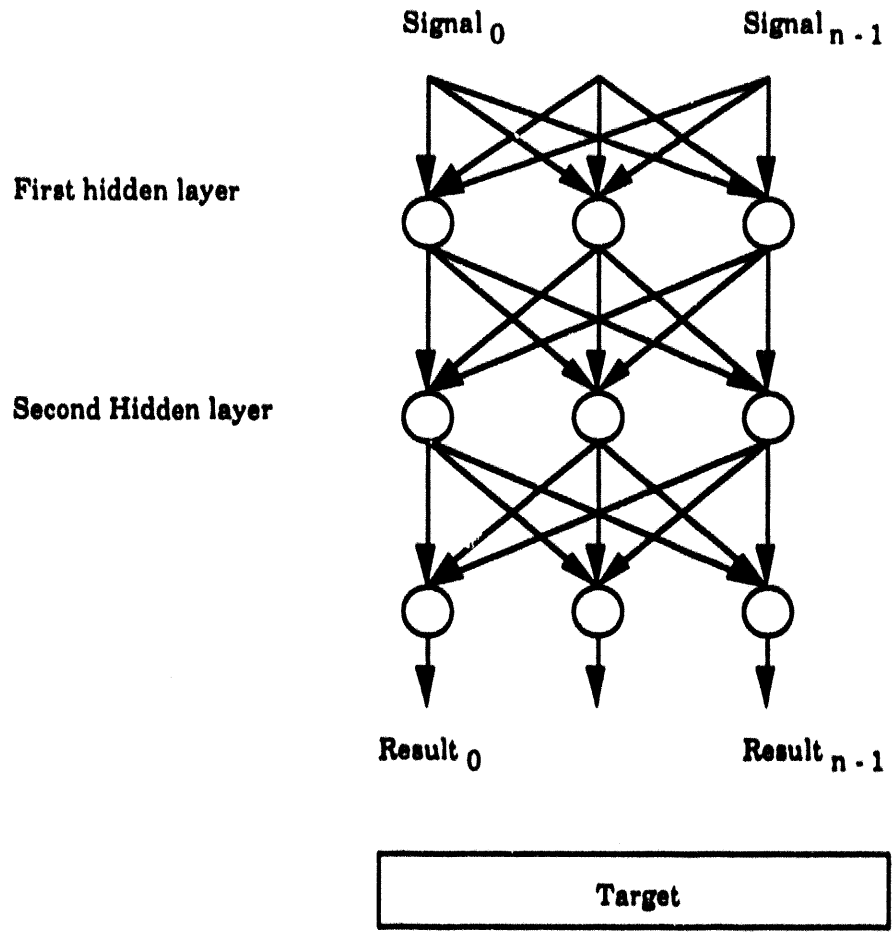

Figure - 3 Multilayer feedforward network

In order to propagate the signal down we present a set of arguments to the network and perform the calculations using equation 1 for each node *N* in each layer *l*. Since these calculations are independent , they may be executed in parallel.

Sisal, a functional language, supports parallel loops in the form of for expressions. Such constructions simplify parallel program development. Our code looks like this:

```
function generate_sout(level, i     : integer;
                       signal       : OneDim;
                       W            : ThrDim;
                       nodes    : OneInt
            returns real)
```

```
for k in 1, nodes[level]
 t_weight := signal[k] * W[level,i,k]
returns value of sum t_weight
end for
end function
```

where the signal[j] represents the incoming arguments to the node and W[level,i,j] the synaptic weights .

To propagate the signal backwards it is necessary to calculate the error each node in each layer. First we calculate the error in the output layer by the equation:

$$\partial_i = Y_i(1 - Y_i)(d_i - Y_i)$$

equation 3

The incoming weights to the output layer where adjusted by the execution of the following function:

```
function weight_adjustment(W      : ThrDim;
                           gain   : real;
                           delta  : OneDim;
                           output : TwoDim;
                           L      : integer;
                           nodes  : OneInt
                    returns TwoDim)

 let
  new_weights:=
  for i in 1, nodes[L] cross k in 1, nodes[L]
  returns
  array of W[level,i,k] + gain * delta * output
  end for
 in
  for i in 1, nodes[L]
  returns
     array of array_addh(new_weights[i], W[level,i,4])
 end let
 end function
```

The calculation of the errors in the two hidden layers is given by:

$$\partial_j = Y_j - 1(1 - Y_j)\sum_k \partial_k W_{jk}$$

equation 4

The dependency of the arguments necessary for the calculation of the errors in the hidden layer makes impossible to execute this task in a parallel form. Sisal supports execution of sequential operations via the for initial construction :

```
function up_signal(output : TwoDim;
                   level  : integer;
                   nodes  : OneInt;
                   desire : OneDim;
                   W      : ThrDim;
                   gain   : real
            returns ThrDim)

            for initial
             L       := level;
             weights:= array[level: output_calculation(output, L,
                                                  desire,nodes, W)
            while L > 1 repeat
             L       := old L - 1;
             weigths:= array_addl(old weights,
                        hidden calculation(output, L, desire, nodes, W, gain)
            returns
             value of weights
            end for
end function
```

The sequence of the operations described were executed until we reached a convergence less than 0.01 between the desire target an the actual output.

4.0 Conclusions and future work

We have presented an study of the properties of parallelism observed during the implementation of a multilayer feedforward in a functional language. During our study we observed that task such as the calculation of the outputs and the weight adjustments of a given node are highly parallel and they can be translated to code in a functional language without too much effort. Our code is easy to understand and follow. In addition due to the

mathematical nature of functional languages the translation of equations to actual code was done without difficulties.

Our future work in this area will be concentrated in the exploration of performance and portability of our code across different machine architectures.

Acknowledgments

I would like to thank the Computer Research Group at Lawrence Livermore National Laboratory for all the support and resources given to make this research possible.

References

[Feo92] Feo, John T. A Comparative Study of Parallel Programming Languages: The Salishan Problem,*Elsevier Sience Publishers(1992)*, pp. 337-366.

[Feo90] Feo, J.T. D.C. Cann and R.R. Oldehoeft, A Report on the SISAL Language Project, *Journal of Parallel and Distributed Computing*, vol. 12, 10 (December 1990), pp. 349-366.

[Lippman87] Lippman, R.P., An Introduction to Computing with Neural Nets, *IEEE ASSP Magazine*, April 1987 pp. 4-22.

[Muller, Reinhardt90] Muller, B. & Reinhardt, J. Neural Networks, An Introduction, *Springer-Verlag (1990)*.

[Provence Naganathan90] Provence ,J. & Naganathan, S., Locally versus globally interlayer connected feedforward neural networks: A performance comparison, *Proc 1990 Applications of Artificial Intelligence VII* , Orlando Florida 1990

SMES
(SPECIAL MEASUREMENT AND EMPLACEMENT SYSTEM)

DORRINE McKINNEY

PERU STATE COLLEGE

LAWRENCE LIVERMORE NATIONAL LABORATORY
LIVERMORE, CALIFORNIA 94550

DECEMBER 18, 1992

Prepared in partial fulfillment of the requirements of the Science and Engineering Research Semester under the direction of Robert E. Knipes and Don Eckert, Research Mentors, at the Lawrence Livermore National Laboratory.

* This research was supported in part by an appointment to the U.S. Department of Energy Science and Engineering Research Semester (hereinafter called SERS) program administered by LLNL under Contract w-7405-Eng-48 with Lawrence Livermore National Laboratory.

INTRODUCTION

SMES

The Special Measurement and Emplacement System places experiments in a hole with a diameter of twelve feet and a depth of two thousand feet. These experiments are fastened to one end of a coax cable. The coax cable is used to support and lower the experiment into the hole. The cable makes a ninety degree transition from the horizontal to the vertical via Teflon coated drums, which are sometimes stationary, sometimes rotating. These experiments have to be placed at varying depths of the entire length of the hole to a precision of plus or minus one-half foot.

Using inputs from the experiments such as location, weight, size of the experiment, data on cable stretch, and coefficient of friction over a ninety degree arc, the system has to place the experiment in the hole with a precision of one-half foot, taking into account the physical parameters described above.

Once the experiments are in place, the hole is backfilled with varying amounts of sand, gravel, and concrete. The system now must compensate for the increased weight on the experiment and on the cable by load-releasing tension.

SMES: SPECIAL MEASUREMENT AND EMPLACEMENT SYSTEM

DORRINE McKINNEY
PERU STATE COLLEGE
NTOD DIVISION

ABSTRACT

SMES was designed to lower cables safely into the ground during downhole operations using on and off relay switches to manually lower cables and potentiometers which control the speed. SMES was automated by interfacing a Robertshaw controller to the existing SMES. Automating SMES was based on six design requirements used to satisfy eleven objectives. The design requirements consisted of a Robertshaw controller, software, tachometer, encoder, strain link, and computer. The eleven objectives consist of the following: individual feeding of the cable, manual override, alarms, stemming level measurements, tension measurements, depth measurements, speed measurements, data received from a disk, continuous data printout, trend data printout, and graphic display. Automating SMES has improve safety, fielding proficiency, and operational control.

EXPLANATION OF METHODS USED

SMES was designed using Quality Function Deployment (QFD), Total Quality Management (TQM), and Taguchi methods. Before automating SMES a brain storming meeting was called to acquire the objectives of how the users would like the system to operate. After receiving valuable information from the brain storming meeting, SMES was upgraded based on eleven objectives. These objectives originated out of the desire to improve safety, operational control and fielding proficiency of the SMES. Each objective is outlined below, with a brief description.

Objective 1 (Individual feeding of the cable)

Individual cables are lowered to a specified depth. The cable travels in either a forward or reverse direction.

Objective 2 (Manual Override)

The system places the emergency relay switch to the off position and allows the user to operate the skid manually. The manual operation uses local control push buttons.

Objective 3 (Alarms)

Alarm values are placed in the software for the transducers. If the measured values from the transducers reach an alarm value inputted into the software, the computer makes a continuous beep, which is the indicator for the alarm.

Objective 4 (Stemming level Measurement)

The stemming level measures of the amount of sand, gravel, and concrete used to backfill the hole.

Objective 5 (Tension Measurements)

Tension measurements are the amount of tension on the cable during the downhole operation.

Objective 6 (Depth Measurements)

Depth measurements is the depth of the cable.

Objective 7 (Speed Measurements)

Speed measurements is the speed of the cable going downhole.

Objective 8 (Receive data from a disk)

A disk supplied by a physicist to give the Robertshaw controller the necessary data normally inputted by the user before the operation of SMES.

Objective 9, 10, 11 (Printouts of continuous data, trend data, and graphics)

Continuous data is read from the transducers.

After acquiring the objectives for the system, six design requirements were used to satisfy the eleven objectives. The first design requirement is a controller. The controller consists of analog

inputs, analog outputs, contact inputs, and contact outputs. There are twenty analog inputs per skid to read voltage from the strain link and the tachometer. Ten analog outputs send a setpoint (constant speed reference) to the DC drives. Ten contact inputs monitor the encoder pulses and thirty-one contact outputs to control the feed of the cable. Within the controller, a voltage input and a voltage output card are used to receive and return voltage to the SMES along with analog input and analog output slaves. The second design requirement is the software used to program the controller and send data to the peripheral components. The next three design requirements are transducers. The strain link measures the tension of the cable, the tachometer measures the speed of the cable, and the encoder measures the depth of the cable. The final design requirement is the computer. The computer monitors data coming in and going out. It also displays graphics, trend data, and updated data from the transducers.

After acquiring the eleven objectives and satisfying the objectives with the design requirements, we began to upgrade the system.

Upgrading the system required basic components which consist of a computer, DMS (Database Management System), DCM controller, and the skid. Figure 1 contains a computer. The computer is used to monitor various signals that are sent from the skid controller. The computer is also an easier method of programming the DCM controller and displaying data.

Figure 2 connects the computer with a DMS (Database Management System) by using a RS-232 cable. The standard

interface cable is used for the serial connection of computer controlled devices. The DMS manages data coming in and going out. [1]

Figure 3 connects the DCM controller to the DMS using a two-wire interconnect. The controller is considered the heart of the operation of SMES. It is a microprocessor-based system which stores preprogrammed information for later recalls and communicates with the computer for constant updates on the operation of the skid. The controller is also used to control speed, depth, and tension on the cable, as well as peripheral components within the work cell. [1]

Figure 4 shows 1-10 tensioners that comprises an entire skid, and Figure 5 shows the connections that were made between the controller and the skid to give SMES automatic control. The purpose of my project was to automate SMES by interfacing the Robertshaw controller with the existing SMES. In order to satisfy the individual feeding of the cable, each tensioner connects to a contact output of the controller. Contact output consists of on and off relay switches. To control the switches, a start and stop command is needed in the software. RF allows the cable to travel in a forward direction and RR allows the cable to travel in a reverse direction. The schematic for the automatic control of SMES is shown in Figure 7. Auto energizes the local control push buttons on the skid. Auto is also in Figure 7. The analog output is connected to the DC drive to give the drive a set voltage on which to operate. The schematic containing the DC drive is shown in Figure 9. The contact inputs monitor incoming pulses from the encoder. The pulses are calculated to give the user cable depth. The final connection is the analog input of the controller to the tachometer feedback and the strain link. Each

transducer outputs a voltage that is received by the analog input. The schematic showing the connection from the strain link to the analog input in shown in Figure 8. The analog and contact input send information to the computer screen and printer to display data on the tension, depth, and speed of the cable. The tachometer input measurement is compared with the analog output setpoint (speed reference voltage). Using PID-control, a loop point is placed in the software and the error is compensated to control speed.

Presentation of Data

The data from the strain link and the tachometer is given below.

Strain link measurements

.961 MV	Top of the hole
.965 MV	20 FT
.970 MV	40 FT
.979 MV	60 FT
.982 MV	80 FT
.986 MV	100 FT

Tachometer, Speed Reference, and FT/MIN Measurements

Tensioner 3, Skid 15

FT/MIN	Tachometer Output (V)	Speed Reference (V)
39.5	37.3 ± .4	11
33.6	35 ± .4	10
36.9	28 ± .4	8
20.1	21 ± .2	6
13.4	14 ± .2	4
6.6	7 ± .1	2

Tensioner 2, Skid 15

FT/MIN	Tachometer Output (V)	Speed Reference (V)
35.8	38 ± .4	11
33.3	35.2 ± .4	10
26.7	28.2 ± .2	8
20	21.1 ± .2	6
13.4	14.2 ± .1	4
6.7	7.1 ± .1	2

Discussion and analysis of results

The system was given various tests after the Robertshaw controller was interfaced with SMES. The results of the test showed that SMES has the ability to automatically control cables to operate in a forward and reverse direction. A software program was used to test the cable traveling in a forward and reverse direction. Using a separate test program, the system was tested for manual override and local control. The systems performed well in automatically shutting down and releasing the local control push buttons to allow the user to operate the skid manually. Alarm values were placed in the software to test the alarm. Displays of data messages telling the user which tensioner was operating and the direction of the cable were obtained. The test results show that the system has the ability to perform individual feeding of the cable, manual override, alarms, and displaying data.

More testing is needed before the system can operate by itself. Measurements from the stain link, tachometer feedback, and the encoder must be tested using a computer program, so that the values coming from the transducer can be compared with specified values in the software. The reason for the comparison is to determine if the system can correct itself once the tension or the speed of the cable reaches a high or low value. The system also needs to be tested with a load on the cable to get final results and data for the system.

Summary

Special Measurement and Emplacement System (SMES) is used to lower cables into the ground during downhole operations. SMES has been upgraded by interfacing the Robertshaw controller with the existing SMES. The system was designed using QFD, TQM, and Taguchi methods. There were eleven objectives and six design requirements use to automate SMES. Test results show that the system can perform individual feeding of the cable, manual override, alarms, and display data. The results also show that more testings of the transducer are needed before the system can operate by itself. The benefits of an automating SMES is that it improves safety, operational control, and fielding proficiency. It also reduces man-hour and critical path-time.

ACKNOWLEDGMENTS

I would like to thank the following people for their understanding, honesty, and patience.

1. Robert E. Knipes
2. Don Eckert
3. Bill Pittman

Over the last 4 months, I have gained invaluable knowledge in the field of electronics and robotics engineering that I will use in my future endeavors. I would like to send special thanks to my mentors Robert E. Knipes and Don Eckert. I would also like to thank the two REECO technicians.

REFERENCE

1 Malcolm, Douglas R. ,Jr., Robotics An Introduction , New York: Delmar Publisher, second edition, 1988

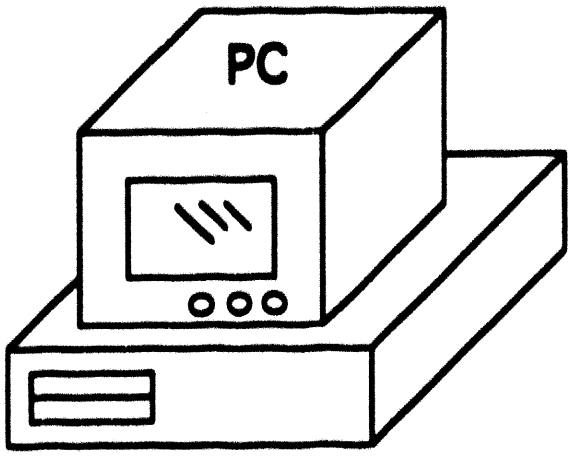

Figure 1

Figure 2

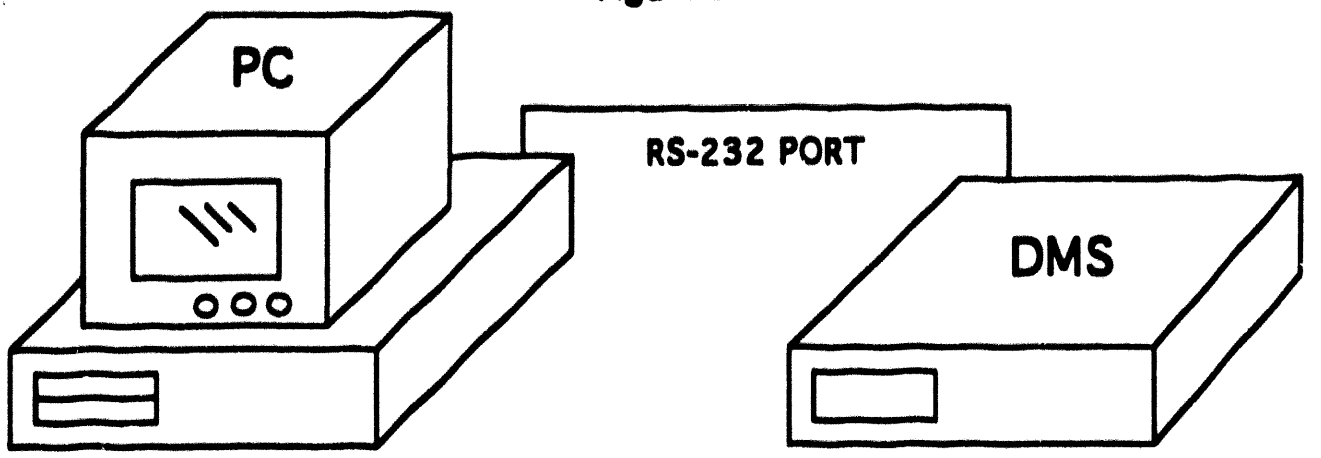

Figure 3

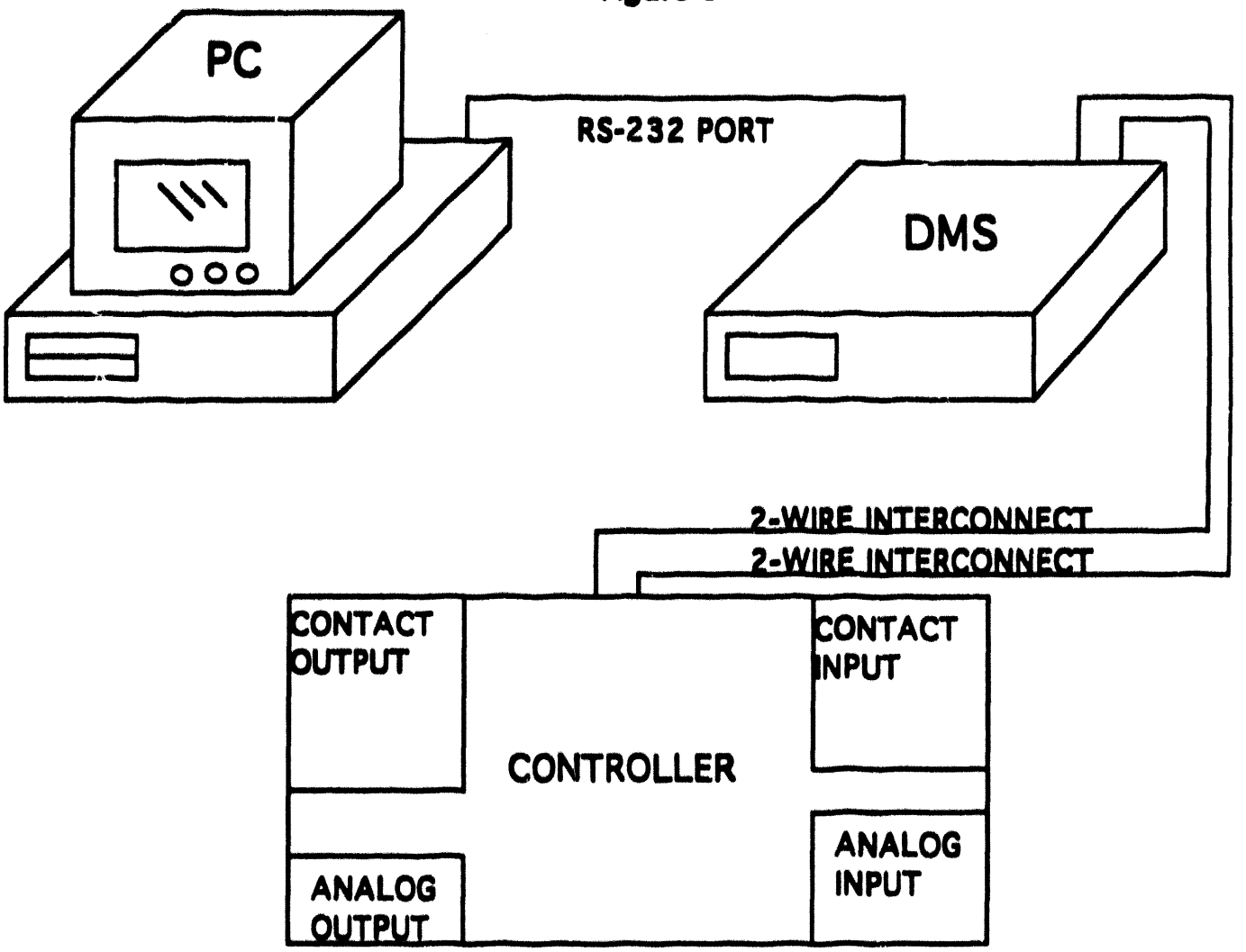
PC
RS-232 PORT
DMS
2-WIRE INTERCONNECT
2-WIRE INTERCONNECT
CONTACT OUTPUT
CONTACT INPUT
CONTROLLER
ANALOG INPUT
ANALOG OUTPUT

Figure 4

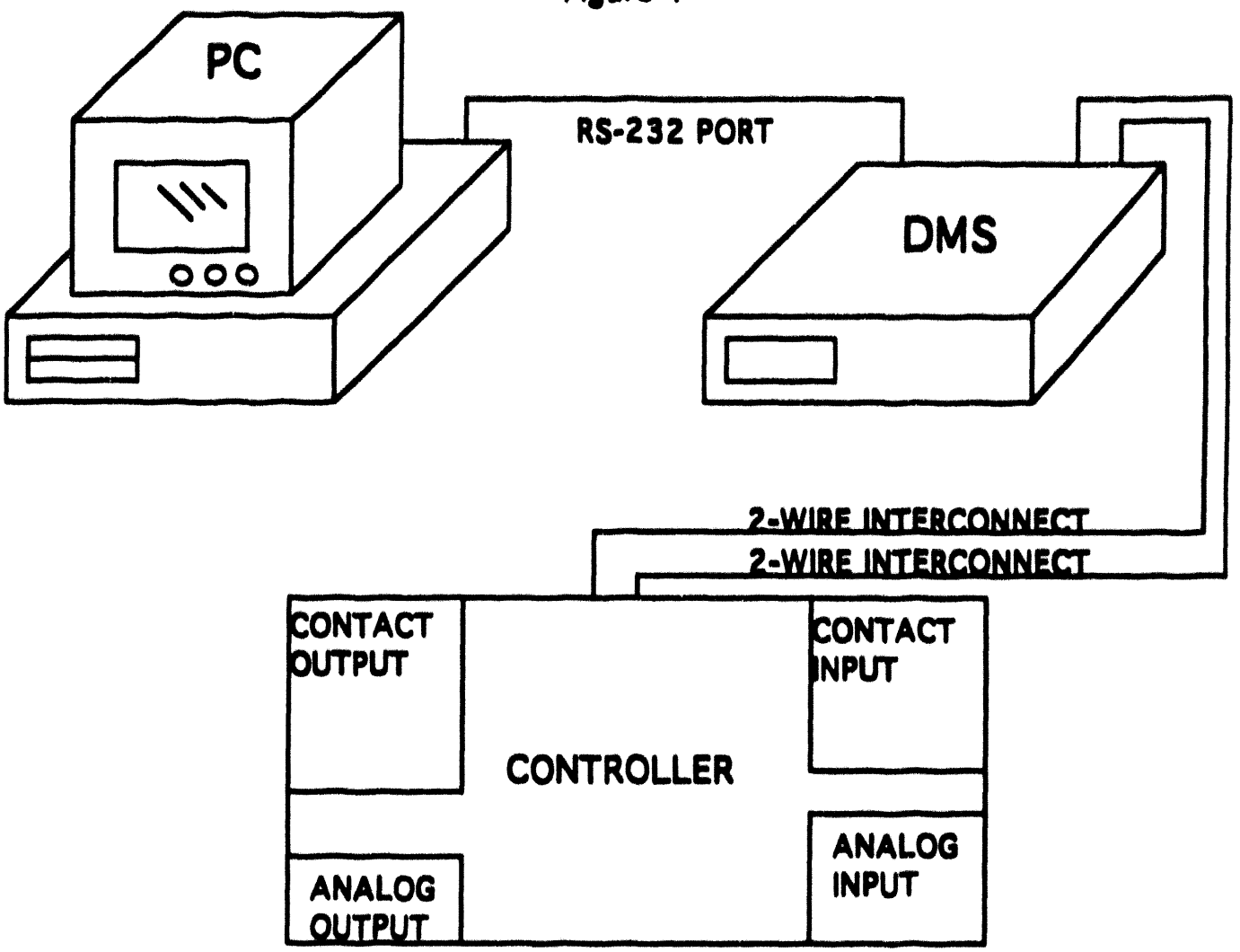
PC
RS-232 PORT
DMS
2-WIRE INTERCONNECT
2-WIRE INTERCONNECT
CONTACT OUTPUT
CONTACT INPUT
CONTROLLER
ANALOG INPUT
ANALOG OUTPUT

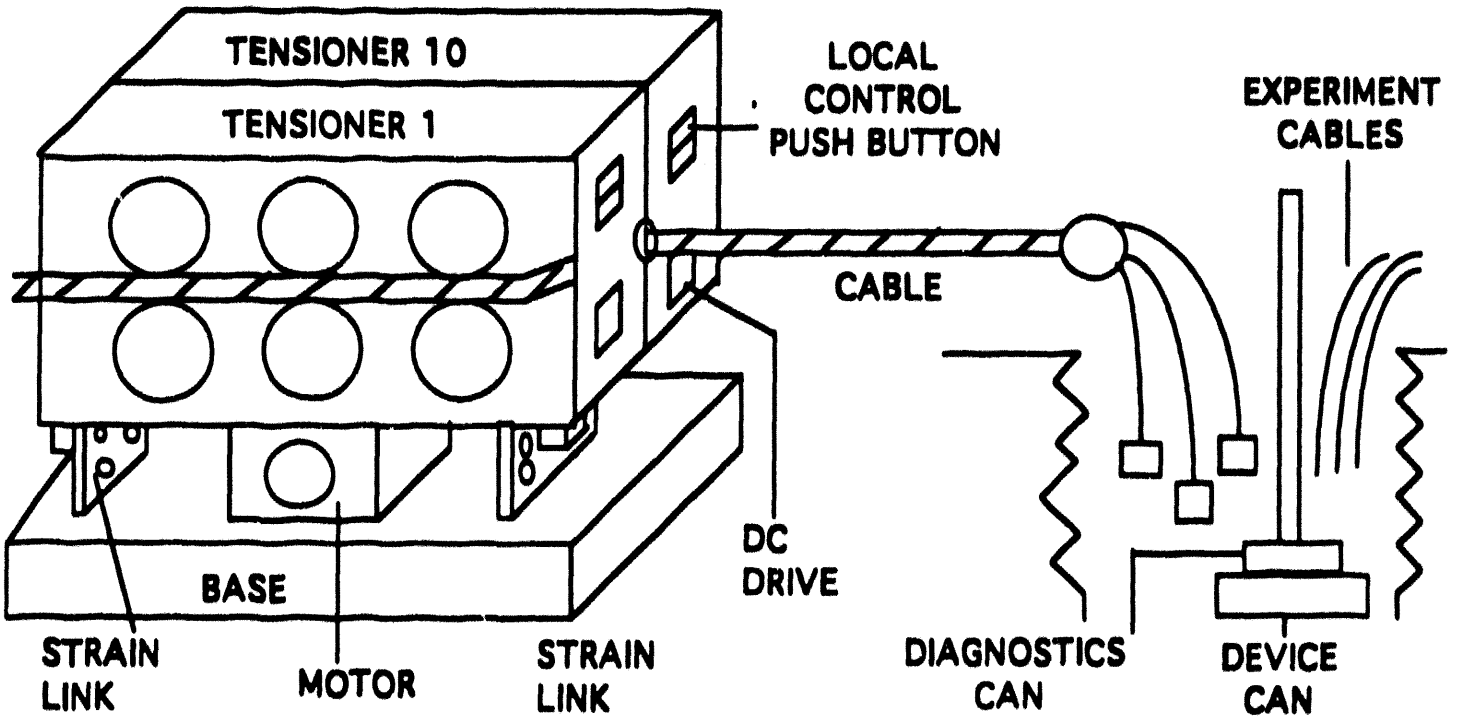
TENSIONER 10
TENSIONER 1
LOCAL CONTROL PUSH BUTTON
EXPERIMENT CABLES
CABLE
DC DRIVE
BASE
STRAIN LINK
MOTOR
STRAIN LINK
DIAGNOSTICS CAN
DEVICE CAN

Figure 5

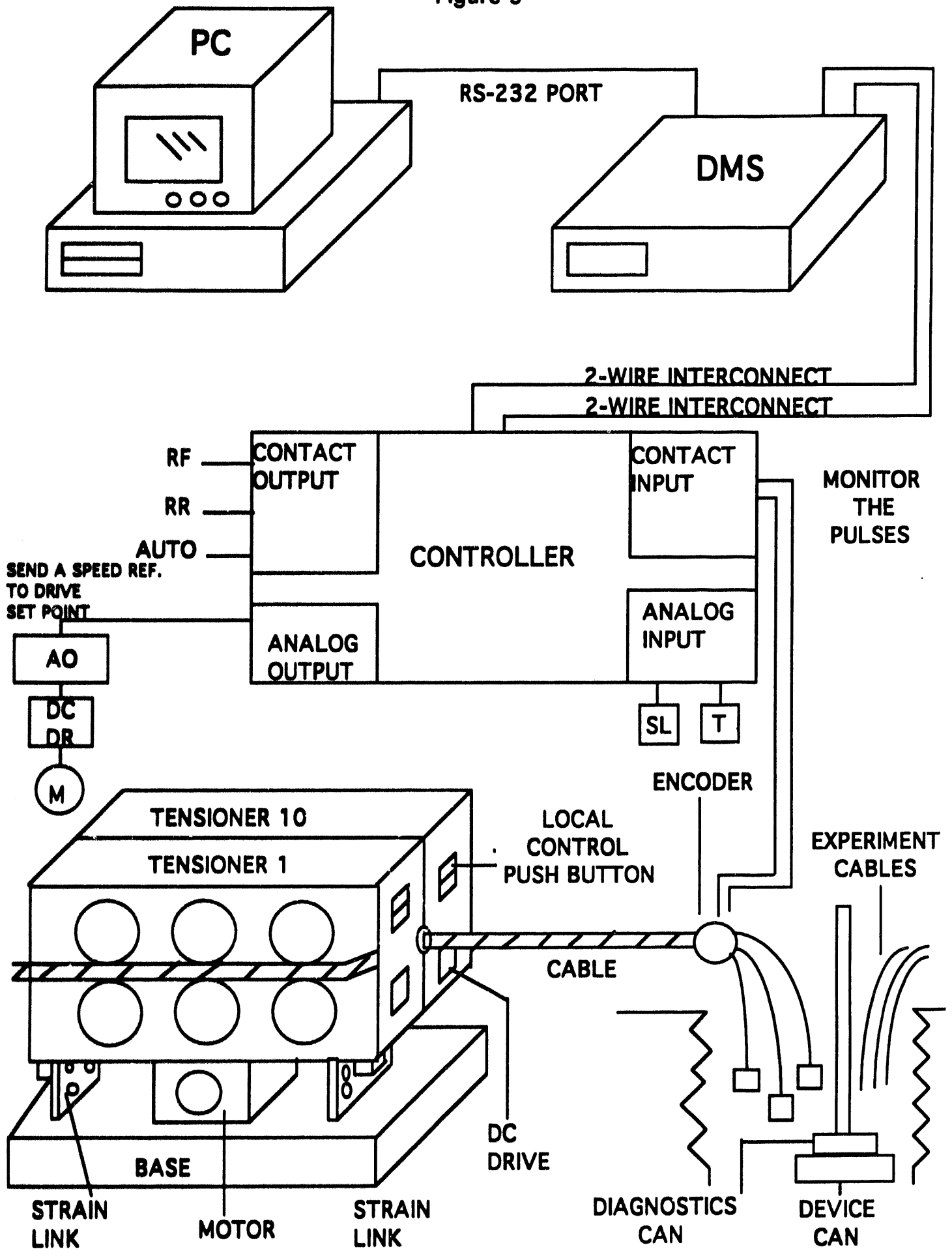
PC
RS-232 PORT
DMS
2-WIRE INTERCONNECT
2-WIRE INTERCONNECT
RF
RR
AUTO
SEND A SPEED REF.
TO DRIVE
SET POINT
CONTACT
OUTPUT
CONTACT
INPUT
MONITOR
THE
PULSES
CONTROLLER
ANALOG
OUTPUT
ANALOG
INPUT
AO
DC
DR
M
SL
T
ENCODER
TENSIONER 10
TENSIONER 1
LOCAL
CONTROL
PUSH BUTTON
EXPERIMENT
CABLES
CABLE
BASE
DC
DRIVE
STRAIN
LINK
MOTOR
STRAIN
LINK
DIAGNOSTICS
CAN
DEVICE
CAN

FIGURE 6

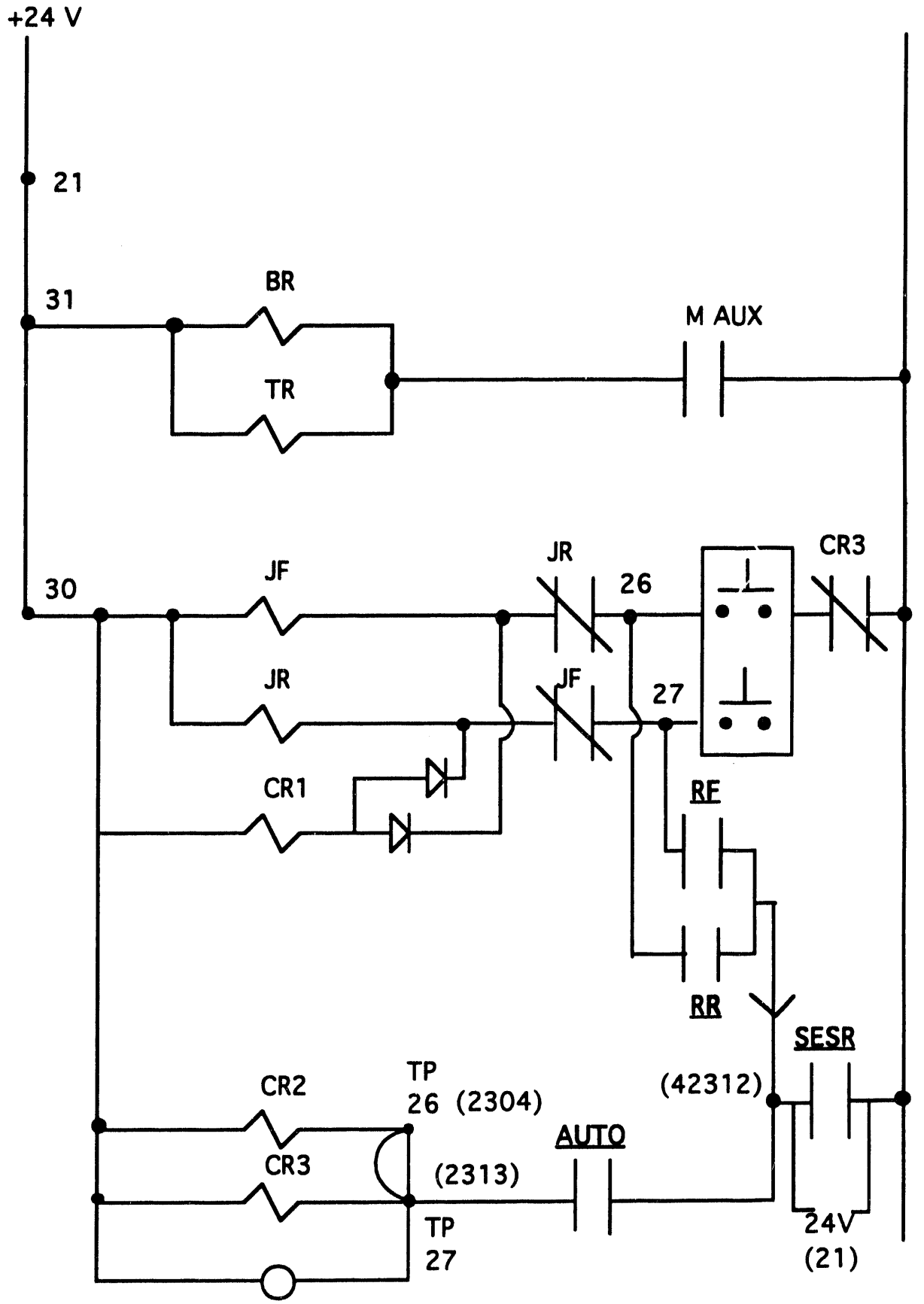
+24 V
21
31
BR
TR
M AUX
30
JF
JR
26
CR3
JR
JF
27
CR1
RF
RR
SESR
(42312)
CR2
TP
26 (2304)
AUTO
CR3
(2313)
TP
27
24V
(21)

FIGURE 7

STRAIN LINK

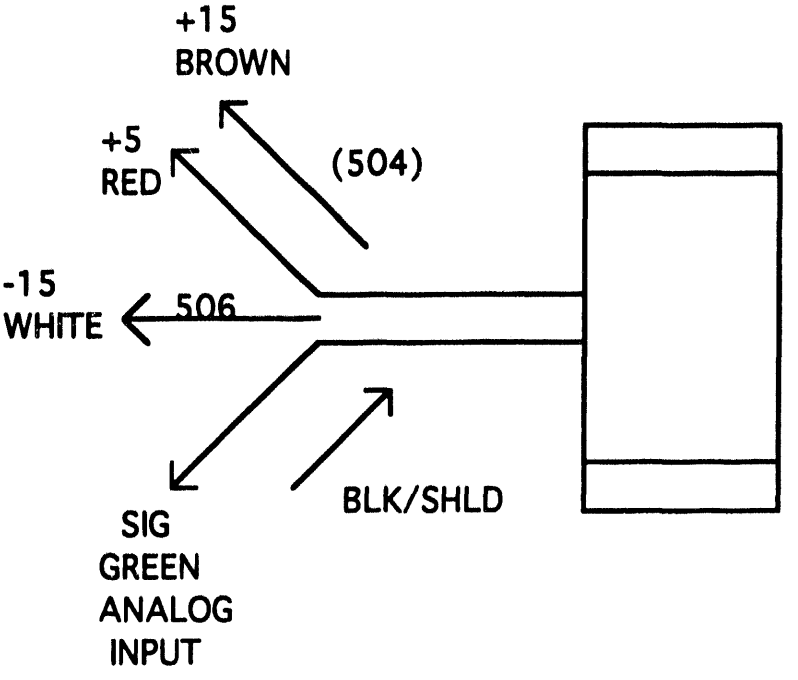

NOTE: +5 VOLTS IS PICKED UP FROM THE POWER SUPPLY W/D 704323-BX.

FIGURE 8

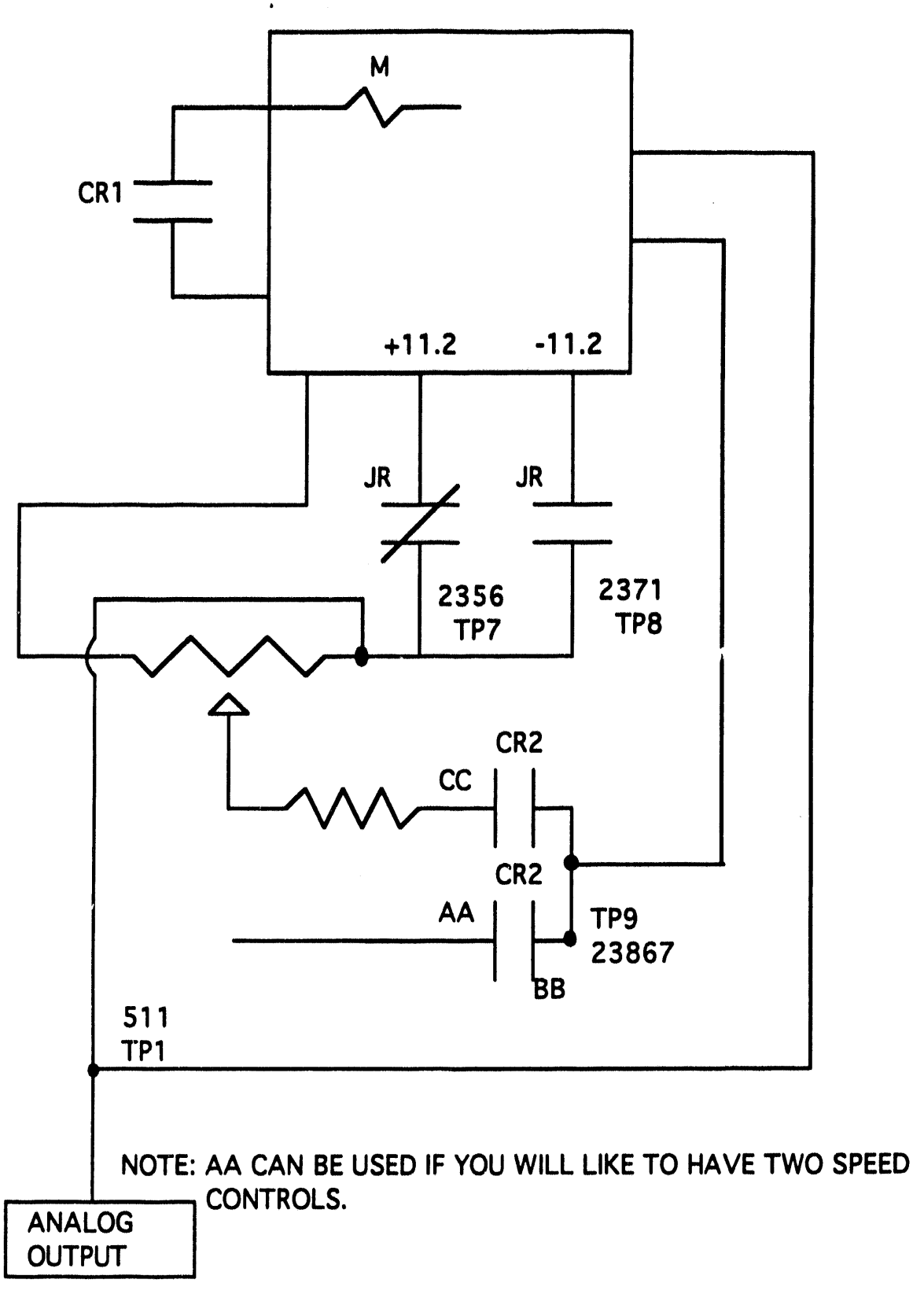

NOTE: AA CAN BE USED IF YOU WILL LIKE TO HAVE TWO SPEED CONTROLS.

Implementation of the Schwarz Alternating Method Using a Functional Language*

John S. Muller

University at Stony Brook
State University of New York

Computing Research Group
Lawrence Livermore National Laboratory
Livermore, California 94550

12/18/92

ABSTRACT

Using SISAL, a portable functional language, we implemented Schwarz Alternating Method (SAM) on multi-processor architectures. SAM is a numerical technique used for solving elliptic partial differential equations with boundary conditions, while SISAL is a portable functional language with syntax similar to other high level languages such as Pascal or Ada. In SISAL it is easy to parallelize algorithms for different multi-processor architectures. As a result, it is the ideal language for those with little or no knowledge of parallel computing. We use SISAL to exploit SAM's natural parallelism, but also demonstrate how it takes advantage of parallelism no matter what architecture is used and can be employed with minimal effort by the programmer. We show performance results on a variety of architectures.

Prepare in partial fulfillment of the requirements of the Science and Engineering Research Semester under the direction of Thomas DeBoni and John T. Feo, Research Mentor, in the Lawrence Livermore National Laboratory.

*This research was supported in part by and appointment to the U.S. Department of Energy Science and Engineering Research Semester (hereinafter called SERS) program administered by LLNL under Contract W-7405-Eng-48 with Lawrence Livermore National Laboratory.

By acceptance of this article, the publisher or recipient acknowledges the U.S. Government's right to retain a non-exclusive, royalty-free license in and to any copyright covering this article.

1.0 Introduction

Today's scientific applications are complex and are computationally intensive. Sequential processors are unable to provide us with the computational power we need to solve these current and future applications. An approach to achieving this computational power is through parallel processing. However we face a roadblock that prevents us from reaching this destination. The problem is that it is difficult to program parallel machines with languages such as FORTRAN. Some approaches to getting around this roadblock include improving the compiler, extending existing languages, or using new languages such as SISAL. The first approach has been tried and it has not been found to be successful. The second approach is to extend existing languages, but this approach does not address the fundamental problems associated with parallel computing. Perhaps the only solution is to use a new language such as SISAL (Streams and Iterations in a Single Assignment Language).

2.0 Imperative vs. Declarative Languages

Before discussing SISAL and using it to implement the Schwarz Alternating method (SAM), it is important to discuss two classes of computer languages. These two classes are commonly referred to as imperative and declarative languages.

Imperative or procedural languages are based on the Von Neuman model. In this scheme, programs are based on the computer's memory and on the sequencing of instructions. In imperative languages, assignment statements involve updating the contents of a memory cell. Therefore, it is up to the programmer to worry about the algorithm as well as how to compute certain values, sequencing and memory management. When parallel architectures are introduced than the programmer is responsible for communication, synchronization, and resource management. If this is done incorrectly, the results are non-deterministic, not portable, and subject to poor performance, resource conflicts, and deadlock.

Declarative or applicative languages may be viewed as strongly typed imperative languages without assignment statements. Declarative languages are based on mathematical ideas and deal with data values rather than memory locations. As a result, they introduce an alternative way to express data values or calculations. Declarative languages have a property called referential transparency; in other words, they are free from side effects. Because of referential transparency, declarative languages introduce no control dependencies, and instruction sequence is only constrained by data dependence. Considering the properties of declarative languages, the programmer only needs to worry

about what values to compute, and not how these are computed. This creates an easier job for the programmer and produces more reliable code.

3.0 SISAL

SISAL was developed in 1983 through the collaborated efforts of Lawrence Livermore National Laboratory (LLNL), the University of Manchester (England), Digital Equipment Corporation (DEC), and Colorado State University[1]. It is considered to be part of a subclass of declarative languages called functional languages and was derived from a data flow language called VAL (Value oriented Algorithmic Language) developed by Jack Dennis[2]. The SISAL language definition has remained stable since 1985, providing a solid test environment for functional programming development. Currently LLNL and Colorado State University are involved the research areas of SISAL[3].

Why was SISAL developed when many other languages are used by the business and research communities? There were several reasons for SISAL development. One major reason was that developers wanted to define a general-purpose functional language that hides all the details of parallelism. They wanted this functional language to be used to implement large scale scientific applications. During the development of SISAL, the developers achieved many goals, including a functional language that provides the same execution performance as an imperative language, a portable language between different architecture's and developed optimization techniques for parallel computing[1, 3, 4].

SISAL offers many advantages when solving problems that imperative languages are unable to offer. These advantages include:

- Deterministic because it always produces correct results regardless of the architecture which is something imperative languages are unable to do or guarantee
- Portability regardless the underlying architecture. SISAL programs may be run sequentially or parallel without any modifications
- Implicit parallelism since it produces parallel code while hiding responsibilities and problems introduced by programming in parallel.
- Performs as fast and in many cases better than imperative languages
- Free from side effects or aliases
- Never introduces time dependent errors
- Never alters memory from the programmers perspective
- Shorter programs since less information needs to be specified

[1, 3].

Like many good things in life, however SISAL has some drawbacks. The three major drawbacks of the language are that it doesn't provide interactive I/O, doesn't provide higher order functions, and that it is unable to handle interrupts. Some may even argue SISAL biggest drawback is that it is a functional language and is unable to offer assignments, side effects, and control flow. Rather than debating this issue, I quote from David A. Turner, who states, "The functional programmer sounds rather like a mediaeval monk, denying himself of the pleasures of life in the hope that it will make him virtuos. To those more interested in the material benefits, these 'advantages' are totally unconvincing"[5].

4.0 Schwarz Alternating Method (SAM)

4.1 Elliptical Partial Differential Equations (PDEs)

A partial differential equation (PDE) is an equation that states a relationship between a function of several independent variables and the partial derivatives of this function with respect to these variables. The general equation of PDE for two independent variables is:

$$Af_{xx} + Bf_{xy} + Cf_{yy} + Df_x + Ef_y + Ff = G$$

The PDE is then classified based on the sign of the discriminant B^2-4AC. When the discriminant is negative, the PDE is classified as elliptic.

Elliptical Partial Differential Equations (PDEs) are present in many scientific and engineering applications. We will look at the Laplace equation and Poisson equation, which are the most common and apply to problems such as mass diffusion, heat diffusion(i.e., conduction), neutron diffusion, electrostatic, and inviscid incompressible fluid flow. The Laplace equation is defined by $f_{xx} + f_{yy} = 0$. The Poisson equation is defined by $f_{xx} + f_{yy} = F(x,y)$ and it is just the Laplace equation with a nonhomogeneous term F(x,y).

For simplicity of demonstrating how to solve the Laplace equation we will look at the heat diffusion problem, as defined in [6]. In the heat diffusion problem we are given a rectangular plate of height h and width w. Each boundary of the plate is held at some constant temperature, which we know. We will then need to determine the temperature (T) distribution at each point (x, y) on the plate (Fig.1).

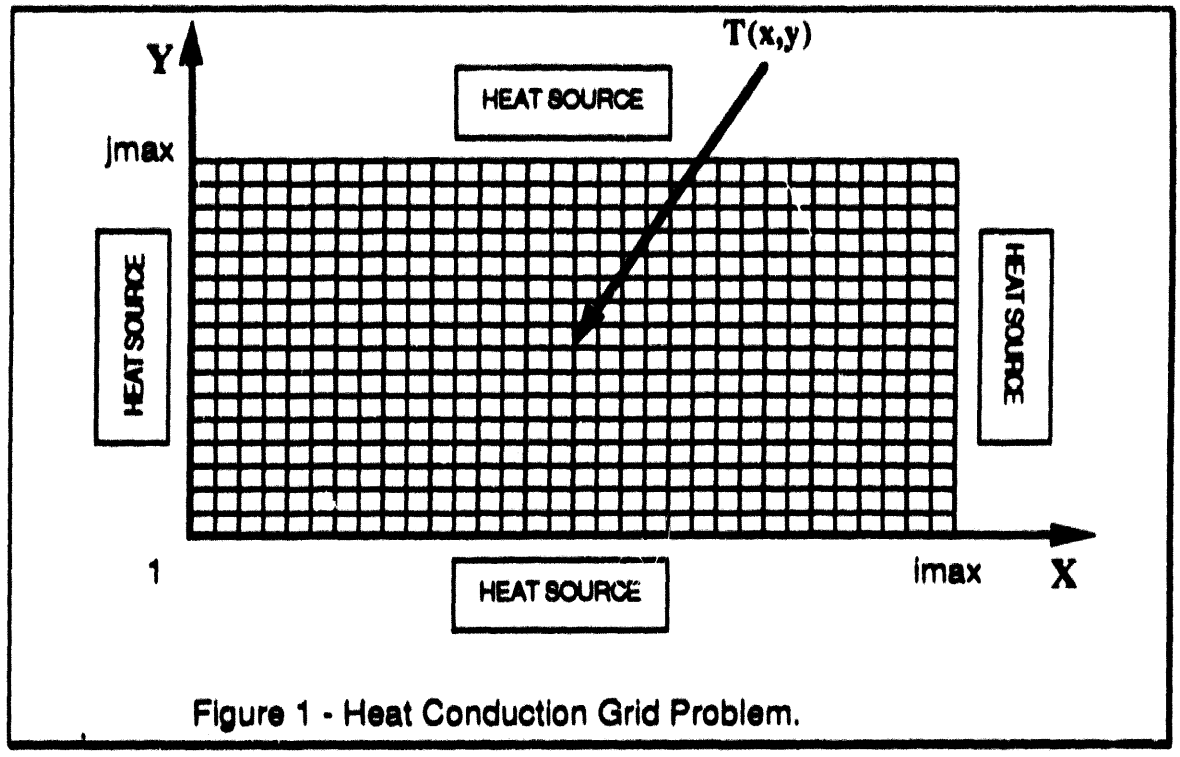

Figure 1 - Heat Conduction Grid Problem.

This distribution may be determined by solving the system of five-point finite difference equation (FDE):

$$T_{I+1,J} + \beta^2 T_{I,J+1} + T_{I-1,J} + \beta^2 T_{I,J-1} - 2(1+\beta^2)T_{I,J} = 0$$

Note that β is the grid aspect ratio defined as $\beta = \Delta x / \Delta y$. If we solve the five-point FDE for $T_{I,J}$ we obtain the following equation:

$$T_{I,J} = \frac{T_{I+1,J} + \beta^2 T_{I,J+1} + T_{I-1,J} + \beta^2 T_{I,J-1}}{2(1+\beta^2)}$$

It is interesting to note that $T_{I,J}$ is just the average of its neighbors in the special case of $\Delta x = \Delta y$ for the Laplace equation and may be expressed by this equation:

$$T_{I,J} = \frac{1}{4}(T_{I+1,J} + T_{I,J+1} + T_{I-1,J} + T_{I,J-1})$$

The solution to the Poisson equation may be found just as easily. The only difference is that we evaluate the nonhomogeneous term at each node and add it to the finite difference approximation of exact partial derivatives. So for the heat conduction problem the adjusted equation is:

$$T_{I+1,J} + \beta^2 T_{I,J+1} + T_{I-1,J} + \beta^2 T_{I,J-1} - 2(1+\beta^2)T_{I,J} = -\Delta x^2 (\frac{Q_{I,J}}{k})$$

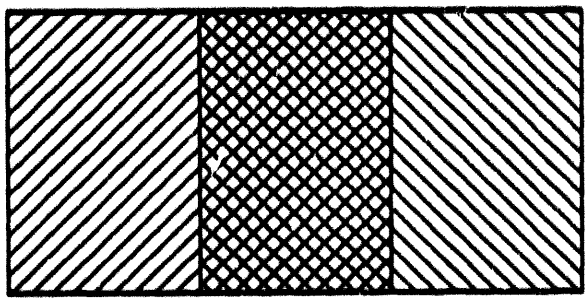

Subregion S1

Subregion S2

Subregion S3 which consists of the S1 union S2. The solution of S1 and S2 will converge to the solution of S3.

Figure 2 - Description of SAM.

The term $-\Delta x^2 (Q_{i,j} / k)$ is the nonhomogeneous term F(x,y) with $Q_{i,j}$ defined as the energy generation rate per unit volume (J / s-cm^3) at grid point (i,j) and k is thermal conductivity of the solid (J / cm-s-C).

4.2 SAM

Schwarz Alternating Method is an old mathematical technique that may be used to solve elliptical partial PDEs. The basic concept of SAM is to divide the solution space into two overlapping regions or disks. At this point the elliptical PDE may be solved on each subregion and a sequence of solutions may be constructed which converges to the solution of the union (Fig. 2).

SAM has the following advantages because correctness of the solution is not affected by:

- The number of subproblems or their geometric shape is unrestricted
- The solution techniques that are used for each subproblem
  (A different technique for the same subproblem may be used at each stage)
- The type of boundary values used for artificial boundaries in the decomposition
- The size of the overlapping area
- The number of partitions

We have chosen to implement SAM in SISAL because we wanted to show how well SISAL handles decomposition problems. SAM offers many advantages for parallel execution because the algorithm contains parallelism, local communication patterns, and hides global information which will be pointed out later.
[7]

5.0 Algorithm

Due to the nature of SISAL, it was very easy to express SAM in SISAL. For purposes of explaining the algorithm that was used, I will look at the heat conduction problem divided into two subproblems.

For the heat conduction problem we would take two points p1 and p2. Points p1 and p2 are separated by a distance of Δx (Fig. 3). This divides the initial problem into two smaller subproblems. Subproblem 1's horizontal grid points range from 1 to p2 while subproblem 2 horizontal grid points ranged from p1 to imax (Fig 4.). We approximate the solutions for the new boundaries along column p2 of subproblem 1 and column p1 of subproblem 2. Each subproblem can now be solved independently. We do this by sending each subproblem to a processor and solving using the congient gradiant method. It is worth noting that this is where same exploits parallelism in its algorithm. It is clear that there is no need for global information at this point.

Once we have reached a solution we will check to see if $\|Ax-b\| < \varepsilon$ (In our implementation, $\varepsilon = 1 \times 10^{-12}$). If this condition has not been met then the solution has not converged yet and we must resolve the problem. However this time we will approximate the boundary p2 in subproblem 1 with the solution of p2 in subproblem 2. We will also do the same for p1 in subproblem 2 by approximating it with the solution of p1 in subproblem 1. We will now send each subproblem to a processor and solve again. This process continues until the solution converges. There is no need for the processors to communicate until solutions have been found and therefore there are no local communication patterns. This in turn makes SAM a good parrallel algorithm.

6.0 Hardware

We provide performance results on a Silicon Graphics Inc. (SGI) machine and two vector supercomputers. The SGI is a scalar IRIS 340 machine consisting of four 33 MHz MIPS R3000 chips. It has shared memory and consists of a two level cache resulting in sever penalty if a cache miss occurs. The SGI machine is able to obtain 7 to 10 MFLOPS peak per processor and 3 to 4 MFLOPS sustained.

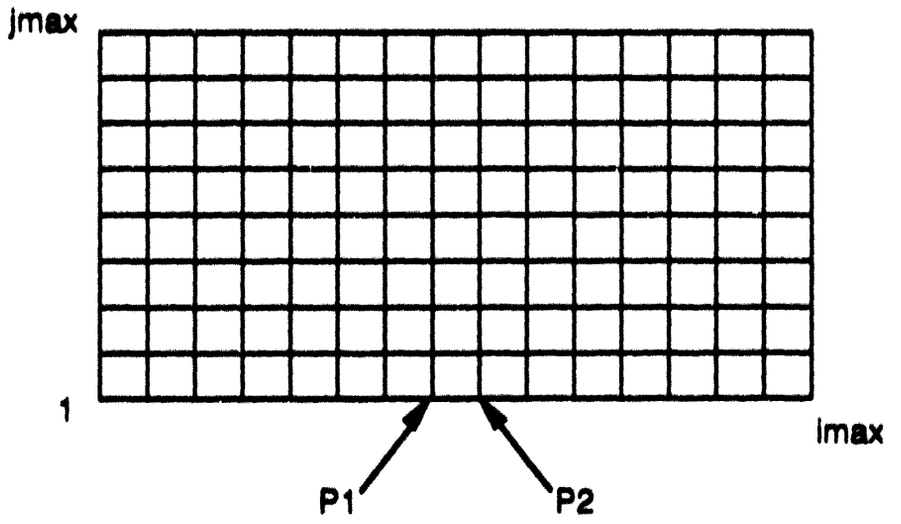

Figure 3 - SAM applied to the Heat Conduction Problem.

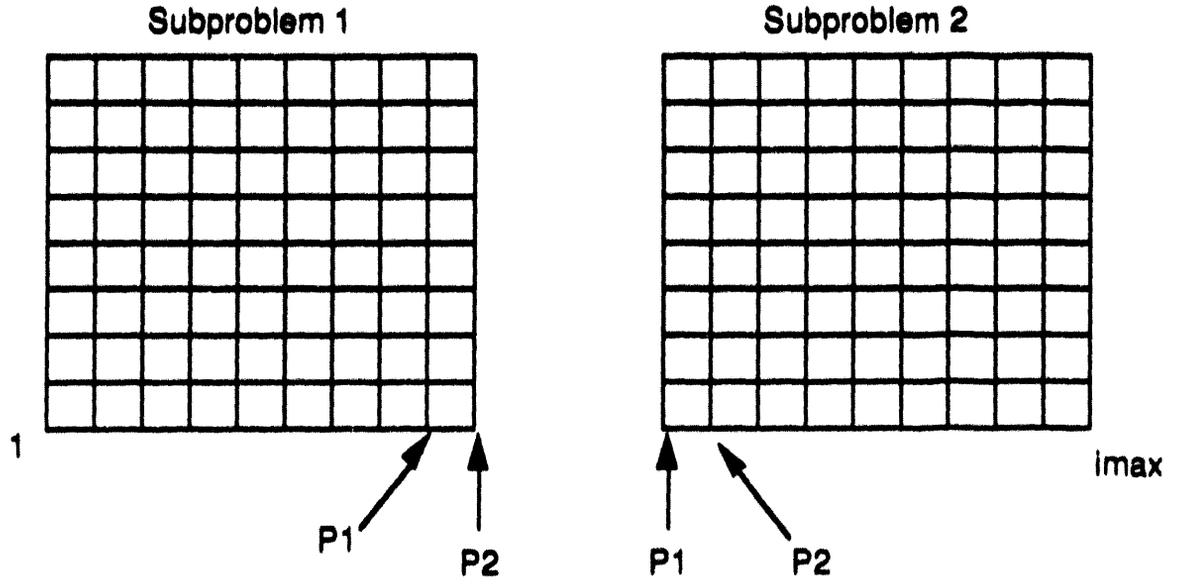

Figure 4 - Then divide the original problem (Fig. 3) into 2 subproblems.

Our second machine is the Cray-2, which is an eight processor vector machine with a vector length of 64. The Cray-2 has 250 MFLOPS peak per processor and 14 to 25 MFLOPS per processor sustained. It is capable of performing 1 billion floating point operations per second per CPU.

The last machine is the Cray Y-MP C90 which is a 16 processor vector machine with a vector length of 128. It has a peak of 500 MFLOPS per processor and 80 to 100 MFLOPS per processor sustained. It can perform 500 million floating point operations per second per CPU.

7.0 Performance results

Tables 1 to 3 show our performance results on the architectures described above for solving a 300 x 300 grid problem divided into 10 subproblems. The workers column represents the number of processors used, Time Sec is the runtime in seconds, Mem Mb column is the memory used in megabytes, speedup column shows the speedup for 1 to 4 processors, and MFLOPS column shows the number of millions of floating point operations per second. Tables 4 to 6 show our performance results on a 300 x 300 grid problem divided into 30 subproblems.

Runtimes decrease as we would expect when we go from 10 subproblems to 30 subproblems. However the Cray C90 runtime didn't decrease that much. I do not know the reason for this at this time.

The amount of memory used increased as the number of processors increased. When going to 10 subproblems to 30 subproblems, the amount of memory used decreased on all machines except the C-90 which remained fairly constant

The speedup curves may be seen in fig. 5 and fig. 6. On the 10 subproblem, the C90 is very close to theoretical maximum, which is an excellent result. The SGI speedup is a little low, the reasons are unexamined at this time. The Cray-2 speedup is terrible. I suspect these results are false since my runs had alot of memory disk swaps and I didn't have dedicated cpu time. On the 30 subproblem, the speedups for the C90 and SGI improved compared to the 10 subproblem except for when using 4 processors on the C90. We expected that the speedup would increase which is especially true for the SGI. Again the Cray-2 results are not right for the same results mentioned above.

Machine	Workers	Time Sec	Mem Mb	Speedup	MFLOPS
SGI	1	239.620	19.317	1.000	2.524
SGI	2	132.930	21.565	1.803	4.550
SGI	3	111.607	24.095	2.147	5.419
SGI	4	98.113	26.767	2.442	6.165

Table 1: 300x300 problem divided into 10 subproblems on SGI.

Machine	Workers	Time Sec	Mem Mb	Speedup	MFLOPS
Cray-2	1	37.519	19.333	1.000	16.120
Cray-2	2	24.225	21.939	1.549	24.967
Cray-2	3	22.095	24.404	1.698	27.374
Cray-2	4	12.650	27.366	2.966	47.812

Table 2: 300x300 problem divided into 10 subproblems on Cray-2.

Machine	Workers	Time Sec	Mem Mb	Speedup	MFLOPS
Cray C90	1	12.524	17.925	1.000	48.293
Cray C90	2	6.668	18.649	1.878	90.705
Cray C90	3	4.597	19.463	2.724	131.569
Cray C90	4	3.574	20.257	3.504	169.229

Table 3: 300x300 problem divided into 10 subproblems on Cray-C90.

Machine	Workers	Time Sec	Mem Mb	Speedup	MFLOPS
SGI	1	100.240	17.899	1.000	2.494
SGI	2	53.235	18.621	1.883	4.696
SGI	3	39.040	19.433	2.568	6.403
SGI	4	33.010	20.224	3.037	7.572

Table 4: 300x300 problem divided into 30 subproblems on SGI.

Machine	Workers	Time Sec	Mem Mb	Speedup	MFLOPS
Cray-2	1	27.413	17.925	1.000	9.119
Cray-2	2	14.516	18.649	1.888	17.220
Cray-2	3	11.482	19.704	2.387	21.770
Cray-2	4	9.129	20.423	3.003	27.382

Table 5: 300x300 problem divided into 30 subproblems on Cray-2.

Machine	Workers	Time Sec	Mem Mb	Speedup	MFLOPS
Cray C90	1	12.485	17.925	1.000	20.021
Cray C90	2	6.600	18.649	1.892	37.874
Cray C90	3	4.560	19.463	2.738	54.817
Cray C90	4	3.569	20.233	3.498	70.038

Table 6: 300x300 problem divided into 30 subproblems on Cray-C90.

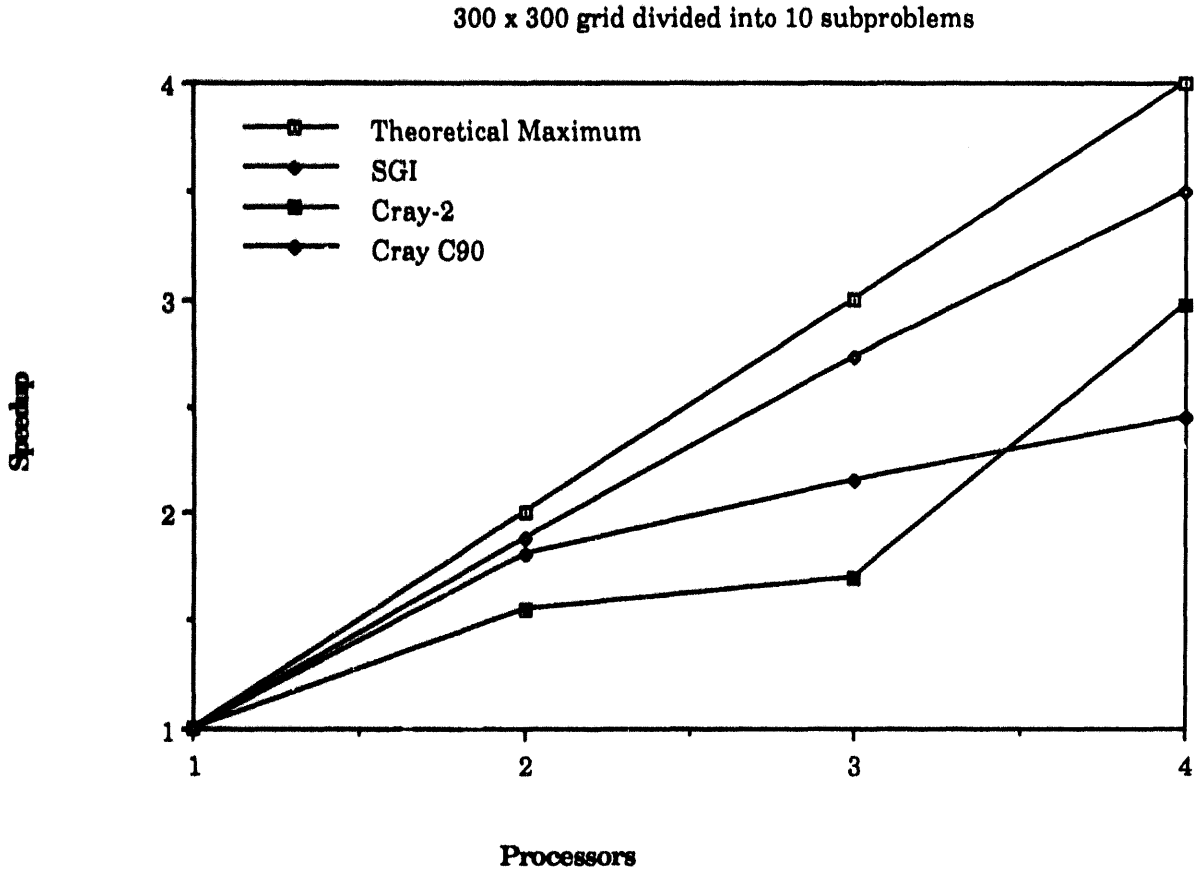

Figure 5 - Speedup for 10 subproblems on 300x300 problem.

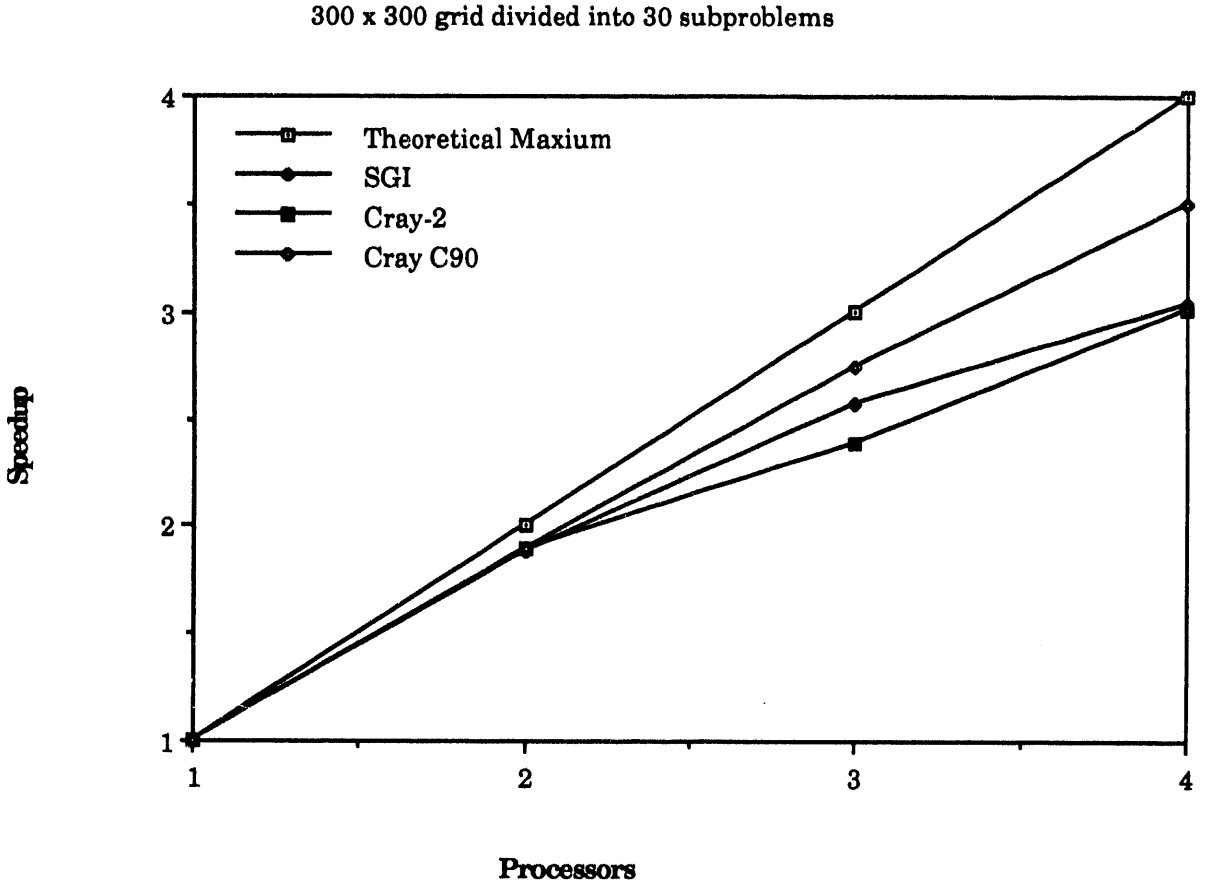

Figure 6 - Speedup for 30 subproblem of a 300 x 300 grid.

8.0 Future

There are many things that we were unable to get to or try that we want to persue in the future.

We may want to see the effect of splitting the problem horizontally instead of vertically like we did in this problem. Another interesting approach that we may want to take is to split the problem horizontally and vertically It would be interesting to see the amount of parallelism that we may be able to exploit this way.

Also we would like to see how different grid sizes may change our results. Right now we are working with problems where $\Delta x/\Delta y=1$.

We also need to investigate and compare the speedups of different size problems and the speedup change when you change the number of subproblems on a wider range.

9.0 Conclusion

In conclusion I first would like to discuss how I perceive SISAL and functional languages. I found that learning to think and program in a functional language was not a hard task to overcome. The hardest part of learning the language for me was overcoming the single assignment paradigm . I found that it was very natural to express the solution to mathematical problems, in particular problems involving matrices and vectors.

One noteworthy feature of SISAL was that I was able to see where the parallelism was going to take place due to its syntax. Before learning SISAL, I did not know a thing about programming in parallel architectures. Within a week, I was writing and running programs without any effort due to SISAL's implicit parallelism.

The quality that makes SISAL stand out from the rest is the fact that it is portable between different architectures. When I did my timings on the SGI machine and the Cray's, I used the exact source code. All I had to do was recompile the source code, without modifications, on each machine and my program ran giving me determinate results. If I wanted to use one or sixteen processors the source code doesn't change.

When splitting the HTP into subproblems it was easy to do in SISAL. All I had to worry about was the algorithm and SISAL took care of the parallelism and architecture for me. If I would have done it in an imperative language such as Fortran than I would have had to worried about communication, synchronization and resource management.

Now don't get me wrong, I am not trying to preach SISAL as being the only language of the nineties. SISAL still has some shortcomings and the biggest problem that I found was that it did not provide higher order functions. For me this caused a problem because every time I changed my problem to have different boundary conditions I would have to

modify my source code and recompile. If I would have been able to pass the initial boundary conditions as a function to the main then this would have simplified things very much. My solution to this was to use a header file with a #define defining my boundary condition this way the change was localized and I only needed to modify one piece of the code.

Another shortcoming that I found was that SISAL doesn't provide interactive I/O. This was not a problem for me to solve my particular problem, but it would of been nice to have to aid me in debugging and is something I am used to from other languages. However it is not really needed since SISAL has a very nice debugging tool called TWINE. Although SISAL could provide a better way for input and output. Its current method FIBRE provides method for input and output, but I feel it is a very poor approach and can be done a better way.

And finally I would like to conclude on the issues of using imperative languages to program parallel architectures. The issue is not whether imperative languages such as FORTRAN is good or bad. Rather the issue is whether languages like FORTRAN are appropriate for parallel computing. The designers had in mind von Neuman sequential machines when they designed FORTRAN. Multiple processors never crossed the designer's minds. Imperative languages with extensions are not appropriate for programming parallel machines.

We need the tomorrow solutions to solve problems of today, not yesterdays solutions. We need to take a new approach to designing programming languages, such as SISAL. The SISAL designers targeted parallel machines when they designed SISAL. SISAL may not be the solution, but it is a step to the solution. It is a approach in the direction of what we need in parallel programming languages.

10.0 Acknowledgments

At this point I want to thank the following people, especially the CRG folks, for the help and knowledge they shared with me in completing this project. A brief thanks in alphabetical order to Vince Beckner, Walter Cedeno, Thomas DeBoni, John Feo, Christopher Frerking, James McGraw, Judy Michels, Patrick Miller, Garry Rodrigue, Bert Still, and Richard Wolski.

Also would like to thank Barry Goldman and the SERS program, without them I would never have had the opportunity to do this research program.

Bibliography

[1] [illegible]
pg 1

[2] McGraw, James R., "The VAL Language: Description and Analysis," Journal ACM Trans. on Programming Languages and Systems 1992, January vol 1, pp 44-82

[3] DeBoni, Tom, A SISAL Tutorial - A Gentle Introduction to Functional Parallel Programming, Unpublished paper, pg 1-3

[4] Feo, John T., A Comparative Study of Parallel Programming Languages: The Salishan Problems, North Holland 1992, pg 337-339

[5] Turner, David A. - Research Topics in Functional Programming Addison-Wesley Publishing Company 1990, pg 18

[6] Hoffman, Joe D. - Numerical Methods for Engineers and Scientists McGraw-Hill, Inc 1992, pg 372, 376, 403-423, 441-443

[7] Tang, Wei Pai, Schwarz Splitting and Template Operators Ph.d. thesis, Stanford University, pg 1,4,5

Adsorption Characteristics of Nitric Oxide on Copper Catalysts

Tim Onasch
Carleton College
Physical Chemistry

ABSTRACT

Previous experiments have shown that copper reduces nitric oxide (NO) gas to N_2 and O_2, indicating the potential use of copper as a catalyst to control exhaust emissions from cars. We will be carrying out infrared studies of the vibrational frequencies of NO adsorbed onto copper ions matrixed in zeolite and aerogel supports. To augment these studies, we used the Columbus system of computer codes to investigate a simple NO-copper model in the restricted Hartree-Fock (H-F) approximation. This is a preliminary theoretical study of NO interacting with a copper ion on a catalytic surface. We compared the total H-F energies of the model at the equilibrium bond distances in the

a) linear Cu^{+1} - N=O b) linear Cu^{+1} - O=N and c) bent Cu^{+1} - N(=O)

conformations, to determine the preferred geometry of adsorption. Preliminary results indicate that the linear Cu^{+1}-ON system is lowest in energy. We characterized the NO-copper interaction by examining the electron densities, the total potential energy curves, and the vibrational frequencies of the free and adsorbed NO molecule. Similar studies have also been done on NO adsorbed onto copper oxide, an overall neutral system.

Introduction:

Along with the increasing concern for our environment, there has been a rising awareness of the environmentally destructive nature of present automotive technologies. Developing new technologies that will decrease the emission levels of harmful substances, such as hydrocarbons, carbon monoxide and nitrogen oxides, from car exhaust and still allow the car to operate at the same high standards, is a must. The government of the United States has already taken a step in this direction by creating a timetable for the reduction of exhaust emission levels. (Fig. 1 Truex) The challenge is now for the automotive industry to meet these standards.

This paper reports on a project that is part of a much larger cooperative effort between car industries and several national labs, including Lawrence Livermore National Laboratory, aimed at developing a more fuel efficient lean burn engine that will meet the increasingly more stringent federal emission standards. Figure 2 clearly shows that a major complication in shifting an engine from a typical intake composition of 14.7:1 air to fuel ratio by weight, to a lean burn with intakes of 16:1 or 17:1 air to fuel ratio is the dramatic increase in nitrogen oxides emissions (Truex). Since conventional three-way catalysts will control hydrocarbon and carbon monoxide levels, but not nitrogen oxide levels at lean burn conditions, new catalytic materials are being developed. (Fig. 3) Copper zeolites and aerogels are examples of NO_X reducing catalysts under development.

The goal of this project was to study the adsorption of nitric oxide (NO) gas on copper catalysts, to better understand the chemistry involved in the first step of the catalysis process. Two approaches were used in the investigation. The first was the experimental characterization of the vibrational frequencies of NO adsorbed onto copper sites on the surface of various aerogel and zeolite catalysts by infrared spectroscopy. And the second approach was the development of theoretical models to interpret the experimental results and further define the nature of the active sites.

Experimental:

In their study of the mechanisms and kinetics of nitric oxide reduction by carbon monoxide over a copper oxide catalyst, London and Bell measured the infrared spectra of adsorbed NO (London, 1973a). Vibrational bands were observed at 1890, 1605, 1575, and 1510 cm^{-1} for a temperature range of 33°C and a NO partial pressure of 0.05 atm. These are all shifted from the 1876 cm^{-1} band of free NO. Based on the small positive shift of the 1890 cm^{-1} band they concluded that the NO bond was not greatly perturbed by adsorption and the Cu-NO bond is relatively weak. They were unable to assign a unique identidy to the adsorbtion site. However, based on the molecular orbital calculations of Blyholder and Allen (Blyholder, 1965), they speculated that bonding in the configuration Cu-N-O would lead to a stronger NO bond and possibly a positive shift in the vibrational frequency. The remaining bands at 1605, 1575, and 1510 cm^{-1} were not assigned but appeared to be due to NO. In a later study London and Bell assigned the active site for NO reduction by CO as either Cu or Cu^{+} and suggested that NO dissociates on adsorption (London, 1973b).

Fu *et al.* carried out a more recent infrared study of NO adsorbed on a $CuO/\gamma\text{-}Al_2O_3$ catalyst (Fu). They concluded that both Cu^{+2} and Cu^{+1} ions coexisted on the surface and assigned the bands at 1888 cm^{-1} to NO on Cu^{+2} in CuO. A shoulder at 1862 cm^{-1} was assigned to Cu^{+2} in $CuAl_2O_4$. The band observed at 1800 cm^{-1} was assigned to NO adsorbed on Cu^{+1}. When the temperature was increased from 123 K to 173 K, the 1800 cm^{-1} feature disappeared. In the presence of CO, Fu *et al* found that NO was selectively adsorbed on the Cu^{+2} sites. These observations led them to conclude that NO was more strongly adsorbed on the Cu^{+2} sites. The reasons for the stronger vibrational shift of the weaker adsorbing Cu^{+1} site was not explained.

The purpose of the experimental part of the present project was to design and assemble an apparatus to take infrared spectra of nitric oxide adsorbed onto copper sites on various samples of copper zeolite and aerogel catalysts to agument the existing experimental data.

A Barnes Analytical / Spectra-Tech diffuse reflectance accessory with a large/small interchangeable sample cup and a catalytic high pressure/high temperature flow through cell was obtained. Using the diffuse reflectance technique on a BioRad FTIR, preliminary spectra were

taken of silica aerogel and various samples of transition metal doped silica aerogels and transition metal oxide aerogels.

A system was designed and assembled to control the temperature and flow through capabilities of the catalytic cell. NO (1000 ppm in Ar) gas was connected in preparation of the adsorption studies, with pure Ar as a purge gas.

However it was not possible to complete any adsorption experiments with the catalytic cell in the allotted time period.

Theoretical Modeling:

The purpose of this part of the study was to develop preliminary theoretical models of nitric oxide adsorbed onto copper sites on a surface using the restricted Hartree-Fock method. These models would then be improved and refined in future studies using experimental data from previous work as a guideline for the accuracy of the models. The models that agreed with the experimental data would then be used to interpret the observed vibrational frequency shifts of a nitric oxide (NO) molecule as it adsorbs onto the surface of a copper catalyst. Obtaining a better understanding of the preferred state of the copper ions and the preferred geometry of adsorption in terms of the orbitals involved is a valuable step towards understanding the mechanism of the catalyzed reduction reaction. An understanding of the mechanism could possibly help tailor a catalyst that has the highest turn over rate for the conditions. Having the understanding of the reaction mechanism could save the time and effort in synthesizing new and better catalytic material, and could also be used to apply to future problems of similar nature.

This section of the paper is broken down into six parts. The first is a description of the models used in this preliminary study. The second is an introductory discussion of the restricted Hartree-Fock method of solving the schroedinger equation for molecular orbitals. The third and fourth parts are a description of the computer codes used and the procedure of inputting the data for calculations. The fifth is a discussion of the results obtained during this study and the sixth part contains the conclusions drawn and the suggested directions for future studies of the reduction of NO by copper catalysts.

Models:

Three models were chosen for this preliminary study with the simple copper components representing possible copper sites on a surface. (See below.)

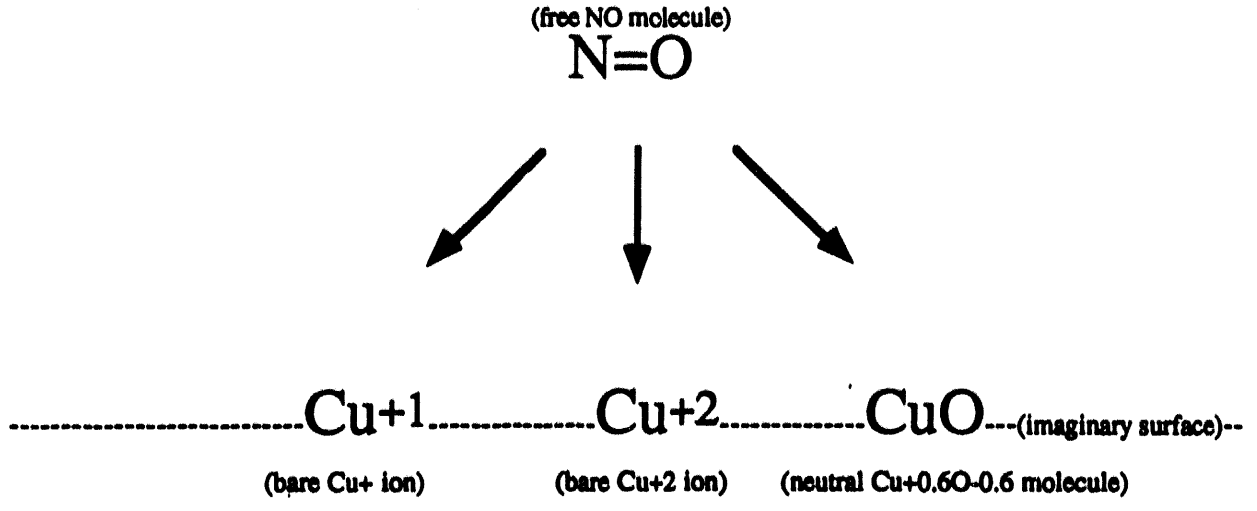

The first two models contain only three atoms: NO interacting with a bare copper ion having either a plus one or plus two charge. These two models were chosen because previous work indicated that both Cu+1 and Cu+2 ions coexist on a copper catalyst surface (Fu 89). The third model is of NO interacting with a copper oxide (CuO) molecule. This model was chosen because CuO is the source of copper on many copper catalysts. The last model also allows the NO molecule to interact with a copper atom having a valence state that is less than a full positive charge.

Restricted Hartree-Fock Method:

The restricted Hartree-Fock method was used to analyze the models for this introductory study because of its simplicity and its relatively short computation time. The restricted Hartree-Fock (H-F) method is an approximation method for solving the Schroedinger equation for atoms or molecules more complicated then the hydrogen atom.[1] While the H-F method is not the most accurate method for obtaining solutions for the Schroedinger equation, it is useful because it carries with it the concept of atomic orbitals and their interactions which lead to the formation of molecular orbitals.

The Schroedinger equation, $H\Psi = E\Psi$ where H is a hamiltonian operator, describes the relationship between the total energy and the wave functions for the electrons of a system. For systems of more then one electron the equation is insoluble because of the terms arising from inter-electronic repulsions, and therefore has to be solved by an approximation method. The H-F method is based on the variational principle. The variational principle states that the Schroedinger equation can be solved in terms of E_{trial}, the energy of the system, using any trial wave function, Ψ, with the result that $E_{trial} \geq E$. In other words, a trial wave function could be chosen such that

---

1 The reason why these calculations are called **restricted** H-F calculations is because electrons with paired spins are forced to occupy the same spatial orbitals.

$E_{trial} = E$. For the H-F case, however, there exists a limit as to how close E_{trial} can get to E. The reason for the limit is implicit in the form of trial wave function that the H-F method uses, and it is the trade-off for being able to describing the molecular orbitals in terms of atomic orbitals.

For closed shell (2N-electron) problems the Hartree-Fock method uses a wave function of the form, $\Psi = A[(\phi_1\alpha)(\phi_1\beta)(\phi_2\alpha)(\phi_2\beta)...(\phi_n\alpha)(\phi_n\beta)]$ where A is the antisymmetrizer and $\phi_n\alpha$ is an electron in the n^{th} orbital with spin α. The wave function is a simple multiplication of the functions of the individual electrons in terms of what orbital they occupy and what spin they have. When dealing with a molecular system, the ϕ_n are functions describing molecular orbitals. The molecular orbitals used in restricted Hartree-Fock calculations are linear combinations of atomic orbitals:

$$\phi_i = \sum C_i * X_n$$

Where C_i is a constant and X_n is a function describing atomic orbitals.

Using this form for the wave function the variational method is applied to the Schroedinger equation and the Hartree-Fock equations are formed (McQuarrie 308):

$$H^{HF}{}_i\phi_i = \varepsilon_i\phi_i \qquad i = 1,2,3... \text{ N (orbitals)}$$

ϕ_i - molecular orbital wave function
ε - orbital energy
H^{HF} - Hartree-Fock Operator

$$H^{HF} = 2f_ih + (2J_i - K_i)$$

f_i - fractional occupation number
h - single electron hamiltonian
J_i - Coulomb operator
K_i - Exchange operator

For the open shell general case, the variational method is applied with the wave function, $\Psi = A[(\phi_1\alpha)(\phi_1\beta)(\phi_2\alpha)(\phi_2\beta)...(\phi_n\alpha)]$ where A is the antisymmetrizer and where not all the orbitals ϕ_n are occupied by two electrons. For this general case the Hartree-Fock operator becomes (Bobrowicz 85):

$$H^{HF} = H^{HF}{}_{(closed)} + 2f_ih + (a_{ij}J_i + b_{ij}K_i)$$

f_i - fractional occupation number
$h = -1/2\nabla^2{}_j - Z/r_j$
a_{ij}, b_{ij} - coupling coefficients
$J_i = (ii|jj) = \langle\phi_i|J_j|\phi_i\rangle = \langle\phi_j|J_i|\phi_j\rangle$

$$K_i = (ij|ij) = \langle\phi_i|K_j|\phi_i\rangle = \langle\phi_j|K_i|\phi_j\rangle$$

From this it can be seen that the form of the Hartree-Fock operator changes depending upon whether the system is closed shell or open shell and depending upon how the open shell electrons are coupled.

Since the J and K integrals are dependent upon all of the ϕ_i orbitals, the H-F equation is a set of N coupled equations and an initial guess for all of the ϕ_i orbitals has to be made. With the initial set of ϕ_i orbitals the Hartree-Fock equation can be used to calculate new orbitals which are just different linear combinations of the original atomic orbital functions. These new orbitals can then be used to resolve the H-F equation and obtain another set of orbitals. The driving force for the calculations is to find the electronic state which has the lowest possible total energy. This process, called the self-consistent field method, is carried out until the cycle where the ϕ_i orbitals calculated are the same as the ϕ_i orbitals used for the calculations. It is at this point where the total system energy is at its lowest value: E_{trial} is as close to E as possible for the calculation.

The output of a restricted H-F calculation are the wave functions for the molecular orbitals of a system and the orbital energies associated with the orbitals. Contour plots can be made of the wave functions and/or the square of the wave functions to give a graphic representation of the shape of the orbitals, indicating the electron probability density, and the interactions happening between the orbitals. From the orbital energies, the total energy of the system can be calculated using the following equation[2]:

$$E = 2\Sigma\varepsilon_i - \Sigma(2J_{ij} - K_{ij})$$

The total energy can then be plotted verus the bond distances in the molecule, producing a potential energy curve. From the potential energy curve, the equilibrium bond distance and the binding energy can be obtained. (See below.)

The potential energy curve can be fitted to an anharmonic oscillator model to obtain the vibrational energies for the quantized vibrational levels of the bond. The difference of the energies of the first two vibrational levels gives the frequency of absorbed electromagnetic radiation for that bond.

---

2 Where the last term corrects for the fact that the electron repulsion term was counted twice in order for each Hartree-Fock operator to be uniform for each molecular orbital, allowing the H-F operator to take on a general form.

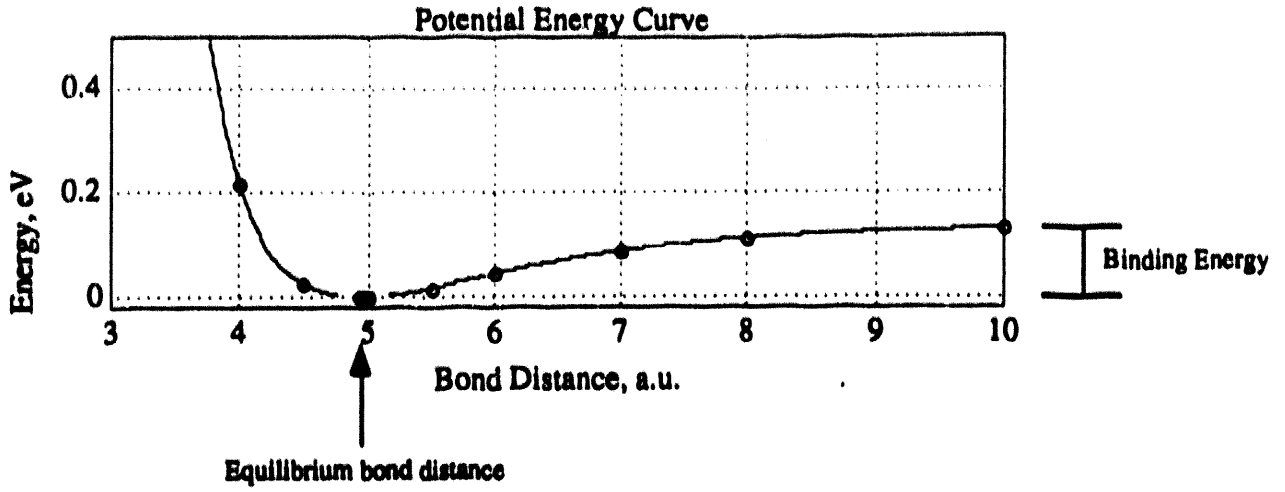

Computer Codes:

The actual calculations to solve the equations for the molecular orbitals and orbital energies are carried out with matrix Hartree-Fock computer codes. The two codes used for this project are The Ohio State University Symmetry by Equal Contribution Molecular Integrals Program (SAINT) and The Ohio State Restricted Hartree-Fock Self-Consistent-Field and Two-Configuration MCSCF Program (SCFPQ) (Pitzer).

These two codes are designed to take advantage of certain features of the matrix Hartree-Fock method: the molecular orbitals are linear combinations of atomic orbital functions and only the constant term C_i is variable during the iterative self-consistent field method of solving the H-F equations. Because of these two criteria, the constant terms can be factored out of the integrals over the single electron Hamiltonian, the Coulomb operator, and the Exchange operator. The integral for the single electron Hamiltonian will be used to illustrate this point:

molecular orbitals: $\phi_i = \Sigma\, C_i * X_n$

single hamiltonian operator: $h = -1/2\nabla^2_j - Z/r_j$

single hamiltonian integral:

$$\langle\phi_i^*|h|\phi_i\rangle = \Sigma_n\Sigma_m\langle C^*_{ni} * X_n^* \,|h|\, C_{mi} * X_m\rangle$$

$$= \Sigma_n\Sigma_m(C^*_{ni} * C_{mi})\langle X_n \,|h|\, X_m\rangle$$

This effectively breaks the calculations down into two parts. The first being the calculation of the integrals involving X_n, where $\langle X_n|h|X_m\rangle$ can be evaluated for every ϕ_i, and the second part being the iterative process of inserting a C_i for every orbital i, summing the terms, solving for the orbital energies, ε, determining the total system energy, selecting new C_i for each orbital and recalculating until a convergence is reached for the total system energy.

The molecular integrals program transforms a basis set of atomic orbials into symmetry orbitals and evaluates the the single electron hamiltonian, Coulomb, and Exchange integrals of the Hartree-Fock equations involving X_n. The output for the molecular integrals program stores the integrals in a disk file to be read by the SCF program, and prints out the coefficients and exponents of the symmetry orbitals.

The Restricted Hartree-Fock SCF program then takes the calculated integrals and carries out the SCF iterations, allowing the coefficients of the symmetry orbitals to vary, until the energy converges. The output of the H-F SCF program prints out the coefficients of the molecular orbitals in terms of the symmetry orbitals, the total energy of the system, and the atomic population analysis, which indicates how the electrons are distributed among the s, p, and d orbitals of each atom.

Calculation Details:

The input required for the molecular integrals program consists of the coefficients and the exponents of the basis set of the atomic orbitals and the symmetry and spatial arrangement of the atoms in the molecule to be analyzed. The atomic orbital functions used in the basis sets for this project were gaussian distribution functions of the form:

$$X_n = N * x^l y^m z^n * \exp(-\alpha r^2)$$

N - normalization coefficient
$x^l y^m z^n$ - function in terms of x,y,z that determines whether the orbital is s,p,d...
$\exp(-\alpha r^2)$ - gaussian distribution function

All of the calculations for this project were done with the all electron Gaussian basis set given in Fig. 4. The size of the basis sets used for the individual atoms were: Cu [14s11p6d/10s9p3d], N [9s5p/4s3p], and O [9s5p/4s3p], which means that the copper atom had a basis set of 14 atomic s-orbital functions contracted to 10 atomic s-orbital functions, 11 p-functions contracted to 9 p-

functions, and 6 d-functions contracted to 3 d-functions, and so on for the N and O atoms. A contracted atomic orbital function has the form:

$$X_c = \Sigma_n C_{cn} * X_n$$

C_{cn} - contraction coefficient

The symmetry and the spatial arrangement of the molecules studied depended upon the purpose of the calculations done. The linear molecule of NO and the linear geometries of simple models studied in this project have $C_{\infty v}$ symmetry, however, for convenience the linear N=O calculations were done with no symmetry and the linear N=O - Cu models were calculated with C_{2v} symmetry. The bent geometries had C_s symmetry, which was used in the calculations.

The spatial arrangement of the atoms allows the total system energies to be determined at different bond distances and geometries of bonding. This data can be then be plotted as potential energy curves.

The input required for the Restricted Hartree-Fock SCF program consists of placing the electrons into the orbitals and entering the coupling coefficients. By using C_{2v} symmetry for the linear N=O - Cu models, the position of the open shell orbital could be controlled. The single electron could be placed into orbitals of different symmetry, corresponding to the p_x, p_y, and p_z orbitals. The coupling coefficients are the a_{ij} and b_{ij} in the Hartree-Fock operator which describe the state of the open shell electrons.

Results and Discussion:

The results for the Cu^{+1} model are summarized in table one. A comparison of the adsorption energies for the Cu^{+1} model shows that the linear geometry where the oxygen end of the nitric oxide molecule is interacting with the Cu^{+1} ion has the largest binding energy and is therefore the preferred geometry of adsorption. This result suggests that the open shell on the nitrogen does not play a significant role in determining the geometry of adsorption. This is reasonable because the bare Cu^{+1} ion is a closed shell system, and does not have any open shell orbitals to interact with the nitrogen.

A examination of the bond distances listed in table one illustrates this point. For the linear cases, where the nitrogen's open shell is angled ninety degrees to the copper ion, the copper-oxygen bond is about 0.14 a.u. shorter then the copper-nitrogen bond. In the bent cases, where the nitrogen's open shell is pointed directly towards the copper ion, the copper-oxygen bond is again 0.13 a.u. shorter then the copper-nitrogen bond. The pattern is evident in the comparison of the potential energy curves for all four cases. (Fig. 6 and 7) Relative to the copper-oxygen bond,

which is an interaction of two closed shell systems, the position of the nitrogen open shell orbital has little effect on the adsorption interaction.

Table one:

Results for Cu^{+1} - NO model

Geometry[3]	Bond Distances (atomic units) Cu - N -or- Cu - O	N=O	Adsorption Energies (eV)	Vibrational Frequencies (cm-1)	Vib. Freq. shifts (Relative to Calc. NO Vib. Freq.) (cm-1)
Cu^{+1} - N=O	4.17	2.15	0.454	2092.6	101.7
Cu^{+1} - O=N	4.03	2.19	0.696	1929.2	-61.7
Cu^{+1} - N ‖ O	4.94	2.17	0.137	2002.4	11.5
Cu^{+1} - N ‖ O	5.13	2.18	0.127	1974.2	-16.7
Cu^{+1} - O ‖ N	4.81	2.19	0.194	1954.8	-36.1

The presence of the bare Cu^{+1} ion in the model may allow the electrostatic interactions between the positive charge and the dipole moment of the nitric oxide to heavily influence the adsorption interaction. The electrostatic theory offers an explanation for why the preferred geometry for the linear case has the oxygen end adsorbed onto the copper ion. The dipole of the nitric oxide molecule is oriented such that the more electro-negative oxygen has the partial negative charge leaving the nitrogen with a partial positive charge. The positive copper ion is attracted to the partially negative oxygen and repulsed by the partially positive nitrogen. The same explanation works for the bent cases, where again the oxygen end adsorbs stronger than the nitrogen to the copper ion.

The electrostatic theory discussed to this point has taken a classical approach to explain the results. However, this approach breaks down when the linear geometries are compared to the bent

3 The states calculated for the bent configurations were all $^2A'$ states, where the open shell on the nitrogen atom was in the plane of the copper, nitrogen, and oxygen system. The other state, the $^2A''$, had the open shell on the nitrogen pointing out of the plane of the three atoms. The $^2A''$ state was a anti-bonding state. (Fig. 5)

geometries. A quantum electrostatics approach is necessary to explain why the linear geometry with the nitrogen end of the NO molecule adsorbed onto the copper ion is more stable then any of the bent cases despite the fact that the nitrogen has the partial positive charge of the dipole. Quantum electrostatics deals with the interplay of two interactions: one attractive and one repulsive. The attractive interaction is a charge induced polarization where the positive copper ion interacts with the existing dipole on the NO molecule as well as with an additional induced moment caused by the polarization of the NO orbitals. The repulsive interaction is the overlap repulsion of orbitals as dictated by the Pauli exclusion principle.

The equilibrium bond distance is at the point where the two interactions are balanced to give the minimum energy. The attractive and repulsive interactions for the Cu^{+1} - N (O) bond of the linear models leads to an equilibrium distance of ~4 atomic units. In the bent cases the equilibrium distance is ~5 atomic units for the Cu^{+1} - N (O) bond. The cause of this effect is the greater electron density the copper ion "sees" in the bent case which gives rise to larger Pauli repulsions. Because of its geometry the bent case brings the second atom of NO closer to the copper ion then the linear model, and so the equilibrium Cu^{+1} - N (O) bond distance increases over the linear case.

Table two:

Results for CuO - NO model

Geometry	Bond Distances (atomic units) Cu - N -or- Cu - O	N=O	Adsorption Energies (eV)	Vibrational Frequencies (cm-1)	Vib. Freq. shifts (Relative to Calc. NO Vib. Freq.) (cm-1)
CuO - N=O	3.93	2.16	0.381	2052.0	61.1
CuO - O=N	3.96	2.18	0.421	1981.5	-9.4

The electrostatic interactions outlined above are not as obvious in the preliminary results obtained for the CuO model. (See table two.) The copper ion does not have a full positive charge like the Cu^{+1} model, but instead has a charge of about +0.58. The preferred geometry of adsorption was again found to be the copper-oxygen interaction. However, the difference between the adsorption energies of the copper-oxygen and the copper-nitrogen bonds is much less then was expected. While the charge on the copper ion was decreased by about 40%, the difference in adsorption energies decreased by almost 80%. Another indication that something else is involved is the fact that for the CuO model, the copper-nitrogen bond is actually shorter then the copper-oxygen bond. So while the previous electrostatic arguments seem to hold true for the CuO model,

there are other factors involved. An example may be the open shell on the oxygen atom of the CuO molecule which is coupled to the open shell on the nitrogen as a triplet state. More calculations needs to be done for the CuO model before any definite conclusions can be made.

Another preliminary calculation that pertains to the discussion of electrostatic interactions is the singlet state of the Cu^{+2} model. (Fig. 8) The Hartree-Fock method converges to the lowest energy possible and in this case it converged along the energy curves corresponding to two different states. It is possible to extrapolate back to obtain an understanding of what the two separate potential energy curves should look like, and these interpretations are drawn in as dotted lines.[4] Because the copper ion contains a full positive two charge and the open shell on the copper ion is overlapped with the open shell on the nitrogen atom of NO with the electrons coupled in a singlet state, the most stable products made are the Cu^{+1} ion and the NO positive ion. These two ions are repulsive to each other and therefore dissociate.

There does appear to be a meta-stable state, where the potential energy curve has a relative minimum. This state has both Cu^{+1} - NO^{+1} and Cu^{+2} - NO character to it. This meta-stable state is a result of the open shell orbitals bonding covalently, however, it is meta-stable because the stronger electrostatic interactions of the system causes the dissociation of the system into the lower energy Cu^{+1} and NO^{+1} as the distance is increased.

Several future studies of interest would be to try and determine what the separate effects of electrostatic interactions and open shell - open shell interactions have on the adsorption of NO onto a copper site. With a better understanding of the separate effects, the combined effects might be easier to interpret. Two suggested models for these studies would be Cu^{0}, which has an open shell but no charge, and Cu^{+2} with the open shell in a different plane than the open shell on the nitrogen atom. The second model suggested would better represent a Cu^{+2} ion on a surface where the open shell would probably lie in the plane of the ligands, which would present a closed shell to the NO molecule, while still retaining the +2 charge. In order for the last model to support the previously presented electrostatic theory, one would expect to find that the copper-oxygen bond would be more stable than the copper-nitrogen bond, and the copper-oxygen interaction would be stronger than it was for the Cu^{+1} or CuO models.

Referring again to table one, there is a correlation between the NO bond distances of the adsorbed species and the corresponding vibrational frequencies. Knowing that the equilibrium bond distance of free NO is 2.174 atomic units, see table two, it can be seen that the NO bond distances follow the same trends as the vibrational frequency shifts. When the NO bond gets shorter then the frequency shift is in a positive direction, indicating that there is an increase in

---

4 Note, the dashed lines are not drawn to scale. Future generalized valence bond calculations are needed to obtain the actual energy curves for the two separate states.

bonding character for the NO molecule. The opposite is true when the NO bond is longer where there is a decrease in bonding character in the NO molecule.

These interactions can be seen in the comparison of the molecular orbitals for free NO and the Cu+1 - NO and Cu+1 - ON models. (Fig. 9, 10, and 11)[5] The Cu+1 - ON molecular orbitals have a lot of copper d-orbital characteristics mixed in. Because each molecular orbital is restricted by the Pauli exclusion principle to have no more then the density of two electrons, the presence of the copper d-orbital character indicates that electron density is being drawn away from the NO orbitals. This fits with the increased NO bond distance and the vibrational frequency is shifted lower for the Cu^{+1} - ON case.

In the Cu^{+1} - NO case there is very little evidence of copper d-orbital character mixing in with the NO orbitals shown in figure 10. While this would make sense in that the NO bond is not strengthened relative to the free NO molecule, it does not account for the decrease in NO bond distance, or why the vibrational frequency shifts higher. The shorter bond distance and the higher frequencies indicate that the NO bond is being strengthened. Further examination of the molecular orbitals and their corresponding orbital energies will have to be pursued before any definite conclusions can be determined.

A plot of the total charge densities, the summation of the electron densities of all of the molecular orbitals of a system, for the NO free molecule and the two linear geometries shows the slight bonding interactions that are taking place. (Fig. 12)

The vibrational frequencies in table one were calculated by fitting the potential energy curves for the models to an anharmonic oscillator model. For a diatomic molecule, the fundamental vibrational frequency is a function in terms of the reduced mass, μ.

$$\nu = 1/(2\pi) * (k/\mu)^{1/2}$$

$$\mu = (m_1 + m_2)/(m_1 m_2)$$

For calculating the vibrational frequencies of NO and NO^{+1} the method was straight forward, however, calculating the vibrational frequencies of NO adsorbed onto Cu^{+1} requires a decision about which atoms are moving. The first time that the vibrational frequencies were calculated for

---

5 The Hartree-Fock method allows for the delocalization of orbitals having the same symmetry. Because of this, the open shell on the nitrogen and the closed shell on the oxygen in the same plane are allowed to mix and form two new orbitals that have pi-bonding and pi-antibonding character to them. Of the molecular orbitals plotted in figures 10 and 11, the π_y orbitals represent the open shell - closed shell delocalized molecular bonds. These π bonds are not true π bonds in that they retain a fair amount of their localized characteristics. Notice the higher electron density around the oxygen atom for the π_y orbital and the great electron density around the nitrogen atom for the π_y^* orbital.

the Cu^{+1} - N=O model, the N was considered to be bound to the copper ion and so only the oxygen atom was vibrated to obtain the potential energy curve for the NO bond. The vibrational frequencies were then calculated using the atomic mass of oxygen for the reduced mass term. This led to vibrational frequencies of about 1400 cm^{-1}, and vibrational shifts from the calculated free NO molecule of around 500 cm^{-1}. For weak adsorption of NO, a shift of 500 cm^{-1} is not physically reasonable. Our calculations have shown the adsorption of NO onto a copper site is a fairly minor perturbation of the NO bonding. The potential energy curve was recalculated moving both the N and O atoms and used along with the proper reduced mass of NO to recalculate the vibrational frequencies. These results gave more reasonable shifts (relative to the calculated free NO vibrational frequencies) as shown in table one.

The 500 cm^{-1} shifts obtained from the first calculations were reconsidered when it was noticed that previous experimental studies had found vibrational frequencies of a similar order (London 35). Our work offers the possible interpretation of the observed low vibrational frequency bands to be NO interacting with or replacing the oxygen ligands present on the surface of copper oxide catalysts (London 39). The two methods used for this project to calculate the vibrational frequencies lend support to this interpretation and are described below.

For the case where the adsorption of NO onto copper sites is taken to be only a minor perturbation of the NO bonding, both the nitrogen and oxygen atoms are vibrated in the presence of a fixed copper ion. A simple representation would look like the following:

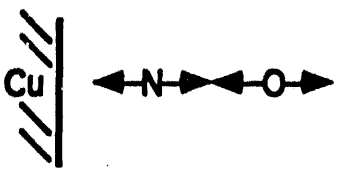

The other case considers the bond between the copper and nitrogen to be strong, as if the nitrogen was bound to the surface of the catalyst and only the oxygen is free to vibrate.

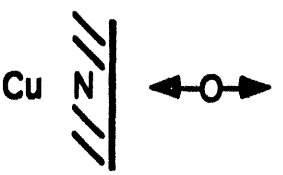

It is for this last case that the low vibrational frequencies were calculated, indicating tht the experimental frequencies could possibly be NO chemically incorporated into the surface of the matrix.

Keeping in mind that these preliminary models are just the first step in developing a good theoretical model that would agree with experimental data, it is important to compare the results of the preliminary calculations to the experimental data to obtain an understanding of the accuracy of both the models and the methods. Table two compares the theoretical and experimental results for the free NO molecule and the ionized positive ion of NO. The NO^+ represents an extreme excited state of the NO molecule. Ionizing the NO molecule acts as a major perturbation of the NO bonding character, going from a molecule with double bond character to an ion with triple bond character. Such an extreme situation was chosen for the comparison of the results of the Restricted Hartree-Fock method because in such an extreme case the errors present in the method would be obvious.

Table three:

		Theoretical Data	Experimental Data	Error
N=O (free molecule):				
Bond Distance	(a.u.)	2.175	2.17472	
Total Energy	(a.u.)	-129.1997	-	
Vibrational Frequency	(cm-1)	1990.9	1876.1	≈6%
$N=O^+$ (free molecule):				
Bond Distance	(a.u.)	1.99	2.00672	
Total Energy	(a.u.)	-128.8350	-	
Vibrational Frequency	(cm-1)	2560.5	2345	≈9%
Vibrational Frequency Shift	(cm-1)	569.6	468.9	≈20%
Ionization Potential	(eV)	9.92	9.3	

(Thulstrup)

A comparison of the bond distances between the theoretical and experimental data suggests that the restricted Hartree-Fock method is fairly accurate in determining the equilibrium bond distances. Table three also clearly shows the error involved in the calculation of the ionization potential and the discrepancies that exist between the experimental and theoretical values for the vibrational frequencies.

The sensitivity of the calculated vibrational frequency to the errors of the restricted Hartree-Fock method can best be seen in a comparison between the calculated H-F potential energy curve and the experimentally determined energy curve for free N=O (Gilmore). The following graph shows that while the equilibrium bond distances are almost the same for both curves and the error

in the H-F calculations is in the slightly different shapes of the energy wells leading to the discrepancy in the vibrational frequencies.

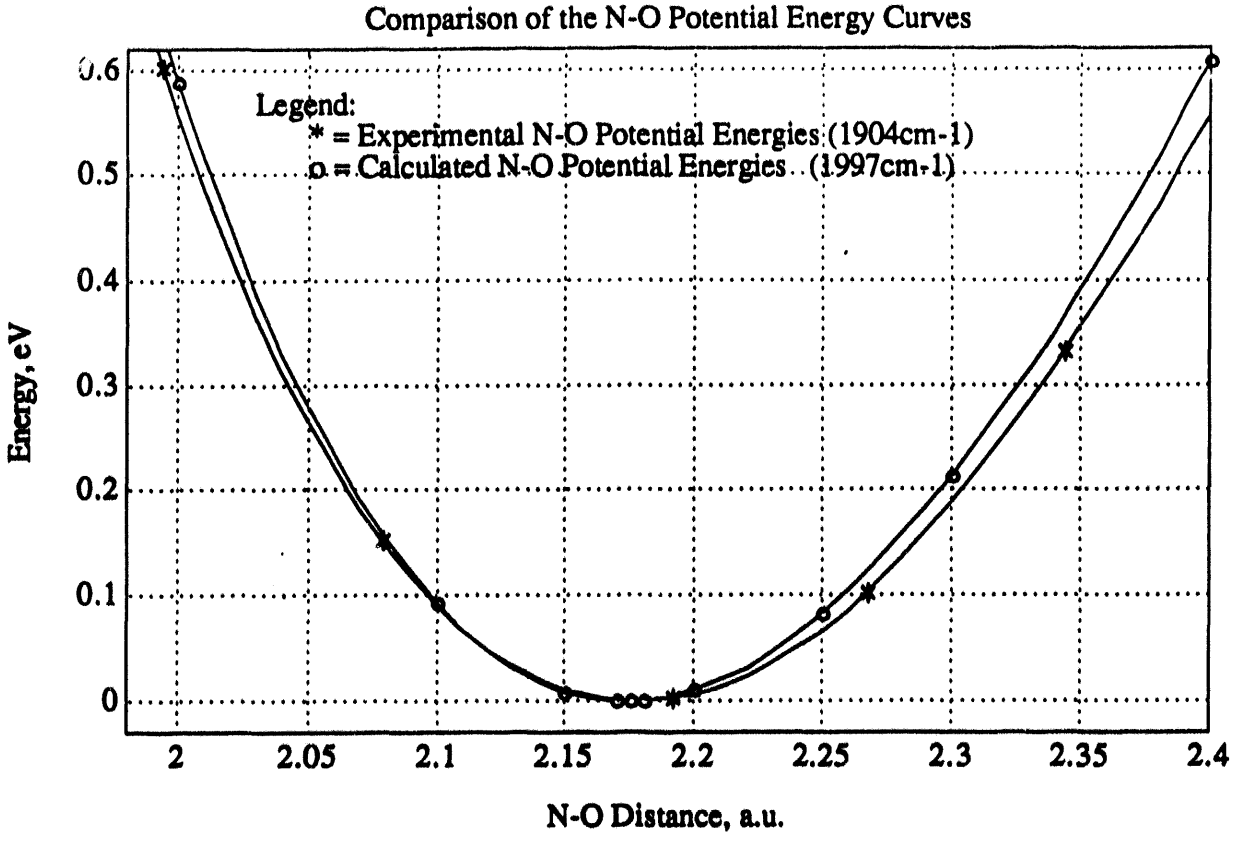

The information presented on table three also indicates that the errors of the restricted Hartree-Fock method are not constant from state to state. The Hartree-Fock method does not deal with different bonding characteristics in a consistent manner. This makes the comparison between the results for different adsorbtion states difficult.

The errors of the Restricted Hartree-Fock method are known. The errors are sensitive to the basis set chosen to represent the atomic orbitals on the atoms involved in the system. A small basis set does not allow for enough flexibility to accurately describe the molecular interactions that occur. Another known source of error lies in the fact that the restricted Hartree-Fock method does not take electron correlation into consideration.

Conclusions:

The restricted Hartree-Fock method does not offer the accuracy to meet the goals of this project. More accurate calculations of the vibrational frequencies and the corresponding shifts are needed in order to obtain a theoretical model that can reproduce experiment.

Since the errors in the restricted Hartree-Fock method are now quantified, the next step would be to correct for them by including larger basis sets and electron correlation. Preliminary calculations have been started for the free NO molecule using a larger basis set then the one used for the work presented in this paper. Empty d-orbitals have been placed on the oxygen and nitrogen atoms in the NO molecule to allow for great flexibility in describing the molecular orbital electron densities. Configuration interaction calculations are also being planned. Configuration Interaction calculations includes the electron correlation that is missing from the restricted Hartree-Fock method.

Alarge amount of data has been calculated for the Cu^{+1} model, and while correlations between the theoretical data obtained and previous experimental data cannot be conclusively drawn because of limited accuracy, this project has taken the first step towards developing a theoretical model of NO adsorbed onto a copper site on a surface. The results from the model have hinted at several possible trends, such as the dominate role of the electrostatic interaction for Cu^{+1} closed shell sites and raised other important questions that will naturally lead to further development of a final model.

Future studies will consist of completing the restricted Hartree-Fock analysis of the Cu+2 and CuO models so that all three models can be cross compared to determine information about the adsorption that takes place on different copper sites. These models can then be analyzed with the configuration interaction methods and larger basis sets.

In addition new models that incorporate a better represent the surface of a copper catalyst must be developed. Our most stable adsorption model for the interaction with Cu^{+1} has a binding energy of about 0.6eV which is too large to be an accurate model of the actual surface adsorption. This is caused by the strong electrostatic interactions of the bare Cu^{+1} ion. A more realistic model would be to place the Cu^{+1} ion in a cluster of oxygen atoms (and other metal ions) to represent the surface of a oxide aerogel catalyst. These improved surface models could then be analyzed with the same approach that was determined accurate enough for calculating vibrational frequencies but with a relatively short computational time. Finally, the model that is developed can be used to the reaction mechanism of the reduction of nitric oxide on a copper catalyst.

Bobrowicz, Frank W. and William A. Goddard III. "The Self-Consistent Field Equations for Generalized Valence Bond and Open-Shell Hartree-Fock Wave Functions." Modern Theoretical Chemistry 3: Methods of Electronic Structure Theory. Schaefer III, Henery F. ed. Plenum Press: New York, 79-127 (1977).

Fu, Yilu; Tian, Yangchao; and Lin, Peiyan. "A Low-Temperature IR Spectroscopic Study of Selective Adsorption of NO and CO on CuO/γ-Al2O3." Journal of Catalysis. **132**, 85-91 (1991).

Gilmore, Forrest R. "Potential Energy Curves for N2, NO, O2 and corresponding ions." J. Quant. Spectrosc. Radiat. Transfer. **5**, 369-390 (1965)..

London, Jack W. and Bell, Alexis T. "Infrared Spectra of Carbon Monoxide, Carbon Dioxide, Nitric Oxide, Nitrogen Dioxide, Nitrous Oxide, and Nitrogen Adsorbed on Copper Oxide." Journal of Catalysis. **31**, 32-40 (1973a).

London, Jack W. and Bell, Alexis T. "Infrared Spectra of Carbon Monoxide, Carbon Dioxide, Nitric Oxide, Nitrogen Dioxide, Nitrous Oxide, and Nitrogen Adsorbed on Copper Oxide." Journal of Catalysis. **31**, 96-109 (1973b).

McQuarrie, Donarld A. Quantum Chemistry. University Science Books: California, 1983.

Pitzer, R.M. *et al.* "Input Description for the Ohio State University Symmetry by Equal Contribution Molecular Integrals Program" and "Input Description for the Ohio State Restricted Hartree-Fock Self-Consistent-Field and Two-Configuration MCSCF Program."

Thulstrup, E.W. and Y. Oehrn. "Configuration Interaction Studies of NO and NO+ with Comparisons to Photoelectron Spectra." The journal of Chemical Physics. **57**, (9) 3716-3726 (11-1-1972).

Truex, T.J.; Searles, R.A.; and D.C. Sun. "Catalysts for Nitrogen Oxides Control under Lean Burn Conditions." Platinum Metals Rev. **36**, (1) 2-11 (1992).

The U.S. Federal Standards include a timetable for the progressive reduction of pollutant emissions in exhaust gas:

▨ hydrocarbon reduction from 0.41 g/mile in 1991, to 0.125 g/mile in 2004

▨ carbon monoxide reduction from 3.4 g/mile in 1991 to 1.7 g/mile in 2004

▨ nitrogen oxides reduction from 1.0 g/mile in 1991 to 0.2 g/mile in 2004

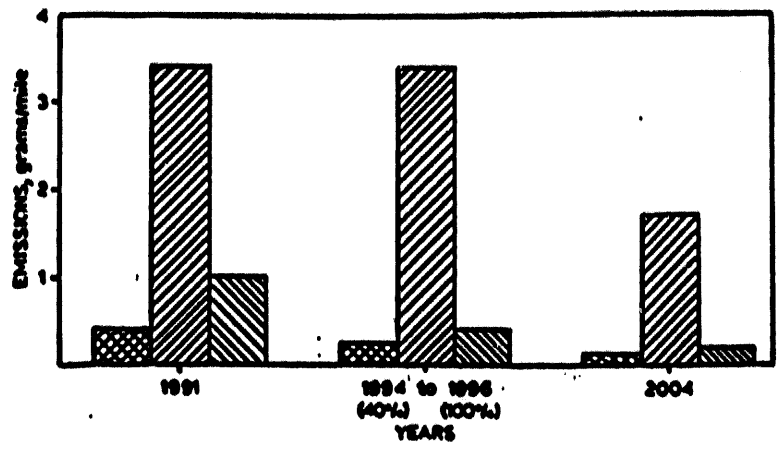

Fig. 1

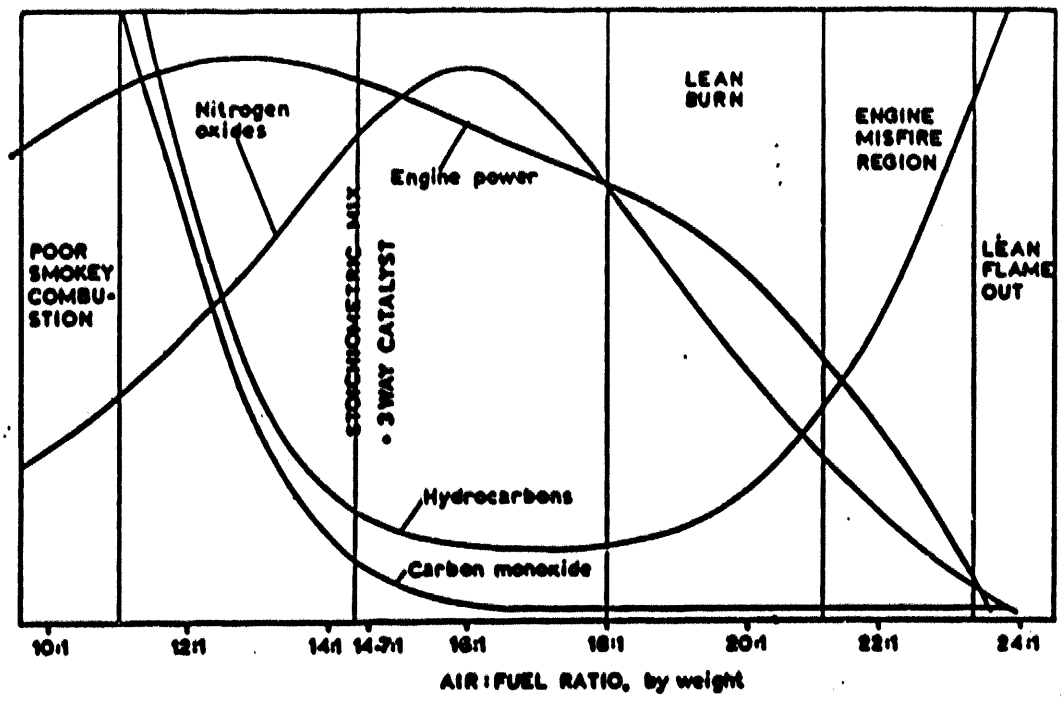

Fig. 2 These four curves indicate trends which apply to all petrol engines. Under lean burn operation fuel is burnt with an excess of air at ratios of up to 24 parts of air to 1 part of fuel, and it can be seen that nitrogen oxides and carbon oxides emissions are at a minimum, but that hydrocarbon emissions can rise at the start of unstable combustion. When there is excess fuel, the engine power is high but high levels of hydrocarbons and carbon monoxide are emitted. Peak combustion temperatures occur just on the lean side of the stoichiometric composition and result in the highest emissions of nitrogen oxides

Fig. 2

Synthesis, Characterization, and Modeling Work Together in the Development of Aerogel Catalysts

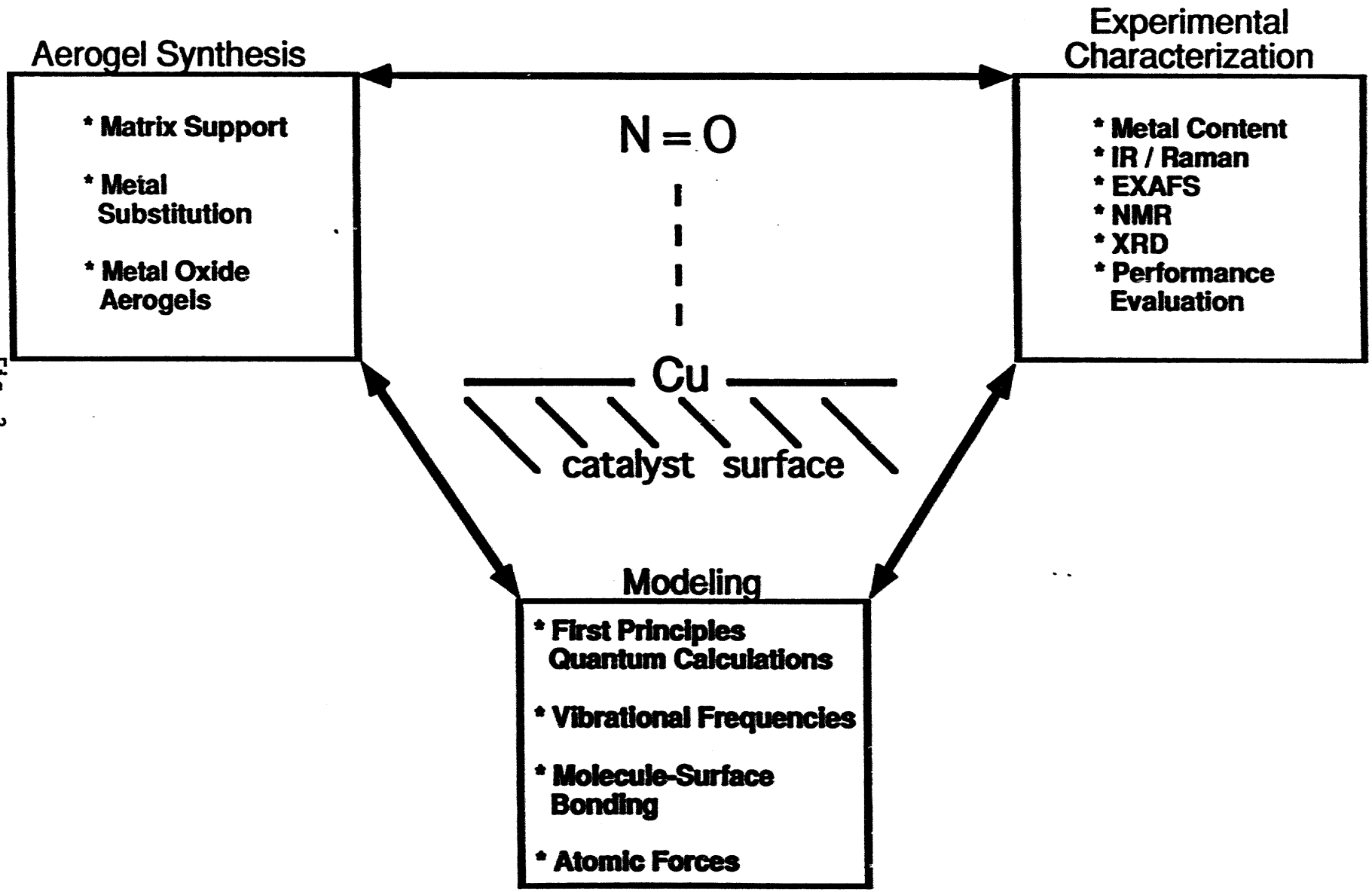

Fig. 3

Basis set used:

Cu [14s11p6d/10s9p3d]

s type gaussians on Cu		p type gaussians on Cu		d type gaussians on Cu	
coefficient	exponent	coefficient	exponent	coefficient	exponent
contracted [5s/1s]:		contracted [3p/1p]:		contracted [4d/1d]:	
337200.0	0.00028	2245.29	0.00226	53.65	0.03311
50072.9	0.00217	532.106	0.01841	15.07	0.17945
11373.4	0.01122	172.195	0.08646	5.104	0.44509
3239.82	0.04462			1.727	0.56330
1071.97	0.13836				
uncontracted:		uncontracted:		uncontracted:	
395.099	1.0	65.3239	1.0	0.5283	1.0
158.399	1.0	27.0551	1.0	0.1491	1.0
67.3591	1.0	11.7435	1.0		
22.2963	1.0	4.69382	1.0		
9.39357	1.0	1.90667	1.0		
2.57848	1.0	0.711445	1.0		
0.964080	1.0	0.155065	1.0		
0.113303	1.0	0.046199	1.0		
0.040791	1.0				

N [9s5p/4s3p]				O [9s5p/4s3p]			
s type gaussians on N		p type gaussians on N		s type gaussians on O		p type gaussians on O	
coefficient	exponent	coefficient	exponent	coefficient	exponent	coefficient	exponent
contracted [6s/1s]:		contracted [6s/1s]:		contracted [6s/1s]:		contracted [6s/1s]:	
5909.44	0.002004	26.786	0.038244	7816.54	.002031	35.1832	0.040023
887.451	0.015310	5.9564	0.243846	1175.82	.015436	7.9040	0.253849
204.749	0.074293	1.7074	0.817193	273.188	.073771	2.3051	0.80642
59.8376	0.253364			81.1696	.247606		
19.9981	0.600576			27.1836	.611832		
2.6860	0.245111			3.4136	.241205		
uncontracted:		uncontracted:		uncontracted:		uncontracted:	
7.1927	1.0	0.5314	1.0	9.5322	1.0	0.7171	1.0
0.7000	1.0	0.1654	1.0	0.9398	1.0	0.2137	1.0

Fig. 4. The Gaussian basis sets used on N, O, and Cu in the Hartree-Fock calculations of free and adsorbed nitric oxide.

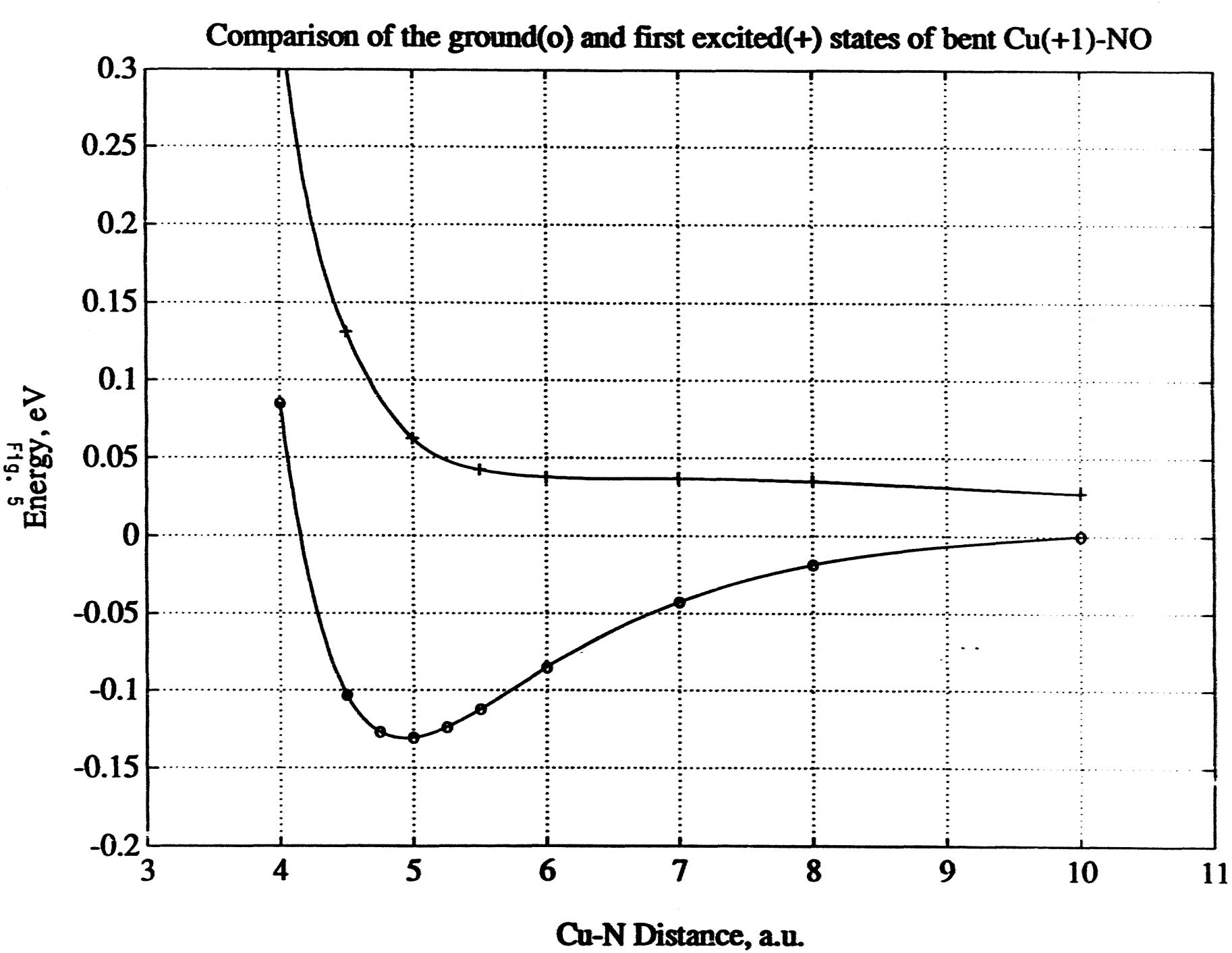
Comparison of the ground(o) and first excited(+) states of bent Cu(+1)-NO
Energy, eV
Fig. 5
Cu-N Distance, a.u.
0.3
0.25
0.2
0.15
0.1
0.05
0
-0.05
-0.1
-0.15
-0.2
3
4
5
6
7
8
9
10
11

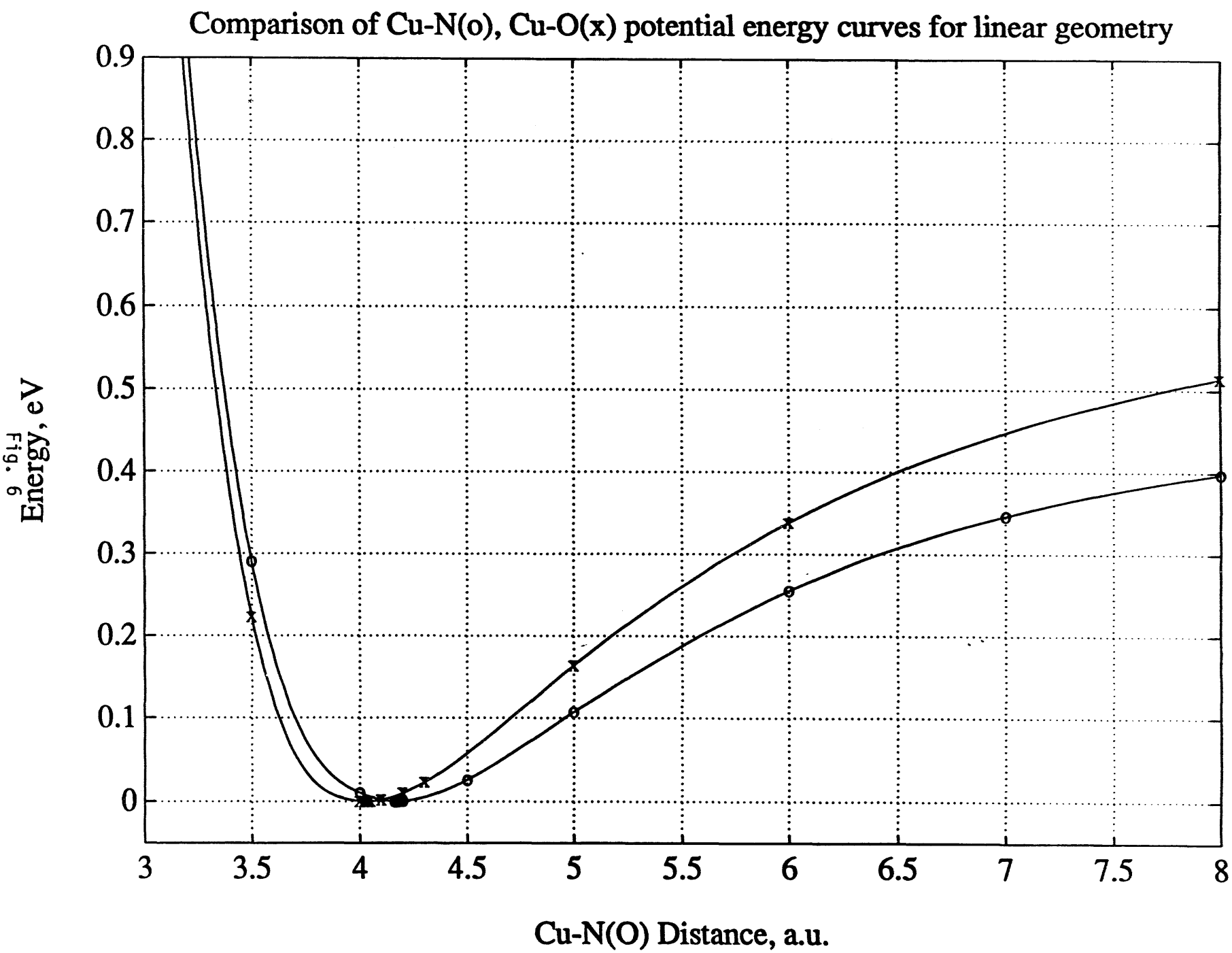
Comparison of Cu-N(o), Cu-O(x) potential energy curves for linear geometry
Energy, eV
Fig. 6
0.9
0.8
0.7
0.6
0.5
0.4
0.3
0.2
0.1
0
3
3.5
4
4.5
5
5.5
6
6.5
7
7.5
8
Cu-N(O) Distance, a.u.

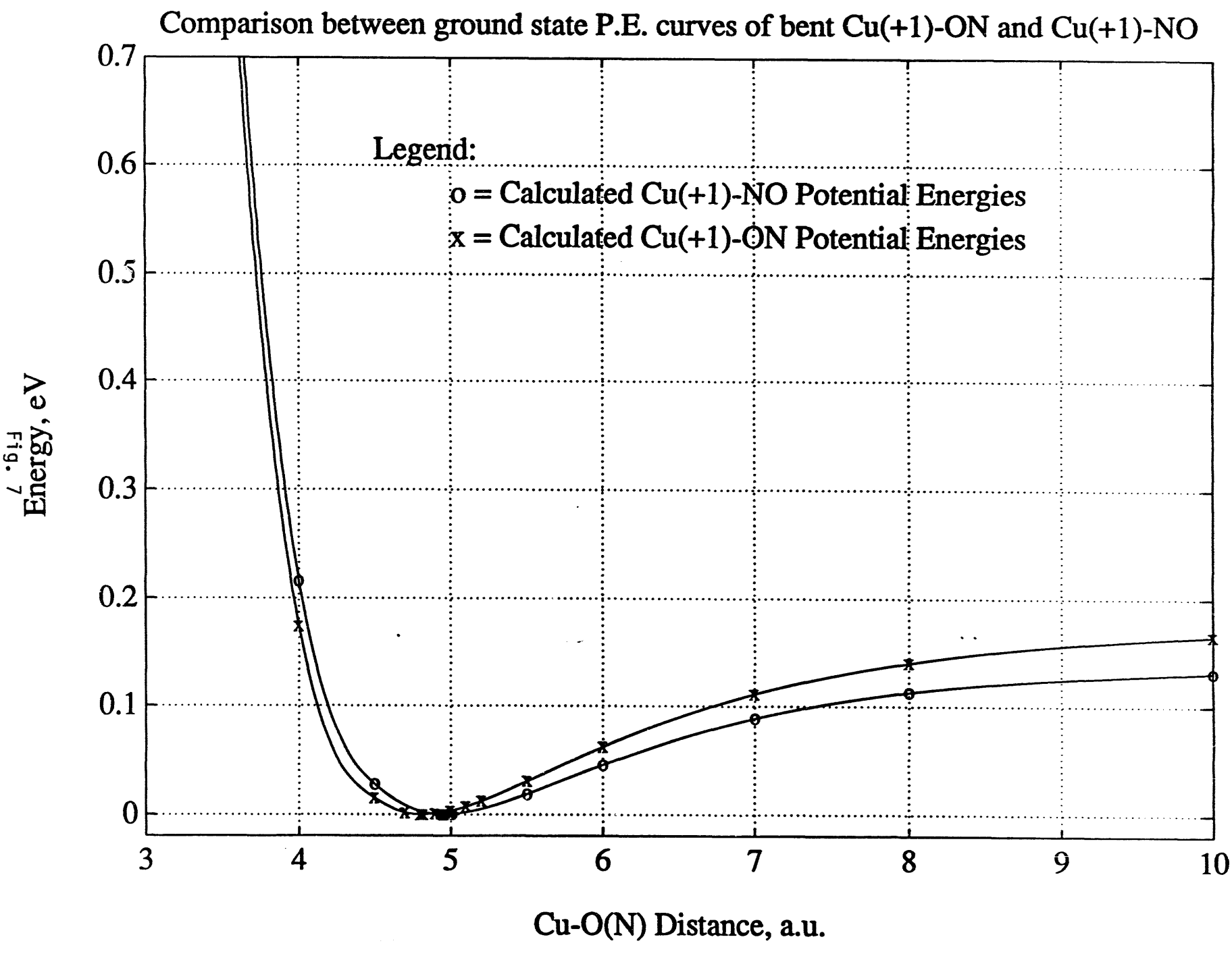
Comparison between ground state P.E. curves of bent Cu(+1)-ON and Cu(+1)-NO
Legend:
o = Calculated Cu(+1)-NO Potential Energies
x = Calculated Cu(+1)-ON Potential Energies
Energy, eV
Cu-O(N) Distance, a.u.
0.7
0.6
0.5
0.4
0.3
0.2
0.1
0
3
4
5
6
7
8
9
10

Fig. 7

Fig. 8

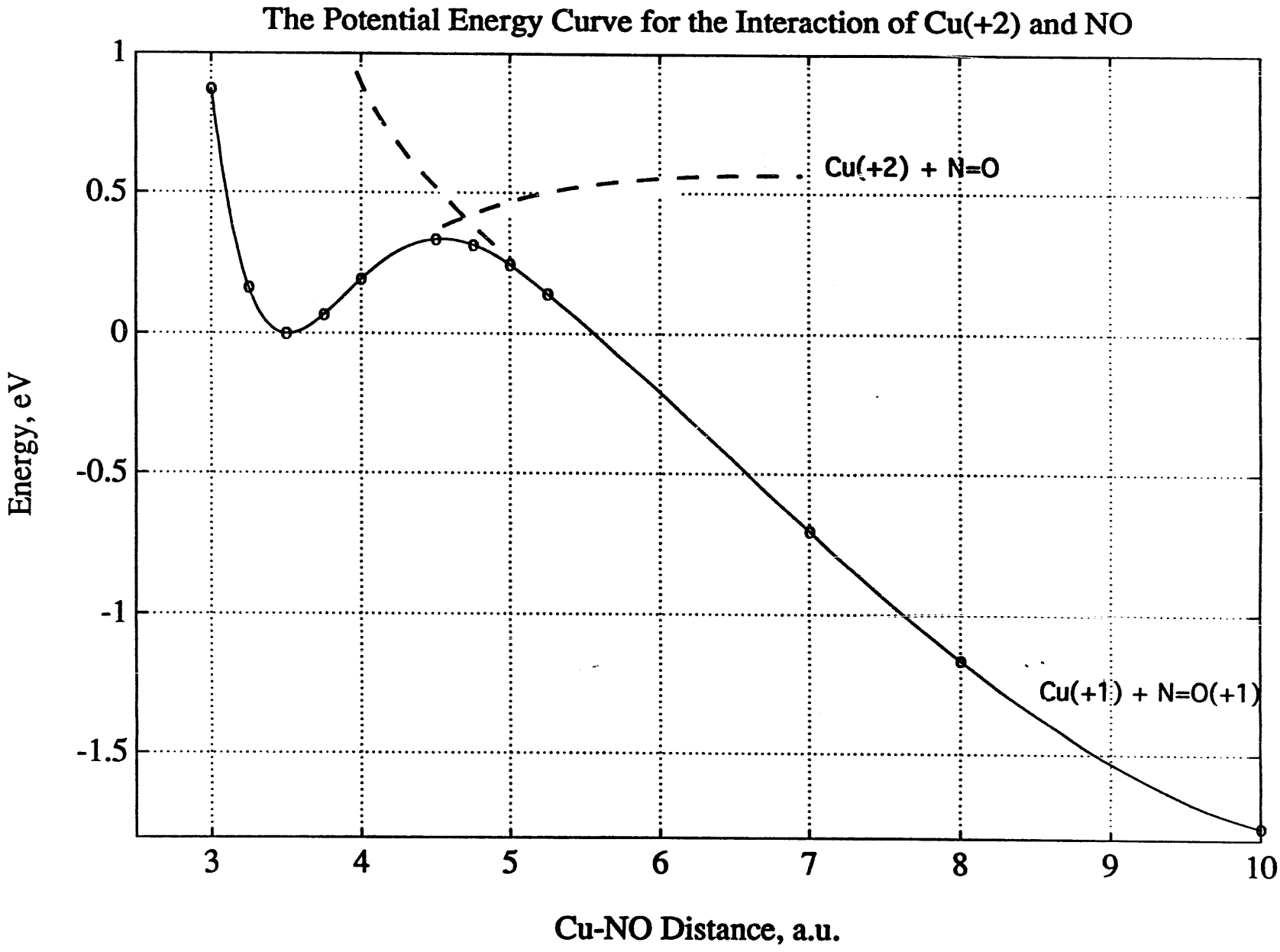
The Potential Energy Curve for the Interaction of Cu(+2) and NO
Energy, eV
1
0.5
0
-0.5
-1
-1.5
3
4
5
6
7
8
9
10
Cu-NO Distance, a.u.
Cu(+2) + N=O
Cu(+1) + N=O(+1)

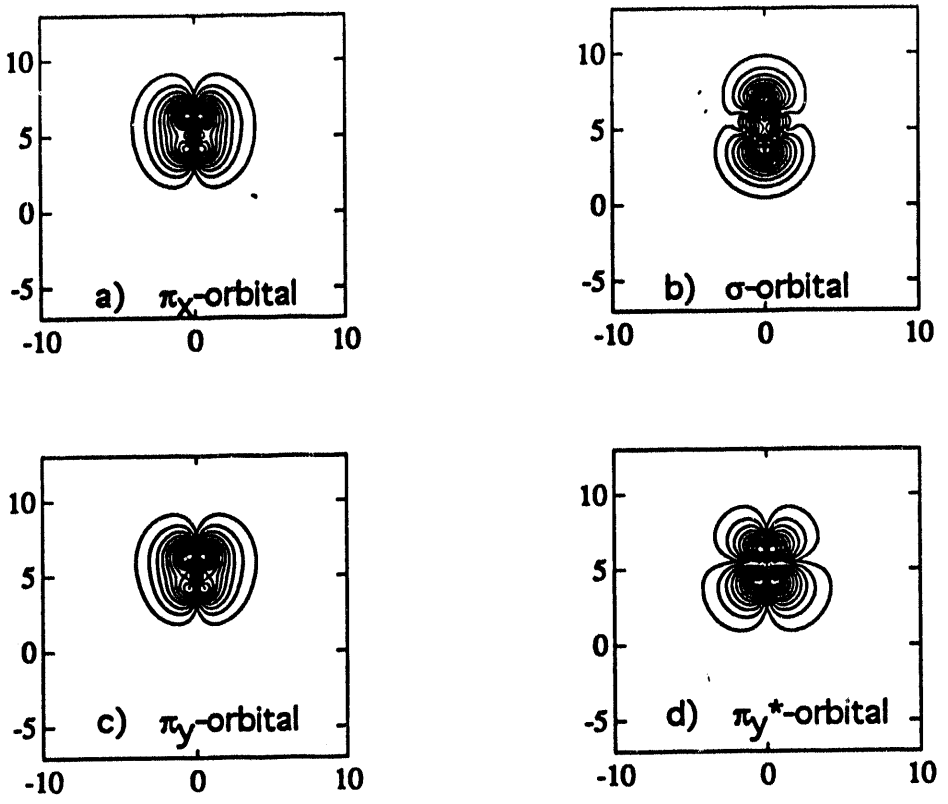

Fig. 9. Contour plots of the electron density for the valence Hartree-Fock orbitals of free nitric oxide.

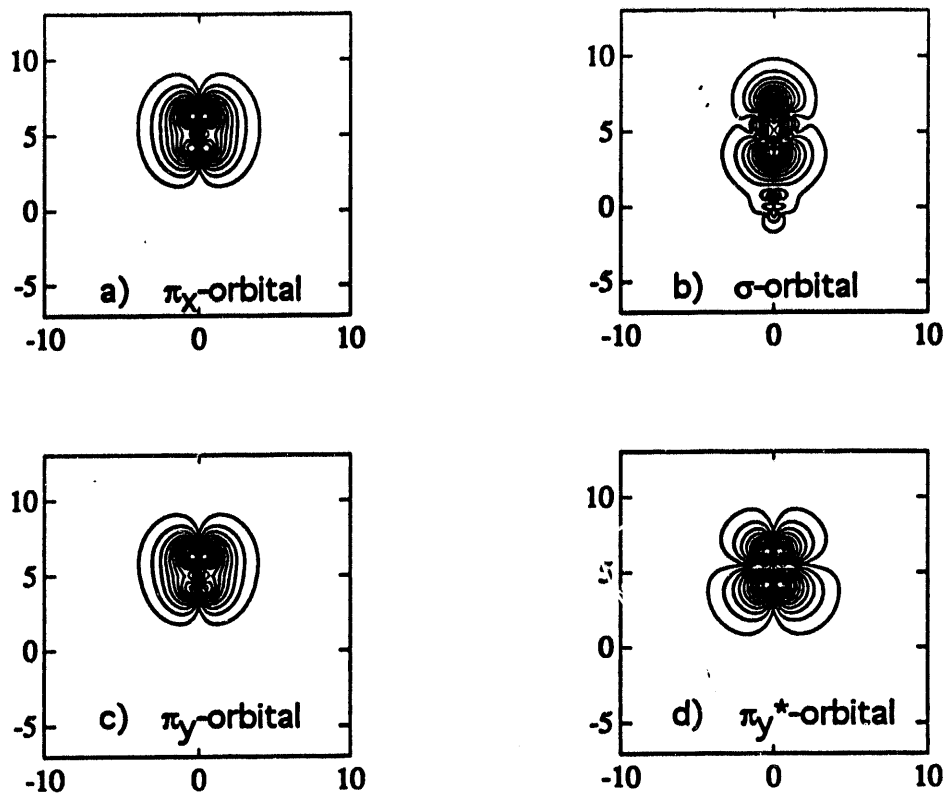

Fig. 10. Contour plots of the electron density for the valence Hartree-Fock orbitals of nitric oxide adsorbed on Cu^+ in the linear Cu-N-O configuration.

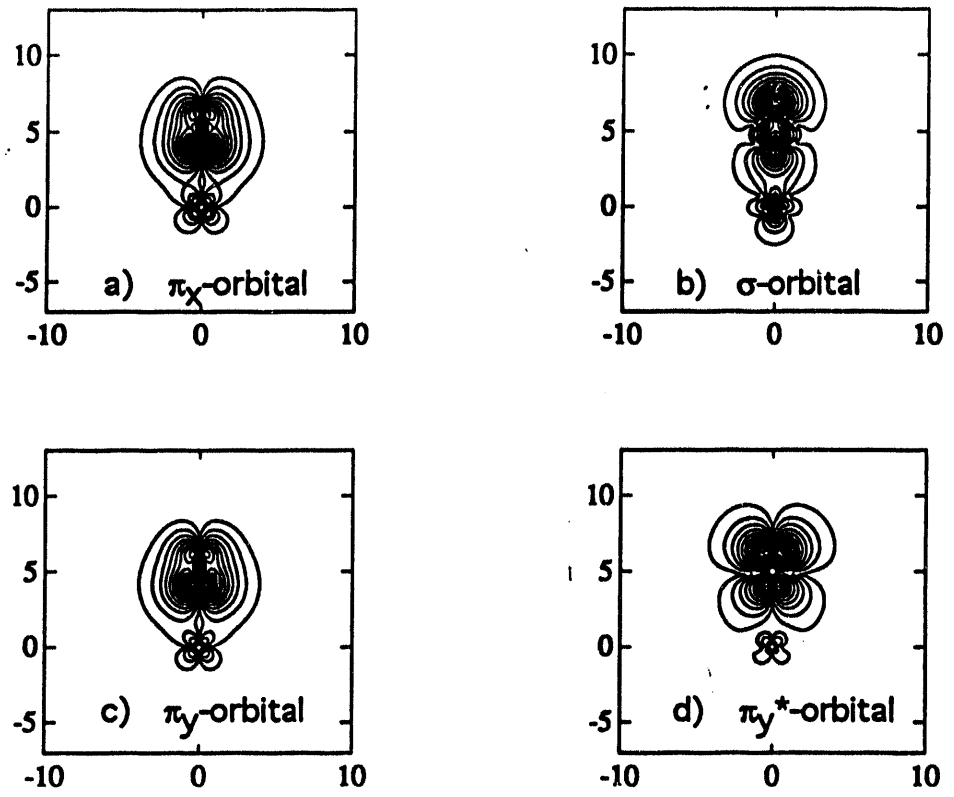

Fig. 11. Contour plots of the electron density for the valence Hartree-Fock orbitals of nitric oxide adsorbed on Cu^+ in the linear Cu-O-N configuration.

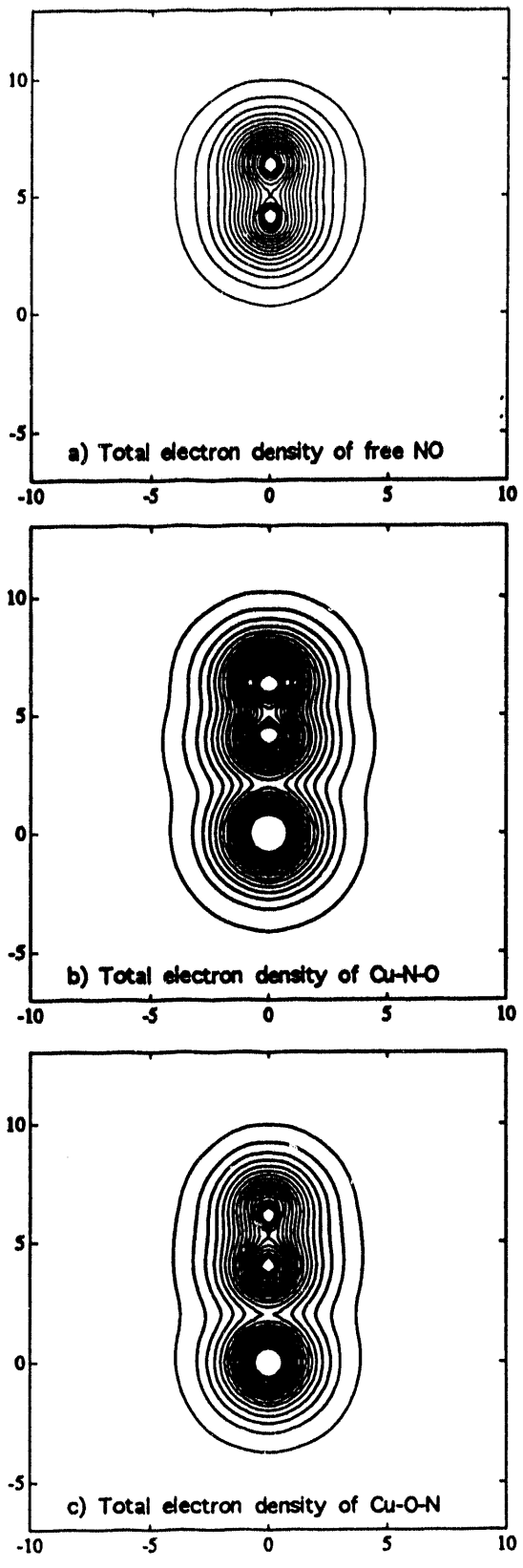

Fig. 12. Comparison of the total electron density for free nitric oxide to NO adsorbed on Cu+ in the Cu-N-O and Cu-O-N linear configurations.

Fabrication of Silicon Membranes Using Electrochemical Etching

Michael A. Stolze
Washington University In St. Louis
Engineering Research

ABSTRACT

An electrochemical etch-stop was evaluated as a technique for producing silicon membranes for use in micromechanical pumps and valves. To begin the process, n-type layers were formed on the back of p-type silicon wafers, creating a diode. The wafers were then etched in hot potassium hydroxide under a reverse-biased voltage. The etching continued until current began to flow through the diode. At this point, an oxide layer formed, halting the etch and reducing the current flow. It was expected that this etch-stop would not take place until the etch reached the p-n junction, but measurements showed that the samples were passivating before this. The premature passivation was expained by experiments showing that current was leaking through the reverse-biased diode.

Fabrication of Silicon Membranes Using Electrochemical Etching

Michael A. Stolze
Wahington University In St. Louis
Engineering Research

December 18, 1992

ABSTRACT

An electrochemical etch-stop was evaluated as a technique for producing silicon membranes for use in micromechanical pumps and valves. To begin the process, n-type layers were formed on the back of p-type silicon wafers, creating a diode. The wafers were then etched in hot potassium hydroxide under a reverse-biased voltage. The etching continued until current began to flow through the diode. At this point, an oxide layer formed, halting the etch and reducing the current flow. It was expected that this etch-stop would not take place until the etch reached the p-n junction, but measurements showed that the samples were passivating before this. The premature passivation was expained by experiments showing that current was leaking through the reverse-biased diode.

I. Introduction

Silicon membranes have sparked a great deal of interest in recent years. Many useful devices have been developed using thin, flexible membranes as sensors or actuators. These include miniaturized pumps and valves [1], and pressure sensors [2]. Precise dimensional control is required to reduce the size of these devices and to improve their quality. The p-n junction etch-stop is an electrochemical technique that has been widely used to produce membranes with precise thicknesses.

It has been known since 1970 that the etching of silicon in potassium hydroxide (KOH) can be halted if a sufficiently positive voltage, called the passivation potential, is applied to the silicon. To control the depth where the passivation potential occurs, a reverse biased p-n junction is used. In a reverse-biased p-n junction, almost no current flows and the voltage change occurs in the space charge region near the junction (fig. 1). During etching, the wafer is placed within a fixture that protects the contact on the back of the wafer and allows this to be connected to a potentiostat (fig. 2). The p-type

material will etch in KOH, giving off hydrogen gas, until the etching reaches the junction. At this point the diode is destroyed and current is able to flow. Since the n-type material is at the passivation potential, etching (and the hydrogen bubbles) will stop. The mechanism that causes this is not completely understood, but it involves the formation of an oxide layer by an oxidation-reduction reaction [3]. The oxide insulates the etching site and halts the current flow. The changes in current provide an indication of both the start and the finish of the etch-stop. In short, the etch removes the p-type silicon, leaving behind an n-type membrane.

In this paper I will discuss our efforts to produce membranes using an electrochemical etch-stop. The report will include sample fabrication methods, electrochemical etching techniques, and the results we observed. The difficulties we encountered will be given particular attention along with some possible remedies.

II. Experimental

All samples were fabricated from two inch p-type wafers. The wafers were polished on both sides and had a nominal thickness of 220 12 microns. They were coated with a 0.5 micron thick thermal oxide, then a 0.1 micron nitride film. Etching windows were opened in the nitride with a carbon hexafluoride plasma etch, then in the oxide with buffered hydrofluoric acid to remove the oxide film. We etched the samples for three hours in 44% KOH at 75 C to save time during the electrochemical etch. Doping windows were opened on the other side of the wafer using the same techniques, but without the KOH etch. These windows were aligned with the etch windows, but were slightly larger.

Simulations using the Supreme 3 computer program determined the doping recipe for a junction depth of three microns (fig. 3). The wafers were n-doped in a phosphorus oxychloride ($POCl_3$) furnace for 30 minutes at 925 C. The wafers were then placed in a drive-in furnace at 1050 C for ten hours and 45 minutes. The first hour of the drive-in was under a dry oxygen atmosphere. This formed an oxide cap to prevent the phosphorus from diffusing out through the surface. The rest of the drive-in was under dry nitrogen. According to the simulation, the concentration of phosphorus reached a maximum value of approximately 10^{19} atoms/cm^3 at the surface of the wafer. The sheet resistance varied between 3.8 and 9.5 ohms/square depending on the placement of the wafers in the doping furnace. This concentration of phosphorus atoms is low enough to avoid introducing large amounts of stress into the membranes[4]. The wafers were then given an RCA clean to remove the oxide, and an aluminum/1% silicon alloy was sputtered on to make an ohmic contact.

All samples were held within a stainless steel/polypropylene fixture during etching. This fixture used viton o-rings to seal the back side of the wafer from the solution. An aluminum plate connected the contact on the back of the wafer to the potentiostat. This contact was insulated from the solution. For some experiments, single chips were etched. To make this possible, a stainless steel disk with a small hole was used to reduce the size of the fixture's opening.

A two electrode configuration could possibly be used to bias the sample for chemical etching, but this does not allow control of the solution voltage. A three-electrode configuration (fig. 4), adds a

saturated calomel electrode (SCE) as a reference. The potentiostat is then able to maintain a constant, reproducible solution voltage. To do this, the potentiostat compares the voltage between the working electrode (the silicon wafer) and the reference electrode to a user-defined voltage. The current through the counter elctrode is then adjusted to nullify any voltage difference. No current flows through the reference electrode , so the interface between the reference and the solution remains constant. The counter electrode is actually grounded, but all potentials are measured with respect to the SCE reference[5].

Several types of electrical and electrochemical measurements were made. I mounted the samples in the fixture and etched in 44% KOH at 75 C to remove the native oxide as well as a doped surface layer from when the diode was formed. Some samples were removed from the KOH to make a "dry test" before continuing the etch. Contact was made at the etch surface using indium gallium eutectic and a sharp metal probe. Contact at the doped surface was made within the etching fixture, the same way as during the etch. I then used the potentiostat to scan across a voltage range and an x-y recorder to measure the I-V curve for the diode (fig. 5). This gave the electrical characteristics of the diode.

To determine the electrochemical characteristics of the sample, I replaced the fixture in the KOH. After the etching began, the potentiostat scanned through a set voltage range at a rate of one or two millivolts per second. The x-y recorder plotted the I-V curve (fig. 6). All voltages were measured with respect to the SCE reference electrode. From this experiment, the passivation potential

of a particular sample could be found. Changes in current , as well as the lack of hydrogen bubbles, indicated when the etch-stop had occurred.

The potentiostat was then disconnected until the sample began to etch. A voltage was applied that was 0.1 to 0.5 volts lower than the passivation potential found using the polarization curve. A strip-chart recorder was used to measure current vs. time. I hoped that the sample would contine to etch and not passivate until the etch approached the junction.

III. Results and Discussion

A major difficulty we encountered was wafer breakage of the wafers during the etch. Pressure from the fixture often caused the wafers to break during the etch if the fixture was clamped too tightly. To test the fixture, a low-pressure air hose was attached to the fixture and the fixture was immersed in water. I then loosened the screws until bubbles began to leak from the fixture. This showed that while the screws did not have to be extremely tight, they did have to be tightened evenly.

The earliest samples were adapted from a mask made for a micropump which included pass through holes. These holes were insulated from the ohmic contact and were etched chemically. Because of this and the fact that some wafers were thinner near one edge, these holes tended to etch through before the etch-stop occurred. KOH entered the fixture through these holes and dissolved the aluminum contact, terminating the experiment

The next set used a different pattern, but this pattern included scribe lines. The lines were narrow enough to terminate before

etching through, but etch-through still occurred where two lines instersected. Hardman #501 extra-fast setting epoxy was used to cover these intesections. It was effective in stopping the etch, but the wafers still broke at the scribe lines.

Another source of leakage was failure of the o-rings. Some viton o-rings decayed so much that the solution took on a yellowish tint from dissolved viton. Other viton o-rings, from a different supplier, held up well. The small silicon o-rings that were used to etch single chips held up extremely well.

To save time we decided to modify our fixture to etch single chips instead of whole wafers. This involved making a steel disk with at small hole in the middle. The chip could be placed in the fixture with this disk on top. KOH entered the hole to etch the chip, but a silicone o-ring kept the KOH out of the rest of the fixture. During most of the early runs with this set-up, the chips would not etch except when a negative voltage was applied. Silicon samples placed in the same solution etched as expected. An electrochemical coupling between the sample and the steel plate was suggested [6]. I placed small pieces of silicon coated with oxide and nitride around the edges of the plate. This insulated the plate from the sample and allowed etching to proceed normally. I also observed this phenomenon when small amounts of KOH seeped into the fixture.

After these problems had been solved, I was able to etch samples to completion. The etch depth was measured using a microscope with differential focus. A high-powered objective lens was focused on the surface of the wafer, then at the bottom of the etch. The microscope was calibrated to measure the distance the

stage moved during this focusing. The thickness of the sample was measured the same way, with the difference between the two measurements giving the membrane thickness. The samples I made had thicknesses between 20 and 30 microns. While the thinnest ones were translucent, this was still much thicker than the three microns we had hoped for. From this I concluded that the diode were leaking current. since even a high resistance leak can cause the membranes to passivate prematurely [7]. The leakage current had been measured during a dry test at 0.09 mA/mm^2.

Kloeck *et al.* suggest a method for successfully etching leaky diodes. In their article they discuss a four-electrode configuration similar to the three-electrode configuration , but with a separate voltage applied to the p-type material. This allows control of the potential at the etch surface even with leakage currents of up to ten milliamps. The disadvantage of this is that it makes the sample fabrication more complicated.

The diode leakage current could also be reduced by using improved fabrication techniques. A getter could be used to remove impurities from the junction. A guard ring could be formed to prevent current from leaking at the edges of the diode. Better diodes would eliminate the need fro a four terminal configuration and improve the yield from an electrochemical etch-stop.

IV. Conclusion

An electrocemical process for producing thin membranes in silicon was evaluated. We constructed fixtures for the single-sided etching of two-inch wafers and chips. Technical problems, including wafer breakage, o-ring failure, unwanted electrochemical effects,

and diode leakage current were identified. We found and tested remedies for all of these except diode leakage current.

We verified that the p-n junction etch-stop behaved as reported in the literature. Polarization curves were recorded which agreed with previously published results. Current through the diode during passivation was measured and this was found to be a reliable indicator of when the etch-stop occurred.

While we were able to electrically control the etch, stopping and starting the reaction by adjusting the applied voltage, we did not achieve the thickness control we wanted. We have solved most of the technical problems, with the exception of the diode leakage current. Once this is remedied, the electrochemical etch-stop will be a useful and versatile technique for producing membranes and other structures.

V. Acknowledgments

Throughout this project, Jim Folta has been my mentor and guide. Edmund Hee was an invaluable teacher and assistant during the fabrication of my samples, not to mention providing me with tea and fig newtons. Bill Goward, Bill Guthreau, and Doug Elsea provided technical help at crucial points in this research.

VI. References

1) J. A. Folta, N. F. Raley, and E. W. Hee, "Design, Fabrication, and Testing of a Miniature Pump,"1992

2)B. Kloeck, S.D. Collins, N.F. De Rooij, and R.L. Smith, "An Electrochemical Etch-stop for Precision Thickness Control of Silicon

Membranes," IEEE Transactions on Electron Devices, Vol. 36, No. 4, 1989.

3)O. J. Glembocki, R.E. Stahlbush, and M. Tomkiewicz,"Bias-dependent Etching of Silicon in Aqueous KOH," J. Electrochem. Soc.:Solid State Science and Technology, Vol.132, No. 1, 1985.

4)W.R. Bunyan and K.E. Bean, Semiconductor Integrated Circuit Processing Technology, p. 444, Addison Wesley Publishing Co., 1990.

5)B. Kloeck *et al.*

6)Jim Folta, Personal Communication, 1992

7) B Kloeck *et al.*

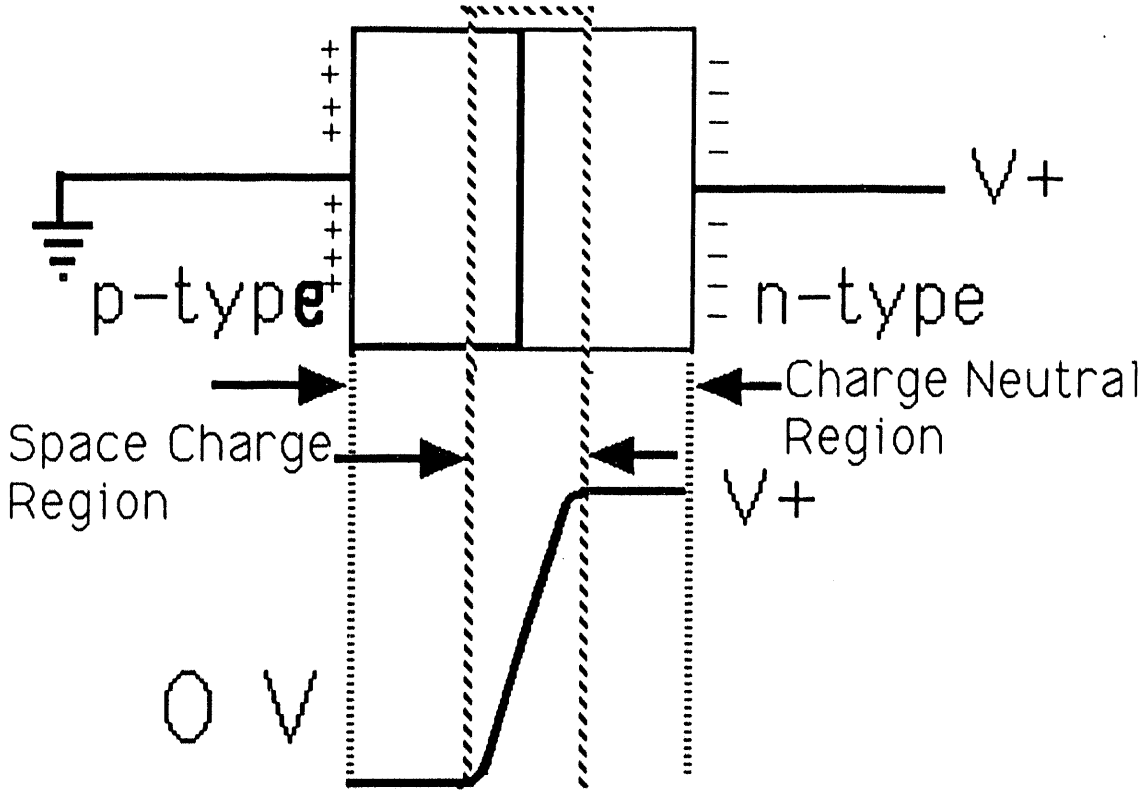

Figure 1. Voltage throughout a reverse-biased p-n junction.

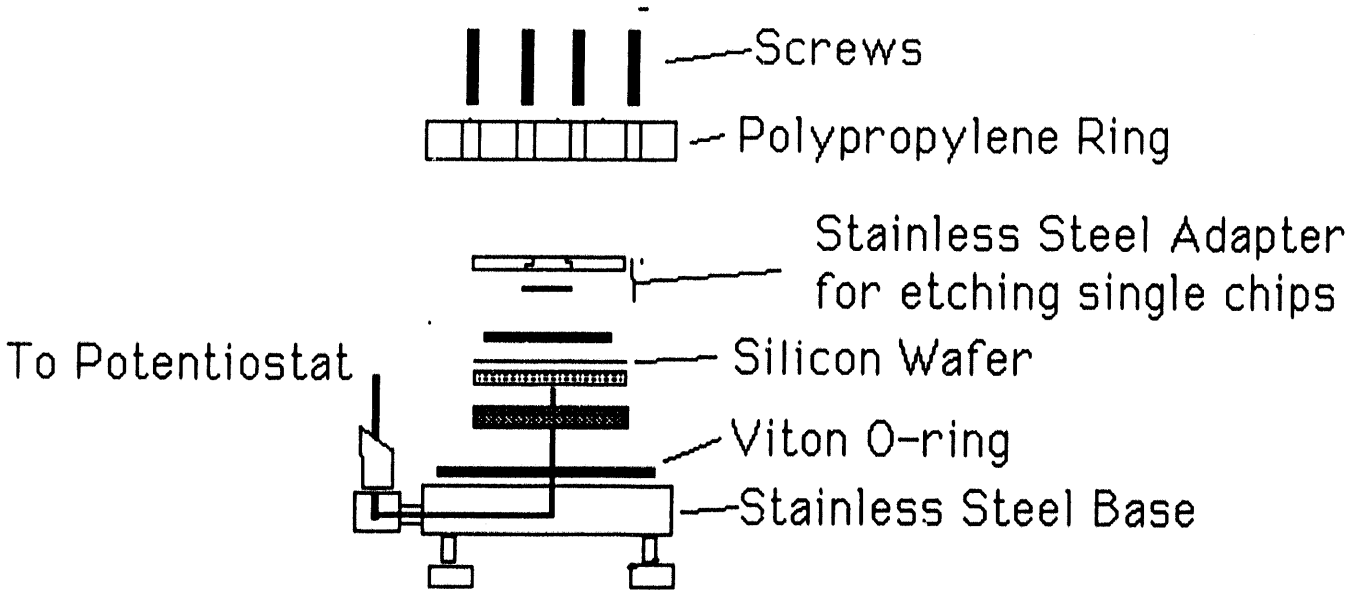

Fig 2. The fixture protects the back of the wafer during etching and allows connection to a potentiostat.

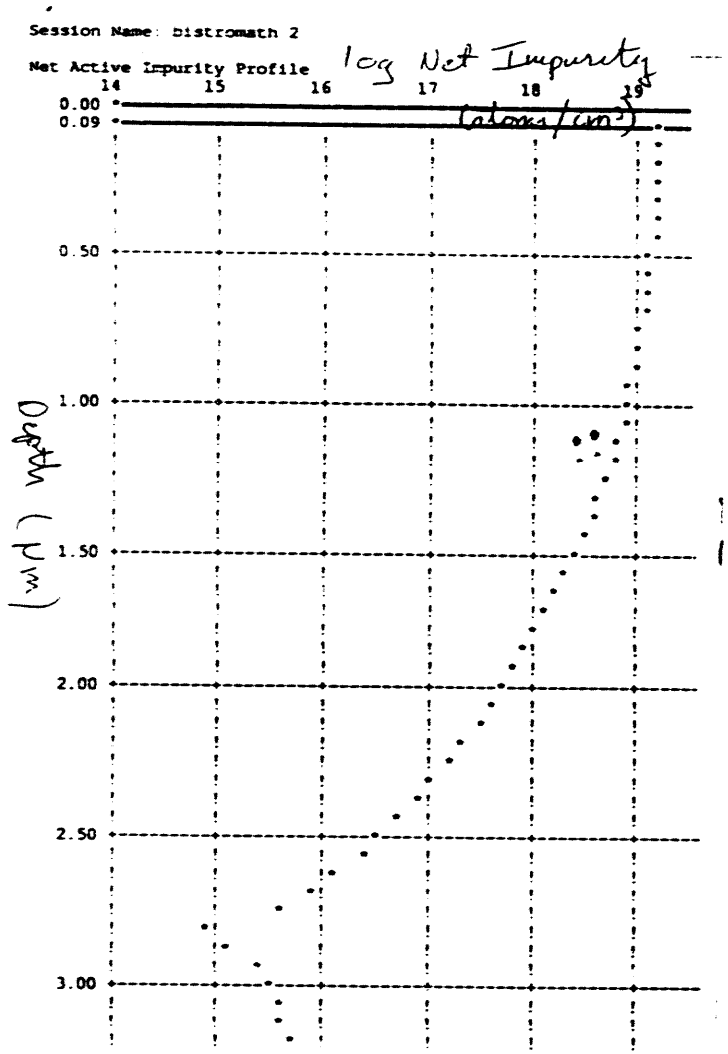

Session Name: bistromath 2

Fri Oct 2 15:11:22 1992

Commands input from file: esd1002

```
 1... Title Membrane for peristaltic pump
 2... $ Electrochem. Etch-stop
 3... $ Phosphorus CVD modeling
 4... Initialize <100> Silicon Boron Concentration=5E15
  ... + thickness=3.5 dx=0.023
 5... Comment Diffuse phosphorus using POCl3 CVD
 6... Diffusion Temperature=925 Time=30 phosphorus
  ... + SolidSolubility
 7... Diffusion Temperature=1050 Time=60 DryO2
 8... Diffusion Temperature=1050 Time=185
 9... Savefile Name=esd1002.struc structur
10... Print All Layers
11... Plot Active Net lp.plot
12... Stop
```

Membrane for peristaltic pump
Electrochem. Etch-stop
Phosphorus CVD modeling

phosphorus using POCl3 CVD

layer no.	material type	thickness (microns)	dx (microns)	dxmin	top node	bottom node	orientation or grain size
2	OXIDE	0.0893	0.0100	0.0010	346	348	
1	SILICON	3.4607	0.0230	0.0010	349	500	<100>

Integrated Dopant

layer no.	Net active	Net chemical	Total active	Total chemical
2	0.0000e+00	6.0965e+12	0.0000e+00	6.2406e+12
1	1.5768e+15	1.5807e+15	1.5801e+15	1.5839e+15
sum	1.5768e+15	1.5868e+15	1.5801e+15	1.5902e+15

Integrated Dopant

layer no.	BORON active	BORON chemical	PHOSPHORUS active	PHOSPHORUS chemical
2	0.0000e+00	7.2039e+10	0.0000e+00	6.1686e+12
1	1.6333e+12	1.6333e+12	1.5785e+15	1.5823e+15
sum	1.6333e+12	1.7053e+12	1.5785e+15	1.5885e+15

Junction Depths and Integrated Dopant Concentrations for Each Diffused Region

layer no.	region no.	type	junction depth (microns)	net active Qd	total chemical Qd
2	1	n	0.0000	0.0000e+00	6.2406e+12
1	2	n	0.0000	1.5771e+15	1.5835e+15
1	1	p	2.7929	2.6790e+11	3.9956e+11

Fig. 3 - Supreme 3 was used to simulate the wafer processing

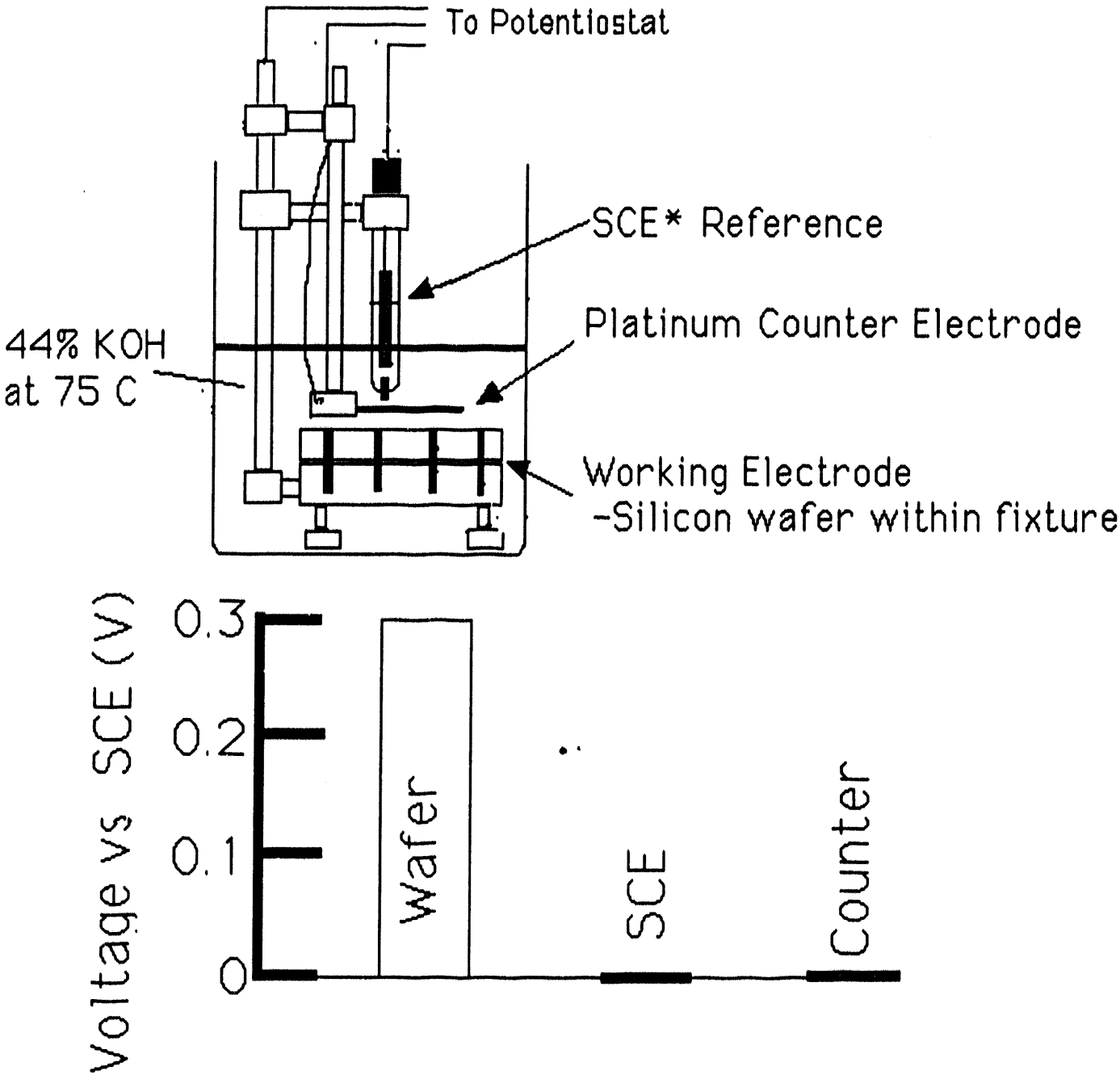

Fig. 4. A three electrode configuration was used to control solution potential during electrochemical etching.

Fig. 5

Diode test done after etching using GaIn eutectic. Leakage current was 0.09 $\frac{mA}{mm^2}$ at 1V.

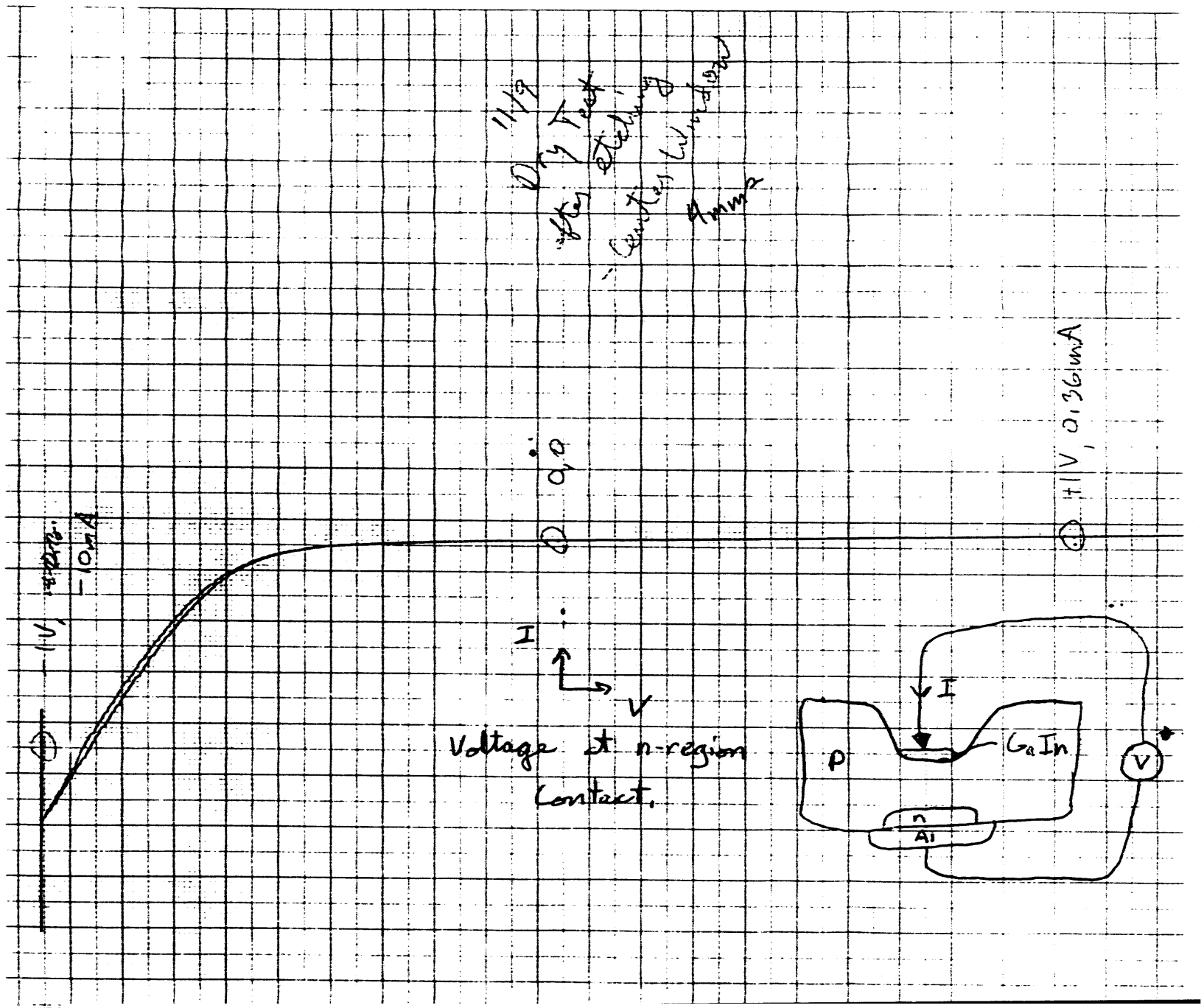

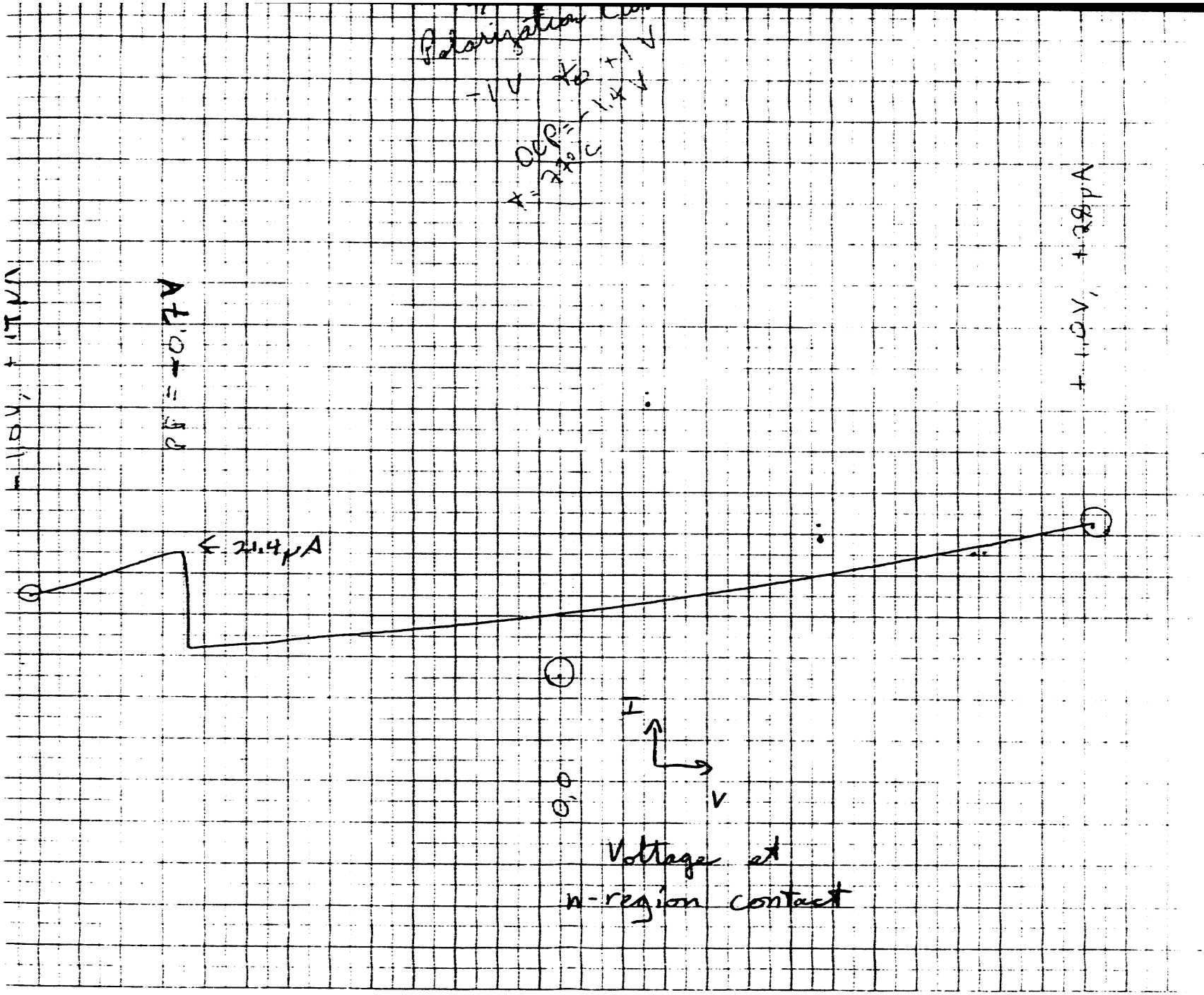

Fig. 6
Polarization curve made during electrochemical etching. The voltage was scanned from -1 to +1 V at 1-2 mV/sec. Passivation occured at -0.7 with a peak current of 21.4μA

END

DATE
FILMED
12/15/93